Methods in Molecular Biology 2275

Springer Protocols

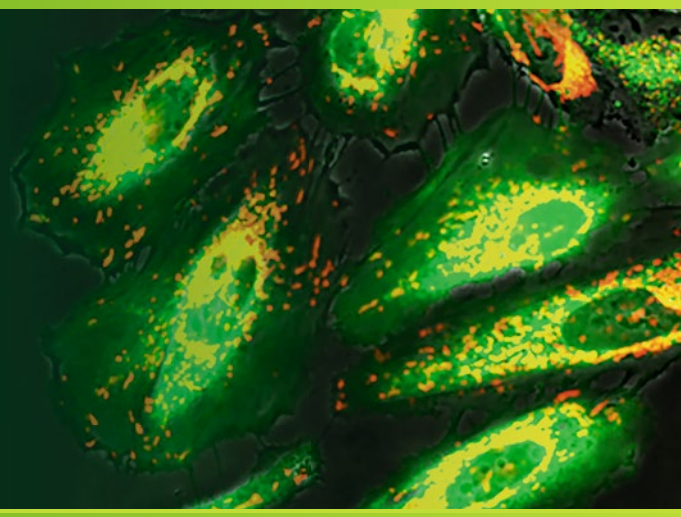

Volkmar Weissig
Marvin Edeas *Editors*

# Mitochondrial Medicine

## Volume 1: Targeting Mitochondria

*Second Edition*

Humana Press

# METHODS IN MOLECULAR BIOLOGY

*Series Editor*
**John M. Walker**
**School of Life and Medical Sciences**
**University of Hertfordshire**
**Hatfield, Hertfordshire, UK**

For further volumes:
http://www.springer.com/series/7651

For over 35 years, biological scientists have come to rely on the research protocols and methodologies in the critically acclaimed *Methods in Molecular Biology* series. The series was the first to introduce the step-by-step protocols approach that has become the standard in all biomedical protocol publishing. Each protocol is provided in readily-reproducible step-by-step fashion, opening with an introductory overview, a list of the materials and reagents needed to complete the experiment, and followed by a detailed procedure that is supported with a helpful notes section offering tips and tricks of the trade as well as troubleshooting advice. These hallmark features were introduced by series editor Dr. John Walker and constitute the key ingredient in each and every volume of the *Methods in Molecular Biology* series. Tested and trusted, comprehensive and reliable, all protocols from the series are indexed in PubMed.

# Mitochondrial Medicine

## Volume 1: Targeting Mitochondria

### Second Edition

Edited by

**Volkmar Weissig**

*Department of Pharmaceutical Sciences, Midwestern University College of Pharmacy, Glendale, AZ, USA*

**Marvin Edeas**

*Cochin Hospital, Cochin Institute, INSERM U1016, Paris, France*

Humana Press

*Editors*
Volkmar Weissig
Department of Pharmaceutical Sciences
Midwestern University
College of Pharmacy
Glendale, AZ, USA

Marvin Edeas
Cochin Hospital
Cochin Institute, INSERM U1016
Paris, France

ISSN 1064-3745 ISSN 1940-6029 (electronic)
Methods in Molecular Biology
ISBN 978-1-0716-1261-3 ISBN 978-1-0716-1262-0 (eBook)
https://doi.org/10.1007/978-1-0716-1262-0



This Humana imprint is published by the registered company Springer Science+Business Media, LLC, part of Springer Nature.
The registered company address is: 1 New York Plaza, New York, NY 10004, U.S.A.

# Preface

It is our distinct pleasure to present the second edition of MiMB *Mitochondrial Medicine* to the ever increasing number of scientists and physicians who are as fascinated by this tiny organelle as we are. We started working on the first edition in September 2014 and were able to bring about one year later two volumes with a total of 70 chapters to the market. As of today (July 2020), 195K downloads have been recorded for Volume I[1] and 90K downloads for volume II[2]. In light of the rapidly growing and expanding field of Mitochondrial Medicine, we readily accepted the invitation to compile a second edition, which we started to work on in March 2019. This second edition as offered here involves a total of 88 chapters with 45 of them written by new contributors who were not part of our first edition. The first and second editions combined subsequently present work from 115 mitochondrial laboratories from around the globe. We therefore believe these five volumes combined to be the most comprehensive source of know-how in the wide-ranging field of Mitochondrial Medicine.

Dividing 87 chapters equally over three volumes proved to be a bit challenging. We chose the subtitle ***Targeting Mitochondria*** for volume I, ***Assessing Mitochondria*** for volume II, and ***Manipulating Mitochondria and Disease Specific Approaches*** for volume III while of course being well aware of significant overlaps between these three areas of research. For example, it is quite obvious that mitochondria are being targeted for the purpose of either assessing them or to manipulate them. We therefore ask all authors not to be too critical regarding the placement of their particular chapter. The reader we believe will anyway choose to download a chapter of his/her interest quite independently of its placement in one of the three volumes.

All chapters in these three volumes were written for graduate students, postdoctoral associates, independent investigators in academia and industry as well as physicians by leading experts in their particular field. We are extremely grateful to them for having found the time to either update their chapter from the first edition or to write a new chapter. We will not forget that for many if not all of our contributors the worldwide COVID-19 pandemic posed additional and unexpected hurdles towards finishing their manuscript in due time. Thank you to all!

The idea for our original book proposal leading to the first edition of MiMB *Mitochondrial Medicine* originated in our efforts to organize a series of annual conferences on Targeting Mitochondria (www.targeting-mitochondria.com), the tenth one of which meanwhile has taken place in November 2019 in Berlin, Germany. Due to the ongoing pandemic, our 11th conference (October 29–30, 2020) will be a virtual one but we are sure it will not be less exciting than all the previous editions.

[1] https://link.springer.com/book/10.1007/978-1-4939-2257-4

[2] https://link.springer.com/book/10.1007/978-1-4939-2288-8

Last but not least we would like to sincerely thank John Walker, the series editor of *Methods in Molecular Biology*, for having invited us to compile this second edition and for his unlimited guidance and help throughout the entire process. We also owe sincere thanks to Patrick Marton, the Executive Editor of the Springer Protocol Series, for always having been available in assisting us throughout the entire project.

***Glendale, AZ, USA*** ***Volkmar Weissig***
***Paris, France*** ***Marvin Edeas***

# Contents

# Contributors


Mohammed Almuteri • *Department of Pharmaceutical Sciences, School of Pharmacy-Boston, MCPHS University, Boston, MA, USA*

Alejandro Baeza • *Dpto. Materiales y Producción Aeroespacial, ETSI Aeronáutica y del Espacio, Universidad Politécnica de Madrid, Madrid, Spain*

Parul Benien • *Department of Pharmaceutical Sciences, School of Pharmacy-Boston, MCPHS University, Boston, MA, USA*

Hong Bi • *School of Chemistry and Chemical Engineering, Anhui University, Hefei, China*

Lucia Biasutto • *CNR Institute of Neurosciences, Padova, Italy; Department of Biomedical Sciences, University of Padova, Padova, Italy*

Susan S. Bird • *Thermo Fisher Scientific, Cambridge, MA, USA*

Mark Böhlke • *Department of Pharmaceutical Sciences, School of Pharmacy-Boston, MCPHS University, Boston, MA, USA*

Cecilia Bombelli • *CNR-ISB, Sede Secondaria di Roma-Meccanismi di Reazione c/o Department of Chemistry, Sapienza University, Roma, Italy*

Federico Bordi • *Physics Department, Sapienza University, Roma, Italy*

Fernanda Borges • *CIQUP/Department of Chemistry and Biochemistry, Faculty of Sciences, University of Porto, Porto, Portugal*

Sergio Bova • *Department of Pharmaceutical and Pharmacological Sciences, University of Padova, Padova, Italy*

Margaret Anne Brimble • *School of Chemical Sciences, University of Auckland, Auckland, New Zealand*

Marisa Brini • *Department of Biology, University of Padua, Padova, Italy*

Milica Bugarski • *Institute of Anatomy, University of Zurich, Zurich, Switzerland*

Karin B. Busch • *Department of Biology, Institute of Molecular Cell Biology, University of Münster, Münster, Germany*

M. Cagalinec • *Department of Cellular Cardiology, Institute of Experimental Endocrinology, Biomedical Research Center, Slovak Academy of Sciences, Bratislava, Slovakia; Department of Neurophysiology and Neuropharmacology, Center for Physiology and Pharmacology, Medical University of Vienna, Vienna, Austria; Centre of Excellence for Advanced Materials Application (CEMEA), Slovak Academy of Sciences, Bratislava, Slovakia*

Fernando Cagide • *CIQUP/Department of Chemistry and Biochemistry, Faculty of Sciences, University of Porto, Porto, Portugal*

Andrew G. Cairns • *School of Chemistry, University of Glasgow, Glasgow, UK*

Tito Calì • *Department of Biomedical Sciences, University of Padua, Padua, Italy; Padova Neuroscience Center (PNC), University of Padua, Padua, Italy*

Rita Casadio • *Biocomputing Group, University of Bologna, Bologna, Italy*

Stefano Casciardi • *Department of Occupational and Environmental Medicine, Epidemiology and Hygiene, National Institute for Insurance against Accidents at Work (INAIL), Rome, Italy*

Francesca Ceccacci • *CNR-ISB, Sede Secondaria di Roma-Meccanismi di Reazione c/o Department of Chemistry, Sapienza University, Roma, Italy*

Laurent Chatre • *Institut Pasteur, Stem Cells and Development, Department of Developmental and Stem Cell Biology, CNRS UMR3738 Team "Stability of Nuclear and Mitochondrial DNA", Paris, France; Normandie Université, UNICAEN, CEA, CNRS, ISTCT/CERVOxy group, GIP Cyceron, Caen, France*
D. Chorvat Jr • *Department of Biophotonics, International Laser Centre, Slovak Centre of Scientific and Technical Information, Bratislava, Slovakia*
Alessia Ciogli • *Department of Chemistry and Technology of Drug, Sapienza University, Roma, Italy*
Marcel Culcasi • *Aix Marseille Univ, CNRS, ICR, UMR 7273, Sondes Moléculaires en Biologie et Stress Oxydant, Marseille, France*
Gerard G. M. D'Souza • *Massachusetts College of Pharmacy and Health Sciences, Boston, MA, USA; Department of Pharmaceutical Sciences, School of Pharmacy-Boston, MCPHS University, Boston, MA, USA*
Andrea De Nadai • *Department of Chemical Sciences, University of Padua, Padua, Italy*
Bryan C. Dickinson • *Department of Chemistry, The University of Chicago, Chicago, IL, USA*
Marco Diociaiuti • *Centro Nazionale Malattie Rare, Istituto Superiore di Sanità, Roma, Italy*
Tamer Elbayoumi • *Department of Pharmaceutical Sciences, College of Pharmacy-Glendale Campus, Midwestern University, Glendale, AZ, USA; College of Pharmacy-Glendale Campus, Nanomedicine Center of Excellence, Midwestern University, Glendale, AZ, USA*
Piero Fariselli • *Biocomputing Group, University of Bologna, Bologna, Italy*
Alessia Forgiarini • *Department of Pharmaceutical and Pharmacological Sciences, University of Padova, Padova, Italy*
Samayita Ganguly • *Department of Pharmaceutical Sciences, College of Pharmacy-Glendale Campus, Midwestern University, Glendale, AZ, USA; College of Pharmacy-Glendale Campus, Nanomedicine Center of Excellence, Midwestern University, Glendale, AZ, USA*
Rose M. Gathungu • *Metabolomics Core Facility, European Molecular Biology Lab, Heidelberg, Germany*
Susan Ghazi • *Institute of Anatomy, University of Zurich, Zurich, Switzerland*
Sander Grefte • *Human and Animal Physiology, Wageningen University & Research, Wageningen, Netherlands*
Andrew M. Hall • *Institute of Anatomy, University of Zurich, Zurich, Switzerland; Department of Nephrology, University Hospital Zurich, Zurich, Switzerland*
Hideyoshi Harashima • *Laboratory for Molecular Design of Pharmaceutics, Faculty of Pharmaceutical Sciences, Hokkaido University, Sapporo, Japan*
Micael Hardy • *Aix Marseille University, CNRS, ICR, UMR 7273, Marseille, France*
Richard C. Hartley • *School of Chemistry, University of Glasgow, Glasgow, UK*
Erik Hedman • *Centre for Inherited Metabolic Diseases, Karolinska University Hospital, Stockholm, Sweden*
Takuya Hidaka • *Department of Chemistry, Graduate School of Science, Kyoto University, Kyoto, Japan*
Brian Hopkins • *Landcare Research, Lincoln, New Zealand*
Richard W. Horobin • *Chemical Biology and Precision Synthesis, School of Chemistry, The University of Glasgow, University Avenue, Glasgow, Scotland, UK*
Outi Itkonen • *Laboratory Division HUSLAB, Helsinki University Central Hospital, Helsinki, Finland*

B. Kalyanaraman • *Department of Biophysics and Free Radical Research Center, Medical College of Wisconsin, Milwaukee, WI, USA*

Dong-Yeon Kim • *Innovation Center for Molecular Probe Development, Department of Nuclear Medicine, Chonnam National University Medical School and Hwasun Hospital, Hwasun, South Korea*

Werner J. H. Koopman • *Human and Animal Physiology, Wageningen University & Research, Wageningen, Netherlands; Department of Biochemistry, Radboud Institute for Molecular Life Sciences, Radboud Center for Mitochondrial Medicine, Radboudumc, Nijmegen, The Netherlands*

Bruce S. Kristal • *Division of Sleep and Circadian Disorders, Department of Medicine, Brigham and Women's Hospital, Boston, MA, USA; Division of Sleep Medicine, Department of Medicine, Harvard Medical School, Boston, MA, USA*

Alexander R. Lippert • *Department of Chemistry, Center for Drug Discovery, Design, and Delivery (CD4), Southern Methodist University, Dallas, TX, USA*

Victoria Lopez • *Dpto. Química en Ciencias Farmacéuticas, Universidad Complutense de Madrid, Instituto de Investigación Sanitaria, Hospital 12 de Octubre i+12, Plaza Ramón y Cajal s/n. CIBER de Bioingeniería, Biomateriales y Nanomedicina, CIBER-BBN, Madrid, Spain*

Maria Lozoya • *Department of Pharmaceutical Sciences, Midwestern University College of Pharmacy Glendale, Glendale, AZ, USA*

Giovanna Mancini • *CNR-ISB, Monterotondo, Italy*

A. Marcek Chorvatova • *Department of Biophotonics, International Laser Centre, Slovak Centre of Scientific and Technical Information, Bratislava, Slovakia; Department of Biophysics, Faculty of Natural Sciences, University of Ss. Cyril and Methodius, Trnava, Slovakia*

Pier Luigi Martelli • *Biocomputing Group, University of Bologna, Bologna, Italy*

Andrea Mattarei • *Department of Pharmaceutical and Pharmacological Sciences, University of Padova, Padova, Italy*

Stephen J. McQuaker • *School of Chemistry, University of Glasgow, Glasgow, UK*

Ahmed Mehanna • *Department of Pharmaceutical Sciences, School of Pharmacy-Boston, MCPHS University, Boston, MA, USA*

Jung-Joon Min • *Innovation Center for Molecular Probe Development, Department of Nuclear Medicine, Chonnam National University Medical School and Hwasun Hospital, Hwasun, South Korea*

K. Mitra • *Department of Genetics, University of Alabama at Birmingham, Birmingham, AL, USA*

Michael P. Murphy • *MRC Mitochondrial Biology Unit, Wellcome Trust/MRC Building, Cambridge, UK*

Valentina Mussi • *CNR-IMM Institute of Microelectronics and Microsystems, Roma, Italy*

Elizabeth J. New • *School of Chemistry, The University of Sydney, Sydney, NSW, Australia*

Catarina Oliveira • *CIQUP/Department of Chemistry and Biochemistry, Faculty of Sciences, University of Porto, Porto, Portugal*

Paulo J. Oliveira • *CNC—Center for Neuroscience and Cell Biology, UC Biotech, University of Coimbra, Cantanhede, Portugal*

Genny Orso • *Department of Pharmaceutical and Pharmacological Sciences, University of Padova, Padova, Italy*

Ganesh N. Pandian • *Institute of Integrated Cell Material Sciences (WPI-iCeMS), Kyoto University Institute for Advanced Study, Kyoto, Japan*

Cristina Paradisi • *Department of Chemical Sciences, University of Padova, Padova, Italy*
Diana Pendin • *Neuroscience Institute, Padua Section, National Research Council, Padua, Italy; Department of Biomedical Sciences, University of Padua, Padua, Italy*
Consuelo Petrocchi • *Aix Marseille Univ, CNRS, ICR, UMR 7273, Sondes Moléculaires en Biologie et Stress Oxydant, Marseille, France*
Sylvia Pietri • *Aix Marseille Univ, CNRS, ICR, UMR 7273, Sondes Moléculaires en Biologie et Stress Oxydant, Marseille, France*
Radoslaw Podsiadly • *Institute of Polymer and Dye Technology, Lodz University of Technology, Lodz, Poland*
Raffaele Proroga • *Department of Chemistry, Sapienza University, Roma, Italy*
David Rennison • *School of Chemical Sciences, University of Auckland, Auckland, New Zealand*
Miria Ricchetti • *Institut Pasteur, Stem Cells and Development, Department of Developmental and Stem Cell Biology, CNRS UMR3738 Team "Stability of Nuclear and Mitochondrial DNA", Paris, France*
Bettina Rieger • *Department of Biology, Institute of Molecular Cell Biology, University of Münster, Münster, Germany*
Verónica Rodríguez-García • *Departamento de Ciencia de los Materiales, ETSI Caminos, Canales y Puertos, Universidad Politécnica de Madrid C/Profesor Aranguren s/n, Madrid, Spain*
Edoardo Rossi • *Department of Chemistry, Sapienza University, Roma, Italy*
Stefano Sarti • *Physics Department, Sapienza University, Roma, Italy*
Castrense Savojardo • *Biocomputing Group, University of Bologna, Bologna, Italy*
Simona Sennato • *CNR-ISC-UOS Sapienza c/o Physics Department, Sapienza University, Roma, Italy*
Shrey Shah • *Department of Pharmaceutical Sciences, School of Pharmacy-Boston, MCPHS University, Boston, MA, USA*
Adam Sikora • *Institute of Applied Radiation Chemistry, Lodz University of Technology, Lodz, Poland*
B. Spurlock • *Department of Genetics, University of Alabama at Birmingham, Birmingham, AL, USA*
Irina G. Stavrovskaya • *Neurology Department, Columbia University Medical Center, New York, NY, USA*
Hiroshi Sugiyama • *Department of Chemistry, Graduate School of Science, Kyoto University, Kyoto, Japan; Institute of Integrated Cell Material Sciences (WPI-iCeMS), Kyoto University Institute for Advanced Study, Kyoto, Japan*
Giacomo Tartari • *Biocomputing Group, University of Bologna, Bologna, Italy*
José Teixeira • *CIQUP/Department of Chemistry and Biochemistry, Faculty of Sciences, University of Porto, Porto, Portugal; CNC—Center for Neuroscience and Cell Biology, UC Biotech, University of Coimbra, Cantanhede, Portugal*
Sophie Thétiot-Laurent • *Aix Marseille Univ, CNRS, ICR, UMR 7273, Sondes Molé culaires en Biologie et Stress Oxydant, Marseille, France*
Nicola Vajente • *Neuroscience Institute, Padua Section, National Research Council, Padua, Italy*
María Vallet-Regí • *Dpto. Química en Ciencias Farmacéuticas, Universidad Complutense de Madrid, Instituto de Investigación Sanitaria, Hospital 12 de Octubre i+12, Plaza Ramón y Cajal s/n. CIBER de Bioingeniería, Biomateriales y Nanomedicina, CIBER-BBN, Madrid, Spain*

Maria Rocio Villegas • *Dpto. Química en Ciencias Farmacéuticas, Universidad Complutense de Madrid, Instituto de Investigación Sanitaria, Hospital 12 de Octubre i +12, Plaza Ramón y Cajal s/n. CIBER de Bioingeniería, Biomateriales y Nanomedicina, CIBER-BBN, Madrid, Spain*

Zifei Wang • *School of Chemical Sciences, University of Auckland, Auckland, New Zealand*

Volkmar Weissig • *Department of Pharmaceutical Sciences, Midwestern University College of Pharmacy Glendale, Glendale, AZ, USA*

Yuma Yamada • *Laboratory for Molecular Design of Pharmaceutics, Faculty of Pharmaceutical Sciences, Hokkaido University, Sapporo, Japan*

Nusem Yu • *Department of Pharmaceutical Sciences, Midwestern University College of Pharmacy Glendale, Glendale, AZ, USA*

Ye Zhang • *School of Chemistry and Chemical Engineering, Anhui University, Hefei, China*

Jacek Zielonka • *Department of Biophysics and Free Radical Research Center, Medical College of Wisconsin, Milwaukee, WI, USA*

# Chapter 1

# Using QSAR Models to Predict Mitochondrial Targeting by Small-Molecule Xenobiotics Within Living Cells

**Richard W. Horobin**

## Abstract

Prediction of mitochondrial targeting, or prediction of exclusion from mitochondria, of small-molecule xenobiotics (biocides, drugs, probes, toxins) can be achieved using an algorithm derived from QSAR modeling. Application of the algorithm requires knowing the chemical structures of all ionic species of the xenobiotic compound in question, and for certain numerical structure parameters (*AI*, *CBN*, log *P*, $pK_a$, and *Z*) to be obtained for all such species. Procedures for specification of the chemical structures; estimation of the structure parameters; and application of the algorithm are described in an explicit protocol.

**Key words** Biocide, Lipophilicity, Localization, Pharmaceutical, $pK_a$, Probe, Structure parameter, Electric charge

## 1 Introduction

Many small-molecule (*see* **Note 1**) xenobiotics—biocides, fluorescent probes, pharmaceuticals, toxins, and so on—localize in and interact with the mitochondria of living cells ([1–4] respectively). Such targeted uptake is sometimes due to the evolved nanomachinery of receptors and transporters [5]. However, in many cases mitochondrial accumulation is largely or partly driven by less complex physicochemical effects. For instance, lipophilic cationic xenobiotics interact with the electrical membrane potential of respiring mitochondria [6], and can also form complexes with the cardiolipin of the inner mitochondrial membrane [7]. Lipophilic weak acid xenobiotics are ion-trapped within mitochondria, since the internal pH of these organelles when respiring is higher than that of the cytosol [8]. Such effects have been numerically modelled, so that if the chemical structure of the xenobiotic is known, then the compound's mitochondrial uptake (or exclusion) can be predicted. Two strategies have had some success in this regard. The first

Volkmar Weissig and Marvin Edeas (eds.), *Mitochondrial Medicine: Volume 1: Targeting Mitochondria*, Methods in Molecular Biology, vol. 2275, https://doi.org/10.1007/978-1-0716-1262-0_1,

**Table 1**
**Numerical structure parameters relevant to predicting the intracellular mitochondrial targeting of small-molecule xenobiotics**

| Structure parameter (with standard abbreviation) | Physicochemical feature described or modeled |
|---|---|
| Amphiphilicity index (*AI*) | Models hydrophobicity of the nonhydrophilic domain, an aspect of amphiphilicity |
| Conjugated bond number (*CBN*) | Models overall size of a conjugated, usually aromatic, domain or domains |
| Lectric charge (*Z*) | Describes overall electric charge carried by a molecular species |
| Logarithm of the octanol–water partition coefficient (log *P*) | Models lipophilicity (positive values) or hydrophilicity (negative values) |
| Negative logarithm of equilibrium constant of ionized/nonionized species for acids and bases ($pK_a$) | Indicates acid or base strength, strong acids have low values while strong bases have high values |

involves a physicochemical first principles model [9], the second uses a correlation-based quantitative structure activity relations (QSAR) approach [10]. Neither strategy is universally applicable [11], and it is the QSAR approach which is utilized in this chapter.

The QSAR approach involves building correlational models which relate various physicochemical features of xenobiotics to their observed intracellular localization (within mitochondria and other structures) inside live cells. Localization within different cell structures results from different combinations of physicochemical properties. These physicochemical features, such as electric charge and lipophilicity, are specified or modeled using numerical structure parameters. Those relevant to mitochondrial localization are listed and described in Table 1. Targeting of mitochondria can be due to several different mechanisms, and consequently arises with diverse chemical classes of xenobiotics. QSAR models for each of the mechanisms are available. An algorithmic integration of these QSAR models, plus models accounting for competitive uptake into certain other cell structures, is provided in Fig. 1. The underlying QSAR modeling approach to predicting intracellular localization of xenobiotics, including details of the QSAR models contributing to Fig. 1, has been reviewed [10].

To predict mitochondrial targeting, the following procedures are required. First, the chemical structure or structures of interest must be established. Then the required numerical structure parameters must be obtained for each structure. Finally, for each chemical structure, the parameter values must be inserted into the algorithmic integration of QSAR models set out in Fig. 1, to obtain a set of targeting predictions for the xenobiotic species of interest. Since the underlying QSAR models are simplistic, these predictions are indicative rather than prescriptive.

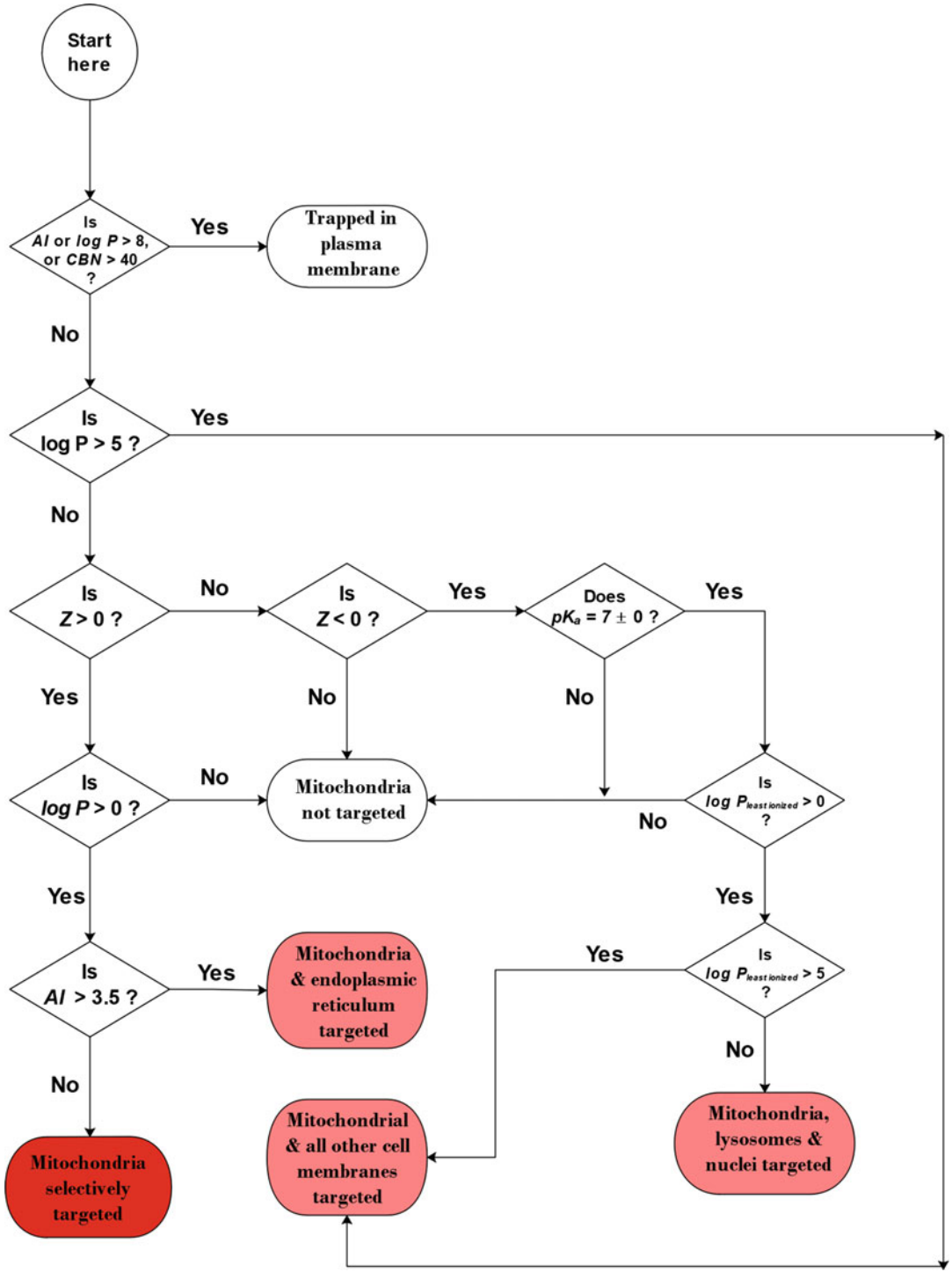


**Fig. 1** Algorithm predicting the mitochondrial targeting (or nontargeting) of small-molecule xenobiotic species within living cells. Structure parameter values must be inserted as appropriate to obtain such predictions. Structure parameter abbreviations (*AI*, *CBN*, log *P*, $pK_a$, and *Z*) are explicated in Table 1. log $P_{\text{least ionized}}$ is the log *P* value of the least ionized species present

## 2 Materials

To carry out the procedures described in Subheading 3, a number of procedural and informational resources are required, and are provided and considered in the present section. The first, based on published QSAR models as described in Subheading 1, is an algorithm predicting whether a given molecular structure (defined in terms of structure parameters) is likely to exhibit mitochondrial targeting or not. This algorithm is provided in Fig. 1. Suggestions for obtaining or checking chemical structures (Subheading 2.1), for assessing whether chemical or biochemical modification has occurred (Subheading 2.2) and which ionized species are likely to be present (Subheading 2.3) are also provided. Moreover, since targeting predictions require the values of the structure parameters for each of the chemical structures of interest to be inserted into the algorithm, procedures for obtaining these values from published sources (Subheadings 2.3 and 2.5) or by estimation (Subheadings 2.3–2.6), are given.

### *2.1 Information Sources Giving Chemical Structures of Xenobiotics*

1. Sources of chemical structures vary in three significant ways. Firstly, the source may be encyclopedic or domain specific. Secondly, the source may be hardcopy or online. Thirdly, the source may be freely accessible, or at least accessible via public libraries, or be proprietary. With these factors in mind, useful places to start looking for information are suggested in Table 2.
2. If the chemical structure of a xenobiotic of interest is already known, it is nevertheless advisable to check this against recognized information sources (*see* **Note 2**), as above.

### *2.2 Information Sources Concerning Chemical or Biochemical Modification of Xenobiotics Within, or Adjacent to, Cells*

There is much published information concerning metabolic modification of xenobiotics. As this can be categorized in an analogous way to the information concerned with structure identity, here it is merely noted as an example that, for pharmaceuticals and related materials, useful free online sources for starting a search are the Biocatalysis/Biodegradation database [44] and the UW Drug Interaction Solutions database [45].

### *2.3 Information Sources and Procedures for Specifying Ionized Chemical Species Derived from the Xenobiotic of Interest*

1. Inspect the structure of the xenobiotic, and identify any acid or basic grouping(s); *see* **Note 3**.
2. Look up or estimate, see below for both approaches, the micro $pK_a$ values (*see* **Note 4**) of the acidic and basic groupings in the compound of interest.
3. There are very many listings of $pK_a$ values. For instance, a six-volume compilation of critically selected values was made by Smith and Martell [12], for which an updated (2012) electronic version is available [13]. More readily accessible are

**Table 2**
**Varying types of information sources for chemical structures of several kinds of xenobiotics**

| Classes of xenobiotics | Typical hardcopy sources | Typical online sources |
|---|---|---|
| Encyclopedic, no particular class | *Merck Index, 15th edn.* [31] | *Merck Index Online** [32]<br>*ChemIDPlus* [14]<br>*ChemSpider* [20] |
| Dyes or fluorescent probes | *Colour Index*, 3rd edn [33]<br>*Conn's biological stains*, 9th edn [34] and 10th edn [35] | *Colour Index International** [36]<br>*Molecular Imaging and Contrast Agent Database* [37] |
| Herbicides | *Herbicide handbook*, 10th edn [38] | *Weed Science Society of America* [39] |
| Pharmaceuticals | *Basic and clinical pharmacology* [40] | *DrugBank* [15]<br>*PubChem* [21] |
| Surfactants | *Surfactants and interfacial phenomena*, 4th edn [41] | Try the "encyclopedic" online sources noted above |
| Toxicants | Too wide a field for a single volume, but [42] is a good starting point | The *Toxnet* database was closed in late 2019; however, much of its content was transferred to the *PubChem* [21] and *PubMed* [46] databases, or to the *PubMed Bookshelf*. For details, see the transition pages on [43] |

Online sources not freely available are indicated by a superscripted asterisk,*

the $pK_a$ values provided by free online sources, such as ChemIDplus [14] and DrugBank [15]; but *see* **Note 5**.

4. When, as if often the case, no reported micro $pK_a$ value can be found, there are many ways of estimating $pK_a$ values. A useful summary of manual procedures, with numerous worked examples, was assembled by Perrin, Dempsey, and Serjeant [16]. There are also numerous software packages which provide $pK_a$ estimates of specified chemical structures. Some packages are commercial, such as those from ACD/Labs [22] and ChemSilico [23]. Such sources may provide free access to a restricted component of the system. There are also excellent free packages such as the widely used ALOGPS [24].
5. If no reported or estimated value is available, make a guesstimate of the $pK_a$ value (*see* **Note 3**).
6. In whatever way $pK_a$ values are obtained, they must then be used to decide which ionic species are likely to be present, both extra- and intracellularly. As this will be influenced by the local pH as well as the $pK_a$ of the xenobiotic, the following generalizations may be useful. Extracellular cellular pH is commonly near 7, although obviously there are many exceptions which must be taken into account. Usual intracellular pHs are 7 in the

cytosol, up to half a pH unit higher in respiring mitochondria and within the nucleus, but one pH unit lower in the trans-Golgi network, and up to 1.5 pH units lower in lysosomes.

7. Draw the chemical structures of each ionic species thought to be present.

### 2.4 Procedures for Specifying CBN Values

1. Inspect the chemical structure diagram of the molecular species concerned, and identify all conjugated components (*see* **Note 3**).
2. First look for the carbon units of homo- and heterocyclic aromatic rings, as well as those of any conjugated polyene chains.
3. Next identify any heteroatoms carrying lone pairs (e.g., nitrogen, oxygen or sulfur) and multiatom units (e.g., amino, carbonyl, nitroxy, sulfoxy, or more complex moieties) within these rings or chains.
4. Now find any atoms (e.g., halogens, nitrogen, oxygen, sulfur) or multiatom units (e.g., amido, carbonyl, carboxy, hydroxy, nitro and nitroxy, sulfoxy and sulfonyl, or more complex moieties) which may be conjugated with aromatic rings or conjugated polyene chains.
5. Once such conjugated units have been identified and marked onto the structure diagram, the *CBN* value may be obtained by counting the total number (*see* **Note 6**) of conjugated bonds seen in the molecule (*see* **Notes 7** and **8**).

### 2.5 Information Sources and Procedures for Obtaining log P Values

1. A collection of more than 15,000 critically selected experimentally determined log *P* values has been accumulated and published by the Pomona College MedChem Project [17, 18]. This dataset, now expanded to more than 55,000 compounds, is currently available online via the MedChem database [19]. More accessible are the log *P* values given in free online sources such as ChemIDplus [14], ChemSpider [20], DrugBank [15], and PubChem [21]; but *see* **Note 5**.
2. When information sources do not provide a log *P* value for the structure of interest, the parameter can be estimated using software-implemented systems (*see* **Note 9**). There are numerous software packages which provide log *P* estimates. Commercial examples include ACD/Labs [22] and ChemSilico [23], and such sources may provide free access to a restricted component of the system. There are also excellent free packages such as the widely used ALOGPS [24].
3. Whichever approach is adopted to obtaining log *P* values, check carefully to see if the micro log *P* values for ionized species are actually available (*see* **Note 10**).

4. If no micro value is available at this stage, use the manual procedure of Hansch and Leo, described in detail in [18] (*see* **Note 11**).

### 2.6 Procedure for Obtaining Amphiphilic Index (AI) Values

1. This parameter models the hydrophobicity of the lipophilic domain of amphiphilic molecules. Consequently, the first step is to decide if the xenobiotic molecule is in fact amphiphilic, that is to say has distinct and significant hydrophilic and hydrophobic domains (*see* **Note 3**). If amphiphilic, the boundary of the hydrophobic domain should then be identified, following which its *AI* value can be estimated. If this boundary is unclear, then a series of *AI* estimates of slightly different regions will be required to assess the most plausible value (*see* **Note 12**). If more than one hydrophobic domain exists, then unless all can be present in one "super domain" (this may only be assessable using 3D models) it is unlikely that the molecule will be significantly amphiphilic.
2. As the *AI* parameter amounts to the notional log *P* of a submolecular fragment, it cannot be measured experimentally by partitioning, and, as no tabulations of the parameter are available, it must be estimated. Estimation can be attempted by any of the procedures described in **item 2** of Subheading 2.5, above. Note that some software packages reject substructures as chemically invalid; sometimes this can be circumvented by insertion of a dummy value. However, if this problem is unavoidable the manual procedure described in **item 4** of Subheading 2.5 must be used.

## 3 Methods

### 3.1 Establishing Chemical Structures

1. Draw the chemical structure of the xenobiotic of interest, in the form it will take when within, or in contact with, a live cell (*see* **Note 2**). Information sources to assist with this are provided in Subheading 2.1.
2. Draw the chemical structure(s) of any reaction product (s) resulting from chemical or biochemical modification of the xenobiotic when within, or adjacent to, a live cell (*see* **Note 13**). Information sources to assist this are provided in Subheading 2.2.
3. Draw the chemical structure(s) of any ionized species likely to arise from the chemical structure adjacent to or within the live cell (*see* **Note 14**). For procedures and information sources, *see* Subheading 2.3.

### 3.2 Estimating Structure Parameters for each Compound and each Ionized Species

1. For each chemical structure estimate the various structure parameters required (*AI*, *CBN*, log *P*, $pK_a$, and *Z*), as described below (*see* **Note 15**).
2. Obtain the electric charge (*Z*) by inspection of the structure diagram and summation of the formal charges. The $pK_a$ values are obtained as described in Subheading 2.3.
3. Obtain the conjugated bond number (*CBN*) using the procedure given in Subheading 2.4.
4. Obtain the logarithm of the octanol–water partition coefficient (log *P*) using the information sources or procedures given in Subheading 2.5.
5. Obtain the amphiphilic index (*AI*) using the procedure described in Subheading 2.6.
6. Tabulate these structure parameters for each chemical structure.

### 3.3 Predicting Mitochondrial Targeting/ Nontargeting Using the QSAR Algorithm (See *Note 16*)

1. For each chemical structure, and with the tabulation of its structure parameters to hand, go to "Start here" in the predictive QSAR algorithm given in Fig. 1.
2. Step through the algorithm, by inserting the structure parameter values when called for. Record whether the xenobiotic species is predicted as being trapped in the plasma membrane, or as entering the cell but not targeting mitochondria, or as targeting mitochondria plus other structures, or as targeting mitochondria selectively (*see* **Note 17**).
3. Finally, if more than one compound or ionized species are considered present, aggregate the predictions for the various species of the xenobiotic compound (*see* **Note 18**).

## 4 Notes

1. "Small molecule" excludes nanoparticular materials, which are not modelable by the QSAR procedures underlying this protocol [25]. However, some polymeric species can be modeled, if they lack secondary structure. It is this latter factor, rather than size as such, which is inconsistent with QSAR modeling of the type used here.
2. Chemical structures given in handbooks, vendors' catalogs or research papers can be in error or be misleading (e.g., [26, 27]). And consider **Note 3**.
3. If not sure about this, befriend a chemist.
4. Micro $pK_a$ values relate to specific ionizable groupings within the xenobiotic. Check that $pK_a$ values cited for a compound are in fact of this type. For compounds containing multiple

ionizable moieties, a single "blended" experimental $pK_a$ value may be cited, which is not what is required here. For discussion of this issue *see* ([16] p. 17; and [28]).

5. When using such information sources, remember that micro values may not be provided, and that values given are often estimates.
6. A molecule may contain a single conjugated region, or multiple regions separated by nonconjugated bridging moieties such as methylene groups.
7. Avoid counting those nonconjugated bonds which link isolated conjugated rings or chains. Avoid counting bonds linking conjugated rings or chains which are not all in a single plane.
8. For worked examples of the procedure *see* [26].
9. Such procedures vary widely, as do validities of outcome. If this is a concern, read and consider a critical review of outcomes and ease of use of a number of computational methods [29].
10. Software packages do not necessarily permit estimation of the log *P* for ionic species. Even if the structure of an ion is entered, the log *P* estimates generated by some software may refer to the corresponding unionized species.
11. The procedure of Hansch and Leo is complicated. Do not assume it can be picked up in an hour or so.
12. For small molecules with little conformational flexibility, the hydrophilic and hydrophobic zones will usually be easy to assess from a 2D structure diagram. With more flexible or complex molecules, inspection of 3D structures may be necessary, and in such cases the plausibility of the *AI* parameter will be reduced.
13. For instance, acids can result from hydrolysis of esters, catalyzed by cellular esterases.
14. Chemical structures shown in hardcopy and online documentation are often those of nonionized species, even if under physiological conditions the actual species present include anionic or cationic molecules. Often, multiple ionic species must be considered.
15. This is necessary as each ionized species is distributed intracellularly as if it were a separate compound [30].
16. Subheading 3.3 should not be read as implying that localization is wholly controlled by the physicochemical character of the xenobiotic molecule. Obviously, cell properties also influence localization patterns.
17. As the underlying QSAR models are dichotomous, any given species should fall into only one of these categories. However,

if structure parameter values fall onto or near the boundaries of key regions in the parameter spaces of the QSAR models, predictive ambiguity may arise.

18. Presence of multiple species, or indeed multiple compounds, does not preclude all chemical structures having the same mitochondrial targeting properties, although this is of course not always the case.

## Acknowledgements

RWH thanks Prof. Graeme Cooke, School of Chemistry, University of Glasgow, for providing facilities.

### References

1. Lin W, Yuan D, Deng Z, Niu B, Chen Q (2019) The cellular and molecular mechanism of glutaraldehyde-didecyldimethylammonium bromide as a disinfectant against *Candida albicans*. J Appl Microbiol 126:102–112
2. Wang W, Liu Y, Niu J, Lin W (2019) Fluorescence imaging of mitochondria with three different sets of signals based on fluorene cation fluorescent probe. J Fluoresc 29:1457–1465
3. Zeilonka J, Joseph J, Sikora A, Hardy M, Ouari O, Vasquez-Vivar J, Cheng G, Lopez M, Kalyanaraman B (2017) Mitochondria-targeted triphenylphosphoniuim-based compounds: syntheses, mechanisms of action, and therapeutic and diagnostic applications. Chem Rev 117:10043–10120
4. Natalie A, Duggett LA, Griffiths SJL, Flatters JL (2017) Paclitaxel-induced painful neuropathy is associated with changes in mitochondrial bioenergetics, glycolysis, and an energy deficit in dorsal root ganglia neurons. Pain 158:1499–1508
5. Chamberlain GR, Tulumello DV, Kelley SO (2013) Targeted delivery of doxorubicin to mitochondria. ASC Chem Biol 8:1389–1395
6. Creed S, McKenzie M (2019) Measurement of mitochondrial membrane potential with the fluorescent dye tetramethylrhodamine methyl ester. Methods Mol Biol 1928:69–76
7. Leung CW, Hong Y, Hanske J, Zhao E, Chen S, Pletneva EV, Tang BZ (2013) Superior fluorescent probe for detection of cardiolipin. Anal Chem 86:1263–1268
8. Rashid F, Horobin RW (1991) Accumulation of fluorescent non-cationic probes in mitochondria of cultured cells: a proposed mechanism, and some implications. J Microsc 163:233–241
9. Trapp S, Horobin RW (2005) A predictive model for the selective accumulation of chemicals in tumor cells. Eur Biophys J 34:959–966
10. Horobin RW, Rashid-Doubell F, Pediani JD, Milligan G (2013) Predicting small molecule fluorescent probe localization in living cells using QSAR modeling. 1. Overview and models for probes of structure, properties and function in living cells. Biotech Histochem 88:440–460
11. Horobin RW, Trapp S, Weissig V (2007) Mitochondriotropics: a review of their mode of action, and their applications for drug and DNA delivery to mammalian mitochondria. J Control Release 121:125–136
12. Smith RM, Martell AE (1974) Critical stability constants, vol 1–6. Plenum Press, New York
13. Smith RM, Martell AE, Motekaitis RJ (2012) NIST critically selected stability constants, version 8.0, NIST standard reference database 46. US Department of Commerce, Gaithersburg MD
14. ChemIDplus. chem.nim.nih.gov/chemidplus. US National Library of Medicine, Bethesda, MA. Accessed 12 Dec 2019
15. DrugBank. www.drugbank.ca. The University of Alberta, Canada. Accessed 12 Dec 2019
16. Perrin DD, Dempsey B, Sarjeant EP (1981) pKa predictions for organic acids and bases. Chapman & Hall, London
17. Leo A, Hansch C, Elkins D (1971) Partition coefficients and their uses. Chem Rev 71:525–616
18. Hansch C, Leo A (1979) Substituent constants for correlation analysis in chemistry and biology. Wiley-Interscience, New York. Chapter IV

19. MedChem database. www.daylight.com/medchem.html. Accessed 12 Dec 2019
20. ChemSpider. www.chemspider.com. The Royal Society of Chemistry. Accessed 12 Dec 2019
21. PubChem. pubchem.ncbi.nim.nih.gov. National Center for Biotechnology Information, US National Library of Medicine, Bethesda, MA, USA. Accessed 12 Dec 2019
22. ACD/Labs. www.acdlabs.com. Advanced Chemical Development, Inc. Accessed 12 Dec 2019
23. ChemSilico. www.chemsilico.com. Daylight Chemical Information Systems, Inc. Accessed 12 Dec 2019
24. ALOGPS v. 2.1. www.vcclab.org/lab/alogps. Virtual Computational Chemistry Laboratory, Institute of Structural Biology, HelmholstZentrum, Munich. Accessed 12 Dec 2019
25. Horobin RW (2010) Can QSAR models describing small-molecule xenobiotics give useful tips for predicting uptake and localization of nanoparticles in living cells? And if not, why not? In: Weissig V, D'Souza GGM (eds) Organelle-specific pharmaceutical nanotechnology. Wiley, Hoboken NJ, pp 193–206
26. Horobin RW, Rashid-Doubell F (2013) Predicting small molecule fluorescent probe localization in living cells using QSAR modeling. 2. Specifying probe, protocol an cell factors; selecting QSAR models; predicting entry and localization. Biotech Histochem 88:461–476
27. Stockert JC, Abasolo MI (2011) Inaccurate chemical structures of dyes and fluorochromes found in the literature can be problematic for teaching and research. Biotech Histochem 86:52–60
28. Avdeef A (2003) Adsorption and drug development. Solubility, permeability and charge state. Wiley-Interscience, Hoboken NJ. Chapter 6
29. Mannhold R, Poda GI, Ostermann C, Tetko IV (2009) Calculation of molecular lipophilicity: state-of-the-art and comparison of log P methods on more than 96,000 compounds. J Pharm Sci 98:861–893
30. Franco A, Trapp S (2008) Estimation of the soil-water partition coefficient normalized to organic carbon for ionizable organic chemicals. Environ Toxicol Chem 27:1995–2004
31. O'Neil MJ (2013) Merck Index: an encyclopedia of chemicals, drugs and biologicals, 15th edn. Royal Society of Chemistry, London
32. Merck Index Online. www.rsc.org/merck-index. Royal Society of Chemistry. Accessed 12 Dec 2019
33. Colour Index (1971) Society of Dyers & Colourists, 3rd edn. Bradford, and American Association of Textile Chemists and Colourists, Research Triangle Park NC
34. Lillie RD (1977) H.J.Conn's biological stains. A handbook on the nature and uses of the dyes imployed in the biological laboratory, 9th edn. Williams & Wilkins, Baltimore
35. Horobin RW, Kiernan JA (2002) Conn's biological stains. A handbook of dyes, stains and fluorochromes for use in biology and medicine, 10th edn. Oxford, BIOS
36. Colour Index International, 4th ed. Online. www.colour-index.com. Society of Dyers & Colourists and American Association of Textile and Colour Chemists. Accessed 12 Dec 2019
37. Molecular imaging and contrast agent database. www.ncbi.nlm.nih.gov/pubmed. Accessed 12 Dec 2019
38. Shaner DL (2014) Herbicide handbook, 10th edn. Weed Science Society of America, Lawrence KS
39. Weed Science Society of America. wssa.net/weed/herbicides. Weed Science Society of America, Lawrence KS. Accessed 12 Dec 2019
40. Katzung BG (2017) Basic and clinical pharmacology, 14th edn. McGraw-Hill Education/Medical, New York
41. Rosen MJ, Kunjappu JT (2012) Surfactants and interfacial phenomena, 4th edn. Wiley, Hoboken NJ
42. Rossoff IS (2001) Encyclopedia of clinical toxicology. CRS Press, Boca Raton
43. ToxNet. toxnet.nim.nih.gov. US National Library of Medicine, Bethesda, MA. Accessed 12 Dec 2019
44. Biocatalysis/Biodegration database. umbbd.ethz.ch. The University of Minnesota. Accessed 12 Dec 2019
45. UW Drug Interaction Solutions database. www.druginteractionsolutions.org The University of Washington. Accessed 12 Dec 2019
46. PubMed. www.ncbi.nim.nih.gov/pubmed. Accessed 12 Dec 2019

# Chapter 2

# DQAsomes as the Prototype of Mitochondria-Targeted Pharmaceutical Nanocarriers: An Update

**Volkmar Weissig, Maria Lozoya, Nusem Yu, and Gerard G. M. D'Souza**

## Abstract

DQAsomes (dequalinium-based liposome-like vesicles) are the prototype for all mitochondria-targeted vesicular pharmaceutical nanocarrier systems. First described in 1998 in a paper which has been cited as of May 2020 over 150 times, DQAsomes have been successfully explored for the delivery of DNA and low-molecular weight molecules to mitochondria within living mammalian cells. Moreover, they also appear to have triggered the design and development of a large variety of similar mitochondria-targeted nanocarriers. Potential areas of application of DQAsomes and of related mitochondria-targeted pharmaceutical nanocarriers involve mitochondrial gene therapy, antioxidant and updated therapy as well as apoptosis-based anticancer chemotherapy. Here, detailed protocols for the preparation, characterization, and application of DQAsomes are given and most recent developments involving the design and use of DQAsome-related particles are highlighted and discussed.

**Key words** DQAsomes, DQAplex, Dequalinium, Mitochondria, Pharmaceutical nanocarriers, Mitochondria, Gene therapy, Chemotherapy, Paclitaxel, Transfection, Apoptosis

## 1 Introduction

### *1.1 DQAsomes—The Early Years*

The accidental discovery of the vesicle-forming capacity of dequalinium chloride (DQA) at the end of the 1990s [1] led to the development of the first mitochondria-targeted vesicular nanocarrier system [2, 3]. Dequalinium (1,1′-decamethylene bis (4-aminoquinaldinium chloride)) is a cationic bolaamphiphile composed of two quinaldinium rings linked by ten methylene groups (*see* Fig. 1).

Under certain experimental conditions as it will be described in detail below, DQA self-assembles into liposome-like vesicles named DQAsomes (DeQAlinium-based lipoSOMES) at that time. Data obtained from freeze fracture electron microscopy, electron microscopy, photon correlation spectroscopy, and Monte Carlo computer simulations [1, 4] strongly support the hypothetical vesicular structure of DQAsomes presented in Fig. 2.

Volkmar Weissig and Marvin Edeas (eds.), *Mitochondrial Medicine: Volume 1: Targeting Mitochondria*, Methods in Molecular Biology, vol. 2275, https://doi.org/10.1007/978-1-0716-1262-0_2,

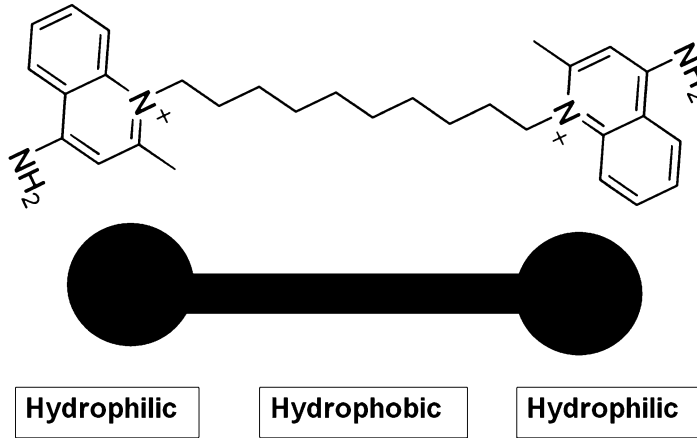


**Fig. 1** Chemical structure of dequalinium chloride with overlaid shapes depicting the molecule's amphipathic character

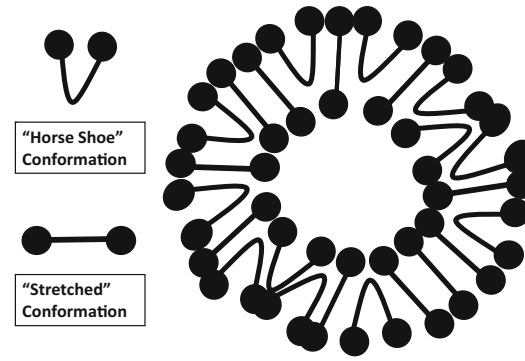


**Fig. 2** Hypothetical scheme illustrating the self-assembly behavior of dequalinium cations into liposome-like vesicles including the depiction of two possible conformations of the bolaamphiphile

A limited structure–activity study [5] involving nine derivatives of DQA revealed that replacing the methyl group in DQA by an aliphatic hexyl ring (informally called "cyclohexyl-DQA," *see* compound **1** in Fig. 3) appears to confer unexpected superior vesicle forming properties to this bolaamphiphile. Vesicles made from cyclohexyl-DQA have in contrast to vesicles made from DQA a much narrower size distribution which hardly changes at all, even after storage at room temperature for over 5 months. In contrast to DQAsomes, bolasomes made from cyclohexyl-DQA are also stable upon dilution of the original vesicle preparation. While DQAsomes slowly disintegrate over a period of several hours, bolasomes made from cyclohexyl-DQA do not show any change in size distribution following dilution. The critical vesicle concentration (CVC) of

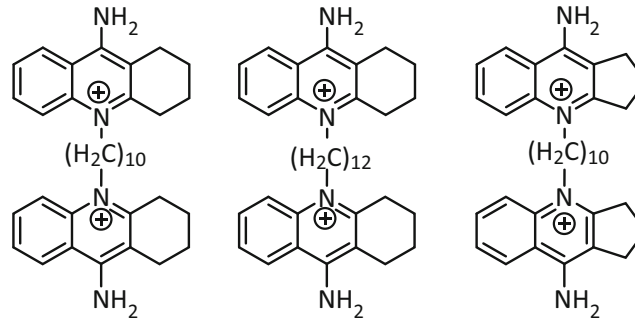


**Fig. 3** Chemical structures of "cyclohexyl-DQA" (compound **1**) and two newly synthesized and tested dequalinium derivatives. In compound **2** the alkyl chain between the heterocycles was extended by two methylene groups "12-cyclohexyl-DQA" [7], in compound **3** the cyclohexyl ring was replaced with a cyclopentyl ring "10-cyclopentyl-DQA" [6]

**Table 1**
**Size distribution of vesicles prepared from three different dequalinium derivatives as shown in Fig. 3**

| Compound as shown in Fig. 3 | Average size (nm) | Polydispersity index | References |
|---|---|---|---|
| 1. "cyclohexyl-DQA" | 168 ± 3 | 0.167 ± 0.002 | [7] |
| 2. "12-cyclohexyl DQA" | 188 ± 3 | 0.158 ± 0.009 | [7] |
| 3. "10-cyclopentyl-DQA" | 454 ± 187 | 0.438 ± 0.010 | [6] |

DQA was estimated to lie between 3 and 5 mM, while cyclohexyl-DQA still forms stable vesicles at 0.36 mM indicating a significant lower CVC [4]. These findings suggest that the cyclohexyl residue attached to the heterocycle in DQA-like bolaamphiphiles favors self-association of the planar ring system. It was speculated that the cyclohexyl ring sterically prevents the free rotation of the hydrophilic head of the amphiphile around the $CH_2$ axis, thus contributing to improved intermolecular interactions between the amphiphilic monomers [5].

The importance of the cyclohexyl ring for the ability of the bola amphiphile to form stable and well defined vesicles with a narrow size distribution was underlined in two more recent studies.

In compound **3** (Fig. 3) the cyclohexyl ring was replaced with a cyclopentyl ring [6] and in compound **2** (Fig. 3) the hydrophobic alkyl chain linking both hydrophilic heterocycles was extend by two methylene groups [7].

From Table 1 it can be seen that extending the hydrophobic alkyl chain by two methylene groups has hardly any impact on the small vesicle size and the narrow size distribution. However,

replacing the cyclohexyl ring by a cyclopentyl ring leads, under identical preparation conditions as described in detail below, to vesicles which are much larger in diameter and which also have a much wider size distribution.

DQA has been used for over 50 years as an antimicrobial agent in over-the-counter mouthwashes, lozenges, and ointments. The pharmacological activities of DQA have been widely studied revealing a variety of subcellular targets such as $K^+$ channels, F1-ATPase, calmodulin, and proteinase K, reviewed in [2]. In 1987 DQA was shown to exclusively localize inside mitochondria in living mammalian cells [8]. Mechanistic aspects of DQA's inherent affinity for energized mitochondria have been discussed on theoretical grounds in 2007 by combining a quantitative structure–activity relationship model with a Fick–Nernst–Planck physicochemical model [9]. The strong affinity of DQA for mitochondria combined with its ability to form cationic liposome-like vesicles (DQAsomes) have led to the proposal of using DQAsomes as the first potential mitochondria-targeted DNA delivery system [10, 11]. In a series of papers, it was demonstrated that DQAsomes meet all essential criteria [11] for a mitochondrial transfection vector. First, DQAsomes form stable complexes with plasmid DNA which are protected from DNase digestion [12]. Second, DQAsome–DNA complexes ("DQAplexes") release DNA at mitochondria-like membranes [13] and upon contact with isolated mouse liver mitochondria [14]. Third, DQAsomes mediate the cellular uptake and delivery of plasmid DNA toward mitochondria in living mammalian cells and finally, fourth, it was shown that plasmid DNA conjugates delivered into mammalian cells by DQAsomes colocalize with mitochondria [15]. Any further progress toward the functional expression of a transgene expression was hampered by the unavailability of an appropriate gene construct suited for transcription and translation inside mammalian mitochondria. This hurdle, however, was apparently overcome in 2011. Using immunofluorescence and a combination of immunohistochemical and molecular based techniques it was shown by Lyrawati et al. [16] that DQAsomes seem to be capable of delivering an artificial mini-mitochondrial genome construct encoding green fluorescence protein to the mitochondrial compartment of a mouse macrophage cell line resulting in the expression of GFP mRNA and protein. Although the reported transfection efficiency was with 1–5% very low, this was and still is, nevertheless, the first claim for f a successful functional transgene expression within living mammalian mitochondria. It appears as reasonable to assume that further optimization of DQAsomal mitochondrial transfection will eventually provide ways to manipulate the mitochondrial genome in living mammalian cells and probably pave the way toward direct mitochondrial gene therapy. Some limited progress into this direction has been reported in 2017 (*see* below under Subheading 1.2).

DQAsomes have also been extensively explored for the mitochondria-targeted delivery of low-molecular weight compounds. For example, preparing DQAsomes in the presence of paclitaxel (detailed protocol below) results in a stable colloidal solution of the drug with an average size distribution between 400 and 600 nm [17]. Cryo-electron and transmission electron microscopic images of paclitaxel incorporated into DQAsomes showed reproducibly rod-like shaped structures approximately 400 nm in length, which is surprising considering the spherical nature of empty DQAsomes [17]. Considering the reproducible stoichiometric composition of 2 mole dequalinium per 1 mole paclitaxel it has later been speculated that the colloidal solution of DQAsomal paclitaxel might actually contain crystal-like solid nanoparticles instead of vesicles with encapsulated paclitaxel [2]. Nevertheless, formulating paclitaxel with DQA increases the solubility of the drug in comparison to free paclitaxel by a factor of roughly 3000, thereby presenting an alternative to Cremophor-based formulations of the highly insoluble paclitaxel. A series of studies has clearly demonstrated that DQAsomal preparations of paclitaxel increase the drug's efficiency in triggering apoptosis by directly acting on mitochondria: First, in contrast to the free drug which randomly diffuses throughout the cytosol, fluorescently labeled paclitaxel formulated with DQAsomes was shown to colocalize with mitochondria [18]. Second, DQAsomal paclitaxel was shown to trigger cell death via apoptosis in cancer cells [18]. Third, DQAsomal paclitaxel was found to inhibit the tumor growth in nude mice bearing human colon carcinoma cells by about 50%, while the free drug at the concentration used did not have any impact on tumor growth [17].

An independent study by Vaidya et al. [19] has confirmed the rod-like structure of paclitaxel formulated with DQAsomes, their colocalization with mitochondria as well as the resulting increased apoptotic activity of paclitaxel [19]. To further increase the apoptotic activity of DQAsomal paclitaxel these authors successfully conjugated folic acid to the surface of DQAsomes in order to make them specific for tumor cells overexpressing the folate receptor.

### 1.2 DQAsomes: The Recent Years

In 2014, the formulation of curcumin-loaded DQAsomes for pulmonary delivery has been described [20]. Curcumin is a potent antioxidant with anti-inflammatory properties, which however has a very low bioavailability following oral administration due to its water insolubility. DQAsomes loaded with curcumin were found to have hydrodynamic diameters between 170 and 200 nm and a zeta potential of approximately +50 mV. The encapsulation efficiency under the chosen experimental conditions was 90% and the drug loading of DQAsomes was determined to be up to 61%. Curcumin encapsulated into DQAsomes was shown to display enhanced antioxidant activity in comparison to free curcumin. Curcumin-loaded

DQAsomes have been discussed by these authors as a promising inhalation formulation with mitochondrial targeting ability, potentially opening a new approach for efficient curcumin delivery for effective treatment of acute lung injury [20].

A surprising property of DQAsomes was described in 2018 [21]. While studying the anticancer efficiency of DQAsomes it was found that dequalinium applied to cell cultures in form of DQAsomes possesses an affinity toward human adipose-derived mesenchymal stem cells (AD-MSCs) and appears to promote their differentiation into osteoblasts without inducing cytotoxic effects. FACS data demonstrated that DQAsomes do not induce cell cycle arrest, apoptosis or cellular generation of reactive oxygen species in AD-MSCs. The authors discussed a role for DQAsomes in maintaining the balance between osteogenic and adipogenic differentiation of human AD-MSCs. In conclusion, Bae et al. [21] hypothesize that their findings may lead to potential applications of DQAsomes in the fields of bone tissue engineering and regenerative medicine.

The same group reported in 2017 a novel nanosome system composed of dequalinium, 1,2 dioleoyl-3-trimethylammonium-propane (DOTAP) and 1,2-dioleoyl-*sn*-glycero-3-phosphoethanolamine (DOPE), called DQA80, for enhanced mitochondria-targeted gene delivery and expression [22]. Citing the low efficiency of expression as a limitation these authors reported a potential approach to improve expression of the construct described in 2011 by Lyrawati et al. [16].They combined dequalinium chloride at varying molar ratios with DOTAP and DOPE and determined the physical stability of the resulting nanosomes [22]. The most stable preparation was reported to be the one prepared with a DOTAP–DOPE–DQA molar ratio of 10:10:80. Named DQA80s, these hybrid nanosomes are arguably the next evolution of DQAsomes for mitochondrial delivery of DNA constructs. Bae et al. reported that DQA80s mediated luciferase expression levels that were several orders of magnitude greater than those mediated by DQAsomes when using a luciferase reporter construct designed for nuclear expression. The levels of DQA80s mediated expression were comparable to those resulting from DOTAP/DOPE alone and were one order of magnitude less than levels achieved by the commercially available delivery systems lipofectamine and PEI. Despite this reported high level of nuclear transfection, the authors found that the DQA80s were able to localize DNA in the region of the mitochondria and that DQA80s mediated measurable levels of GFP expression from the same construct as the one used by Lyrawati et al. [16]. Interestingly, DOTAP/DOPE and DQAsomes mediated measurable levels of GFP expression albeit significantly lower than those mediated by DQA80s. Although promising, the fact that the study also reports that the DQA based preparations result in mitochondrial depolarization

highlights the potential toxicity of DQA as a limitation for mitochondrial DNA delivery. Finally, it is our opinion that the lack of clear evidence that recoded constructs designed for mitochondrial expression do not result in any nuclear-cytosolic transcription and or translation is, nevertheless, reason for concern that neither of the two groups which reported transgene expression in mammalian mitochondria have properly addressed yet.

A paper from 2018 describes the use of multifunctional pH-sensitive DQAsomes for the mitochondria-targeted delivery of doxorubicin [23]. The authors synthesized a pH responsive PEG–cholesterol conjugate and linked the human epidermal growth factor peptide (HER-2 peptide) to the distal end of the PEG chain. This HER-2-peptide-$PEG_{2000}$-Schiff base-cholesterol (HPSC) was then used to modify the surface of doxorubicin-loaded DQAsomes. Cholesterol serves as a DQAsomal membrane anchor for the PEG-HER-2-peptide. The Schiff base is pH-sensitive and releases the PEG-HER-2-peptide from the DQAsomal surface in an acidic environment. The authors tested their formulation using human breast cancer cell and DOX-resistant breast cancer cell lines (MCF-7 and MCF-7/ADR). Cellular uptake and mitochondria-targeting assays demonstrated that HPS-DQAsomes were able to deliver the therapeutic agent (doxorubicin) to mitochondria, thereby inducing a mitochondria-driven apoptosis process. In conclusion the authors suggested the utilization of multifunctional pH-sensitive HPS-DQAsomes as a novel and versatile approach for overcoming multidrug resistance in cancer cells [23].

The affinity of dequalinium cations for mitochondria was most recently utilized for the targeting of resveratrol-loaded liposomes to mitochondria [24]. Mitochondriotropic liposomes bearing triphenylphosphonium cations as mitochondrial targeting ligand on their surface have been described for the first time in 2005 [25] and their usefulness for the delivery of drugs to mitochondria in vitro and in vivo has been demonstrated in 2008 [26]. In the most recent study, instead of linking triphenylphosphonium residues to the liposomal surface the authors modified the surface of liposomes with dequalinium cations linked to the distal PEG end of distearoylphosphatidylethanolamine polyethylene glycol (DQA-DSPE-PEG), as shown in Fig. 4.

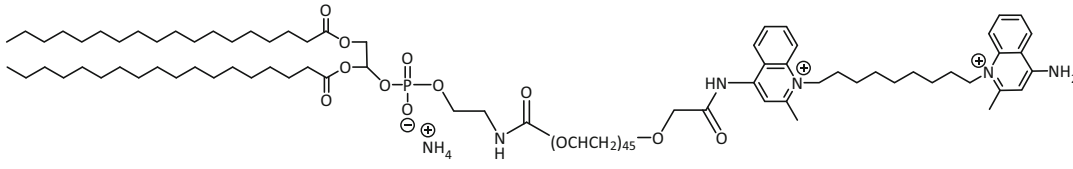


**Fig. 4** Chemical structure of DQA-DSPE-PEG, according to [24]

The enhanced cellular uptake and selective accumulation of DQA-DSPE-PEG liposomes with incorporated resveratrol at or in mitochondria were demonstrated using confocal microscopy and via resveratrol quantification in the intracellular organelle, using LC-MS/MS. In addition, the authors observed the induction of cytotoxicity in cancer cells caused by the generation of reactive oxygen species and via the dissipation of the mitochondrial membrane potential.

A very different, non–mitochondria-related use of DQAsomes and Bolasomes composed of dequalinium derivatives have been described by David Stewart's group. In 2016 these investigators explored complexes formed from phosphorothioate gapmer antisense oligonucleotides with cationic dequalinium–derived bolasomes as a potential treatment for *Clostridium difficile* [7]. Anaerobic *C. difficile* log phase cultures were treated with serial doses of oligonucleotide–bolasome complexes or equivalent amounts of empty bolasomes for 24 h. The authors reported that antisense gapmers for four specific gene targets achieved nanomolar minimum inhibitory concentrations for *C. difficile* [7], while no inhibition of bacterial growth was observed from treatments at matched dosages of scrambled gapmer nanocomplexes or plain, oligonucleotide-free bolasomes compared to untreated control cultures [7]. In 2018, the same group extended their studies testing the antibacterial activities of gapmer oligonucleotides complexed with cationic bolasomes against cultures of *E. coli*, *B. fragilis*, *E. faecalis*, and again *C. difficile* [6]. Their data confirm that complexes of cationic dequalinium–based bolasomes and antisense oligonucleotides are effective against *C. difficile* while sparing other bacteria.

In the following the preparation, characterization, and use of DQAsomes will be described. The same protocol can be used (and has been used by us) to prepare bolasomes composed of any dequalinium derivatives.

## 2 Materials

1. Rotary evaporator.
2. Fluorescence spectrophotometer.
3. Dequalinium chloride (*see* **Note 1**).
4. Paclitaxel.
5. SYBR™ Green I.
6. HEPES: 5 mM HEPES, pH 7.2, salt-free (*see* **Note 2**).
7. Methanol.
8. CellScrub buffer.
9. Solid Phase Extraction (SPE) column (J.T.Baker BAKER BOND Octadecyl 40 μm Prep LC Packing).

## 3 Methods

### 3.1 Preparation of Empty DQAsomes

1. Dissolve 26 mg dequalinium chloride (10 mM final) in about 2 ml methanol.
2. Remove the organic solvent using a rotary evaporator.
3. Add 5 ml salt-free HEPES buffer (*see* **Note 3**).
4. Sonicate the suspension of dequalinium chloride using a probe sonicator until a clear opalescent solution is obtained. To prevent overheating of the sonicated material, the round-bottom flask has to be cooled with ice water (*see* **Note 4**).
5. Centrifuge the colloidal solution containing DQAsomes for 10 min at 3000 × *g* at room temperature to remove any undissolved solid material (*see* **Note 5**).
6. Carefully collect the supernatant. Store at 4 °C.

### 3.2 Quantification of the Dequalinium Chloride Concentration in DQAsomes

1. Make a 1 mM stock solution of dequalinium chloride by dissolving 5.2 mg in 10 ml methanol.
2. Prepare a standard curve for dequalinium chloride by measuring its fluorescence over a concentration range between 0.0 and 0.01 mM ($\lambda_{EM}$ 380 nm, $\lambda_{EX}$ 283 nm).
3. Dissolve 0.02 ml DQAsomes in 3 ml methanol and measure fluorescence ($\lambda_{EM}$ 380 nm, $\lambda_{EX}$ 283 nm).
4. Calculate dequalinium concentration using the previously obtained standard curve.

### 3.3 Transfection of Mammalian Cells with DQAplexes

Appropriate DQAplexes, that is, DNA constructs (linear or circular) complexed with DQAsomes, should be prepared after the DNA binding capacity of each new DQAsome preparation has been determined in order to choose the correct DQAsome–DNA ratio, that is, to exclude the presence of any excess of free DNA. The absolute DNA Binding Capacity (DBC) has been defined [4] as the amount of DNA (μg) divided by that amount of dequalinium or any other suitable bolaamphiphile (nmole), which is necessary to completely prevent the DNA from interacting with SYBR™, resulting in 100% loss of fluorescence:

$$\text{Absolute DBC [μg/nmole]} = \text{μg DNA/nmole Bolaamphiphile} \quad (1)$$

1. Mix 1 μl water containing 625 ng plasmid DNA with 2.5 ml 5 mM HEPES, pH 7.4.
2. Add 0.5 ml SYBR™ solution (SYBR™ stock 1: 5000 in HEPES).
3. While continuously stirring, measure fluorescence ($\lambda_{EX}$ 497 nm, $\lambda_{EM}$ 520 nm) as a function of time, until a steady fluorescence signal is obtained.

4. Add step-wise aliquots between 1 and 20 μl of the DQAsome (bolasome) solution until fluorescence decreased either to background level or by at least 25%.
5. Calculate the absolute DBC following Eq. (1).
6. Dilute separately the appropriate amounts of DNA (oligonucleotides or plasmid DNA) and DQAsomes in serum-free cell medium. Allow both dilutions to stand for 10 min at room temperature and then mix them together. Allow the mixture of DNA and DQAsomes to stand at room temperature for another 5 min before adding to the cell culture well.
7. Grow cells in appropriate cell culture medium until approximately 60–80% confluence.
8. Incubate cells for 5–10 h with 1 mg DNA complexed with DQAsomes (*see* **Note 6**).
9. Remove the medium containing noninternalized material.
10. Wash cells thoroughly with CellScrub buffer to remove surface associated complex.
11. Analyze transfected cells using the appropriate method depending on the nature of the transgene encoded by the pDNA used (*see* **Note 7**).

### *3.4 Encapsulation of Paclitaxel into DQAsomes (See Note 8)*

1. Dissolve 26 mg (10 mM final) dequalinium chloride and 42.1 mg (10 mM final) paclitaxel in methanol in a round bottom flask.
2. Remove the organic solvent with a rotary evaporator.
3. Add 5 mM HEPES and probe sonicate the suspension until a clear opaque solution is obtained. Cool the round bottom flask in ice water during sonication (*see* **Note 9**).
4. To remove undissolved material, centrifuge for 10 min at 3000 × *g*.

### *3.5 Quantitative DQA and Paclitaxel Determination in Paclitaxel-Loaded DQAsomes*

The solubility of paclitaxel in water at 25 °C at pH 7.4 is with 0.172 mg/l (0.2 μM), extremely low, making any separation procedure of nonencapsulated paclitaxel from DQAsomes unnecessary, that is, in an aqueous environment, only paclitaxel encapsulated in DQAsomes stays in colloidal solution. However, for control, a paclitaxel suspension was probe sonicated under identical conditions used for the encapsulation of paclitaxel into DQAsomes, but in the complete absence of dequalinium chloride. As expected, upon centrifugation, no paclitaxel was detectable in the supernatant. The amount of dequalinium in DQAsomes is measured using fluorescence spectroscopy (excitation 335 nm, emission 360 nm). At these wavelengths, paclitaxel does not display any fluorescence and therefore does not interfere with the determination of dequalinium. Paclitaxel is quantified via UV spectroscopy.

The UV spectra of paclitaxel and dequalinium in methanol strongly overlap between 200 and 240 nm. Therefore, before measuring the amount of paclitaxel encapsulated into DQAsomes, dequalinium has to be quantitatively removed from the preparation.

1. Dissolve 0.02 ml Paclitaxel-loaded DQAsomes in 3 ml methanol and measure fluorescence as described above under Subheading 3.2.
2. Equilibrate the solid phase extraction (SPE) column with methanol.
3. Load column with 1 ml water.
4. Apply 0.02 ml Paclitaxel-loaded DQAsomes previously dissolved in methanol/water = 10/1, v/v.
5. Elute dequalinium from the column by washing it with a discontinued methanol/water gradient (1 ml methanol–water (1:4, v/v), followed by 1 ml methanol/water (3:2, v/v)).
6. Elute paclitaxel from the SPE column by washing with 1 ml 100% methanol.
7. Measure the absorption of paclitaxel via UV spectroscopy at 230 nm (*see* **Note 10**).

## 4 Notes

1. Alternatively, Dequalinium acetate can be used. Although not studied in detail, it has been found that DQA acetate seems to form DQAsomes with a narrower size distribution and almost instantaneously upon hydration with salt-free buffer.
2. All buffer solutions used for the preparation of DQAsomes must be salt-free. There are two forms of HEPES, HEPES salt free and HEPES potassium. HEPES potassium should not be used due to the higher pH which would result in the need for titration with acid that results in salt being formed. Traces of salt disrupt DQAsomes from being formed during the sonication process.
3. Alternatively, DQAsomes can also be formed in distilled water.
4. If no clear opalescent solution is formed after 30–45 min sonication, the buffer used most likely contained traces of salt. Another reason if no clear opalescent solution is formed 30–45 min after sonication, the ice bath could be at too low of a temperature, thus hindering the change to the opalescent solution. This can be remedied by around the 30 min of sonification intermittently removing the ice bath for short intervals of 30 s repeatedly until a clear opalescent solution is formed.

5. If centrifuge is set to is set −4 °C the dequalinium will crash out of solution resulting in the white dequalinium being on the wall of the centrifuge tube and the solution will be clear not opaque. Solution will remain opaque if centrifuged at room temperature, 25 °C.
6. All incubations should be performed in serum free medium to eliminate possible precipitation events associated with the interaction of the vesicular carriers with serum proteins.
7. For fluorescence microscopic analysis, grow cells on 22 mm circular coverslips in six well cell culture plates. After washing cells with CellScrub buffer to remove surface associated complex (**step 10**), incubate them with the required dye following the dye-specific protocol. The cells are then washed in sterile phosphate buffered saline (PBS) and mounted on slides in Fluoromount G medium for analysis by confocal fluorescence microscopy.
8. The same protocol has been followed for the encapsulation of other water-insoluble low-molecular weight drugs like etoposide (V. Weissig, S. M. Cheng, unpublished).
9. This step can take up to 1 h. It has been observed, though rarely, that the sonicated suspension of dequalinium chloride and paclitaxel turns into a highly viscous gel. This gel formation is not understood and has not been further investigated.
10. The lack of any absorption at 315 nm demonstrates the complete absence of dequalinium in the sample used for the determination of paclitaxel.

## Acknowledgements

The author (VW) would like to thank his former graduate student Dr. Shing-Ming Cheng for his outstanding contributions to work described in this chapter and Dr. Chuck Veltri for drawing the chemical structures in Figs. 3 and 4.

### References

1. Weissig V, Lasch J, Erdos G et al (1998) DQAsomes: a novel potential drug and gene delivery system made from Dequalinium. Pharm Res 15:334–337
2. Weissig V (2011) From serendipity to mitochondria-targeted nanocarriers. Pharm Res 28:2657–2668
3. Weissig V (2011) Mitochondrial delivery of biologically active molecules. Pharm Res 28:2633–2638
4. Weissig V, Moegel HJ, Wahab M, Lasch J (1998) Computer simulations of DQAsomes. Proc Intl Symp Control Rel Bioact Mater 25:312
5. Weissig V, Lizano C, Ganellin CR, Torchilin VP (2001) DNA binding cationic bolasomes with delocalized charge center: a structure-activity relationship study. S.T.P. pharma. Sciences 11:91–96
6. Sharma AK, Krzeminski J, Weissig V et al (2018) Cationic amphiphilic bolaamphiphile-based delivery of antisense oligonucleotides provides a potentially microbiome sparing

treatment for *C. difficile*. J Antibiot (Tokyo) 71 (8):713–721

7. Hegarty JP, Krzeminski J, Sharma AK et al (2016) Bolaamphiphile-based nanocomplex delivery of phosphorothioate gapmer antisense oligonucleotides as a treatment for *Clostridium difficile*. Int J Nanomedicine 11:3607–3619
8. Weiss MJ, Wong JR, Ha CS et al (1987) Dequalinium, a topical antimicrobial agent, displays anticarcinoma activity based on selective mitochondrial accumulation. Proc Natl Acad Sci U S A 84:5444–5448
9. Horobin RW, Trapp S, Weissig V (2007) Mitochondriotropics: a review of their mode of action, and their applications for drug and DNA delivery to mammalian mitochondria. J Control Release 121:125–136
10. Weissig V, Torchilin VP (2000) Mitochondriotropic cationic vesicles: a strategy towards mitochondrial gene therapy. Curr Pharm Biotechnol 1:325–346
11. Weissig V, Torchilin VP (2001) Towards mitochondrial gene therapy: DQAsomes as a strategy. J Drug Target 9:1–13
12. Lasch J, Meye A, Taubert H et al (1999) Dequalinium vesicles form stable complexes with plasmid DNA which are protected from DNase attack. Biol Chem 380:647–652
13. Weissig V, Lizano C, Torchilin VP (2000) Selective DNA release from DQAsome/DNA complexes at mitochondria-like membranes. Drug Deliv 7:1–5
14. Weissig V, D'SOuza GG, Torchilin VP (2001) DQAsome/DNA complexes release DNA upon contact with isolated mouse liver mitochondria. J Control Release 75:401–408
15. D'Souza GG, Boddapati SV, Weissig V (2005) Mitochondrial leader sequence--plasmid DNA conjugates delivered into mammalian cells by DQAsomes co-localize with mitochondria. Mitochondrion 5:352–358
16. Lyrawati D, Trounson A, Cram D (2011) Expression of GFP in the mitochondrial compartment using DQAsome-mediated delivery of an artificial mini-mitochondrial genome. Pharm Res 28:2848–2862
17. Cheng SM, Pabba S, Torchilin VP, Fowle W, Kimpfler A, Schubert R, Weissig V (2005) Towards mitochondria-specific delivery of apoptosis-inducing agents: DQAsomal incorporated paclitaxel. J Drug Deliv Sci Technol 15:81–86
18. D'Souza GG, Cheng SM, Boddapati SV et al (2008) Nanocarrier-assisted sub-cellular targeting to the site of mitochondria improves the pro-apoptotic activity of paclitaxel. J Drug Target 16:578–585
19. Vaidya B, Paliwal R, Rai S, Khatri K, Goyal AK, Mishra N, Vyas SP (2009) Cell-selective mitochondrial targeting: a new approach for cancer therapy. Cancer Therapy 7:141–148
20. Zupancic S, Kocbek P, Zariwala MG et al (2014) Design and development of novel mitochondrial targeted nanocarriers, DQAsomes for curcumin inhalation. Mol Pharm 11:2334–2345
21. Yoonhee Bae MKJ, Mun JY, Mallick S, Song SJ, Kim DM, Ko KS, Han J, Choi JS (2018) DQAsome nanoparticles promote osteogenic differentiation of human adipose-derived mesenchymal stem cells. Bull Kor Chem Soc 39:97–104
22. Bae Y, Jung MK, Song SJ et al (2017) Functional nanosome for enhanced mitochondria-targeted gene delivery and expression. Mitochondrion 37:27–40
23. Shi M, Zhang J, Li X et al (2018) Mitochondria-targeted delivery of doxorubicin to enhance antitumor activity with HER-2 peptide-mediated multifunctional pH-sensitive DQAsomes. Int J Nanomedicine 13:4209–4226
24. Kang JH, Ko YT (2019) Enhanced subcellular trafficking of resveratrol using mitochondriotropic liposomes in cancer cells. Pharmaceutics 11(8):423
25. Boddapati SV, Tongcharoensirikul P, Hanson RN et al (2005) Mitochondriotropic liposomes. J Liposome Res 15:49–58
26. Boddapati SV, D'Souza GG, Erdogan S et al (2008) Organelle-targeted nanocarriers: specific delivery of liposomal ceramide to mitochondria enhances its cytotoxicity in vitro and in vivo. Nano Lett 8:2559–2563

# Chapter 3

# Synthesis and Characterization of Mitochondria-Targeted Triphenylphosphonium Bolaamphiphiles

**Francesca Ceccacci, Simona Sennato, Edoardo Rossi, Raffaele Proroga, Stefano Sarti, Marco Diociaiuti, Stefano Casciardi, Valentina Mussi, Alessia Ciogli, Federico Bordi, Giovanna Mancini, and Cecilia Bombelli**

## Abstract

In this chapter we describe: (1) the procedure for the synthesis of four single chain bolaamphiphiles, displaying chains of 12, 16, 20 and 30 methylene units and triphenylphosphonium moieties as headgroups (**TPP1**-**TPP4**); (2) the methods used to characterize **TPP1**-**TPP4** spontaneous aggregation in aqueous solution. We illustrate the determination of Krafft point and cac by conductivity measurements and the procedures used to investigate dimensions, morphology, and stability by dynamic and dielectrophoretic laser light scattering, dialysis, transmission electron microscopy, and Raman spectroscopy measurements.

**Key words** Triphenylphosphonium bolaamphiphiles, Kolbe electrolysis, Thermomorphic electrolytic solution, U-shaped/extended conformation, Equilibrium systems, Kinetic traps

## 1 Introduction

Bolaamphiphiles are a class of surfactants displaying a peculiar molecular structure, characterized by two hydrophilic headgroups linked by one or more hydrophobic chains. This distinctive structural feature is responsible for the well-known bolaamphiphile polymorphism as it affects, as expected, the self-assembling of the monomers in aqueous solution, where a wide range of aggregates can spontaneously grow, from micelles and vesicles to nanotubes and nanoribbons. [1] In fact, if for all amphiphiles in general the aggregate morphology is controlled by the molecular structure of the monomer, in the case of bolaamphiphiles the connection between the two headgroups introduces an additional parameter that controls self-assembly, the monomer conformation. Inside the aggregate, bolaamphiphile monomers can assume an extended conformation or a U-shaped one, which can give rise, in principle, to a monolayer or a bilayer membrane respectively; actually, inside

Volkmar Weissig and Marvin Edeas (eds.), *Mitochondrial Medicine: Volume 1: Targeting Mitochondria*, Methods in Molecular Biology, vol. 2275, https://doi.org/10.1007/978-1-0716-1262-0_3,

the aggregates these two monomer arrangements can coexist, leading to intermediate organizations between pure monolayer and pure bilayer [2, 3]. Some bolaamphiphiles are able to form very stable monolayer vesicles, characterized by low solute permeability and stability to mechanical stress and elevated temperatures. In nature, their polymorphism contributes to confer unique characteristics to archaebacterial membranes, [4] while in the world of nanotechnology it makes bolaamphiphiles very attractive for the formulation of polymolecular aggregates or nanomaterials to be used in a wide range of applications: membrane models, sensing, electronics, imaging, drug and gene delivery [5]. In this respect, many synthetic bolaamphiphiles displaying specific moieties on the headgroups or in the chains have been prepared, in order to endow liposomes with specific properties, suitable for definite applications [6–9]. It is the case of dequalinium [10, 11] and triphenylphosphonium (**TPP**) cationic bolaamphiphiles for mitochondrial targeting. Many **TPP** bolaamphiphiles have been synthesized and have been shown to enter mitochondria, displaying at the same time some toxicity [12, 13]. Some investigations associate such toxicity with the crowding of bolaamphiphile cationic charge inside mitochondria, with consequent depolarization of organelle membrane; others studies correlate such toxicity mainly to bolaamphiphile ability in disrupting membrane [14]. In our opinion, in order to deeply understand the effects and, in general, the biological performances of a bolaamphiphile, the interplay between chemical structure, colloidal behavior, and physicochemical properties cannot be ignored. For this reason, we have decided to prepare and fully characterize four single chain bolaamphiphiles (**TPP1**-**TPP4**) displaying chains of 12, 16, 20 and 30 methylene units and triphenylphosphonium (**TPP**) moieties as headgroups. The colloidal behavior of these amphiphiles was investigated with the final aim of using them, in the near future, as mitochondria-targeted elements in liposome formulations.

The physicochemical features of **TPP1**-**TPP4** aggregates spontaneously formed in aqueous solution were studied by means of different techniques, in order to investigate different aspects of **TPP1**-**TPP4** self-assembly, from aggregation conditions parameters (cac, Krafft point) to morphology (dynamic and dielectrophoretic laser light scattering, TEM), stability (dialysis, dynamic and dielectrophoretic laser light scattering), and conformation of the monomer inside the aggregate (Raman spectroscopy). As the reader will realize in the following Subheadings 3 and 4, both obtaining pure **TPP** amphiphiles in acceptable yields and understanding the morphology of **TPP** aggregates are demanding and challenging tasks, especially in the case of longer chains. For this reason, the use of many techniques and experimental accuracy is required as well as the resort to some expedients.

## 2 Materials

### 2.1 Synthesis of Triphenylphosphonium Bolaamphiphiles TPP1-TPP4

1. 1,16-dihydroxyhexadecane.
2. $PBr_3$.
3. $NaHCO_3$.
4. $Na_2SO_4$.
5. Electrolytic solution: mix 80 mL of $CH_3CN$, 40 mL of $CH_3OH$, and 40 mL of Pyridine, then add KOH (240 mg), which slowly solubilizes, finally add 80 mL of cyclohexane. At room temperature two phases are present, at 311 K the mixture turns to one phase.
6. Kolbe electrolysis apparatus; electrodes: 25 mm × 50 mm Pt plates.
7. 11-bromoundecanoic acid.
8. 16-bromohexadecanoic acid.
9. RCA solution: Mix $H_2O$–$H_2O_2$ 30%–$NH_3$ 33% (5:1:1 v/v), heat to 75 °C. The Pt-plates are immersed in the hot solution and left there until they turn sleek (about 15 min). Let the solution cool down to room temperature, take the Pt-plates and wash them thoroughly with $H_2O_{dd}$ (*see* **Note 1**).
10. 1,12-dibromododecane.

### 2.2 Chromatography of Tripheny-lphosphonium Bolaamphiphiles TPP1-TPP4

1. The chromatographic system was a Shimadzu Nexera UHPLC LC-30A (Shimadzu, Milan, Italy), equipped with a SPD-M20A photodiode array detector (2.5 μL detector flow cell volume; filter time constant of 0.002 s and data collection rate of 100 Hz).
2. Column inlet (450 mm × 0.13 mm ID) and outlet (1040 mm × 0.13 mm ID) vipers were used, producing an extra column volume of 20 μL (*see* **Note 2**).
3. UHPLC columns: Titan™ C18 column (100 × 2.1 mm ID, 1.9 μm, 80 Å, Supelco) and Ascentis® Express C18 column (150 × 2.1 mm ID, 2.7 μm Sigma).
4. Eluents for **TPP1**-**TPP3**: (A) $H_2O/CH_3CN$ 90/10 + 20 mM $NH_4OAc$ and (B) $CH_3OH/CH_3CN/H_2O$ 50/40/10 + 20 mM $NH_4OAc$ (*see* **Notes 3** and **4**).
5. Eluents for **TPP4**: (A) $H_2O/CH_3CN$ 90/10 + 20 mM $NH_4OAc$ and (B) $CH_3OH/CH_3CN$ 50/50 + 20 mM $NH_4OAc$ (*see* **Notes 3** and **4**).

### 2.3 Conductivity Experiments on Bolaamphiphiles TPP1-TPP4

Conductivity measurements were carried out on a Hanna conductometer, HI-9932, equipped with a jacketed cell (5 cm × 11 cm-internal diameter and height), maintained at the desired temperature by a thermostatting apparatus.

### 2.4 Dialysis Experiments on Aqueous Solutions of TPP1-TPP4 Above the cac

1. Activation of dialysis tubing cellulose membrane: the membrane contains glycerol and sulfur compounds that must be removed before use by the following procedure. Wash the tube in running water for 3–4 h, paying attention to rinse out also the inside of the tube. Then immerse the tube in a 0.3% (w/v) solution of sodium sulfide at 80 °C for 1 min. Rinse with hot water (60 °C) for 2 min, acidify with a 0.2% (v/v) solution of sulfuric acid, and rinse again with hot water to remove the acid.
2. UV-vis measurements were carried out on a Cary 300 UV–vis double beam spectrophotometer, in a quartz cuvette of 1 cm path length.

### 2.5 Dynamic and Dielectrophoretic Light Scattering (DLS, DELS) Measurements

Dynamic and Dielectrophoretic light scattering (DLS, DELS) measurements were performed by NanoZetasizer apparatus (Malvern, UK), equipped with a 4 mW HeNe laser source employing a backscattering configuration and a thermostatted cell-holder. Disposable 2.5 mL polystyrene cuvette with 1 cm path length have been used for DLS measurements, U-shaped disposable cuvettes (model DTS 1070) have been used for DELS measurements.

### 2.6 Transmission Electron Microscopy (TEM)

1. TEM measurements were carried out by both a Zeiss 902 microscope, operating at 80 kV, and TECNAI 12 G2 Twin FEI microscope, operating at 120 kV. Images were acquired by a digital charge-coupled device camera, model Proscan (Proscan Elektronische Systeme, Lagerlechfeld, Germany) HSC2 (1024 × 1024 pixels), thermostatted by a Peltier cooler in the Zeiss instrument and by a slow-scan charge coupled device camera (Gatan 794 IF) in the FEI instrument.
2. Stain solution: phosphotungstic acid aqueous solution 2% w/v buffered at pH 7.40 with NaOH.

### 2.7 Raman Characterization of Tripheny-lphosphonium Bolaamphiphiles TPP1-TPP4

Raman measurements were realized with a DXR Thermo Fisher Scientific Raman Microscope, with a 532 nm excitation, 10 mW power and a long-distance 50× objective, with each spectrum resulting from 5 s acquisition time and 100 accumulations.

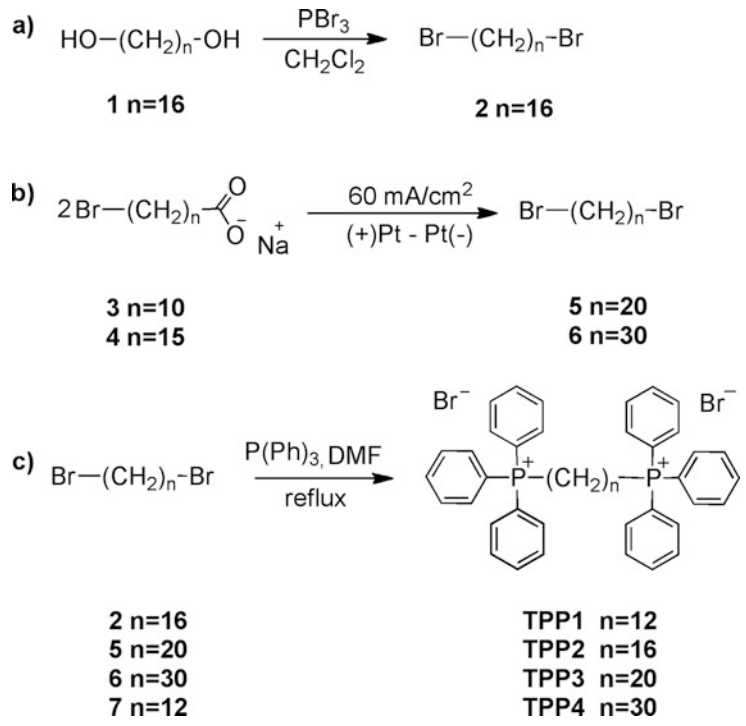


**Scheme 1** Synthetic pathway for the preparation of bolaamphiphiles **TPP1-TPP4**

## 3 Methods

### *3.1 Synthesis of Tripheny-lphosphonium Bolaamphiphiles TPP1-TPP4*

Synthetic pathway for the preparation of bolaamphiphiles **TPP1-TPP4** is depicted in Scheme 1.

#### *3.1.1 1,16-Dibromohexadecane*

1. Dissolve 1.0 g of 1,16-dihydroxyhexadecane **1** in 9 mL of anhydrous $CH_2Cl_2$.
2. When the solution is clear, add 0.68 g of $PBr_3$ under inert atmosphere at 0 °C. Keep the solution under stirring at room temperature for 18 h.
3. Monitor the reaction course by TLC (TLC: $Et_2O$–hexane = 9:1 to see the product; $Et_2O$ to see the diol).
4. Workup: neutralize the reaction solution with $NaHCO_3$ sat. and wash the aqueous phase with $CH_2Cl_2$ (3 × 50 mL). Collect the organic phases, wash them with brine, dry over $Na_2SO_4$ and filter. Remove the solvent under reduced pressure to obtain the crude product as brown viscous oil. Purification of the crude product by chromatography (silica, hexane, crude product/silica = 1:40) yields 0.64 g (1.6 mmol, 43%) of **2** as an off-white solid.

**Fig. 1** Electrolytic solution in the electrolytic cell: (**a**) above the switching temperature is monophasic; (**b**) below the switching temperature is biphasic (picture taken at the end of the reaction)

$^{1}$H-NMR ($CDCl_3$) ppm: 3.40 (4H, t, $J_{H-H} = 7.0$ Hz, $H_\alpha$); 1.84 (4H, q, $J_{H-H} = 7.0$ Hz, $H_\beta$); 1.50–1.10 (24H, m).

$^{13}$C-NMR ($CDCl_3$) ppm: 34.1; 32.9; 29.7; 29.6; 29.5; 29.4, 28.8; 28.2.

GC-MS: 55 (100); 69 (80); 83 (50); 97 (40); 135 (45); 149 (10); 384 (1).

*3.1.2 1,20-Dibromoeicosane* ***5***

1. Pour 240 mL of the electrolytic solution in the electrolytic cell, add 2.1 g (8.1 mmol) of 11-bromoundecanoic acid **3** and heat to 318 K to obtain a monophasic system (*see* **Note 5**) (Fig. 1).
2. When the acid is completely dissolved and only one phase is present, run the electrolysis at 318 K, under 0.8 A, for 40 min (TLC: hexane to see the product, RF 0.53; $Et_2O$–hexane = 8:2 to see the acid) (*see* **Notes 6** and **7**). Cool the solution to room temperature to reobtain a biphasic system. Wash the upper cyclohexanic phase with 1 M HCl, (*see* **Note 8**) with brine, dry over $Na_2SO_4$, and filter. Finally concentrate the solution under reduced pressure to obtain the crude product as a yellow solid (*see* **Note 9**). Purification of the residue is made by chromatography (silica, hexane, crude product/silica = 1:100) and yields 1.2 g of product **5** (white powder, 65% yield).

   $^{1}$H-NMR ($CDCl_3$) ppm: 3.39 (4H, t, $CH_2$ α); 1.84 (4H, q, $CH_2$ β); 1.41–1.24 (32H, om).

   $^{13}$C-NMR ($CDCl_3$) ppm: 33.9; 32.7; 29.5; 29.5; 29.4; 29.4; 29.3; 28.6; 28.0.

### 3.1.3 1,30-Dibromotricontane **6**

1. Pour 240 mL of the electrolytic solution in the electrolytic cell, add 0.48 g (1.4 mmol) of 16-bromohexadecanoic acid **4** and heat to 327 K to obtain a monophasic system (*see* **Note 5**) (Fig. 1).
2. When the acid is completely dissolved and only one phase is present, run the electrolysis at 327 K, under 0.8 A for 20 min (TLC: hexane to see the product, RF 0.45; $Et_2O$–hexane = 9:1 to see the acid) (*see* **Notes 6** and **7**). Cool the solution to room temperature to reobtain a biphasic system and concentrate the upper cyclohexanic phase under reduced pressure to obtain the crude product as yellowish solid. Purification of the residue is made by chromatography (silica, hexane, crude product/silica = 1:100) to obtain 0.16 g of product **6** (white powder, 38% yield).

   $^1$H-NMR ($\delta CDCl_3$, 300 MHz) ppm: 3.41 (4H, t, $J_{H-H}$ = 7 Hz, $CH_2$ α); 1.85 (4H, q, $J_{H-H}$ = 6.7 Hz, $CH_2$ β); 1.41–1.24 (52H, om, aliphatic).

   $^{13}$C-NMR ($\delta CDCl_3$, 75.5 MHz) ppm: 34.2; 32.9; 29.8; 29.7; 29.6; 29.5; 28.9; 28.3.
3. Clean the Pt-Plates with RCA solution.

### 3.1.4 General Procedure for the Quaternization Reaction to Achieve ***TPP1-TPP4***

1. Dissolve 2.2 mmol of α,ω-dibromoalkane in 10 mL of DMF and add 1.5 g (5.7 mmol) of $PPh_3$ under inert atmosphere, at room temperature.
2. Keep the resulting solution under stirring for 4 h at 393 K (TLC: hexane to see the reagents; EtOH–$CH_2Cl_2$ = 9:1 to see the product), then cool and concentrate it under reduced pressure to obtain a viscous brown oil.
3. Add $CH_3OH$ to the crude product and concentrate the resulting solution under reduced pressure. Repeat the procedure twice and then keep the residue under high vacuum to completely remove DMF (*see* **Note 10**). Dissolve again the crude product in $CH_3OH$ and add *cold* $Et_2O$. After stirring the mixture, two phases separate, an upper ethereal one and a brown oil. Remove the ethereal phase and wash the oil again with cold $Et_2O$ until $PPh_3$ is completely removed (check by TLC: hexane). Dry the oil under reduced pressure and then wash it with cold $Et_2O$, under sonication. Remove $Et_2O$, dry again, then wash with hexane under sonication. Remove the hexane and dry again under reduced pressure to obtain the product as a white powder (*see* **Note 11**).
4. Dodecane-1,12-diylbis(triphenylphosphonium)bromide **TPP1** (91%) $^1$H-NMR($CD_3OD$) ppm: 7.90–7.75 (30H, om, ar); 3.50–3.35 (4H, m, $H_\alpha$); 1.83–1.42 (8H, m, $H_\beta$, $H_\gamma$); 1.40–1.15 (12H, om). $^{13}$C-NMR($CD_3OD$) ppm: 136.2 (d, $J_{C-P}$ = 2.9 Hz); 134.8 (d, $J_{C-P}$ = 9.9 Hz); 131.5 (d, $J_{C-P}$ = 12.5 Hz); 120.0 (d, $J_{C-P}$ = 86.2 Hz); 31.6 (d, $J_{C-}$

$_P$ = 16.0 Hz); 30.5; 30.3; 29.9; 23.5 (d, $J_{C-P}$ = 4.4 Hz); 22.7 (d, $J_{C-P}$ = 50.9 Hz). *FIA-MS-(ESI)*: 346.25 *m/z* $[C_{48}H_{54}P_2]^{2+}$.

5. Hexadecane-1,16-diylbis(triphenylphosphonium) bromide **TPP2** (90%) $^1$H-NMR ($CD_3OD$) ppm: 7.92–7.75 (30H, om, ar); 3.50–3.36 (4H, m, $H_\alpha$), 1.75–1.48 (8H, om, $CH_2$ β, γ); 1.45–1.17 (20H, om). $^{13}$C-NMR($CD_3OD$) ppm: 134.9 (d, $J_{C-P}$ = 3.0 Hz); 133.5 ($J_{C-P}$ = 10.0 Hz); 130.1 (d, $J_{C-P}$ = 12.5 Hz); 118.6 (d, $J_{C-P}$ = 86.3 Hz); 30.2 (d, $C_\gamma$, $J_{C-P}$ = 16.1 Hz); 29.4; 29.2; 29.0; 28.6; 22.2 (d, $C_\beta$, $J_{C-P}$ = 4.4 Hz); 21.3 (d, $C_\alpha$, $J_{C-P}$ = 50.9 Hz). *FIA-MS-(ESI)*: 374.42 *m/z* $[C_{52}H_{62}P_2]^{2+}$.
6. Eicosane-1,20-diylbis(triphenylphosphonium) bromide **TTP3** (60%) $^1$H-NMR($CD_3OD$) ppm: 7.89–7.74 (30H, m); 3.46–3.31 (4H, m, $CH_2\alpha$); 1.82–1.58 (8H, om, $CH_2$ β, γ); 1.35–1.25 (28H, om). $^{13}$C-NMR($CD_3OD$) ppm: 136.2 (d, $J_{C-P}$ = 2.8 Hz); 134.8 (d, $J_{C-P}$ = 10 Hz); 131.5 (d, $J_{C-P}$ = 12 Hz); 120.0 (d, $J_{C-P}$ = 86 Hz); 31.6 (d, $J_{C-P}$ = 16 Hz); 30.8; 30.7; 30.5; 30.4; 29.9; 23.5 (d, $J_{C-P}$ = 7.5 Hz); 22.7 (d, $J_{C-P}$ = 51 Hz). *FIA-MS-(ESI)*: 402.50 *m/z* $[C_{56}H_{70}P_2]^{2+}$.
7. Tricontane-1,30-diylbis(triphenylphosphonium) bromide **TPP4** (40%) $^1$H-NMR (δ $CD_3OD$, 300 MHz) ppm: 8.98–7.68 (30H, m); 3.46–3.33 (4H, m); 1.78–1.45 (8H, m); 1.40–1.19 (48 H, m). $^{13}$C-NMR (δ $CD_3OD$, 75.5 MHz) ppm: 136.2 (d, $J_{C-P}$ = 2.9 Hz); 134.8 (d, $J_{C-P}$ = 10 Hz); 131.5 (d, $J_{C-P}$ = 12.5 Hz); 120.3 (d, $J_{C-P}$ = 90.6 Hz); 31.6 (d, $J_{C-P}$ = 16 Hz); 31.7; 31.5; 30.8; 30.7; 30.6; 30.4; 29.5; 25.4; 23.6 (d, $J_{C-P}$ = 7.5 Hz); 22.7 (d, $J_{C-P}$ = 52 Hz). *FIA-MS-(ESI)*: 472.58 *m/z* $[C_{66}H_{90}P_2]^{2+}$.

### 3.2 HPLC Analysis for TPP Bolaamphiphiles

#### 3.2.1 HPLC Analysis for TPP1-TPP3

1. Samples are dissolved in $CH_3OH$ (1 mg/mL c.a.).
2. Set column Titan™ C18 temperature at 30 °C (*see* **Note 12**).
3. Perform gradient elution: 0–7 min, 0% B, 7–17 min, 100% B; flow rate: 0.6 mL/min.
4. Set the photodiode array detector between 190 and 340 nm.
5. Perform the elaboration data at 254 nm.

#### 3.2.2 HPLC Analysis for TPP4

1. Sample is dissolved in $CH_3OH$ (1 mg/mL c.a.).
2. Set Ascentis® Express C18 column temperature at 30 °C (*see* **Note 12**).
3. Perform gradient elution: 0–10 min, 0% B, 10–15 min, 100% B; flow rate: 0.5 mL/min.
4. Set the photodiode array detector between 190 and 340 nm.
5. The elaboration data is performed at 214 nm.

## 3.3 Conductivity Experiments on Bolaamphiphiles TPP1-TPP4

### 3.3.1 Krafft Point of TPP1-TPP4

1. Make some preliminary evaluations by visual inspection to find a concentration condition of the amphiphile that is above the cac. To do this, dissolve in water an amount of the amphiphiles, add the amphiphile until you see foaming by shaking. If required, heat the solution to dissolve the powder and check if foam appears after shaking.
2. Prepare 20 mL of a solution at the concentration you have found, if necessary heat to obtain a clear solution, and pour it in the jacketed cell for conductivity experiments.
3. Keep the solution at 277 K overnight.
4. Check the solution: if it is clear after one night at 277 K, the Krafft temperature for that concentration of the amphiphile is below 277 K and the Krafft point as well; on the contrary, if some precipitate is present you can carry out the experiment for Krafft point and Krafft temperature determination by conductivity measurements (*see* **Note 13**).
5. Link the cell to the thermostatting apparatus, add a magnetic stirrer and insert the electrode in the cell. Keep the mixture under stirring and register conductivity at increasing temperature (Rate: 0.2 degree/min) (*see* **Note 14**).
6. When the Krafft point is reached, an abrupt increase in conductivity is observed, parallel to a sudden increase in the amphiphile solubility. Keep increasing the temperature to completely solubilize the precipitate. The temperature at which the solution becomes clear is the Krafft temperature for that concentration of amphiphile. After the precipitate is completely dissolved, keep increasing temperature for other 10°.
7. In the curve "conductivity vs. *T*," the point where the conductivity increases abruptly corresponds to the Krafft point whereas the Krafft temperature can be individuated by the last break. In Fig. 2, an example of Krafft point plot is reported.

### 3.3.2 Determination of the cac of TPP1-TPP4

1. Prepare a 10 mM ethanolic solution of **TPP** (*see* **Note 15**).
2. Add a magnetic stirrer and 20.0 mL of $H_2O_{dd}$ in the jacketed cell for conductivity experiments and then add the electrode, set the temperature of the thermostatting apparatus at 298 K.
3. Add, under stirring, small aliquots of the ethanolic solution to water and record conductivity (*see* **Note 16**).
4. Plot the values of "conductivity vs **TPP** concentration," the cac is the concentration corresponding to an abrupt reduction of the slope in the curve. The value of cac can be determined by the intersection between the curves before and after the change in slope (Fig. 3).

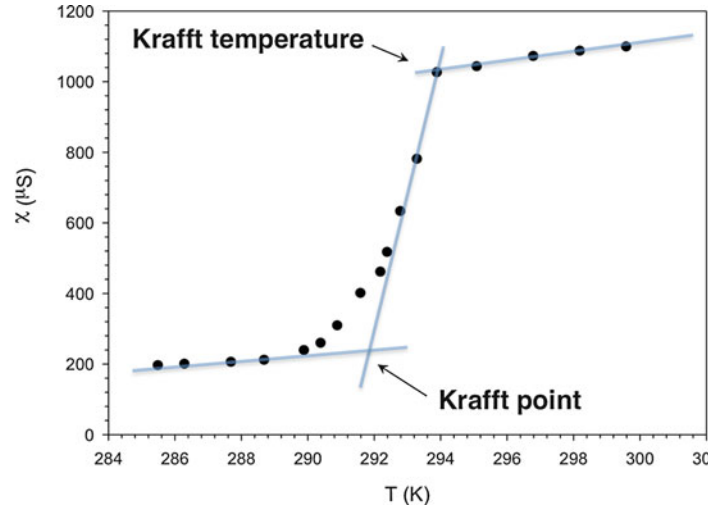


**Fig. 2** An example of plot for Krafft point determination by conductivity measurements

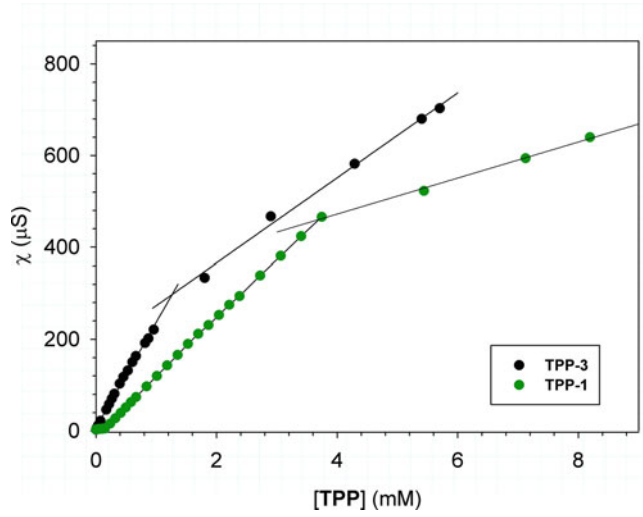


**Fig. 3** Examples of plot of conductivity vs [**TPP**] for cac measurement (black circle for **TPP1**, green circle for **TPP3**)

### *3.4 Dialysis Experiments on TPP1-TPP4*

1. Prepare 2 mL of a 10 mM solution of **TPP** in $H_2O_{dd}$ (*see* **Note 17**).
2. Close one end of an activated dialysis tubing cellulose membrane (7 × 3 cm) (*see* **Note 18**) by a tight knot, leaving a piece of tube of about 2 cm at the end of the tube.
3. Fill the tube with 1 mL of **TPP** solution, using a Pasteur pipette, and check for leakage, in case of leakage tie another knot. Finally, close the tube with another knot at the other end (*see* **Note 19**).

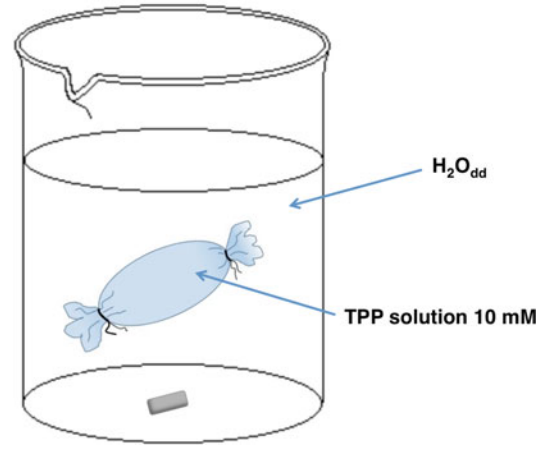


**Fig. 4** Representation of a dialysis system, with the dialysis tube immersed in $H_2O_{dd}$

4. Add 25 mL of $H_2O_{dd}$ and a magnetic stirrer in a beaker, and then immerse the dialysis tube (Fig. 4).
5. Dialyze against 25 mL of $H_2O_{dd}$, changing the external medium every 15 min for 1 h and maintaining the diffusate solution under stirring (*see* **Note 20**).
6. At the end of the dialysis, carefully cut the tube beneath one of the two knots, and recover **TPP** solution with a Pasteur pipette. Work above a beaker to avoid waste of solution in case the tube slips from your hand.
7. Determine **TPP** concentration in the sample by UV measurements, before and after dialysis (*see* **Note 21**).

### *3.5 DLS and DELS Measurements*

#### *3.5.1 Size Measurements*

1. Drop 1 mL of the 10 mM aqueous solutions of **TPP1**-**TPP4** in a 2.5 mL polystyrene cuvette with 1 cm optical path length with an Eppendorf pipette (single-channel, volume 1 mL).
2. Perform measurements with automatic selection of attenuation, position of the beam in the cell and duration of the measurements, so that the best condition in terms of signal will be determined by the software. Insert data of sample refractive index and solvent viscosity.
3. Fix the temperature and wait some minutes to allow thermal equilibration of the sample.
4. Check that the preliminary optimization procedure performed by the instrument at varying position of the laser beam from the cell wall, attenuation of the signal and acquisition time, is successful to get the highest amplitude of the measured correlogram.

**Table 1**
**Hydrodynamic size of the TPP samples obtained by General Purpose NNLS analysis**

| | Diameter[a,b] (nm) | Peak width (nm) |
|---|---|---|
| **TPP1** | 70<br>235 | 10<br>55 |
| **TPP2** | 90<br>500 | 10<br>80 |
| **TPP3** | 100<br>329 | 20<br>30 |
| **TPP4** | 200 | 60 |

[a]The average hydrodynamic diameters and the associated peak width of the size distribution have been obtained by NNLS intensity-weighted distribution analysis. Statistical errors are within 5%
[b]For **TPP1**-**TPP3** surfactants two distinct populations with different size are found. The population with the smallest size is the most abundant according to NNLS number-weighted analysis

5. Perform at least three repeated measurements for each sample (after the preparation and at different time intervals) to check the stability of the dispersion over time.
6. To determine the hydrodynamic size, the analysis software gives the possibility to consider two different fits of the correlation function: (1) a cumulant analysis [15] and (2) a distribution analysis by a General Purpose algorithm [16] (*see* **Note 22**). If a PDI index larger than 0.2 is observed, as in the case of aqueous solutions of **TPP1**-**TPP4**, consider that the cumulant method cannot be fully appropriate since it is not able to resolve the size distribution. Analyze data by the general-purpose algorithm implemented with NNLS inversion to determine the intensity-weighted size distribution of the various population of particles present in the sample. Data of the hydrodynamic size of the samples can be obtained by considering the value of the peak mean and the corresponding width of the intensity-weighted size distribution determined by General Purpose (NNLS) analysis (Table 1).
7. The whole histogram of the "intensity weighted" NNLS distribution for the **TPP1**-**TPP4** samples can be plotted as a function of the radius (Fig. 5).
8. To evaluate the relative proportion between the different populations, consider the % data obtained by the number-weighted size distribution.

*3.5.2 Zeta Potential Measurements*

1. Drop 850 μL of the 10 mM aqueous solutions of **TPP1**-**TPP4** in a U-cell DTS1070 for DELS measurement, with an Eppendorf pipette (single-channel, volume 1 mL). Pay attention to avoid air bubble in the cell and to fill the cell at the correct level, so that the electrodes are completely wetted.

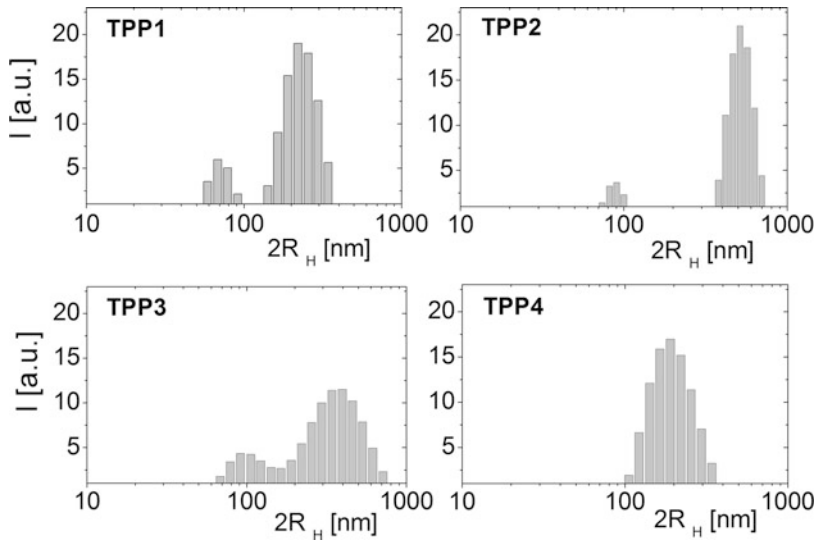


**Fig. 5** DLS intensity-weighed size distribution of **TPP1-TPP4** suspensions by dynamic light scattering (DLS)

2. Choose the automatic operation modality for performing measurements in order to let the instrument the best choice of Voltage parameter with respect to the conductivity of the sample. Choose the solvent used for **TPP1-TPP4** dispersions and insert data on viscosity and dielectric constant.
3. Fix the temperature and wait some minutes to allow thermal equilibration of the sample.
4. Check that the preliminary optimization procedure performed by the instrument at varying Voltage of the applied Electric field is successful to get the highest amplitude of the measured Phase Signal.
5. Perform at least three repeated measurements for each sample and pay attention to the mean $\zeta$-potential of each repeated measurement (*see* **Note 23**). Repeat measurements at different time intervals to check the stability of the dispersion over time.
6. To analyze data, consider the mean values of the $\zeta$-potential and the width of the $\zeta$-potential distribution averaged on the three repeated measurements and report them in a table, as shown in Table 2.

### *3.6 TEM*

1. Prepare the sample by depositing a 20 μL drop of the 10 mM aqueous solutions of **TPP1-TPP4** on a 300 mesh copper grid for electron microscopy, covered with a thin (about 20 nm) amorphous carbon film, by using an Eppendorf pipette (single-channel, volume 200 μL). In Fig. 6 are reported TEM images of **TPP1-TPP4** samples obtained by the procedure described.
2. Let the sample deposit on the grid and then remove the excess of solution by placing the grid on filter paper.

**Table 2**
**ζ-potential of the TPP samples obtained by DELS measurements**

| | ζ-Potential[a,b] (mV) | Peak width (mV) |
|---|---|---|
| **TPP1** | 40 | 8 |
| **TPP2** | 50 | 6 |
| **TPP3** | 57 | 7 |
| **TPP4** | 65 | 8 |

[a]Statistical errors are within 5%
[b]For **TPP1**-**TPP3** surfactants two distinct populations with different size are found. The average ζ-potential and the width of the corresponding distribution can be attributed to the population with the smallest size, which is the most abundant according to NNLS number-weighted analysis

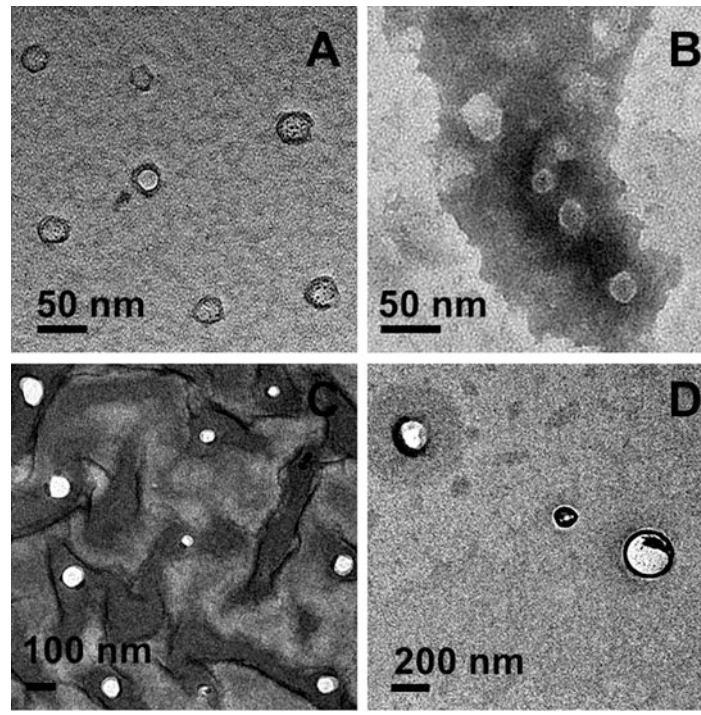


**Fig. 6** TEM images obtained on **TPP1-TPP4** samples by negative PTA staining. Note that the magnification used to acquire the images is different and in each image is shown the corresponding bar of length

3. Stain the sample by depositing 20 μL of stain solution and remove the excess by filter paper.
4. On a single grid you could find a lot of different types of aggregates, differing in nature, size and density because sample deposition is a very delicate and empirical process. For this reason, it is important to acquire many images from the same

grid in order to point out the most representative and statistically significant morphology of the analyzed sample.

5. To enhance contrast and resolution, acquire images by using the "electron energy loss filter" (EFTEM) (*see* **Note 24**).
6. Perform Image analysis and quantification by the digital image analyzer analy-SIS 3.0 (SIS GmbH, Germany), which gives the possibility to enhance the contrast and sharpness of the acquired images and perform morphological quantification and statistics. To avoid systematic errors, perform dimensional measurements after a careful magnification calibration of the whole imaging system on the basis of reference standards.

### *3.7 Raman Analysis of Bolaphosphonium TPP1-TPP4 Solutions*

1. Drop 100 μL of the 10 mM aqueous solutions of **TPP1**-**TPP4** on an aluminum covered glass slide with an Eppendorf pipette (single-channel, volume 200 μL (*see* **Note 25**).
2. Perform Raman measurements with a 532 nm excitation, 10 mW power, a long-distance 50× objective, and so that each spectrum results from 5 s acquisition time and 100 accumulations. A typical spectrum corresponding to the sample **TPP3** is presented in Fig. 7. The inset shows a magnification of the spectral region around 2900 $cm^{-1}$ containing important contributions associated to the packing and conformation properties of the samples.

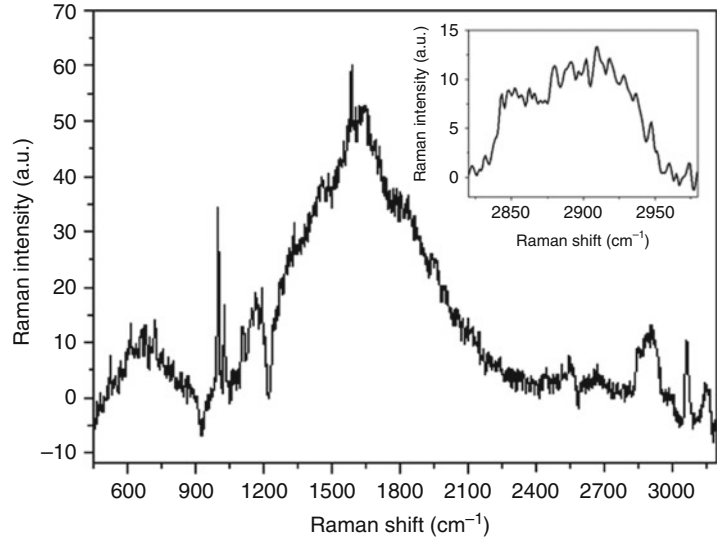


**Fig. 7** A typical Raman spectrum corresponding to the sample **TPP3**, collected by the descripted apparatus and with the indicated acquisition parameters. The inset shows a magnification of the spectral region around 2900 $cm^{-1}$ containing important contributions associated to the packing and conformation properties of the samples

3. To collect the spectra, focus the laser spot on the surface of the aluminum covered slide.
4. Before analyzing the data, subtract the baseline to each spectrum.
5. To compare the spectra, execute multipeak fitting by considering Lorentz band shapes and three main spectral contributions in the spectral region corresponding to C–H stretching vibrations from 2820 to 2980 $cm^{-1}$ [17–20].

## 4 Notes

1. **WARNING**!! To clean plates with RCA solution, use the safety equipment and follow all the safety procedures: work under a hood!
2. The reduced extra-column volume notably increases the efficiency of columns in the UHPLC regime.
3. The small amount of acetonitrile in eluent A minimize the growth of mold.
4. The buffer concentration was calculated on the total volume of each eluent. When you are preparing the eluent, dissolve the buffer in water and then add the organic counterpart.
5. To perform this reaction, a thermomorphic system is required, composed of two phases (one is $CH_3OH/CH_3CN$/Pyridine, the other is cyclohexane) [21]. Such biphasic system becomes monophasic by heating and the temperature at which this change is observed is the switching temperature. For the system $CH_3OH/CH_3CN$/Pyridine and cyclohexane, the switching temperature is 311 K. When a compound is dissolved in the mixture, the switching temperature increases. Therefore, the switching temperature increases from 311 to 318 K when **3** is dissolved in the mixture whereas in the case of **4**, the switching temperature becomes 327 K.
6. Note that a current density of 60 $mA/cm^2$ is required for the reaction to occur. So find the proper current that gives the required current density according to the surface dimension of the Pt-plates.
7. Check the reaction by TLC after 20 min, if you see traces of the reagent (even more than traces) stop the reaction. Remember that longer reaction times result in a yield decrease! This is due mainly to dehalogenation side reactions, both on the reagent and the product [22].
8. This washing serves to remove pyridine from cyclohexanic phase.

9. Check the $CH_3OH/CH_3CN$/Pyridine solution to see if the product is present and, in case, wash the solution with cyclohexane to extract the product.
10. At this point, the product should appear as a sticky foam. If it is still an oil, repeat the procedure once again.
11. The procedure of washing with $Et_2O$ and hexane helps in removing the impurities (mainly $PPh_3$) and in obtaining the product as powder. When $Et_2O$ is added to the oil, a precipitation of the product may occur, but this is not sufficient to have a pure product. Therefore, in case of precipitation, it is better to add a small volume of methanol to dissolve the precipitate and wash the methanolic solution with $Et_2O$. As the purification proceeds, the residue obtained after removal of the solvent becomes a foam. To render this foam a powder, it is possible to wash it again with cold $Et_2O$, sonicate the mixture, remove $Et_2O$ and dry again under reduced pressure. A final step with hexane can be useful (but sometimes not necessary) to have the product as a white powder.
12. Temperature between 303 and 308 K helps to reduce the peak bandwidth. **WARNING!!** The temperature to be used is related to the stability of the product!
13. Aggregates are present in solution if such solution is in the region comprised between the Krafft boundary and cac curve (Fig. 8).

    For the determination of the temperature of Krafft point, one of the most used techniques is conductivity [23–27].

    The general protocol for the sample preparation of this experiment is the following: to a proper amount of surfactant, a proper volume of Milli-Q water is added and the mixture is heated to obtain a clear solution above the cac (a 10 mM clear

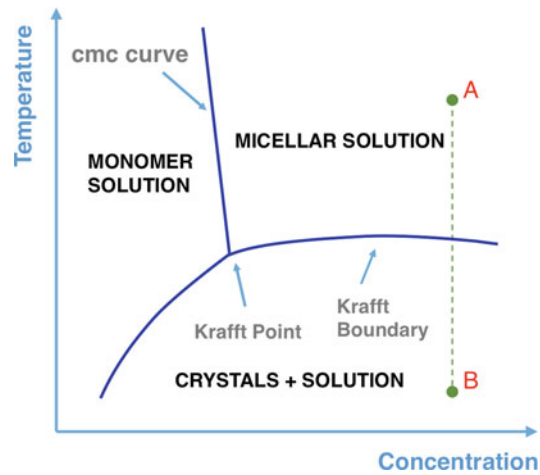


**Fig. 8** Phase diagram temperature vs. concentration of a common surfactant

solution can be described, as an example, by point A in Fig. 8); the solution is then kept at 277 K overnight before starting measurements. To perform the experiment, you need to have an initial solution with a precipitate at 277 K, the temperature from which you start the experiment [28]. The solution with the precipitate can be represented by point B in Fig. 8. If after 24 h at 277 K the solution is clear, then the Krafft point of the surfactant is below this temperature and you are not able to determine it precisely because the conductometer works in the range 0–333 K. This is the case of **TPP1**-**TPP4** bolaamphiphiles. Therefore, for amphiphile solutions above the cac that are clear at 277 K, usually a definite Krafft point is not reported, since it is operatively difficult to determine it, but rather it is indicated that the Krafft point is <277 K [29].

14. Although the rate used is approximately 0.2 degree/min, before increasing the temperature verify that the conductivity value is stable because the solubilization of the amphiphile may require more time.

15. When you deal with an amphiphile whose behavior is not known and not easily predictable (i.e., you do not know if it gives micelles or liposomes in aqueous solution), the procedure to determine the cac is slightly different from the general one. In the general approach, a concentrated aqueous solution of surfactant is gradually added to water and conductivity is recorded at increasing surfactant concentration in the cell. In the case of amphiphiles that give rise to liposome in solution, it is not possible to use a water stock solution of surfactant. In this case, in fact, the stock solution will be made of liposomes, which generally are not equilibrium system; thus, once they are formed, they do not break upon dilution. Imagining of performing the conductivity experiment with such a solution, upon adding the liposome solution, liposomes will simply be diluted in water, and the conductivity registered at increasing amphiphile concentration would be simply the conductivity of liposome at increasing concentration.

    For this reason, the amphiphile stock solution is made in ethanol, a solvent in which, in principle, the amphiphile should not aggregate (this assumption must be verified by DLS before carrying out the conductivity experiment). However, care must be taken in the choice of the concentration of the stock solution: it should be such that at the end of the experiment the total volume of ethanol added must not exceed 3% of the total volume of the solution. The presence of a larger amount of ethanol in solution would in fact influence the aggregation of the amphiphile, thus affecting the final value of cac.

16. Choose the concentration of **TPP** ethanolic solution and the proper volumes for aliquot additions in order to explore the concentration range $10^{-6}$ to $10^{-2}$ M.
17. In order to obtain a clear solution above the cac, the mixture of **TPP** and water was heated.
18. Molecular weight cut-off = 14,000, proteins of molecular weight 12,000 or greater will be retained. Tube external surface 10 $cm^2$.
19. To avoid leaking of the solution from the tube, additional closure clamps just above the knots are also recommended.
20. Stirring will allow dialysis tube to slowly float; the floating should not be too quick in order to avoid membrane disruption.
21. UV spectra were recorded after proper dilution of the samples (about 1:70).
22. Cumulant and distribution analysis allow determining the mean value (1) or the distribution (2) of the Diffusion coefficient $D$, respectively. Thanks to the Stokes–Einstein relationship $RH = kBT/6\pi\eta D$, where $kB$ is the Boltzmann's constant, $T$ is the temperature, and $\eta$ the solvent viscosity, it is possible to convert the average value or the distribution of the diffusion coefficients $D$ of the particles into the mean value or the distribution of the effective hydrodynamic radii, RH, respectively. In detail, by the cumulant analysis the logarithm of the correlation function versus delay time is fitted with a linear regression. The slope leads to a mean particle diameter ($z$-average) size and the curvature leads to a parameter called the second cumulant or polydispersity (PDI) which represents an average parameter of sample homogeneity.
23. If a systematic deviation occurs, it may be the sign of sample heating and damage, whose extent is larger for highly conductive samples. In this case, decrease the number of subruns performed in each measurement and insert a pause between the repeated measurements.
24. Energy filtering allows the suppression of the contribution of inelastic scattering that typically occurs when the sample is mainly made of light elements as in the case of biological samples. Such filtering reduces chromatic aberration [30] which is usually the main factor in determining the maximum attainable resolution in a conventional TEM, when working with soft samples [31].
25. Due to the low concentration of the investigated samples, the dropping of the aqueous solutions of **TPP1**-**TPP4** on an adequate substrate is preferred for the Raman measurements with respect to the use of a quartz cuvette because it allows to

better focus the excitation laser and to acquire the spectral signal with higher efficiency.

## Acknowledgments

We are grateful to Alessandro Latini (Sapienza University of Rome) for his highly qualified advice on electrolysis; we are also grateful to Roberto Moscardelli (CNR-ISB) and Enrico Rossi (CNR-ISB) for technical support.

### References

1. Shimizu T, Masuda M, Minamikawa H (2005) Supramolecular nanotube architectures based on amphiphilic molecules. Chem Rev 105:1401–1444
2. Lee KP, Papahadjopoulos-Sternberg B, Wong D, Waigh RD, Watson DG, Gray AI, McCarthy D, McAllister M, Schätzlein AG, Uchegbu IF (2004) Highly hydrophilic fused aggregates (microsponges) from a C12 spermine bolaamphiphile. J Phys Chem B 108:8129–8135
3. Di Meglio C, Rananavare SB, Svenson S, Thompson DH (2000) Bolaamphiphilic phosphocholines: structure and phase behavior in aqueous media. Langmuir 16:128–133
4. Siliakus MF, van der Oost J, Kengen SWM (2017) Adaptations of archaeal and bacterial membranes to variations in temperature, pH and pressure. Extremophiles 21:651–670
5. Nurajea N, Baib H, Suc K (2013) Bolaamphiphilic molecules: assembly and applications. Prog Polym Sci 38:302–343
6. Lainè C, Mornet E, Lemiègre L, Montier T, Cammas-Marion S, Neveu C, Carmoy N, Lehn P, Benvegnu T (2008) Folate-equipped pegylated archaeal lipid derivatives: synthesis and transfection properties. Chem Eur J 14:8330–8340
7. Brard M, Lainè C, Rethore G, Laurent I, Neveu C, Lemiègre L, Benvegnu T (2007) Synthesis of archaeal bipolar lipid analogues: a way to versatile drug/gene delivery systems. J Org Chem 2:8267–8279
8. Ray S, Das AK, Banerjee A (2007) pH-responsive, bolaamphiphile-based smart metallo-hydrogels as potential dye-adsorbing agents, water purifier, and vitamin B12 carrier. Chem Mater 19:1633–1639
9. Dakwar GR, Abu Hammad I, Popov M, Linder C, Grinberg S, Hedelman E (2012) Delivery of proteins to the brain by bolaamphiphilic nano-sized vesicles. J Control Release 160:315–321
10. Weissing V (2011) From serendipity to mitochondria-targeted nanocarriers. PharmRes 28:2657–2668
11. Men Y, Wang X, Li R, Zhang Y, Tian W, Yao H, Ju R, Ying X, Zhou J, Li N, Zhang L, Yu Y, Lu W (2011) The efficacy of mitochondrial targeting antiresistant epirubicin liposomes in treating resistant leukemia in animals. Int J Nanomedicine 6:3125–3137
12. Ross MF, Da Ros T, Blaikie FH, Prime TA, Porteous CM, Severina II, Skulachev VP, Kjaergaard HG, Smith RAJ, Murphy MP (2006) Accumulation of lipophilic dications by mitochondria and cells. Biochem J 400:199–208
13. Severina II, Vyssokikh MY, Pustovidko AV, Simonyan RA, Rokitskaya TI, Skulachev VP (2007) Effects of lipophilic dications on planar bilayer phospholipid membrane and mitochondria. Biochim Biophys Acta 1767:1164–1168
14. Benien P, Solomon MA, Nguyen P, Sheehan EM, Mehanna AS, D'Souza GGM (2016) Hydrophobized triphenyl phosphonium derivatives for the preparation of mitochondriotropic liposomes: choice of hydrophobic anchor influences cytotoxicity but not mitochondriotropic effect. J Liposome Res 26:21–27
15. Koppel DE (1972) Analysis of macromolecular polydispersity in intensity correlation spectroscopy: the method of cumulants. J Chem Phys 57:4814–4820
16. Lawson CL, Morrison ID (1974) Solving least squares problems. A FORTRAN Program and Subroutine Called NNLS. Prentice-Hall, Englewood Cliffs, NJ
17. Gaber BP, Yager P, Peticolas WL (1978) Interpretation of biomembrane structure by Raman difference spectroscopy. Nature of the

endothermic transitions in phosphatidylcholines. Biophys J 21:161–176

18. Snyder RG, Scherer JR, Gaber BP (1980) Effects of chain packing and chain mobility on the Raman spectra of biomembranes. Biochim Biophys Acta 601:47–53
19. Gaber BP (1977) On the quantitative interpretation of biomembrane structure by Raman spectroscopy. Biochim Biophys Acta 465:260–274
20. Yellin N, Levin IW (1977) Hydrocarbon chain disorder in lipid bilayers. Temperature dependent Raman spectra of 1,2-diacyl phosphatidylcholine-water gels. Biochim Biophys Acta 489:177–190
21. Okada Y, Kamimura K, Chiba K (2012) Cycloalkane-based thermomorphic systems for organic electrochemistry:an application to Kolbe-coupling. Tetrahedron 68:5857–5862
22. Wiebe A, Gieshoff T, Mçhle S, Rodrigo E, Zirbes M, Waldvogel SR (2018) Electrifying organic synthesis. Angew Chem Int Ed 57:5594–5619
23. Bello C, Bombelli C, Borocci S, di Profio P, Mancini G (2006) Role of the spacer stereochemistry on the aggregation properties of cationic Gemini surfactants. Langmuir 22:9333–9338
24. Andreani R, Bombelli C, Borocci S, Lah J, Mancini G, Paolo Mencarelli P, Vesnaverc G, Villani C (2004) New biphenylic derivatives: synthesis, characterisation and enantiodiscrimination in chiral aggregates. Tetrahedron Asymmetry 15:987–994
25. Bombelli C, Bordi F, Borocci S, Diociaiuti M, Lettieri R, Limongelli F, Mancini G, Sennato S (2011) New pyrenyl fluorescent amphiphiles: synthesis and aggregation properties. Soft Matter 7:8525
26. Bartoloni A, Bombelli C, Borocci S, Bonicelli MG, Galantini L, Giansanti L, Ierino M, Mancini G, Muschietti A, Sperduto C (2013) Synthesis and physicochemical characterization of pyrrolidinium based surfactants. J Colloid Interface Sci 392:297–303
27. Borocci S, Ceccacci F, Galantini L, Mancini G, Monti D, Scipioni A, Venanzi M (2003) Deracemization of an axially chiral biphenylic derivative as a tool for investigating chiral recognition in self-assemblies. Chirality 15:441–447
28. Bales BL, Benrraou M, Zana R (2002) Krafft temperature and micelle ionization of aqueous solutions of cesium dodecyl sulfate. J Phys Chem B 106:9033–9035
29. Sakai T, Ikoshi R, Toshida N, Kagaya M (2013) Thermodynamically stable vesicle formation and vesicle-to-micelle transition of single-tailed anionic surfactant in water. J Phys Chem B 117:5081–5089
30. Egerton RF (1986) Electron energy loss spectroscopy. Plenum Press, New York
31. Diociaiuti M (2006) Electron energy loss spectroscopy microanalysis and imaging in the transmission electron microscope: example of biological applications. J Electron Spectrosc Relat Phenom 143:189–203

# Chapter 4

# Synthesis and Evaluation of $^{18}$F-Labeled Fluoroalkyl Triphenylphosphonium Salts as Mitochondrial Voltage Sensors in PET Myocardial Imaging

**Dong-Yeon Kim and Jung-Joon Min**

## Abstract

We have previously reported that radiolabeled phosphonium cations accumulate in the mitochondria down a transmembrane potential gradient. We present an optimized procedure for synthesis of three [$^{18}$F]-labeled fluoroalkyl triphenylphosphonium salts ([$^{18}$F]FATPs) via two-step simple nucleophilic substitution reactions to develop new myocardial imaging agents for positron emission tomography (PET). The total reaction time of [$^{18}$F]FATPs was within 60 min, and the overall decay-corrected radiochemical yield was approximately 15–30% (decay corrected). Radiochemical purity was >98% according to analytical high-performance liquid chromatography (HPLC). The specific activity of [$^{18}$F]FATPs was >6.1 TBq/μmol. The [$^{18}$F]FATPs exhibited higher first-pass extraction fraction values in isolated heart, higher uptake in the myocardium, and a more rapid clearance from the liver and lung than [$^{13}$N]$NH_3$ in normal rats. The images from rats with an occluded left coronary artery demonstrated sharply defined myocardial defects in the corresponding area of the myocardium. This imaging technology may enable high-throughput, multiple studies daily and wide distribution of PET myocardial studies in clinic.

**Key words** Myocardium, Imaging, Mitochondrial voltage sensors, Positron Emission Tomography, Triphenylphosphonium

## 1 Introduction

Since the 1970s, single-photon emission computed tomography (SPECT) has been the demonstrably superior method for detecting myocardial abnormalities, and the clinical value of nuclear cardiology continues to evolve [1, 2]. SPECT technologies using $^{201}$Tl, $^{99m}$Tc-sestamibi, and $^{99m}$Tc-tetrofosmin are the mainstay of myocardial perfusion imaging tests in the diagnosis of coronary artery disease (CAD) and assessment of myocardial infarction (MI) [3, 4]. However, the technical limitations of photon-attenuation correction and suboptimal spread of radioactivity in organs adjacent to the heart may compromise the delineation of small lesions and

Volkmar Weissig and Marvin Edeas (eds.), *Mitochondrial Medicine: Volume 1: Targeting Mitochondria*, Methods in Molecular Biology, vol. 2275, https://doi.org/10.1007/978-1-0716-1262-0_4,

limit the diagnostic accuracy of SPECT [4]. Positron emission tomography (PET) has several technical merits over SPECT, such as higher spatial resolution and more accurate attenuation correction. Because of these advantages, PET can accurately diagnose the presence of small lesions in CAD and enables quantitative measurement of myocardial tracer uptake [5]. However, the short half-life of PET tracers that are currently used for myocardial imaging, including [$^{13}$N]$NH_3$ (half-life: 9.97 min), $^{82}$Rb (1.27 min), and [$^{15}$O]$H_2O$ (2.04 min), limit the widespread clinical use of PET owing to the need for a nearby cyclotron or generator. A physical advantage of $^{18}$F is its longer half-life (109.8 min); therefore, a $^{18}$F-labeled myocardial imaging agent would overcome the limitations imposed by the current PET tracers and facilitate clinical protocols [6, 7].

### 1.1 The Rationale of [$^{18}$F]-Labeled Fluoroalkyl Triphenylphosphonium Salts ([$^{18}$F]FATPs)

The mitochondrial membrane potential (MMP) is higher in cardiomyocytes than in normal epithelial cells, and loss of MMP is an early event in cell death caused by myocardial ischemia [8, 9]. Similar to SPECT agents such as [$^{99m}$Tc]-sestamibi and [$^{99m}$Tc]-tetrofosmin, phosphonium cations accumulate in cardiomyocytes. This accumulation occurs because the density of mitochondria in cardiomyocytes is high and also because mitochondria have a high electrochemical transmembrane (inside-negative) potential, down which the cations move [10]. Therefore, radiolabeled phosphonium cations are promising candidates for myocardial imaging [11, 12].

The first radiolabeled phosphonium cation studied for use in PET was [$^{11}$C]triphenylmethylphosphonium ([$^{11}$C]TPMP) [13]. [$^{11}$C]TPMP PET studies were performed to evaluate the membrane potential of heart tissue in canine models, which was determined to be 148.1 ± 6.0 mV (inside negative). In addition, PET studies showed that the [$^{11}$C]TPMP accumulated in the heart immediately after its intravenous injection and then remained with a high heart-to-blood ratio (greater than 46:1) and heart-to-lung ratio (14:1) [14, 15]. However, [$^{11}$C]TPMP use is limited because of the short half-life of $^{11}$C (20 min). To provide a tracer similar to [$^{11}$C]TPMP but with a longer half-life, the synthesis and evaluation of $^{18}$F-labeled phosphonium cations were investigated [15]. Among them, 4-[$^{18}$F]fluorobenzyltriphenylphosphonium ([$^{18}$F]FBnTP) showed excellent results as a myocardial perfusion agent. [$^{18}$F]FBnTP was synthesized using four-step procedures. The 4-trimethylammoniumbenzaldehyde was used as a precursor and a third intermediate, 4-[$^{18}$F]fluorobenzyl bromide, reacted with triphenylphosphine to yield [$^{18}$F]FBnTP. [$^{18}$F]FBnTP is metabolically stable and demonstrates excellent characteristics as a cardiac imaging agent in healthy and CAD disease models [16–18]. In a separate study, direct fluorination of tetraphenylphosphonium was investigated [19]. (4-[$^{18}$F]Fluorophenyl)

triphenylphosphonium ([$^{18}$F]TPP) was synthesized via a direct nucleophilic substitution reaction of [$^{18}$F]fluoride using 4-nitrophenyltriphenylphosphonium as a precursor.

Clearance of radiotracer from the liver depends on its lipophilicity. Although there is little information available with regard to the optimal lipophilicity needed for high myocardial selectivity of a radiotracer, a predictive model has been reported for the selective accumulation of phosphonium cations in myocardial cells [20]. Furthermore, because the alkyl group increases hydrophobicity, the hydrophobic interaction between the triphenylphosphonium cation and the lipid core is attractive owing to the hydrophobicity of the lipophilic phosphonium cation and increased entropy [21–23]. Thus, we synthesized several kinds of radiolabeled phosphonium salts, and assessed lipophilicity at different carbon chain lengths and functional groups to find the optimum [24–28]. Highly lipophilic structures such as benzene rings were not adopted to avoid delayed washout from the liver. The (3-[$^{18}$F]fluoropropyl) triphenylphosphonium cation [15] (a shorter-chain analog) had lower uptake by myocardial tissue, whereas the (8-[$^{18}$F]fluorooctyl)triphenylphosphonium cation (a longer-chain analog) had higher liver uptake and delayed clearance.

Three [$^{18}$F]FATPs {(5-[$^{18}$F]fluoropentyl)triphenylphosphonium cation ([$^{18}$F]FPTP), (6-[$^{18}$F]fluorohexyl)triphenylphosphonium cation ([$^{18}$F]FHTP), (2-(2-[$^{18}$F]fluoroethoxy)ethyl) triphenylphosphonium cation ([$^{18}$F]FETP)} were synthesized very easily from the reaction of triphenylphosphine with a precursor that has appropriate cationic activity and lipophilicity for penetration of the mitochondrial membrane and accumulation inside (log $P = 1.31 \pm 0.02$, $1.78 \pm 0.05$, $0.89 \pm 0.02$, each tracer) [25, 26, 28]. [$^{18}$F]FATPs have good myocardial uptake and retention, and fast clearance from other organs leading to high myocardial selectivity.

### 1.2 Limitations

Some limitations to the application of [$^{18}$F]FATPs in clinic should be considered. First, although our current preclinical findings of stable uptake and excellent pharmacokinetics of [$^{18}$F]FATPs suggest that the tracers may be suitable for clinical studies, it should be remembered that they were obtained in an experimental study of rodent models. Further preclinical application is being addressed with a pig model that more closely resembles the human heart in its size, heart rate, myocardial blood flow, and mitochondrial density. Second, our study was limited to acute MI with permanent left coronary artery (LCA) ligation. This model is well suited to determining myocardial defects but is not identical to the clinical situation in which hemodynamically relevant stenosis is unmasked by a stress-induced increase of myocardial blood flow. Further studies are needed to validate [$^{18}$F]FATPs PET for the detection of small lesions of myocardial ischemia and scars of chronic infarctions.

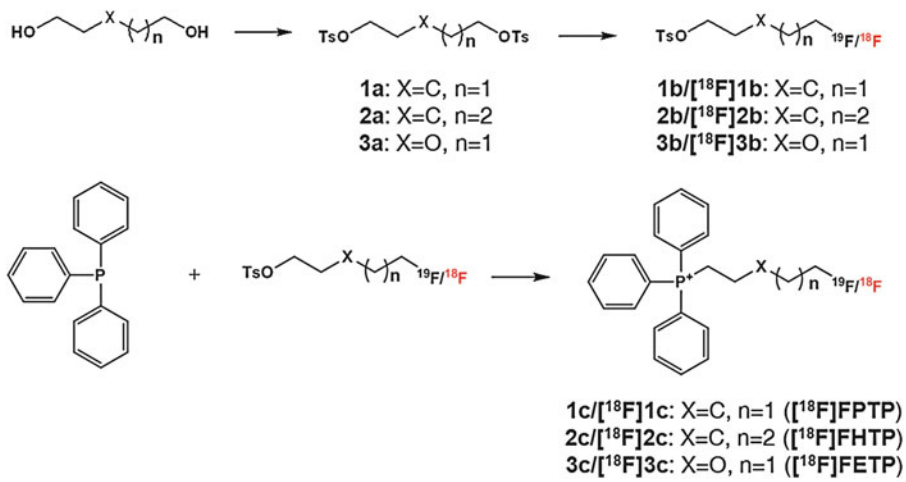


**Fig. 1** Synthesis scheme and structure of [$^{18}$F]-labeled fluoroalkyl triphenylphosphonium salts ([$^{18}$F]FATPs). ((5-[$^{18}$F]fluoropentyl)triphenylphosphonium cation (**[$^{18}$F]1c**: **[$^{18}$F]FPTP**), (6-[$^{18}$F]fluorohexyl)triphenylphosphonium cation (**[$^{18}$F]2c**: **[$^{18}$F]FHTP**), (2-(2-[$^{18}$F]fluoroethoxy)ethyl)triphenylphosphonium cation (**[$^{18}$F]3c**: **[$^{18}$F]FETP**))

### *1.3 Experimental Design*

The total radiosynthesis of [$^{18}$F]FATPs is shown in Fig. 1. The [$^{18}$F]FATPs were radiolabeled via two-step nucleophilic substitution reactions of no-carrier-added [$^{18}$F]fluoride with the precursor α, ω-di-tosyloxyalkane (pentane-1,5-diyl bis (4-methylbenzenesulfonate; **1a**, hexane-1,6-diyl bis (4-methylbenzenesulfonate); **2a**, 2,2′-oxybis(ethane-2,1-diyl) bis (4-methylbenzenesulfonate); **3a**) in the presence of 4,7,13,16,21,24-hexaoxa-1,10-diazabicyclo[8.8.8] hexacosane (Kryptofix 2.2.2) and $K_2CO_3$. The semipreparative and analytical HPLC system was used for purification and identification. The first-pass extraction fraction (EF) values of radiotracers were measured in isolated rat hearts perfused by the Langendorff method [29]. The LCA ligation was performed on 8-week-old male Sprague–Dawley (SD) rats for MI models. Animal care, all experiments, and euthanasia were performed in accordance with protocols approved by the Chonnam National University Animal Research Committee and the Guide for the Care and Use of Laboratory Animals (8th edition, *The National Academies Press.* 2010). Dynamic small-animal PET images were acquired for 70 min (10 s × 12f, 20 s × 9f, 30 s × 10f, 60 s × 10f, 300 s × 6f, 600 s × 2f) after injection of [$^{18}$F]FATPs (37 MBq). Images were reconstructed using the three-dimensional ordered-subset expectation maximization algorithm with four iterations. Analysis of the small-animal PET images was performed with the PMOD software package (PMOD Technologies Ltd) [30, 31].

## 2 Materials

### 2.1 Column Solvents

1. Column solvent A: Prepare a solution by mixing a solvent of methylene chloride, *n*-hexane, and acetone in a ratio of 48:50:2 (vol:vol:vol), and store this solution in a refrigerator.
2. Column solvent B: Prepare a solution by mixing a solvent of methylene chloride, *n*-hexane, and acetone in a ratio of 49:50:1 (vol:vol:vol)), and store this solution in a refrigerator.
3. Column solvent C: Prepare a solution by mixing a solvent of methylene chloride and methanol in a ratio of 9:2 (vol:vol), and store this solution in a refrigerator.

### 2.2 Solutions

1. Phosphate-buffered saline (PBS): Dissolve 1 PBS tablet in 100 mL of sterile distilled water (S.DW), autoclave, and keep at room temperature.
2. TTC solution (1%): Prepare 0.1 M $Na_2HPO_4$ and 0.1 M $NaH_2PO_4$ in S.DW. Dissolve 1.0 g of TTC powder in a solution mixture of 77.4 mL of $Na_2HPO_4$ and 22.6 mL of $NaH_2PO_4$.

### 2.3 Other Supplies

1. Sep-Pak cartridge preconditioning: Activate the Accell Plus QMA Carbonate Sep-Pak light cartridge with 10 mL of water. For the Sep-Pak C18 cartridge, activate with 10 mL of ethanol followed by 20 mL of water.
2. Semipreparative high-performance liquid chromatography (HPLC) system for purification:

   Use a Phenomenex Luna C18 HPLC column (250 × 10 mm, 5 μm) with acetonitrile–PBS = 45:55 ([$^{18}$F]1c, [$^{18}$F]3c) and acetonitrile–PBS = 50:50 ([$^{18}$F]2c) over 30 min at a flow rate of 1 mL min$^{-1}$. Set up the UV lamp at 254 nm.
3. Analytical HPLC system for quality control: Use a Waters Atlantis C18 HPLC column (4.6 × 250 mm, 5 μm) with acetonitrile–PBS = 45:55 ([$^{18}$F]1c, [$^{18}$F]3c) and acetonitrile–PBS = 50:50 ([$^{18}$F]2c) over 30 min at a flow rate of 1 mL min$^{-1}$. Set up the UV lamp at 254 nm.
4. Micro-PET/CT scanner: Calibrate the micro-PET/CT animal scanner according to the manufacturer's protocol.

## 3 Methods

### 3.1 Preparation of Fluoroalkyl Triphenylphosphonium Salts

#### 3.1.1 Synthesis of α, ω-di-Tosyloxyalkane (1a-3a)

1. Add alkane-α, ω-diol (pentane-1,5-diol: 1.56 g, hexane-1,6-diol: 1.77 g, 2,2′-oxydiethanol: 1.59 g, 15.0 mmol) to *p*-toluenesulfonyl chloride (8.58 g, 45.0 mmol) in 30.0 mL of anhydrous pyridine at 0 °C.
2. Continue stirring the mixture at room temperature for 3 h.
3. Quench with 3.0 mL of water and stir for a further 30 min.
4. Add methylene chloride and 1.0 M HCl to the reaction mixture, and extract the pyridine from the organic phase.
5. Wash the organic phase with water and brine, dry over sodium sulfate, and filter.
6. After evaporation of the solvent, purify the solution by column chromatography (column solvent A).
7. Recrystallize **1a**-**3a** from methylene chloride–*n*-hexane. This should result in a yield of **1a**: 5.07 g, 82%; **2a**: 5.12 g, 80%; and **3a**: 5.28 g, 85% as a white powder (*see* **Note 1**).

#### 3.1.2 Synthesis of ω-Fluoroalkyl Tosylate (1b-3b)

1. Add anhydrous acetonitrile (3.0 mL) to tetrabutylammonium fluoride trihydrate (TBAF, 1.43 g, 4.54 mmol) and evaporate the mixture under reduced pressure to remove the water.
2. Add **1a**-**3a** (**1a**: 1.87 g; **2a**: 1.94 g; **3a**: 1.88 g, 4.54 mmol) in 10.0 mL of anhydrous acetonitrile to the reaction flask.
3. Connect a reflux condenser to the reaction flask and reflux the mixture at 85 °C for 4 h.
4. Evaporate the solvent under reduced pressure and purify the solution by column chromatography (column solvent B). This should result in a yield of **1b**: 0.60 g, 51%; **2b**: 0.60 g, 48%; and **3b**: 0.67 g, 56% yield as yellow oil (*see* **Note 2**).

#### 3.1.3 Synthesis of Fluoroalkyl Triphenylphosphonium Salts (1c-3c)

1. Add triphenylphosphine (1.0 g, 3.81 mmol) in 10.0 mL anhydrous acetonitrile to **1b**-**3b** (**1b**: 0.09 g; **2b**: 1.05 g; **3b**: 1.0 g, 3.81 mmol).
2. Connect a reflux condenser to the reaction flask and reflux the mixture for 19 h.
3. Evaporate the solvent under reduced pressure.
4. Purify the solution by column chromatography (column solvent C). This should result in a yield of **1c**: 1.03 g, 77%; **2c**: 1.03 g, 74%; and **3c**: 1.01 g, 75%.

### 3.2 Radiosynthesis of [$^{18}$F]Fluoroalkyl Triphenylphosphonium Salts

#### 3.2.1 Preparation of Activated [$^{18}$F]Fluoride

1. Load aqueous [$^{18}$F]fluoride from cyclotron onto an Accell Plus QMA Carbonate Sep-Pak light cartridge.
2. Elute the [$^{18}$F]fluoride from the cartridge with an aqueous potassium carbonate solution (25.0 mmol) into the reaction vessel.
3. Add 4.0 mg of Kryptofix 2.2.2 in 1.0 mL of acetonitrile to the reaction vessel and dry the radioactive solution under nitrogen at 100 °C.
4. Dry the residue by azeotropic distillation with 1 mL of acetonitrile.
5. Repeat two times more to add anhydrous acetonitrile and evaporate solvent to remove the water completely (*see* **Note 3**).

#### 3.2.2 Radiolabeling of Fluoroalkyl Triphenylphosphonium Salts

1. Add 4.0 mg of **1a**-**3a** dissolved in 1.0 mL of anhydrous acetonitrile to the reaction vessel.
2. Heat the mixture for 5 min at 90 °C in the closed state.
3. Check the first [$^{18}$F]fluorination yield by radio TLC (10 × 100 mm plate, develop the TLC plate with column solvent B) (*see* **Note 4**).
4. Load radioactive solution onto a Sep-Pak Silica cartridge.
5. Elute the **[$^{18}$F]1b**-**[$^{18}$F]3b** from the cartridge to a second reaction vessel with 1.0 mL of anhydrous acetonitrile.
6. Add 6.0 mg of triphenylphosphine dissolved in 1.0 mL toluene to the second reaction vessel.
7. Heat the reaction vessel at 220 °C for 3 min with no separation step (*see* **Note 5**).

#### 3.2.3 HPLC Purification

1. Cool the solution and load onto a Sep-Pak C18 cartridge and elute with 1 mL of HPLC system eluent.
2. Inject solution into a semipreparative HPLC column system for purification.
3. Collect the radioactive peak corresponding to **[$^{18}$F]1c**-**[$^{18}$F]3c**, and measure the recovered activity (*see* **Note 6**).

#### 3.2.4 Quality Control and Preparation of In Vivo Experiments

1. Perform the quality control assessments by taking a small aliquot: measure radiochemical purity, confirm product identity (coinjection with reference compound) and determine specific activity by using the analytical HPLC system.
2. Dry the collected fraction and make isotonic with sodium chloride.
3. Pass through a 0.20 μm membrane filter into a sterile multidose vial for in vivo experiments.

### 3.3 Preparation of [$^{13}$N]$NH_3$

1. Produce [$^{13}$N]$NO_x$ via $^{16}$O(p, α)$^{13}$N reaction on a GE PETtrace cyclotron (10 μA irradiation beam for 10 min).
2. Deliver [$^{13}$N]$NO_x$ to disposable unit and react with Devarda's alloy and sodium hydroxide.
3. Dissolve the radioproduct in 0.9% sodium chloride.
4. Pass through a 0.20 μm membrane filter into a sterile multidose vial for in vivo studies.

### 3.4 Perfused Isolated Rat Heart Study

1. Excise heart quickly from anesthetized rats (intraperitoneal sodium pentobarbital [0.25 mL]; Merial GmbH).
2. Place heart in ice-chilled Krebs–Henseleit bicarbonate buffer (glucose at 10 mmol/L), and cannulated via the aorta.
3. Perfuse the heart with Krebs–Henseleit buffer, oxygenated with a mixture of 95% oxygen and 5% carbon dioxide (flow velocities, 0.5, 4.0, 8.0, and 16.0 mL/min).
4. Stabilize the heart for a period of 15 min, after which a bolus injection of approximately 0.925 MBq each of **[$^{18}$F]1c**-**[$^{18}$F]3c** or **[$^{13}$N]$NH_3$**.
5. Measure whole-heart radioactivity over 10 min with a pair of bismuth germinate detectors and calculate the total coincidence counting rate.
6. Analyze the curve by fitting an exponentially decaying function to the data representing the tissue washout component (from 100 to 600 s).
7. Extrapolate the fitted curve to the time of the maximum counting rate and divide by the measured maximum counting rate (ratio: EF value, Table 1 and Fig. 2).

**Table 1**
**First-pass extraction fraction values (EF%) of [$^{18}$F]1c-[$^{18}$F]3c and [$^{13}$N]$NH_3$ at different flow rates**

| | [$^{18}$F]1c | [$^{18}$F]2c | [$^{18}$F]3c | [$^{13}$N]$NH_3$ |
|---|---|---|---|---|
| 0.5 mL/min ($n = 2$) | 41.26 ± 11.51 | 45.30 ± 8.78 | 33.89 ± 10.30$^{*}$ | 49.30 ± 4.05 |
| 4.0 mL/min ($n = 2$) | 30.18 ± 8.90$^{\dagger}$ | 31.59 ± 8.73$^{\dagger}$ | 24.35 ± 4.38$^{*}$ | 15.18 ± 7.29 |
| 8.0 mL/min ($n = 2$) | 23.21 ± 6.62$^{\dagger}$ | 22.57 ± 6.47$^{*}$ | 19.70 ± 3.05$^{*}$ | 12.89 ± 6.30 |
| 16 mL/min ($n = 2$) | 18.50 ± 4.65$^{\dagger}$ | 18.43 ± 3.57$^{\dagger}$ | 13.94 ± 1.72$^{\dagger}$ | 7.38 ± 3.80 |

Data are expressed as mean ± SD. EF values were measured three times in each isolated heart. $^{*}$ $P < 0.05$ vs. $^{13}$N-$NH_3$ by Mann–Whitney test. $^{\dagger}$ $P < 0.01$ vs. $^{13}$N-$NH_3$ by Mann–Whitney test

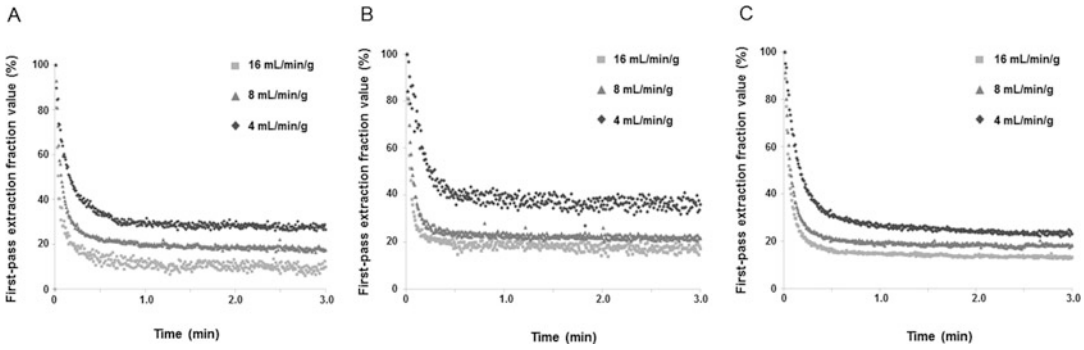


**Fig. 2** First-pass EFs as function of blood flow. Smoothed time–activity curves obtained from sequential measurements of single rat heart are shown. Flow velocities and EFs are indicated ($n = 6$, each flow). (**a**) **[$^{18}$F]1c** (**b**) **[$^{18}$F]2c** (**c**) **[$^{18}$F]3c**

### *3.5 Preparation of Animals*

*3.5.1 Surgery Preparation and Animal Anesthetization*

1. Clean the surgical table with 70% alcohol, unfold all surgical instruments and place on a surgery cover.
2. Turn on the heating pad and set the temperature to 30 °C, check oxygen level and connection with the ventilator.
3. Pour around 20 mL of PBS solution in a petri dish and dissolve 1–2 mg of tetracycline into it. From here on, this solution is referred to as PBS*.
4. Make ketamine and Rompum mixture at a ratio of ketamine–Rompum = 1:2. (Dose: ketamine 10 mg per kilogram body mass, 2% Rompum at 0.4 mL per kilogram body mass).
5. Anesthetize the rat with 2.5% isoflurane mixed with oxygen in an anesthesia chamber for 5 min, and then induce deeper anesthesia by intramuscular injection of the ketamine and Rompum mixture into the left thigh.
6. Take the rat out, remove the hair from its neck and left chest with animal clippers, lay the rat on the heating pad in a supine position, and fix with surgical tape.

*3.5.2 Preparation of MI Model*

1. Turn on the surgical light, and sterilize the surgical parts with iodine tincture and then 70% alcohol.
2. Make a 5 mm incision (over the larynx) in the neck in the longitudinal direction, cut through the lipid, and separate the muscle to expose the larynx.
3. Remove the needle cover and gently insert the angiocath through the larynx, about half the length of the angiocath (*see* **Note 7**).
4. Turn on the ventilator; set the oxygen flow to around 2 L min$^{-1}$, the frequency to 85–90 breaths per minute (bpm), and the amplitude to around 2; and connect the ventilator to the angiocath. Check that the animal's heart is beating and that there are chest fluctuations (*see* **Note 8**).

5. Draw an imaginary line with PBS* from the xiphoid process upward and leftward at an angle of 45° to the body axis and make a 2 cm incision through the skin. Separate the pectoralis into two layers with curved blunt scissors.
6. Expose the chest wall, make a small hole in the center between the fifth and sixth ribs, and then gently enlarge the incision to a width of 5 mm with blunt curved scissors.
7. Gently insert the retractors, rotate the retractors 180° (keeping the handle on the left side), and then open the retractors to exposure the heart.
8. Break the pericardium with two curved blunt forceps, identify the LCA, and ligate the LCA at 2–3 mm below the left auricle with 5–0 suture silk (*see* **Note 9**).
9. Clean up any debris and blood inside the thoracic cavity with PBS* gauze and remove the retractors. Insert a 10 mL syringe capped with a 16-gauge angiocath, and close the chest cavity by suturing the fifth and sixth ribs with 3–0 absorbable suture silk using the "figure 8 suture method" [32].
10. Gently retract the syringe plunger to remove 6–8 mL air from the thoracic cavity to maintain negative pressure, relocate the pectoralis, and close the skin with 3–0 suture silk in a point suture manner.
11. Close the incision in the neck with 3–0 suture silk in a point suture method, clean the surgical area with PBS* gauze, and remove surgical tape.
12. Transfer the rat into a new cage with the angiocath and remove it latter when the rat begins to wake up. Keep the rat in a warm place and supply with water and food (*see* **Note 10**).

### 3.6 Protocol of PET Imaging

#### 3.6.1 Preparation of Small Animals

1. First, anesthetize the normal rats and MI model rats by applying isoflurane (3%) mixed with oxygen 1.5 L $min^{-1}$ for approximately 3 min. Secure the anesthetized rats to a bed using a belt.
2. Transfer the rats to the gantry of the micro-PET. Alter the isoflurane concentration to 1.5–2.0%.

#### 3.6.2 Data Acquisition

1. Inject the rats with tracer (activity 37 MBq/200 μL) and measure the radioactivity for 70 min. Control the isoflurane concentration at ~1.0–1.5%, calibrating to the MI model rat's condition.
2. Separate the data counts into static and dynamic fractions.
3. Reconstruct the static and dynamic data over a 70 min period (10 s × 12f, 20 s × 9f, 30 s × 10f, 60 s × 10f, 300 s × 6f, 600 s × 2f) using the three-dimensional ordered subsets expectation maximization (OSEM3D) method. Set each parameter (filter, value, the number of iterative) to the default value.

(a) Image size is 128 (default).

(b) Image data type is Intel/VAX 4-byte float (default).

(c) Requested resolution (mm) is set to 1.5.

(d) The number of the iterations is set to 4.

4. Process the final reconstructed image using PMOD 3.2 (*see* **Note 11**) (Figs. 3 and 4).

### 3.7 MI Confirmation by TTC Staining Procedures

1. Remove the 1% TTC working solution from storage at 4 °C and warm it in a water bath at 37 °C.
2. Anesthetize the rat using isoflurane and then sacrifice it with 100 μL of ketamine via tail vein injection.
3. Open the chest cavity with bone scissors and gently exteriorize the heart, wash in PBS, and remove as much blood as possible.
4. Take photos with a digital camera, and then use a blade to slice the heart tissue into three 2 mm-thick slices vertically from the cardiac apex to the ligation site.
5. Transfer the sliced tissues into a 50 mL tube with 5–10 mL warmed 1% TTC solution and keep in the water bath with gentle shaking for around 5–10 min.
6. Closely observe the tissues for color change (normal tissue will be stained a dull-red color, while the defective area will be stained white), and once the tissue color becomes constant or well stained, stop the staining step.
7. Take out the tissues and arrange them in the same direction on a black background card, take photos, and determine the defective area by checking which tissue regions are pale (*see* **Note 12**) (Fig. 5).

## 4 Notes

1. A possible low yield of the labeling precursor, that is, below 70%, might be caused by traces of water present in pyridine. In this case, use dry pyridine.
2. Water present in TBAF can cause a low yield of fluorination. In this case, add additional anhydrous $CH_3CN$ and evaporate to remove $H_2O$ in reaction.
3. If the [$^{18}$F]fluoride is not completely eluded from the QMA cartridge, a high-capacity cartridge might have been used. In that case, switch to a smaller-capacity cartridge (46 mg) or use more elution solution.
4. Water present in precursor can cause a low yield of [$^{18}$F]fluorination. In this case, add additional anhydrous $CH_3CN$ and evaporate to remove $H_2O$ in reaction or store the precursor in desiccator.

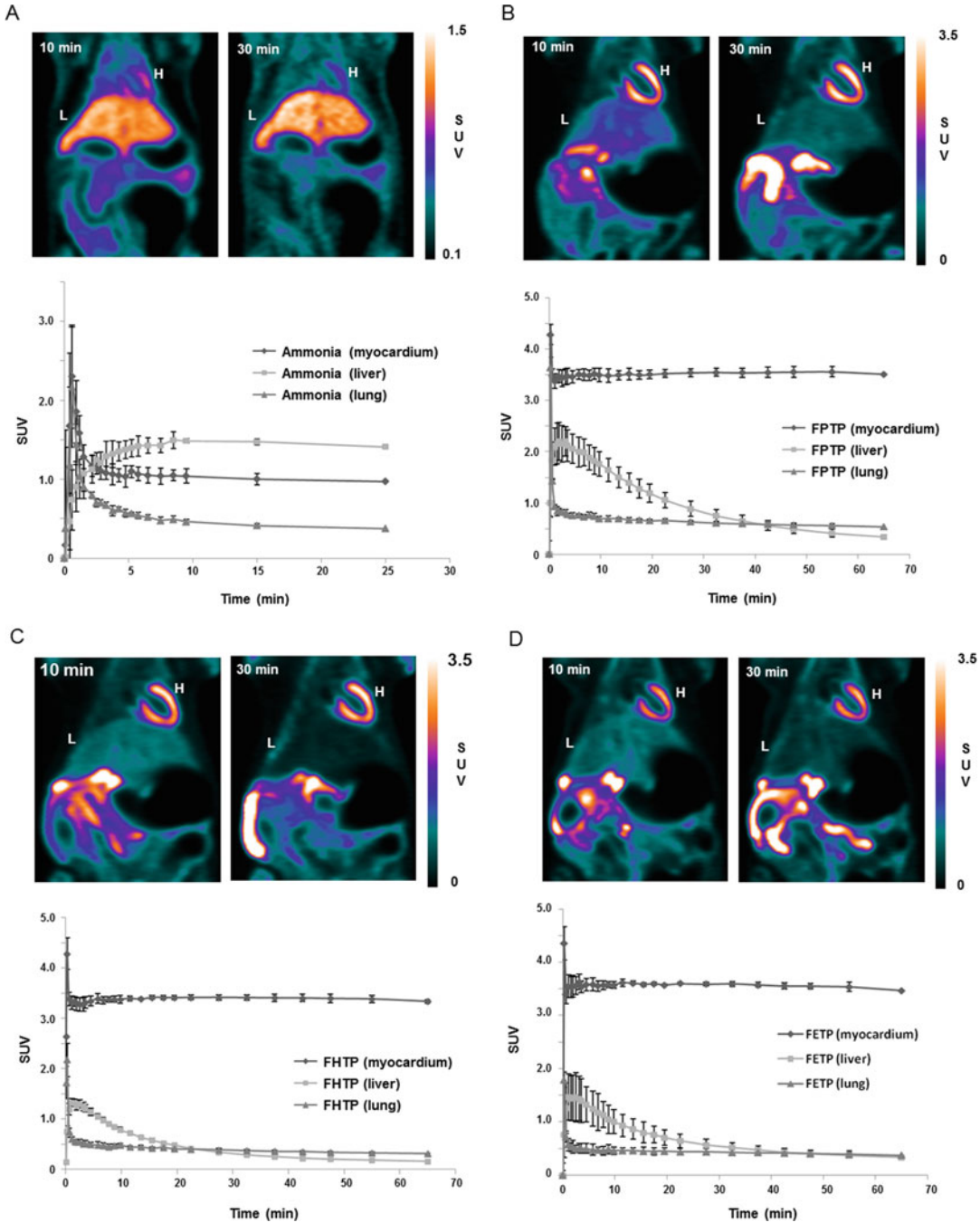


**Fig. 3** Coronal small-animal PET images and time–activity curves of normal rats after intravenous injection of 37 MBq of (**a**) **[$^{13}$N]NH$_3$**, (**b**) **[$^{18}$F]1c**, (**c**) **[$^{18}$F]2c**, or (**d**) **[$^{18}$F]3c** ($n = 3$, each tracer). Heart was visible, with excellent heart-to-background contrast at each time point after **[$^{18}$F]1c**-**[$^{18}$F]3c** injection. *H* heart, *L* liver, *SUV* standardized uptake value

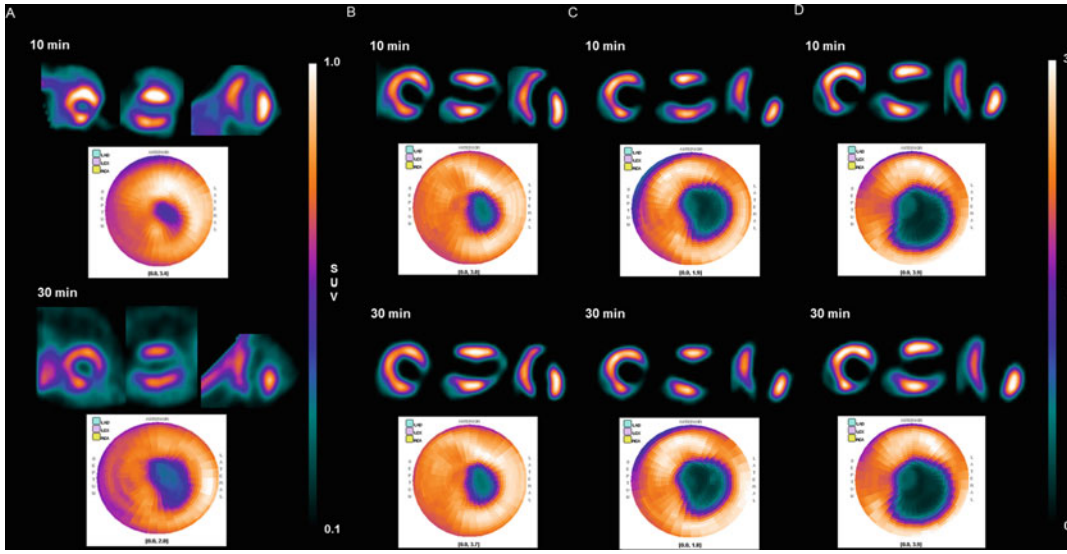


**Fig. 4** Short-, vertical long-, and horizontal long-axis and polar map images of (**a**) **[$^{13}$N]$NH_3$**, (**b**) **[$^{18}$F]1c**, (**c**) **[$^{18}$F]2c**, or (**d**) **[$^{18}$F]3c** in each representative animal. Data were collected between 0–10 and 20–30 min after radiotracer injection (37 MBq). *SUV* standardized uptake value

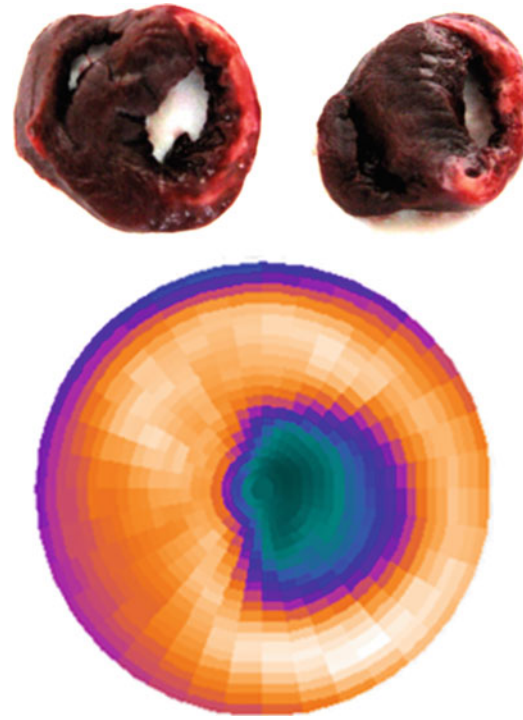

**Fig. 5** MI confirmation of heart by TTC staining and comparison of TTC staining images with polar map image after **[$^{18}$F]1c** injection (37 MBq)

5. A possible low yield of the radio coupling reaction might be caused by improper reaction temperature. In this case, Increase the reaction temperature to 240 °C or heat the reaction vessel for 5 min.
6. A possible low specific activity of [$^{18}$F]1c–[$^{18}$F]3c might be caused impurity which is eluted from the C18 cartridge. In this case, elute the C18 cartridge with 1.5 mL HPLC system eluent.
7. Insufficient anesthetization or nerve compression lead to reflex contraction can fail to insert angiocath. In this case, inject additional ketamine and Rompum mixture, about 1/3 primary dose or gently rotate and push the angiocath into the trachea.
8. A possible respiratory arrest might be caused high oxygen pressure. In this case, decrease the oxygen to suitable pressure; gently push the chest to aid recovery.
9. Lots of bleeding or too fast heart beating can fail LCA ligation. In this case, be carefully when opening the thoracic cavity and breaking the pericardium, clean up blood with PBS* gauze or give the animal additional anesthetic, continue ligation when it has calmed down.
10. Pneumothorax or large-scale pulmonary congestion can cause animal death after surgery. In this case, tightly close the chest wall and remove enough air from the thoracic cavity to maintain negative pressure or be careful when opening the thoracic cavity and inserting the retractors, and throughout try to avoid touching the lungs.
11. A possible animal death for acquisition might be caused high concentration of isoflurane. In this case, reduce the concentration of isoflurane less than 1%.
12. A possible imprecise detection of infarction region might be caused by a mistake of LCA ligation. In this case, clarify the LCA before ligation and ligate tightly.

## Acknowledgments

This research was supported by the Pioneer Research Center Program through the National Research Foundation of Korea, funded by the Ministry of Science and ICT (2015M3C1A3056410), by the Basic Science Research Program through the National Research Foundation of Korea (NRF), funded by the Ministry of Education (2017R1D1A1B03029055) and by the Bio & Medical Technology Development Program of the NRF funded by the Korean government (MSIT) (No.2019M3E5D1A026795912).

## References

1. Ohira H et al (2013) Current and future clinical applications of cardiac positron emission tomography. Circ J 77:836–848
2. Small GR et al (2013) Advances in cardiac SPECT and PET imaging: overcoming the challenges to reduce radiation exposure and improve accuracy. Can J Cardiol 29:275–284
3. Schwaiger M, Melin J (1999) Cardiological applications of nuclear medicine. Lancet 354:661–666
4. Gibbons RJ et al (2004) The quantification of infarct size. J Am Coll Cardiol 44:1533–1542
5. Knuuti J, Bengel FM (2008) Positron emission tomography and molecular imaging. Heart 94:360–367
6. Huisman MC et al (2008) Initial characterization of an $^{18}$F-labeled myocardial perfusion tracer. J Nucl Med 49:630–636
7. Yu M et al (2007) BMS-747158-02: a novel PET myocardial perfusion imaging agent. J Nucl Cardiol 14:789–798
8. Summerhayes IC et al (1982) Unusual retention of rhodamine 123 by mitochondria in muscle and carcinoma cells. Proc Natl Acad Sci U S A 79:5292–5296
9. Chen LB (1988) Mitochondrial membrane potential in living cells. Annu Rev Cell Biol 4:155–181
10. Min JJ et al (2004) Tetraphenylphosphonium as a novel molecular probe for imaging tumors. J Nucl Med 45:636–643
11. Kroemer G (2003) Mitochondrial control of apoptosis: an introduction. Biochem Biophys Res Commun 304:433–435
12. Ross MF et al (2005) Lipophilic triphenylphosphonium cations as tools in mitochondrial bioenergetics and free radical biology. Biochemistry (Mosc) 70:222–230
13. Fukuda H et al (1986) Use of $^{11}$C-triphenylmethylphosphonium for the evaluation of membrane potential in the heart by positron emission tomography. Eur J Nucl Med 11:478–483
14. Krause BJ et al (1994) Myocardial perfusion with [$^{11}$C]methyl triphenyl phosphonium: measurements of the extraction fraction and myocardial uptake. J Nucl Biol Med 38:521–526
15. Ravert HT et al (2004) Radiosynthesis of 3-[$^{18}$F]fluoropropyl and 4-[$^{18}$F]fluorobenzyl triarylphosphonium ions. J Label Compd Radiopharm 47:469–476
16. Madar I et al (2007) Assessment of severity of coronary artery stenosis in a canine model using the PET agent $^{18}$F-fluorobenzyltriphenyl phosphonium: comparison with $^{99m}$Tc-tetrofosmin. J Nucl Med 48:1021–1030
17. Madar I et al (2007) Characterization of membrane potential-dependent uptake of the novel PET tracer $^{18}$F-fluorobenzyl triphenylphosphonium cation. Eur J Nucl Med Mol Imaging 34:2057–2065
18. Madar I et al (2006) Characterization of uptake of the new PET imaging compound $^{18}$F-fluorobenzyltriphenyl phosphonium in dog myocardium. J Nucl Med 47:1359–1366
19. Cheng Z et al (2005) Synthesis of (4-[$^{18}$F] fluorophenyl)triphenylphosphonium as a potential imaging agent for mitochondrial dysfunction. J Label Compd Radiopharm 48:131–137

20. Zhou Y, Liu S (2011) $^{64}$Cu-labeled phosphonium cations as PET radiotracers for tumor imaging. Bioconjug Chem 22:1459–1472
21. Demura M, Kamo N, Kobatake Y (1987) Binding of lipophilic cations to the liposomal membrane: thermodynamic analysis. Biochim Biophys Acta 820:303–308
22. Ono A et al (1994) Activation energy for permeation of phosphonium cations through phospholipid bilayer membrane. Biochemistry 33:4312–4318
23. Smith RA et al (2004) Targeting coenzyme Q derivatives to mitochondria. Methods Enzymol 382:45–67
24. Kim DY et al (2007) Synthesis of (4-[$^{18}$F]fluorophenyl)triphenylphosphonium as a mitochondrial voltage sensor for PET. Nucl Med Mol Imaging 41:561–565
25. Kim DY et al (2012) Synthesis of [$^{18}$F]-labeled (2-(2-fluoroethoxy)ethyl)triphenylphosphonium cation as a potential agent for myocardial imaging using positron emission tomography. Bioorg Med Chem Lett 22:319–322
26. Kim DY et al (2012) Synthesis of [$^{18}$F]-labeled (6-fluorohexyl)triphenylphosphonium cation as a potential agent for myocardial imaging using positron emission tomography. Bioconjug Chem 23:431–437
27. Kim DY et al (2012) Synthesis of [$^{18}$F]-labeled (2-(2-fluoroethoxy)ethyl)tris(4- methoxyphenyl)phosphonium cation as a potential agent for positron emission tomography myocardial imaging. Nucl Med Biol 39:1093–1098
28. Kim DY et al (2012) Evaluation of a mitochondrial voltage sensor, ($^{18}$F-fluoropentyl)triphenylphosphonium cation, in a rat myocardial infarction model. J Nucl Med 53:1779–1785
29. Kim DY et al (2015) Comparison of $^{18}$F-labeled fluoroalkylphosphonium cations with $^{13}$N-$NH_3$ for PET myocardial perfusion imaging. J Nucl Med 56:1581–1586
30. Schepis T et al (2007) Absolute quantifi cation of myocardial blood flow with $^{13}$N-ammonia and 3-dimensional PET. J Nucl Med 48:1783–1789
31. Siegrist PT et al (2008) $^{13}$N-ammonia myocardial perfusion imaging with a PET/CT scanner: impact on clinical decision making and cost-effectiveness. Eur J Nucl Med Mol Imaging 35:889–895
32. Zhao J, Huangfu X (2007) Arthroscopic treatment of nonunited anterior cruciate ligament tibial avulsion fracture with figure-of-8 suture fixation technique. Arthroscopy 23:405–410

# Chapter 5

# Novel Mitochondria-Targeted Triphenylphosphonium Conjugates of Linear β-Phosphorylated Nitrones: Preparation, $^{31}$P NMR Mitochondrial Distribution, EPR Spin Trapping Reporting, and Site-Directed Antiapoptotic Properties

**Consuelo Petrocchi, Sophie Thétiot-Laurent, Marcel Culcasi, and Sylvia Pietri**

## Abstract

The mitochondrion can be considered as the metabolic powerhouse of the cell, having a key impact on energy production, cell respiration, and intrinsic cell death. Mitochondria are also the main source of endogenous reactive oxygen species, including free radicals (FR), which are physiologically involved in signaling pathways but may promote cell damage when unregulated or excessively formed in inappropriate locations. A variety of chronic pathologies have been associated with FR-induced mitochondrial dysfunctions, such as cancer, age-related neurodegenerative diseases, and metabolic syndrome.

In recent years drug design based on specific mitochondria-targeted antioxidants has become a very attractive therapeutic strategy and, among target compounds, nitrones have received growing attention because of their specific affinity toward FR. Here, we describe protocols dealing with the preparation, mitochondria permeation assessment, electron paramagnetic resonance (EPR) spin trapping setting, and antiapoptotic properties evaluation of a series of new linear nitrones vectorized by a triphenylphosphonium cation and labeled with a diethoxyphosphoryl moiety as $^{31}$P nuclear magnetic resonance (NMR) reporter with antioxidant property.

**Key words** Mitochondria-targeted nitrones, $^{31}$P NMR, EPR spin trapping, Mitochondrial permeability, $H_2O_2$-induced apoptosis

## 1 Introduction

In aerobic metabolism mitochondria play a crucial role in ATP synthesis and oxidative phosphorylation. These organelles are also central to a range of vital processes such as calcium homeostasis, amino acid, and heme biosynthesis. The mitochondrion is also the most important site for reactive oxygen species (ROS) formation

Volkmar Weissig and Marvin Edeas (eds.), *Mitochondrial Medicine: Volume 1: Targeting Mitochondria*, Methods in Molecular Biology, vol. 2275, https://doi.org/10.1007/978-1-0716-1262-0_5,

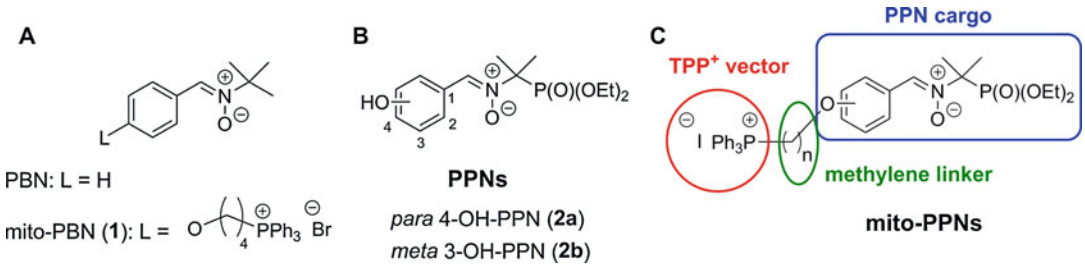


**Fig. 1** Molecular structures of (**A**) PBN and mito-PBN (**1**), (**B**) monohydroxylated PPNs (**2**), and (**C**) mito-PPNs iodides

which are involved in cellular signaling and apoptosis [1]. Under adverse conditions excess, unbalanced mitochondrial ROS production (among them are free radicals (FR)) contributes to the initiation and progression of a variety of chronic diseases such as cancer, neurodegenerative diseases, diabetes, and ischemic syndrome [2].

It is therefore increasingly considered that designing specifically targeted antioxidants and/or modulators of FR production may be an interesting strategy in the treatment of mitochondrial dysregulation [3]. By incorporating a lipophilic cation such as triphenylphosphonium ($TPP^+$) as a mitochondrial vector, a wide range of targeted compounds with antioxidant properties (e.g., vitamin E or quinones) can be used as cargo, being able to cross the mitochondrial inner membrane by diffusion [4]. As a class of potential target drugs, derivatives of α-phenyl-*N*-*tert*-butyl nitrone (PBN; Fig. 1A) have received particular attention in the past decade because their unique FR scavenging properties can result in inhibition of oxidative stress that underlies several ROS-induced pathologies [5]. On these combined bases the $TPP^+$–PBN conjugate bromide, mito-PBN (**1**; Fig. 1A) has demonstrated promising pharmacological activity in several preclinical studies [4, 6]. In $TPP^+$ conjugates accumulation within the mitochondrion is due to accelerated free diffusion from the extracellular space into the cytosol because of the cell negative plasma membrane potential and, in the case of mito-PBN, the concentration within the mitochondrial matrix may be 1000-fold that in the extracellular medium [6, 7]. It has been shown that in mitochondria targeted compounds having $TPP^+$ as the vector, the length of the alkyl linker and the antioxidant functional group (e.g., a quinone, vitamin E, or a stable nitroxide FR) are crucial in determining the biological properties, including cytotoxicity [7].

Besides, linear nitrones such as PBN are spin-trapping agents widely used in electron paramagnetic resonance (EPR) studies of FR formation and introduction of a diethoxyphosphoryl group $(EtO)_2P(O)$ within the PBN structure leads to increased lifetime of the spin adducts ([8] and cited references) and may bring about a better biocompatibility [9]. Based on this concept we designed PPNs, a new generation of phosphorylated PBN hybrids such as

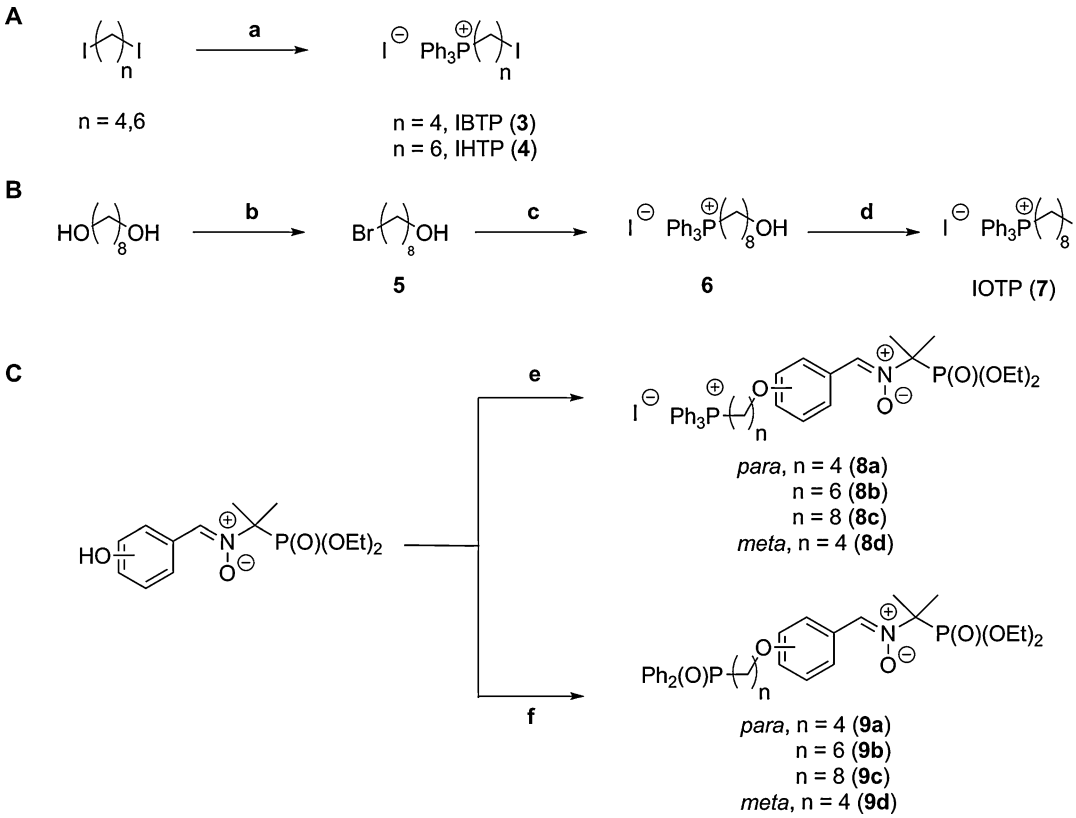


**Scheme 1** Synthesis of (**A**) 4- and 6-methylene linkers (IBTP **3** and IHTP **4**); (**B**) 8-methylenes linker (IOTP **7**); (**C**) mito-PPNs (**8a–d**) and non–mitochondria-targeted nitrones (**9a–d**). Reagents and conditions: (**a**) $PPh_3$, 120 °C, dark, 1.5 h; (**b**) HBr, toluene, 150 °C, 1 day; (**c**) $PPh_3$, acetonitrile, 85 °C, 2 days; (**d**) HI, acetonitrile, 100 °C, 5 h; (**e**) (**1**) $K_2CO_3$, acetonitrile, TA, 30 min; (**2**) **3**, **4**, or **7**, acetonitrile, 60 °C, 12 h; (**f**) (**1**) NaH, acetonitrile, TA, 30 min; (**2**) **3**, **4**, or **7**, acetonitrile, 40 °C, 12 h

compounds **2a,b** (Fig. 1B) having an aryl moiety present in several natural antioxidant phenolics. Expectedly, these low-toxic compounds were better oxidative stress EPR probes than PBN itself, and they demonstrated increased antioxidant action in vitro and vasoprotective effect in precontracted rat aortic rings due to enhanced nitric oxide donation property [8].

Recently the usefulness of introducing a $(EtO)_2P(O)$ group in $TPP^+$ vectorized compounds was demonstrated in a series of linear α-aminophosphonates which showed enhanced properties as mitochondrial pH probes [10, 11]. In the present study, we have extended these studies to design novel $TPP^+$-vectorized phosphorylated PBN derivatives. These new mito-PPNs, all iodides, were constructed from cargo compounds **2a,b**, functionalized with various linkers composed of methylene units before grafting of a $TPP^+$ vector (Fig. 1C). In this paper the synthesis and analytical data of four mito-PPNs **8a–d** (Scheme 1) are described, together

with detailed protocols for determining characteristic EPR signatures of selected spin adducts, in vitro antioxidant properties, and cytotoxicity. Also given are protocols for (1) implementing a whole perfused rat liver model to measure mitochondrial permeation of mito-PPNs versus analogs **9a–d** lacking the $TPP^+$ group (Scheme 1), and (2) assessing their protective effect versus the nonnitronyl methyltriphenylphosphonium bromide (TPMP) in a cellular model of hydrogen peroxide ($H_2O_2$)-induced apoptosis.

## 2 Materials

### 2.1 Chemical Synthesis and Analysis

1. Triphenylphosphine (harmful, health hazard).
2. 1,4-diiodobutane (irritant).
3. 1,6-diiodohexane (irritant).
4. 1,8-octanediol (irritant).
5. Methyltriphenylphosphonium bromide (acute toxic, irritant, environmental hazard).
6. 48% hydrobromic acid (corrosive, irritant).
7. Sodium hydroxide (corrosive).
8. 36% hydrochloric acid (corrosive, irritant).
9. 57% hydroiodic acid (corrosive, irritant).
10. Sodium thiosulfate (irritant).
11. Sodium sulfate (corrosive, irritant).
12. Potassium carbonate (irritant).
13. Magnesium sulfate (irritant).
14. 60% dispersion in mineral oil sodium hydride (flammable).
15. Diethyl ether (flammable, harmful).
16. Dichloromethane (harmful, health hazard).
17. Toluene (irritant, flammable, health hazard).
18. Acetonitrile (harmful, irritant, flammable).
19. Nitrones 4-OH-PPN (**2a**) and 3-OH-PPN (**2b**, Fig. 1B) prepared according to [8].
20. Doubly distilled deionized water (15 MΩ) used for all solutions and buffers.
21. Reactions monitored on silica gel 60 aluminum TLC-plates with F254 as indicator.
22. UV lamp (to check TLC plates at 254 nm).
23. Flash chromatography purifications on silica gel 60 (230–400 mesh).
24. NMR Tubes.

25. 99.8 atom% D Deuterochloroform (acute toxic, irritant, health hazard).
26. 99.8 atom% D Tetradeuteromethanol (flammable, acute toxic, health hazard).
27. Tetramethylsilane (flammable, irritant).
28. 85% Orthophosphoric acid (corrosive).
29. Analytical $^{1}H$ NMR (300, 400 or 500 MHz), $^{13}C$ NMR (75, 100 or 125 MHz), and $^{31}P$ NMR (121.5, 162 or 202.5 MHz) spectra are recorded in $CDCl_3$ or $CD_3OD$ on Bruker Avance III NanoBay 300 or 400 MHz and Bruker Avance I 500 MHz spectrometers. Chemical shifts ($\delta$) are reported in parts per million (ppm) relative to TMS ($^{1}H$ and $^{13}C$) or external $H_3PO_4$ ($^{31}P$). Coupling constants ($J$) are reported in Hertz (Hz) and abbreviations of multiplicity are as follows: s, singlet; d, doublet; t, triplet; quint, quintuplet; m, multiplet; dd, doublets of doublet; br, broad.
30. Melting points are determined on a Büchi Melting Point M-560 apparatus (Büchi, Essen, Germany) and are uncorrected.
31. Melting points capillary tubes.
32. HRMS are done on a Q-STAR Elite apparatus (Applied Biosystems, USA). Analytical experiments are performed at the local unit Spectropole-Aix-Marseille University (Saint-Jérôme Etoile, Marseille, France).

### 2.2 Cell Culture and Cytotoxicity Studies

1. Methyltriphenylphosphonium bromide (acute toxic, irritant, environmental hazard).
2. Dimethyl sulfoxide (irritant).
3. Murine 3T3 NIH fibroblasts (ATCC–LGC Promochem, Molsheim, France).
4. Dulbecco's Modified Eagle's Minimum Media (DMEM).
5. Phenol red-free DMEM.
6. Glucose.
7. Fetal calf serum (from Gibco Life Technologies, Thermo Fisher Scientific, Illkirch, France).
8. Penicillin.
9. Streptomycin.
10. Triton X-100.
11. Fluorescein diacetate.
12. Phosphate buffer saline (PBS, Life Technology Corp.; St Aubin, France).

13. 3-(4,5-Dimethyl-2-thiazolyl)-2,5-diphenyl-2*H*-tetrazolium bromide (MTT).
14. 0.2-μm Millipore filter.
15. Incubator set at 37 °C and 5% $CO_2$ atmosphere.
16. 24-well plates.
17. 96-well black plates for fluorescence determination.
18. Microscope.
19. Spectrophotometer for fluorescence determination at 535 nm, following excitation at 485 nm.
20. Microplate reader to assess cell viability at 570 nm.
21. Prepare fresh stock solutions of nitrones and TPMP in DMSO (1–5 mM) and pass all media through a 0.2-μm Millipore filter before use.
22. Maintain 3T3 NIH fibroblasts at 37 °C in a 5% $CO_2$-humidified atmosphere in DMEM containing 1% glucose and supplemented with 10% fetal calf serum, 100 U/mL penicillin, and 100 mg/mL streptomycin [12]. Cells are plated in 24-well dishes and medium is replenished every 2–3 days until confluency, checked by microscopic observation. For cell exposure 10-μL aliquots of nitrone or TPMP stock solutions are transferred into each well of confluent cells previously filled with phenol red-free DMEM containing 1% glucose, in order to reach a final volume of 0.5 mL/well, test compounds concentration of 0.1 μM to 0.2 mM and 0.1% DMSO (v/v). Incubate wells for 24 h at 37 °C in a 5% $CO_2$-humidified atmosphere, sample supernatants for extracellular LDH assay, treat wells with 1% Triton X-100, gently scrape the cells and keep them at −80 °C for total LDH or ATP measurement (see below).
23. Use a commercial kit for LDH determination (*see* [8]).
24. Assay ATP in thawed cells resuspended in PBS supplemented with 100 μL/well 0.1%Triton X-100 using the luminescence-based kit, for example, the luciferin-luciferase reagent Biofax A® (Yelen, Ensuès la Redonne, France; http://www.yelen-analytics.com) as described in [8].
25. Assay cytotoxicity in cells by the fluorometric microculture cytotoxicity assay (FMCA) in PBS 1× (+/+) containing fluorescein diacetate (4.8 μM; and 3% Triton X-100, using excitation at 485 nm and detection at 535 nm as described in [8].
26. Assay cell viability at 570 nm using a microplate reader by the MTT assay in DMEM containing PBS 1× (+/+), MTT and DMSO as described in [8].

### 2.3 EPR Spectrometry

EPR spectra can be recorded using any conventional X-band (9.79 GHz) spectrometer equipped with a standard cylindrical $TM_{110}$ resonant cavity, provided the instrument is located in an established EPR facility, with the possible help of an experienced coworker for the computer simulation and interpretation of the signal. Here, a Bruker ESP 300 spectrometer has been used, with a 100 KHz field modulation and operating at a microwave power of 10 mW. For determining $g$-factors of spin adducts, a Bruker ER 035 M gaussmeter and a HP 5350B frequency counter are operated.

### 2.4 Mitochondrial Permeation Capacity

Mitochondrial and cytosolic distribution of nitrones are investigated according to earlier work [10, 13].

1. Sprague-Dawley male rats (120 g) used for liver perfusion and mitochondrial preparation are from CERJ (Le Genest St Isle, France) and fed ad libitum with a standard Teklad 2016 diet (Harlan Laboratories, Gannat, France). Animals are maintained in the local animal house under conventional conditions, in a room with controlled temperature (21–25 °C) and a reverse 12 h light/dark cycle. All animal procedures used are in strict accordance with the Directive 2010/63/EU of the European Parliament. The CNRS and Aix-Marseille University have currently valid licenses for animal experimentation (agreement C13-055-06/D 13-055-8) delivered by the French Government.
2. Sodium pentobarbital.
3. Krebs-Henseleit (KH): 1.2 mM $KH_2PO_4$, 119 mM NaCl, 4.8 mM KCl, 1.2 mM $MgSO_4$, 25 mM $NaHCO_3$ and 1.3 mM $CaCl_2$, bubbled with a 95% $O_2$ and 5% $CO_2$ gas mixture (pH 7.35).
4. 0.25 M solution of sucrose in ice-cold KH buffer.
5. 10 mM 4-(2-hydroxyethyl)-1-piperazineethanesulfonic acid (HEPES) solution in ice-cold KH buffer, pH 7.5.
6. Dichloromethane (harmful, health hazard).
7. Dimethyl sulfoxide (irritant).
8. Filtrate through four layers of cheesecloth, centrifuged at 750 × $g$ for 10 min at 2 °C.
9. Isolate mitochondria as a subcellular purified fraction ([13] and references therein).
10. NMR tubes.
11. Hexadeuterodimethyl sulfoxide (irritant).
12. 85% orthophosphoric acid (corrosive).
13. Determine mitochondrial permeation analysis by recording $^{31}P$ NMR (242.94 MHz) spectra in DMSO-$d_6$ on a Bruker Avance

III 600 MHz spectrometer equipped with a BBFO+ probe. Chemical shifts ($\delta$) are reported in parts per million (ppm) relative to external $H_3PO_4$ ($^{31}P$).

### 2.5 Apoptosis Determination in Schwann Cells

Schwann cells freshly prepared from bilateral sciatic nerves of Sprague-Dawley male rats (120 g) [15] are kindly provided by the Institute of Neuroscience, Hôpital de la Timone, Marseille. Cells are made apoptotic by treatment with $H_2O_2$ according to [14]. The cytoprotective properties of test nitrones are evaluated as detailed in [8].

1. Culture Schwann cells in DMEM/Ham's F-12 medium according to [14, 15].
2. $H_2O_2$ (oxidizer, irritant, corrosive).
3. Reagents for MTT and LDH assays (see above).
4. Test compounds solutions (0.1–1 μM) in culture medium + 0.1% DMSO.

## 3 Methods

### 3.1 Synthesis of (4-Iodobutyl) triphenylphosphonium Iodide (IBTP, 3) [16]

Triphenylphosphine (1 g, 3.82 mmol) and 1,4-diiodobutane (6 g, 19 mmol) are stirred for 1.5 h at 120 °C in the dark. The reactional mixture is triturated in diethyl ether (50 mL). The yellow pale solid is filtered and air-dried (2.15 g, 98%): $^1H$ NMR (300 MHz, $CDCl_3$) $\delta$ 7.85 (m, 3H, H-4′), 7.82 (m, 6H, H-3′), 7.72 (m, 6H, H-2′), 3.78 (m, 2H, 1–$CH_2$), 3.33 (t, $J = 6.2$ Hz, 2H, 4–$CH_2$), 2.21 (quint, $J = 6.6$ Hz, 2H, 3–$CH_2$), 1.82 (m, 2H, 2–$CH_2$); $^{13}C$ NMR (75 MHz, $CDCl_3$) $\delta$ 135.2 (d, $J = 3.3$ Hz, 3C, C-4′), 133.7 (d, $J = 9.9$ Hz, 6C, C-2′), 130.6 (d, $J = 12.7$ Hz, 6C, C-3′), 118.0 (d, $J = 86.4$ Hz, 3C, C-1′), 32.4 (d, $J = 17.1$ Hz, 3–$CH_2$), 23.2 (d, $J = 3.9$ Hz, 2–$CH_2$), 21.9 (d, $J = 51.2$ Hz, 1–$CH_2$), 7.7 (4–$CH_2$); $^{31}P$ NMR (121 MHz, $CDCl_3$) $\delta$ 24.49.

### 3.2 Synthesis of (6-Iodohexyl) triphenylphosphonium Iodide (IHTP, 4)

Triphenylphosphine (1 g, 3.82 mmol) and 1,6-diiodohexane (5 g, 15 mmol) are stirred for 1.5 h at 120 °C in the dark. The oily residue is triturated in the minimum of dichloromethane and diethyl ether (50 mL) is added. The upper phase is removed and the operation is repeated twice on the oily residue. A brown-red oil is obtained (1.5 g, 65%): $^1H$ NMR (300 MHz, $CDCl_3$) $\delta$ 7.80 (m, 9H, H-3′ et H-4′), 7.70 (m, 6H, H-2′), 3.69 (m, 2H, 1–$CH_2$), 3.09 (t, $J = 7.0$ Hz, 2H, 6–$CH_2$), 1.74 (m, 6H, 2–$CH_2$, 4–$CH_2$ and 5–$CH_2$), 1.42 (m, 2H, 3–$CH_2$); $^{13}C$ NMR (75 MHz, $CDCl_3$) $\delta$ 135.2 (d, $J = 2.8$ Hz, 3C, C-4′), 133.7 (d, $J = 9.9$ Hz, 6C, C-2′), 130.6 (d, $J = 12.6$ Hz, 6C, C-3′), 118.0 (d, $J = 85.8$ Hz, 3C, C-1′), 32.8 (5–$CH_2$), 29.9 (4–$CH_2$), 29.2 (d, $J = 16.5$ Hz, 3–$CH_2$), 22.9 (d, $J = 50.6$ Hz, 1–$CH_2$), 22.4 (d, $J = 4.4$ Hz, 2–$CH_2$), 7.5 (6–$CH_2$); $^{31}P$ NMR (121 MHz, $CDCl_3$) $\delta$ 24.23.

### 3.3 Synthesis of 8-Bromo-Octanol (5)

1,8-octanediol (3 g, 20.5 mmol) is dissolved in toluene (40 mL) and 48% hydrobromic acid (1.6 mL, 30.8 mmol) is slowly added. The solution is stirred at 150 °C for 24 h. The reactional mixture is washed with water (30 mL). The residue is diluted in dichloromethane (30 mL), washed with aqueous solutions of 10%-NaOH (30 mL), 10%-HCl (30 mL), water (2 × 30 mL) and brine (30 mL). The organic phase is dried over $MgSO_4$ and concentrated to yield **5** as a yellow oil (3.2 g, 77%): $^1$H NMR (400 MHz, $CDCl_3$) $\delta$ 3.64 (t, $J = 6.8$ Hz, 2H, 1–$CH_2$), 3.41 (t, $J = 6.8$ Hz, 2H, 8–$CH_2$), 1.86 (quint, $J = 7.0$ Hz, 2H, 7–$CH_2$), 1.57 (m, 2H, 2–$CH_2$), 1.43 (m, 2H, 6–$CH_2$), 1.34 (m, 6H, 3–$CH_2$, 4–$CH_2$ and 5–$CH_2$); $^{13}$C NMR (100 MHz, $CDCl_3$) $\delta$ 63.0 (1–$CH_2$), 31.0 (8–$CH_2$), 32.8 (2–$CH_2$*), 32.7 (7–$CH_2$*), 29.2 (5–$CH_2$), 28.7 (4–$CH_2$), 28.1 (6–$CH_2$), 25.6 (3–$CH_2$), *may be reversed.

### 3.4 Synthesis of (8-Hydroxyoctyl) triphenylphosphonium Bromide (6)

Compound **5** (2 g, 9.6 mmol) and triphenylphosphine (2.8 g, 10.5 mmol) are stirred in acetonitrile (100 mL) at 85 °C for 2 days. The reaction mixture is concentrated, the residual oil is dissolved in the minimum of dichloromethane and diethyl ether (60 mL) is added dropwise. When the organic phase is translucent, it is removed and the operation repeated twice. The residue is dried under vacuum to yield **6** as a yellow oil (3.5 g, 78%): $^1$H NMR (300 MHz, $CDCl_3$) $\delta$ 7.84 (m, 3H, H-4′), 7.81 (m, 6H, H-3′), 7.73 (m, 6H, H-2′), 3.73 (m, 2H, 1–$CH_2$), 3.59 (t, $J = 6.6$ Hz, 2H, 8–$CH_2$), 1.64 (m, 4H, 2–$CH_2$, 7–$CH_2$), 1.52 (m, 4H, 6–$CH_2$, 3–$CH_2$), 1.29 (m, 4H, 4–$CH_2$ and 5–$CH_2$); $^{13}$C NMR (75 MHz, $CDCl_3$) $\delta$ 134.1 (d, $J = 2.2$ Hz, 3C, C-4′), 133.6 (d, $J = 9.9$ Hz, 6C, C-2′), 130.5 (d, $J = 12.7$ Hz, 6C, C-3′), 118.2 (d, $J = 85.8$ Hz, 3C, C-1′), 62.1 (8–$CH_2$), 32.4 (7–$CH_2$), 30.1 (d, $J = 16.0$ Hz, 3–$CH_2$), 28.6 (4–$CH_2$ and 5–$CH_2$), 25.4 (6–$CH_2$), 22.7 (d, $J = 50.1$ Hz, 1–$CH_2$), 22.3 (d, $J = 3.9$ Hz, 2–$CH_2$); $^{31}$P NMR (121 MHz, $CDCl_3$) $\delta$ 24.35.

### 3.5 Synthesis of (8-Iodooctyl) triphenylphosphonium Iodide (IOTP, 7) (Adapted from [17])

Compound **6** (0.35 g, 0.74 mmol) is dissolved in acetonitrile (5 mL) and a commercial 57% hydriodic acid solution (1.7 mL, 4.4 mmol) is slowly added. The mixture is stirred at 100 °C for 5 h. The reaction is quenched by addition of an aqueous 5%-NaOH solution (3 mL). After settling, the organic layer is concentrated and diluted in dichloromethane (10 mL),washed with water (2 × 10 mL), and with an aqueous saturated solution of $Na_2S_2O_3$ (10 mL). The organic layer is dried over $Na_2SO_4$ and concentrated to give **7** as a pale brown oil (0.46 g, 98%): $^1$H NMR (400 MHz, $CDCl_3$) $\delta$ 7.83 (m, 3H, H-4′), 7.81 (m, 6H, H-3′), 7.77 (m, 6H, H-2′), 3.68 (m, 2H, 1–$CH_2$), 3.15 (t, $J = 7.0$ Hz, 2H, 8–$CH_2$), 1.79 (m, 2H, 2–$CH_2$), 1.65 (m, 4H, 3–$CH_2$ and 7–$CH_2$), 1.35–1.20 (m, 6H, 4–$CH_2$, 5–$CH_2$ and 6–$CH_2$); $^{13}$C NMR (75 MHz, $CDCl_3$) $\delta$ 135.1 (d, $J = 2.8$ Hz, 3C, C-4′), 133.7 (d, $J = 9.9$ Hz, 6C, C-2′), 130.5 (d, $J = 12.6$ Hz, 6C, C-3′), 118.2 (d,

$J = 85.8$ Hz, 3C, C-1′), 33.3 (7–$CH_2$), 30.3 (d, $J = 15.4$ Hz, 3–$CH_2$), 30.2 (6–$CH_2$), 28.9 (4–$CH_2$*), 28.0 (5–$CH_2$*), 23.1 (d, $J = 50.1$ Hz, 1–$CH_2$), 22.5 (d, $J = 4.4$ Hz, 2–$CH_2$), 7.5 (8–$CH_2$), *may be reversed; $^{31}$P NMR (162 MHz, $CDCl_3$) $\delta$ 24.23.

### 3.6 General Procedure for the Tripheny-lphosphonium Nitrone Iodides (8a–d)

The appropriate OH-PPN (**2a** or **2b**) derivative (1 eq.) and $K_2CO_3$ (2.5 eq.) are dissolved in acetonitrile (32 mM) under a $N_2$-atmosphere. The mixture is stirred for 30 min at room temperature. A solution of the appropriate linker IBTP **3**, IHTP **4** or IOTP 7 (1 eq.) in acetonitrile (32 mM) is added dropwise at 0 °C and the mixture is stirred for 12 h at 60 °C, allowed to cool at room temperature, filtered under vacuum, and concentrated. The residue is dissolved in dichloromethane (volume equal to the initial acetonitrile volume),washed with an aqueous 1% HCl solution (3× volume of dichloromethane). The organic layer is dried over $MgSO_4$, filtered, and concentrated. The residual oil is dissolved in the minimum of dichloromethane and diethyl ether (20 × volume of dichloromethane) is added dropwise while maintaining the stirring. Once the organic layer is translucent, the supernatant is removed and the operation repeated twice. The residue is dried under vacuum to afford the desired compound.

1. Synthesis of 2-(diethoxyphosphoryl)-*N*-(4-(4-(triphenylphosphono)butoxy)benzylidene)propan-2-amine oxide iodide (**8a**). The title compound is obtained from 4-OH-PPN **2a** (0.1 g, 0.32 mmol) and IBTP **3** (0.2 g, 0.32 mmol). Compound **8a** is obtained as a brown pale sticky oil (0.1 g, 40%): $^1$H NMR (500 MHz, $CDCl_3$) $\delta$ 8.21 (d, $J = 8.9$ Hz, 2H, H-2), 7.80 (m, 9H, H-2″ and H-4″), 7.70 (m, 1H, HCNO), 7.66 (m, 6H, H-3″), 6.83 (d, $J = 8.9$ Hz, 2H, H-3), 4.18 (m, 4H, 2 × –OC$H_2$$CH_3$), 4.11 (t, $J = 5.6$ Hz, 2H, 1′–$CH_2$), 3.80 (m, 2H, 4′–$CH_2$), 2.22 (m, 2H, 2′–$CH_2$), 1.86 (m, 2H, 3′–$CH_2$), 1.82, (s, 3H, C($CH_3$)$_2$), 1.79 (s, 3H, C($CH_3$)$_2$), 1.31 (t, $J = 7.0$ Hz, 6H, 2 × –$OCH_2CH_3$); $^{13}$C NMR (125 MHz, $CDCl_3$) $\delta$ 160.1 (C-4), 135.1 (d, $J = 1.9$ Hz, C-4″), 133.6 (d, $J = 10.6$ Hz, C-2″), 132.6 (d, $J = 5.8$ Hz, HCNO), 131.0 (C-2), 130.5 (d, $J = 12.5$ Hz, C-3″), 123.8 (C-1), 118.0 (d, $J = 85.4$ Hz, C-1″), 114.2 (C-3), 72.3 (d, $J = 154.5$ Hz, *C*($CH_3$)$_2$), 66.4 (1′–$CH_2$), 63.2 (d, $J = 6.7$ Hz, 2 × –O$CH_2CH_3$), 29.0 (d, $J = 16.3$ Hz, 2′–$CH_2$), 23.2 (C(*C*$H_3$)$_2$), 22.3 (d, $J = 50.9$ Hz, 4′–$CH_2$), 19.3 (d, $J = 2.9$ Hz, 3′–$CH_2$), 16.4 (d, $J = 5.8$ Hz, 2 × –$OCH_2$*C*$H_3$); $^{31}$P NMR (121.5 MHz, $CDCl_3$) $\delta$ 24.61, 23.35; HRMS-ESI: calcd. for $C_{36}H_{44}NO_5P_2^+$ $[M]^+$ 632.2689, found 632.2690.

2. Synthesis of 2-(diethoxyphosphoryl)-*N*-(4-(6-(triphenylphosphono)hexyloxy)benzylidene)propan-2-amine oxide iodide (**8b**). The title compound is obtained from 4-OH-PPN **2a** (0.15 g, 0.47 mmol) and IHTP **4** (0.28 g, 0.47 mmol). Compound **8b** is obtained as a yellow oil (0.13 g, 35%): $^{1}$H NMR (300 MHz, $CDCl_3$) $\delta$ 8.24 (d, $J$ = 8.8 Hz, 2H, H-2), 7.82 (m, 6H, H-2″), 7.74 (m, 6H, H-3″), 7.72 (m, 3H, H-4″), 7.64 (d, $J$ = 2.2 Hz, 1H, HCNO), 6.87 (d, $J$ = 8.8 Hz, 2H, H-3), 4.20 (m, 4H, 2 × –OC$H_2$CH$_3$), 3.96 (t, $J$ = 6.2 Hz, 2H, 1′–CH$_2$), 3.74 (m, 2H, 6′–CH$_2$), 1.85 (s, 3H, C(CH$_3$)$_2$), 1.80 (s, 3H, C(CH$_3$)$_2$), 1.74 (m, 6H, 2′–CH$_2$, 3′–CH$_2$ and 5′–CH$_2$), 1.49 (m, 2H, 4′–CH$_2$), 1.32 (t, $J$ = 7.1 Hz, 6H, 2 × –OCH$_2$C$H_3$); $^{13}$C NMR (75 MHz, $CDCl_3$) $\delta$ 160.6 (C-4), 135.1 (d, $J$ = 2.8 Hz, C-4″), 133.7 (d, $J$ = 9.9 Hz, C-2″), 132.8 (d, $J$ = 6.6 Hz, HCNO), 131.0 (C-2), 130.5 (d, $J$ = 12.7 Hz, C-3″), 123.5 (d, $J$ = 1.7 Hz, C-1), 118.1 (d, $J$ = 85.8 Hz, C-1″), 114.3 (C-3), 72.2 (d, $J$ = 154.6 Hz, $C$(CH$_3$)$_2$), 67.7 (1′–CH$_2$), 63.3 (d, $J$ = 6.6 Hz, 2 × –OCH$_2$CH$_3$), 30.0 (d, $J$ = 16.0 Hz, 4′–CH$_2$), 28.7 (2′–CH$_2$), 25.6 (3′–CH$_2$), 23.3 (C($CH_3$)$_2$), 23.0 (d, $J$ = 50.1 Hz, 6′–CH$_2$), 22.6 (d, $J$ = 4.4 Hz, 5′–CH$_2$), 16.4 (d, $J$ = 6.1 Hz, 2 × –OCH$_2$$CH_3$); $^{31}$P NMR (121.5 MHz, $CDCl_3$) $\delta$ 24.35, 23.40; HRMS-ESI: calcd. for $C_{38}H_{48}NO_5P_2^+$ $[M]^+$ 660.3002, found 660.3004.

3. Synthesis of 2-(diethoxyphosphoryl)-*N*-(4-(8-(triphenylphosphono)octyloxy)benzylidene)propan-2-amine oxide iodide (**8c**). The title compound is obtained from 4-OH-PPN **2a** (0.19 g, 0.6 mmol) and IOTP **7** (0.37 g, 0.6 mmol). Compound **8c** is obtained as a yellow oil (0.12 g, 25%): $^{1}$H NMR (300 MHz, $CDCl_3$) $\delta$ 8.23 (d, $J$ = 8.8 Hz, 2H, H-2), 7.78 (m, 6H, H-2″), 7.69 (m, 9H, H-3″ and H-4″), 7.64 (d, $J$ = 2.2 Hz, 1H, HCNO), 6.86 (d, $J$ = 8.8 Hz, 2H, H-3), 4.17 (m, 4H, 2 × –OC$H_2$CH$_3$), 3.93 (t, $J$ = 6.4 Hz, 2H, 1′–CH$_2$), 3.62 (m, 2H, 8′–CH$_2$), 1.83 (s, 3H, C(CH$_3$)$_2$), 1.78 (s, 3H, C(CH$_3$)$_2$), 1.68 (m, 2H, 6′–CH$_2$), 1.64–1.61 (m, 4H, 2′–CH$_2$ and 7′–CH$_2$), 1.37 (m, 6H, 3′–CH$_2$, 4′–CH$_2$ and 5′–CH$_2$), 1.29 (t, $J$ = 7.1 Hz, 6H, 2 × –OCH$_2$C$H_3$); $^{13}$C NMR (75 MHz, $CDCl_3$) $\delta$ 160.6 (C-4), 135.1 (d, $J$ = 2.8 Hz, C-4″), 133.6 (d, $J$ = 9.9 Hz, C-2″), 132.8 (d, $J$ = 7.9 Hz, HCNO), 131.0 (C-2), 130.6 (d, $J$ = 12.7 Hz, C-3″), 123.5 (d, $J$ = 1.6 Hz, C-1), 118.1 (d, $J$ = 85.8 Hz, C-1″), 114.3 (C-3), 72.2 (d, $J$ = 154.6 Hz, $C$(CH$_3$)$_2$), 68.0 (1′–CH$_2$), 63.2 (d, $J$ = 6.6 Hz, 2 × –OCH$_2$CH$_3$), 30.3 (d, $J$ = 16.0 Hz, 6′–CH$_2$), 29.0 (d, $J$ = 16.0 Hz, 3′–CH$_2$ and 4′–CH$_2$), 28.8 (2′–CH$_2$), 25.8 (5′–CH$_2$), 23.3 (C($CH_3$)$_2$), 23.0 (d, $J$ = 49.5 Hz, 8′–CH$_2$), 22.5 (d, $J$ = 4.4 Hz, 7′–CH$_2$), 16.4 (d, $J$ = 6.1 Hz,

2 × –$OCH_2CH_3$); $^{31}P$ NMR (121.5 MHz, $CDCl_3$) $\delta$ 24.19, 23.34; HRMS-ESI: calcd. for $C_{40}H_{52}NO_5P_2^+$ $[M]^+$ 688.3315, found 688.3315.

4. Synthesis of 2-(diethoxyphosphoryl)-*N*-(3-(4-(triphenylphosphono)butoxy)benzylidene)propan-2-amine oxide iodide (**8d**). The title compound is obtained from 3-OH-PPN **2b** (0.15 g, 0.47 mmol) and IBTP **3** (0.30 g, 0.47 mmol). Compound **8d** is obtained as a yellow oil (0.11 g, 30%): $^1H$ NMR (400 MHz, $CD_3OD$) $\delta$ 8.20 (brs, H-2), 8.01 (d, $J = 2.2$ Hz, 1H, HCNO), 7.90 (m, 6H, H-2″), 7.80 (m, 6H, H-3″), 7.75 (m, 3H, H-4″), 7.63 (brd, $J = 8.0$ Hz, 1H, H-6), 7.36 (t, $J = 8.0$ Hz, 1H, H-5), 7.01 (dd, $J = 8.3$ and 2.5 Hz, 1H, H-4), 4.21 (m, 4H, 2 × –$OCH_2CH_3$), 4.11 (t, $J = 5.8$ Hz, 2H, 1′–$CH_2$), 3.52 (m, 2H, 4′–$CH_2$), 2.05 (quint, $J = 6.5$ Hz, 2H, 2′–$CH_2$), 1.90 (m, 2H, 3′–$CH_2$), 1.86, (s, 3H, $C(CH_3)_2$), 1.82 (s, 3H, $C(CH_3)_2$), 1.33 (t, $J = 7.0$ Hz, 6H, 2 × –$OCH_2CH_3$); $^{13}C$ NMR (75 MHz, $CD_3OD$) $\delta$ 160.0 (C-3), 136.4 (d, $J = 2.8$ Hz, 3C, C-4″), 135.9 (d, $J = 6.6$ Hz, HCNO), 135.0 (d, $J = 9.0$ Hz, 6C, C-2″), 133.0 (d, $J = 1.1$ Hz, C-1), 131.7 (d, $J = 12.6$ Hz, 6C, C-3″), 130.6 (C-5),123.9 (C-6), 119.9 (d, $J = 86.4$ Hz, 3C, C-1″), 119.0 (C-2), 115.9 (C-4), 75.1 (d, $J = 160.1$ Hz, $C(CH_3)_2$), 67.8 (1′–$CH_2$), 65.0 (d, $J = 7.2$ Hz, 2 × –$OCH_2CH_3$), 30.7 (d, $J = 16.5$ Hz, 2′–$CH_2$), 23.9 ($C(CH_3)_2$), 22.4 (d, $J = 72.4$ Hz, 4′–$CH_2$), 20.4 (d, $J = 3.9$ Hz, 3′–$CH_2$), 17.0 (d, $J = 6.0$ Hz, 2 × –$OCH_2CH_3$); $^{31}P$ NMR (121.5 MHz, $CD_3OD$) $\delta$ 23.90, 23.24; HRMS-ESI: calcd. for $C_{36}H_{44}NO_5P_2^+$ $[M]^+$ 632.2689, found 632.2690.

### 3.7 General Procedure for the Diphenylphosphonyl nitrones (9a–d)

The appropriate PPN derivative (1 eq.) is dissolved in acetonitrile (63 mM) and 60%-NaH (2.5 eq.) is added portionwise at 0 °C. The slurry is stirred 30 min at room temperature. A solution of the appropriate linker **3**, **4** or **7** (1.2 eq.) in acetonitrile (76 mM) is slowly added at 0 °C and the reactional mixture is then stirred for 12 h at 40 °C. Cold water (half the total volume of acetonitrile) is added and the solution is extracted with dichloromethane (3 × volume of water). The organic layers are gathered and concentrated. The residual oil is dissolved in the minimum of dichloromethane and diethyl ether (5 × volume of dichloromethane) is added dropwise while maintaining the stirring. Once the organic layer is translucent it is filtered and the operation repeated twice. The organic layers are gathered, dried over $MgSO_4$, filtered and concentrated to afford the desired compounds.

1. Synthesis of 2-(diethoxyphosphoryl)-*N*-(4-(4-(diphenylphosphoryl)butoxy)benzylidene)propan-2-amine oxide (**9a**). The title compound is obtained from

4-OH-PPN **2a** (0.2 g, 0.63 mmol) and IBTP **3** (0.43 g, 0.76 mmol). Compound **9a** is obtained as a yellow pale oil (0.23 g, 64%): $^{1}$H NMR (300 MHz, $CDCl_3$) $\delta$ 8.12 (d, $J = 8.5$ Hz, 2H, H-2), 7.62 (m, 4H, H-2″), 7.54 (brs, 1H, HCNO), 7.37 (m, 6H, H-4″ and H-3″), 6.74 (d, $J = 8.5$ Hz, 2H, H-3), 4.08 (m, 4H, 2 × –OC$H_2$CH$_3$), 3.86 (t, $J = 5.8$ Hz, 2H, 1′–$CH_2$), 2.24 (m, 2H, 4′–$CH_2$), 1.78 (m, 4H, 2′–$CH_2$ and 3′–$CH_2$), 1.72, (s, 3H, C($CH_3$)$_2$), 1.68 (s, 3H, C($CH_3$)$_2$), 1.20 (t, $J = 7.0$ Hz, 6H, 2 × –OCH$_2$C$H_3$); $^{13}$C NMR (75 MHz, $CDCl_3$) $\delta$ 160.4 (C-4), 132.9 (d, $J = 6.1$ Hz, HCNO), 132.6 (d, $J = 98.5$ Hz, C-1″), 131.4 (d, $J = 2.8$ Hz, C-4″), 130.8 (C-2), 130.7 (d, $J = 9.4$ Hz, C-2″), 128.6 (d, $J = 11.6$ Hz, C-3″), 123.6 (d, $J = 1.7$ Hz, C-1), 114.1 (C-3), 72.2 (d, $J = 154.6$ Hz, $C$($CH_3$)$_2$), 67.1 (1′–$CH_2$), 63.3 (d, $J = 6.6$ Hz, 2 × –O$CH_2$CH$_3$), 30.0 (d, $J = 14.3$ Hz, 2′–$CH_2$), 29.2 (d, $J = 72.1$ Hz, 4′–$CH_2$), 23.3 (C($CH_3$)$_2$), 18.4 (d, $J = 3.3$ Hz, 3′–$CH_2$),16.4 (d, $J = 6.0$ Hz, 2 × –OCH$_2$$C$H$_3$); $^{31}$P NMR (121.5 MHz, $CDCl_3$) $\delta$ 32.29, 23.34; MS-ESI: $m/z$ (%): 572.2 (100) [M + H]$^+$, 594.2 (10) [M + Na]$^+$.

2. Synthesis of 2-(diethoxyphosphoryl)-*N*-(4-(6-(diphenylphosphoryl)hexyloxy)benzylidene)propan-2-amine oxide (**9b**). The title compound is obtained from 4-OH-PPN **2a** (0.2 g, 0.63 mmol) and IHTP **4** (0.43 g, 0.76 mmol). Compound **9b** is obtained as a yellow oil (0.17 g, 43%): $^{1}$H NMR (300 MHz, $CDCl_3$) $\delta$ 8.24 (d, $J = 8.8$ Hz, 2H, H-2), 7.71 (m, 4H, H-2″), 7.63 (d, $J = 2.3$ Hz, 1H, HCNO), 7.47 (m, 4H, H-3″), 7.44 (m, 2H, H-4″), 6.86 (d, $J = 8.8$ Hz, 2H, H-3), 4.18 (m, 4H, $J = 7.3$ Hz, 2 × –OC$H_2$CH$_3$), 3.93 (t, $J = 6.3$ Hz, 2H, 1′–$CH_2$), 2.27 (m, 2H, 6′–$CH_2$), 1.83, (s, 3H, C($CH_3$)$_2$), 1.78 (s, 3H, C($CH_3$)$_2$), 1.70 (m, 2H, 5′–$CH_2$*), 1.63 (m, 2H, 2′–$CH_2$*), 1.44 (m, 4H, 3′–$CH_2$ and 4′–$CH_2$), 1.30 (t, $J = 7.1$ Hz, 6H, 2 × –OCH$_2$C$H_3$), *may be reversed; $^{13}$C NMR (75 MHz, $CDCl_3$) $\delta$ 160.6 (C-4), 133.0 (d, $J = 97.9$ Hz, C-1″), 132.8 (d, $J = 5.5$ Hz, HCNO), 131.3 (d, $J = 2.8$ Hz, C-4″), 130.8 (C-2), 130.7 (d, $J = 8.8$ Hz, C-2″), 128.6 (d, $J = 11.5$ Hz, C-3″), 123.4 (d, $J = 1.7$ Hz, C-1), 114.2 (C-3), 72.1 (d, $J = 154.6$ Hz, $C$($CH_3$)$_2$), 67.8 (1′–$CH_2$), 63.3 (d, $J = 7.1$ Hz, 2 × –O$CH_2$CH$_3$), 30.5 (4′–$CH_2$), 29.5 (d, $J = 72.1$ Hz, 6′–$CH_2$), 28.7 (2′–$CH_2$), 25.4 (3′–$CH_2$), 23.3 (C($CH_3$)$_2$), 21.4 (d, $J = 3.8$ Hz, 5′–$CH_2$), 16.4 (d, $J = 6.0$ Hz, 2 × –OCH$_2$$C$H$_3$); $^{31}$P NMR (121.5 MHz, $CDCl_3$) $\delta$ 32.51, 23.38; MS-ESI: $m/z$ (%): 600.3 (100) [M + H]$^+$, 622.3 (8) [M + Na]$^+$.

3. Synthesis of 2-(diethoxyphosphoryl)-*N*-(4-(8-(diphenylphosphoryl)octyloxy)benzylidene)propan-2-amine oxide (**9c**). The title compound is obtained from 4-OH-PPN **2a** (0.13 g,

0.4 mmol) and IOTP **7** (0.25 g, 0.4 mmol). Compound **9c** is obtained as a yellow oil (0.08 g, 32%): $^{1}$H NMR (300 MHz, $CDCl_3$) $\delta$ 8.25 (d, $J$ = 8.8 Hz, 2H, H-2), 7.72 (m, 4H, H-2″), 7.65 (d, $J$ = 2.3 Hz, 1H, HCNO), 7.46 (m, 6H, H-3″ and H-4″), 6.89 (d, $J$ = 8.8 Hz, 2H, H-3), 4.19 (m, 4H, $J$ = 7.3 Hz, 2 × –OC$H_2$CH$_3$), 3.96 (t, $J$ = 6.3 Hz, 2H, 1′–$CH_2$), 2.25 (m, 2H, 8′–$CH_2$), 1.84, (s, 3H, C($CH_3$)$_2$), 1.78 (s, 3H, C($CH_3$)$_2$), 1.74 (m, 2H, 7′–$CH_2$), 1.62 (m, 4H, 2′–$CH_2$ and 3′–$CH_2$), 1.39 (m, 6H, 4′$CH_2$, 5′–$CH_2$ and 6′–$CH_2$), 1.30 (t, $J$ = 7.1 Hz, 6H, 2 × –OCH$_2$C$H_3$); $^{13}$C NMR (75 MHz, $CDCl_3$) $\delta$ 160.5 (C-4), 133.0 (d, $J$ = 97.9 Hz, C-1″), 132.8 (d, $J$ = 5.5 Hz, HCNO), 131.6 (d, $J$ = 2.8 Hz, C-4″), 130.9 (C-2), 130.6 (d, $J$ = 8.8 Hz, C-2″), 128.5 (d, $J$ = 11.5 Hz, C-3″), 123.3 (d, $J$ = 1.7 Hz, C-1), 114.1 (C-3), 72.1 (d, $J$ = 154.6 Hz, $C$(CH$_3$)$_2$), 67.7 (1′–$CH_2$), 63.2 (d, $J$ = 7.1 Hz, 2 × –O$CH_2$CH$_3$), 30.5 (6′–$CH_2$), 29.5 (d, $J$ = 72.1 Hz, 8′–$CH_2$), 28.9 (3′–$CH_2$ and 4′–$CH_2$), 28.7 (2′–$CH_2$), 25.7 (5′–$CH_2$), 23.2 (C($C$H$_3$)$_2$), 21.3 (d, $J$ = 3.8 Hz, 7′–$CH_2$),16.4 (d, $J$ = 6.0 Hz, 2 × –OCH$_2$$C$H$_3$); $^{31}$P NMR (121.5 MHz, $CDCl_3$) $\delta$ 32.67, 23.44; HRMS-ESI: calcd. for $C_{34}H_{48}NO_6P_2^+$ [M + H]$^+$ 628.2951, found 628.2948.

4. Synthesis of 2-(diethoxyphosphoryl)-*N*-(3-(4-(diphenylphosphoryl)butoxy)benzylidene)propan-2-amine oxide (**9d**). The title compound is obtained from 3-OH-PPN **2b** (0.2 g, 0.63 mmol) and IBTP **4** (0.43 g, 0.76 mmol). Compound **9d** is obtained as a yellow oil (0.19 g, 53%): $^{1}$H NMR (500 MHz, $CD_3OD$) $\delta$ 8.12 (brs, H-2), 7.88 (d, $J$ = 2.4 Hz, 1H, HCNO), 7.77 (m, 4H, H-2″), 7.70 (brd, $J$ = 7.9 Hz, 1H, H-6), 7.59 (m, 2H, H-4″), 7.52 (m, 4H, H-3″), 7.33 (t, $J$ = 7.9 Hz, 1H, H-5), 6.99 (dd, $J$ = 7.9 and 2.3 Hz, 1H, H-4), 4.21 (m, 4H, 2 × –OC$H_2$CH$_3$), 4.02 (t, $J$ = 6.1 Hz, 2H, 1′–$CH_2$), 2.50 (m, 2H, 4′–$CH_2$), 1.92 (quint, $J$ = 6.7 Hz, 2H, 2′–$CH_2$), 1.84 (s, 3H, C($CH_3$)$_2$), 1.81 (s, 3H, C($CH_3$)$_2$), 1.77 (m, 2H, 3′–$CH_2$),1.33 (t, $J$ = 7.2 Hz, 6H, 2 × –OCH$_2$C$H_3$); $^{13}$C NMR (125 MHz, $CD_3OD$) $\delta$ 160.2 (C-3), 136.1 (d, $J$ = 6.4 Hz, HCNO), 133.7 (C-4″), 133.5 (d, $J$ = 98.9 Hz, C-1″), 132.9 (C-1), 131.8 (d, $J$ = 9.2 Hz, C-2″), 130.6 (C-5), 130.1 (d, $J$ = 11.9 Hz, C-3″), 123.7 (C-6), 119.0 (C-2), 115.6 (C-4), 74.7 (d, $J$ = 159.5 Hz, $C$(CH$_3$)$_2$), 68.3 (1′–$CH_2$), 65.0 (d, $J$ = 6.4 Hz, 2 × –O$CH_2$CH$_3$), 31.0 (d, $J$ = 14.7 Hz, 2′–$CH_2$), 29.4 (d, $J$ = 72.4 Hz, 4′–$CH_2$), 23.6 (C($C$H$_3$)$_2$), 19.4 (d, $J$ = 3.7 Hz, 3′–$CH_2$), 16.8 (d, $J$ = 5.5 Hz, 2 × –OCH$_2$$C$H$_3$); $^{31}$P NMR (101.3 MHz, $CD_3OD$) $\delta$ 36.93, 23.24; MS-ESI: *m/z* (%): 572.2 (100) [M + H]$^+$, 594.2 (46) [M + Na]$^+$.

### 3.8 Cell Cultures and Cytotoxicity Assays for Nitrones 8(a–d) and 9(a–d)

1. Renew the medium of confluent cells and expose them for 24 h to test compounds (0.01 μM to 0.2 mM) in wells containing a final 0.1% DMSO concentration in DMEM (vehicle).
2. Assess cytotoxicity at the end of drug exposure: remove 10 μL of medium from each well for determining extracellular LDH release as described in [8]. Remove the remaining incubation medium, wash cells two times with PBS 1× (+/+) and determine cytotoxicity using ATP, FMCA, and MTT assays (*see* [8]).
3. Cytotoxicities, as assessed by the MTT assay, are significantly decreased in all new $(EtO)_2P(O)$-substituted linear nitrones as compared to TPMP and mito-PBN (Fig. 2A), consistent with our previous work on relevant cyclic structures [9]. Of interest, comparison of $IC_{50}$ values obtained in **8**- versus **9**-type nitrones (Fig. 2A) suggests that the presence of a $TPP^+$ moiety somewhat increases the cytotoxicity of mito-PPNs, a property reported earlier [7, 18]. The same trend is obtained using the other endpoints of viability and/or necrosis (LDL release, ATP depletion and FMCA assay; data not shown).

### 3.9 Protocol: EPR Spin Trapping of n-Octyloxyl Radical

1. Prepare a stock solution containing 25% v/v of 1-octanol (Sigma-Aldrich) in dry DMSO.
2. Use Eppendorf tubes (1.5 mL) for preparing a 0.5-mL aliquot of nitrones **1**, **8c** or **8d** (final concentration, 50 mM) in stock solution.
3. Add ~1 mg of $Pb(OAc)_4$ to the aliquot and vortex for 5 s.
4. Quickly add the resulting dark red mixture into a 50 μL glass capillary, seal it at both ends with Noxygen wax, and center it in the resonant EPR cavity.
5. Record the EPR spectrum at room temperature within 60 s after addition of $Pb(OAc)_4$. Typical EPR settings used: modulation amplitude, 0.028–0.063 mT; receiver gain, $1.6–2.2 \times 10^5$, time constant, 81.92 ms; sweep rate, 0.12 mT/s, field resolution, 4096 points. Due to the relatively good persistency of the signals, up to 5 individual spectra are averaged.
6. Transfer spectral data to a computer and use simulation software WinSim ([19]; https://www.niehs.nih.gov/research/resources/software/tox-pharm/tools/index.cfm) for calculating $a_N$, $a_H$ and $a_P$ coupling constants of spin adducts (Table 1).
7. Figure 3 illustrates the good EPR spin trapping property in vitro of nitrones **8c,d** compared to **1** toward *n*-octyloxyl radical, a model lipophilic alkoxyl radical mimicking those that can transiently form in cells undergoing lipid peroxidation (*see* **Note 1**).

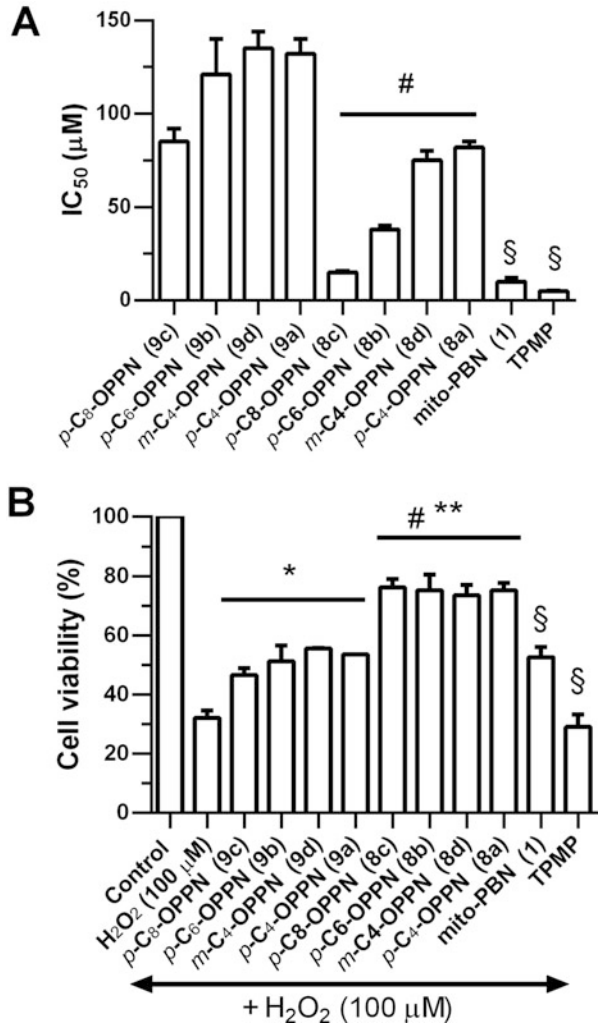


**Fig. 2** (**A**) $IC_{50}$ values after 24 h exposure of normal murine 3T3 fibroblasts, and (**B**) antiapoptotic activity in Schwann cells treated by $H_2O_2$ (100 μM) for 16 h of new nitrones. $IC_{50}$, defined as the concentration resulting in 50% cell viability, was calculated from concentration-response curves (0.1 μM to 0.2 mM). Schwann cells were preincubated with nitrones (0.1 μM) for 8 h before $H_2O_2$ exposure. Data from MTT assay are means ± SD of 3–6 independent experiments made in triplicate. Statistics: one-way ANOVA ($p < 0.05$) followed by Duncan test: $^{\#}p < 0.05$ versus **9**-type nitrones; $^{\S}p < 0.05$ versus **8**- and **9**-type nitrones; $^{*}p < 0.05$ and $^{**}p < 0.01$ versus $H_2O_2$-treated cells. New nitrones were given acronyms to visualize structure–activity effects

### *3.10 Protocol: Isolated Liver Experiments and Subcellular Mitochondrial and Cytosolic Fractions Preparation [10, 13]*

Animals are deeply anesthetized by intraperitoneal injection of sodium pentobarbital (100 mg/kg). After the opening of the abdomen wall, the portal vein is cannulated (antegrade perfusion) and the liver is perfused at 37 °C in a nonrecirculating mode by a KH bicarbonate buffer. The starting perfusion rate is set at 20 mL/min (*see* **Note 2**). The excised liver is weighed, and the perfusion is adjusted to a flow rate of 3 mL/min/g of wet weight. After a 30 min equilibration period, an aliquot of the stock solution of **8a** or **9a** nitrone in DMSO is added to the perfusion medium to

**Table 1**
**Calculated EPR parameters of selected *n*-octyloxyl spin adducts**

| Nitrone | $a_N$ (mT) | $a_H$ | $a_P$ | *g*-factor |
|---|---|---|---|---|
| **1** | 1.368 | 0.196 | – | 2.0060 |
| **8c** | 1.266 | 0.133 | 4.031 | 2.0062 |
| **8d** | 1.259 | 0.133 | 3.994 | 2.0062 |

Spectra are recorded at room temperature in DMSO

achieve a final concentration of 1 μM, and the perfusion is extended for 1 h. The perfusate is then switched to an ice-cold KH buffer for 10 min (*see* **Note 3**), and the liver is homogenized in five volumes of a solution containing 0.25 M sucrose and 10 mM HEPES. After filtration, the homogenate is centrifuged at 750 × *g* for 10 min at 2 °C, the mitochondrial and cytosolic fractions are isolated from the supernatant by differential centrifugation as previously described [10, 13] and finally resuspended in 1 mL KH buffer. These samples are extracted at 20 °C with dichloromethane (2 × 5 mL), and the combined organic layers are concentrated under reduced pressure to give a dry residue. Data are pooled from 3 to 4 livers/test compound. Each residue is subsequently dissolved in 20 μL of DMSO and frozen until $^{31}$P NMR analysis.

### 3.11 $^{31}$P NMR on Mitochondrial and Cytosolic Extracts

1. Dilute the mitochondrial or cytosolic residues with DMSO-$d_6$ (500 μL) and transfer the solution into a 5-mm NMR tube. Record the $^{31}$P NMR spectrum under DMSO-$d_6$ lock solutions using a ZGIG sequence with a 30° (17.07 μs) pulse width, acquisition time of 0.84 s, repetition delay of 2.00 s, and a 32 scans acquisition. Spectra of mitochondrial and cytosolic repartition for nitrones **8a** and **9a** are shown in Fig. 4 (here, we used a Bruker Avance III spectrometer operating at a phosphorus frequency of 242.94 MHz).
2. $^{31}$P NMR spectra of Fig. 4a, c show that the $TPP^+$ vectorized nitrone **8a** distributed both in mitochondria and cytosol (with a mitochondrial–cytosolic ratio of 2:1), based on the detection of the $P(O)(OEt)_2$ ($\delta$ 24.1 ppm) and $TPP^+$ ($\delta$ 24.6 ppm) peaks, whereas its diphenylphosphonyl structural analog **9a** is found only in cytosol, based on the detection of the $P(O)(OEt)_2$ ($\delta$ 24.1 ppm) and $P(O)Ph_2$ ($\delta$ 31.1 ppm) peaks (Fig. 4b, d) (*see* **Note 4**).

### 3.12 Apoptosis Experiments

1. Expose Schwann cells to different $H_2O_2$ concentrations for 16 h. Perform the MTT and LDH assays to determine the cell damage and select the appropriate $H_2O_2$ concentration to establish the model of oxidative stress [14] (*see* **Note 5**).

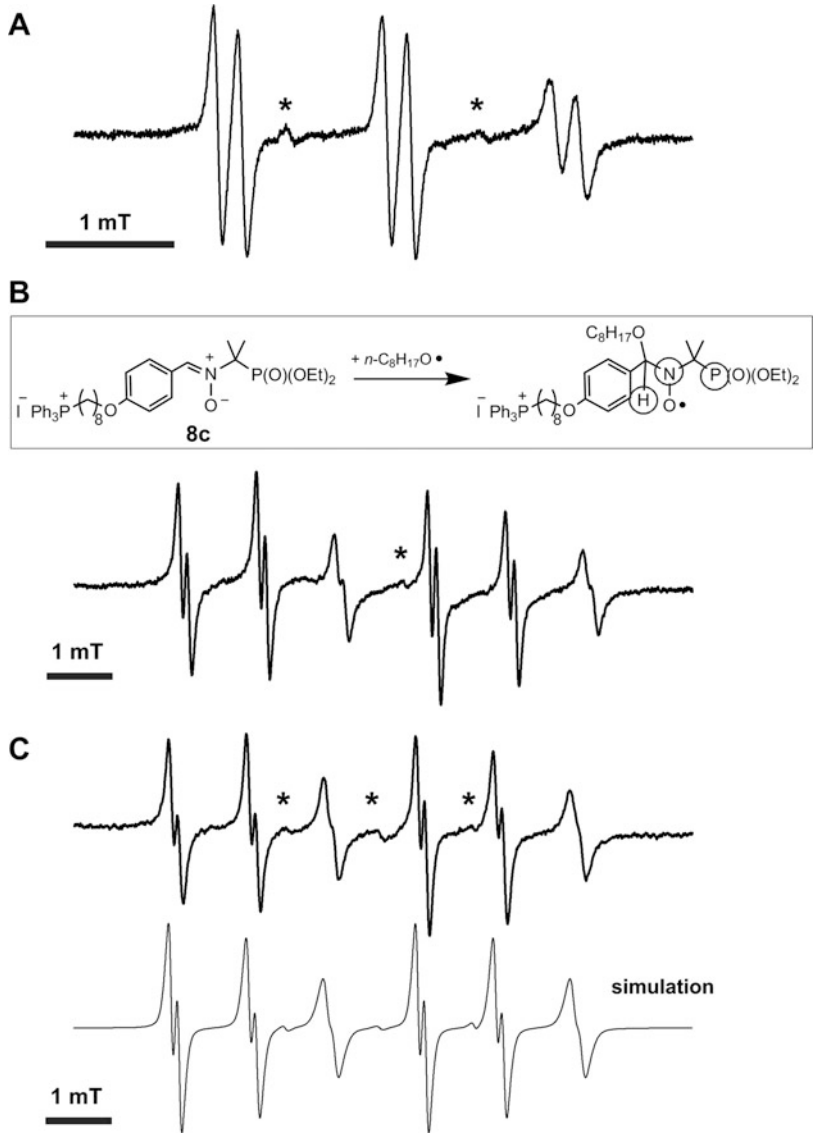


**Fig. 3** EPR spectra of *n*-octyloxyl radical adducts formed upon reaction of lead tetraacetate with DMSO solutions containing 25% v/v 1-octanol and ~50 mM of nitrones **1** (**A**), **8c** (**B**), or **8d** (**C**), showing signal simulation. Insert: Spin trapping reaction for nitrone **8c** showing coupling nuclei in circles. Signals were obtained at room temperature by signal averaging 3 (**A**), 1 (**B**), or 5 (**C**) scans. Asterisks indicate EPR lines belonging to trace unknown spin adducts (<5% of total signal). For simulated signal of (**C**), a good fit was obtained by assuming an additional triplet with $a_N = 1.525$ mT (0.7% of total signal)

2. Incubate Schwann cells with test nitrone and TPMP solutions (0.1–1 μM) for 8 h and then add $H_2O_2$ (100 μM) for 16 h. Perform the MTT and LDH assays to determine cell damage.
3. Cell viability, as assessed by the MTT assay, dropped by 70% upon treatment with $H_2O_2$. As compared to TPMP all nitrones (at 0.1 μM) better inhibited this $H_2O_2$-induced apoptosis of

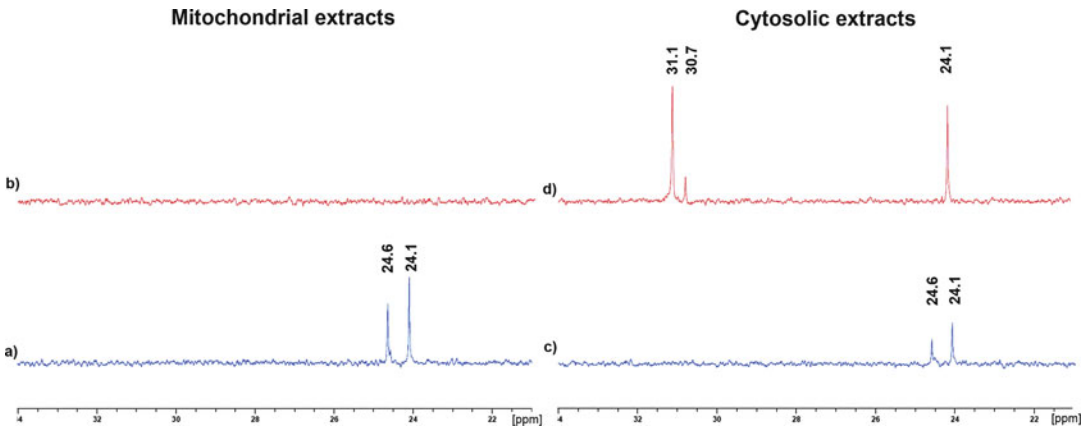


**Fig. 4** $^{31}P$ NMR signals in DMSO-$d_6$ recorded from samples of mitochondrial (**a**, **b**) and cytosolic (**c**, **d**) extracts from the same rat liver that underwent a 60 min normothermic perfusion with Krebs–Henseleit buffer containing 1 μM of **8a** (**a**, **c**) or **9a** (**b**, **d**). Chemical shifts (in ppm relative to 85% $H_3PO_4$ in $D_2O$): $(EtO)_2P(O)$-, 24.1 and $Ph_3P^+$-, 24.6 (**8a**) or $P(O)Ph_2$- 31.1 (**9a**) in DMSO-$d_6$

the cells (Fig. 2B), suggesting that direct FR scavenging may be a relevant protective mechanism both in cytosol and mitochondria. Despite $TPP^+$ vectorized compounds of **8**-type have shown enhanced toxicity versus **9**-type derivatives (Fig. 2A) they are yet found significantly more efficient against apoptosis (Fig. 2B). In the $H_2O_2$-based apoptosis model and cell type selected here, this suggests that specifically targeting the mitochondria would be a better therapeutic strategy. The shortest methylene chain lengths ($n = 4$ versus $n = 6$ or 8) are found to alleviate the $TPP^+$ induced cytotoxicity property in mito-PPNs, but not in their phosphonyl analogs (Fig. 2a), while no such structural effect is evident in apoptosis experiments (Fig. 2B).

## 4 Notes

1. Spin trapping is a widely used technique where an unstable free radical reacts with a molecule (mostly a nitrone in biological studies) to form a reasonably more stable, EPR detectable spin adduct (generally a nitroxide). Under certain conditions EPR parameters of a biological spin adduct (e.g., coupling constants, *see* Fig. 3) are characteristic of the trapped radical, the assignment of which must be confirmed by suitable controls, or comparison with the literature or spin adduct databases [20]. To the authors' knowledge a few *n*-octyloxyl spin adducts have been reported, using nonphosphorylated cyclic nitrones [21].
2. It is assumed that the liver weight represents about 4% of the body weight (i.e., 6–8 g).

3. This step is assumed to completely remove the test compound from the extracellular space.
4. Compounds **8** and **9** bear two phosphorus atoms, yielding two $^{31}P$ NMR peaks. It has been demonstrated that the chemical shift associated with the $TPP^+$ group remains constant at ~24.6 ppm [10] while the one associated with the $(EtO)_2P(O)$ group is ~24.1 ppm [8, 10]. A third peak is observed in the cytosolic extract (30.7 ppm) of nitrone **9a** (Fig. 4d) and is probably due to degradation or liver metabolism of compound **9a** during the recirculating process.
5. Here the $H_2O_2$ concentration that induced ~60% of cell viability in this oxidative stress-induced model of apoptosis is 100 μM.

## Acknowledgments

The study was supported by fundings of the Agence Nationale de la Recherche, France (ANR JCJC MitoDiaPM- N° ANR-17-CE34-0006-01). The support of the work of C.P. by the French Research Ministry (MNERT) is gratefully acknowledged. The authors thank M. Cassien, E. Ricquebourg, M. Robin, and V. Pique for discussion and expert technical help.

### References

1. van der Bliek AM, Sedensky MM, Morgan PG (2017) Cell biology of mitochondrion. Genetics 207(3):843–871
2. Jones DP, Sies H (2015) The redox code. Antioxid Redox Signal 23(9):734–746
3. Pfeffer G, Majamaa K, Turnbull DM, Chinnery PF (2012) Treatment for mitochondrial disorders. Cochrane Database Syst Rev 4: CD004426. https://doi.org/10.1002/14651858.
4. Murphy MP (2008) Targeting lipophilic cations to mitochondria. Biochim Biophys Acta Bioenerg 1777:1028–1031
5. Floyd RA, Kopke RD, Choi CH, Foster SB, Doblas S, Towner RA (2008) Nitrones as therapeutics. Free Radic Biol Med 45:1361–1374
6. Murphy MP, Echtay KS, Blaikie FH et al (2003) Superoxide activates uncoupling proteins by generating carbon-centered radicals and initiating lipid peroxidation. Studies using a mitochondria-targeted spin trap derived from α-phenyl-***N-tert***-butylnitrone. J Biol Chem 278(49):48534–48545
7. Reily C, Mitchell T, Chacko BK et al (2013) Mitochondrially targeted compounds and their impact on cellular bioenergetics. Redox Biol 1:86–93
8. Cassien M, Petrocchi C, Thétiot-Laurent S et al (2016) On the vasoprotective mechanisms underlying novel β-phosphorylated nitrones: focus on free radical characterization, scavenging and NO-donation in a biological model of oxidative stress. Eur J Med Chem 119:197–217
9. Maurelli E, Culcasi M, Delmas-Beauvieux MC et al (1999) New perspectives on the cardioprotective phosphonate effect of the spin trap 5-(diethoxyphosphoryl)-5-methyl-1-pyrroline *N*-oxide: an hemodynamic and 31-P NMR study in rat hearts. Free Radic Biol Med 27:34–41
10. Culcasi M, Casano G, Lucchesi C et al (2013) Synthesis and biological characterization of new aminophosphonates for mitochondrial pH determination by $^{31}P$ NMR spectroscopy. J Med Chem 56(6):2487–2499
11. Culcasi M, Thétiot-Laurent S, Atteia A, Pietri S (2015) Mitochondrial, acidic, and cytosolic pHs determination by 31P NMR spectroscopy: design of new sensitive targeted pH probes. In:

Weissig V, Edeas M (eds) Mitochondrial medicine. Methods in Molecular Biology, vol 1265. Humana Press, New York, pp 135–147

12. Culcasi M, Benameur L, Mercier A et al (2012) EPR spin trapping evaluation of ROS production in human fibroblasts exposed to cerium oxide nanoparticles: evidence for NADPH oxidase and mitochondrial stimulation. Chem Biol Interact 199(3):161–176
13. Cova D, De Angelis L, Monti E, Piccinini F (1992) Subcellular distribution of two spin trapping agents in rat heart: possible explanation for their different protective effects against doxorubicin-induced cardiotoxicity. Free Radic Res Commun 15(6):353–360
14. He B, Wu F, Fan L et al (2018) Carboxymethylated chitosan protects Schwann cells against hydrogen peroxide-induced apoptosis by inhibiting oxidative stress and mitochondria dependent pathway. Eur J Pharmacol 825:48–56
15. Kaewkhaw R, Scutt AM, Haycock JW (2012) Integrated culture and purification of rat Schwann cells from freshly isolated adult tissue. Nat Protoc 7(11):1996–2004
16. Lin TK, Hughes G, Muratovska A et al (2002) Specific modification of mitochondrial protein thiols in response to oxidative stress: a proteomics approach. J Biol Chem 277 (19):17048–17056
17. Klein SM, Zhang C, Jiang YL (2008) Simple synthesis of fresh alkyl iodides using alcohols and hydroiodic acid. Tetrahedron Lett 49 (16):2638–2641
18. Bergeron KL, Murphy EL, Majofodun O et al (2009) Arylphosphonium salts interact with DNA to modulate cytotoxicity. Mutat Res 673:141–148
19. Duling DR (1994) Simulation of multiple isotropic spin trap EPR spectra. J Magn Reson B 104:105–110
20. Buettner GR (1987) Spin trapping: ESR parameters of spin adducts. Free Radic Biol Med 3 (4):259–303
21. Stolze K, Udilova N, Nohl H (2002) Spin adducts of superoxide, alkoxyl, and lipid-derived radicals with EMPO and its derivatives. Biol Chem 383(5):813–820

# Chapter 6

# Insights on Targeting Small Molecules to the Mitochondrial Matrix and the Preparation of MitoB and MitoP as Exomarkers of Mitochondrial Hydrogen Peroxide

**Andrew G. Cairns, Stephen J. McQuaker, Michael P. Murphy, and Richard C. Hartley**

## Abstract

Small molecules can be physicochemically targeted to the mitochondrial matrix using the lipophilic alkyltriphenylphosphonium (TPP) group. Once in the mitochondria the TPP conjugate can detect or influence processes within the mitochondrial matrix directly. Alternatively, the conjugate can behave as a prodrug, which is activated by release from the TPP group either using an internal or external instruction. Small molecules can be designed that can be used in any cell line, tissue, or whole organism, allow for temporal control, and can be applied in a reversible dose-dependent fashion. An example is the detection and quantification of hydrogen peroxide in mitochondria of whole living organisms by MitoB. Hydrogen peroxide produced within the mitochondrial matrix is involved in signaling and implicated in the oxidative damage associated with aging and a wide range of conditions including cardiovascular disease, neurodegeneration, and cancer. MitoB accumulates in mitochondria and is converted into the exomarker, MitoP, by hydrogen peroxide in the mitochondrial matrix. The hydrogen peroxide concentration is determined from the ratio of MitoP to MitoB after a period of incubation, and this ratio is determined by mass spectrometry using d15-MitoP and d15-MitoB as internal standards. Here we discuss the targeting of small molecules to the mitochondrial matrix using TPP, and describe the synthesis of MitoB and MitoP and the deuterated standards necessary for quantification of hydrogen peroxide in the mitochondrial matrix of whole living organisms.

**Key words** Mitochondria, Targeting, Reactive oxygen species, Exomarker, Oxidative stress, Hydrogen peroxide, Chemical biology, Mass spectrometry, Drug delivery

## 1 Introduction

### *1.1 Mitochondria-Targeted Drugs, Prodrugs, and Bioactives*

Small molecules are useful both as medicines and as tools to elucidate biological processes [1]. A key advantage to small molecules is that in theory they can be used in any cell line, tissue, organ, or organism. Their use does not require the manipulation of proteins and gene expression through mutation and RNA-dependent gene silencing, so they can be applied to native tissues and organisms.

Volkmar Weissig and Marvin Edeas (eds.), *Mitochondrial Medicine: Volume 1: Targeting Mitochondria*, Methods in Molecular Biology, vol. 2275, https://doi.org/10.1007/978-1-0716-1262-0_6,

Furthermore, a small molecule that is useful for the study of a biological process can often be a lead compound for drug discovery, and vice versa.

Mitochondria play a central role in metabolism, supplying most of the ATP used by cells, and also are key to signaling, homeostasis, and the events leading up to apoptosis and necrosis [2, 3]. Mitochondrial dysfunction contributes to wide range of pathologies including cardiovascular diseases, neurodegeneration, and cancer [2], and is implicated in the process of aging itself [4–6].

Drugs can act on targets in the mitochondria without having an independent mechanism for their accumulation there. However, efficacy would be increased and side-effects decreased if the concentration of a drug is elevated near its site of action. For this reason, it is desirable to have a mechanism of targeting small molecules to the mitochondria, and in particular the mitochondrial matrix where much of metabolism is sited (Fig. 1). Targeting of a bioactive compound or sensor to mitochondria requires selective

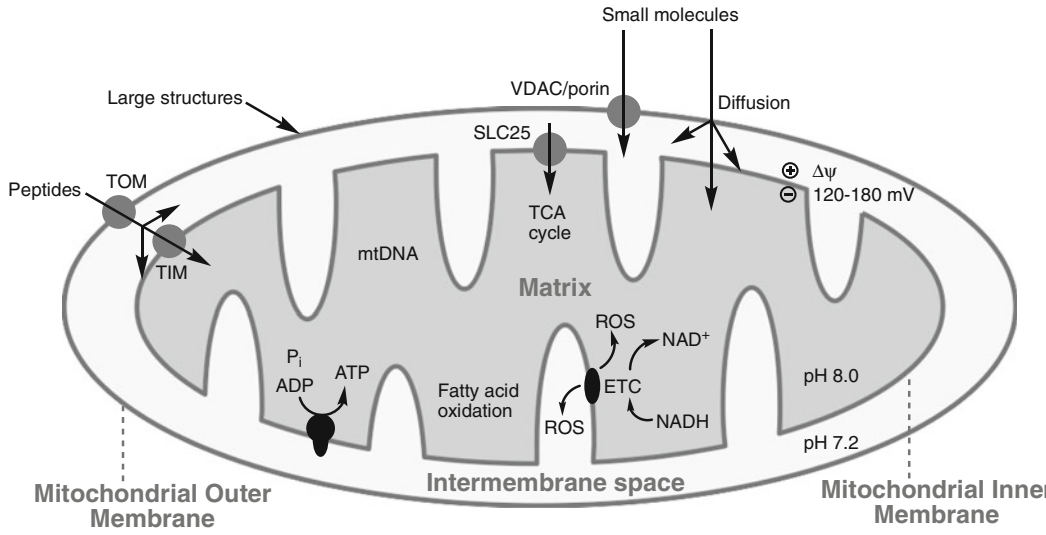


**Fig. 1** Delivery to particular subcompartments is necessary for targeting, for example the biochemistry of the tricarboxylic acid (TCA) cycle can only be accessed if the molecule can reach the matrix. There are a number of routes that allow particular localizations. Large structures may associate with the outer membrane. Relatively small molecules (including some peptides) may diffuse freely across the outer and inner membranes provided they are sufficiently lipophilic. Small charged or highly polar molecules may be transported across the mitochondrial outer membrane through the voltage dependent anion channel (VDAC) and may enter the matrix through one of the SLC25 family of mitochondrial carriers. Most peptides cannot cross membranes by free diffusion but may cross the mitochondrial outer membrane if recognized by the translocase of the outer membrane (TOM) and traverse the mitochondrial inner membrane if recognized by the translocase of the inner membrane (TIM). Even if not specifically targeted to a subcompartment by a particular mechanism of uptake, bioactive molecules or sensors may be localized through their interactions with a particular protein or lipid, such as cardiolipin, but only if an appropriate mechanism for crossing the intervening membrane or membranes allows this

delivery to a particular mitochondrial subcompartment. Delivery to the outside of the mitochondrial outer membrane (MOM), or to the intermembrane space or to the matrix will dramatically affect what processes can be influenced effectively by a bioactive compound and what effects a sensor may detect. For example, some anticancer drugs that induce apoptosis exert their effect on targets in the MOM [7–9], while some compounds that limit ischemic reperfusion injury act on succinate dehydrogenase located on the matrix side of the MIM [10, 11]. Colocalization of a fluorescent compound with fluorescently labelled mitochondria in cells is often presented as sufficient evidence of successful targeting. Unfortunately, the diffraction limited optics of normal microscopy do not allow suborganellar resolution without the use of super-resolution techniques [12]. Thus, a compound may be colocalized with mitochondria, but still not delivered to the correct site for its proposed mode of action.

There are a variety of approaches for the delivery of molecular cargo to mitochondria [13]. These include nanoparticles and liposomes [14–16], and peptide sequences [17, 18], but the most general method of delivery involves conjugating the small molecule to a lipophilic cation [3, 19]. The last of these takes advantage of the membrane potential across the mitochondrial inner membrane (MIM) to target compounds specifically to the mitochondrial matrix.

The electron transport chain (ETC) sited in the MIM pumps protons out of the mitochondrial matrix into the intermembrane space between the MIM and the mitochondrial outer membrane. This gives rise to a small difference in pH and a high membrane potential due to charge separation across the MIM, because the positively charged protons are not accompanied by anions. Thus, the membrane potential ($\Delta\psi$) across the MIM is negative on the matrix side. A proton-motive force resulting from the membrane potential and to a lesser extent the pH gradient drives the production of ATP from ADP and phosphate by ATP-synthase [20].

Targeting to the mitochondrial matrix can be achieved by incorporating a lipophilic cation in the drug (Fig. 2). Lipophilic cations can cross the MIM freely by diffusion both in and out. The positive charge leads to accumulation within the mitochondrial matrix as a result of $\Delta\psi$. The process is governed by the Nernst equation so that for every 60 mV there is a tenfold accumulation in the matrix relative to the cytosol. This results in a several-hundred-fold higher concentration in the matrix for $\Delta\psi$ between 120 and 180 mV. There is also a small plasma $\Delta\psi$ that leads to a 3–10 fold accumulation of lipophilic cations within the cell, and this means that the concentration within the mitochondrial matrix may be over a thousand-fold that outside the cell [3, 19].

It is important to note that the individual lipophilic cations freely diffuse in and out of the mitochondria. If such diffusion is

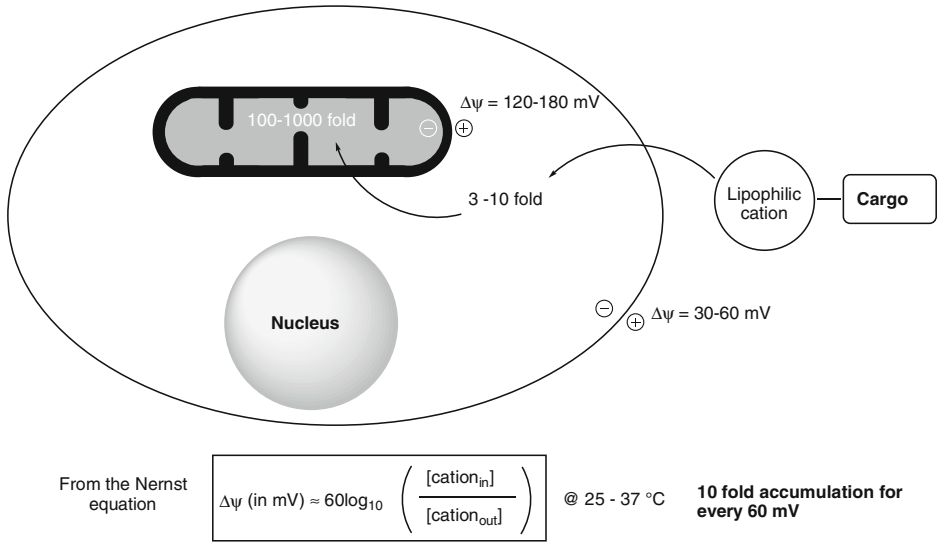


**Fig. 2** The accumulation of lipophilic cation conjugates in the mitochondrial matrix due to the plasma membrane potential and the greater membrane potential across the mitochondrial inner membrane

implausible due to size, for example some nanoparticles too large to cross the MIM [21], then an alternative explanation for accumulation is necessary and the specific localization within the mitochondria needs to be elucidated. Furthermore, the higher concentration within the matrix does not cancel the charge inside; the overall ratio is maintained by the membrane potential driven by the ETC and is independent of the concentration of lipophilic cation used; for example, a 300:1 ratio would be maintained if it were 300 nM:1 nM or if it were 3 μM:10 nM.

The lipophilic cation of choice is the alkyltriphenylphosphonium (TPP) cation [3, 19, 22] because it has been extensively validated in vivo, including in humans; for example, volunteers in a phase II clinical trial of MitoQ were dosed orally with this mitochondria-targeted antioxidant for 1 year without safety issues [23] (Fig. 3a). Conjugates of TPP diffuse freely across membranes and the cationic nature of the compounds gives them good water solubility. The ease with which lipophilic cations cross membranes is best modelled by calculating the transfer energy of the solvated cation from water to an alkane solvent (hexane or octane) [24, 25]. It is important to note that this is not bulk partitioning, which also involves the solubility of the counter-anion. In order to accumulate in the membrane-potential dependent way, the cation must cross alone so that there is movement of charge [25]. Variations of the TPP head group have been studied and 3,5-dimethyl substitution provides a good balance of synthetic accessibility and increased uptake [26]. TPP is shaped like an inside-out umbrella, which limits the solvent accessible charge so that it is not highly

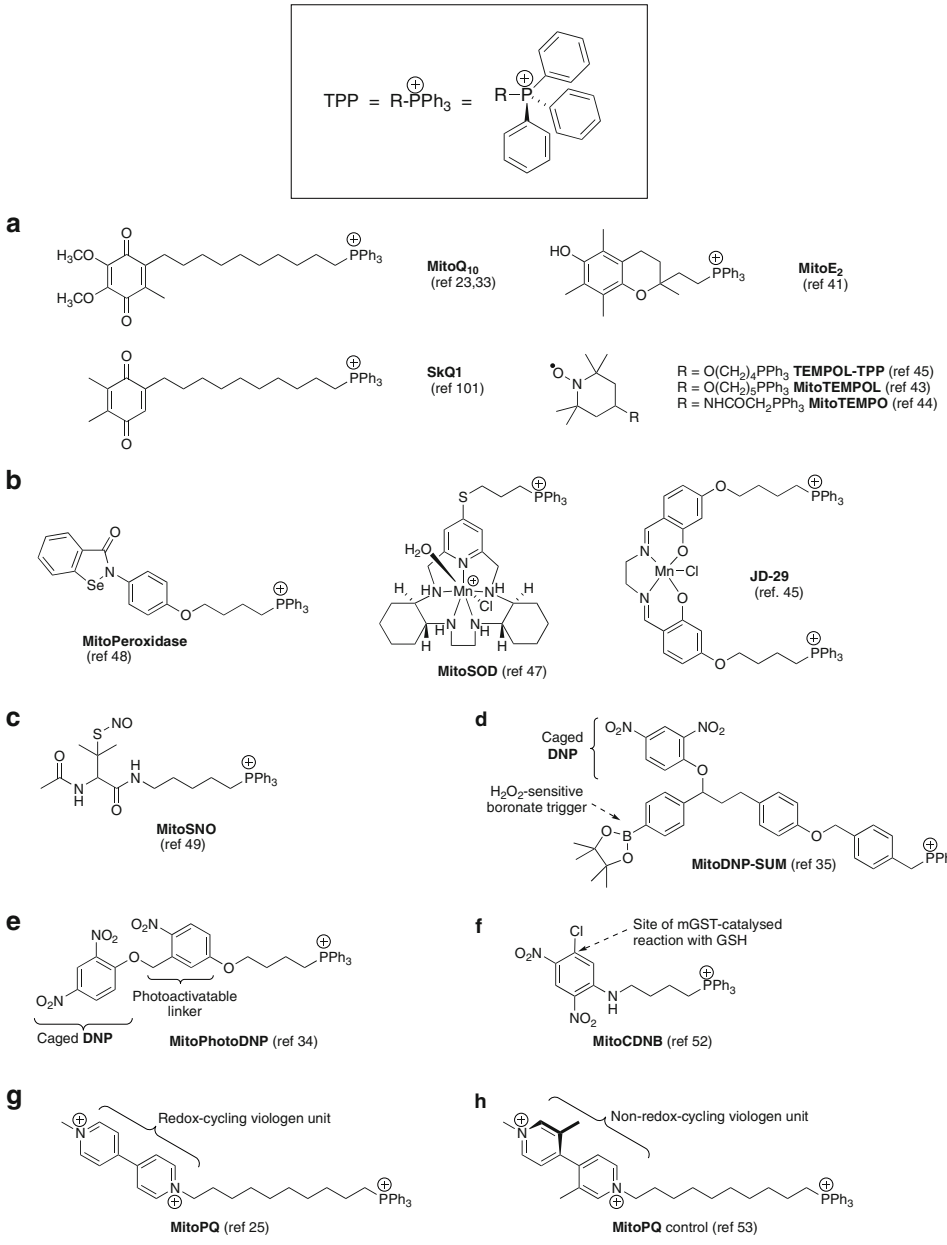


**Fig. 3** Example bioactives targeted to the mitochondria by TPP. (**a**) Antioxidants that react directly with ROS (some require in situ reduction to produce the active drug). (**b**) Antioxidants that catalyze the decomposition of ROS. (**c**) A potential antioxidant drug that inhibits the production of mitochondrial ROS. (**d**) A potential prodrug that reduces the $\Delta\psi$ in response to ROS. (**e**) A potential prodrug that depolarizes the MIM in response to UV light. (**f**) A prooxidant that selectively removes the mitochondrial thiol antioxidant defense. (**g**) A prooxidant, MitoParaquat, that selectively generates superoxide from molecular oxygen in the mitochondrial matrix, thus elevating mitochondrial ROS. (**g**) A control compound for use with MitoParaquat in whole living organisms

solvated in water and can transfer easily through membranes [25]. This shape also prevents the cation intercalating into double stranded nucleic acids, which can be a problem for planar lipophilic cations such as phenanthridinium ions [27]. The TPP group is small, having a hydrophobic radius of about 4.2 Å [20], and so does not sterically impede diffusion across membranes. It is also easily introduced by chemical synthesis (see below).

On the other hand, the TPP cation is not a universal mitochondria-targeting group. The mechanism of uptake matters: if the TPP conjugate as a whole is too polar or too large, this is likely to preclude free diffusion across membranes [28–31]. Under these circumstances, colocalization with the mitochondria is not a sufficient indicator of delivery to the mitochondrial matrix. Further evidence is needed. TPP's mechanism of targeting requires uptake to be $\Delta\psi$-dependent. This can be tested by showing that accumulation is significantly decreased or abolished when an uncoupler, such as FCCP, is used [20]. Uncouplers translocate protons across the MIM thereby removing $\Delta\psi$ and uncoupling the activity of the electron transport chain from ATP synthase. If necessary, the small effect of the pH gradient across the MIM can be separated from the larger effect of $\Delta\psi$ by using nigericin. This $K^+/H^+$ exchanger replaces the pH gradient with a greater $\Delta\psi$ to maintain the same proton-motive force [20], resulting in an increase in the uptake of compounds, such as simple TPP conjugates, that accumulate driven by $\Delta\psi$ independent of pH.

A wide range of TPP conjugates have been synthesized and shown to accumulate in mitochondria (Fig. 3). Generally, the cargo to which the TPP is conjugated is not itself charged. However, carboxylic acids that exist predominantly in their anionic carboxylate form at pH 7 can be targeted to mitochondria using TPP. Indeed, zwitterionic carboxylate **1** accumulates to a greater extent than the simple triphenylmethylphosphonium cation. At first sight this may seem perplexing as the zwitterion **1** has no overall charge (Fig. 4) [32]. The key feature of this system is that the zwitterionic

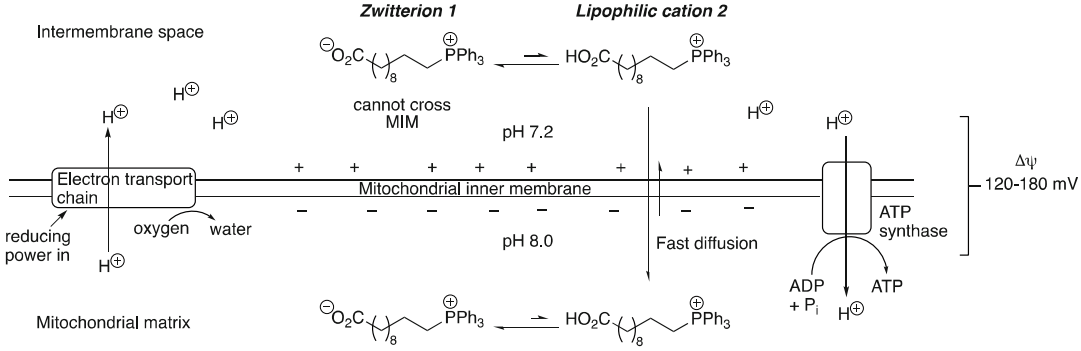


**Fig. 4** Mechanism of accumulation of a zwitterionic TPP-carboxylate conjugate in the mitochondrial matrix

form **1** is too polar to cross membranes but it is in equilibrium with the monocationic carboxylic acid **2**, which is a lipophilic cation and can diffuse freely across the MIM. The carboxylic acid form **2** partitions across the membrane in accordance with the Nernst equation. The carboxylic acid **2** inside the matrix is also in equilibrium with the deprotonated membrane-impermeant zwitterion **1**. If the pH were the same on the inside and outside of the MIM, the zwitterionic form **1** would accumulate to the same degree as the carboxylic acid **2**. However, the pH inside is higher than outside, so accumulation of the zwitterionic form inside is greater than would be expected from the Nernst equation alone.

The TPP conjugate could be a drug itself, as is the case of MitoQ (Fig. 3a) [33] and most other drug candidates that use the TPP targeting group (Fig. 5a). In theory, a TPP-drug would distribute throughout the body, concentrating in tissues with high mitochondrial content, such as muscle and liver. However, what if selectivity for a single tissue or site is important? In these cases a prodrug strategy is appropriate whereby the inactive prodrug distributes to all mitochondria, but the drug is released from the TPP targeting group only within particular mitochondria or inside the mitochondria of particular tissues.

Prodrug activation could either be by an instruction from outside the living cells (Fig. 5b) or by a process within the mitochondria (Fig. 5c), and we have demonstrated both approaches

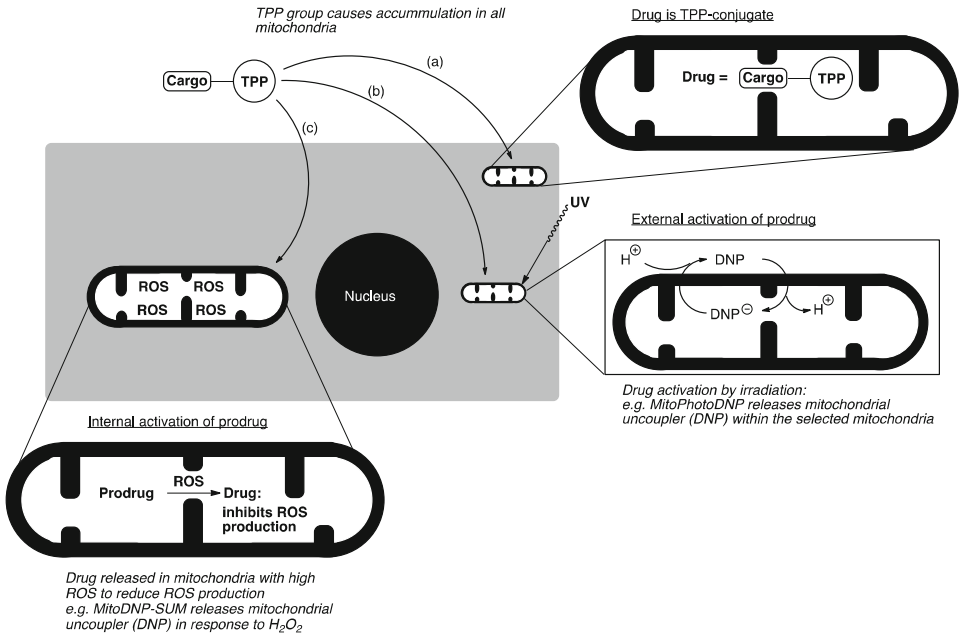


**Fig. 5** TPP-drug conjugates that (**a**) act directly as drugs, (**b**) are prodrugs that release the drugs in response to an instruction from outside the mitochondria, and (**c**) are prodrugs that release the drugs in response to an instruction from within the mitochondria

[34, 35]. MitoPhotoDNP [34] is a UV light-activated mitochondrial uncoupler (Figs. 3e and 5b). It accumulates in all mitochondria in accordance with the Nernst equation, but can be activated within particular mitochondria by irradiation with UV light to release the proton translocator, 2,4-dinitrophenol (DNP). DNP crosses the MIM in both its protonated phenol form and its deprotonated phenoxide form (DNP−), and so it abolishes the membrane potential of the selected mitochondria, uncoupling the ETC from ATP-synthase. This gives sustained depolarization of discrete mitochondria and has been used to show that the interconnected mitochondrial network in muscle allows energy supply by a minimal diffusion of metabolites and electrical conduction across the network [36].

Each cell contains many mitochondria and it is likely that some function well, while others are dysfunctional. The production of reactive oxygen species (ROS) as a result of reduction of oxygen to superoxide by complex I of the ETC in particular, is implicated in a wide range of diseases (Fig. 6) [2, 11]. Reverse electron transport through the ETC contributes to the production of superoxide [10, 11, 37] and is greatest when the membrane potential is high

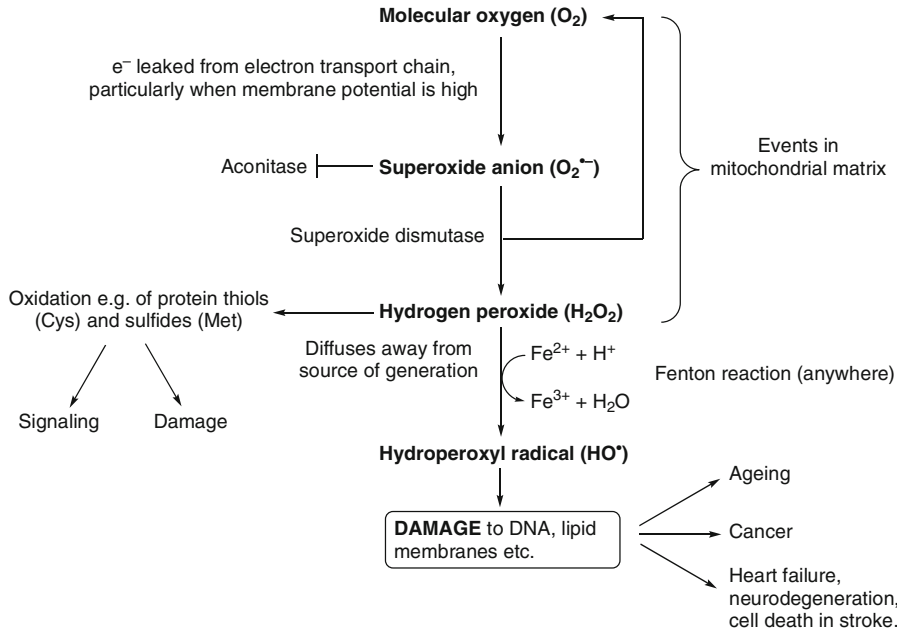


**Fig. 6** ROS and their generation in the mitochondrial matrix. ROS generation is initiated by reduction of molecular oxygen to superoxide by the electron transport chain, in particular complexes I and III. Superoxide can damage the iron-sulfur cluster of aconitase, an enzyme in the TCA cycle, and so is rapidly dismutated to oxygen and hydrogen peroxide by superoxide dismutase. Hydrogen peroxide is relatively stable and can diffuse out of the matrix. It can oxidize protein thiols (Cys) and sulfides (Met), and so signal redox status but may also cause damaging oxidative stress if the antioxidant defense is insufficient. Where accessible redox active metals are available, hydrogen peroxide is converted to the hydroxyl radical, which is highly damaging

[38]. Superoxide rapidly disproportionates to hydrogen peroxide and molecular oxygen under catalysis from superoxide dismutase (SOD) [39], and elevated mitochondrial hydrogen peroxide levels appear to contribute to the aged phenotype. Indeed, the free radical theory of aging suggests that mitochondrial ROS are the main driving force of aging. It may be tempting to suggest that antioxidants would slow the process of aging and provide a panacea for the treatment of diseases where damage is mediated or accentuated by oxidative stress. However, this has not proved to be the case [40], possibly because the antioxidants are not distributing to the regions where they are needed. Non-targeted antioxidants may also interfere with intracellular signaling, which is partly mediated by hydrogen peroxide and other ROS.

Targeting antioxidants to the mitochondria ameliorates oxidative damage at the site where most endogenous ROS are generated. Thus, the TPP-antioxidant conjugates MitoQ [23, 33], MitoE [41], and the various TPP-nitroxide conjugates [42–45] are effective antioxidants that scavenge ROS (Figs. 3a and 5a); some of these require in situ reduction to generate the active antioxidant and this provides a route for regeneration. Thus, even though they react stoichiometrically, each molecule can quench many ROS as a result of recycling. MitoQ is an example of this: it is activated as an antioxidant by reduction by the ETC within the mitochondrial matrix, and is rapidly reactivated after oxidation by ROS [46]. Mechanistic mimetics of SOD and peroxidase have also been targeted to mitochondria (Fig. 3b) [45, 47, 48]; although these are true catalysts, their turnover rates are significantly slower than endogenous enzymes. On the other hand, the TPP conjugate, MitoSNO (Fig. 3c), reduces the production of ROS by inhibiting the mechanism of ROS generation [49]. In principle, this is a more efficacious approach because MitoSNO stoichiometrically inhibits the catalytic generation of ROS by the ETC, so that each molecule of MitoSNO prevents the formation of many ROS molecules. MitoSNO limits the damage caused by myocardial infarction in vivo by nitrosating Cys39 on the ND3 subunit of complex I of the ETC [50]. The nitrosation is reversible, but inhibits the ETC during reperfusion, so minimizing the production of the ROS responsible for reperfusion injury. Importantly, the protein thiol target is only exposed under anoxia: this gives selectivity for affecting dysfunctional mitochondria in the presence of functional mitochondria in other tissues.

MitoSNO acts directly on its target, which is exposed during ischemia. An alternative approach would be to control the release of a drug so that it is only present in dysfunctional mitochondria. Selectivity would then be achieved through activation of a prodrug by processes associated with dysfunctional mitochondria. MitoDNP-SUM is a prototypical example of such a prodrug (Figs. 3d and 5c) [35]. ROS are generated when the potential

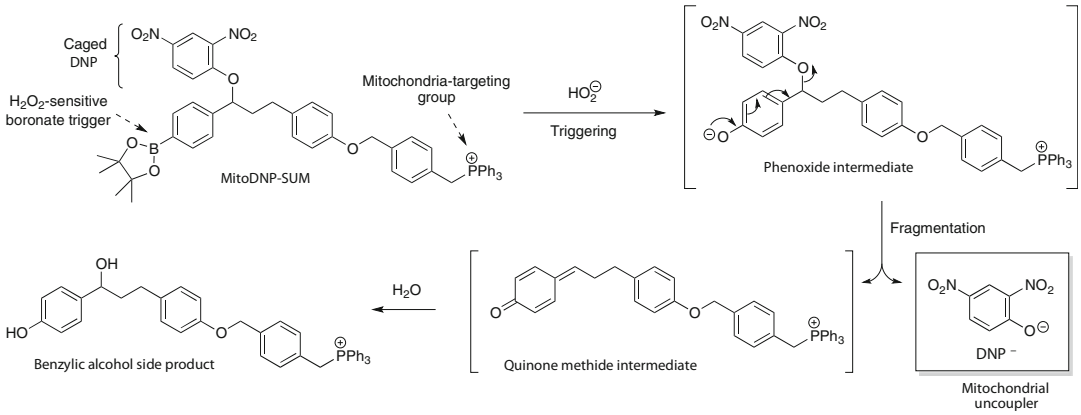


**Fig. 7** Release of a mitochondrial uncoupler from the mitochondria-targeted prodrug, **MitoDNP-SUM**

across the MIM is elevated. MitoDNP-SUM accumulates in all mitochondria in accordance with the Nernst equation, and is activated by hydrogen peroxide to release the proton-translocator, DNP. Proton translocation across the MIM is known to reduce the membrane potential. In principle, this provides a negative feedback as mitochondria with lower membrane potentials produce fewer ROS and even a small drop in the membrane potential leads to a large drop in ROS production. The release of DNP from MitoDNP-SUM is mediated by the reaction between the hydroperoxide anion and the arylboronate unit (Fig. 7) [35, 51]. This produces a phenoxide intermediate, which then fragments to release DNP− and a quinone methide, which rapidly reacts to give a benzylic alcohol side product. Mitochondria-targeted prooxidants are also useful to test the effects of ROS generated in the mitochondrial matrix or to enhance these effect when toxicity is desired (Fig. 3f, g). MitoCDNB selectively depletes the mitochondrial pool of glutathione (GSH) catalyzed by mitochondrial glutathione *S*-transferase, and inactivates mitochondrial thioredoxin-reductase, both of which are important to the mitochondrial antioxidant defense (Fig. 3f) [52]. The effects of MitoCDNB also illustrate the important point that TPP conjugates can provide selectivity for mitochondrial matrix enzymes over similar enzymes in the cytosol, even when there is no difference in the chemical reactivity of the bioactive moiety toward the enzymes and enzyme-catalyzed processes in the two locations and the TPP conjugate must traverse the cytosol to accumulate in the matrix. MitoParaquat demonstrates an alternative prooxidant mechanism, instead of chemically knocking down the antioxidant defense, it selectively generates superoxide in the mitochondrial matrix (Fig. 3g) [25]. Its viologen unit is reduced by complex I of the ETC and the resulting radical cation is then reoxidized by molecular oxygen generating superoxide so that it acts as a redox cycler generating

superoxide catalytically. Interestingly, very low levels of MitoParaquat protect mice against ischemic reperfusion injury to their hearts when dosing is carried out before ischemia, an example of hormesis [53]. In order to confirm that the effect was due to the redox cycling action of MitoParaquat, a very similar compound that could not redox cycle was used as a control (Fig. 3h).

### 1.2 Mitochondria-Targeted Sensors

Mitochondrial ROS appear to be important to a wide range of diseases [2, 3]. Furthermore, there is growing evidence that different ROS have different effects, and that these effects are location and concentration dependent [54]. Therefore, a range of mitochondria-targeted sensors have been reported (Fig. 8). Nitrone spin traps have been made that react with the highly reactive radicals involved in oxidative stress to give longer lived nitroxyl radicals that can be detected by EPR spectrometry, for example MitoPBN [55], MitoSpin [56], MitoBMPO [57], and Mito-DEPMPO (Fig. 8a) [58, 59]. Often, the hyperfine couplings allow the type of radical trapped to be identified. The adducts of oxygen-centred radicals are generally short-lived, and superoxide adducts are particularly unstable. However, MitoBMPO and Mito-DEPMPO produce distinct, detectable superoxide adducts [57–59]. Unfortunately, high concentrations of the traps are necessary making in vivo work impractical.

An alternative is to detect ROS using fluorescence [60]. Superoxide can be detected by Mito-HE (commercially called Mito-SOX™ red, Fig. 8b) [61], an analogue of hydroethidine targeted to the mitochondria by TPP, which gives a specific hydroxylated *N*-alkylphenanthridinium salt, HO-Mito-Etd$^+$, upon reaction with superoxide. The product can be detected using its fluorescence at 579 nm when excited at 510 nm, or by excitation at 396 nm. Exciting at 396 nm minimizes confusion arising from other phenanthridinium cations produced by nonspecific oxidation. The detection method in cellulo relies on the fluorescence enhancement that occurs when the phenanthridinium cations intercalate into double-stranded nucleic acids. Since other phenanthridinium cations also fluoresce, efforts have been made to distinguish and quantify the products of hydroethidine oxidation by HPLC [62]. The interaction with double-stranded nucleic acids is problematic for in cellulo monitoring of mitochondrial superoxide because the fluorescence enhancement depends on the availability of double-stranded nucleic acids, and because it could affect signaling and also cause redistribution of the fluorophore resulting in artefacts. To overcome these complications and to enhance the selectivity for detection of superoxide over other ROS, the hydroethidine analogue MitoNeoD was developed as a superoxide sensor (Fig. 8b) [63]. The addition of neopentyl groups prevents intercalation into double-stranded nucleic acids and the C-6 deuteration slows nonspecific oxidation relative to reaction with superoxide.

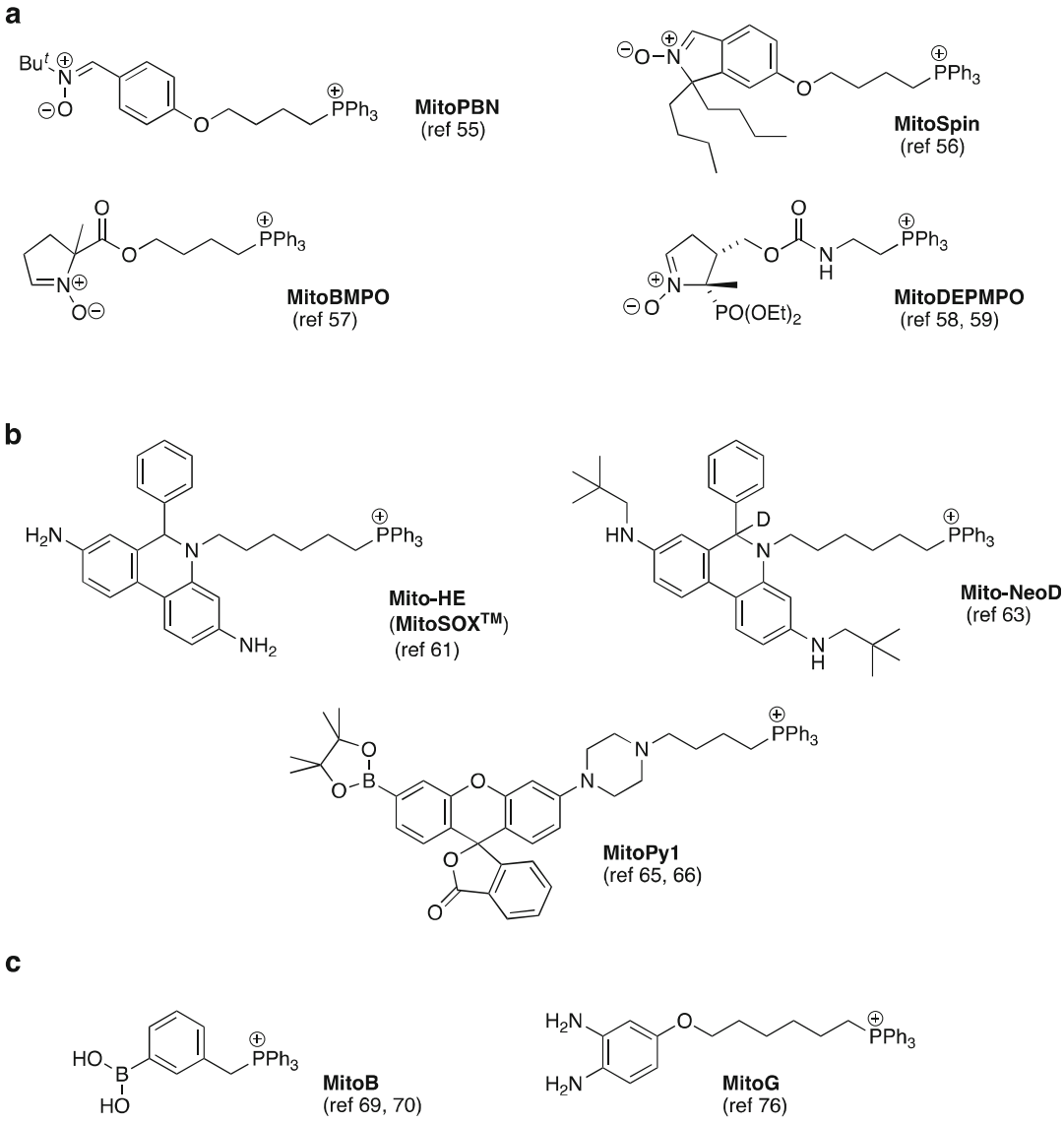


**Fig. 8** Examples of mitochondria-targeted sensors for detecting ROS and the products of oxidation within the mitochondrial matrix. (**a**) Nitrone spin traps for detecting free radicals. (**b**) Probes for detecting ROS through fluorescence. (**c**) Probes for detecting ROS and products of oxidation through an exomarker approach utilizing mass spectrometry

These modifications allow for better monitoring in cellulo, and consistent extraction and quantification by mass spectrometry when MitoNeoD is used for the exomarker approach to quantify mitochondrial superoxide in whole living organisms [63, 64].

The specific reaction between an arylboronate and hydrogen peroxide or peroxynitrite to give a phenol has been used as an on-switch for a mitochondria-targeted prefluorophore, MitoPy1 (Fig. 8b) [65, 66]. The reaction is irreversible, so the rate of

increase of fluorescence indicates the concentration of hydrogen peroxide present. Fluorescent probes are easy to use in cell-based studies, but are less useful in whole organisms due to autofluorescence and limited light penetration. One solution is to express luciferase in an organism and then use a so-called peroxy caged luciferin (e.g., PCL-2) [67, 68], which is uncaged by hydrogen peroxide by the mechanism discussed above. The luciferin then undergoes a chemiluminescent reaction catalyzed by the expressed luciferase leading to emission of light in response to hydrogen peroxide. However, there is no mitochondria-targeted version of this compound yet.

The lack of effective methods of detecting specific mitochondrial ROS in vivo had meant that surprisingly little was known about the concentrations of these species in whole living organisms. This was a serious short-coming because mitochondrial ROS are implicated in a wide range of diseases and in aging itself [2, 3]. To tackle this deficiency in methods, we disclosed that a mitochondria-targeted arylboronate MitoB can be used to determine directly changes in the concentration of mitochondrial hydrogen peroxide in whole organisms (Fig. 8c) [69, 70]. We first reported the use of MitoB in living flies (Drosophila melanogaster), nematodes (*Caenorhabditis elegans*), and mice, including providing a detailed step by step protocol [69, 70]. Since these reports include detailed descriptions of how MitoB is employed, we will only provide a very brief overview of the main features of this probe. On the other hand, we include here a detailed protocol for the synthesis and purification of MitoB and all the chemical standards needed for its use.

MitoB has a TPP group that causes it to accumulate in mitochondria. Following injection into the organism, MitoB rapidly distributes to the various tissues of the body so that about 90% of the probe is intracellular and 98% of this is within the mitochondria. It reacts with hydrogen peroxide to give the phenol, MitoP (Fig. 9). More precisely, it reacts with the conjugate base of hydrogen peroxide, the hydroperoxide anion, so that the higher pH of the mitochondrial matrix gives an additional four-fold acceleration relative to reaction in the cytosol. Selectivity is ensured by using two different types of reactivity displayed by hydrogen peroxide: it is a nucleophile and it has a leaving group. With the exception of peroxynitrite and HOCl, other ROS do not react with MitoB to give this product [71, 72]. Unlike probes that rely on simple oxidation, the incorporation of an atom from the reacting molecule, hydrogen peroxide, provides a molecular memory of the reactant detected. Importantly, the rate constant for reaction between the mitochondrial peroxidase, peroxiredoxin III, and hydrogen peroxide is over a million times higher than that for reaction with MitoB [69]. Since MitoB reacts slowly, it does not itself influence the hydrogen peroxide concentration.

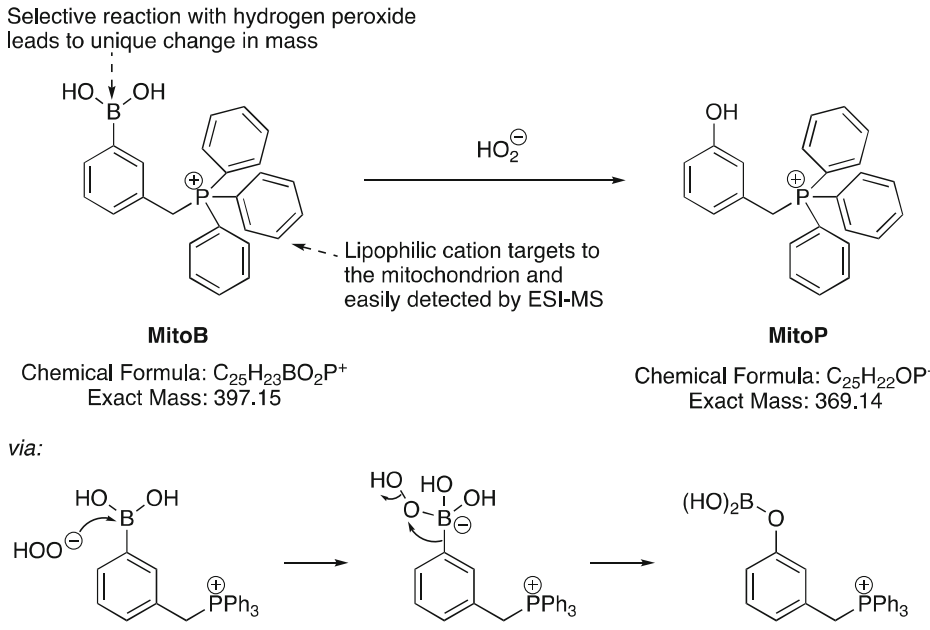


**Fig. 9** Reaction of **MitoB** to produce **MitoP**

Both MitoB and MitoP can be easily detected by electrospray ionization mass spectrometry (ESI-MS) with high sensitivity, because each molecule already bears a fixed positive charge and does not need to be ionized to be detected. As MitoB is converted irreversibly into MitoP, the ratio of MitoP to MitoB increases with time. The rate of this increase reflects the concentration of hydrogen peroxide. The concentration of MitoB in the mitochondrial matrix is about 3000 times the extracellular concentration, and this combined with higher proportion of hydrogen peroxide in its deprotonated form means that MitoP production occurs almost exclusively in the mitochondrial matrix (Fig. 10). Expressing the amount of MitoP and MitoB as a ratio corrects for absolute concentration.

To date, we have determined the ratio of MitoP to MitoB following euthanizing the animals, but in principle the ratio of MitoP to MitoB in fluids such as blood or urine might be used to monitor hydrogen peroxide concentrations continuously because both MitoP and MitoB freely diffuse in and out of mitochondria. However, in all cases quantification requires correction for extraction efficiency. This is done by adding a known quantity of d15-MitoB and deuterated d15-MitoP after the experiment is complete and before extraction of the MitoB and MitoP. For convenience both deutero standards are prepared from perdeutero triphenylphosphine so that there are 15 labels in each. Thus, the amount of MitoP ($m/z$ 369) is determined by comparison with d15-MitoP ($m/z$ 384), and the amount of MitoB ($m/z$ 397) is

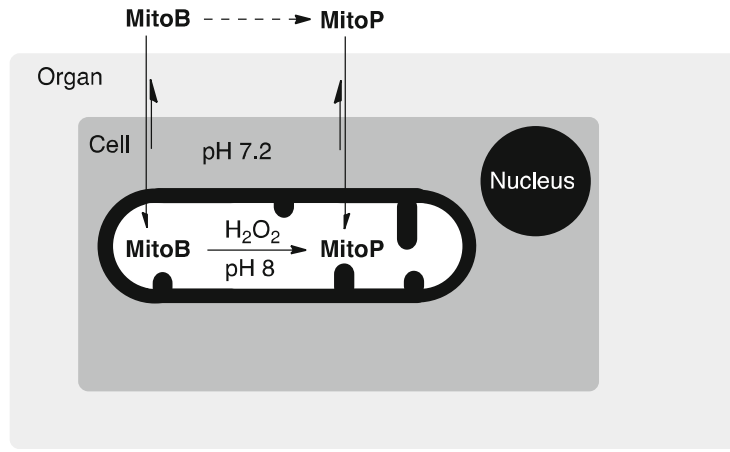


**Fig. 10** The molecular probe, MitoB, is converted into the exomarker, MitoP, by reaction with hydrogen peroxide inside the mitochondria, because its concentration within these organelles is approximately 3000 times the extracellular concentration and because the matrix pH is about 0.8 pH units more alkali than the cytosol. The ratio of MitoP/MitoB after a fixed period reflects the intramitochondrial [$H_2O_2$]

determined relative to d15-MitoB ($m/z$ 412). Liquid chromatography (LC) is used to separate the TPP compounds from other endogenous compounds extracted with them. Often the TPP compounds elute at the same time, and the compounds are detected simultaneously using multiple reaction monitoring [for details of this and the comparison with the deutero standards *see* Cochemé et al. [69, 70]]. Depending on the LC system used, there may be some or complete separation of MitoB from MitoP, and indeed partial separation of the deutero labeled and unlabeled version of the compounds is also possible [73–75]. Therefore, it is important to sample the ions over the whole peak so that the proportions are correct.

MitoP is an exomarker [64] of mitochondrial hydrogen peroxide in living organisms (Fig. 9). This is similar to a biomarker, but is produced by a specific transformation of an exogenous probe, in this case MitoB. Whereas biomarkers may be produced by a range of processes, a small molecule probe can be designed to detect a specific endogenous compound, in this case hydrogen peroxide, in a particular place, for example the mitochondria. Exomarkers have the advantage that they are neither produced nor degraded by endogenous processes and so reflect more accurately the concentration of the species they are designed to detect. An exomarker approach to the detection of mitochondrial glyoxal and methylglyoxal has also been developed using MitoG (Fig. 8c) [76].

Since the original work [69, 70] in living flies (Drosophila melanogaster), nematodes (*Caenorhabditis elegans*), and mice,

MitoB/MitoP has been used widely in these and other organisms. We have applied this methodology in a wild species, brown trout (*S*almo *t*rutta) [77, 78]. This raises the possibility of using the probe in ecological studies, and the development of MitoB protocols for aquatic organisms was outlined based on this experience [79]. MitoB has also been successfully used in rats [80] and marine sculpins [81], and in various tissue types, including liver [79, 82], brain [83], muscle [4, 79], fat [84], heart [85–87], lung [88, 89], kidney [4, 80], arterial [89–91], fibroblast [92], spleen [93], colon [93], T cells [94], and induced pluripotent stem cells [95]. In addition to metabolic studies applications have included studies of reperfusion injury [10, 85–87], macrophage [96] and T cell regulation [94], cancer metastasis [88, 97] β-cell proliferation [84], preeclampsia [80], hypertension [89] and food supplements [93]. The ubiquity of hydrogen peroxide and its direct origin from superoxide make its measurement an excellent surrogate for overall mitochondrial ROS generation. In addition to acting as a proxy for total mitochondrial ROS, MitoB has been applied to study hydrogen peroxide production specifically as a signaling molecule [95]. MitoB has been used to quantify hydrogen peroxide relative to superoxide levels in order to understand the transport and regulation of superoxide dismutase (SOD) [89, 90]. The utility of this approach is enhanced by development of analogous targeted exomarkers for superoxide [63], glyoxal [76] and hydrogen sulfide [98], which use the same approach as MitoB and can be used in concert to offer opportunities to investigate the balance of the ROS species and gasotransmitters involved in signaling and damage.

Here we present again the detailed protocols for the preparation of MitoB, d15-MitoB, MitoP, and d15-MitoP, which we first provided in an earlier edition of *Methods in Molecular Biology* [99].

## 2 Materials

### 2.1 Equipment for Synthesis

1. UV lamp (to check TLC plates, 254 nm).
2. Oven (200 °C+ capable).
3. Fridge (0–5 °C capable).
4. Stirring/heating plate with temperature probe.
5. Oil bath or alternative heating media.
6. Rotary evaporator (in fume hood) attached to vacuum line.
7. Vacuum pump (weak vacuum, 100 mbar sufficient).
8. Vacuum line (<20 mbar).
9. Inert gas supply (approximately atmospheric pressure, balloon sufficient), attached to a short needle.

10. Dewar-type bowl (large enough for the 50 mL flask and coolant).
11. Thermometer (effective down to at least −20 °C).
12. Desiccator.
13. 1× clamp stand and appropriate clamps.
14. 2 × 50 mL round bottomed flask.
15. 3 × 100 mL round bottomed flask.
16. 2 × 250 mL round bottomed flask.
17. 1 × condenser (appropriate to fit flask) and connections to attach water.
18. 5× Suba-Seals to fit condenser and flasks.
19. 2× Magnetic stirrer bar.
20. 100 or greater mL Buchner flask and small Buchner funnel with filter paper or equivalent filtration set up.
21. 1 L or greater mL Buchner flask and large (500 mL) Buchner funnel with filter paper or equivalent filtration set up.
22. 50 mL beaker.
23. 2× 1 L beaker or conical flask.
24. Appropriate sample vials (10 mL).
25. Glass pipettes and pipette teats.
26. 1 mL syringes and appropriate needles.
27. 2× 20 mL syringe.
28. 1× 50 mL syringe.
29. 4× long metal needle.
30. Chromatography grade silica gel ($SiO_2$) and acidified sand.
31. 2× TLC plates and appropriate tank.
32. NMR tube and access to NMR machine.

### 2.2 Synthesis of MitoB

1. Toluene (irritant, health hazard, flammable).
2. Triphenylphosphine (harmful, health hazard).
3. (3-bromomethyl)phenylboronic acid (irritant).
4. Dimethyl sulfoxide (irritant).
5. Distilled water.
6. Diethyl ether (flammable, harmful).
7. $d_6$-Dimethyl sulfoxide (irritant).

### 2.3 Synthesis of d15-MitoB

The same materials as for MitoB, except replace triphenylphosphine with d15-triphenylphosphine.

### 2.4 Synthesis of MitoP

1. 3-hydroxymethylbenzylalcohol (harmful/irritant, corrosive).
2. Phosphorus tribromide (1 M solution in dichloromethane, corrosive, harmful/irritant).
3. Anhydrous pyridine (harmful/irritant, flammable).
4. Anhydrous acetonitrile (harmful/irritant, flammable).
5. Anhydrous toluene (irritant, health hazard, flammable).
6. Triphenylphosphine (harmful, health hazard).
7. Ethyl acetate (irritant, flammable).
8. Diethyl ether (harmful, flammable).
9. Dichloromethane (harmful, health hazard).
10. Ethanol (flammable).
11. Distilled water.
12. Dry ice ($CO_{2(s)}$, may cause burns, $CO_{2(g)}$ hazardous above 1.5% concentration).
13. Acetone or 2-isopropanol (flammable, irritant).
14. $d_6$-Dimethyl sulfoxide.
15. Magnesium Sulfate.

### 2.5 Synthesis of d15-MitoP

The same materials as for MitoP, except replace triphenylphosphine with d15-triphenylphosphine.

## 3 Method

### 3.1 Overview of Procedure for the Synthesis of MitoB and d15-MitoB

MitoB was prepared from commercially available 3-(bromomethyl)phenylboronic acid using triphenylphosphine to displace the benzylic bromide (Fig. 11). The procedure produces the bromide salt (MW 477.14). The reaction is carried out in boiling toluene under reflux and the MitoB bromide precipitates from solution. The solid MitoB bromide is collected by filtration and then recrystallized from DMSO. MitoB is an arylboronic acid and can dehydrate to form a trimer, so a final recrystallization from water is carried out to ensure MitoB bromide is entirely in the boronic acid form. d15-MitoB bromide is prepared in exactly the same way except d15-triphenylphosphine is used instead of triphenylphosphine.

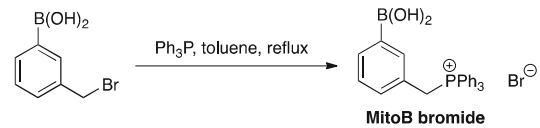


**Fig. 11** Synthesis of **MitoB** bromide

### 3.2 Setup for Preparation of MitoB and d15-MitoB (See Note 1)

1. For the preparation of MitoB, weigh out 1.00 g (4.65 mmol, 1.00 eq.) 3-(bromomethyl)phenylboronic acid and 1.34 g (5.11 mmol, 1.10 eq.) triphenylphosphine and add both to the 50 mL round bottomed flask containing the magnetic stirrer bar (*see* **Note 2**). Alternatively, for the preparation of d15-MitoB, weigh out 1.00 g 3-(bromomethyl)phenylboronic acid and 1.42 g d15-triphenylphosphine and add both to the 50 mL round bottomed flask.
2. Clamp the flask around the ground glass joint to the clamp stand, arranged so it is centrally positioned in the heating medium on top of the stirrer plate. Add 25 mL toluene.
3. Attach the condenser to the flask, adding a Suba-Seal and inert gas inlet to the top of the condenser by way of a needle piercing the Suba-Seal. Attach water supply to the condenser.
4. Insert a second needle in the Suba-Seal to act as an outlet and purge the flask and condenser with the inert gas for 5 min.
5. Start the stirring and then set the reaction to heat to reflux. The boiling point of toluene is 110–111 °C.
6. When the boiling temperature is reached, continue to heat the reaction under reflux for 6 h for complete conversion to product, which precipitates as a solid (*see* **Note 2**).
7. Turn off heat and remove the reaction from the heat source by moving clamp arm bearing the flask upward. Allow to cool for 30 min. Meanwhile heat 20 mL toluene to 70 °C in the 100 mL round bottomed flask.
8. Filter under vacuum to collect the solid MitoB bromide. Re-use the filtrate to wash out the contents of the round bottomed flask pouring the washings over the filter cake of MitoB bromide. Wash out the flask twice with the hot toluene (10 mL each wash, preheated to 70 °C) again pouring the washings over the filter cake of MitoB bromide. Finally wash the filter cake followed with 30 mL diethyl ether. Allow the material to further dry under vacuum for 20 min.

### 3.3 Purification of MitoB

1. Add approximately 500 mg of solid crude MitoB bromide to 0.7 mL of dimethyl sulfoxide and heat to dissolve in a sample vial. Allow the material to cool, crystallize, and settle (1 h) (*see* **Note 3**).
2. Carefully remove the dimethyl sulfoxide with a pipette (leave the crystals behind).
3. Repeat **steps 1** and **2** with more solid crude MitoB bromide, reusing the dimethyl sulfoxide from the previous crystallization (*see* **Note 4**) and an additional 0.1 mL (measured with a 1 mL syringe and used to wash the residual material through the empty pipette following transfer) until all crude material has

been recrystallized (you will now have up to five vials each containing approximately 400 mg recrystallized material).

4. After removing the dimethyl sulfoxide from each sample vial, add 1.5 mL of hot distilled water, agitate and allow to settle before carefully removing the liquid with a pipette, leaving the solid MitoB bromide in the vial. Combine these waste aqueous solutions and the final waste dimethyl sulfoxide, then collect any further crystals formed, retrieving the final batch of crystals by vacuum filtration if necessary, reusing the previously mentioned apparatus.
5. Combine the batches of crystallized MitoB bromide in a 100 or greater mL round bottomed flask, using hot distilled water in 1 mL aliquots to wash any residual solid into the flask.
6. Add distilled water to a volume of 40–50 mL and heat to 80 °C on the rotary evaporator at ambient pressure for 1 h, then allow the heating bath to cool to 50 °C and carefully concentrate the water under vacuum until a white solid is observed forming on the flask walls (*see* **Note 5**).
7. When solid is observed, remove the flask and allow it to cool. The MitoB bromide continues to precipitate from solution. Collect the solid by filtering under vacuum as previously, allowing 30 min to 1 h (depending on vacuum strength) to dry the solid material. The filtrate can be reused to obtain more MitoB bromide if desired, by further concentrating as in **step 5**.
8. Collect the material in a preweighed vial and check purity (if possible) by $^{1}$H NMR in $d_6$-dimethyl sulfoxide, with approx. 2 mg of material in a 0.5 mL sample (s*ee* **Note 6**).

   Approximate Yield: 70%.

### 3.4 Characterization Data for MitoB

$\delta_H$ (500 MHz, $d_6$-dimethyl sulfoxide): 7.95 [2H, s, B(O**H**)$_2$], 7.92–7.86 (3H, m, 3 × *p*-PPh$_3$), 7.77–7.68 (7H, m, 6 × *o*-PPh$_3$, H4), 7.67–7.58 (6H, 6 × *m*-PPh$_3$), 7.46 (1H, s, H2), 7.18 (1H, t, $J$ = 7.6 Hz, H5), 6.94 (1H, d, $J$ = 7.6 Hz, H6), 5.11 (2H, $J$ = 15.6 Hz, C**H**$_2$Ph). $\delta_C$ (100 MHz, $d_6$-dimethyl sulfoxide): 136.88 (d, $J$ = 5.6 Hz, CH), 134.94 (d, $J$ = 2.4 Hz, CH), 133.93 (d, $J$ = 9.8 Hz, CH), 133.78 (d, $J$ = 3.6 Hz, CH), 132.25 (d, $J$ = 5.2 Hz, CH), 129.95 (d, $J$ = 12.5 Hz, CH), 127.60 (d, $J$ = 2.8 Hz, CH), 126.67 (d, $J$ = 8.5 Hz, C), 117.75 (d, $J$ = 85.5 Hz, C), 28.15 (d, $J$ = 46.5 Hz, CH$_2$).

$\delta_P$ (162 MHz, $d_6$-dimethyl sulfoxide) 23.15 (s).

IR (ATR, cm$^{-1}$): 3322 (OH), 2928 (ArH, v. weak), 2882 (ArH), 2789 (ArH, v. weak), 1549 (Ar, v. weak), 1485 (Ar, weak), 1435 (Ar, strong). LRMS (ESI): 397 [M+ (phosphonium cation), 100%].

HRMS: 397.1518 [M+ (phosphonium cation)]. $C_{25}H_{23}BO_2P$ requires 397.1524.

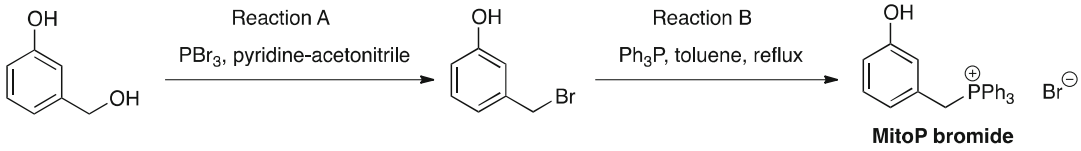


**Fig. 12** Synthesis of **MitoB** bromide

Microanalysis: $C_{25}H_{23}BBrO_2P$ requires C: 62.93% H: 4.86%, found C: 62.90% H: 4.80%.

### 3.5 Characterization Data for d15-MitoB

$\delta_H$ (400 MHz, $d_6$-dimethyl sulfoxide): 92:8 mixture of $d_{15}$:$d_{14}$: 7.97 [2H, s, B(O**H**)$_2$], 7.74–7.69 (1H, m, H4), 7.46 (1H, s, H2), 7.17 (1H, t, $J$ = 7.6 Hz, H5), 6.94 (1H, d, $J$ = 7.6 Hz, H6), 5.12 (2H, $J$ = 15.6 Hz, C**H**$_2$Ph). $\delta_C$ (100 MHz, $d_6$-dimethyl sulfoxide): 137.02 (d, $J$ = 5.6 Hz, CH), 135.08–134.22 (m, CD), 133.92 (d, $J$ = 2.7 Hz, CH), 134.22–133.12 (m, CD), 132.43 (d, $J$ = 5.5 Hz, CH), 130.05–129.15 (m, CD), 127.75 (d, $J$ = 2.6 Hz, CH), 126.84 (d, $J$ = 8.6 Hz, C), 117.67 (d, $J$ = 85.4 Hz, C), 28.27 (d, $J$ = 46.5 Hz, CH2). $\delta_P$ (162 MHz, $d_6$-dimethyl sulfoxide): 23.01 (s). IR (ATR, $cm^{-1}$): 3236 (OH), 2928 (ArH, v. weak), 2882 (ArH), 1543 (Ar), 1485 (Ar), 1424 (Ar, moderately strong). LRMS (ESI): 412 [M+(phosphoniumcation), 100%]. HRMS: 412.2460 [M+(phosphonium cation)]. $C_{25}H_{23}$ [11]$BO_2P$ requires 412.2465. Microanalysis: $C_{25}H_8D_{15}BBrO_2P$ requires C: 61.00% H: 1.64% D: 6.14%, found C: 60.90% H: 1.64% D: 6.17%.

$d_{14}$ peaks observed: $\delta_H$ (400 MHz, $d_6$-dimethyl sulfoxide): 7.89 (0.02H, d, $J$ = 2.0 Hz, $p$-PPh$_3$), 7.63 (0.03H, d, $J$ = 12.7 Hz, $o$-PPh$_3$), 7.24 (0.03H, d, $J$ = 8.0 Hz, $m$-PPh$_3$).

### 3.6 Overview of Procedure for the Synthesis of MitoP and d15-MitoP (See Note 7)

MitoP is prepared in two steps by an adaptation of the procedure described by Dawson et al. [100] (Fig. 12). First, in reaction A, 3-hydroxybenzyl alcohol is converted into the 3-(bromomethyl)phenol by reaction with phosphorus tribromide in a mixture of anhydrous pyridine and anhydrous acetonitrile. The reaction is water-sensitive and phosphorus tribromide reacts violently with water. 3-(Bromomethyl)phenol is a reactive compound and should be used for the next step soon after preparation. The second step, reaction B, involves displacing the benzylic bromide with triphenylphosphine to give MitoP bromide. The reaction is carried out in boiling toluene under reflux and MitoP bromide precipitates from solution. Often the MitoP is essentially pure after workup, but recrystallization from ethanol is possible if impure material is obtained. d15-MitoP bromide is prepared by using d15-triphenylphosphine instead of triphenylphosphine in reaction B.

### 3.7 Setting up Reaction A

1. Dry one 50 mL and two 100 mL round bottomed flasks and appropriate stirrer bars, the metal needles and the condenser overnight in a dry 250 °C oven. Alternatively, the flasks can be dried under vacuum with a heat gun or Bunsen burner (do not do this with the condenser). The dry glassware, needles and stirrer bars should be allowed to cool under vacuum and kept in a sealed desiccator prior to use.
2. Prepare a −15 °C bath on a stirrer plate by adding dry ice to 2-isopropanol or acetone in a Dewar, checking with a thermometer. Err on the cold side: somewhat below −15 °C is acceptable, but above this temperature is not satisfactory (*see* **Note 8**).
3. Attach anhydrous acetonitrile, phosphorus tribromide solution and anhydrous pyridine to an inert gas supply.
4. Set up the 50 mL flask in the Dewar, sealing with a Suba-Seal and connecting to inert gas.

### 3.8 Reaction A

1. Add 14.1 mL phosphorus tribromide solution and 5 mL acetonitrile to a 100 mL round bottomed flask using long needles attached to syringes, then stir the mixture. Immediately return the acetonitrile needle and syringe to a dry, inert environment for later use (putting the needle back through a seal into the dry solvent container with the syringe still attached is sufficient). Quench the phosphorus tribromide needle into 20 mL dichloromethane then add 5 mL ethanol to this solution. Dispose of this as toxic waste.
2. Add 0.75 mL anhydrous pyridine dropwise over 10 min with a needle and syringe to the stirring mixture (*see* **Note 9**).
3. Dissolve 5 g 3-hydroxymethylbenzyl alcohol in 15 mL anhydrous acetonitrile and 0.25 mL anhydrous pyridine in a 50 mL round bottomed flask (*see* **Note 10**), then add the solution to the reaction mixture dropwise over 10 min using a long needle and 20 mL syringe. An additional 2 mL anhydrous acetonitrile can then be used to wash any residual material from the 50 mL round bottomed flask into the reaction mixture.
4. Allow the reaction to stir and warm gradually to room temperature over 4 h.

### 3.9 Workup of Reaction A (See Note 11)

1. Prepare 2 L 19:1 dichloromethane–ethyl acetate.
2. Use 300 mL of this solution to make a slurry with approximately 250 mL $SiO_2$ in a 1 L beaker or conical flask, then load this into the large Buchner funnel. Allow the solvent to run through to incipient wetness, agitating gently to aid silica settling, then top with a 1 cm layer of acidified sand.

3. Transfer the reaction mixture from reaction A to a 250 mL round bottomed flask, washing the residue in with dichloromethane (*see* **Note 12**), then remove the solvent under reduced pressure in a fume hood, disposing of the distillate as toxic waste.
4. Dissolve the residue in 100 mL dichloromethane, then wash with 100 mL $H_2O$, reextracting with a further 100 mL dichloromethane (*see* **Note 11**).
5. Add the combined dichloromethane solutions to the silica in the Buchner funnel, allowing the solvent to run through under atmospheric pressure until no residual solvent remains above the silica layer, discarding the resulting filtrate. Add 1 cm sand and elute the compound under vacuum with the dichloromethane–ethyl acetate solution, collecting fractions of approximately 300 mL (*see* **Note 13**), then spotting each on a silica TLC plate in turn and stopping when the last fraction shows no UV activity under an appropriate lamp. Confirm the product fractions by TLC ($R_f$ = 0.57 in 9:1 dichloromethane–ethyl acetate) and combine these in a 1 L beaker or conical flask.
6. Add magnesium sulfate to the filtrate and swirl, then filter the solution, using dichloromethane to wash any residual material from the magnesium sulfate.
7. Half fill a 250 mL round bottomed flask with a portion of the solution, and remove the solvent under reduced pressure, add a further portion of the solution and repeat until all the material is contained in the flask and all solvent has been removed.

### 3.10 Characterization Data for 3-(Bromomethyl)Phenol

$\delta_H$ (500 MHz, $CDCl_3$): 7.21 (1H, t, $J$ = 7.9 Hz, H5) 6.97 (1H, d, broad, $J$ = 7.7 Hz, H4), 6.88 (1H, t, $J$ = 2.1 Hz, H2), 6.77 (1H, ddd, $J$ = 8.1, 2.5, 0.7 Hz, H6), 4.44 (2H, s, $CH_2$). $\delta_C$ (100 MHz, $CDCl_3$): 155.75 (C), 139.56 (C), 120.20 (CH), 121.63 (CH), 116.07 (CH), 115.69 (CH), 33.27 ($CH_2$). IR (ATR $cm^{-1}$): 3354 (O–H), 1591 ($C_{Ar}C_{Ar}$), 1489 ($C_{Ar}C_{Ar}$), 1456 ($C_{Ar}C_{Ar}$). LRMS ($EI^+$): 187.99 ($^{81}BrM^+$, 31%), 185.99 ($^{81}BrM^+$, 33%), 107.06 [($M^+$ − Br), 100%]. HRMS: 187.9652 and 185.9686. $C_7H_7OBr$ requires 187.9660 and 185.9680. MP: 60–63 °C.

### 3.11 Setting up Reaction B

1. Add 70 mL dry toluene, a suitable stirrer bar and 10 g triphenylphosphine to the reaction A product.
2. Attach the condenser to the water and round bottomed flask; put under inert gas and heat to reflux while stirring for 6 h.

### 3.12 Work Up of Reaction B

1. Warm 100 mL toluene to 70 °C in a 250 mL round bottomed flask.
2. Filter the reaction mixture vacuum, reusing the filtrate to wash out the contents of the flask, then wash out the flask with a further 2 × 50 mL 70 °C toluene and use these to further wash

the filter cake, followed by 100 mL diethyl ether. Allow the material to further dry under vacuum for 20 min.

3. Check purity by $^{1}$H NMR in $d_6$-dimethyl sulfoxide. Proceed to Subheading 3.13 only if necessary.

   Approximate Yield (2 steps): 75%.

### 3.13 Purification (if Necessary)

1. Add ethanol to the impure solid in a ratio of 15 mL/g in a large round bottomed flask (100 mL for 1 g, *see* **Note 14**) then heat the mixture to 80 °C until the solid dissolves.
2. Remove the flask from the heat, allow to cool and seal with a Suba-Seal (*see* **Note 15**), then place in a fridge (approx. 5 °C) for 5–6 h (*see* **Note 16**).
3. Decant the solvent from the crystals, then redissolve the crystals in a minimal quantity of warm ethanol and add distilled water to reach an approximate ratio of 2:1 ethanol–water mix.
4. Carefully remove the solvent mixture under reduced pressure to retrieve the pure solid (*see* **Note 17**).

### 3.14 Characterization Data for MitoP Bromide

$\delta_H$ (400 MHz, $d_6$-dimethyl sulfoxide): 9.54 (1H, s, OH), 7.94–7.86 (3H, m, 3 × *p*-H $PPh_3$), 7.78–7.70 (6H, m, 6 × *m*-H $PPh_3$), 7.70–7.60 (6H, m, 6 × *o*-H $PPh_3$), 7.00 (1H, t, $J = 7.8$ Hz, H-5), 6.68 (1H, broad d, $J = 8.0$ Hz, H-6), 6.41 (1H, broad s, H-2), 6.36 (1H, broad d, $J = 7.1$ Hz H-4), 5.06 (2H, d, $J = 15.6$ Hz, $CH_2$). $\delta_C$ (100 MHz, $d_6$-dimethyl sulfoxide): 157.54 (d, $J = 3.2$ Hz, C), 135.10 (d, $J = 1.9$ Hz, CH), 134.03 (d, $J = 9.8$ Hz, CH), 130.11 (d, $J = 12.5$ Hz, CH), 129.75 (d, $J = 2.2$ Hz, CH), 129.05 (d, $J = 8.3$ Hz, C),121.39 (d, $J = 5.5$ Hz, CH), 117.98 (d, $J = 85.6$ Hz, C), 117.83 (d, $J = 5.6$ Hz, CH), 115.33 (d, $J = 3.1$ Hz, CH), 28.13 (d, $J = 46.6$ Hz, $CH_2$). $\delta_P$ (162 MHz, $d_6$-dimethyl sulfoxide): 23.03(s). IR (ATR, $cm^{-1}$): 3079 (OH), 2889 (ArH), 2858 (ArH), 2787 (ArH), 1611 (Ar), 1568(Ar). LRMS (ESI): 369 [M+(phosphonium cation), 100%]. HRMS:369.1399 [M+(phosphonium cation)]. $C_{25}H_{22}OP$ requires 369.1403. Microanalysis: $C_{25}H_{22}BrOP$ requires C: 66.83% H: 4.94%, found C: 66.89% H: 4.98%.

### 3.15 Characterization Data for d15-MitoP Bromide

$\delta_H$ (400 MHz, $d_6$-dimethyl sulfoxide): 9.55 (1H, s, OH), 7.00 (1H, t, $J = 7.8$ Hz, H-5), 6.69 (1H, broad d, $J = 8.0$ Hz, H-6), 6.42 (1H, broad s, H-2), 6.36 (1H, broad d, $J = 7.2$ Hz, H-4), 5.08 (2H, d, $J = 15.7$ Hz, $CH_2$). $\delta_C$ (100 MHz, $d_6$-dimethyl sulfoxide): 157.54 (d, $J = 3.1$ Hz, C), 134.90–134.23 (m, CD), 134.08–133.12 (m, CD), 130.08–129.20 (m, CD), 129.73 (d, $J = 3.4$ Hz, CH),128.57 (d, $J = 8.6$ Hz, C), 121.39 (d, $J = 5.6$ Hz, CH), 117.85 (d, $J = 5.5$ Hz, CH), 117.76 (d, $J = 85.4$ Hz, C), 115.32 (d, $J = 3.4$ Hz, CH), 28.16 (d, $J = 46.6$ Hz, $CH_2$). $\delta_P$ (162 MHz, $d_6$-dimethyl sulfoxide): 22.92 (s). IR (ATR, $cm^{-1}$): 3080 (OH), 2889 (ArH), 2858 (ArH), 2787

(ArH), 1617 (Ar), 1609 (Ar), 1587 (Ar). LRMS (ESI): 384 [M +(phosphonium cation),100%]. HRMS: 384.2336 [M+ (phosphonium cation)]. $C_{25}H_7D_{15}OP$ requires 384.2344. Microanalysis: $C_{25}H_7D_{15}BrOP$ requires C: 64.66% H: 1.52% D: 6.51%, found C: 64.69% H: 1.52% D: 6.69%.

## 4 Notes

1. Although reasonably dry conditions and toluene are preferable, use of all reagents including toluene as supplied commercially produces acceptable results for this synthesis.
2. Where more than one size is suitable for **step 4**, (Subheading 3.2) a larger stirrer bar is preferred, as substantial precipitate is generated and may impede a smaller one.
3. The synthesis as outlined does not require a centrifuge for Subheading 3.3, **step 1**, and the yield given can be achieved without one. However, where available use of a centrifuge to settle the fine precipitate from the crystallizations will make the purification considerably easier.
4. Re-use of the recrystallization liquors (Subheading 3.3, **steps 1–3**) is important as excess dimethyl sulfoxide is relatively difficult to remove, and MitoB is fairly soluble in this solvent—the first 500 mg batch will saturate the solvent. Recrystallization of all the material in a larger quantity of dimethyl sulfoxide works but has a detrimental impact on yield.
5. Protodeboronation is possible in **step 6** (Subheading 3.3); increasing the temperature of the aqueous crystallization beyond 80 °C appears to accelerate this reaction. If this product is observed, repeating **step 6** (Subheading 3.3) and concentrating the sample less may be sufficient to remove this; otherwise repeat Subheading 3.3. $^1$H NMR of impurity: $\delta_H$ (400 MHz, $d_6$-dimethyl sulfoxide): 7.95–7.87 (3H, m, 3 × *p*-$PPh_3$), 7.79–7.70 (6H, m, 6 × *o*-$PPh_3$), 7.69–7.61 (6H, 6 × *m*-$PPh_3$), 7.34–7.27 (1H, m, H4), 7.23 (2H, t, $J = 7.7$ Hz, H2, H6), 6.99–6.93 (2H, m, H3, H5), 5.14 (2H, d, $J = 15.8$ Hz, C**H**$_2$Ph).
6. The concentration of the $^1$H NMR sample for Subheading 3.3, **step 8** is not experimentally vital, but is specified as much stronger samples will show a second set of peaks if the $d_6$-dimethyl sulfoxide is dry; these represent trimerization of the boronic acid within the NMR sample rather than degradation of the material. If side peaks are observed, add a drop of water to the NMR to check trimerization is not responsible.

7. If possible higher purity 3-hydroxymethylbenzyl alcohol (95%) should be used, as this allows the compound to be isolated in sufficient purity to avoid recrystallization (Subheading 3.6).
8. Care should be taken in preparation of cold bath (Subheading 3.7, **step 2**) not to add a large excess of dry ice, as temperatures significantly below the freezing point of acetonitrile can be achieved with such conditions.
9. Addition of the pyridine will produce white gas. Addition of a vent will dissipate this; however, positive argon pressure should be maintained while the vent is in place (Subheading 3.8, **step 1**).
10. Dissolution of the starting material is slow in Subheading 3.8, **step 3**. Sonication significantly speeds up this process.
11. Subheading 3.9, and particularly **step 4**, should be performed quickly—the product is not stable indefinitely and will react with water present to reform starting material. Even the crystalline solid isolated (**step 7**) may decompose relatively quickly if not used, especially if heated or impure. For this reason it is not desirable to heat this compound strongly to remove solvent traces. These will not interfere with the following reaction anyway, but may instead be removed under higher vacuum if desired.
12. During **step 3** (Subheading 3.9), a significant portion of the material will appear to be insoluble; however, the desired product will dissolve in dichloromethane.
13. Only a small number of fractions (5 or less) are expected for **step 5** (Subheading 3.9). Do not increase the solvent polarity as side products or starting material may elute.
14. The procedure outlined for recrystallization (Subheading 3.13) uses enough ethanol to fully dissolve 1 g of Mito P. This will often be unnecessary where purity is high (90%+) already. Less ethanol can be used; it is not necessary to fully dissolve the material prior to cooling in these cases.
15. Reasonable substitutes may be used for the Suba-Seal (Subheading 3.13, **step 2**); be aware, however, that warm ethanol vapor will start to dissolve Parafilm and that the drop in temperature on cooling will result in a vacuum and make glass stoppers difficult to remove.
16. In our experience 80%+ of the Mito P will crystallize out in the time given (Subheading 3.13, **step 2**), but it is likely that leaving the crystallization longer would increase the yield slightly.
17. Evaporation in ethanol–water mix is to remove residual ethanol (Subheading 3.13, **step 4**). Care is required as "bumping" is likely toward the end of this evaporation (the use of the larger

flask size somewhat mitigates this problem). In our experience traces of ethanol are difficult to remove from solid even with prolonged heating under vacuum.

## Acknowledgments

AC funded through a European Research Council Advanced Grant (322784) to Neil Metcalfe, SJMcQ through Lloyds TSB Foundation for Scotland and the Royal Society of Edinburgh. We thank the EPSRC National Mass Spectrometry Service at Swansea University for ESI-MS, both LRMS and HRMS.

### References

1. Arrowsmith CH, Audia JE, Austin C (2015) The promise and peril of chemical probes. Nat Chem Biol 11:536–541
2. Murphy MP, Hartley RC (2018) Mitochondria as a therapeutic target for common pathologies. Nat Rev Drug Discov 17:865–886
3. Smith RAJ, Hartley RC, Murphy MP (2011) Mitochondria-targeted small molecule therapeutics and probes. Antioxid Redox Signal 15:3021–3038
4. Logan A, Shabalina IG, Prime TA et al (2014) In vivo levels of mitochondrial hydrogen peroxide increase with age in mtDNA mutator mice. Ageing Cell 13:765–768
5. Lepez-Otin C, Blasco MA, Partridge L et al (2013) The hallmarks of aging. Cell 153:1194–1217
6. Hernandez-Segura A, Nehme J, Demaria M (2018) Hallmarks of cellular senescence. Trends Cell Biol 28:436–453
7. Abate M, Festa A, Falco M et al (2020) Mitochondria as playmakers of apoptosis, autophagy and senescence. Semin Cell Dev Biol 98:139–153
8. Adams JM, Cory S (2018) The BCL-2 arbiters of apoptosis and their growing role as cancer targets. Cell Death Differ 25:27–36
9. Lopez J, Tait SWG (2015) Mitochondrial apoptosis: killing cancer using the enemy within. Br J Cancer 112:957–962
10. Chouchani ET, Pell VR, Gaude E et al (2014) Ischaemic accumulation of succinate controls reperfusion injury through mitochondrial ROS. Nature 515:431–435
11. Chouchani ET, Pell VR, James AM et al (2016) A unifying mechanism for mitochondrial superoxide production during ischemia-reperfusion injury. Cell Metab 23:254–263
12. Jakobs S, Wurm CA (2014) Super-resolution microscopy of mitochondria. Curr Opin Chem Biol 20:9–15
13. Jean SR, Tulumello DV, Wisnovsky SP et al (2014) Molecular vehicles for mitochondrial chemical biology and drug delivery. ACS Chem Biol 9:323–333
14. Weissig V (2015) DQAsomes as the prototype of mitochondria-targeted pharmaceutical nanocarriers: preparation, characterization, and use. Methods Mol Biol 1265:1–11
15. Donahue ND, Acar H, Wilhelm S (2019) Concepts of nanoparticle cellular uptake, intracellular trafficking, and kinetics in nanomedicine. Adv Drug Deliv Rev 143:68–96
16. Guo X, Wei X, Chen Z et al (2020) Multifunctional nanoplatforms for subcellular delivery of drugs in cancer therapy. Prog Mater Sci 107:100599
17. Jean SR, Ahmed M, Lei EK et al (2016) Peptide-mediated delivery of chemical probes and therapeutics to mitochondria. Acc Chem Res 49:1893–1902
18. Mitchell W, Ng EA, Tamucci JD (2020) The mitochondria-targeted peptide SS-31 binds lipid bilayers and modulates surface electrostatics as a key component of its mechanism of action. J Biol Chem 295:7452–7469
19. Nicholls DG, Ferguson SJ (2013) Bioenergetics 4. Academic Press, London
20. Murphy MP, Smith RAJ (2007) Targeting antioxidants to mitochondria by conjugation to lipophilic cations. Annu Rev Pharmacol Toxicol 47:629–656
21. Horobin RW (2010) Can QSAR models describing small-molecule xenobiotics give useful tips for predicting uptake and localization of nanoparticles in living cells? And if not, why not? In: Weissig V, D'Souza GG (eds)

Organelle-specific pharmaceutical nanotechnology. Wiley, New York

22. Zielonka J, Joseph J, Sikora A et al (2017) Mitochondria-targeted triphenylphosphonium-based compounds: syntheses, mechanisms of action, and therapeutic and diagnostic applications. Chem Rev 117:10043–10120
23. Snow BJ, Rolfe FL, Lockhart MM et al (2010) A double-blind, placebo-controlled study to assess the mitochondria-targeted antioxidant MitoQ as a disease-modifying therapy in Parkinson's disease. Mov Disord 25:1670–1674
24. Rokitskaya TI, Luzhkov VB, Korshunova GA et al (2019) Effect of methyl and halogen substituents on the transmembrane movement of lipophilic ions. Phys Chem Chem Phys 21:23355–23363
25. Robb EL, Gawel JM, Aksentijevic D et al (2015) Selective superoxide generation within mitochondria by the targeted redox cycler MitoParaquat. Free Radic Biol Med 89:883–894
26. Hu Z, Sim Y, Kon OL et al (2017) Unique Triphenylphosphonium derivatives for enhanced mitochondrial uptake and photodynamic therapy. Bioconjug Chem 28:590–599
27. Ihmels H, Otto D (2005) Intercalation of organic dye molecules into double-stranded DNA general principles and recent developments. In: Wurthner F (ed) Supermolecular dye chemistry, vol 258. Springer, New York, pp 161–204
28. Yang CY, Cai SJ, Liu HL et al (1997) Immobilized artificial membranes—screens for drug membrane interactions. Adv Drug Deliv Rev 23:229–256
29. Lipinski CA, Lombardo F, Dominy BW et al (2012) Experimental and computational approaches to estimate solubility and permeability in drug discovery and development settings. Adv Drug Deliv Rev 64:4–17
30. Ross MF, Da Ros T, Blaikie FH et al (2006) Accumulation of lipophilic dications by mitochondria and cells. Biochem J 400:199–208
31. Ong HC, Hu Z, Coimbra JTS et al (2019) Enabling mitochondrial uptake of lipophilic dications using methylated triphenylphosphonium moieties. Inorg Chem 58:8293–8299
32. Finichiu PG, James AM, Larsen L et al (2013) Mitochondrial accumulation of a lipophilic cation conjugated to an ionisable group depends on membrane potential, pH gradient and pK(a): implications for the design of mitochondrial probes and therapies. J Bioenerg Biomembr 45:165–173
33. Kelso GF, Porteous CM, Coulter CV et al (2001) Selective targeting of a redox-active ubiquinone to mitochondria within cells—antioxidant and antiapoptotic properties. J Biol Chem 276:4588–4596
34. Chalmers S, Caldwell ST, Quin C et al (2012) Selective uncoupling of individual mitochondria within a cell using a mitochondria-targeted photoactivated protonophore. J Am Chem Soc 134:758–761
35. McQuaker SJ, Quinlan CL, Caldwell ST et al (2013) A prototypical small-molecule modulator uncouples mitochondria in response to endogenous hydrogen peroxide production. Chembiochem 14:993–1000
36. Glancy B, Hartnell LM, Malide D et al (2015) Mitochondrial reticulum for cellular energy distribution in muscle. Nature 523:617–620
37. Robb EL, Hall AR, Prime TA et al (2018) Control of mitochondrial superoxide production by reverse electron transport at complex I. J Biol Chem 293:9869–9879
38. Lambert AJ, Brand MD (2004) Superoxide production by NADH: ubiquinone oxidoreductase (complex I) depends on the pH gradient across the mitochondrial inner membrane. Biochem J 382:511–517
39. Murphy MP (2009) How mitochondria produce reactive oxygen species. Biochem J 417:1–13
40. Halliwell B (2013) The antioxidant paradox: less paradoxical now? Br J Clin Pharmacol 75:637–644
41. Smith RAJ, Porteous CM, Coulter CV, Murphy MP (1999) Selective targeting of an antioxidant to mitochondria. Eur J Biochem 263:709–716
42. Dhanasekaran A, Kotamraju S, Karunakaran C et al (2005) Mitochondria superoxide dismutase mimetic inhibits peroxide-induced oxidative damage and apoptosis: role of mitochondrial superoxide. Free Radic Biol Med 39:567–583
43. Trnka J, Blaikie FH, Smith RAJ, Murphy MP (2008) A mitochondria-targeted nitroxide is reduced to its hydroxylamine by ubiquinol in mitochondria. Free Radic Biol Med 44:1406–1419
44. Dikalova AE, Bikineyeva AT, Budzyn K et al (2010) Therapeutic targeting of mitochondrial superoxide in hypertension. Circ Res 107:106–116
45. Dessolin J, Schuler M, Quinart A et al (2002) Selective targeting of synthetic antioxidants to mitochondria: towards a mitochondrial medicine for neurodegenerative diseases? Eur J Pharmacol 447:155–161

46. James AM, Sharpley MS, Manas AR et al (2007) Interaction of the mitochondria-targeted antioxidant MitoQ with phospholipid bilayers and ubiquinone oxidoreductases. J Biol Chem 282:14708–14718
47. Kelso GF, Maroz A, Cochemé HM et al (2012) A mitochondria-targeted macrocyclic Mn(II) superoxide dismutase mimetic. Chem Biol 19:1237–1246
48. Filipovska A, Kelso GF, Brown SE et al (2005) Synthesis and characterization of a triphenylphosphonium-conjugated peroxidase mimetic—insights into the interaction of ebselen with mitochondria. J Biol Chem 280:24113–24126
49. Prime TA, Blaikie FH, Evans C et al (2009) A mitochondria-targeted S-nitrosothiol modulates respiration, nitrosates thiols, and protects against ischemia-reperfusion injury. Proc Natl Acad Sci U S A 106:10764–10769
50. Chouchani ET, Methner C, Nadtochiy SM et al (2013) Cardioprotection by S-nitrosation of a cysteine switch on mitochondrial complex I. Nat Med 19:753–759
51. Quin C, Robertson L, McQuaker SJ et al (2010) Caged mitochondrial uncouplers that are released in response to hydrogen peroxide. Tetrahedron 66:2384–2389
52. Booty LM, Gawel JM, Cvetko F et al (2019) Selective disruption of mitochondrial thiol redox state in cells and in vivo. Cell Chem Biol 26:449–461
53. Antonucci S, Mulvey JF, Burger N et al (2019) Selective mitochondrial superoxide generation in vivo is cardioprotective through hormesis. Free Radic Biol Med 134:678–687
54. Murphy MP, Holmgren A, Larsson NG et al (2011) Unraveling the biological roles of reactive oxygen species. Cell Metab 13:361–366
55. Murphy MP, Echtay KS, Blaikie FH et al (2003) Superoxide activates uncoupling proteins by generating carbon-centered radicals and initiating lipid peroxidation—studies using a mitochondria-targeted spin trap derived from alpha-phenyl-*N*-tert-butylnitrone. J Biol Chem 278:48534–48545
56. Quin C, Trnka J, Hay A et al (2009) Synthesis of a mitochondria-targeted spin trap using a novel Parham-type cyclization. Tetrahedron 65:8154–8160
57. Xu YK, Kalyanaraman B (2007) Synthesis and ESR studies of a novel cyclic nitrone spin trap attached to a phosphonium group-a suitable trap for mitochondria-generated ROS? Free Radic Res 41:1–7
58. Hardy M, Chalier F, Ouari O et al (2007) Mito-DEPMPO synthesized from a novel NH2-reactive DEPMPO spin trap: a new and improved trap for the detection of superoxide. Chem Commun 10:1083–1085
59. Hardy M, Rockenbauer A, Vasquez-Vivar J et al (2007) Detection, characterization, and decay kinetics of ROS and thiyl adducts of Mito-DEPMPO spin trap. Chem Res Toxicol 20:1053–1060
60. Dickinson BC, Srikun D, Chang CJ (2010) Mitochondrial-targeted fluorescent probes for reactive oxygen species. Curr Opin Chem Biol 14:50–56
61. Robinson KM, Janes MS, Pehar M et al (2006) Selective fluorescent imaging of superoxide in vivo using ethidium-based probes. Proc Natl Acad Sci U S A 103:15038–15043
62. Kalyanaraman B, Dranka BP, Hardy M et al (2014) HPLC-based monitoring of products formed from hydroethidine-based fluorogenic probes—the ultimate approach for intra- and extracellular superoxide detection. Biochim Biophys Acta 1840:739–744
63. Shchepinova MM, Cairns AG, Prime TA et al (2017) MitoNeoD: A mitochondria-targeted superoxide probe. Cell Chem Biol 24:1285–1298
64. Logan A, Cochemé HM, Pun PBL et al (2014) Using exomarkers to assess mitochondrial reactive species in vivo. Biochim Biophys Acta 1840:923–930
65. Dickinson BC, Lin VS, Chang CJ (2013) Preparation and use of MitoPY1 for imaging hydrogen peroxide in mitochondria of live cells. Nat Protoc 8:1249–1259
66. Dickinson BC, Chang CJ (2008) A targetable fluorescent probe for imaging hydrogen peroxide in the mitochondria of living cells. J Am Chem Soc 130:9638–9639
67. Van de Bittner GC, Bertozzi CR, Chang CJ (2013) Strategy for dual-Analyte luciferin imaging: in vivo bioluminescence detection of hydrogen peroxide and caspase activity in a murine model of acute inflammation. J Am Chem Soc 135:1783–1795
68. Van de Bittner GC, Dubikovskaya EA, Bertozzi CR, Chang CJ (2010) In vivo imaging of hydrogen peroxide production in a murine tumor model with a chemoselective bioluminescent reporter. Proc Natl Acad Sci U S A 107:21316–21321
69. Cochemé HM, Quin C, McQuaker SJ et al (2011) Measurement of $H_2O_2$ within living drosophila during aging using a ratiometric mass spectrometry probe targeted to the

mitochondrial matrix. Cell Metab 13:340–350

70. Cochemé HM, Logan A, Prime TA et al (2012) Using the mitochondria-targeted ratiometric mass spectrometry probe MitoB to measure $H_2O_2$ in living drosophila. Nat Protoc 7:946–958
71. Sikora A, Zielonka J, Lopez M et al (2009) Direct oxidation of boronates by peroxynitrite: mechanism and implications in fluorescence imaging of peroxynitrite. Free Radic Biol Med 47:1401–1407
72. Sikora A, Zielonka J, Adamus J et al (2013) Reaction between peroxynitrite and triphenylphosphonium-substituted arylboronic acid isomers: identification of diagnostic marker products and biological implications. Chem Res Toxicol 26:856–867
73. Turowski M, Yamakawa N, Meller J et al (2003) Deuterium isotope effects on hydrophobic interactions: the importance of dispersion interactions in the hydrophobic phase. J Am Chem Soc 125:13836–13849
74. Eltayar N, Vandewaterbeemd H, Gryllaki M et al (1984) The lipophilicity of deuterium atoms—a comparison of shake-flask and hplc methods. Int J Pharm 19:271–281
75. Tanaka N, Thornton ER (1976) Isotope-effects in hydrophobic binding measured by high-pressure liquid-chromatography. J Am Chem Soc 98:1617–1619
76. Pun PBL, Logan A, Darley-Usmar V et al (2014) A mitochondria-targeted mass spectrometry probe to detect glyoxals: implications for diabetes. Free Radic Biol Med 67:437–450
77. Salin K, Auer SK, Rudolf AM et al (2015) Individuals with higher metabolic rates have lower levels of reactive oxygen species in vivo. Biol Lett 11:20150538
78. Salin K, Villasevil EM, Anderson GJ et al (2018) Decreased mitochondrial metabolic requirements in fasting animals carry an oxidative cost. Funct Ecol 32:2149–2157
79. Salin K, Auer SK, Villasevil EM et al (2017) Using the MitoB method to assess levels of reactive oxygen species in ecological studies of oxidative stress. Sci Rep 7:41228
80. Williamson RD, McCarthy FP, Manna S (2020) L-(+)-Ergothioneine significantly improves the clinical characteristics of pre-eclampsia in the reduced uterine perfusion pressure rat model. Hypertension 75:561–568
81. Lau GY, Arndt S, Murphy MP et al (2019) Species- and tissue-specific differences in ROS metabolism during exposure to hypoxia and hyperoxia plus recovery in marine sculpins. J Exp Biol 222:jeb206896
82. Gallego-Villar L, Rivera-Barahona A, Cuevas-Martin C et al (2016) In vivo evidence of mitochondrial dysfunction and altered redox homeostasis in a genetic mouse model of propionic acidemia: implications for the pathophysiology of this disorder. Free Radic Biol Med 96:1–12
83. Lopez-Fabuel I, Le Douce J, Logan A et al (2016) Complex I assembly into supercomplexes determines differential mitochondrial ROS production in neurons and astrocytes. Proc Natl Acad Sci U S A 113:13063–13068
84. Kusminski CM, Ghaben AL, Morley TS et al (2020) A novel model of diabetic complications: adipocyte mitochondrial dysfunction triggers massive beta-cell hyperplasia. Diabetes 69:313–330
85. Dare AJ, Logan A, Prime TA et al (2015) The mitochondria-targeted anti-oxidant MitoQ decreases ischemia-reperfusion injury in a murine syngeneic heart transplant model. J Heart Lung Transplant 34:1471–1480
86. Frankenreiter S, Bednarczyk P, Kniess A et al (2017) cGMP-elevating compounds and ischemic conditioning provide Cardioprotection against ischemia and reperfusion injury via cardiomyocyte-specific BK channels. Circulation 136:2337–2355
87. Hancock M, Hafstad AD, Nabeebaccus AA et al (2018) Myocardial NADPH oxidase-4 regulates the physiological response to acute exercise. Elife 7:41044
88. Brinker AE, Vivian CJ, Beadnell TC et al (2020) Mitochondrial haplotype of the host stromal microenvironment alters metastasis in a non-cell autonomous manner. Cancer Res 80:1118–1129
89. Schultz A, Olorundami OA, Teng RJ et al (2019) Decreased OLA1 (Obg-like ATPase-1) expression drives ubiquitin-proteasome pathways to downregulate mitochondrial SOD2 (superoxide dismutase) in persistent pulmonary hypertension of the newborn. Hypertension 74:957–966
90. Zemanovic S, Ivanov MV, Ivanova LV et al (2018) Dynamic phosphorylation of the C terminus of Hsp70 regulates the mitochondrial import of SOD2 and redox balance. Cell Rep 25:2605–2616
91. Yu EPK, Reinhold J, Yu H et al (2017) Mitochondrial respiration is reduced in atherosclerosis, promoting necrotic Core formation and reducing relative fibrous cap thickness. Arterioscler Thromb Vasc Biol 37:2322–2332

92. Maresca A, Del Dotto V, Capristo M et al (2020) DNMT1 mutations leading to neurodegeneration paradoxically reflect on mitochondrial metabolism. Hum Mol Genet 29 (11):1864–1188
93. Pei R, Liu J, Martin DA et al (2019) Aronia berry supplementation mitigates inflammation in T cell transfer-induced colitis by decreasing oxidative stress. Nutrients 11:1316
94. Secinaro MA, Fortner KA, Dienz O et al (2018) Glycolysis promotes caspase-3 activation in lipid rafts in T cells. Cell Death Dis 9:62
95. Hamalainen RH, Ahlqvist KJ, Ellonen P et al (2015) mtDNA mutagenesis disrupts pluripotent stem cell function by altering redox signaling. Cell Rep 11:1614–1624
96. Formentini L, Santacatterina F, Nunez de Arenas C (2017) Mitochondrial ROS production protects the intestine from inflammation through functional M2 macrophage polarization. Cell Rep 19:1202–1213
97. He C, Danes JM, Hart PC et al (2019) SOD2 acetylation on lysine 68 promotes stem cell reprogramming in breast cancer. Proc Natl Acad Sci U S A 116:23534–23541
98. Arndt S, Baeza-Garza CD, Logan A et al (2017) Assessment of $H_2S$ in vivo using the newly developed mitochondria-targeted mass spectrometry probe MitoA. J Biol Chem 292:7761–7773
99. Cairns AG, McQuaker SJ, Murphy MP, Hartley RC (2015) Targeting mitochondria with small molecules: the preparation of MitoB and MitoP as exomarkers of mitochondrial hydrogen peroxide. In: Weissig V, Edeas M (eds) Mitochondrial medicine. Methods in molecular biology, vol 1265. Humana press, New York, NY
100. Dawson MI, Hobbs PD, Kuhlmann K et al (1980) Retinoic acid analogs—synthesis and potential as cancer chemopreventive agents. J Med Chem 23:1013–1022
101. Skulachev VP, Anisimov VN, Antonenko YN et al (2009) An attempt to prevent senescence: a mitochondrial approach. Biochim Biophys Acta 1787:437–461

# Chapter 7

# Synthesis of Triphenylphosphonium Phospholipid Conjugates for the Preparation of Mitochondriotropic Liposomes

**Parul Benien, Mohammed Almuteri, Shrey Shah, Mark Böhlke, Ahmed Mehanna, and Gerard G. M. D'Souza**

## Abstract

Surface modification of liposomes with a ligand is facilitated by the conjugation of the ligand to a hydrophobic molecule that serves to anchor the ligand to the liposomal bilayer. We describe here a simple protocol to conjugate a triphenylphosphonium group to several commercially available functionalized phospholipids. The resulting triphenylphosphonium-conjugated lipids can be used to prepare liposomes that preferentially associate with mitochondria when exposed to live mammalian cells in culture.

**Key words** Mitochondriotropic, Liposomes, Triphenylphosphonium

## 1 Introduction

There has been a growing interest in mitochondria-specific drug delivery over the last decade and even a cursory survey of the literature reveals that triphenylphosphonium (TPP) has been proven to be a versatile mitochondriotropic ligand for many delivery strategies [1–10]. TPP has been conjugated to various biologically active molecules and has improved the mitochondrial accumulation and therapeutic activities of these molecules [11–14]. TPP has also been the ligand of choice for the design of pharmaceutical carriers with mitochondria-specific accumulation [15, 16]. Our efforts in mitochondria-specific delivery have focused on liposomes as the delivery platform with early formulations that were based on the use of stearyl triphenylphosphonium (STPP) [17–20]. STPP allows for the surface modification of liposomes with TPP residues by virtue of the stearyl chain serving as a lipid anchor for TPP in the liposomal bilayer. In an effort to allow more flexibility in the lipid composition of the liposomal

Volkmar Weissig and Marvin Edeas (eds.), *Mitochondrial Medicine: Volume 1: Targeting Mitochondria*, Methods in Molecular Biology, vol. 2275, https://doi.org/10.1007/978-1-0716-1262-0_7,

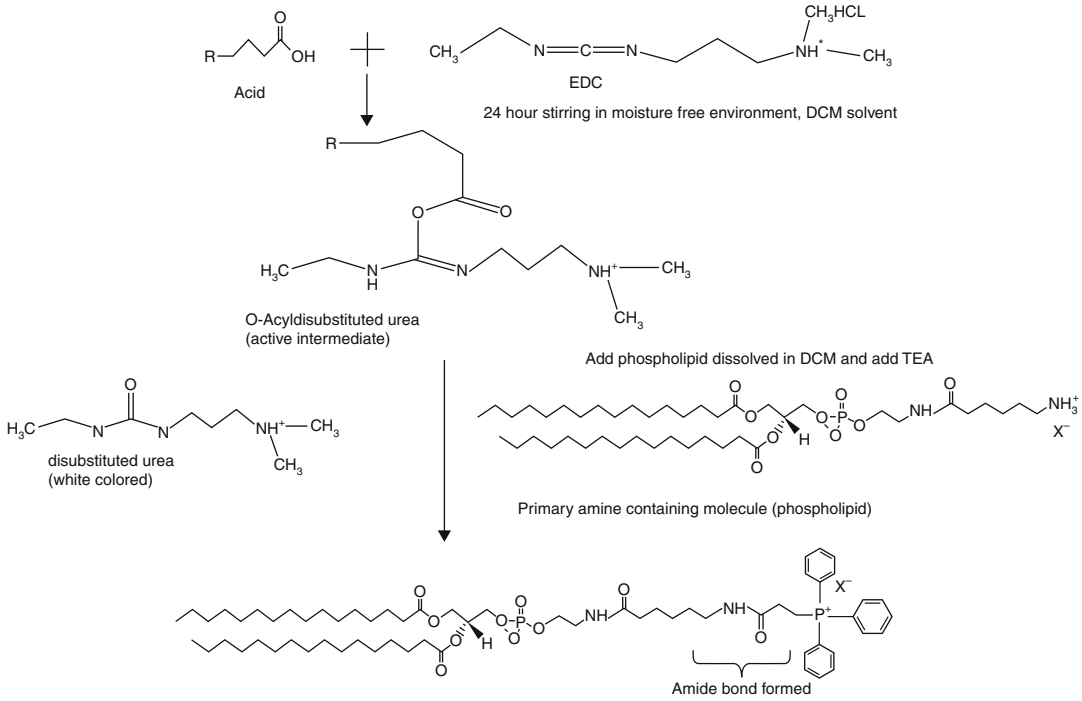


**Fig. 1** Schematic representation of the synthesis of triphenylphosphonium modified phospholipid

formulation and to study the potential effect of the lipid anchor on the mitochondrial compatibility of the mitochondriotropic liposomal platform, we developed a simple approach for the conjugation of TPP to commercially available functionalized phospholipids. A schematic of the synthetic procedure is shown in Fig. 1. This protocol has been used successfully to prepare several TPP modified phospholipids. It should be noted, however, that the aim of the protocol has been to produce a usable concentration of modified phospholipid and not to produce a highly purified product free of all traces of unmodified lipid. Our studies have confirmed that liposomes prepared from these lipids have greater cell biocompatibility compared to liposomes prepared with STPP [21].

## 2 Materials

### 2.1 Synthesis

1. 1-Ethyl-3-[3-dimethylaminopropyl] carbodiimide hydrochloride.
2. 2-Carboxyethyl-triphenylphosphonium bromide.
3. 1,2-dipalmitoyl-*sn*-glycero-3-phosphoethanolamine-*N*-(hexanoylamine) (Avanti Polar Lipids, Alabaster, AL).
4. Dichloromethane.
5. Triethylamine ≥99%.
6. Sodium sulfate, anhydrous, 99%.

7. Whatman filter paper.
8. 20 mL Scintillation vials, borosilicate glass with screw cap.
9. Spinbar® Magnetic stir bars, one each 2 × 7 mm and 7 × 35 mm.
10. 100 mL Pyrex graduated media bottle.

### 2.2 Purification

1. Chloroform ≥99.5%.
2. Methanol HPLC grade.
3. Silica gel 60F.
4. Sand—acid washed.
5. Burette, acrylic 50 mL.
6. Disposable Borosilicate glass tubes, 12 × 75 mm.

### 2.3 TLC Analysis

1. TLC glass plates, Silica gel 60 $F_{254}$ (EMD Chemicals, Billerica, MA).

### 2.4 Miscellaneous Equipment

1. Magnetic stirrer.
2. Rotary evaporator.
3. Handheld UV lamp.

## 3 Methods

Unless otherwise indicated all steps are performed at room temperature.

### 3.1 Dehydration of Solvents

1. Shake sufficient amount of anhydrous sodium sulfate (2 g for each 10 mL of solvent) with dichloromethane (DCM) in an airtight vial until the sodium sulfate floats. Filter through Whatman filter paper and collect the dried solvent in a fresh airtight vial (*see* **Note 1**).
2. Follow the same procedure as above to prepare dried triethanolamine (TEA).

### 3.2 Synthesis

1. Weigh 41.5 mg (~100 mmol) 2-Carboxyethyl-triphenylphosphonium bromide (TPP-Br) (*see* **Note 2**) and dissolve in 2 mL (*see* **Note 3**) dried DCM in a vial (solution 1).
2. Weigh 19.2 mg (~100 mmol) EDC HCl and dissolve in 2 mL (*see* **Note 3**) dried DCM in a vial (solution 2).
3. Place the small (2 × 7 mm) magnetic stir bar inside the vial that contains solution 2 (*see* **Note 4**). Add 200 μL of TPP-Br solution (solution 1) to the EDC HCl solution (solution 2) with continuous stirring. Cap the vial and continue stirring.

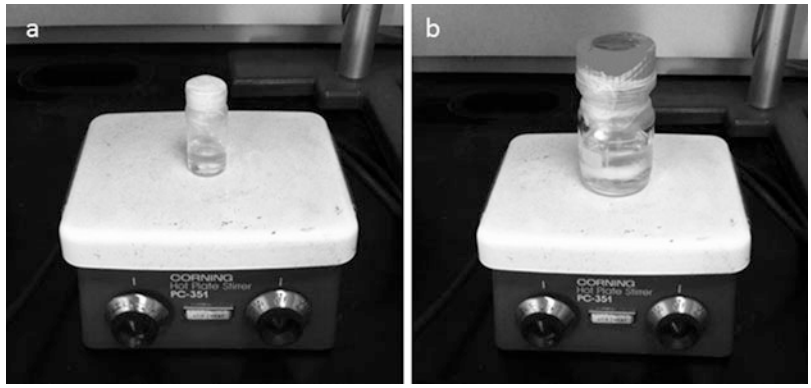


**Fig. 2** Apparatus setup for synthetic process. (**a**) Activation of triphenyl phosphonium (**step 4** of Subheading 3.2) (**b**) Synthesis of triphenyl phosphonium modified lipid (**step 8** of Subheading 3.2)

When the solution turns clear add another 200 μL of solution 1. Continue in this fashion until all of solution 1 has been added to solution 2 (*see* **Note 5**).

4. After all of the TPP-Br solution has been added to the EDC HCl solution, cap the vial and wrap with Parafilm to ensure that the vial remains airtight. Keep the sealed vial on the magnetic stirrer and let the reaction run with continuous stirring until the liquid in the vial turns clear, usually 24–48 h. *See* Fig. 2a for how the setup should look at this stage.
5. Dissolve 80.5 mg (~100 mmol) of 1,2-dipalmitoyl-*sn*-glycero-3-phosphoethanolamine-*N*-(hexanoylamine) in 2 mL dried DCM and then add 28 mL of TEA (~200 mmol).
6. Transfer the activated EDC-TPP to a larger bottle (e.g., a 100 mL glass media bottle) and place the large (7 × 35 mm) magnetic stir bar inside it and transfer to a magnetic stirrer. Slowly add the dissolved lipid dropwise while stirring, over a period of 1 h.
7. If the solution is not clear, add 2 mL aliquots of DCM and TEA with stirring, until it turns clear.
8. Seal the bottle and wrap with Parafilm (*see* Fig. 2b for how the setup should look at this stage). Let the reaction run on the magnetic stirrer for 24 h or until a white insoluble precipitate of isourea is visible.
9. Stop the reaction, filter to get rid of the isourea and transfer the contents to a 100 mL round bottom flask (which should be completely dry) and evaporate to dryness on a rotary evaporator at 37 °C.

### 3.3 Purification

1. While the product is being dried, prepare the mobile phase and the silica gel column for the purification step. The mobile phase composition is methanol–chloroform–water (25:4:2). 500 mL is usually sufficient to carry out all subsequent steps.
2. Prepare the column in an appropriately sized burette with an inner diameter of approximately 1 cm. Suspend sufficient silica gel 60F in the mobile phase to form a slurry that when poured into the burette and allowed to settle will yield a column 10–12 cm high. Pour a layer of sand (approximately 2–2.5 cm) over the top of the silica column to ensure that the silica does not get disturbed when adding the eluent. Wash the column with a couple of column volumes of mobile phase before use in the purification. At no point during preparation or purification should the column be allowed to dry.
3. After complete evaporation, dissolve the solid that is left in the flask from **step 9** of the synthesis in the minimum amount of mobile phase that completely dissolves the solid.
4. Pour the concentrated reaction mixture dissolved in the mobile phase onto the column and start collecting 0.5 mL fractions in disposable culture tubes. About 48 to 60 fractions are usually needed.
5. Run TLC and observe which fractions have the modified lipid. Apply four fractions per TLC slide using TLC capillary tubes, immerse in jars containing 5 mL mobile phase with filter papers surrounding each plate. Allow the mobile phase to reach at least two-thirds of the way up the TLC plate.
6. On observing in UV light, the modified lipid fraction is visible at the top of the TLC plate. Combine fractions with spots on the upper half of the TLC plate (*see* Fig. 3) in a 100 mL round bottom flask and evaporate to dryness on rotary evaporator at 37 °C.

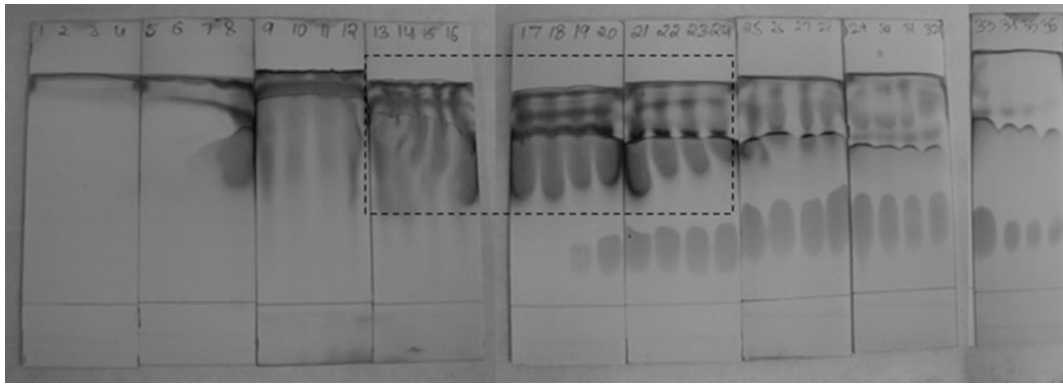

**Fig. 3** TLC analysis of collected fractions from column chromatography. Dashed box indicates fractions that were collected. For ease of photography, plates were developed in iodine vapor. Routine inspection was with UV illumination as described in **step 6** of Subheading 3.3

7. Collect the powder left in the round bottom flask, weigh and then dissolve in chloroform to yield the working stock of modified lipid (*see* **Note 6**).

## 4 Notes

1. As an extra precaution seal vials with Parafilm for storage. Wherever possible choose vials such that head space is minimized above the surface of the solvent and prepare several in advance of starting the synthesis.
2. TPP-Br is a white powder. Do not use if the powder has turned brown.
3. 2 mL of the solvent is usually enough. If still not soluble, add more as needed.
4. Use a vial for the EDC HCl solution that can also accommodate the entire volume of the TPP-Br solution to be added.
5. Ensure not to add further drops until the solution is clear and also ensure to seal the vial quickly after each addition, as EDC is prone to degradation by moisture.
6. For the sake of simplicity, the synthesis described in detail is for the conjugation of TPP to 1,2-dipalmitoyl-*sn*-glycero-3-phosphoethanolamine-*N*-(hexanoylamine). However, we have successfully used the same approach for modifying 1,2-dioleoyl-*sn*-glycero-3-phosphoethanolamine-*N*-(hexanoylamine) (DO) and 1,2-dimyristoyl-*sn*-glycero-3-phosphoethanolamine-*N*-(hexanoylamine) (DM), both of which are available from Avanti Polar Lipids. The reagent amounts and steps remain the same for the other lipids. However, the oleoyl lipid is most difficult to dissolve, so it may need more of the solvents in **step 7** of the synthesis than the other two types of lipids. As a further confirmation of the success of the synthesis and purification, NMR can be used to verify the presence of the desired product (*see* Fig. 4).

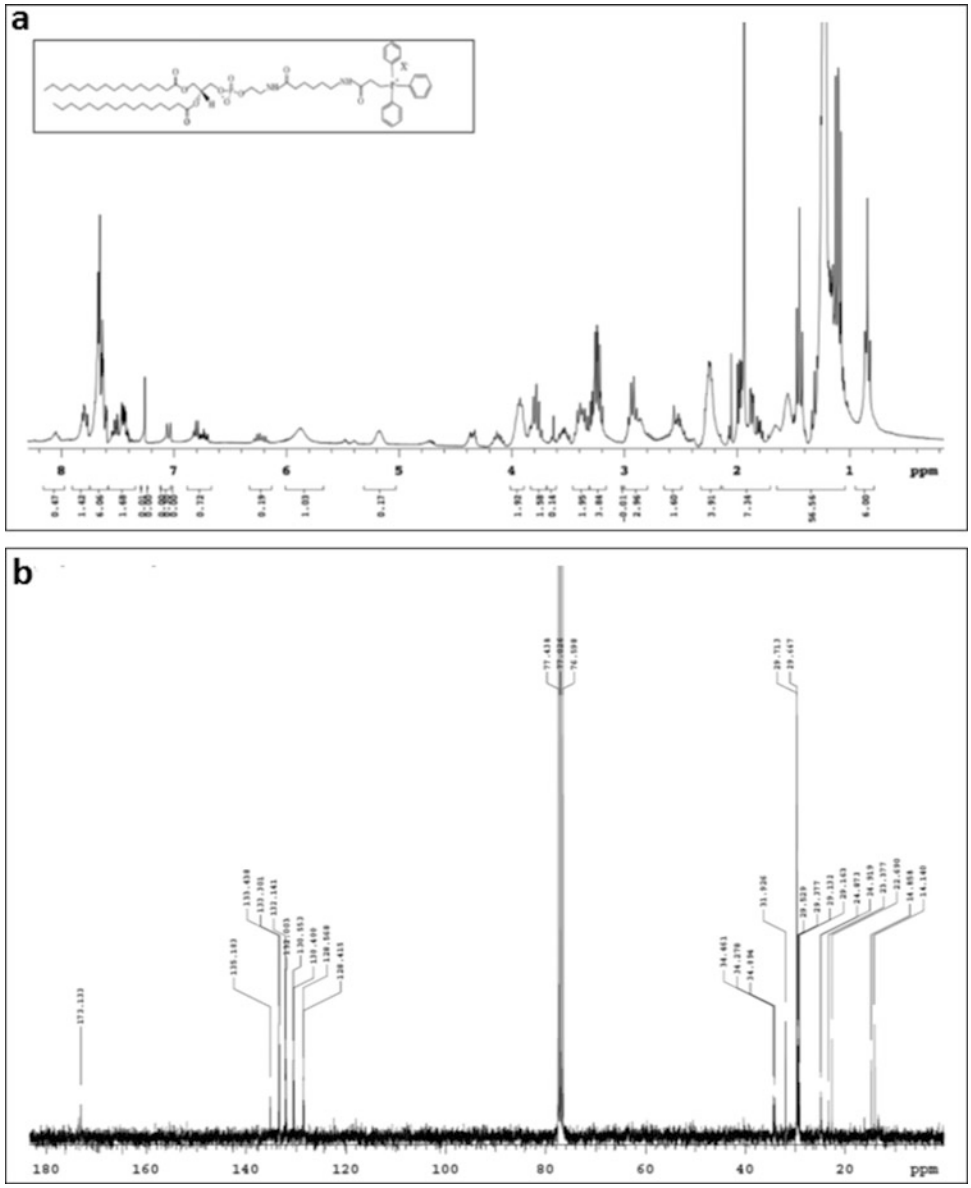


**Fig. 4** NMR spectra of triphenylphosphonium modified phospholipid. (**a**) $^{1}H$ NMR spectrum. Inset represents the chemical structure of the modified phospholipid with molecular formula $C_{63}H_{96}N_2O_{10}P_2Br$ and molecular weight of 1183.29 g/mol. (**b**) $^{13}C$ NMR spectrum. Both spectra were obtained on a Varian 300 MHZ instrument (Agilent Technologies, Santa Clara, CA) using 1024 scans for the $^{13}C$ spectrum and 16 scans for the $^{1}H$ spectrum. The $CDCl_3$ solvent peak appears at 77.026 ppm and 7.26 ppm in the $^{13}C$ NMR spectrum and the $^{1}H$ proton spectrum, respectively

## Acknowledgments

This work was supported by funds from MCPHS University School of Pharmacy—Boston.

## References


1. Luft R (1994) The development of mitochondrial medicine. Proc Natl Acad Sci U S A 91 (19):8731–8738
2. Murphy MP, Smith RA (2000) Drug delivery to mitochondria: the key to mitochondrial medicine. Adv Drug Deliv Rev 41(2):235–250
3. Martinou JC, Green DR (2001) Breaking the mitochondrial barrier. Nat Rev Mol Cell Biol 2 (1):63–67
4. Fulda S, Galluzzi L, Kroemer G (2010) Targeting mitochondria for cancer therapy. Nat Rev Drug Discov 9(6):447–464
5. Weissig V (2011) Mitochondrial delivery of biologically active molecules. Pharm Res 28 (11):2633–2638
6. D'Souza GG et al (2011) Approaches for targeting mitochondria in cancer therapy. Biochim Biophys Acta 6:689–696
7. Weissig V (2011) From serendipity to mitochondria-targeted nanocarriers. Pharm Res 28(11):2657–2668
8. Yamada Y, Harashima H (2008) Mitochondrial drug delivery systems for macromolecules and their therapeutic application to mitochondrial diseases. Adv Drug Deliv Rev 60 (13–14):1439–1462
9. Murphy MP (2008) Targeting lipophilic cations to mitochondria. Biochim Biophys Acta 1777(7–8):1028–1031
10. Zielonka J et al (2017) Mitochondria-targeted triphenylphosphonium-based compounds: syntheses, mechanisms of action, and therapeutic and diagnostic applications. Chem Rev 117 (15):10043–10120
11. Kolevzon N et al (2011) Multiple triphenylphosphonium cations as a platform for the delivery of a pro-apoptotic peptide. Pharm Res 28(11):2780–2789
12. Smith RA, Hartley RC, Murphy MP (2011) Mitochondria-targeted small molecule therapeutics and probes. Antioxid Redox Signal 15(12):3021–3038
13. Murphy MP, Smith RA (2007) Targeting antioxidants to mitochondria by conjugation to lipophilic cations. Annu Rev Pharmacol Toxicol 47:629–656
14. Jameson VJ et al (2015) Synthesis of triphenylphosphonium vitamin E derivatives as mitochondria-targeted antioxidants. Tetrahedron 71(44):8444–8453
15. Cuchelkar V, Kopeckova P, Kopecek J (2008) Novel HPMA copolymer-bound constructs for combined tumor and mitochondrial targeting. Mol Pharm 5(5):776–786
16. Marrache S, Dhar S (2012) Engineering of blended nanoparticle platform for delivery of mitochondria-acting therapeutics. Proc Natl Acad Sci U S A 109(40):16288–16293
17. Boddapati SV et al (2005) Mitochondriotropic liposomes. J Liposome Res 15(1–2):49–58
18. Boddapati SV et al (2008) Organelle-targeted nanocarriers: specific delivery of liposomal ceramide to mitochondria enhances its cytotoxicity in vitro and in vivo. Nano Lett 8 (8):2559–2563
19. Patel NR et al (2010) Mitochondria-targeted liposomes improve the apoptotic and cytotoxic action of sclareol. J Liposome Res 20 (3):244–249
20. Solomon MA, Shah SA, D'Souza GG (2012) In vitro assessment of the utility of stearyl triphenyl phosphonium modified liposomes in overcoming the resistance of ovarian carcinoma Ovcar-3 cells to paclitaxel. Mitochondrion 3 (5):464–472
21. Benien P et al (2016) Hydrophobized triphenyl phosphonium derivatives for the preparation of mitochondriotropic liposomes: choice of hydrophobic anchor influences cytotoxicity but not mitochondriotropic effect. J Liposome Res 26(1):21–27

# Chapter 8

# Imaging Mitochondrial Hydrogen Peroxide in Living Cells

**Alexander R. Lippert, Bryan C. Dickinson, and Elizabeth J. New**

## Abstract

Hydrogen peroxide ($H_2O_2$) produced from mitochondria is intimately involved in human health and disease, but is challenging to selectively monitor inside living systems. The fluorescent probe MitoPY1 provides a practical tool for imaging mitochondrial $H_2O_2$ and has been demonstrated to function in a variety of diverse cell types. In this chapter, we describe the synthetic preparation of the small molecule probe MitoPY1, methods for validating this probe in vitro and in live cells, and an example procedure for measuring mitochondrial $H_2O_2$ in a cell culture model of Parkinson's disease.

**Key words** Hydrogen peroxide, Fluorescent probes, Boronate, Fluorescence microscopy, Mitochondria, Triphenylphosphonium cations

## 1 Introduction

Mitochondria are vital organelles that not only house the electron transport chain and oxidative phosphorylation machinery but also play key regulatory roles for many processes including apoptosis [1], metabolism, and proliferation [2]. Given their fundamental importance in human biology, there has been extensive interest in studying the mitochondria for their role in disease genesis and as potential therapeutic targets [3]. Mitochondria are an important site for the production of reactive oxygen species (ROS), a family of distinct oxygen derivatives with unique physical properties and biological activities [4]. These ROS are generated as presumably undesired side products of the mitochondrial electron transport chain and often mediate deleterious effects associated with disease and aging [5–7]. However, some ROS are now known to function as signaling agents to modulate cellular processes. For example, hydrogen peroxide ($H_2O_2$) has emerged as an important ROS due, in part, to its ability to mediate signaling cascades involved in redox homeostasis [8]. Determining $H_2O_2$ levels in mitochondria in living cells in real time, however, remains a significant challenge [9].

Volkmar Weissig and Marvin Edeas (eds.), *Mitochondrial Medicine: Volume 1: Targeting Mitochondria*, Methods in Molecular Biology, vol. 2275, https://doi.org/10.1007/978-1-0716-1262-0_8,

Small molecule fluorescent probes have enabled the imaging of a wide range of analytes [10]. Boronate-based probes, in particular, offer a method for the selective imaging of $H_2O_2$ by using the chemoselective and biocompatible oxidation of boronates into phenols [11]. For example, the first-generation probe PF1, based on a caged fluorescein, displays the remarkable ability to selectively visualize exogenously added $H_2O_2$ in living cells [12]. This strategy has been generalized to develop boronate-based $H_2O_2$ probes with a wide range of optical properties [13, 14]. One general challenge in the use of a small molecule fluorescent probe is to control its subcellular localization so that it accumulates in the region of interest within a cell. Mitochondrial localization of a small molecule can be achieved by appending an alkylated triphenyl phosphonium tag as first described by Murphy and Smith [15]. This methodology utilizes the fact that lipophilic cations tend to accumulate in the mitochondria due to the highly negative mitochondrial membrane potential [16]. We show here that a mitochondrially localizing $H_2O_2$ probe can be designed based on the PF dye series by incorporation of a triphenyl phosphonium tag to provide the probe MitoPY1, which can be used to selectively image $H_2O_2$ in the mitochondria of living cells [17, 18]. MitoPY1 has been successfully utilized to study mitochondrial $H_2O_2$ levels in many cell models, including cultured cancer cells [19–22] immortalized cells expressing copper-handling mutations [23], primary cells from *X. leavis* embryos [24], primary rat neurons [25–27] and osteoblasts [28], mouse sperm [29], primary mouse cardioymyocytes [30] and immune cells [31, 32] and cannulated isolated human arterioles [33, 34].

The protocol outlined in this chapter provides a detailed description of the synthesis of MitoPY1 and its application to imaging $H_2O_2$ in the mitochondria of living cells. As a working example, we use MitoPY1 to image mitochondrial $H_2O_2$ in a cellular model of Parkinson's disease.

## 2 Materials

### 2.1 Synthetic Chemistry Components

#### 2.1.1 Step 1: Synthesis of Fmoc-Piperazine Rhodol

1. 2-(2,4-dihydroxybenzoyl)benzoic acid [35] (*see* **Note 1**).
2. 1-(2-hydroxyphenyl)-piperazine.
3. Trifluoroacetic acid (TFA).
4. Diethyl ether.
5. Methanol.
6. 9-fluoreneylmethyl chloroformate (Fmoc-Cl).
7. Sodium bicarbonate ($NaHCO_3$).

8. Rotary evaporator.
9. Acetonitrile.
10. Ethyl acetate.
11. Hexanes.
12. Silica gel.
13. Sodium sulfate.

*2.1.2 Step 2: Synthesis of Fmoc-Piperazine Rhodol Triflate*

1. *N*-Phenyl bis(trifluoromethanesulfonamide).
2. Sodium carbonate ($Na_2CO_3$).
3. Dimethyl formamide (DMF).

*2.1.3 Step 3: Synthesis of Fmoc-Piperazine Rhodol Boronate*

1. Pd(dppf)$Cl_2$·$CH_2Cl_2$.
2. Potassium acetate (KOAc).
3. Toluene.
4. Microwave reactor.

*2.1.4 Step 4: Synthesis of MitoPY1*

1. Piperidine.
2. (4-iodobutyl)triphenylphosphonium iodide [36] (*see* **Note 2**).
3. Glovebox.
4. Dichloromethane.

***2.2 Cellular Imaging Components (See Note 3)***

1. Eppendorf tubes.
2. Fluorescence spectrometer (*see* **Note 4**).
3. Human embryonic kidney cells (HEK293T).
4. Dulbecco's modified Eagle medium (DMEM).
5. Fetal bovine serum (FBS).
6. Trypsin.
7. Cell culture dishes appropriate for microscopy (*see* **Note 5**).
8. Dimethyl sulfoxide (DMSO).
9. Dulbecco's phosphate buffered saline (DPBS).
10. Hydrogen peroxide ($H_2O_2$).
11. Paraquat.
12. Glutamine.
13. Poly-L-lysine.
14. Inverted confocal microscope (*see* **Note 6**).

## 3 Methods

### 3.1 Synthetic Chemistry (Fig. 1)

#### 3.1.1 Synthesis of Fmoc-Piperazine Rhodol

1. Add 2-(2,4-dihydroxybenzoyl) benzoic acid (1.0 equiv., *see* **Note 1**) and 1-(3-hydroxyphenyl)-piperazine (1.0 equiv.) to a heavy walled pressure flask (*see* **Note 7**).
2. Add 16 mL TFA per 1 g 2-(2,4-dihydroxybenzoyl) benzoic acid to the flask. Seal the flask and stir for 3 h in an oil bath held at 95 °C (*see* **Note 8**).
3. Cool the reaction to room temperature and add 240 mL diethyl ether per 1 g 2-(2,4-dihydroxybenzoyl) benzoic acid. A solid red precipitate should be observed.
4. Collect the precipitate by filtration and immediately dissolve in methanol (*see* **Note 9**).

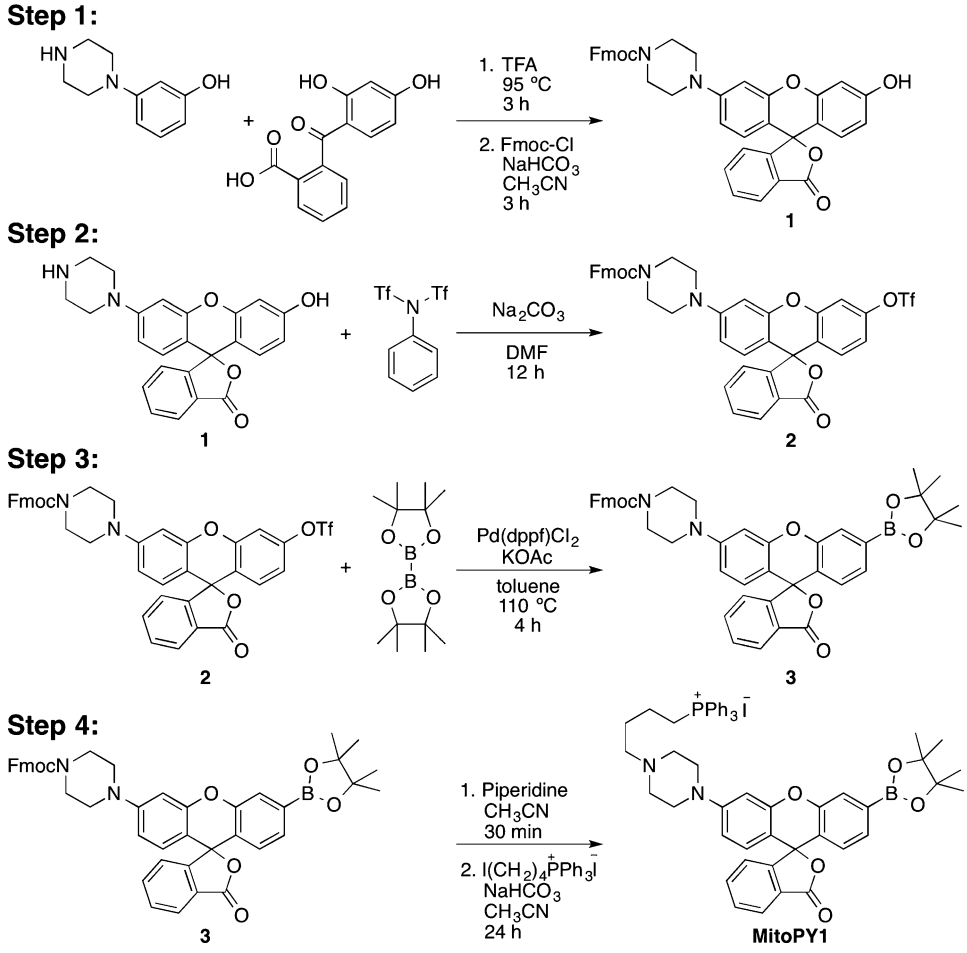


**Fig. 1** Stepwise synthetic scheme for the preparation of MitoPY1

5. Transfer to a round-bottom flask and dry under high vacuum. Add this unpurified product to a dry Schlenk tube (*see* **Note 10**).
6. Add Fmoc-Cl (0.68 equiv.), $NaHCO_3$ (1.7 equiv.), and approximately 8 mL anhydrous acetonitrile per 1 g 2-(2,4-dihydroxybenzoyl) benzoic acid, enough to dissolve the material. Stir under ambient temperature for 3 h.
7. Dilute the reaction in ethyl acetate and then wash with water (*see* **Note 11**).
8. Evaporate the organic layer using a rotary evaporator. This crude product can be purified by silica column chromatography, eluting with 1:1 hexanes–ethyl acetate (*see* **Note 12**) to provide Fmoc-piperazine rhodol as a red solid in 39% yield.

*3.1.2 Synthesis of Fmoc-Piperazine Rhodol Triflate*

1. Add the Fmoc-piperazine rhodol (1 equiv.), *N*-phenyl bis(trifluoromethanesulfonamide) (2 equiv.), and $Na_2CO_3$ (10 equiv.) to a dry Schlenk tube (*see* **Note 10**).
2. Add 2 mL anhydrous DMF per 100 mg Fmoc-piperazine. Fill the flask with nitrogen and stir at ambient temperature for 12 h. After this time, dilute reaction in ethyl acetate and wash with water (*see* **Note 11**).
3. Evaporate the organic layer using a rotary evaporator.
4. Purify using silica column chromatography (*see* **Note 12**), eluting with 1:1 hexanes–ethyl acetate to give Fmoc-piperazine rhodol triflate as a white solid in 46% yield.

*3.1.3 Synthesis of Fmoc-Piperazine Rhodol Boronate*

1. Add the Fmoc-piperazine rhodol triflate (1 equiv.), Pd(dppf)-$Cl_2$·$CH_2Cl_2$ (0.3 equiv.), bis(pinacolato)diboron (1.0 equiv.), KOAc (10 equiv.), and 4.5 mL toluene per 100 mg Fmoc-piperazine rhodol triflate to a dry pressure flask (*see* **Note 7**) inside an inert atmosphere glove box. Remove the tube from the box and heat at 110 °C in a microwave reactor for 4 h.
2. Cool to ambient temperature and transfer to a round-bottomed flask using dichloromethane. Concentrate using a rotary evaporator.
3. Purify by silica column chromatography (*see* **Note 12**), eluting with 1:1 hexanes–ethyl acetate to yield Fmoc-piperazine rhodol boronate as a white solid in 74% yield.

*3.1.4 Synthesis of MitoPY1*

1. Add the Fmoc-piperazine rhodol boronate (1 equiv.) to a round-bottomed flask and dissolve in 15 mL 15% piperidine in acetonitrile per 100 mg Fmoc-piperazine rhodol boronate. Stir under ambient temperature for 30 min.
2. Evaporate all solvent using a rotary evaporator. Transfer the reaction vessel into an inert atmosphere glovebox. Add

(4-iodobutyl)triphenylphosphonium iodide (2 equiv., *see* **Note 2**), $NaHCO_3$ (5 equiv.), and 1.5 mL acetonitrile per 10 mg Fmoc-piperazine rhodol boronate.

3. Stir the reaction for 24 h under ambient temperature inside the glovebox.
4. Remove the reaction from the glovebox. Filter any solid material and evaporate to dryness using a rotary evaporator.
5. Purify by silica column chromatography (*see* **Note 12**), eluting with 9:9:1 dichloromethane–ethyl acetate–methanol to yield MitoPY1 as a light pink solid in 76% yield.

### 3.2 Cellular Imaging with MitoPY1

#### 3.2.1 Preparation of Aliquots

1. Dissolve MitoPY1 at a concentration of 4.3 mg/mL methanol for a final concentration of 5 mM (*see* **Note 13**).
2. Aliquot 20 μL portions of the MitoPY1 solution into Eppendorf tubes. Allow the methanol to evaporate (*see* **Note 14**).
3. Store dry stocks at −20 °C. On the day of the imaging experiment, dissolve dry stocks in 20 μL DMSO to make 5 mM stock solutions.

#### 3.2.2 Validation of Probe Response to $H_2O_2$ In Vitro

1. Add 2 μL of the 5 mM stock solution of MitoPY1 in DMSO to 1.998 mL of DPBS to make a 5 μM solution of MitoPY1 in DPBS.
2. Separate this solution into two 1 mL aliquots.
3. Prepare a 100 mM solution of $H_2O_2$ by adding 11 μL of 30% (wt/vol) $H_2O_2$ to 989 μL $H_2O$.
4. Treat a 1 mL aliquot of MitoPY1 in DPBS with 1 μL of 100 mM $H_2O_2$ for a final concentration of 100 μM $H_2O_2$. For the negative control, treat the other 1 mL aliquot of 5 μM MitoPY1 in DPBS with 1 μL $H_2O$.
5. Collect the fluorescence spectra with a fluorescence spectrometer (*see* **Note 4**), using an excitation wavelength of 503 nm and collecting the spectrum between 513 nm and 650 nm, with an emission maximum at $\lambda_{em} = 530$ nm. An increase in fluorescence intensity should be observed for the aliquot that was treated with $H_2O_2$ compared with the aliquot treated with $H_2O$ (Fig. 2a).

#### 3.2.3 Cell Culture

1. Maintain HEK 293T cells in exponential growth as a monolayer in DMEM supplemented with 10% FBS (*see* **Note 15**).
2. One or two days before imaging, seed a 24-well plate (*see* **Note 5**) with cells (*see* **Note 16**). At this stage, cytotoxicity (*see* **Note 17**) and mitochondrial membrane potential (MMP, *see* **Note 18**) can be measured to ensure that the probe is not perturbing normal mitochondrial function.

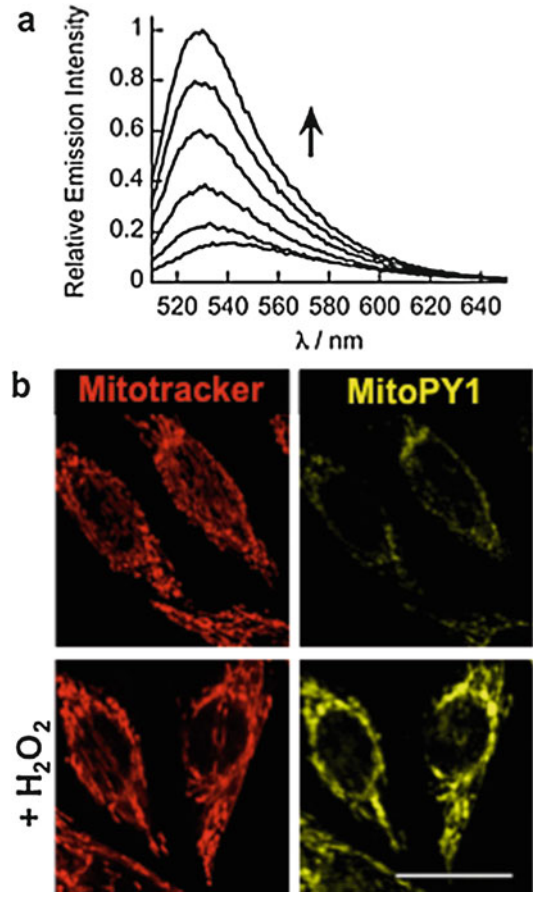


**Fig. 2** (**a**) Fluorescence turn-on response of 5 μM MitoPY1 to $H_2O_2$. Time points represent 0, 5, 15, 30, 45, and 60 min after the addition of 100 μM $H_2O_2$. $\lambda_{ex} = 503$ nm. (**b**) Imaging mitochondrial $H_2O_2$ in live cells with MitoPY1. HeLa cells loaded with 5 μM MitoPY1 and 50 nM MitoTracker Deep Red for 20 min at 37 °C and then stimulated with either $H_2O$ control or 100 μM $H_2O_2$ for 40 min. Scale bar = 20 μm. (Adapted with permission from Dickinson, B. C. and Chang, C. J. (2008) A Targetable Fluorescent Probe for Imaging Hydrogen Peroxide in the Mitochondria of Living Cells. *J Am Chem Soc* 130, 9638–9639. Copyright 2008 American Chemical Society)

### *3.2.4 Validation of Probe Response to Mitochondrial $H_2O_2$ in Cell Culture*

1. Add 12 μL of 5 mM MitoPY1 in DMSO to 6 mL DPBS for a final concentration of 10 μM MitoPY1.
2. Remove the 24-well plate from the incubator and replace the medium in six of the wells with 1 mL of the 10 μM MitoPY1 solution in DPBS (*see* **Note 19**).
3. Add MitoTracker Deep Red at a concentration of 25–100 nM (*see* **Note 20**).

4. After 30 min of incubation at 37 °C to allow dye uptake into cells (*see* **Note 21**), wash the cells with 2 × 1 mL DPBS (*see* **Note 22**).
5. Treat three wells with 100 μM $H_2O_2$ in 1 mL DPBS and the other three wells with 1 mL DPBS as a control.
6. Image the cells using a fluorescence microscope (*see* **Note 6**). Either a 488 nm or 510 nm excitation wavelength may be used with a collection window between 527 and 580 nm. MitoTracker Deep Red can then be imaged using a 633 nm excitation wavelength with a collection window between 666 and 698 nm. The mean fluorescence intensity of the $H_2O_2$-treated cells should be significantly higher than the control cells (*see* **Note 23**). An example of these results is shown in Fig. 2b.

#### *3.2.5 Imaging of Mitochondrial $H_2O_2$ in a Cellular Model of Parkinson's Disease*

Once the synthesized MitoPY1 has been validated in vitro and in cells, biological imaging experiments may be performed. As an example, an imaging experiment that uses an overnight exposure to 1 mM paraquat as a cellular model of Parkinson's disease will be described.

1. The day before imaging, prepare a 1 mM solution of paraquat in DMEM containing 10% FBS and 2 mM glutamine.
2. Remove the medium from three wells and replace with 1 mL of the 1 mM paraquat solution.
3. Incubate for 24 h at 37 °C.
4. Remove the 24-well plate from the incubator and replace the medium of the three paraquat-treated wells and three untreated control wells (*see* **Note 24**).
5. Replace with 1 mL of the 10 μM MitoPY1 solution in DPBS.
6. Add MitoTracker Deep Red at a concentration of 25–100 nM (*see* **Note 20**).
7. After 30 min to allow dye uptake into cells (*see* **Note 21**), wash the cells with 2 × 1 mL DPBS (*see* **Note 22**).
8. Image the cells using a fluorescence microscope (*see* **Note 6**). Either a 488 nm or 510 nm excitation wavelength may be used, with a collection window between 527 and 580 nm. MitoTracker Deep Red can then be imaged using a 633 nm excitation wavelength with a collection window between 666 and 698 nm. Relative quantification of mitochondrial $H_2O_2$ can be evaluated by measuring the mean pixel intensity of the fluorescence images (*see* **Note 23**).

## 4 Notes

1. 2-(2,4-dihydroxybenzoyl) benzoic acid can be prepared by an adapted literature procedure. [17] Briefly, dissolve resorcinol (1.1 equiv.) and phthalic anhydride (1.0 equiv.) in 30 mL dry nitrobenzene per 1 g of phthalic anhydride under an inert atmosphere. Cool the reaction mixture to 0 °C and add aluminum(III) chloride (2.3 equiv.). The reaction mixture should turn dark green. Stir the suspension for 16 h and then pour into a rapidly stirring mixture of 2:1 hexanes–1 M HCl. Filter the precipitate. The solid can be recrystallized from methanol–water.
2. (4-Iodobutyl)triphenylphosphonium iodide can be prepared from a literature procedure. [18] Briefly, add 1,4-diodobutane (5 equiv.) to triphenylphosphine (1 equiv.) in a screw-top pressure flask. Cover the flask with aluminum foil to block out any light and heat at 100 °C for 1.5 h. After cooling to ambient temperature, wash the resulting yellow solid three times with diethyl ether. Dissolve the solids in a small amount of dichloromethane, and then add diethyl ether. A yellow solid should precipitate. Carefully decant the solvent by slowly pouring the liquid into another flask or gently pipetting the solvent without removing any solids. Repeat this process three times, combine all solids and remove any residual solvent under high vacuum. The synthesized (4-iodobutyl)triphenylphosphonium iodide should be used immediately or stored in the dark at −20 °C.
3. Given components are for HEK293T cells, but these can be adapted to other cell lines as needed.
4. A plate reader with fluorescence mode can also be used to validate the probes in vitro.
5. When using an inverted microscope, cells must be imaged through a thin layer of glass to minimize refraction. Cells can be grown in chamber slides (e.g., Nunc makes LabTek chambered cover glass with 1, 2, 4, or 8 wells) or in glass-bottomed multiwell plates (MatTek corporation supplies such plates). Alternatively, cells can be grown on sterile coverslips in plastic multiwell plates and mounted onto glass slides immediately before imaging. Experiments described here involve use of a 24-well glass-bottomed plate.
6. Imaging may be performed with an inverted or an upright fluorescence microscope. In addition, these dyes can be analyzed by flow cytometry. If an upright microscope is used, the cells should be grown on sterile coverslips. Twelve millimeter round coverslips fit easily into 24-well plates, so cells can be grown as described below (*see* **Note 15**). Immediately before

the imaging experiment, wash the cells with DPBS, pick up the coverslip with forceps, and transfer it to a 4 cm diameter Petri dish containing 2 mL phenol red-free DMEM and any dyes of interest. This Petri dish can be placed on the microscope stage, and the appropriate objective can be dipped into the medium.

7. The flask should have a recommended working pressure of at least 60 psi. These flasks are available from Chemglass (CG-1880-10). Ensure that there are no cracks or deformities in the glass and use a blast shield in case of explosion.
8. A silicone oil bath on a hotplate-stirrer equipped with temperature control can be used.
9. After the filtration, the crude product tends to turn into an oil, most likely due to residual TFA. Immediate dissolution into methanol followed by evaporation usually results in a solid product.
10. Schlenk tubes are available from Chemglass (AF-0537). The Schlenk tube should be predried in an oven for 4 h at 130 °C, and then attached to a Schlenk line using a gas inlet adapter. With the stopcock closed, open the flask to the high vacuum. Vacuum for 10–15 min and then fill with dry $N_2$ using the Schlenk line. Attach the stopcock side of the Schlenk tube to the $N_2$ line and begin a positive flow of $N_2$. Open the stopcock and replace the gas inlet adaptor with a septum. A round-bottomed flask equipped with a septum can alternatively be used in this step.
11. This operation is typically performed with a separatory funnel. Pour the reaction mixture into the separatory funnel. Next, add the water or other aqueous solution to the funnel. Shake the separatory funnel, being sure to release pressure at regular intervals by pointing the vent away from the face or body. The mixture will separate into two phases, with the water composing the bottom layer and the ethyl acetate composing the top layer. If the organic solvent used is dichloromethane, it will fall to the bottom layer because dichloromethane is denser than water. Remove the stopper, open the stopcock, and collect the desired layer.
12. Silica chromatography can be performed by the method of Still [37]. Add a small piece of cotton to a chromatography column and attach the tip to a house vacuum line. Push the cotton down with a wooden rod, using the house vacuum line to hold it in place if necessary. Add a small layer of sand (~1–2 cm), and then add silica gel (~15–25 cm, depending on the amount of material and width of the column). Tap gently to make a flat layer and then turn on the vacuum to pack the silica gel. Keep under house vacuum for 10–15 min. Add another layer of sand (~1–2 cm). Prepare eluent (~1 L) and then carefully pour into

the column with the vacuum on, being careful not to upset the silica bed. For best results the top of the silica layer should be flat. Close the stopcock and turn off the vacuum before any solvent enters the vacuum line. Remove the vacuum line and clean the column tip with acetone. Fill the column with eluent and then push through using air pressure. Allow the solvent to empty until just above the sand layer. Close the stopcock. Dissolve the crude product in the minimum amount of dichloromethane, or other low polarity solvent that dissolves the crude material, and then gently add it to the column using a pipette to drip it slowly down the side of the column. Open the stopcock and allow the crude product to be adsorbed to the top of the silica layer, washing with the minimum amount of eluent or dichloromethane. Once the product has been adsorbed, fill the reservoir with eluent and collect the eluent that comes off of the column into different test tubes. Analyze the test tubes using thin layer chromatography, and then combine and evaporate the fractions that contain the pure product.

13. The concentration of MitoPY1 can be confirmed by using the extinction coefficient of 14,200 $M^{-1}$ $cm^{-1}$ at 510 nm.
14. The evaporation can be accomplished by placing the tubes in a fume hood overnight; by blowing air or nitrogen gas over the tubes, taking care to avoid splashing; or by placing in a vacuum desiccator.
15. Cells should be maintained between 10% and 90% confluence in a 37 °C, 5% $CO_2$ tissue culture incubator. HEK293T cells typically double every 36 h, so maintaining exponential growth will require passage of the culture twice a week. Culture cells in a T75 culture flask. At 100% confluence, the flask will hold approximately $1 \times 10^7$ cells. All manipulations that expose cells should be performed in a sterile laminar flow hood. For passaging, remove the medium from the flask by aspirating or carefully decanting. Wash with 2 mL DPBS. Add 0.05% trypsin in DMEM at 37 °C and incubate for 2 min. After confirming that cells have detached from the plastic, add 10 mL DMEM and determine cell density using a hemocytometer. Pellet the cells at $500 \times g$ for 5 min, remove the supernatant by aspiration or decanting, and resuspend the cells in DMEM. These cells can then be added to new flasks containing medium. For propagating cells, seed $1 \times 10^6$ cells into 10 mL DMEM in a T75 culture flask.
16. Cells should be plated in phenol red-free medium to avoid fluorescence background from the media, and an appropriate cell number plated for 50–70% confluence on the day of imaging. 100% confluence in a 24-well plate corresponds to approximately $5 \times 10^5$ cells. Seeding $2 \times 10^5$ cells overnight will typically give an appropriate confluence. Use between 0.5 and 1.0 mL medium per well.

17. A number of mitochondrially localizing compounds disrupt mitochondrial function, causing cell death. It is therefore valuable to confirm cell viability upon treatment with MitoPY1 or similar cellular probes. Cell viability can be confirmed by a number of standard assays. Simple methods include counting of cell populations treated with trypan blue or propidium iodide, which only stain dead or dying cells. For more robust statistics, plate readers or flow cytometers enable collection of data from much larger numbers of cells. The colorimetric MTT or WST-1 assays can be performed in a multiwell plate and analyzed on a plate reader. Flow-cytometric methods include concurrent use of a live stain (such as Calcein AM) with a dead stain (such as propidium iodide).
18. Molecules that localize to the mitochondria can interact with the mitochondrial membrane, thus perturbing the membrane potential and hence overall mitochondrial function. Measurement of MMP in the presence of MitoPY1 can confirm that this sensor does not act in such a way. MMP can be measured by flow-cytometric assays that utilize two different mitochondrial dyes, such as in the method described by Pendergrass et al. [38].
19. For short-term experiments in robust cell lines, a laminar flow hood is usually not necessary. For longer-term experiments and/or sensitive cell lines, it is best to perform all cellular operations in a laminar flow hood with sterile solutions.
20. MitoTracker Deep Red is available from Life Technologies and should be used according to the manufacturer's instructions. This dye will confirm mitochondrial localization and serves as an important control.
21. Depending on the cell type, the optimal time for cellular uptake ranges from 15 to 40 min.
22. Wash cells by removing the medium and adding 1 mL of DPBS warmed to 37 °C, and repeating this step with an additional 1 mL of DPBS at 37 °C.
23. Mean fluorescence intensity is typically quantified in ImageJ (National Institutes of Health) by setting identical thresholds in both wells, such that the intracellular fluorescence in both images is selected. Other quantification methods can be used, but these should be clearly reported to ensure lab-to-lab reproducibility.
24. In general, it is best to have at least three biological replicates for every experiment to ensure reproducibility and significance.

## References


1. Desagher S, Martinou JC (2000) Mitochondria as the central control point of apoptosis. Trends Cell Biol 10:369–377
2. McBride HM, Neuspiel M, Wasiak S (2006) Mitochondria: more than just a powerhouse. Curr Biol 16:R551–R560
3. Ernstner L, Schatz G (1981) Mitochondria: a historical review. J Cell Biol 91:227s–255s
4. Yang K, Kolanowski JL, New EJ (2017) Mitochondrially targeted fluorescent redox sensors. Interface Focus 7:20160105
5. Petros JA, Baumann AK, Ruiz-Pesini E, Amin MB, Sun CQ, Hall J, Lim SD, Issa MM, Flanders WD, Hosseini SH, Marshall FF, Wallace DC (2005) mtDNA mutations increase tumorigenicity in prostate cancer. Proc Natl Acad Sci U S A 102:719–724
6. Fato R, Bergamini C, Leoni S, Strocchi P, Lenaz G (2008) Generation of reactive oxygen species by mitochondrial complex I: implications in neurodegeneration. Neurochem Res 33:2487–2501
7. Lenaz G, Bovina C, D'Aurelio M, Fato R, Formiggini G, Genova ML, Giuliano G, Pich MM, Paolucci U, Castelli GP, Ventura B (2002) Role of mitochondria in oxidative stress and aging. Ann N Y Acad Sci 959:199–213
8. Veal EA, Day AM, Morgan BA (2007) Hydrogen peroxide sensing and signaling. Mol Cell 26:1–14
9. Kolanowski JL, Kaur A, New EJ (2016) Selective and reversible approaches towards imaging redox signaling using small molecule probes. Antiox Redox Signal 24:713–730
10. New EJ (2016) Harnessing the potential of small molecule intracellular fluorescent sensors. ACS Sensors 1:328–333
11. Lippert AR, Van de Bittner GV, Chang CJ (2011) Boronate oxidation as a bioorthogonal reaction approach for studying the chemistry of hydrogen peroxide in living systems. Acc Chem Res 44:293–804
12. Chang MCY, Pralle A, Isacoff EY, Chang CJ (2004) A selective, cell-permeable optical probe for hydrogen peroxide in living cells. J Am Chem Soc 126:15392–15393
13. Miller EW, Albers AE, Pralle A, Isacoff EY, Chang CJ (2005) Boronate-based fluorescent probes for imaging cellular hydrogen peroxide. J Am Chem Soc 127:16652–16659
14. Dickinson BC, Huynh C, Chang CJ (2010) A palette of fluorescent probes with varying emission colors for imaging hydrogen peroxide signaling in living cells. J Am Chem Soc 132:5906–5915
15. Murphy MP, Smith RAJ (2007) Targeting antioxidants to mitochondria by conjugation to lipophilic cations. Annu Rev Pharmacol Toxicol 47:629–656
16. Ross MF, Kelso GF, Blaike FH, James AM, Cochemé HM, Filipovska A, Da Ros T, Hurd TR, Smith RAJ, Murphy MP (2005) Lipophilic triphenylphosphonium cations as tools in mitochondrial bioenergetics and free radical biology. Biochem Mosc 70:222–230
17. Dickinson BC, Chang CJ (2008) A targetable fluorescent probe for imaging hydrogen peroxide in the mitochondria of living cells. J Am Chem Soc 130:9638–9639
18. Dickinson BC, Lin VS, Chang CJ (2013) Preparation and use of MitoPY1 for imaging hydrogen peroxide in live cells. Nat Protoc 8:1249–1259
19. Pallichankandy S, Rahman A, Thayyullathil F, Galadari S (2015) ROS-dependent activation of autophagy is a critical mechanism for the induction of anti-glioma effect of sanguinarine. Free Radic Biol Med 89:708–720
20. Lin L, Li D, Alesi GN, Fan J, Kang H-B, Lu Z, Boggon TJ, Jin P, Yi H, Wright ER, Duong D, Seyfried NT, Egnatchik R, DeBerardinis RJ, Magliocca KR, He C, Arellano ML, Khoury HJ, Shin DM, Khuri FR, Kang S (2015) Glutamate dehydrogenase 1 signals through antioxidant glutathione peroxidase 1 to regulate redox homeostasis and tumor growth. Cancer Cell 27:257–270
21. Li B, Iglesias-Pedraz JM, Chen L-Y, Yin F, Cadenas E, Reddy S, Comai L (2014) Down-regulation of the Werner syndrome protein induces a metabolic shift that compromises redox homeostasis and limits proliferation of cancer cells. Aging Cell 13:367–378
22. Cao Y, Qiu T, Kathayat RS, Azizi S-A, Thorne AK, Ahn D, Fukata Y, Fukata M, Rice PA, Dickinson BC (2019) ABHD10 is an S-depalmitoylase affecting redox homeostasis through peroxiredoxin-5. Nat Chem Biol 15:1232–1240
23. Zlatic SA, Vrailas-Mortimer A, Gokhale A, Carey LJ, Scott E, Burch R, McCall MM, Rudin-Rush S, Bowen Davis J, Hartwig C, Wener E, Li L, Petris M, Faundez V (2018) Rare disease mechanisms identified by genealogical proteomics of copper homeostasis mutant pedigrees. Cell Systems 6:368–380
24. Sidlauskaite E, Gibson JW, Megson IL, Whitfield PD, Tovmasyan A, Batinic-Haberle I, Murphy MP, Moult PR, Cobley JN (2018) Mitochondrial ROS cause motor deficits

induced by synaptic inactivity: implications for synapse pruning. Redox Biol 16:344–351

25. Rodella U, Scorzerto M, Duregotti E, Negro S, Dickinson BC, Chang CJ, Yuki N, Rigoni M, Montecucco C (2016) An animal model of Miller fisher syndrome: mitochondrial hydrogen peroxide is produced by the autoimmune attack of nerve terminals and activates Schwann cells. Neurobiol Dis 96:95–104
26. Zhang Y-P, Zhang Y, Xiao Z-B, Zhang Y-B, Zhang J, Li Z-Q, Zhu Y-B (2018) CFTR prevents neuronal apoptosis following cerebral ischemia reperfusion via regulating mitochondrial oxidative stress. J Mol Med 96:611–620
27. Sanders LH, McCoy J, Hu X, Mastroberardino PG, Dickinson BC, Chang CJ, Chu CT, Van Houten B, Greenamyre JT (2014) Mitochondrial DNA damage: molecular marker of vulnerable nigral neurons in Parkinson's disease. Neurobiol Dis 70:214–223
28. Huang T-C, Chiu P-R, Chang W-T, Hsieh B-S, Huang Y-C, Cheng H-L, Huang L-W, Hu Y-C, Chang K-L (2018) Epirubicin induces apoptosis in osteoblasts through death-receptor and mitochondrial pathways. Apoptosis 23:226–236
29. Gray JE, Starmer J, Lin VS, Dickinson BC, Magnuson T (2013) Hydrogen peroxide and defective cholesterol efflux prevent in vitro fertilization by cryopreserved inbred mouse sperm. Biol Reprod 89(17):1–12
30. Pisarenko O, Shulzhenko V, Studneva I, Pelogeykina Y, Timoshin A, Anesia R, Valet P, Parini A, Kunduzova O (2015) Structural apelin analogues: mitochondrial ROS inhibition and cardiometabolic protection in myocardial ischaemia reperfusion injury. Brit J Pharmacol 172:2933–2945
31. Abuaita BH, Schultz TL, O'Riordan MX (2018) Mitochondria-derived vesicles deliver antimicrobial reactive oxygen species to control phagosome-localized *Staphylococcus aureus*. Cell Host Microbe 25:625–636
32. Tkachev V, Goodell S, Opipari AW, Hao L-Y, Franchi L, Glick GD, Ferrara JLM, Byersdorfer CA (2015) Programmed Death-1 controls T cell survival by regulating oxidative metabolism. J Immunol 194:5789–5800
33. Chabowski DS, Kadlec AO, Ait-Aissa K, Hockenberry JC, Pearson PJ, Beyer AM, Gutterman DD (2018) Lysophosphatidic acid acts on LPA1 receptor to increase H2O2 during flow-induced dilation in human adipose arterioles. Brit J Pharmacol 175:4266–4280
34. Beyer AM, Zinkevich N, Miller B, Liu Y, Wittenburg AL, Mitchell M, Galdieri R, Sorokin A, Gutterman DD (2017) Transition in the mechanism of flow-mediated dilation with aging and development of coronary artery disease. Basic Res Cardiol 12:5
35. Chang CJ, Nolan EM, Jaworski J, Okamoto KI, Hayashi Y, Sheng M, Lippard SJ (2004) ZP8, a neuronal zinc sensor with improved dynamic range; imaging zinc in hippocampal slices with two-photon microscopy. Inorg Chem 43:6774–6779
36. Lin TK, Hughes G, Muratovska A, Blaikie FH, Brookes PS, Darley-Usmar V, Smith RAJ, Murphy MP (2002) Specific modification of mitochondrial protein thiols in response to oxidative stress. J Biol Chem 277:17048–17056
37. Still WC, Kahn M, Mitra A (1978) Rapid chromatographic techniques for peparative separation with moderate resolution. J Org Chem 43:2923–2925
38. Pendergrass W, Wolf N, Poot M (2004) Efficacy of MitoTracker green™ and CMXrosamine to measure changes in mitochondrial membrane potentials in living cells and tissues. Cytometry A 61A:162–169

# Chapter 9

# Synthesis and Testing of Novel Isomeric Mitochondriotropic Derivatives of Resveratrol and Quercetin

**Lucia Biasutto, Andrea Mattarei, and Cristina Paradisi**

## Abstract

Resveratrol and quercetin are among the most studied plant polyphenols, and have many health-promoting actions. Strategies to accumulate them into mitochondria may be of therapeutic relevance, since these compounds are redox active and are well known to impact mitochondria and mitochondrial proteins. We report here the procedures to synthesize mitochondria-targeted resveratrol and quercetin derivatives; the synthetic strategies reported are however expected to be adaptable to other polyphenols with similar reactivity at the phenolic hydroxyls.

Mitochondrial targeting can be achieved by conjugation with triphenylphosphonium, a lipophilic cation; this was linked via a butyl spacer forming an ether bond with one of the phenolic oxygens. The first step toward the synthesis of all mitochondriotropic derivatives described in this work is the production of a regiospecific -(4-*O*-chlorobutyl) derivative. Triphenylphosphonium ($P^+Ph_3I^-$) is then introduced through two consecutive nucleophilic substitution steps: $-Cl \rightarrow -I \rightarrow -P^+Ph_3I^-$. Pure mono-substituted chlorobutyl regioisomers are obtained by purification from the reaction mixture in the case of resveratrol, while specific protection strategies are required for quercetin to favor alkylation of one specific hydroxyl.

Functionalization of the remaining hydroxyls can be exploited to modulate the physicochemical properties of the derivatives (i.e., water solubility, affinity for cell membranes); we report here synthetic protocols to obtain acetylated and methylated analogs.

A brief description of some methods to assess the accumulation of the derivatives in mitochondria is also given; the proposed techniques are the use of a $TPP^+$-selective electrode (with isolated rat liver mitochondria) and fluorescence microscopy (with cultured cells).

**Key words** Quercetin, Resveratrol, Mitochondria, Triphenylphosphonium, Regioselectivity

## 1 Introduction

Plant polyphenols are a large family of natural compounds with many potential benefits for health care [1–4]. Resveratrol and quercetin are among the most studied and interesting members of this family; at least in vitro, they show promising effects for the prevention and/or therapy of pathophysiological conditions ranging from aging to cancer [5–7]. Their effects are ascribed to their redox properties, but also to interaction with proteins [8–19].

Volkmar Weissig and Marvin Edeas (eds.), *Mitochondrial Medicine: Volume 1: Targeting Mitochondria*, Methods in Molecular Biology, vol. 2275, https://doi.org/10.1007/978-1-0716-1262-0_9,

When used at concentrations in the tens of μM range [17, 18, 20–23], quercetin and resveratrol were shown be cytotoxic on cultured cancer cells; these concentrations however are not expected to be reached in vivo, due to the low bioavailability and rapid metabolism of these natural compounds [24–30]. To overcome these problems, strategies to overcome low bioavailability and/or achieve high local concentrations of the active compound at specific sites of action have been developed [31–33].

Mitochondria are emerging as an ideal target for cancer therapy; they play a key role in fundamental cellular processes such as metabolism, $Ca^{2+}$ and redox signaling and apoptosis and, despite their altered bioenergetic and/or biosynthetic status, their functionality is maintained and is essential for cancer cells [34–36].

Both resveratrol and quercetin are well known to impact mitochondria and mitochondrial proteins (e.g., [14, 16, 20, 22, 23]), and act as anti- or prooxidants depending on concentration and circumstances [8, 9]. Their mitochondrial targeting turned out to be an effective way to reach higher local concentrations of the compounds, with a consequent potentiation of their effects [37–41]. Accumulation in these organelles was achieved through conjugation of the polyphenol kernel with a butyltriphenylphosphonium lipophilic cation, which allows permeation of the construct through biological membranes (thanks to the delocalization of the positive charge) and, most importantly, its accumulation in compartments held at more negative potentials, such as the mitochondrial matrix, in accordance to the Nernst's law [42–44].

The first step toward the synthesis of all our mitochondriotropic derivatives is the production of a regiospecific -(4-*O*-chlorobutyl) derivative. Chloride is then substituted by iodide, a better leaving group which is displaced in a second nucleophilic substitution by triphenylphosphine. This two-step procedure allows the use of milder reaction conditions; direct substitution $–Cl \rightarrow –P^{+}Ph_3I^{-}$ would require high reaction temperatures, with consequent risks of product decomposition.

Since the conjugation position may significantly affect the chemical and biological properties of the derivative [39, 41], strategies to achieve regioselective alkylation are described. Direct partial alkylation of resveratrol leads to a mixture of the two monosubstituted isomers (3- and 4′-), which can then be separated/purified by flash chromatography. On the other hand, synthesis of mono-alkylated quercetin isomers requires the adoption of protecting strategies to favor the reaction of a specific hydroxyl (Scheme 1). This avoids the formation of complex mixtures of mono- and di-substituted products, with consequent purification problems and low recovery yields. Conjugation at position 3 is achieved through a diphenylmethane ketal protection of the 3′- and 4′-OH of the catechol ring [45], which otherwise are the most reactive

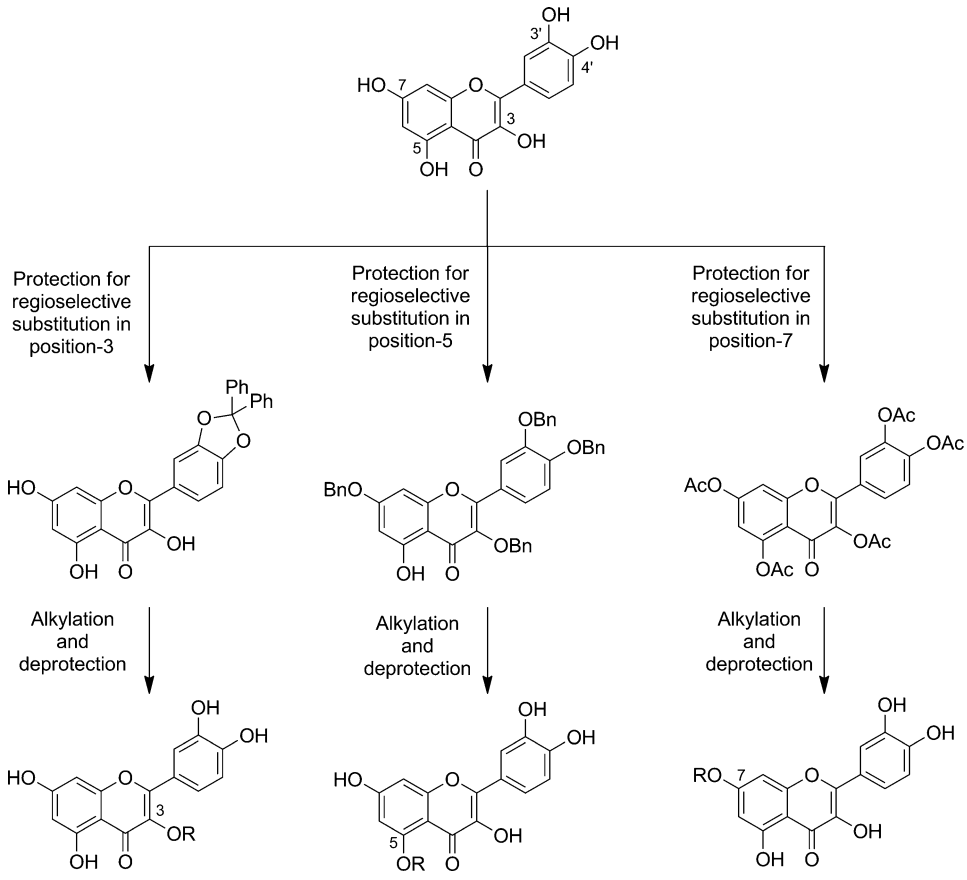


**Scheme 1** Protection strategies to allow regioselective monoalkylation of quercetin. *Ph* phenyl, *Bn* benzyl, *Ac* acetyl

[46]. Alkylation at position 5- of quercetin is performed exploiting the relative resistance of the 5-OH group toward benzylation when mild reaction conditions are used (3.5 equivalents of benzyl bromide and $K_2CO_3$, from 0 °C to room temperature over 2 h) [45]. The 5-OH group is indeed less acidic than the other quercetin phenolic functions, because of its involvement in an intramolecular H-bond with the 4-keto group of the quercetin backbone [47]. 3,3′,4′,7-tetrabenzyl quercetin is thus synthesized; it is then regioselectively alkylated in position-5 and debenzylated through a palladium hydroxide-catalyzed hydrogenation reaction, to afford 5-(4-*O*-chlorobutyl)quercetin. Functionalization of 7-OH can be achieved via imidazole-promoted regioselective deacetylation and alkylation of 3,3′,4′,5,7-pentaacetyl quercetin [39, 48]. Selective functionalization of 3′- and 4′-OH was not considered, since the catechol moiety on the C-ring is known to be largely responsible of the redox properties of the molecule [49], and it was also reported to be essential for interaction of quercetin with target proteins [11, 50].

The physicochemical properties of mitochondriotropic derivatives can be further modulated by functionalization of the remaining hydroxyls in the molecule; synthetic strategies to produce acetylated and methylated analogs are presented here. Acetylation or methylation is usually performed on the -(4-*O*-chlorobutyl) derivative; if the -(4-*O*-iodobutyl)-derivative is used, reaction yields are lower because of side reactions (i.e., dimerization) due to the higher electrophilicity of alkyl iodides compared to chlorides. Also acetylation/methylation of the -(4-*O*-triphenylphosphoniumbutyl) derivative is not recommended, because of purification problems.

Two methods are finally proposed to assess mitochondrial accumulation of the derivatives. A $TPP^+$-selective electrode can be used; uptake and release of the mitochondriotropic derivative by isolated rat liver mitochondria is associated to a decrease or increase in its concentration in the incubation medium, respectively (associated with a deflection of the electrode readout). In the second approach, the (weak) fluorescence of mitochondriotropic derivatives is exploited to monitor their accumulation in in situ mitochondria, using fluorescence microscopy and cultured cells; a $\Psi_m$-dependent fluorescence increase and decrease is observed upon mitochondrial accumulation of the compound and uncoupling, respectively.

## 2 Materials

### 2.1 Synthesis of Resveratrol and Quercetin Derivatives

1. Chemicals and solvents of laboratory grade, used as received, without further purification.
2. Thin layer chromatography equipment (TLC): silica gel supported on plastic (Macherey-Nagel Polygram®SIL G/UV254, silica thickness 0.2 mm), or silica gel supported on glass (Fluka) (silica thickness 0.25 mm, granulometry 60 Å, medium porosity), Spectroline® E-Series UV lamp, glass containers.
3. Flash chromatography equipment: glass column (5 mm ÷ 50 mm diameter, 80 ÷ 120 cm length) with reductions, silica gel (Macherey-Nagel 60, 230–400 mesh granulometry (0.063–0.040 mm)), air pressure line.

### 2.2 Assessment of Accumulation into Mitochondria—$TPP^+$-Selective Electrode with Isolated Rat Liver Mitochondria

1. Isolated rat liver mitochondria, prepared as described in [51].
2. $TPP^+$-selective electrode, prepared as described in [51]. A calomel electrode is used as reference.
3. Assay medium: 200 mM sucrose, 10 mM HEPES, 5 mM succinate, 1 mM $NaH_2PO_4$, 1.25 μM rotenone, pH 7.4 (adjusted with KOH).

### 2.3 Assessment of Accumulation into Mitochondria—and Cultured Cells

1. Human colon carcinoma cell line HCT116 or human hepatocarcinoma cell line HepG2.
2. High glucose DMEM (Dulbecco's Modified Eagle Medium) cell culture medium, supplemented with 10% FBS (fetal bovine serum), 10 mM HEPES, 100 U/mL penicillin G, 0.1 mg/mL streptomycin, 2 mM glutamine, 1.5 g/L sodium pyruvate and 1% nonessential amino acids.
3. HBSS: 136.9 mM NaCl, 5.36 mM KCl, 1.26 mM $CaCl_2$, 0.81 mM $MgSO_4$, 0.44 mM $KH_2PO_4$, 0.34 mM $Na_2HPO_4$, 5.55 mM Glucose, pH 7.4 (with NaOH).
4. Round coverslips (24 mm diameter).
5. Fluorescence microscope supplied with a 40× objective.

## 3 Methods

Synthetic protocols to obtain specific regioisomeric derivatives of resveratrol or quercetin include some general procedures, which are given at the beginning of this Section. We then proceed and describe the specific procedures to obtain each derivative.

### 3.1 General Procedure—Alkylation of One Hydroxyl Function to Produce a -(4-O-Chlorobutyl) Derivative

The described procedure is summarized in Scheme 2.

1. Dissolve resveratrol or protected quercetin (9.0 mmol, 1.0 eq.) in 30 mL dimethylformamide (DMF).
2. Add 1.4 g of $K_2CO_3$ (9.9 mmol, 1.1 eq.) and 2.31 g of 1-bromo-4-chlorobutane (13.5 mmol, 1.5 eq.) under argon, and stir overnight at room temperature.
3. Dilute the mixture in 100 mL ethyl acetate, transfer the solution into a separating funnel and wash three times with 50 mL of 1 N HCl, discharging the aqueous (bottom) layer after each wash.
4. Collect the organic layer, dry it adding anhydrous $MgSO_4$ (about 5 g) and filter the solution with filter paper.
5. Evaporate the solvent under reduced pressure.
6. Purify the product(s) by flash chromatography.

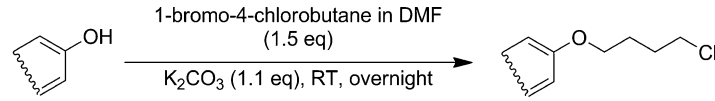


**Scheme 2** Alkylation of one hydroxyl function to produce a -(4-*O*-chlorobutyl) derivative (General procedure Subheading 3.1)

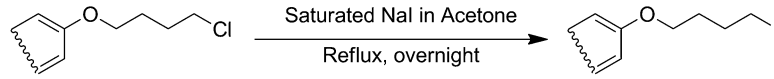


**Scheme 3** –Cl → –I nucleophilic substitution to produce a -(4-*O*-iodobutyl) derivative (General procedure Subheading 3.2)

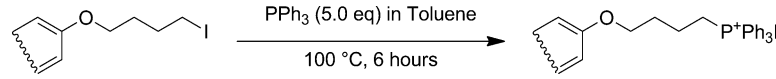


**Scheme 4** –I → $–P^{+}Ph_3I^{-}$ nucleophilic substitution to produce a -(4-*O*-triphenylphosphoniumbutyl) derivative (General procedure Subheading 3.3). *$PPh_3$* triphenylphosphine

### *3.2 General Procedure: –Cl → –I Nucleophilic Substitution to Produce a -(4-O-Iodobutyl) Derivative*

The described procedure is summarized in Scheme 3.

1. Prepare a saturated solution of NaI (about 6 g) in 20 mL of acetone (*see* **Notes 1** and **2**).
2. Dissolve the -(4-*O*-chlorobutyl) derivative (1.5 mmol, 1.0 eq.) into the NaI saturated solution, and heat at reflux overnight.
3. After cooling, dilute the resulting mixture in 100 mL ethyl acetate and filter it using a paper filter. Rinse the solid with 50 mL ethyl acetate and transfer the combined ethyl acetate–acetone solution into a separating funnel.
4. Wash three times with 30 mL of water.
5. Collect the organic layer, dry it adding anhydrous $MgSO_4$ (about 5 g) and then remove the solid by paper filtration.
6. Evaporate the solvent under reduced pressure.
7. Purify the product by flash chromatography (*see* **Note 3**).

### *3.3 General Procedure: –I → $–P^{+}Ph_3I^{-}$ Nucleophilic Substitution to Produce the -(4-O-Triphenylphosphoniumbutyl) Derivative*

The described procedure is summarized in Scheme 4.

1. Dissolve the -(4-*O*-iodobutyl) derivative (1.5 mmol, 1.0 eq.) and 2.0 g of triphenylphosphine (7.5 mmol, 5.0 eq.) in toluene (25 mL).
2. Heat at 100 °C under argon, for 6 h. Follow the reaction course by thin layer chromatography, which shows disappearance of the reactant (the iodide) and the formation of a spot with Rf = 0 corresponding to the triphenylphosphonium derivative.
3. Evaporate the solvent under reduced pressure.
4. Dissolve the resulting solid in the minimum volume (about 3 mL) of acetone (or dichloromethane in the case of acetylated or methylated derivatives).
5. Precipitate the product adding diethyl ether (100 mL).

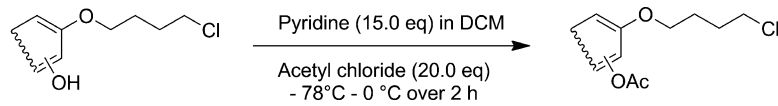


**Scheme 5** Acetylation of -(4-*O*-chlorobutyl) derivatives (General procedure Subheading 3.4). *DCM* dichloromethane

6. Decant the solvent.
7. Repeat **steps 5** and **6** four more times (*see* **Note 4**).
8. Filter the precipitate with paper and desiccate under vacuum (*see* **Note 5**).

### 3.4 General Procedure—acetylation of -(4-O-Chlorobutyl) Derivatives

Acetylated analogs can be synthesized applying this general procedure to 4′-(4-*O*-chlorobutyl) resveratrol and 3-(4-*O*-chlorobutyl) resveratrol (respectively, **R2** and **R3** in Scheme 7), to 3-(4-*O*-chlorobutyl) quercetin (**Q4** in Scheme 8) and to 5-(4-*O*-chlorobutyl) quercetin (**Q15** in Scheme 9). 3,3′,4′,5-tetraacetyl-7-(4-O-chlorobutyl) quercetin (**Q25** in Scheme 10) is directly obtained during the regioselective deacetylation-alkylation of 3,3′,4′,5,7-pentaacetyl quercetin (**Q24** in Scheme 10). The described procedure is summarized in Scheme 5.

1. Prepare a solution of the -(4-*O*-chlorobutyl) derivative (1.0 mmol, 1.0 eq.) and anhydrous pyridine (1.2 g, 15.0 mmol, 15.0 eq.) in dichloromethane (25 mL).
2. Cool the mixture in a dry ice–acetone bath (−78 °C).
3. Add dropwise and under continuous stirring a solution of acetyl chloride (20.0 mmol, 20.0 eq.) in dichloromethane (20 mL) (*see* **Note 6**).
4. Allow the reaction mixture to warm up to room temperature over 2 h.
5. Add dichloromethane (50 mL) and wash the organic phase three times with 1 N HCl (50 mL).
6. Dry over anhydrous $MgSO_4$ (about 5 g) and remove the solid by paper filtration.
7. Evaporate the solvent under reduced pressure.
8. Purify the residue by flash chromatography.

### 3.5 General Procedure—Methylation of -(4-O-Chlorobutyl) Derivatives

Methylated analogs can be synthesized applying this general procedure to 4′-(4-*O*-chlorobutyl) resveratrol and 3-(4-*O*-chlorobutyl) resveratrol (respectively, **R2** and **R3** in Scheme 7), to 3-(4-*O*-chlorobutyl) quercetin (**Q4** in Scheme 8), to 5-(4-*O*-chlorobutyl) quercetin (**Q15** in Scheme 9) and to 7-(4-*O*-chlorobutyl) quercetin (**Q26** in Scheme 10). The described procedure is summarized in Scheme 6.

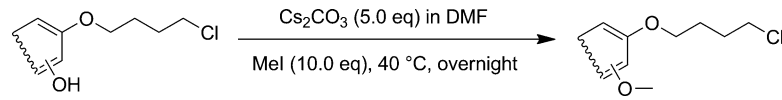


**Scheme 6** Methylation of -(4-*O*-chlorobutyl) derivatives (General procedure Subheading 3.5). *MeI* iodomethane, *DMF* dimethylformamide

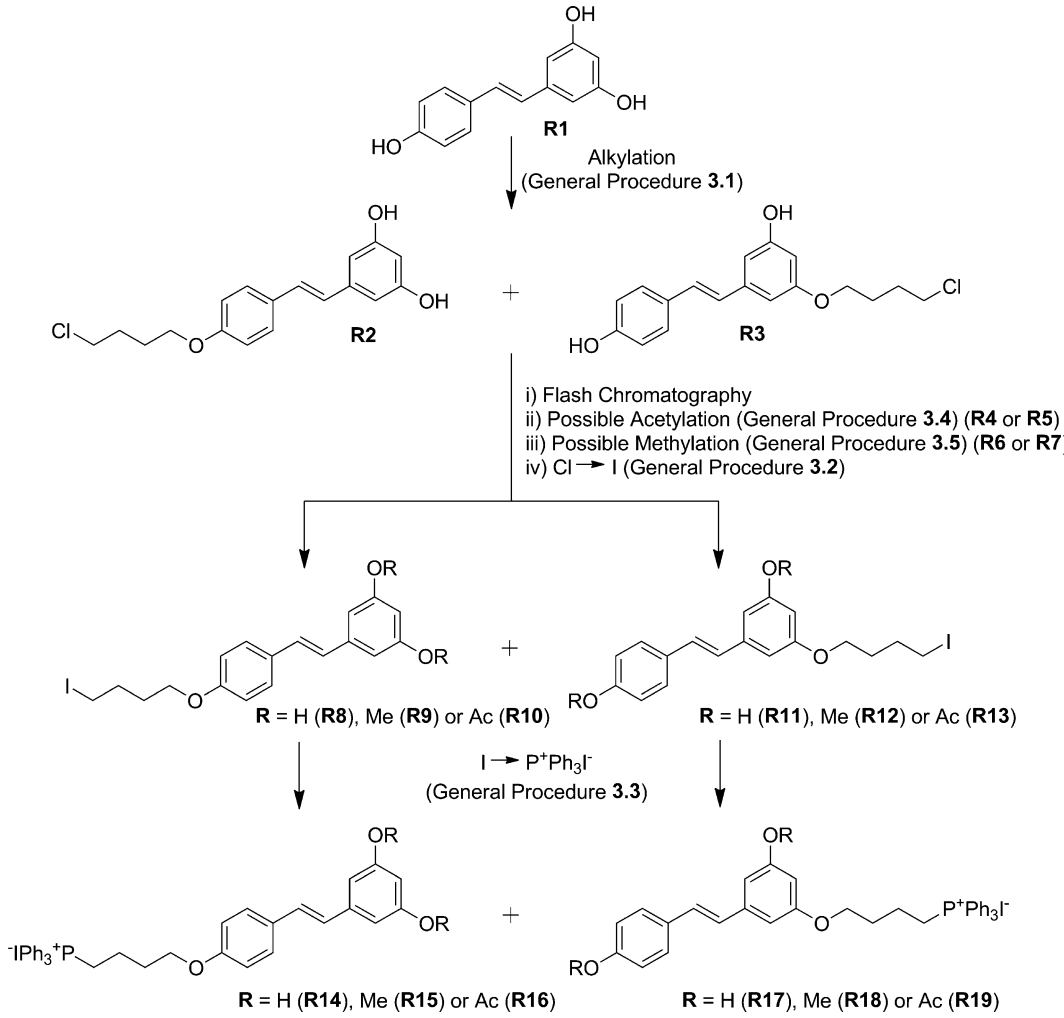


**Scheme 7** Synthesis of 4′-(4-*O*-triphenylphosphoniumbutyl) resveratrol and 3-(4-*O*-triphenylphosphoniumbutyl) resveratrol (Subheading 3.6). *Me* methyl, *Ac* acetyl

1. Dissolve the -(4-*O*-chlorobutyl) derivative (0.5 mmol, 1.0 eq.) in dimethylformamide (20 mL).
2. Add $Cs_2CO_3$ (0.8 g, 2.5 mmol, 5.0 eq.) and iodomethane (0.7 g, 5.0 mmol, 10.0 eq.) under nitrogen, and stir overnight at 40 °C.

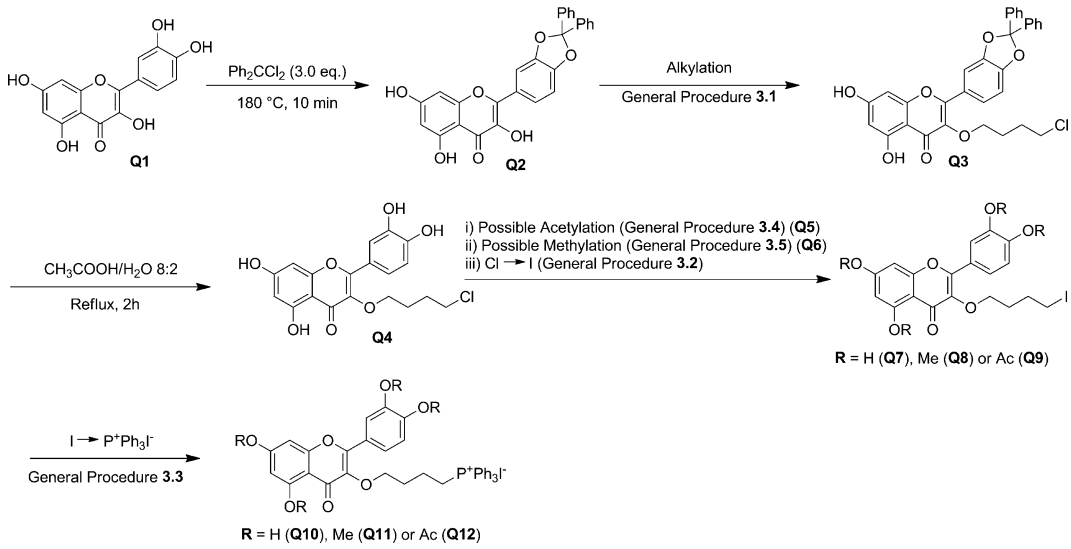


**Scheme 8** Synthesis of 3-(4-*O*-triphenylphosphoniumbutyl) quercetin (Subheading 3.7). *$Ph_2CCl_2$* dichlorodiphenylmethane, *Ph* phenyl, *Me* methyl, *Ac* acetyl

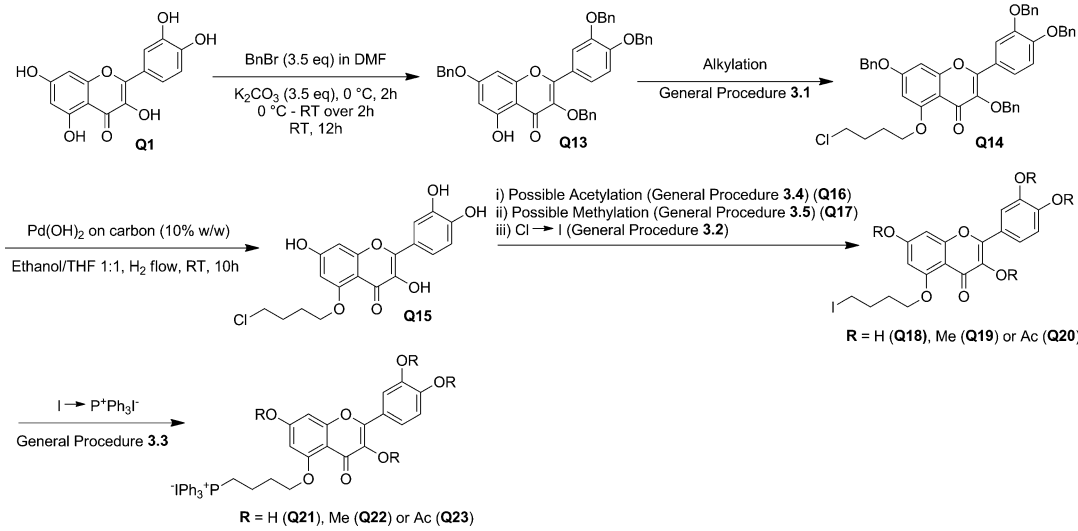


**Scheme 9** Synthesis of 5-(4-*O*-triphenylphosphoniumbutyl) quercetin (Subheading 3.8). *BnBr* benzyl bromide, *DMF* dimethylformamide, *Bn* benzyl, *Me* methyl, *Ac* acetyl

3. Dilute the mixture in dichloromethane (100 mL) and wash three times with 1 N HCl (50 mL).
4. Dry the organic layer over $MgSO_4$ (about 5 g) and remove the solid by paper filtration.
5. Evaporate the solvent under reduced pressure.
6. Purify the residue by flash chromatography.

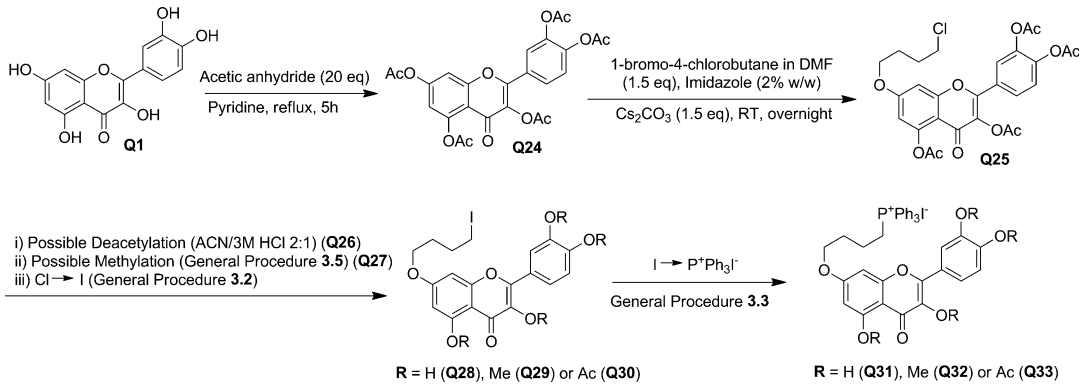


**Scheme 10** Synthesis of 7-(4-*O*-triphenylphosphoniumbutyl) quercetin (Subheading 3.9). *DMF* dimethylformamide, *Me* methyl, *Ac* acetyl

### *3.6 Synthesis of 4′-(4-O-Triphenyl phosphoniumbutyl) Resveratrol and 3-(4-O-Triphenyl phosphoniumbutyl) Resveratrol*

The described procedure is summarized in Scheme 7.

1. Carry out general procedure Subheading 3.1, using resveratrol (**R1**) as starting reagent (*see* **Note 7**). Purify the products (4′-(4-*O*-chlorobutyl) resveratrol (**R2**) and 3-(4-*O*-chlorobutyl) resveratrol (**R3**)) by flash chromatography using dichloromethane–ethyl acetate 9:1 as eluent (*see* **Notes 8** and **9**).
2. Carry out general procedure Subheading 3.2, using 4′-(4-*O*-chlorobutyl) resveratrol (**R2**) and 3-(4-*O*-chlorobutyl) resveratrol (**R3**) as starting reagent. Purify the product (4′- or 3-(4-*O*-iodobutyl) resveratrol, **R8** or **R11**) by flash chromatography using dichloromethane–ethyl acetate 9:1 as eluent (*see* **Note 10**).
3. Carry out general procedure Subheading 3.3, using 4′-(4-*O*-iodobutyl) resveratrol (**R8**) or 3-(4-*O*-iodobutyl) resveratrol (**R11**) as starting reagent (*see* **Note 11**).

### *3.7 Synthesis of 3-(4-O-Triphenyl phosphoniumbutyl) Quercetin*

The described procedure is summarized in Scheme 8.

1. Dissolve 3.0 g of quercetin dihydrate (**Q1**) (8.9 mmol, 1.0 eq.) in 5.1 mL dichlorodiphenylmethane (27.0 mmol, 3.0 eq.).
2. Mix thoroughly, then heat and stir at 180 °C for 10 min (*see* **Notes 12** and **13**).
3. Cool the reaction mixture in ice/water (*see* **Note 14**).
4. Dilute in 15 mL of dichloromethane and sonicate (*see* **Notes 15** and **16**).
5. Purify the reaction product (3′,4′-*O*-diphenylmethane quercetin, **Q2**) by flash chromatography using dichloromethane–ethyl acetate 95:5 as eluent (*see* **Note 17**).
6. Carry out general procedure Subheading 3.1 (*see* **Note 18**). Purify 3′,4′-*O*-diphenylmethane-3-(4-*O*-chlorobutyl) quercetin (**Q3**) by flash chromatography using ethyl acetate–hexane 3:7 as eluent.

7. Dissolve 1.0 g of 3′,4′-*O*-diphenylmethan-3-(4-*O*-chlorobutyl) quercetin (**Q3**) (1.80 mmol, 1 eq.) into a mixture of acetic acid/water 8:2 (50 mL).
8. Heat the solution at reflux for 2 h (*see* **Note 19**).
9. Add 200 mL of ethyl acetate and pour the mixture into a separating funnel.
10. Add a saturated solution of $NaHCO_3$ in water until all the acetic acid is neutralized (about 200 mL) (*see* **Note 20**).
11. Collect the organic layer and wash with 100 mL of a $NaHCO_3$-saturated aqueous solution.
12. Dry the organic phase adding anhydrous $MgSO_4$ (about 5 g) and filter the solution with filter paper.
13. Evaporate the solvent under reduced pressure and purify the derivative (3-(4-*O*-chlorobutyl) quercetin, **Q4**) by flash chromatography using chloroform–acetone 8:2 as solvent (*see* **Note 21**).
14. Carry out general procedure Subheading 3.2. Purify the -(4-*O*-iodobutyl) derivative (**Q7**) by flash chromatography using chloroform–acetone 8:2 as solvent (*see* **Note 22**).
15. Carry out general procedure Subheading 3.3 to obtain 3-(4-*O*-triphenylphosphoniumbutyl) quercetin (**Q10**) (*see* **Note 23**).

### *3.8 Synthesis of 5-(4-O-Triphenyl phosphoniumbutyl) Quercetin*

The described procedure is summarized in Scheme 9.

1. Dissolve 1.0 g of quercetin dihydrate (**Q1**) (3.00 mmol, 1.0 eq.), 1.43 g of $K_2CO_3$ (10.4 mmol, 3.5 eq.) and 1.24 mL of benzyl bromide (10.4 mmol, 3.5 eq.) in 20 mL of dimethylformamide at 0 °C.
2. Stir vigorously at 0 °C for 2 h.
3. Allow the reaction mixture warm to room temperature over 2 h and maintain the stirring for 12 h (*see* **Note 24**).
4. Dilute the resulting mixture in 100 mL of ethyl acetate and wash the organic phase three times with 1 N HCl (50 mL).
5. Dry the organic phase adding anhydrous $MgSO_4$ (about 5 g) and filter the solution with filter paper.
6. Evaporate the solvent under reduced pressure.
7. Purify 3,3′,4′,7-tetrabenzyl quercetin (**Q13**) by flash chromatography using toluene–ethyl acetate 9:1 as eluent (*see* **Note 25**).
8. Carry out general procedure Subheading 3.1. Purify the reaction product (3,3′,4′,7-tetrabenzyl-5-(4-*O*-chlorobutyl) quercetin, **Q14**) by flash chromatography using toluene–ethyl acetate 9:1 as eluent (*see* **Note 26**).

9. Dissolve 0.5 g of 3,3′,4′,7-tetrabenzyl-5-(4-*O*-chlorobutyl) quercetin (**Q14**) (0.66 mmol, 1.0 eq.) into a mixture of ethanol and tetrahydrofuran 1:1 (60 mL).
10. Add palladium hydroxide on carbon (50 mg, 10% w/w) at room temperature and stir for 10 h under a flow of hydrogen (*see* **Notes 27** and **28**).
11. Filter the reaction mixture on Celite® and wash with ethanol (30 mL).
12. Concentrate the filtrate under vacuum and purify 5-(4-*O*-chlorobutyl) quercetin) (**Q15**) by flash chromatography using toluene–methanol 9:1 as eluent (*see* **Note 29**).
13. Carry out general procedure Subheading 3.2. Purify 5-(4-*O*-iodobutyl) quercetin (**Q18**)) by flash chromatography using chloroform–acetone 8:2 as solvent (*see* **Note 30**).
14. Carry out general procedure Subheading 3.3 to obtain 5-(4-*O*-triphenylphosphoniumbutyl) quercetin (**Q21**) (*see* **Note 31**).

### *3.9 Synthesis of 7-(4-O-Triphenyl phosphoniumbutyl) Quercetin*

The described procedure is summarized in Scheme 10.

1. Mix quercetin dihydrate (**Q1**) (1.0 g, 3.00 mmol, 1.0 eq.), acetic anhydride (6.13 g, 60.0 mmol, 20 eq.) and pyridine (15 mL).
2. Heat to reflux and stir for 5 h.
3. Add ice-water (50 g) to the warm mixture.
4. Filter the resulting precipitate and transfer it to a round-bottom flask.
5. Add to the precipitate 50 mL of ethanol and heat to reflux the suspension. Dissolve all the precipitate by adding small portions (5 mL each) of ethanol to the solution at reflux.
6. Cool slowly (over 3 h) the solution to room temperature, then in ice/water.
7. Filter the resulting precipitate (3,3′,4′,5,7-pentaacetyl quercetin [35]), wash with cold ethanol (50 mL).
8. Desiccate under vacuum.
9. Dissolve 3,3′,4′,5,7-pentaacetyl quercetin (**Q24**) (1.50 g, 2.9 mmol, 1.0 eq.) in 30 mL of dimethylformamide.
10. Add 1.43 g of $Cs_2CO_3$ (4.4 mmol, 1.5 eq.), 1.51 g of 1-bromo-4-chlorobutane (8.8 mmol, 3.0 eq.) and 30 mg of imidazole (2% w/w with respect to **Q24**) under argon, and stir for 48 h (*see* **Note 32**).
11. Dilute the mixture in 150 mL ethyl acetate, pour the solution into a separating funnel and wash three times with 100 mL of 0.5 N HCl, discharging the aqueous (bottom) layer after each wash.

12. Collect the organic layer, dry it with anhydrous $MgSO_4$ (about 5 g) and filter with filter paper.
13. Evaporate the solvent under reduced pressure.
14. Purify 3,3′,4′,5-tetraacetyl-7-(4-*O*-chlorobutyl) quercetin (**Q25**) by flash chromatography using dichloromethane–ethyl acetate–hexane 8:2:2 as eluent (*see* **Notes 33** and **34**).
15. Add 3,3′,4′,5-tetraacetyl-7-(4-*O*-chlorobutyl)quercetin (**Q25**) (0.5 g, 0.9 mmol) to a mixture of acetonitrile (60 mL) and 3 M aq. HCl (30 mL).
16. Stir the resulting solution at reflux for 1 h (*see* **Note 35**).
17. Add cold water (200 mL) and ethyl acetate (200 mL).
18. Pour the solution into a separating funnel and wash three times with 100 mL of 0.5 N HCl, discharging the aqueous (bottom) layer after each wash.
19. Collect the organic layer, dry it adding anhydrous $MgSO_4$ (about 5 g) and filter the solution with filter paper.
20. Evaporate the solvent under reduced pressure.
21. Purify 7-(4-*O*-chlorobutyl)quercetin (**Q26**) by flash chromatography using toluene–methanol, 8:2 as eluent (*see* **Note 36**).
22. Carry out general procedure Subheading 3.2. Purify 7-(4-*O*-iodobutyl)quercetin (**Q28**) by flash chromatography using toluene–methanol 8:2 as solvent (*see* **Note 37**).
23. Carry out general procedure Subheading 3.3 to obtain 7-(4-*O*-triphenylphosphoniumbutyl)quercetin (**Q31**) (*see* **Note 38**).

### 3.10 Assessment of Accumulation into Mitochondria—$TPP^+$-Selective Electrode with Isolated Rat Liver Mitochondria

The uptake of mitochondriotropic derivatives by isolated rat liver mitochondria (RLM) can be followed using a $TPP^+$-selective electrode. Uptake of the derivative by RLM can be monitored as a decrease in concentration of the derivative in the assay solution. On the other hand, dissipation of the mitochondrial potential by an uncoupler (e.g., FCCP) or by the onset of the permeability transition (induced by $Ca^{2+}$ in the presence of Pi) causes the release of the derivative from the mitochondrial matrix, with a consequent increase of its concentration in the assay medium.

1. Fill the water-jacketed cell (thermostatted at 20 °C) with medium; maintain the solution under magnetic stirring.
2. At typically 2–3 min intervals (depending on the response speed of the specific electrode), add 2–3 aliquots of the derivative to the medium (typically 0.2 μM final concentration each), waiting for the instrumental readout to stabilize after each addition (*see* **Note 39**).
3. Add RLM (1 mg protein/mL).
4. Add 40 μM $CaCl_2$ or 1 μM FCCP or another uncoupler (e.g., dinitrophenol, 20 μM) to depolarize mitochondria.

### 3.11 Assessment of Accumulation into Mitochondria—with Cultured Cells

The weak fluorescence of mitochondriotropic resveratrol and quercetin derivatives can be exploited to follow their accumulation into the mitochondria of cultured cells (*see* **Note 40**).

1. Plate the cells onto 24-mm glass coverslips, in 6-well plates.
2. Allow cells to grow for 2 days in DMEM at 37 °C, in a humidified atmosphere of 5% $CO_2$.
3. Mount the coverslips onto microscope holders.
4. Wash twice with warm HBSS.
5. Cover the cells with 1 mL DMEM without FBS and phenol red, supplemented with 2 μM Cyclosporin A.
6. Place the cells on the microscope stage.
7. Acquire images at 1–2 min intervals, exciting at 340 nm and collecting fluorescence at $\lambda > 400$ nm.
8. After 5–10 min, carefully withdraw 0.5 mL of the incubation medium, add the desired derivative (1–10 μM final concentration), mix and add the solution back on the cells, at a peripheral point.
9. 30–90 min after addition of the derivative, carefully withdraw 0.5 mL of the incubation medium, add FCCP (1 μM final concentration), mix and add the solution back on the cells, at a peripheral point of the coverslip. This procedure insures adequate mixing.

## 4 Notes

1. The Finkelstein reaction is a one-step nucleophilic substitution reaction ($S_N2$) where an alkyl chloride is converted to an alkyl iodide using sodium iodide as source of iodide anion and dry acetone as solvent. The driving force of this reaction is the production of NaCl, which is nearly insoluble in acetone ($4.2 \times 10^{-4}$ g/kg acetone) compared to the reactant NaI (280 g/kg acetone) [52]. This is also experimentally observable during the reaction's progression as the formation of a white precipitate (NaCl) in acetone.
2. NaI is added to a solution of acetone in small aliquots (about 100 mg) stirring for 1 min after each addition. The saturated solution is obtained when a white precipitate is appreciable at the bottom of the flask after stirring for 5 min. The solution is used without filtering.
3. The Finkelstein reaction is almost quantitative. Only one spot is observed by thin layer chromatography, but purification is recommended in order to eliminate traces of inorganic salts.

4. To minimize product loss, the procedure can be performed in 50 mL centrifuge tubes, and a brief centrifugation step can be introduced before solvent removal to allow better separation of the precipitated product from the solvent.
5. -(4-*O*-triphenylphosphoniumbutyl) derivatives are usually characterized by $^{1}$H-NMR, $^{13}$C-NMR and LC/MS. $CDCl_3$ or DMSO-$d_6$ are good solvents to dissolve the products for NMR analysis. When performing HPLC-UV and/or LC/MS, a reverse phase C18 column with end-capped silica is required to minimize the amount of free silanols in the column, which otherwise can interact with the positively charged derivatives, causing drastic peak tailing [53, 54].
6. A white precipitate (pyridinium chloride) is generated immediately.
7. Follow the reaction course by thin layer chromatography using dichloromethane–ethyl acetate 9:1 as eluent. Progression of the reaction is associated with disappearance of the spot corresponding to resveratrol and the appearance of two new spots, respectively 4′-(4-*O*-chlorobutyl) resveratrol (**R2**, Rf: 0.34) and 3-(4-*O*-chlorobutyl) resveratrol (**R3**, Rf: 0.47).
8. When 2 g of resveratrol are used as starting material, a 30 × 350 mm glass column filled with silica gel (230–400 mesh) using dichloromethane–ethyl acetate 9:1 as eluent allows the efficient purification of the two resveratrol isomers. Expected reaction yield is about 30% for the 4′-substituted isomer (**R2**) and 15% for the 3-substituted isomer (**R3**).
9. From this point, 3- and 4′-substituted isomers are processed independently.
10. Follow the reaction course by thin layer chromatography using dichloromethane–ethyl acetate 9:1 as eluent. TLC will show the formation of just one spot/product, respectively 4′-(4-*O*-iodobutyl) resveratrol (Rf: 0.38) or 3-(4-*O*-iodobutyl) resveratrol (Rf: 0.51). 90% expected yield.
11. Follow the reaction course by thin layer chromatography using dichloromethane–ethyl acetate 9:1 as eluent. Progression of the reaction is associated with disappearance of the starting reactant, respectively 4′-(4-*O*-iodobutyl) resveratrol (**R8**) or 3-(4-*O*-iodobutyl) resveratrol (**R11**) and the formation of a product spot with Rf: 0. 75% expected reaction yield.
12. The protection of the catechol moiety under neat conditions (no solvent). The reaction yield is strongly affected by the proper mixing of quercetin dihydrate and dichlorodiphenylmethane; for this reason, before heating to 180 °C the reaction mixture is sonicated and stirred until it appears as an homogeneous suspension.

13. The reaction generates hydrochloric acid; therefore, it is highly recommended to vent the reaction with argon to a bubbler/trap filled with aqueous base (e.g., 1 N NaOH) to quench escaping gaseous products.
14. After 10 min at 180 °C, the reaction flask is cooled in ice/water solution to avoid possible side reactions of substitution and/or dimerization that can lower the reaction yield.
15. A suspension is formed, which is loaded directly into the chromatography column.
16. Follow the reaction course by thin layer chromatography using dichloromethane–ethyl acetate 95:5 as eluent; many spots will be present, due to alkylation at different positions of the quercetin backbone. The desired catechol-protected quercetin intermediate (**Q2**) is the largest yellow spot with Rf: 0.52.
17. When 3 g of quercetin dihydrate are used as starting material, a 50 × 350 mm glass column filled with silica gel (230–400 mesh) using dichloromethane–ethyl acetate 95:5 as eluent allows the efficient purification of the desired product from the reaction mixture. 70% expected yield.
18. Follow the reaction course by thin layer chromatography using ethyl acetate–hexane 3:7 as eluent. TLC will show the formation of two spots: the desired compound, 3′,4′-*O*-diphenylmethane-3-(4-*O*-chlorobutyl) quercetin (**Q3**, Rf: 0.43) and the disubstituted derivative 3′,4′-*O*-diphenylmethane-3,7-(4-*O*-chlorobutyl) quercetin (Rf: 0.76). 45% expected yield.
19. Follow the reaction course by thin layer chromatography using chloroform–acetone 8:2 as eluent. TLC will show the formation of one spot, the desired derivative, 3-(4-*O*-chlorobutyl) quercetin (**Q4**, Rf: 0.30) and the progressive disappearance of the catechol-protected reagent 3′,4′-*O*-diphenylmethane-3-(4-*O*-chlorobutyl) quercetin (**Q3**, Rf: 0.78).
20. Neutralization is complete when no more carbon dioxide evolves from the solution.
21. 80% expected yield.
22. Follow the reaction course by thin layer chromatography using chloroform–acetone 8:2 as eluent. TLC will show the formation of just one spot/product (3-(4-*O*-iodobutyl) quercetin, **Q7**, Rf = 0.32.) 90% expected yield.
23. 70% expected yield.
24. Follow the reaction course by thin layer chromatography using toluene–ethyl acetate 9:1 as eluent. TLC will show the formation of two spots: the desired compound (3,3′,4′,7-tetrabenzyl quercetin, **Q13**, Rf: 0.51) and the per-benzylated side product (Rf: 0.34).

25. 60% expected yield.
26. Follow the reaction course by thin layer chromatography using toluene–ethyl acetate 9:1 as eluent. TLC will show the formation of one spot, the desired product, 3,3′,4′,7-tetrabenzyl-5-(4-*O*-chlorobutyl) quercetin (**Q14**, Rf: 0.35) and the progressive disappearance of 3,3′,4′,7-tetrabenzyl quercetin (**Q13**, Rf: 0.51). 70% expected yield.
27. Hydrogen gas is bubbled through the mixture at low and constant flow.
28. Follow the reaction course by thin layer chromatography using toluene–methanol 9:1 as eluent. TLC will show the formation of the desired species (5-(4-*O*-chlorobutyl) quercetin, **Q15**, Rf: 0.24) and the progressive disappearance of 3,3′,4′,7-tetrabenzyl-5-(4-*O*-chlorobutyl) quercetin (**Q14**, Rf: 0.78) through the formation of partially benzylated -(4-*O*-chlorobutyl) quercetin derivatives with intermediate Rf value.
29. 85% expected yield.
30. Follow the reaction course by thin layer chromatography using chloroform–acetone 8:2 as eluent. TLC will show the formation of just one spot/product (5-(4-*O*-iodobutyl) quercetin, **Q18**, Rf = 0.28). 90% expected yield.
31. 70% expected yield.
32. Follow the reaction course by thin layer chromatography using dichloromethane–ethyl acetate–hexane 8:2:2 as eluent. TLC will show the formation of the desired compound (3,3′,4′,5-tetraacetyl-7-(4-*O*-chlorobutyl) quercetin, **Q25**, Rf: 0.58) and the progressive disappearance of 3,3′,4′,5,7-pentaacetyl quercetin (**Q24**, Rf: 0.43).
33. 70% expected yield.
34. At this point 3,3′,4′,5-tetraacetyl-7-(4-*O*-chlorobutyl) quercetin (**Q25**) is obtained as a synthesis intermediate; after purification by flash chromatography, it can be used as reagent for the synthesis of 3,3′,4′,5-tetraacetyl-7-(4-*O*-triphenylphosphoniumbutyl) quercetin (**Q33**) (general procedures Subheadings 3.2 and then Subheading 3.3).
35. Follow the reaction course by thin layer chromatography using toluene–methanol 8:2 as eluent. TLC will show the formation of the desired compound (7-(4-*O*-chlorobutyl) quercetin, **Q26**, Rf: 0.32), the progressive disappearance of the reagent (**Q25**, Rf: 0.85) and transient formation of partially acetylated-7-(4-*O*-chlorobutyl) quercetin derivatives (spots with intermediate Rf value).
36. 90% expected yield.

37. Follow the reaction course by thin layer chromatography using toluene–methanol 8:2 as eluent. TLC will show the formation of just one spot/product (7-(4-*O*-iodobutyl)quercetin, **Q28**, Rf = 0.35). 90% expected yield.
38. 70% expected yield.
39. This serves to build a scale to be used to quantify subsequent variations in concentration. The procedure is necessary because each electrode has its own sensitivity and response speed; this is due, for example, to variability in the thickness and/or density of the membrane.
40. Acetylated and methylated quercetin derivatives are the most fluorescent ones.

## Acknowledgments

We thank Dr. M. Zoratti for support and useful discussions. This work was supported by grants from the Fondazione Cassa di Risparmio di Padova e Rovigo (CARIPARO) ("Developing a Pharmacology of Polyphenols"), from the Italian Ministry of the University and Research (PRIN n. 20107Z8XBW_004), and by the CNR Project of Special Interest on Aging.

### References

1. Abbaszadeh H, Keikhaei B, Mottaghi S (2019) A review of molecular mechanisms involved in anticancer and antiangiogenic effects of natural polyphenolic compounds. Phytother Res 33:2002–2014
2. Gorzynik-Debicka M, Przychodzen P, Cappello F, Kuban-Jankowska A, Marino Gammazza A, Knap N, Wozniak M, Gorska-Ponikowska M (2018) Potential health benefits of olive oil and plant polyphenols. Int J Mol Sci 19:686
3. Xing L, Zhang H, Qi R, Tsao R, Mine Y (2019) Recent advances in the understanding of the health benefits and molecular mechanisms associated with green tea polyphenols. J Agric Food Chem 67:1029–1043
4. Silvester AJ, Aseer KR, Yun JW (2019) Dietary polyphenols and their roles in fat browning. J Nutr Biochem 64:1–12
5. Russo GL, Spagnuolo C, Russo M, Tedesco I, Moccia S, Cervellera C (2019) Mechanisms of aging and potential role of selected polyphenols in extending healthspan. Biochem Pharmacol 173:113719
6. Reyes-Farias M, Carrasco-Pozo C (2019) The anti-cancer effect of quercetin: molecular implications in cancer metabolism. Int J Mol Sci 20:3177
7. Jiang Z, Chen K, Cheng L, Yan B, Qian W, Cao J, Li J, Wu E, Ma Q, Yang W (2017) Resveratrol and cancer treatment: updates. Ann N Y Acad Sci 1403:59–69
8. Halliwell B (2008) Are polyphenols antioxidants or pro-oxidants? What do we learn from cell culture and in vivo studies? Arch Biochem Biophys 476:107–112
9. De Marchi U, Biasutto L, Garbisa S, Toninello A, Zoratti M (2009) Quercetin can act either as an inhibitor or an inducer of the mitochondrial permeability transition pore: a demonstration of the ambivalent redox character of polyphenols. Biochim Biophys Acta 1787:1425–1432
10. Calabrese V, Cornelius C, Trovato A, Cavallaro M, Mancuso C, Di Rienzo L, Condorelli D, De Lorenzo A, Calabrese EJ (2010) The hormetic role of dietary antioxidants in free radical-related diseases. Curr Pharm Des 16:877–883
11. Hou DX, Kumamoto T (2010) Flavonoids as protein kinase inhibitors for cancer

chemoprevention: direct binding and molecular modeling. Antioxid Redox Signal 13:691–719

12. Seifried HE, Anderson DE, Fisher EI, Milner JA (2007) A review of the interaction among dietary antioxidants and reactive oxygen species. J Nutr Biochem 18:567–579
13. Harikumar KB, Aggarwal BB (2008) Resveratrol: a multitargeted agent for age-associated chronic diseases. Cell Cycle 7:1020–1035
14. Jardim FR, de Rossi FT, Nascimento MX, da Silva Barros RG, Borges PA, Prescilio IC, de Oliveira MR (2018) Resveratrol and brain mitochondria: a review. Mol Neurobiol 55:2085–2101
15. Sajadimajd S, Bahramsoltani R, Iranpanah A, Kumar Patra J, Das G, Gouda S, Rahimi R, Rezaeiamiri E, Cao H, Giampieri F et al (2019) Advances on natural polyphenols as anticancer agents for skin cancer. Pharmacol Res 151:104584
16. Lejri I, Agapouda A, Grimm A, Eckert A (2019) Mitochondria- and oxidative stress-targeting substances in cognitive decline-related disorders: from molecular mechanisms to clinical evidence. Oxidative Med Cell Longev 2019:9695412
17. Ashrafizadeh M, Ahmadi Z, Farkhondeh T, Samarghandian S (2020) Resveratrol targeting the Wnt signaling pathway: a focus on therapeutic activities. J Cell Physiol 235 (5):4135–4145
18. Tavana E, Mollazadeh H, Mohtashami E, Modaresi SMS, Hosseini A, Sabri H, Soltani A, Javid H, Afshari AR, Sahebkar A (2019) Quercetin: a promising phytochemical for the treatment of glioblastoma multiforme. BioFactors 46:356–366
19. Rauf A, Imran M, Khan IA, Ur-Rehman M, Gilani SA, Mehmood Z, Mubarak MS (2018) Anticancer potential of quercetin: a comprehensive review. Phytother Res 32:2109–2130
20. Lin X, Wu G, Huo WQ, Zhang Y, Jin FS (2012) Resveratrol induces apoptosis associated with mitochondrial dysfunction in bladder carcinoma cells. Int J Urol 19:757–764
21. Delmas D, Solary E, Latruffe N (2011) Resveratrol, a phytochemical inducer of multiple cell death pathways: apoptosis, autophagy and mitotic catastrophe. Curr Med Chem 18:1100–1121
22. Liu KC, Yen CY, Wu RS, Yang JS, Lu HF, Lu KW, Lo C, Chen HY, Tang NY, Wu CC et al (2012) The roles of endoplasmic reticulum stress and mitochondrial apoptotic signaling pathway in quercetin-mediated cell death of human prostate cancer PC-3 cells. Environ Toxicol 29(4):428–439
23. Rodriguez-Enriquez S, Pacheco-Velazquez SC, Marin-Hernandez A, Gallardo-Perez JC, Robledo-Cadena DX, Hernandez-Resendiz I, Garcia-Garcia JD, Belmont-Diaz J, Lopez-Marure R, Hernandez-Esquivel L et al (2019) Resveratrol inhibits cancer cell proliferation by impairing oxidative phosphorylation and inducing oxidative stress. Toxicol Appl Pharmacol 370:65–77
24. Walle T, Hsieh F, DeLegge MH, Oatis JE Jr, Walle UK (2004) High absorption but very low bioavailability of oral resveratrol in humans. Drug Metab Dispos 32:1377–1382
25. Manach C, Williamson G, Morand C, Scalbert A, Remesy C (2005) Bioavailability and bioefficacy of polyphenols in humans. I. Review of 97 bioavailability studies. Am J Clin Nutr 81:230s–242s
26. Dabeek WM, Marra MV (2019) Dietary quercetin and Kaempferol: bioavailability and potential cardiovascular-related bioactivity in humans. Nutrients 11:2288
27. Petersen B, Egert S, Bosy-Westphal A, Muller MJ, Wolffram S, Hubbermann EM, Rimbach G, Schwarz K (2016) Bioavailability of quercetin in humans and the influence of food matrix comparing quercetin capsules and different apple sources. Food Res Int 88:159–165
28. Burak C, Brull V, Langguth P, Zimmermann BF, Stoffel-Wagner B, Sausen U, Stehle P, Wolffram S, Egert S (2017) Higher plasma quercetin levels following oral administration of an onion skin extract compared with pure quercetin dihydrate in humans. Eur J Nutr 56:343–353
29. Svilar L, Martin JC, Defoort C, Paut C, Tourniaire F, Brochot A (2019) Quantification of trans-resveratrol and its metabolites in human plasma using ultra-high performance liquid chromatography tandem quadrupole-orbitrap mass spectrometry. J Chromatogr B Analyt Technol Biomed Life Sci 1104:119–129
30. Garg R, Sardana S (2017) Research Problems Associated with Resveratrol (trans-3, 5, 4′- trihydroxystilbene; RSV) and Various Strategies to Overcome those Problems (Review). Curr Drug Deliv 14:364–376
31. Biasutto L, Mattarei A, La Spina M, Azzolini M, Parrasia S, Szabo I, Zoratti M (2019) Strategies to target bioactive molecules to subcellular compartments. Focus on natural compounds. Eur J Med Chem 181:111557

32. Biasutto L, Mattarei A, Azzolini M, La Spina M, Sassi N, Romio M, Paradisi C, Zoratti M (2017) Resveratrol derivatives as a pharmacological tool. Ann N Y Acad Sci 1403:27–37
33. Biasutto L, Mattarei A, Sassi N, Azzolini M, Romio M, Paradisi C, Zoratti M (2014) Improving the efficacy of plant polyphenols. Anti Cancer Agents Med Chem 14:1332–1342
34. Wallace DC (2012) Mitochondria and cancer. Nat Rev Cancer 12:685–698
35. Denisenko TV, Gorbunova AS, Zhivotovsky B (2019) Mitochondrial involvement in migration, invasion and metastasis. Front Cell Dev Biol 7:355
36. Sica V, Bravo-San Pedro JM, Stoll G, Kroemer G (2020) Oxidative phosphorylation as a potential therapeutic target for cancer therapy. Int J Cancer 146:10–17
37. Biasutto L, Mattarei A, Marotta E, Bradaschia A, Sassi N, Garbisa S, Zoratti M, Paradisi C (2008) Development of mitochondria-targeted derivatives of resveratrol. Bioorg Med Chem Lett 18:5594–5597
38. Mattarei A, Biasutto L, Marotta E, De Marchi U, Sassi N, Garbisa S, Zoratti M, Paradisi C (2008) A mitochondriotropic derivative of quercetin: a strategy to increase the effectiveness of polyphenols. Chembiochem 9:2633–2642
39. Mattarei A, Sassi N, Durante C, Biasutto L, Sandonà G, Marotta E, Garbisa S, Gennaro A, Paradisi C, Zoratti M (2011) Redox properties and cytotoxicity of synthetic isomeric Mitochondriotropic derivatives of the natural polyphenol quercetin. Eur J Org Chem 2011:5577–5586
40. Sassi N, Biasutto L, Mattarei A, Carraro M, Giorgio V, Citta A, Bernardi P, Garbisa S, Szabo I, Paradisi C et al (2012) Cytotoxicity of a mitochondriotropic quercetin derivative: mechanisms. Biochim Biophys Acta 1817:1095–1106
41. Sassi N, Mattarei A, Azzolini M, Bernardi P, Szabo I, Paradisi C, Zoratti M, Biasutto L (2014) Mitochondria-targeted resveratrol derivatives act as cytotoxic pro-oxidants. Curr Pharm Des 20:172–179
42. Murphy MP (2008) Targeting lipophilic cations to mitochondria. Biochim Biophys Acta 1777:1028–1031
43. Smith RA, Hartley RC, Cocheme HM, Murphy MP (2012) Mitochondrial pharmacology. Trends Pharmacol Sci 33:341–352
44. Skulachev VP, Anisimov VN, Antonenko YN, Bakeeva LE, Chernyak BV, Erichev VP, Filenko OF, Kalinina NI, Kapelko VI, Kolosova NG et al (2009) An attempt to prevent senescence: a mitochondrial approach. Biochim Biophys Acta 1787:437–461
45. Bouktaib M, Lebrun S, Atmani A, Rolando C (2002) Hemisynthesis of all the O-monomethylated analogues of quercetin including the major metabolites, through selective protection of phenolic functions. Tetrahedron 58:10001–10009
46. Rao KV, Owoyale JA (1976) Partial methylation of quercetin: direct synthesis of tamarixetin, ombuin and ayanin. J Heterocyclic Chem 13:1293–1295
47. Slabbert NP (1977) Ionisation of some flavanols and dihydroflavonols. Tetrahedron 33:821–824
48. Mattarei A, Biasutto L, Rastrelli F, Garbisa S, Marotta E, Zoratti M, Paradisi C (2010) Regioselective O-derivatization of quercetin via ester intermediates. An improved synthesis of rhamnetin and development of a new mitochondriotropic derivative. Molecules (Basel, Switzerland) 15:4722–4736
49. Metodiewa D, Jaiswal AK, Cenas N, Dickancaite E, Segura-Aguilar J (1999) Quercetin may act as a cytotoxic prooxidant after its metabolic activation to semiquinone and quinoidal product. Free Radic Biol Med 26:107–116
50. Lolli G, Cozza G, Mazzorana M, Tibaldi E, Cesaro L, Donella-Deana A, Meggio F, Venerando A, Franchin C, Sarno S et al (2012) Inhibition of protein kinase CK2 by flavonoids and tyrphostins. A structural insight. Biochemistry 51:6097–6107
51. Serviddio G, Sastre J (2010) Measurement of mitochondrial membrane potential and proton leak. Methods Mol Biol 594:107–121
52. Burgess J (1978) Metal ions in solution. Ellis Horwood Ltd, Chichester
53. Gritti F, Guiochon G (2006) Influence of the degree of coverage of C18-bonded stationary phases on the mass transfer mechanism and its kinetics. J Chromatogr A 1128:45–60
54. McCalley DV (2010) The challenges of the analysis of basic compounds by high performance liquid chromatography: some possible approaches for improved separations. J Chromatogr A 1217:858–880

# Chapter 10

# Bridging the Gap Between Nature and Antioxidant Setbacks: Delivering Gallic Acid to Mitochondria

**Fernando Cagide, Catarina Oliveira, José Teixeira, Paulo J. Oliveira, and Fernanda Borges**

## Abstract

Research on mitochondria-targeted active molecules became a hot topic in the past decade. Development of mitochondria permeability transition pore (mPTP)-targeting agents with clinical applications is needed not only because of the importance of the target in several diseases but also due to the fact that the current developed molecules have shown poor clinical success. In fact, only a reduced percentage reach mitochondria, effectively preventing pathological mPTP opening. The mitochondrial-targeting strategies should be a promising solution to increase the selectivity of compounds to the mPTP, reducing also their potential side effects. Chemical conjugation of bioactive molecules with a lipophilic cation such as the triphenylphosphonium ($TPP^+$) has been established as a robust strategy to specifically target mitochondria. Phytochemicals such as hydroxybenzoic acids are normal constituents of the human diet. These molecules display beneficial healthy effects, ranging from antioxidant action through diverse mechanisms to modulation of mitochondrial-related apoptotic system, although their therapeutic application is limited due to pharmacokinetic drawbacks. Accordingly, the development of a new antioxidant based on the dietary benzoic acid—gallic acid—is described as well as the demonstration of its mitochondriotropic characteristics.

**Key words** Mitochondriotropic antioxidant, Gallic Acid, Smart Carriers, Rat Heart Mitochondria

## 1 Introduction

Mitochondria have an important number of roles in eukaryotic cells: regulation calcium homeostasis, fatty acid oxidation, urea cycle, biosynthesis of lipid and amino acid and, importantly the production of energy in the form of ATP [1]. Under different pathologies, the same reactions that lead to ATP synthesis also result in the production of an excess of reactive oxygen species (ROS) [2]. Since mitochondria are particularly vulnerable to oxidative stress, excessive production of ROS can lead to cell dysfunction and death [3].

Closely involved with the concept of cell death by necroptosis, the mitochondrial permeability transition (mPTP) is a sudden and

Volkmar Weissig and Marvin Edeas (eds.), *Mitochondrial Medicine: Volume 1: Targeting Mitochondria*, Methods in Molecular Biology, vol. 2275, https://doi.org/10.1007/978-1-0716-1262-0_10,

irreversible increase in the permeability of the inner mitochondrial membrane (IMM) to small solutes up to 1.5 kDa, leading to the progressive dissipation of mitochondrial transmembrane potential ($\Delta\psi m$). This unregulated passage of water that follows solute intake into the mitochondrial matrix results in the osmotic swelling of the organelle [4]. For these reasons, the mPTP is a significant event in a large number of human pathologies (e.g., heart failure, stroke, diabetes, liver injury, neurodegenerative disorders. and cancer) [5, 6].

Mitochondrial studies are currently performed on mouse or rat isolated mitochondria primarily from the liver or heart due to the abundance and easy access of these organs. Cardiac mitochondria are often isolated for multiple functional and toxicological studies, being used in different studies for the evaluation of toxicity and the accumulation of a large numbers of compounds [7], as well as to study the effects of different molecules on mPTP opening [8]. The best-characterized mPTP opening mechanism involves the accumulation of $Ca^{2+}$ ions in the mitochondrial matrix [9]. Thus, besides the accumulation of mitochondrial $Ca^{2+}$, major mPTP stimulators include ROS, inorganic phosphate, matrix alkalinization, long-chain fatty acids, atractyloside, and carboxyatractyloside [10].

Research to date suggests that phytochemical antioxidants, such as plant polyphenols, play an important role on the protection of mitochondria against oxidative stress and particularly towards the mPTP opening phenomena [11]. One of the most common plant polyphenols in the diet is gallic acid (3,4,5-trihydroxybenzoic acid) that has an important antioxidant activity as well as the ability to chelate pro-oxidant metals such as Cu and Fe [12, 13]. Moreover, recent study demonstrated that gallic acid prevented mitochondrial swelling induced by different stimuli, suggesting that it acts as a genuine mPTP inhibitor [14]. In spite of these important properties of gallic acid, its high solubility in water and polarity restricts its bioavailability by allowing its easy excretion and making it difficult to pass through lipidic membranes and reach areas where oxidative stress damage occurs such as mitochondria [15]. In fact, a substantial obstacle in the development of mPTP-targeting agents with clinical applications is based in part in the fact that they have low bioavailability, with only a reduced percentage reaching mitochondria, limiting their efficacy in preventing mPTP opening.

The mitochondrial-targeting strategies are a promising solution to increase the selectivity of compounds towards the mPTP, reducing also their potential side effects. Within this framework, several therapeutic approaches targeting mitochondria have been developed, in particular those using triphenylphosphonium cation ($TPP^+$) as a carrier to deliver molecules to mitochondria [16–18]. These types of cations accumulate in the mitochondria due to their net electric charge, and the mitochondrial binding/accumulation can be estimated using a selective $TPP^+$ electrode.

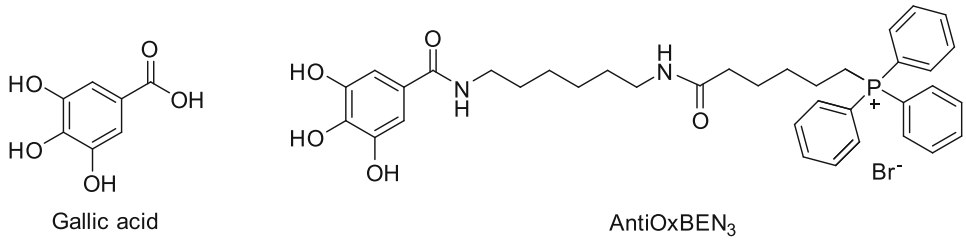


**Fig. 1** Chemical structures of gallic acid and AntiOxBEN$_3$

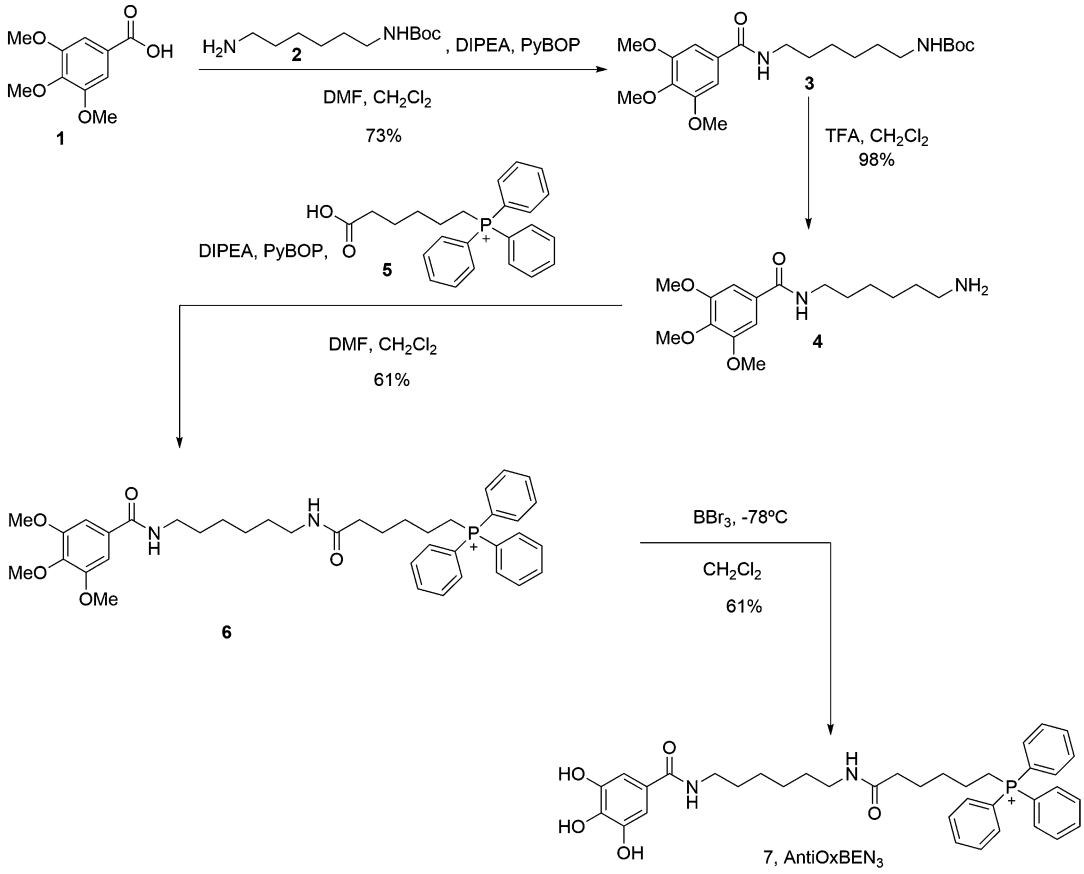


**Scheme 1** Flowchart followed for the synthesis of mitochondriotropic antioxidant AntiOxBEN$_3$

Consequently, it is expected that the use of this type of derivatives will allow the selective targeting of antioxidants to the mitochondria to prevent damage caused by oxidative stress.

Based on this, a mitochondria-targeted antioxidant based on gallic acid was developed, AntiOxBEN$_3$ (*see* Fig. 1, Scheme 1), which strikingly showed potential to inhibit the increase of the inner mitochondrial membrane permeability resulting from mPTP induction [19]. AntiOxBEN$_3$ accumulated several thousand-fold inside isolated rat heart mitochondria, without causing disruption of the oxidative phosphorylation apparatus (*see* Fig. 2).

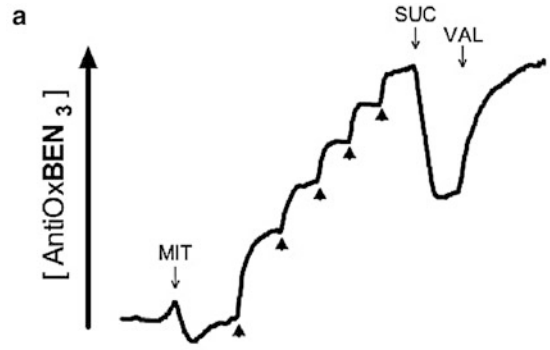


b

| | [ Intramitochondrial ] (mM) | [ Extramitochondrial ] (μM) | Accumulation Ratio |
|---|---|---|---|
| $AntiOxBEN_3$ | 1.38 ± 0.26 | 2.06 ± 0.41 | 2228 ± 167.7 |

**Fig. 2** Mitochondrial heart uptake of $AntiOxBEN_3$. In the presence of rotenone, heart mitochondria were incubated with five sequential 1 μM $AntiOxBEN_3$ additions (black arrowheads) to calibrate the electrode response. Succinate was then added to generate a transmembrane electric potential by being oxidized on mitochondrial Complex II. Accumulated $AntiOxBEN_3$ is subsequently released by adding valinomycin, which depolarizes mitochondrial by promoting potassium mitochondrial influx. By determining the ratio between the accumulated and external $TPP^+$ concentration, a value of around 2250× fold accumulation is obtained. *MIT* mitochondria, *SUC* succinate, *VAL* valinomycin

Because of the important role of the mPTP in different pathologies, including those affecting the cardiovascular system [20], $AntiOxBEN_3$ appears as a solid candidate for developing a novel therapeutic agent that could be used to inhibit excessive pore opening. In this chapter, we measure the mitochondrial uptake of triphenylphosphonium-derived gallic acid antioxidant ($AntiOxBEN_3$) in isolated rat heart mitochondria using a $TPP^+$-selective electrode.

## 2 Materials

### 2.1 Components for Synthesis

All the reagents used for $AntiOxBEN_3$ synthesis were used without further purification. The solvents employed were *pro-analysis* grade. After extraction the organic layers were gathered and dried over $Na_2SO_4$. Solutions were decolorized with activated charcoal when needed. Flash column chromatography was performed using silica gel 60 (0.040–0.063 mm) (*see* **Note 1**).

### 2.2 Rat Mitochondrial Fraction Preparation Components

1. Homogenization medium: 250 mM sucrose, 10 mM HEPES, pH 7.4 (KOH), 1 mM EGTA, supplemented with 0.1% BSA (bovine serum albumin) (fatty acid free). Weigh 171.15 g sucrose, 4.77 g HEPES, and 0.761 g EGTA and transfer to a glass flask. Add water to a volume of 1.8 L. Mix and adjust pH with KOH. Make up to 2 L with water and store at −20 °C (*see* **Note 2**).

2. Resuspension buffer: 250 mM sucrose, 10 mM HEPES, pH 7.2 (KOH). Weigh 87.57 g sucrose and 2.38 g HEPES and transfer to a glass flask. Add water to a volume of 900 mL. Mix and adjust pH with KOH. Make up to 1 L with water and store at −20 °C.
3. Protease: 5 mg/mL of Subtilisin A, Type VIII from *Bacillus licheniformis*. Weigh 5 mg of protease and add water to a final volume of 1 mL. Gently mix and store at −20 °C in 50 μL aliquots.

### 2.3 Components to Evaluate the Mitochondriotropic Features of AntiOxBEN$_3$

1. Reagents for preparation of $TPP^+$-selective electrode: tetraphenylphosphonium, tetraphenylboron, diisooctylphthalate, polyvinylchloride (high molecular weight) and tetrahydrofuran.
2. Reagents for specific techniques: substrate of electron transport chain (succinate), inhibitor of electron transport chain (rotenone) and ionophore (valinomycin).
3. Reaction medium: 120 mM KCl, 10 mM HEPES, pH 7.2, 1 mM EGTA. Weigh 4.47 g KCl, 1.19 g HEPES and 0.190 g EGTA and transfer to a glass flask. Add water to a volume of 450 mL. Mix and adjust pH. Make up to 500 mL with water and store at 4 °C.
4. AntiOxBEN$_3$: prepare a stock solution of 100 mM AntiOxBEN$_3$ by dissolving 7.07 mg in DMSO (100 μL). Dilute it in water to reach a final concentration of 200 μM.

## 3 Methods

### 3.1 Development of the Mitochondriotropic Antioxidant AntiOxBEN$_3$ (Scheme 1)

#### 3.1.1 Synthesis of Tert-Butyl (6-(3,4,5-Trimethoxybenzamido) Hexyl)Carbamate (3)

1. Dissolve, in a round bottom flask, 500 mg of 3,4,5-trimethoxybenzoic acid **1** in 3.9 mL of *N*,*N*-dimethylformamide.
2. Place the mixture at 4 °C, add 0.421 mL of *N*,*N*-diethylpropan-2-amine and 1.668 g of PyBOP dissolved in 3.9 mL of $CH_2Cl_2$. Stir the reaction for half an hour.
3. Add 0.529 mL of *tert*-butyl(6-aminohexyl)carbamate and cool again in an ice bath. Add 1.2 mL of 2-aminoethanol. Stir the reaction 18 h at room temperature.
4. Then, dilute the mixture with 20 mL of $CH_2Cl_2$, wash twice with 20 mL of saturated $NaHCO_3$. Dry it, filter, and evaporate the solvent.
5. Purify the crude product by column chromatography (ethyl acetate–petroleum ether [50%]). Combine the fractions with the desired compound and evaporate the solvent (*see* **Note 3**).

*3.1.2 Synthesis of* N*-(6-Aminohexyl)-3,4,5-Trimethoxybenzamide (**4**)*

1. In a round bottom flask, stir a solution of 1 g of compound **3** and 4 mL of triethylamine in 20 mL of $CH_2Cl_2$ for an hour.
2. Neutralize the reaction with a saturated solution of $NaHCO_3$, separate the organic phase and dry it. Filter and evaporate the solvent.
3. Purify the crude product by column chromatography (methanol–dichloromethane [10%]). Combine the fractions with the desired compound and evaporate the solvent (*see* **Note 3**).

*3.1.3 Synthesis of [5-(6-(3,4,5-Trimethoxybenzamido) hexylamino) carbonylpentyl] triphenylphosphonium Bromide (**6**)*

1. Dissolve 689 mg of compound **4** in 7.4 mL of *N*,*N*-dimethylformamide.
2. Place the solution at 4 °C, add 0.476 mL of *N*,*N*-diethylpropan-2-amine and 1.572 g of PyBOP dissolved in 7.4 mL of $CH_2Cl_2$. Stir the mixture for half an hour.
3. Add 1.218 g of the compound **5**. Heat up the reaction to room temperature stirring the reaction for 20 h.
4. Dilute with 40 mL of $CH_2Cl_2$, wash twice with 20 mL of saturated $NaHCO_3$ and dry it. Filter and evaporate the solvent.
5. Purify the crude product by column chromatography (methanol–dichloromethane [10%]). Combine the fractions with the desired compound and evaporate the solvent (*see* **Note 3**).

*3.1.4 Synthesis of [5–(6-(3,4,5-Trihydroxybenzamido) hexylamino) carbonylpentyl] triphenylphosphonium Bromide (**7**, AntiOxBEN$_3$)*

1. Dissolve 1 g of compound **6** in 7.6 mL of anhydrous dichloromethane. Stir the solution under an inert atmosphere (argon) and cool it to −70 °C.
2. Add 4.3 mL of a solution of boron tribromide (1 M in dichloromethane). Keep the reaction at −70 °C for 10 min. Let the reaction reach room temperature and stir the solution during 12 h.
3. Quench the reaction with a slow and careful addition of 20 mL of water. Remove the solvents.
4. Dissolve the solid in MeOH and dry it. Filter and evaporate the solvent.
5. Purify the crude product by column chromatography (methanol–dichloromethane [10%]). Combine the fractions with the desired compound and evaporate the solvent (*see* **Note 3**).

### 3.2 Isolation of Rat Heart Mitochondrial Fractions

Independently of mitochondrial origin (liver, heart, kidney, or brain), the first important procedure to achieve good and feasible results is the isolation of tightly coupled mitochondrial fractions [21]. The methods for mitochondrial isolation are laboratory-specific and are established to obtain preparations of mitochondria suitable for different applications. Note that all the isolation procedures must be carried out on ice, or in a cold room, and follow a standardized flowchart (Scheme 2).

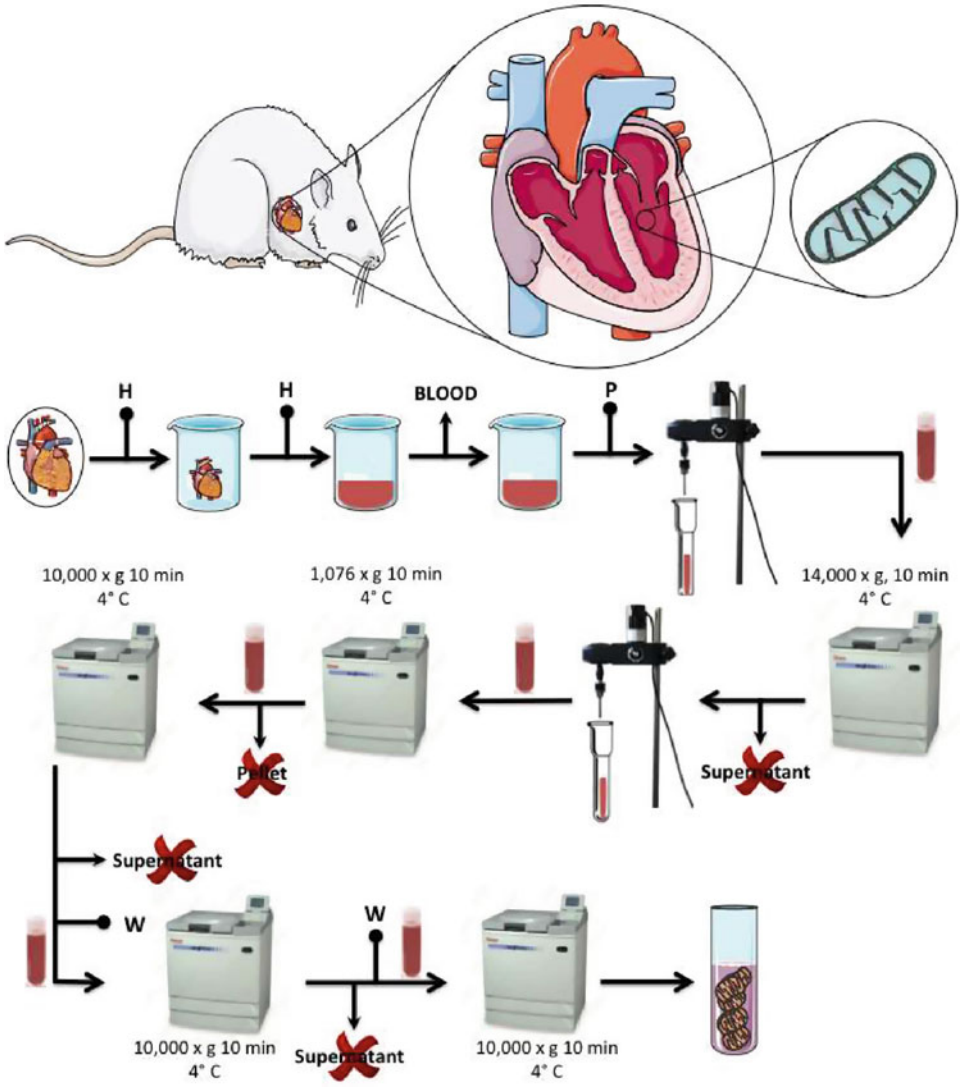


**Scheme 2** General flowchart for isolation of rat heart mitochondrial fractions. All the material was kept on ice during the isolation procedure. *H* homogenization buffer, *P* protease, *W* washing buffer

1. Take a young adult (10–12 weeks old) male or female rat and sacrifice it using a proper and ethic method (e.g., anesthesia with halothane or isoflurane followed by cervical dislocation and decapitation). Bleed the rat into the sink for about 1 min.
2. Open the rat with scissors, remove the connective tissue and fat. Excise the heart from the animal and place it in a beaker containing ice-cold homogenization buffer.
3. Remove, as much as possible, the adhering fat or fibrous tissue, chop up the heart with scissors and drain off the homogenization medium. Add fresh homogenization buffer and repeat the procedure several times to remove blood excess until the liquid comes out clear.

4. Transfer the minced blood-free tissue to a precooled glass Potter-Elvehjem homogenizer and fill it with approximately 40 mL of homogenization medium, supplemented by 0.5 μg/mL of protease. For the isolation of cardiac mitochondrial fractions, the homogenization medium is supplemented with 0.5 μg/mL (40 μL from the 5 mg/mL solution) of Subtilisin A (*see* **Note 4**).
5. Exposure to protease is limited to 2–3 min in order to minimize loss of mitochondrial membrane integrity. Then, homogenize heart gently about 5–8 times with the plunger rotating at 300 rpm (*see* **Note 5**). Always perform all steps under 4 °C.
6. Transfer to a 50 mL centrifuge tube (*see* **Note 6**). Protease needs to be removed from the solution by centrifuging the homogenate at 14,000 × *g* for 10 min, which corresponds to 10,822 rpm in the Sorvall SS-34 rotor using the Sorvall RC 6 Plus centrifuge or equivalent. Decant carefully the supernatant (*see* **Note 7**).
7. Homogenize heart pellet gently once again about 5–8 times with the plunger rotating at 300 rpm (*see* **Note 5**).
8. Transfer to a 50 mL centrifuge tube (*see* **Note 6**). Nuclei, red cells, intact cells and other debris are removed by centrifuging the homogenate at 1076 × *g* for 10 min, which corresponds to 3000 rpm in the Sorvall SS-34 rotor using the Sorvall RC 6 Plus centrifuge or equivalent. Decant carefully the supernatant to a new centrifuge tube (*see* **Note 8**).
9. Centrifuge the supernatant at 10,000 × *g* for 10 min (=9150 rpm) and discard it. The mitochondrial pellet forms a soft brown pellet that should be gently resuspended with a smooth paintbrush and with heart resuspension buffer (*see* **Note 9**).
10. Centrifuge again the suspension at 10,000 × *g* for 10 min. Resuspend the pellet with a paintbrush in heart resuspension medium and repeat the procedure.
11. Suspend carefully the pellet in about 0.5 mL of resuspension buffer. Determine mitochondrial protein content by biuret method calibrated with BSA [22] (*see* **Note 10**).

### 3.3 Uptake of AntiOxBEN$_3$ by Mitochondria

#### 3.3.1 Preparation of TPP$^+$ Selective Electrode

The uptake of AntiOxBEN$_3$ by mitochondria is measured with a TPP$^+$-selective electrode. The electrode is constituted by a polyvinylchloride-based membrane containing tetraphenylboron as an ion-exchanger and prepared according to Kamo et al. [23, 24]: a solution containing 0.34 mg of tetraphenylboron ($Na^+$ salt), 16 mg of polyvinylchloride (high molecular weight), 57 μL of diisooctylphthalate, and tetrahydrofuran (to a final volume of 500 μL) is evaporated on a glass plate enclosed by a 2 cm diameter glass ring to produce a polyvinylchloride membrane.

The ring is covered with a glass beaker and left overnight at room temperature to vaporize tetrahydrofuran and obtain a clear membrane (0.2 mm thick). Then, a piece of membrane is glued with tetrahydrofuran to a 2 mm inner diameter polyvinylchloride tube (*see* **Note 11**). Tetrahydrofuran is evaporated by light sucking and blowing into the tube. Any outstrip membrane material remaining over the tube must be cut out with a razor blade. The whole electrode is filled with 0.1–0.2 mL previously degassed $TPP^+$ 10 mM that works as reference solution. A silver wire coated with AgCl is used to establish the connection to a suitable electrometer. The electrode is soaked overnight in a 10 mM $TPP^+$ solution for conditioning before use.

The electromotive force is measured between the $TPP^+$ electrode and a calomel electrode located in the sample solution. In accordance with the Nernst equation, a good electrode must have a linear voltage response to log [$TPP^+$] and a slope of 59 at 25 °C.

### *3.3.2 Heart Mitochondrial Uptake of AntiOxBEN$_3$*

The heart mitochondrial uptake of AntiOxBEN$_3$ is measured in an open thermostat vessel, at a constant temperature of 37 °C, under efficient magnetic stirring.

1. Add to the reaction chamber 1 mL of reaction medium containing 120 mM KCl, 10 mM HEPES, pH 7.2, and 1 mM EGTA supplemented with rotenone (1.5 μM).
2. Place the pen record after choosing a 50-mV full scale; wait until the trace is stable (select a chart speed of 1 cm/min). Add 0.5 mg mitochondrial heart protein.
3. Mitochondria-targeted agent AntiOxBEN$_3$ will be used to trace a calibration curve. For this, perform five consecutive additions of AntiOxBEN$_3$ (1 μM each one). Between each addition wait until the trace is stable (*see* **Note 12**).
4. Add 10 mM succinate. After AntiOxBEN$_3$ has been accumulated, add 0.2 μg/mL valinomycin. The accumulated AntiOxBEN$_3$ in mitochondria is released once mitochondrial membrane potential is abolished by the influx of potassium (*see* **Note 13**).

## 4 Notes

1. For the synthetic procedures, the use of protective clothing, goggles, gloves and protection mask for solid particles (when silica column is packed) is required. Silica gel causes irritation on respiratory tract and dust beads may cause skin and eyes irritation. For further information, see Merck Index.

2. Aliquot in flasks of approximately 500 mL. 0.1% BSA (10 mL of a stock solution 5% BSA) is added on the day of the experiment to the homogenization buffer.
3. NMR and electrospray ionization mass spectra (ESI-MS) data must be acquired to confirm the structural identity of the compound (for details *see* Ref. 6).
4. For the isolation of cardiac mitochondrial fractions, the homogenization medium is supplemented with 0.5 μg/mL of Subtilisin A, Type VIII from *Bacillus licheniformis* (Sigma-Aldrich) in order to degrade cardiac fibbers.
5. The pestle must reach the bottom of the tube in the first or second pass but caution is needed either for not to create a vacuum or to put the plunger through the bottom of the homogenizer.
6. Balance the content with a water-filled tube. If the homogenate does not fit in one tube, divide it by two tubes.
7. Decant with care the supernatant, essentially devoid of protease, to a precooled glass Potter-Elvehjem homogenizer and fill it with approximately 40 mL of homogenization medium.
8. Decant with care the supernatant, to avoid contamination with debris from pellet.
9. Generally, the pellet has a superficial mobile layer (a "fluffy layer") that must be discarded together with the supernatant as it contains damaged mitochondria.
10. The mitochondrial protein after isolation should be quantified after a 20 min recovery and used within 5–6 h post-isolation, being kept in ice at all times.
11. Care must be taken to avoid the use of excess of tetrahydrofuran as it can cause dissolution of the central core of the membrane.
12. The calibration can be done prior to the addition of mitochondria.
13. To confirm that AntiOxBEN$_3$ is accumulated due to mitochondrial membrane potential, valinomycin should be added to the reaction chamber at the same time than rotenone. When mitochondrial membrane potential is not generated, AntiOxBEN$_3$ is not accumulated by mitochondria.

## Acknowledgments

This work was funded by FEDER funds through the Operational Programme Competitiveness Factors—COMPETE and national funds by FCT—Foundation for Science and Technology under

research grants UID/NEU/04539/2020, UID/QUI/00081/2020, PTDC/BIA-MOL/28607/2017, PTDC/ASP-PES/28397/2017, POCI-01-0145-FEDER-016659, POCI-01-0145-FEDER-028607, and POCI-01-0145-FEDER-006980. F. Cagide, C. Oliveira, and J. Provavelmente já não se aplica grants are supported by FCT, POPH, and FEDER/COMPETE.

## References

1. Bernardi P, Scorrano L, Colonna R, Petronilli V, Di Lisa F (1999) Mitochondria and cell death. Mechanistic aspects and methodological issues. Eur J Biochem 264:687–701
2. Petersen RB, Nunomura A, Lee HG, Casadesus G, Perry G et al (2007) Signal transduction cascades associated with oxidative stress in Alzheimer's disease. J Alzheimers Dis 11:143–152
3. Marchi S, Giorgi C, Suski JM, Agnoletto C, Bononi A et al (2012) Mitochondria-ros crosstalk in the control of cell death and aging. J Signal Transduct 2012:329635
4. Bonora M, Wieckowski MR, Chinopoulos C, Kepp O, Kroemer G et al (2015) Molecular mechanisms of cell death: central implication of ATP synthase in mitochondrial permeability transition. Oncogene 34:1475–1486
5. Brookes PS, Yoon Y, Robotham JL, Anders MW, Sheu SS (2004) Calcium, ATP, and ROS: a mitochondrial love-hate triangle. Am J Physiol Cell Physiol 287:C817–C833
6. Sileikyte J, Forte M (2019) The mitochondrial permeability transition in mitochondrial disorders. Oxidative Med Cell Longev 2019:3403075
7. Oliveira PJ (2011) Mitochondria as a drug target in health and disease. Curr Drug Targets 12:761
8. Bernardi P, Rasola A, Forte M, Lippe G (2015) The mitochondrial permeability transition pore: channel formation by F-ATP synthase, integration in signal transduction, and role in pathophysiology. Physiol Rev 95:1111–1155
9. Izzo V, Bravo-San Pedro JM, Sica V, Kroemer G, Galluzzi L (2016) Mitochondrial permeability transition: new findings and persisting uncertainties. Trends Cell Biol 26:655–667
10. Brenner C, Grimm S (2006) The permeability transition pore complex in cancer cell death. Oncogene 25:4744–4756
11. Sandoval-Acuna C, Ferreira J, Speisky H (2014) Polyphenols and mitochondria: an update on their increasingly emerging ROS-scavenging independent actions. Arch Biochem Biophys 559:75–90
12. Fazary AE, Taha M, Ju Y-H (2009) Iron complexation studies of Gallic acid. J Chem Eng Data 54:35–42
13. Badhani B, Sharma N, Kakkar R (2015) Gallic acid: a versatile antioxidant with promising therapeutic and industrial applications. RSC Adv 5:27540–27557
14. Sun J, Ren DD, Wan JY, Chen C, Chen D et al (2017) Desensitizing mitochondrial permeability transition by ERK-Cyclophilin D Axis contributes to the neuroprotective effect of Gallic acid against cerebral ischemia/reperfusion injury. Front Pharmacol 8:184
15. Benfeito S, Oliveira C, Soares P, Fernandes C, Silva T et al (2013) Antioxidant therapy: still in search of the 'magic bullet'. Mitochondrion 13:427–435
16. Smith RA, Murphy MP (2011) Mitochondria-targeted antioxidants as therapies. Discov Med 11:106–114
17. Teixeira J, Oliveira C, Amorim R, Cagide F, Garrido J et al (2017) Development of hydroxybenzoic-based platforms as a solution to deliver dietary antioxidants to mitochondria. Sci Rep 7:6842
18. Wu S, Cao Q, Wang X, Cheng K, Cheng Z (2014) Design, synthesis and biological evaluation of mitochondria targeting theranostic agents. Chem Commun 50:8919–8922
19. Teixeira J, Oliveira C, Cagide F, Amorim R, Garrido J et al (2018) Discovery of a new mitochondria permeability transition pore (mPTP) inhibitor based on gallic acid. J Enzyme Inhib Med Chem 33:567–576
20. Kwong JQ, Molkentin JD (2015) Physiological and pathological roles of the mitochondrial permeability transition pore in the heart. Cell Metab 21:206–214
21. Schulz S, Lichtmannegger J, Schmitt S, Leitzinger C, Eberhagen C et al (2015) A protocol for the parallel isolation of intact mitochondria from rat liver, kidney, heart, and brain. Methods Mol Biol 1295:75–86

22. Gornall AG, Bardawill CJ, David MM (1949) Determination of serum proteins by means of the biuret reaction. J Biol Chem 177:751–766
23. Kamo N, Kobatake Y (1986) Changes of surface and membrane potentials in biomembranes. Methods Enzymol 125:46–58
24. Kamo N, Muratsugu M, Hongoh R, Kobatake Y (1979) Membrane potential of mitochondria measured with an electrode sensitive to tetraphenyl phosphonium and relationship between proton electrochemical potential and phosphorylation potential in steady state. J Membr Biol 49:105–121

# Chapter 11

# Liposomal Delivery of Cyclocreatine Impairs Cancer Cell Bioenergetics Mediating Apoptosis

**Samayita Ganguly and Tamer Elbayoumi**

## Abstract

Creatine kinase (CK) enzyme overexpression has been suggested to play a role in the process of tumorigenesis and metastasis. Cyclocreatine (CCR) is a substrate analog of creatine kinase (CK), where its phosphorylated form is a poor phosphate donor in comparison with native bioenergetic molecule, creatine phosphate (Cr-P). The compound CCR has been shown to markedly inhibit the growth of a broad spectrum of cancers, both in vitro and in vivo. Intracellularly, CCR is phosphorylated by CK to yield a synthetic phosphagen [(*N*-phosphorylcyclocreatine (CCR~P)], with thermodynamic and kinetic properties distinct from those of creatine phosphate (Cr-P). Distinct inhibition of tumor growth and metastasis has been attributed to CCR accumulation as CCR~P in tumor cells, especially in those expressing a high level of CK protein, with minimal adverse effects. Unfortunately, the clinical use of CCR against malignancies is quite limited due to its amphoteric nature, which accounts for most of its extremely low membrane permeability, as well as limited oral bioavailability (BA) and poor systemic pharmacokinetics (PK).

Our current work describes the encapsulation of CCR, utilizing freeze and thaw vesicles (FTV)—composed mostly of saturated PC, DOPE, and Chol—into stealth™ liposomes, postcoated with 4.5 M% PEG-PE. Following physicochemical characterization, in vitro release and cellular uptake kinetics confirmed efficient delivery of liposomal CCR (CCR-Lip), leading to intracellular accumulation of its CC-P metabolic product. Successful delivery of CCR to cancer cell effectively depleted low energetic cancer cells of ATP significantly mediating myc-induced metabolic changes. CCR-Lip showed significant antimetastatic and anticancer effectiveness against both MCF-7 and PC-3 human carcinoma models ($p < 0.05$–$0.01$), with 4- to 6-fold lower IC50 values vs. closest drug control. Such shift in bioenergetics was coupled via AMPK and phospho-p53 to the mitochondrial apoptosis effector Bak, thus inducing a cell-intrinsic mechanism to counteract uncontrolled neoplastic proliferation, in target cancer cells. Our novel liposomal delivery system of the CCR substrate analog demonstrated strong inhibition of malignant cell bioenergetics, leading to significant antineoplastic and proapoptotic actions, against different cancers.

**Key words** Creatine kinase; phosphagen, Creatine phosphate, Cyclocreatine, Proapoptotic, Cell bioenergetics, Freeze and thaw nanovesicles, Stealth™ liposomes

## 1 Introduction

The creatine kinase–creatine phosphate system is involved in the maintenance of cellular energy homeostasis in tissues with large and

Volkmar Weissig and Marvin Edeas (eds.), *Mitochondrial Medicine: Volume 1: Targeting Mitochondria*, Methods in Molecular Biology, vol. 2275, https://doi.org/10.1007/978-1-0716-1262-0_11,

fluctuating energy demands, such as skeletal muscle, heart, and brain [1, 2]. It is well established that the CK/Cr-P system functions as a spatial and temporal energy buffer in addition to maintaining cellular pH, ATP–ADP ratios, and ADP levels [3].

The key factor responsible for eliciting the decrease in the ATP supply–demand ratio in proliferating cancer cells is the relative lack of ATP. In fact, inefficient ATP production is a familiar attribute of cancer cell-associated metabolic programs, where also MYC protooncogene-mediated metabolic reprogramming has been associated with depletion of cellular ATP levels [3, 4]. In malignancy, myc-induced metabolic reprogramming (metabolic transformation) fuels autonomous patterns of cell proliferation and renders cells "addicted" to reprogrammed metabolic pathway. Such effects can be essentially implicated in cancerous cells undergoing the Warburg transformation or effect [5]. Such Myc-induced reprogramming of malignant cells renders them much more susceptible to apoptosis, if deprived of glucose of glutamine. It also sensitized cells to intrinsic pathway of apoptotic death [5, 6].

Several previous reports have investigated the role of creatine kinase (CK) and its bioenergetic substrates in malignancy [5]. The CK enzyme (in both mitochondria and cytoplasm) has been proposed to play a significant role in the process of tumorigenesis [3, 7]. Preclinical data suggested CK is overexpressed in many tumor types, of diverse origins, and is associated with their metastatic transformation [3, 4, 7]. It is induced by several hormones [8], oncogenes [9], and other elements of signal transduction pathways [10–13].

Cyclocreatine (CCR), a synthetic phosphagen that acts as a substrate analog of CK, has been shown to act as an anticancer agent in a variety of preclinical studies [14–16]. In vitro and animal studies demonstrated CCR is phosphorylated by CK into a synthetic phosphagen [(*N*-phosphorylcyclocreatine(CCR-P), which is thermodynamically and kinetically distinct from natural creatine phosphate (Cr-P) (Fig. 1) [12, 13]. CCR~P has been demonstrated to be a poor substrate for CK and hence provides ATP less readily than creatine. Therefore, intracellular accumulation of this phosphagen, CCR (along with its phosphorylated form, CCR~P), impairs the functions of the creatine kinase–creatine phosphate system, causing depletion of ATP–ADP ratios that is not only detrimental to tumor cell growth, but ultimately sensitizes malignant cells to mitochondria-dependent apoptosis [5, 12, 13].

The bioenergetic substrate, CCR is a hydrophilic and strongly charged small anion, similar to ATP, where they both cannot normally pass the cell membrane in sufficient quantities to satisfy tissue metabolic requirements [17, 18]. Moreover, both Cr and CCR have a very short half-life in the blood, and are rapidly hydrolyzed to ADP, AMP, and adenosine via a cascade of extracellular ectonucleotidases [5, 19]. The nature of the CCR as a small amphoteric molecule, in addition to its limited water solubility, generally

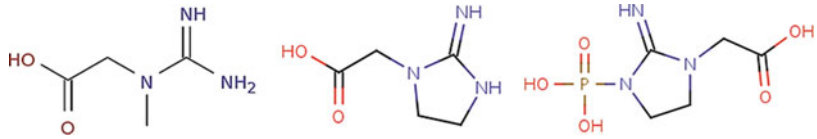


**Fig. 1** Chemical structures of creatine, Cr (**left**); cyclocreatine, CCR (**middle**); and its metabolic phosphagen, cyclocreatine phosphate, CCR~P. (**right**)

contributes to its poor oral bioavailability [20]. At the same time, these characteristics make it an ideal candidate for loading into liposomal nanocarriers, for improved drug delivery (Fig. 2) [5].

Liposomes are one of the most widely studied nanoscale carrier systems. They have been extensively investigated for both controlled release and targeted delivery of many therapeutic macromolecules, thanks to their favorable pharmaceutical characteristics, such as biocompatibility and the ease of large-scale production [21, 22].

Our current work describes the PEGylated liposomal formulation of CCR (CCR-FTV) and, the intracellular accumulation of its CC-P metabolic product, because of efficient CCR-FTV nanodelivery, due to improved solubilization and permeability through lipidic membranes. This approach can effectively deplete low energetic cancer cells of ATP, mediating myc-induced metabolic changes, coupled via 5′ adenosine monophosphate-activated protein kinase, AMPK, and phospho-p53 tumor protein to the mitochondrial permealizer, BCL2 antagonist/killer 1 protein, Bak, thus inducing an intrinsic apoptotic mechanism to cease uncontrolled proliferation (Fig. 3). In addition, our polyethylene glycol, PEG-coated CCR-liposomes (included as 4.5 mol% PEG-PE) can offer prolonged circulation in blood for our synthetic phosphagen drug, as a candidate pharmaceutical platform suitable for systemic administration in potential clinical applications.

## 2 Materials

### *2.1 Preparation of CCR-Loaded Liposomes (Plain and PEGylated)*

1. Chloroform (100%, dry).
2. L-α-phosphatidylcholine, hydrogenated (Soy) (Avanti Polar Lipids, Inc., Alabaster, AL). Dissolve 25.5 mM HSPC in 10 mL chloroform, to make 20 mg/mL HSPC stock solution. Store at −80 °C.
3. Cholesterol (Chol). Dissolve 51.8 mM Chol in 10 mL chloroform, to make 20 mg/mL HSPC stock solution. Store at −80 °C.
4. 1,2-Distearoyl-*sn*-glycero-3-phosphoethanolamine-*N*-[methoxy(polyethylene glycol)-2000] (ammonium salt) (PEG, MW 2000) (Avanti Polar Lipids, Inc., Alabaster, AL), for PEGylated

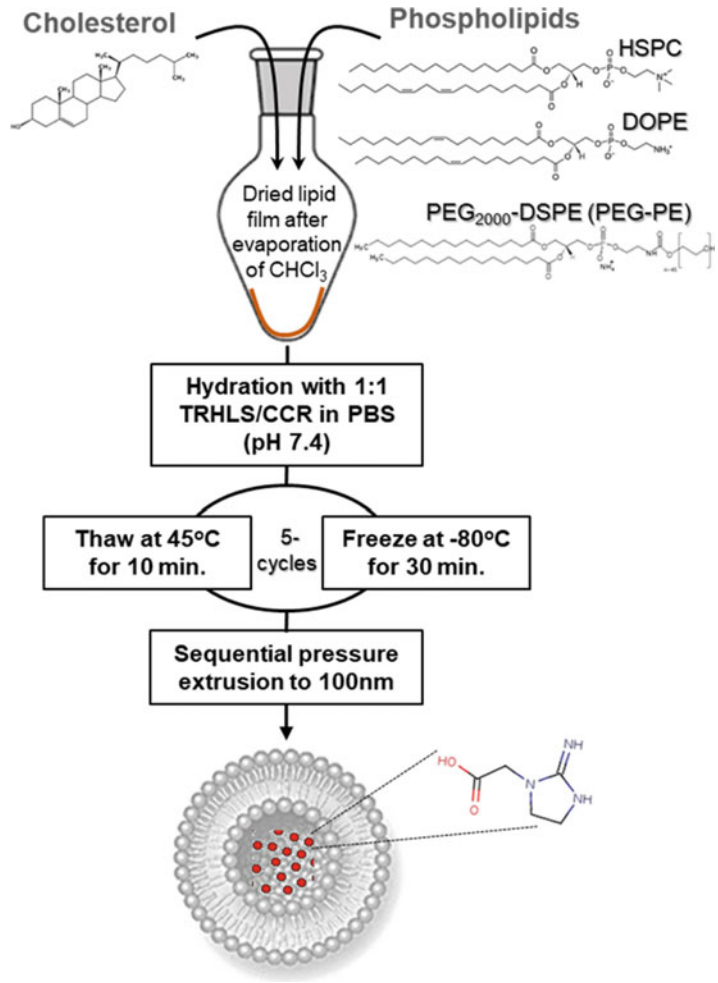


**Fig. 2** Method for preparation of CCR-loaded liposomes, specifically freeze–thaw vesicles (FTV) loaded with CCR

liposomes. Dissolve 3.57 mM $mPEG_{2000}$-DSPE/PEG-PE in 10 mL chloroform, to make 10 mg/mL PEG-PE stock solution. Store at −80 °C.

5. 1,2-Dioleoyl-*sn*-glycero-3-phosphoethanolamine (18:1 (Δ9-Cis) PE or DOPE) (Avanti Polar Lipids, Inc., Alabaster, AL). Dissolve 26.9 mM DOPE in 10 mL chloroform, to make 20 mg/mL DOPE stock solution. Store at −80 °C.
6. 1-Carboxymethyl-2-iminoimidazolidine (cyclocreatine, CCR) (Millipore Sigma, St. Louis, MO).
7. 25 mL pear-shaped and round-bottom glass flasks that fit rotary evaporator spout, for organic/cosolvent evaporation.
8. Rotary evaporator with vertical coiled condenser, RE100-Pro (Scilogix, LLC, Rocky Hill, CT) with rotation speed control,

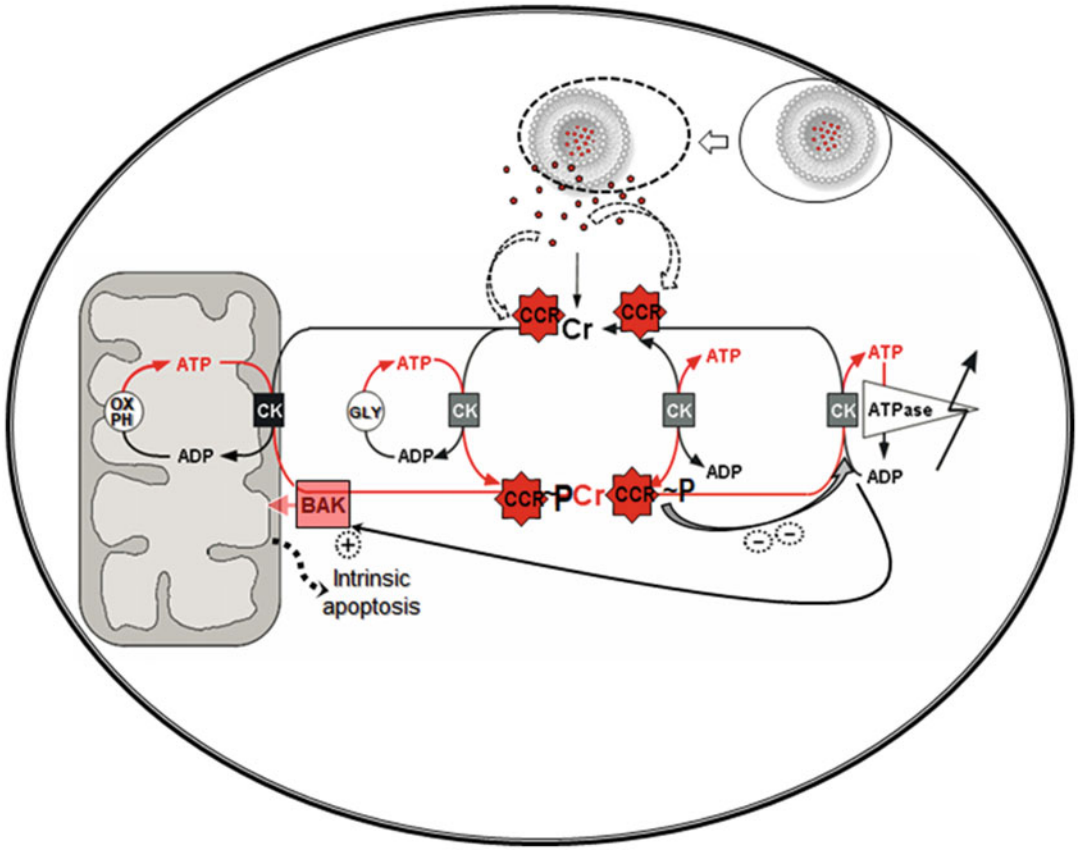


**Fig. 3** Representation of proposed intracellular effect of CCR-FTV liposomal delivery, curtailing CK/Cr-P shuttle, resulting in activation of AMPK, p53, and BAK, triggering mitochondria-mediated apoptosis

connected to a dry-vacuum pump capable of providing at least 100 mTorr of vacuum.

9. Stock (1×) phosphate buffered saline (PBS), pH 7.2. Dissolve 137.9 mM Sodium Chloride (8.0 g), 2.7 mM KCl (0.2 g), 1.8 mM $KH_2PO_4$ (0.24 g), 10 mM $Na_2HPO_4$ (1.44 g) in 800 mL of MQ water. Titrate to pH 7.2 with 1 M HCl, and then adjust final volume to 1 L. Store at 4 °C.
10. Benchtop lyophilizer, FreeZone 4.5 (Labconco, Kansas City, MO).
11. Nitrogen gas source, with flow meter regulator, adjustable from 10 to 60 CF/H.
12. Nitrogen gas operated LIPEX™ extruder (Northern Lipids Inc., Burnaby, BC, CA).
13. LIPEX™-compatible polycarbonate filter disks—size 100 nm, 200 nm, and 400 nm (Northern Lipids Inc., Burnaby, BC, CA).

14. Spectra/Por 6 Standard Regenerated Cellulose (RC) Dialysis Tubing, pretreated, 18 mm flat width, MWCO: 25 kD (25,000 Da) (Spectrum Chemical MFG Corp., New Brunswick, NJ).
15. Noncontact Infrared thermometer with laser sight (Temperature range: −50 °C to 38 °C, and minimum accuracy ±1.5 °C), for accurate measurement of external temperature of the LIPEX™ extruder barrel.
16. Weigh balance (up to 0.001 mg in precision for accuracy).
17. Pipette(s) capable of dispensing at 10 μL, 500 μL, and 1 mL.
18. 5 mL glass vials.
19. Milli-Q (MQ) water.

### 2.2 Determination of CCR Concentration

1. Triton X-100.
2. HPLC 250 × 4.6 mm (4 μm packing vol.) stainless steel column ACE PFP C-18 (Advanced Chromatography Technologies Ltd., Aberdeen, Scotland).
3. Waters 2695 Alliance HPLC system, with UV detector.
4. 25 mM phosphate buffer, pH 5.5. Dissolve 1.2 mM of $Na_2HPO_4{\cdot}7H_2O$ (0.327 g) and 23.8 mM of $NaH_2PO_4{\cdot}H_2O$ (3.28 g) in 800 mL of MQ water. Titrate to pH 5.5 with 1 M HCl, and then adjust final volume to 1 L. Store at 4 °C.
5. Tetrabutylammonium bisulfate (TBA, Sigma).
6. HPLC-grade methanol (Sigma).
7. Speed adjustable/digital orbital mixer.
8. 1 mL HPLC plastic vials.
9. Milli-Q (MQ) water.

### 2.3 Physicochemical Characterization of Prepared CCR-Liposomes (Plain and PEGylated)

1. Pipette(s) capable of dispensing at 10 μL, 500 μL, and 1 mL.
2. 5 mL glass test tubes.
3. Milli-Q (MQ) water.
4. Speed adjustable/digital orbital mixer.
5. Malvern Zetasizer Nano ZS (Malvern Instruments, Westborough, MA).
6. Disposable folded capillary (electrophoretic) cells for zeta potential measurements (Malvern Instruments, Westborough, MA).
7. Disposable low volume (1.5 mL capacity) 12 mm square polystyrene cuvettes, for particle size analysis.

### 2.4 MitoOrange Mitochondrial Polarization Assay

1. One vial of $1 \times 10^5$ cells of model human PC-3 metastatic prostatic carcinoma cell lie (American Type Culture Collection, ATCC catalog# CRL-1435™, Manassas, Virginia).
2. ATCC-formulated F-12 K Medium (F12K).
3. Fetal bovine serum (FBS-added to growth media as 10% vol/vol).
4. Complete serum-free medium (SFM, Gibco Biosciences, Dublin, Ireland).
5. 15 mL polystyrene centrifuge tube (1 per sample).
6. Hemacytometer.
7. Microfuge at 13,000 × *g*, Clinical centrifuge at 100–1000 × *g*.
8. Pipette(s) capable of dispensing at 10 μL, 500 μL, and 1 mL.
9. Graduated cylinder.
10. Cell culture grade sterile dimethyl sulfoxide (DMSO).
11. Vortex mixer.
12. Amber vials or polypropylene tubes for storage at −20 °C.
13. Cell culture plates 96-well opaque-walled plates compatible with fluorimeter, with clear flat bottom.
14. Multichannel pipettor(s), capable of dispensing at 50 μL and 500 μL.
15. Orange mitochondrial membrane potential assay kit (Abcam, Cambridge, MA).
16. Fluorescence plate reader with excitation 530–570 nm and emission 580–620 nm filter pair, Synergy 2 multimode microplate reader (BioTek Instruments, Winooski, VT).

## 3 Methods

### 3.1 Preparation of Empty and CCR-Loaded Freeze–Thaw Vesicles (FTV)/Liposomes

Prepare all FTV liposomal formulations using only clean glassware. Thoroughly clean the glassware and spatulas with concentrated nitric acid followed by ethanol. Make sure no residue of whitish phospholipids or drug remains in the glassware. Furthermore, use MQ water during the entire formulation processes to guarantee purified grade final product (Fig. 2).

1. Turn on the hot plate and adjust to 30 °C. Warm clean 25 mL beaker on the hot plate for 5 min, filled with (1×) phosphate buffered saline (PBS), adjusted to pH 7.2.
2. In a 25 mL pear-shaped glass flask, add phospholipid matrix components, 76.6 mMol of HSPC:DOPE:Chol in 2:1:1 M ratio (as 1.5 mL from 20 mg/mL 18:1 HSPC stock solution in chloroform, and 0.71 mL from 20 mg/mL DOPE stock solution in chloroform, plus 0.3 mL from 20 mg/mL Chol stock solution in chloroform) (*see* **Note 1**).

3. Connect pear-shaped glass flask to the rotary evaporator, and slowly evaporate organic solvent under 100 mTorr (26 Hg) vacuum, set at 50–60 rpm rotation, and 40 °C water bath temperature, for approx. 60 min (*see* **Notes 2** and **3**).
4. Release vacuum pressure, and carefully disconnect flask (*see* **Note 4**).
5. Freeze the diluted FTV dispersion by immersing the flask in liquid nitrogen, then place it into a freeze-drying glass flask, and keep in −80 °C freezer for 1 h.
6. Transfer flask from freezer directly into freeze-drying flask, seal and connect to benchtop lyophilizer, for at least 2 h, to remove any traces of organic solvent (*see* **Note 5**).
7. For empty FTV, using 1 mL pipette, gradually add 3 mL of warm (1×) PBS, pH 7.2, onto the warm mixture inside the 25 mL pear-shaped glass flask, mixing thoroughly but slowly, using vortex mixer at about 1000 rpm for 5 min, or until the entire lipid film on the glass has been dispersed in buffered solution (*see* **Note 6**).
8. Dissolve 25 mg of CCR in 5 mL of warm (1×) phosphate buffered saline and adjust pH 7.2.
9. For CCR-loaded FTV liposomes, using 1 mL pipette, gradually add 3 mL of warm CCR solution in (1×) phosphate buffered saline, pH 7.2, to lipid film in flask.
10. Freeze the dispersion, first by immersing the flask in liquid nitrogen at −80 °C for 5 min, then inside −80 °C freezer for 30 min, followed by thawing at 45 °C for 10 min.
11. Repeat freezing and thawing cycle five times.
12. Transfer the FTV liposomal samples (empty or CCR-loaded) to the LIPEX™ extruder, pass twice under 300 PSI nitrogen gas pressure, using first 400 mm filter disk. Run another two passes using the 200 nm filter, followed by two final passes using the 200 nm filter (*see* **Note 7**).
13. For CCR-loaded FTV samples, add the extruded liposomes to the dialysis bag of MWCO 250,000 Da, seal, and separate nonencapsulated CCR by dialysis against the (1×) PBS, pH 7.2 buffer at 4 °C overnight (*see* **Note 8**).
14. Dilute the liposomal formulations to a final concentration of 10 mg lipids/2.5 mg CCR/mL in phosphate buffered saline, pH 7.2 buffer.
15. Add $CaCl_2$ to a concentration 1.0 mM.
16. Store all FTV formulations at 4 °C for later use.

### 3.2 Determination of CCR

The level of liposomal CCR encapsulation is determined via HPLC.

1. Lyse CCR-containing liposomes with 0.5% (v/v) Triton X-100 in distilled water to release CCR from FTV liposomes.
2. Record the UV absorbance on a Waters 2695 Alliance HPLC system, with UV detector at 210 nm.
3. Perform chromatography, using sample volume of 20 μL, on a 250 × 4.0 mm stainless steel column, packed with 4 μm ACE Cl8. The chromatographic conditions are as follows: isocratic elution at room temperature with mobile phase for the first 10 min consisted of buffer A (25 mM phosphate buffer with 100 mg/L tetrabutylammonium, pH 5.0), then 1:1 vol/vol mixture with buffer B (25 mM phosphate buffer with 100 mg/L TBA, pH 5.0, and 10% acetonitrile) for the following 10 min, all run at a flow rate of 0.5 mL/min.
4. Record CCR-corresponding peaks at 5–6 min elution time.

### 3.3 Physical Characterization of Empty and Drug-Loaded FTV Liposomal Formulations

Produced FTV formulations are characterized for particle size and size distribution using the dynamic light scattering (DLS) technique with a Malvern Zetasizer Nano ZS (Malvern Instruments, Westborough, MA) at 273° fixed angle and at 23 °C temperature.

1. Dilute each FTV formulation, for particle size analysis, using MQ water at about 50 folds vol/vol, in disposable polystyrene cuvettes. The numbered average particle hydrodynamic diameter and the polydispersity index (PDI) will be determined (*see* **Note 9**).
2. For the zeta potential, dilute FTV samples in MQ water, pH 6.8, at 100–200 fold vol/vol, then employ a 1 mL syringe, horizontally, to insert the almost transparent solution carefully inside the folded capillary electrophoretic cell of the Malvern Zetasizer Nano ZS, while making sure to avoid inserting any air bubbles. The average surface charge will be measured (Fig. 2).

### 3.4 Orange Mitochondrial Polarization Assay in Cultured Human Prostatic Carcinoma Cells

Mitochondrial membrane potential, $\Delta\psi_m$, is an important parameter of mitochondrial function used as an indicator of cell health. The loss of mitochondrial membrane potential (MMP) is a hallmark for apoptosis. The Orange Mitochondrial membrane potential assay kit utilizes the lipophilic, cationic dye MitoOrange™ for the detection of the mitochondrial membrane potential change in cells. In normal cells, the orange fluorescence intensity is increased when MitoOrange™ dye is accumulated in the mitochondria. However, in apoptotic cells, the fluorescence intensity of MitoOrange™ dye is decreased following the collapse of MMP (Fig. 4).

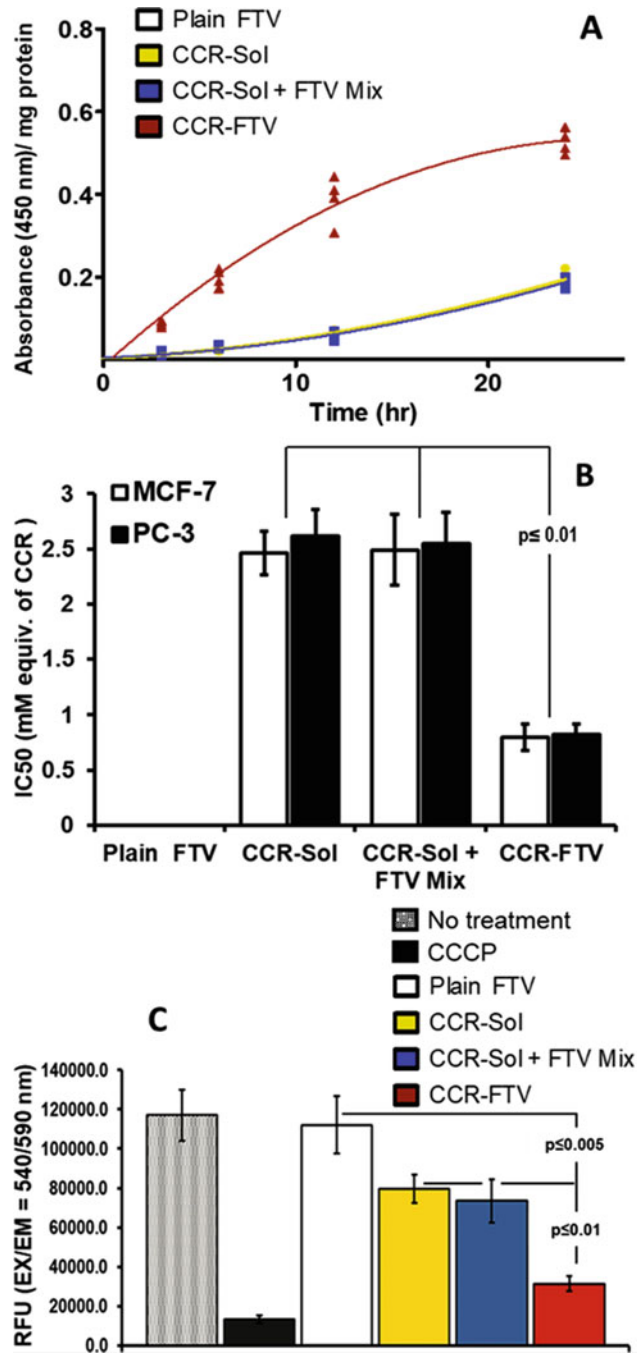


**Fig. 4** In vitro assays of CCR-FTV formulation in human carcinomas. (**a**) Kinetics of cancer cell uptake of CCR formulations; (**b**) ATP-Lite™ assay of cytotoxic effectiveness (expressed as IC50 values) of CCR-FTV liposomes, following 48 h treatment of two human carcinoma cell lines; (**c**) Orange mitochondrial membrane potential assay of CCR-formulations, in PC-3 prostatic small cell carcinoma, 24 h postincubation with 2 mM of CCR-equivalent concentration ($n = 4$, data $\pm$ SE)

1. Set up 96-well assay clear flat bottom plates (opaque/black walled), containing approximately $2 \times 10^4$ cells in 100 μL of complete F12K cell culture media per well.
2. Allow PC-3 cells to attach to the bottom of the plate for 24 h. Cell would be ready to the next step when they are about 60–70% confluent.
3. Add the various vehicle controls, as well as test formulations, containing the different CCR treatments, all diluted 5× at minimum, in SFM and applied to test wells in twofold serial dilution pattern. Make sure the final volume is 100 μL in each well (*see* **Note 10**).
4. Culture cells for 42 h test exposure period (*see* **Notes 11** and **12**).
5. Remove assay plates from 37 °C incubator, and remove all CCR and FTV-containing media and SFM controls.
6. Warm all component of the kit to room temperature.
7. Add 50 μL of the supplied 200× MitoOrange™ Dye into 10 mL of Assay Buffer A, and mix well using vortex mixer, to prepare MitoOrange dye-loading solution.
8. Apply cell wash to all wells containing cells, by carefully and slowly adding 50 μL of Hank's balanced buffer saline (HBS), leaving in well for 5 s, then removing HBS solution, repeat this step twice for the entire plate, taking extreme caution to minimize dislodging attached cells inside each well.
9. Finally, add 100 μL of MitoOrange dye-loading solution to each well.
10. Shake plate for 10 s, to mix reagent well.
11. Incubate at 37 °C, using the same standard cell culture conditions for 20–30 min.
12. Insert the developed plate in the plate reader, and set assay protocol/method to shake plate for 10 s, then record end point fluorescence using ex.540/em.590 nm filter set.

## 4 Notes

1. For PEGylated/Stealth FTV liposomes, containing 4.5 M% of PEG-PE in formulations, add 3.45 mM of PEG-PE (as 0.98 mL from 10 mg/mL of PEG-PE stock solution in) directly as a part of the phospholipid mixture, all dissolved in organic solvent.
2. While the vacuum is best adjusted based on each solvent, for optimized solvent removal via the rotary evaporator system, apply the 20/40/60 "technical" rule, which correlates to at

least 20 °C difference in temperature between the system's main components. Use operating bath temperature of at least 43 °C (glass transition temperature of main phospholipid, HSPC), to yield a solvent vapor temperature of 20 °C, which is subsequently condensed at about 0 °C (using ice–water mix to cool the condenser).

3. For efficient and complete evaporation of organic solvent, make sure to keep the connected pear-shaped flask, is tilted at about 60–45° angle to the plane of the surrounding warm water bath. For improved ethanol evaporation, also increase the flask's rotation speed to about 90 rpm.
4. Complete removal of organic solvent is confirmed when a translucent off-white dry film residue remains in the flask, which may get somewhat opaquer as the flask temperature cools down. The dried lipid film must be clear from any suspending white or yellowish lipid clumps or precipitates. Otherwise, redissolve in another 4 mL of chloroform, and repeat the evaporation process, using slightly lower water bath temperature (−1.0 °C), and vacuum settings.
5. Make sure the benchtop lyophilizer has stabilized (vacuum pressure reached at least $p < 200 \times 10^{-3}$ mbar, condenser temperature $\leq -50$ °C), prior to and after connecting the sample freeze-drying flask, then leave undisturbed for 2 h.
6. Optional: briefly put pear-shaped flask in bath sonicator (only for 2–3 min) to dislodge resistant dried lipid film remains, present on the inside glass wall of flask.
7. Prewarm the thermobarrel LIPEX™ extruder to about 45 °C (measured externally using noncontact IR thermometer), before running the liposomal samples, to guarantee smooth flow-pass through the filter. Make sure to run sample through the larger pore-size filter disk first, before the smaller pore size one, to avoid clogging of the filter disk.
8. Be very careful handling the dialysis tubing—it is very delicate and can be easily damaged when opening/closing the sealing clips. Make sure not to puncture the tubing with the pipette tips, during the introduction or withdrawal of samples.
9. Optional: for enhanced numerical accuracy, compare measured average particle hydrodynamic diameter and the polydispersity index (PDI) for empty and CCR-loaded FTV, consistently using the volume analysis/volume statistics function, available in the output analysis parameters.
10. Perform the twofold serial dilution step by sequentially transferring 100 μL vol. of first row original liposomal dispersion into the following corresponding row of wells, then mixing via 3× repeated pipetting, followed by transferring the same volume (100 μL) into the corresponding subsequent row of wells.

11. Set up quadruplicate wells with untreated cells to serve as a negative vehicle control. Add the same solvent used to deliver the test compounds to the vehicle control wells.
12. Set up quadruplicate wells with cells treated with 25 μM of CCCP, added simultaneously with the MitoOrange dye-loading solution, serving as a positive control, to represent maximum apoptosis.

## References


1. Lillie JW, O'Keefe M, Valinski H, Hamlin HA Jr, Varban ML, Kaddurah-Daouk R (1993) Cyclocreatine (1-carboxymethyl-2-iminoimidazolidine) inhibits growth of a broad spectrum of cancer cells derived from solid tumors. Cancer Res 53:3172–3178
2. Miller EE, Evans AE, Cohn M (1993) Inhibition of rate of tumor growth by creatine and cyclocreatine. Proc Natl Acad Sci U S A 90:3304–3308
3. Martin KJ, Chen SF, Clark GM, Degen D, Wajima M, Von Hoff DD, Kaddurah-Daouk R (1994) Evaluation of creatine analogues as a new class of anticancer agents using freshly explanted human tumor cells. J Natl Cancer Inst 86:608–613
4. Martin KJ, Winslow ER, Kaddurah-Daouk R (1994) Cell cycle studies of cyclocreatine, a new anticancer agent. Cancer Res 54:5160–5165
5. Wyss M, Kaddurah-Daouk R (2000) Creatine and creatinine metabolism. Physiol Rev 80:1107–1213
6. Matthews RT, Ferrante RJ, Klivenyi P, Yang L, Klein AM, Mueller G, Kaddurah-Daouk R, Beal MF (1999) Creatine and cyclocreatine attenuate MPTP neurotoxicity. Exp Neurol 157:142–149
7. Hoosein NM, Martin KJ, Abdul M, Logothetis CJ, Kaddurah-Daouk R (1995) Antiproliferative effects of cyclocreatine on human prostatic carcinoma cells. Anticancer Res 15:1339–1342
8. Ara G, Gravelin LM, Kaddurah-Daouk R, Teicher BA (1998) Antitumor activity of creatine analogs produced by alterations in pancreatic hormones and glucose metabolism. In Vivo 12:223–231
9. Martin K, Winslow E, Okeefe M, Khandekar V, Hamlin A, Lillie J, Kaddurahdaouk R (1996) Specific targeting of tumor cells by the creatine analog cyclocreatine. Int J Oncol 9:993–999
10. Martin KJ, Vassallo CD, Teicher BA, Kaddurah-Daouk R (1995) Microtubule stabilization and potentiation of taxol activity by the creatine analog cyclocreatine. Anti-Cancer Drugs 6:419–426
11. Schiffenbauer YS, Tempel C, Abramovitch R, Meir G, Neeman M (1995) Cyclocreatine accumulation leads to cellular swelling in C6 glioma multicellular spheroids: diffusion and one-dimensional chemical shift nuclear magnetic resonance microscopy. Cancer Res 55:153–158
12. Teicher BA, Menon K, Northey D, Liu J, Kufe DW, Kaddurah-Daouk R (1995) Cyclocreatine in cancer chemotherapy. Cancer Chemother Pharmacol 35:411–416
13. Bergnes G, Yuan W, Khandekar VS, O'Keefe MM, Martin KJ, Teicher BA, Kaddurah-Daouk R (1996) Creatine and phosphocreatine analogs: anticancer activity and enzymatic analysis. Oncol Res 8:121–130
14. Schimmel L, Khandekar VS, Martin KJ, Riera T, Honan C, Shaw DG, Kaddurah-Daouk R (1996) The synthetic phosphagen cyclocreatine phosphate inhibits the growth of a broad spectrum of solid tumors. Anticancer Res 16:375–380
15. Kristensen CA, Askenasy N, Jain RK, Koretsky AP (1999) Creatine and cyclocreatine treatment of human colon adenocarcinoma xenografts: 31P and 1H magnetic resonance spectroscopic studies. Br J Cancer 79:278–285
16. Jeong KS, Park SJ, Lee CS, Kim TW, Kim SH, Ryu SY, Williams BH, Veech RL, Lee YS (2000) Effects of cyclocreatine in rat hepatocarcinogenesis model. Anticancer Res 20:1627–1633
17. Atchison N, Swindlehurst G, Papas KK, Tsapatsis M, Kokkoli E (2014) Maintenance of ischemic beta cell viability through delivery of lipids and ATP by targeted liposomes. Biomater Sci 2:548–559
18. Levchenko TS, Hartner WC, Verma DD, Bernstein EA, Torchilin VP (2010) ATP-loaded liposomes for targeted treatment in models of myocardial ischemia. Methods Mol Biol 605:361–375

19. Maril N, Degani H, Rushkin E, Sherry AD, Cohn M (1999) Kinetics of cyclocreatine and Na(+) cotransport in human breast cancer cells: mechanism of activity. Am J Phys 277: C708–C716
20. Schiffenbauer YS, Meir G, Cohn M, Neeman M (1996) Cyclocreatine transport and cytotoxicity in rat glioma and human ovarian carcinoma cells: 31P-NMR spectroscopy. Am J Phys 270:C160–C169
21. Elbayoumi TA, Torchilin VP (2010) Current trends in liposome research. Methods Mol Biol 605:1–27
22. Elbayoumi TA (2010) Nano drug-delivery systems in cancer therapy: gains, pitfalls and considerations in DMPK and PD. Ther Deliv 1:215–219

# Chapter 12

# Mt-fura-2, a Ratiometric Mitochondria-Targeted $Ca^{2+}$ Sensor. Determination of Spectroscopic Properties and $Ca^{2+}$ Imaging Assays

**Andrea De Nadai, Nicola Vajente, Diana Pendin, and Andrea Mattarei**

## Abstract

$Ca^{2+}$ handling by mitochondria is implicated in energy production, shaping of cytosolic $Ca^{2+}$ rises, and determination of cell fate. It is therefore of crucial interest for researchers to directly measure mitochondrial $Ca^{2+}$ concentration [$Ca^{2+}$] in living cells. Synthetic fluorescent $Ca^{2+}$ indicators, providing a straightforward loading technique, represents a tempting strategy. Recently, we developed a new highly selective mitochondria-targeted $Ca^{2+}$ indicator named mt-fura-2, obtained by coupling two triphenylphosphonium cation-containing groups to the molecular backbone of the cytosolic ratiometric $Ca^{2+}$ indicator fura-2.

The protocols we describe here cover all the significant steps that are necessary to characterize the probe and apply it to biologically relevant contexts. The procedures reported are referred to mt-fura-2 but could in principle be applied to characterize other mitochondria-targeted $Ca^{2+}$ probes. More in general, with the due modifications, this chapter can be considered as a handbook for the characterization and/or application of mitochondria-targeted chemical $Ca^{2+}$ probes.

**Key words** mt-fura-2, $Ca^{2+}$ indicator, $Ca^{2+}$ probe, Mitochondria, Fluorescence, Absorption, Affinity, Quantum yield, $Ca^{2+}$ imaging

## 1 Introduction

Calcium ($Ca^{2+}$) signaling is a master player in essential physiological processes (e.g., muscle contraction, neuronal transmission, cellular motility, and apoptosis). Mitochondria, by taking up and releasing $Ca^{2+}$ to the cytosol, contribute to the shaping of both the amplitude and the time course of cytosolic $Ca^{2+}$ signals. Conversely, $Ca^{2+}$ entered in the mitochondrial matrix through the mitochondrial $Ca^{2+}$ uniporter (MCU) is essential for the regulation of mitochondrial specific functions [1–3]. Indeed, $Ca^{2+}$ handling by mitochon-

Andrea De Nadai and Nicola Vajente contributed equally to this work.

Volkmar Weissig and Marvin Edeas (eds.), *Mitochondrial Medicine: Volume 1: Targeting Mitochondria*, Methods in Molecular Biology, vol. 2275, https://doi.org/10.1007/978-1-0716-1262-0_12,

dria has been implicated in crucial processes such as energy production and determination of cell fate. It is therefore of interest for researchers to directly measure mitochondrial $Ca^{2+}$ concentration [$Ca^{2+}$] in living cells and several attempts have been made in the past years to generate suitable sensors [4]. Genetically encoded $Ca^{2+}$ indicators (GECIs) are quite popular because of their greatest advantage compared to chemical dyes, that is, the existence of strategies for targeting specific subcellular compartments [5]. Despite this obvious advantage, GECIs present some drawbacks, the most relevant being the need for their delivery of invasive or laborious procedures that cannot be applied to all cell types or present safety-related issues (e.g., transfection, viral infection, and electroporation).

Small organic fluorescent $Ca^{2+}$ indicators, providing a straightforward loading technique, represents a tempting strategy, especially but not exclusively for cell types where the delivery of GECIs is troublesome. Chemical $Ca^{2+}$ indicators consist of an organic fluorophore moiety, determining their photophysical properties, and a chelating domain, usually 1,2-bis(*o*-aminophenoxy)ethane-*N*,*N*,*N*′,*N*′-tetraacetic acid (BAPTA), with high selectivity for $Ca^{2+}$ [6]. Acetoxymethyl ester (AM) protected forms of these indicators are the cell-permeant versions that allow their loading into many cells at the same time. This provides the advantage to trap fluorescent $Ca^{2+}$ indicators in the cytosol of living cells, once the AM groups are hydrolyzed by esterases [7], due to the high hydrophilicity of the free acid form. According to the spectral changes occurring upon $Ca^{2+}$ binding, fluorometric $Ca^{2+}$ indicators are classified as intensometric dyes, in which fluorescence varies as a function of $Ca^{2+}$ binding, or as dual-excitation (or -emission) wavelength indicators, that allow for calibrated [$Ca^{2+}$] measurements through excitation or emission ratiometry. Ratiometric dyes minimize the most common problems associated with synthetic indicators, that is, heterogeneous dye loading, photobleaching, dye leakage, and changes in focal plane [4]. Of note, the aforementioned, nonratiometric dyes are unsuitable to quantitatively evaluate $Ca^{2+}$ in mitochondria, where events such as opening of permeability transition pore (PTP) would lead to probe leakage, resulting in a decrease of fluorescence that would be misinterpreted as a decrease of [$Ca^{2+}$].

Recently, we developed a new highly selective mitochondria-targeted $Ca^{2+}$ indicator [8] named mt-fura-2, obtained by coupling two triphenylphosphonium cation-containing groups to the molecular backbone of the cytosolic ratiometric $Ca^{2+}$ indicator fura-2. Using a combination of spectroscopic, biochemical and cell biology techniques, we determined the characteristics of mt-fura-2 and performed mitochondrial matrix [$Ca^{2+}$] measurements in living cells.

Mt-fura-2 shows excitation wavelength shifts upon $Ca^{2+}$ binding and high selectivity for $Ca^{2+}$ over $Mg^{2+}$. The dissociation constant is ~1.5 μM in vitro and its $Ca^{2+}$ binding properties are not affected by pH changes in the physiological range or by the presence of hydrogen peroxide. Upon loading as acetoxymethyl ester, the probe shows proper mitochondrial localization and $[Ca^{2+}]$ measurements can be obtained in cell types where the delivery of GECIs via standard methods is difficult to achieve, that is, primary cultures.

Herein we describe in detail all the protocols necessary to characterize mt-fura-2 and to apply it to biologically relevant contexts. In particular, we will outline the procedures necessary to characterize the probe from a spectroscopic point of view (i.e., absorbance and fluorescence properties, affinity for $Ca^{2+}$, dependence on pH and other interferants) and use it for $[Ca^{2+}]$ measurements in living cells.

## 2 Materials

### 2.1 Solutions and Reagents

All solutions should be prepared using ultrapure water (prepared by purifying deionized water, to attain a sensitivity of 18 MΩ × cm at 25 °C) and analytical grade reagents.

To ensure the lowest contaminating $[Ca^{2+}]$ in the solutions, glassware has to be carefully cleaned with 10 mM HCl, then rinsed abundantly with milliQ water prior to the preparation of each solution.

#### 2.1.1 General Solutions and Reagents

1. mt-fura-2 acetoxymethyl ester (−AM): 1 mM mt-fura-2/AM (synthesized as described in [8] (*see* **Note 1**)) in DMSO; aliquot the solution and store at −20 °C protected from light.
2. mt-fura-2 free acid (–COOH): 1 mM mt-fura-2/COOH (synthesized as described in [8] (*see* **Note 1**)) in DMSO; aliquot the solution and store at −20 °C protected from light.
3. fura-2 free acid (–COOH): 1 mM fura-2/COOH (pentapotassium salt, commercially available) in DMSO; aliquot the solution and store at −20 °C protected from light.
4. Standard $CaCl_2$ solutions: 1 mM, 10 mM, 100 mM $CaCl_2$ in water. Dilute 1 M $CaCl_2$ standard solution (commercially available) in milliQ water.
5. EGTA: 500 mM EGTA, pH 8.0 (buffered with TRIS). Weigh EGTA powder in a beaker on a magnetic stirrer, add 80 mL of milliQ water and keep the suspension in agitation at 37 °C. Adjust the pH to 8 with TRIS base (powder). Note that to dissolve EGTA the suspension must be alkalinized by addition of TRIS. Adjust the volume with milliQ water in a 100 mL volumetric flask. For long-term storage, keep the solution at 4 °C.

*2.1.2 Solutions and Reagents for Spectroscopic Evaluation*

1. Solution for spectroscopic measurements (S): 130 mM KCl, 20 mM NaCl, 20 mM TRIS HCl, and 1 mM $MgCl_2$, pH 7 at 37 °C. Weigh each compound and add it to a beaker on a magnetic stirrer. Add milliQ water to about 900 mL volume. Mix the solution and adjust the pH to 7 at 37 °C using a concentrated solution of KOH. Adjust the volume with milliQ water in a 1 L volumetric flask. The solution can be stored in a glass bottle at 4 °C. For long-term storage, aliquot the solution and keep it at −20 °C.
2. Quinine sulfate stock solution: 3 mM quinine sulfate in 0.1 M $H_2SO_4$.
3. HCl solution: 1 M HCl in milliQ water.
4. KOH solution: 1 M KOH in milliQ water.
5. Solutions of $MgCl_2$, $MnCl_2$ and $ZnCl_2$: 0.1 mM, 1 mM, 10 mM, 100 mM, 1000 mM of the respective salt dissolved in TRIS 20 mM at pH 7.
6. $H_2O_2$ solution: 1 M $H_2O_2$ in milliQ water.

*2.1.3 Solutions and Reagents for Imaging Experiments*

1. Extracellular-like solution (EC): 135 mM NaCl, 20 mM HEPES, 5 mM KCl, 1 mM $MgCl_2$, 10 mM glucose, pH 7.4 at 37 °C. Weigh each compound and add it to a beaker on a magnetic stirrer. Add milliQ water to about 900 mL volume. Mix the solution and adjust the pH to 7 at 37 °C using pellets or a concentrated solution of NaOH. Adjust the volume with milliQ water in a 1 L volumetric flask (*see* **Note 2**). The solution can be stored in a glass bottle at 4 °C. For long-term storage, aliquot the solution and store at −20 °C.
2. Intracellular-like solution (IC): 130 mM KCl, 20 mM HEPES, 10 mM NaCl, 1 mM $MgCl_2$, pH 7 at 37 °C. Weight each compound and add it to a beaker on a magnetic stirrer. Add milliQ water to about 900 mL volume. Mix the solution and adjust the pH to 7.4 at 37 °C using pellets or a concentrated solution of KOH. Adjust the volume with milliQ water in a 1 L volumetric flask (*see* **Note 2**). Store the solution in a glass bottle at 4 °C. For long-term storage, aliquot the solution and store at −20 °C.
3. Pluronic F-127: 20% (w/v) Pluronic F-127 in water. To avoid powder clumping, it is critical to prepare the solution by adding slowly Pluronic-F127 powder while stirring. The solution is stable for a few months at RT. For long-term storage, aliquot the solution and store at −20 °C.
4. Cell culturing medium and transfection reagent for the cell type of choice.
5. Plasmid DNA encoding a mitochondria-targeted fluorescent protein (i.e., mt-RFP, [9, 10]) (*see* **Note 3**).

6. Bovine serum albumin (BSA) solution: 2% (w/v) BSA in water. Weigh BSA and add it slowly while stirring to avoid clumping.
7. Digitonin solution: 100 mM digitonin in water, aliquot and store at −20 °C.
8. CCCP solution: 1 mM CCCP in DMSO, aliquot and store at −20 °C.
9. Cyclosporin A solution: 1 mM cyclosporin A in DMSO, aliquot and store at −20 °C.
10. Histamine solution (*see* **Note 4**): 100 mM histamine in water, aliquot and store at −20 °C.

## 2.2 Equipment

### 2.2.1 General Equipment

1. Set of adjustable volume micropipettes (P10, P20, P200, and P1000).
2. pH-meter: to perform pH dependency measurements a pH-meter equipped with a micro electrode is required (e.g., Metrohm, length 11.3 cm, diameter 6 mm, pH 0–14, 0–80 °C).

### 2.2.2 Equipment for In Vitro Evaluation

1. Standard quartz cuvettes for fluorescence and absorption measurements (optical path = 1 cm).
2. Thermostated Varian Cary 100 spectrophotometer coupled to a H1 lamp for visible wavelengths and a deuterium lamp for $\lambda < 350$ nm or analogous instruments.
3. Thermostated Varian Cary Eclipse fluorometer coupled to a Xenon pulsed source or analogous instruments. The presence of magnetic stirring is recommended.

### 2.2.3 Equipment for Imaging Experiments

1. Confocal microscope equipped with 60–100 × UV-permeable objective; laser lines adequate to excite mt-fura-2 and a spectrally distinct fluorescent protein, for example, UV/405 nm and 543 nm laser lines.
2. Fluorescence microscope suitable for $Ca^{2+}$ imaging experiments that allows to alternate excitation wavelengths. A system adapted for fura-2 imaging is also suitable for mt-fura-2. As an example, the systems we use is composed of: Monochromator equipped with a 50–75 W lamp able to alternate 340–380 nm excitation wavelength; A neutral density filter, a dichroic mirror FF-409-DiO3 and an emission filter 510/84 nm; Objectives 20–40 × UV-permeable; Highly sensitive CCD or sCMOS cameras. A microscope acquisition software that supports online calculation of ratio is not essential but is certainly helpful to monitor $[Ca^{2+}]$ dynamics in real time as the experiment proceeds. We use Roboscope, a custom-made software developed by Catalin Ciubotaru at VIMM, Padua, Italy or Nis-Elements (Nikon). However, other pieces of software (e.g., MetaFluor from Universal Imaging) can be used as well.

3. Perfusion system to ensure exchange of solutions, when necessary along the imaging experiment (*see* **Note 5**). Alternatively, it is possible to use manual addition and mixing (*see* **Note 6**).
4. Open or closed bath imaging chambers (*see* **Note 7**).
5. Temperature control system: in the case of cells that require a temperature higher than RT (most commonly 37 °C), a heating system is required. A chamber heater combined with an in-line solution heater is usually enough to guarantee temperature control. An objective heater can be added (*see* **Note 8**).
6. Offline analysis software: for example, Fiji (National Institutes of Health, NIH) (freeware downloadable at https://imagej.net/ImageJ); Microsoft Excel or an equivalent data analysis software; Origin (OriginLab Corporation) or GraphPad Prism (GraphPad Software, Inc).

## 3 Methods

### 3.1 Before Starting: Determination of the Residual [$Ca^{2+}$] in Solutions

$Ca^{2+}$ is a ubiquitous ion and small but not negligible amounts of it are generally present in the inorganic salts and glassware used to prepare experimental solutions. The determination of the residual [$Ca^{2+}$] present in solution S is required before starting the spectroscopic characterization of mt-fura-2.

1. Switch on the fluorometer and set it at 37 °C at least 1 h before the experiment, in order to allow the stabilization of the experimental temperature and the emission spectra of the lamps.
2. Add 3 mL of solution S in a clean capped cuvette with a magnetic stir bar.
3. Insert the cuvette in the thermostated fluorometer, activate the magnetic stirrer and wait at least 5 min in order to stabilize the temperature before starting the analysis.
4. Add 0.5 μM of commercially available fura-2/COOH (e.g., 1.5 μL of 1 mM solution in DMSO).
5. Set the slits to 5/10 or 2.5/5 nm (excitation/emission) and the photomultiplier tube (PMT) to 600 V or 800 V.
6. Record the excitation spectrum in the wavelength range 300–450 nm, $\lambda_{em} = 510$ nm. This corresponds to residual $Ca^{2+}$ in solution (contaminating $Ca^{2+}$).
7. Add 50 μM EGTA (e.g., 0.3 μL of 500 mM EGTA solution) and record the excitation spectrum using the same instrumental setup. This corresponds to minimal [$Ca^{2+}$].
8. Add 500 μM $Ca^{2+}$ (e.g., 15 μL of 100 mM standard $CaCl_2$ solution) and record the excitation spectrum using the same instrumental setup. This corresponds to maximal [$Ca^{2+}$].

9. Determine the concentration of contaminating $Ca^{2+}$ ions using the Grynkiewicz equation [11]:

$$\left[Ca^{2+}\right] = K_d \times \beta \times \left(\frac{R_{residual} - R_{Ca^{2+}_{min}}}{R_{Ca^{2+}_{max}} - R_{residual}}\right)$$

where $K_d = 224$ nM for fura-2 at 37 °C in solution S, $R = \frac{F_{\lambda_1}}{F_{\lambda_2}}$, $\beta = \frac{F_{\lambda_2,Ca^{2+}_{min}}}{F_{\lambda_2,Ca^{2+}_{max}}}$, $F_{\lambda_1}$ is the fluorescence ($F$) value measured at $\lambda_1 = 340$ nm, and $F_{\lambda_2}$ is the $F$ value measured at $\lambda_2 = 380$ nm.

### 3.2 Investigation of Absorption Properties of mt-fura-2

The UV-Vis absorption spectra of $Ca^{2+}$-free, $Ca^{2+}$-bound, and -AM forms of mt-fura-2 are measured to determine the wavelengths of maximum absorption (*see* **Note 9**).

1. Switch on the UV-Vis spectrophotometer and set it at 37 °C at least 1 h before the experiment, in order to stabilize the experimental temperature and the emission spectra of the lamps.
2. Add 3 mL of solution S in a clean, capped cuvette.
3. Insert the cuvette in the UV-Vis spectrophotometer and wait at least 5 min in order to stabilize the temperature before starting the analysis.
4. Record the baseline between 300 and 600 nm.
5. Add 5 μM mt-fura-2/COOH (e.g., 15 μL of 1 mM solution in DMSO) and mix well (*see* **Note 10**).
6. Add 50 μM EGTA (e.g., 0.3 μL of 500 mM EGTA solution) in order to chelate contaminant $Ca^{2+}$ ions present in solution and mix well (*see* **Note 11**).
7. Record the UV-Vis spectrum (*see* **Note 12**) in the wavelength range 300–600 nm. This corresponds to the spectrum at minimum (virtually zero) $[Ca^{2+}]$ (Fig. 1a).
8. Add 500 μM $Ca^{2+}$ (e.g., 15 μL of 100 mM standard $Ca^{2+}$ solution) and mix well (*see* **Note 13**).
9. Record the UV-Vis spectrum in the wavelength range 300–600 nm. This corresponds to the spectrum at maximum $[Ca^{2+}]$ (Fig. 1a).
10. Wash the cuvette accurately (*see* **Note 14**).
11. If of interest, repeat the procedure to measure the absorbance spectrum of the -AM form of mt-fura-2 (*see* **Note 15**). In this case, since the $Ca^{2+}$ chelating moiety is covered by the AM protecting groups, the absorbance properties of the probe do not change in the presence/absence of $Ca^{2+}$. For this reason, no addition of $Ca^{2+}$ or EGTA is required.

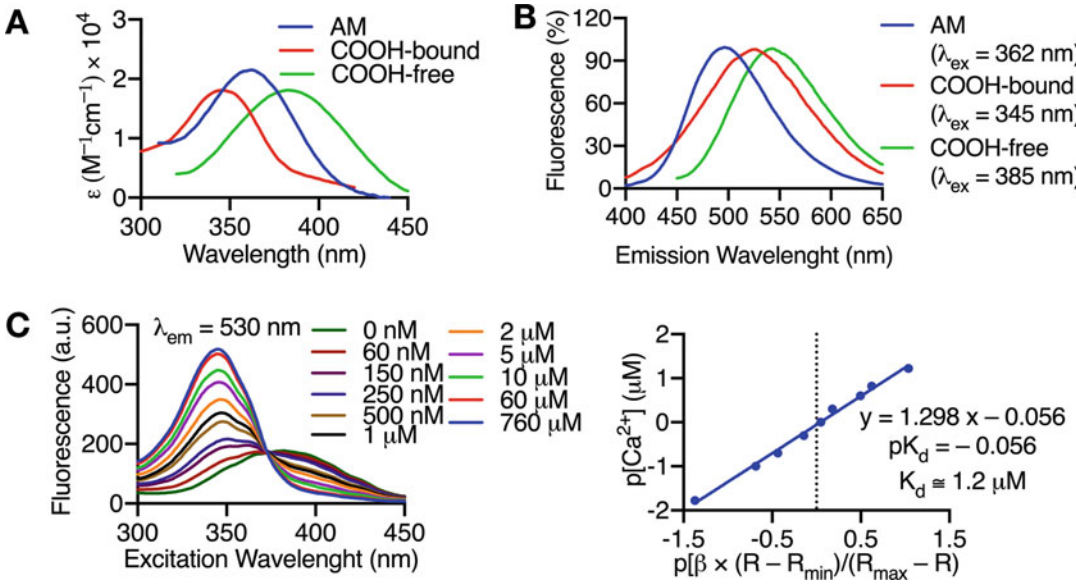


**Fig. 1** (**a**) Absorption spectra of the indicated forms of mt-fura-2 (5 μM) recorded at 37 °C in solution S. (**b**) Normalized emission spectra of the indicated forms of mt-fura-2 (2 μM) recorded at 37 °C in solution S upon excitation at the indicated wavelengths. (**c**) *Left.* Excitation spectra of mt-fura-2/COOH (2 μM) recorded at 37 °C in solution S, in the presence of the indicated [$Ca^{2+}$]. Emission was measured at 530 nm. *Right.* Determination of $K_d$ value by linearization of the experimental data (measured ad $\lambda_{ex} = 340$ nm and 400 nm) according to Grynkiewicz's method. $R_{min} = 0.5$, $R_{max} = 13.3$, $\beta = 4.3$, DR = 26

### *3.3 Investigation of Fluorescence Spectroscopic Properties of mt-fura-2*

#### *3.3.1 Optimization of the Experimental Parameters of the Fluorometer*

A preliminary experiment is necessary to determine the appropriate experimental setup (slit width, PMT voltage, etc.) (*see* **Note 16**) and the wavelengths of maximum emission for the $Ca^{2+}$-free, $Ca^{2+}$-bound and -AM form of the probe.

1. Switch on the fluorometer and set it at 37 °C at least 1 h before the experiment, in order to allow the stabilization of the experimental temperature and the emission spectra of the lamps.
2. Add 3 mL of solution S in a capped cuvette with a magnetic stir bar.
3. Insert the cuvettes in the fluorometer, activate the magnetic stirrer and wait at least 5 min in order to stabilize the temperature before starting the analysis.
4. As a starting set up, set the slits to 5/10 mm and the PMT to 800 V. Set the detection speed at 120 nm × $min^{-1}$.
5. Record the emission spectrum in the wavelength range 380–650 nm, setting $\lambda_{ex} = 361$ nm (maximum absorption of the -AM form, identified in Subheading 3.2), in order to verify the absence of spurious emission bands.
6. Add 1–2 μM of mt-fura-2/AM (e.g., 3–6 μL of 1 mM solution in DMSO).

7. Wait 5 min to allow the automatic mixing of the solution. In the absence of an automatic stirrer, mix manually with a clean pipette.
8. Record the emission spectrum in the wavelength range 380–650 nm, $\lambda_{ex} = 361$ nm (Fig. 1b).
9. Based on the results obtained, adjust the slits width in order to optimize the signal (*see* **Note 17**).
10. Once satisfactory emission spectra have been recorded, identify the wavelength of maximum emission ($\lambda_{em} = 502$ nm for mt-fura-2/AM).
11. Record the excitation spectrum in the wavelength range 300–450 nm, $\lambda_{em} = 502$ nm (maximum emission identified in **step 10**, this Section).
12. Wash the cuvette accurately (*see* **Note 14**).
13. Repeat **steps 2–5**.
14. Add 1–2 μM of mt-fura-2/COOH (e.g., 3–6 μL of 1 mM solution in DMSO) and 500 μM $Ca^{2+}$ (e.g., 15 μL of 100 mM standard $CaCl_2$ solution) (*see* **Note 13**) to obtain saturating [$Ca^{2+}$].
15. Record the emission spectrum in the wavelength range 400–700 nm, $\lambda_{ex} = 345$ nm (wavelength of maximum absorption of the –COOH-$Ca^{2+}$-bound form, identified in Subheading 3.2) and identify the wavelength of maximum emission ($\lambda_{em} = 520$ nm for mt-fura-2/COOH-$Ca^{2+}$-bound) (Fig. 1b).
16. Based on the results obtained, adjust the slits width and PMT voltage in order to optimize the signal (*see* **Note 17**).
17. Record the excitation spectrum in the wavelength range 300–450 nm, $\lambda_{em} = 520$ nm (maximum emission determined in **step 15**, this Section).
18. Wash the cuvette accurately (*see* **Note 14**).
19. Repeat **steps 2–5**.
20. Add 1–2 μM of mt-fura-2/COOH (e.g., 3–6 μL of 1 mM solution in DMSO) and 50 μM EGTA (e.g., 0.3 μL of 500 mM EGTA solution) (*see* **Note 11**) to reach virtually zero [$Ca^{2+}$].
21. Maintaining the experimental parameters optimized for mt-fura-2/COOH-$Ca^{2+}$-bound form in terms of slits width, PMT and scan speed, record the emission spectrum in the wavelength range 450–700 nm, $\lambda_{ex} = 385$ nm (maximum absorption of mt-fura-2/COOH-$Ca^{2+}$-free, identified in Subheading 3.2) and identify the wavelength of maximum emission ($\lambda_{em} = 540$ nm for mt-fura-2/COOH-$Ca^{2+}$-free) (Fig. 1b).

22. Record the excitation spectrum in the wavelength range 300–450 nm, $\lambda_{em}$ = 540 nm (maximum emission identified in **step 21**, this Section).
23. All the spectra obtained can be smoothed using the functions implemented in the software used for data analysis, for example, using the moving-average function by a factor of 4 and a second order polynomial smoothing factor.

### *3.3.2 Determination of $Ca^{2+}$ Binding Properties and Dynamic Range (DR) of mt-fura-2*

Affinity for $Ca^{2+}$ ion (dissociation constant, $K_d$) (*see* **Note 18**) and DR (*see* **Note 19**) are key determinants for a $Ca^{2+}$ probe. Their determination allows to perform quantitative measurements of $[Ca^{2+}]$.

1. Switch on the fluorometer at least 1 h before the experiment and set it at 37 °C, in order to allow the stabilization of the experimental temperature and the emission spectra of the lamps.
2. Add 3 mL of solution S in a capped cuvette with a magnetic stir bar.
3. Insert the cuvette in the fluorometer, activate the magnetic stirrer and wait at least 5 min in order to stabilize the temperature before starting the analysis.
4. Use the experimental setup optimized in Subheading 3.3.1 for mt-fura-2/COOH (e.g., slits 5/10 nm, PMT 800 V, and scan speed 120 nm × $min^{-1}$).
5. Record the excitation spectrum in the wavelength range 300–450 nm (*see* **Note 20**), $\lambda_{em}$ = 530 nm (*see* **Note 21**) in order to verify the absence of spurious excitation bands.
6. Add 2 μM of mt-fura-2/COOH (e.g., 6 μL of 1 mM solution in DMSO).
7. Record the excitation spectrum in the wavelength range 300–450 nm, $\lambda_{em}$ = 530 nm (*see* **Notes 20** and **21**) (Fig. 1c).
8. Add 150–200 nM of $Ca^{2+}$ (e.g., 4.6–6.0 μL of $Ca^{2+}$ 100 μM) corresponding to about 0.1–0.2 × the expected $K_d$ value) and record the excitation spectrum (Fig. 1c).
9. Repeat **step 8** adding progressively increasing $[Ca^{2+}]$ using the standard solutions, until no fluorescence variations are recorded (at least 12–15 spectra until a $[Ca^{2+}]$ of about 100–250 × the expected $K_d$ value is reached) (*see* **Notes 22** and **23**) (Fig. 1c).
10. Wash accurately the cuvette (*see* **Note 14**) and repeat the experiment at least three times.
11. In case the residual $[Ca^{2+}]$ in the solution used is close to the $K_d$, it is advisable to perform measurements as described in

**Table 1**
**Matrices for the calculation of *R* values for each combination of excitation wavelengths. *R* values have been determined in the absence of $Ca^{2+}$ ($R_{min}$ in Matrix A, *left*) and in saturating $Ca^{2+}$ ($R_{max}$ in Matrix B, *right*)**

| Matrix **A** | | | $F_{\lambda_{isos}}$ $\lambda_{isosb}$ | ... $\rightarrow$ | $F_{\lambda_{max}}$ $\lambda_{max}$ | Matrix **B** | | | $F_{\lambda_{isos}}$ $\lambda_{isosb}$ | ... $\rightarrow$ | $F_{\lambda_{max}}$ $\lambda_{max}$ |
|---|---|---|---|---|---|---|---|---|---|---|---|
| $F_{Ca^{2+}_{min}}$ | | Wavelength (nm) | $\lambda_{isosb}$ | ... | $\lambda_{max}$ | $F_{Ca^{2+}_{max}}$ | | Wavelength (nm) | $\lambda_{isosb}$ | ... | $\lambda_{max}$ |
| $F_{\lambda_{min}}$ | $\lambda_{min}$ $\downarrow$ $\lambda_{isosb}$ | $\lambda_{min}$ | $\frac{F_{\lambda_{min}}}{F_{\lambda_{isos}}}$ $A_{11}$ | ... | $\frac{F_{\lambda_{min}}}{F_{\lambda_{max}}}$ $A_{n1}$ | $F_{\lambda_{min}}$ | $\lambda_{min}$ $\downarrow$ $\lambda_{isosb}$ | $\lambda_{min}$ | $\frac{F_{\lambda_{min}}}{F_{\lambda_{isos}}}$ $B_{11}$ | ... | $\frac{F_{\lambda_{min}}}{F_{\lambda_{max}}}$ $B_{n1}$ |
| ... | | ... | ... | ... | ... | ... | | ... | ... | ... | ... |
| $F_{\lambda_{isos}}$ | | $\lambda_{isosb}$ | $\frac{F_{\lambda_{isos}}}{F_{\lambda_{isos}}}$ $A_{1n}$ | ... | $\frac{F_{\lambda_{max}}}{F_{\lambda_{isos}}}$ $A_{nn}$ | $F_{\lambda_{isos}}$ | | $\lambda_{isosb}$ | $\frac{F_{\lambda_{isos}}}{F_{\lambda_{isos}}}$ $B_{1n}$ | ... | $\frac{F_{\lambda_{max}}}{F_{\lambda_{isos}}}$ $B_{nn}$ |

**Table 2**
**Matrix reporting DR values for each combination of excitation wavelengths. DR values have been calculated as the ratio between values in Matrix B and Matrix A (Table 1)**

| | Matrix **DR** | $\lambda_{isosb} \rightarrow \lambda_{max}$ | | |
|---|---|---|---|---|
| | Wavelength (nm) | $\lambda_{isosb}$ | ... | $\lambda_{max}$ |
| $\lambda_{min}$ $\downarrow$ | $\lambda_{min}$ | $DR_{11} = \frac{A_{11}}{B_{11}}$ | ... | $DR_{n1} = \frac{A_{n1}}{B_{n1}}$ |
| | ... | ... | ... | ... |
| $\lambda_{isosb}$ | $\lambda_{isosb}$ | $DR_{1n} = \frac{A_{1n}}{B_{1n}}$ | ... | $DR_{nn} = \frac{A_{nn}}{B_{nn}}$ |

**steps 2–7** also in $Ca^{2+}$-buffered solutions (instead of standard solution S), containing a predetermined amount of free [$Ca^{2+}$] (*see* **Note 24**).

12. Report *F* values recorded at each couple of excitation wavelengths $\lambda_1$ and $\lambda_2$ building the two matrices **A** and **B** (Table 1). Ratio between the values calculated in Matrix **A** and Matrix **B** gives the Matrix **DR** with DR values for each couple of wavelengths $\lambda_1$ and $\lambda_2$ (Table 2). Results can be displayed in a 2D projection as shown in Fig. 2a. Another quick method to determine the wavelengths of maximum DR is described in **Note 25** (Fig. 2b).
13. Determine actual [$Ca^{2+}$] present in solution for each fluorescence spectrum recorded. This is calculated taking into account residual [$Ca^{2+}$] in solution S and the dilution factor due to the addition of solutions (*see* **Note 26**).
14. Determine the $K_d$ in the experimental conditions by interpolating experimental data using Grynkiewicz equation [11]. $pK_d$ is identified by the intercept value of the fitting plot of $p[Ca^{2+}]$ versus $p\left[\beta \times \left(\frac{R-R_{min}}{R_{max}-R}\right)\right]$ (*see* **Note 18**).

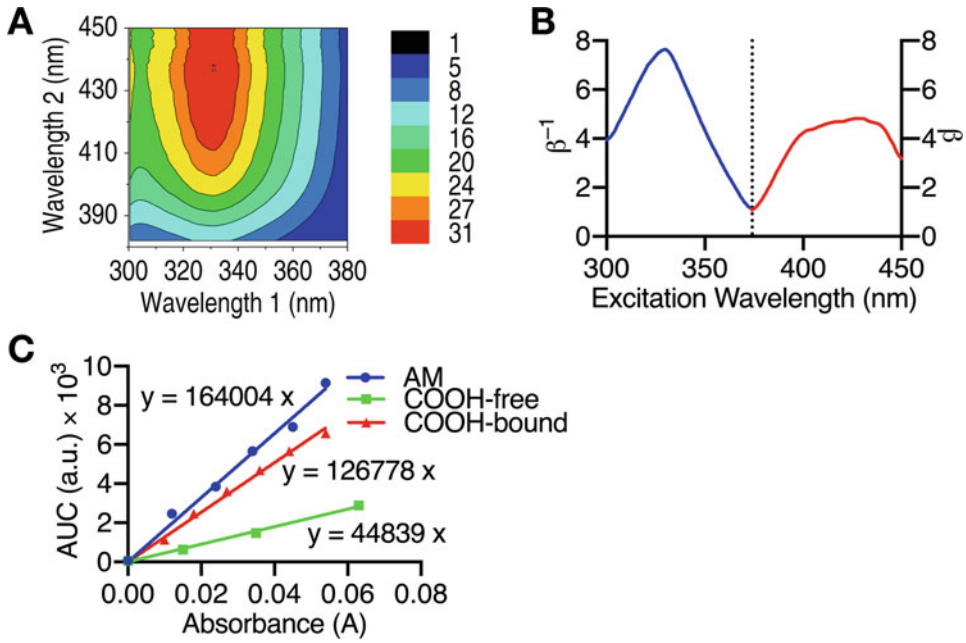


**Fig. 2** (**a**) 2D representation of the DR values calculated for each couple of excitation wavelengths. (**b**) Plot of $\beta$ (for $\lambda > \lambda_{isosbestic}$) and $\beta^{-1}$ (for $\lambda < \lambda_{isosbestic}$). The two maxima indicate the wavelength ranges where DR is maximal. (**c**) Absorbance maximum value plotted against the AUC of the fluorescence emission spectrum obtained at different concentrations for each of the indicated forms of mt-fura-2

*3.3.3 Determination of Fluorescence Quantum Yield (QY)*

1. QY can be determined for each form of the probe (–COOH-$Ca^{2+}$-bound, –COOH-$Ca^{2+}$-free, -AM protected) (*see* **Note 27**) by comparison with QY of the standard Quinine Sulfate in $H_2SO_4$ 0.1 M (*see* **Note 28**) [12].
2. Set the instrumental temperature of the fluorometer and the spectrophotometer at 25 °C (*see* **Notes 29** and **30**).
3. Add 3 mL of $H_2SO_4$ 0.1 M and 2 μM of Quinine sulfate (e.g., 2 μL of 3 mM solution) in a capped fluorescence cuvette.
4. As a starting instrumental setup use slit width 5/5 nm and PMT 600 V. Record the emission fluorescence spectrum by exciting the sample at 345 nm and recording the emission in the range 380–630 nm.
5. Optimize the instrumental setup, in order to reach a maximum value of emitted fluorescence of about 0.15–0.25× the maximum value detectable (generally 150–250 a.u., when maximum is 1000 a.u.). This experimental setup will be used for all the measurements with mt-fura-2 probe forms.
6. Wash the cuvette accurately (*see* **Note 14**).

7. Add 3 mL of $H_2SO_4$ 0.1 M in a fluorescence cuvette, then record the absorption spectrum and the emission spectra of the blank using the optimized experimental parameters ($\lambda_{ex}$ = 345, 361, and 385 nm, $\lambda_{em}$ = 400–650 nm).
8. Add 2 μM of Quinine sulfate (e.g., 2–2.5 μL of 3 mM solution) and record the complete absorbance spectrum.
9. Move the cuvette to the fluorometer and record emission fluorescence spectra upon excitation 345, 361, and 385 nm ($\lambda_{em}$ = 400–650 nm).
10. Repeat the addition of quinine sulfate and the recording of absorbance and fluorescence spectra (**steps 8** and **9**) until an absorbance value closed to 0.1 is obtained or the maximum value of the emitted fluorescence detectable is reached (at least 4–6 additions).
11. Wash the cuvette accurately (*see* **Note 14**).
12. Repeat the operations **7**–**11** using each of the three forms of the probes (mt-fura-2/AM, mt-fura-2/COOH-$Ca^{2+}$-free and -$Ca^{2+}$-bound) using as a solvent solution S. Set the temperature at 37 °C (*see* **Note 30**) while keeping unchanged all the other instrumental parameters. Wavelengths and initial concentrations used for each form are: (1) mt-fura-2/AM: $\lambda_{ex}$ = 361 nm, $\lambda_{em}$ = 400–650 nm, 0.3–0.5 μM/addition; (2) mt-fura-2/COOH-$Ca^{2+}$-free (measured in the presence of EGTA 50 μM): $\lambda_{ex}$ = 385 nm, $\lambda_{em}$ = 450–700 nm, 0.6–1.0 μM/addition; (3) mt-fura-2/COOH-$Ca^{2+}$-bound (measured in the presence of $Ca^{2+}$ 500 μM): $\lambda_{ex}$ = 345 nm, $\lambda_{em}$ = 400–650 nm, 1.0–1.5 μM/addition.
13. Calculate the Area Under the Curve (AUC) of each emission fluorescence spectra recorded (*see* **Note 31**).
14. Plot the AUC values versus the absorbance at the selected $\lambda_{ex}$ for all the concentrations tested of each compound (Fig. 2c).
15. Trace the fitting line forced to pass through the origin for each compound (Fig. 2c).
16. Determine QYs by applying the equation described in **Note 32**.

### 3.4 Determination of the Optimal Excitation Wavelengths at the Microscope

Note that this evaluation can be done only if in your experimental set up the excitation wavelength can be selected specifically, with a precision of at least ±5 nm, for example with a fluorescence microscope equipped with a monochromator.

1. Mount a clean glass coverslip in an imaging chamber and mark the surface with a water-resistant marker.
2. Add on top of the coverslip 1 mL of IC solution.

3. At the fluorescence microscope focus the mark at the surface of the coverslip.
4. Perform a wavelength scan: starting from the excitation wavelength of 320 nm (and until you reach 410 nm), increase $\lambda_{ex}$ by 5–10 nm and record the emitted fluorescence; these values correspond to the background fluorescence.
5. Remove 100 μL of solution from the imaging chamber and put them into an empty tube.
6. Add to the solution in the tube 50 μM mt-fura-2/COOH and 0.5 mM EGTA, to reach minimum $[Ca^{2+}]$, and mix thoroughly.
7. Mix the 100 μL with the solution in the imaging chamber.
8. Perform a wavelength scan as described in **step 4**; these values correspond to the spectrum at minimum $[Ca^{2+}]$.
9. Remove 100 μL of solution from the imaging chamber and put them into an empty tube.
10. Add to the 100 μL in the tube 5 mM $CaCl_2$ to reach maximum $[Ca^{2+}]$ and mix thoroughly.
11. Mix the 100 μL with the solution in the imaging chamber.
12. Repeat the wavelength scan as described in **step 4**; these values correspond to the spectrum at maximum $[Ca^{2+}]$.
13. Discharge the coverslip and wash accurately the imaging chamber (*see* **Note 33**).
14. Repeat **steps 1–13** at least three times.
15. Export the .tif file of the recording of the experiment.
16. Using a software of your choice (see the postmeasurement analysis described in Subheading 3.6.5 for more details), draw a region of interest (ROI) in the field of view and measure the fluorescence intensity (FI) recorded upon excitation at 320 to 410 nm at minimum $[Ca^{2+}]$.
17. Repeat **step 16** with images recorded for the background fluorescence and at maximum $[Ca^{2+}]$.
18. Subtract the FI value of background fluorescence from the FI value at the corresponding wavelength recorded in the presence of minimum or maximum $[Ca^{2+}]$.
19. Plot the data obtained as wavelength versus mean FI (background subtracted).
20. It is possible to proceed calculating R and dynamic range as reported in Subheading 3.3.2 for measurements performed at the fluorometer. However, the highest DR often does not correlate with the best acquisition setup. Indeed, very low signals recorded at minimal $[Ca^{2+}]$ around 340 nm (*see*

**Note 34**) contributes to artificially decrease $R_{min}$. Moreover, UV light induces high cytotoxicity. All these issues must be taken into account when determining the best combination of excitation wavelengths to be used at the fluorescence microscope.

### 3.5 Investigation of the Dependence of Fluorescence Properties by Other Interfering Species

Before starting each experiment, prepare the set up as described in Subheading 3.3.1.

#### 3.5.1 Determination of Dependence of Fluorescence by ROS Species (See **Note 35**)

1. Add mt-fura-2/COOH 2 μM to 6.5 mL of Solution S in a test tube.
2. Split the solution in two cuvettes, 3 mL each.
3. Add 50 μM of EGTA (e.g., 0.3 μL of EGTA 500 mM) in the first cuvette and 500 μM of $Ca^{2+}$ (e.g., 15 μL of $Ca^{2+}$ 100 mM) in the second (about 100–250 × $K_d$).
4. Record the excitation fluorescence spectra.
5. Add 1 mM of $H_2O_2$ (e.g., 3 μL of $H_2O_2$ 1 M) in both cuvettes.
6. Record the excitation fluorescence spectra every 4–5 min for 16–20 min using the cycling mode of the fluorometer.
7. Plot the data and compare the spectra.

#### 3.5.2 Determination of the Affinity for Other Inorganic Cations

BAPTA-based fluorescent dyes show affinity for double charged cations (*see* **Note 36**) that might interfere with $Ca^{2+}$ quantification in biological environment.

1. Add 3 mL of solution S in a cuvette, then add mt-fura-2/COOH (2 μM).
2. Add progressively increasing amount of a cation of interest until no fluorescence variation is recorded.
3. Data can be analyzed as described for $Ca^{2+}$ in Subheading 3.3.2, in order to determine the affinity constant for competitive cations. Alternatively, the concentrations of a cation that determines respectively a fluorescence quench of 10, 50 and 90% can be determined.

#### 3.5.3 Determination of pH Dependence of Fluorescence

pH plays a crucial role in the chelation of $Ca^{2+}$ for BAPTA-based fluorescence probes and it is crucial to verify whether $[H^+]$ could affect $[Ca^{2+}]$ measurements in the physiological pH range (*see* **Note 37**).

1. Add 3 mL of solution S in a cuvette, then add mt-fura-2/COOH (2 μM) and EGTA (50 μM).

2. Acidify progressively the solution by adding HCl 1 M while measuring pH inside the cuvette with a calibrated pH-meter equipped with a microelectrode.
3. When pH 7 is reached, record the excitation fluorescence spectra to investigate the pH dependence of carboxylic $Ca^{2+}$-free form.
4. Increase the pH by adding KOH 1 M while measuring pH inside the cuvette (volume suggested of 10 μL/addition).
5. When pH 9 is reached, record the excitation fluorescence spectra.
6. Repeat the experiment in the presence of 500 μM $Ca^{2+}$ to investigate the pH dependence of carboxylic $Ca^{2+}$-bound form.

### 3.6 Loading and Imaging Procedures in Cells

All the protocols described here have been optimized for HeLa cells, and small adjustments could be required if other cell types are used. The protocols can also be adapted for the loading of cells in suspension.

#### 3.6.1 Cell Culturing and Plating: General Considerations

HeLa cells are kept in culture and transfected following standard protocols. Cells are detached 1 day before the experiment and plated on glass coverslips (*see* **Note 38**). Depending on the diameter of the coverslips and the rate of cell growth, different amount of cells may be seeded; as a rule of thumb, consider that the day of the experiment cells should be around 80–90% confluence. Plated cells are grown in an incubator at 37 °C and 5% $CO_2$ for 24 h before the loading.

#### 3.6.2 Loading of mt-fura-2 in Cultured Cells

Cells are plated on glass coverslips 24 h before loading.

1. Prepare a 10× loading mix (*see* **Note 39**) containing: 0.2% (w/v) Pluronic F-127 (*see* **Note 40**), 10 μM mt-fura-2/AM, and EC + $Ca^{2+}$ solution to reach a final volume of 100 μL. It is crucial to prepare the mix in a tube following the order (*see* **Note 41**): Pluronic–mt-fura-2/AM–EC solution and mix thoroughly by pipetting after the addition of each component.
2. Carefully remove one coverslip from the cell culture medium and place it in an empty plate.
3. Gently wash the cells on the coverslip once with 1 mL of EC + $Ca^{2+}$ solution prewarmed at 37 °C.
4. Bath the cells with 900 μL of EC + $Ca^{2+}$ prewarmed at 37 °C.
5. Add the 100 μL of mt-fura-2 loading solution to the 900 μL of EC + $Ca^{2+}$ and mix gently by pipetting.
6. Incubate the cells with mt-fura-2 for 35 min (*see* **Note 42**) at 37 °C (*see* **Note 43**).
7. Move the coverslip to a new well filled with 1 mL of fresh EC + $Ca^{2+}$ solution, prewarmed at 37 °C.
8. Incubate in EC + $Ca^{2+}$ for 10 min (*see* **Note 44**) at 37 °C.

### 3.6.3 Evaluation of Subcellular Localization of mt-fura-2

Cells are plated on glass coverslips 24 h before transfection. Note that the amount of cells plated has to be scaled to obtain 60% confluence the day of transfection.

1. Transfect the cells with mt-RFP encoding plasmid DNA (*see* **Note 45**) following standard protocols and incubate at 37 °C and 5% $CO_2$ for 24 h.
2. Load the cells with mt-fura-2 as described in Subheading 3.6.2.
3. Move the coverslip from the plate to an imaging chamber and cover the cells with 1 mL of EC + $Ca^{2+}$ solution prewarmed at 37 °C.
4. Place the imaging chamber in a suitable heating system, to keep the temperature at 37 °C during imaging.
5. Acquire images of live cells at the confocal microscope (*see* **Note 46**), using UV/405 nm to visualize mt-fura-2 and the proper excitation/emission parameters for the selected fluorescent protein. As an example, in case of a mt-RFP, we used a 543 nm laser line.
6. Analyze acquired images using for example ImageJ software; use the "Coloc 2" plugin to calculate the Pearson's and Mander's colocalization coefficients.

### 3.6.4 $Ca^{2+}$ Imaging: IP3-Mediated ER $Ca^{2+}$ Release

1. Load the cells with mt-fura-2/AM following the protocol described in Subheading 3.6.2.
2. Mount the coverslip into an imaging chamber and bath cells with 1 mL of EC + $Ca^{2+}$ prewarmed at 37 °C.
3. Place the imaging chamber in a suitable heating system, in order to keep the temperature at 37 °C during imaging.
4. Set the peristaltic pump by positioning an input and an output tube on the opposite borders of the imaging chamber and start the perfusion of EC + $Ca^{2+}$ (*see* **Note 47**).
5. Set the microscope with the best illumination wavelength couple, previously determined (Subheading 3.4) and select exposure time and interval between subsequent acquisitions (*see* **Note 48**).
6. Use bright-field illumination to focus on cells.
7. Switch to fluorescence illumination and choose the field of view: every cell should be loaded with mt-fura-2, however some fields of view may contain cell debris or cells where loading is not exclusively mitochondrial (Fig. 3a).
8. If the acquisition software allows so, define the regions of interest (ROIs) (*see* **Note 49**) (Fig. 3a).
9. Start the recording.

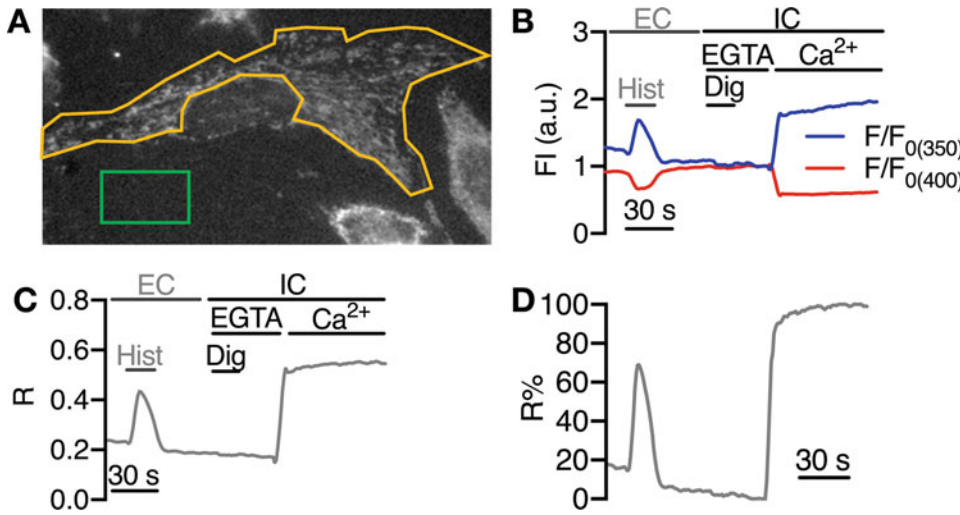


**Fig. 3** (**a**) HeLa cells loaded with mt-fura-2/AM and imaged at a fluorescence microscope. Green square has been selected as a background ROI, orange polygonal ROI delineates the region of the cell occupied by mitochondrial network. (**b**) Representative traces of the $F/F_0$ values obtained upon excitation at $\lambda_{ex} = 350$ nm (blue line) and 400 nm (red line) during a typical imaging experiment. $F_0$ value has been calculated as the mean of 10 points recorded at the minimal [$Ca^{2+}$]. Stimuli were applied as indicated, while cells are bathed in EC solution (gray) or IC solution (black). Hist, histamine; Dig, digitonin. (**c**) Representative trace of the Ratio calculated as $R = F_{350}/F_{400}$ relative to the imaging experiment described in **b**. (**d**) Changes in $R$ normalized to $R_{max}$, calculated as: $R\% = (R - R_{min})/(R_{max} - R_{min}) \times 100$ where $R_{max}$ and $R_{min}$ are the $R$ values obtained upon permeabilization at saturating [$Ca^{2+}$] and in the absence of $Ca^{2+}$, respectively

10. Record for a couple of minutes to allow equilibration of the cells (*see* **Note 50**). This measurement corresponds to resting mitochondrial [$Ca^{2+}$].
11. Change the solution in EC + $Ca^{2+}$ + 100 μM Histamine (or another IP3-generating stimulus, *see* **Note 51**).
12. After the peak in R value due to mitochondrial uptake of $Ca^{2+}$ released from the ER, change the solution perfusing EC solution + EGTA (500 μM) for a few minutes.
13. Change the solution perfusing IC containing EGTA (500 μM) for 30 s.
14. Permeabilize the cells with IC solution containing digitonin (100 μM) and EGTA (500 μM) for 1 min (*see* **Note 52**).
15. Change the solution perfusing IC containing EGTA (500 μM), CCCP (1 μM), and Cyclosporin A (800 nM) (*see* **Note 53**) until a plateau in $R$ values is reached; this value is considered the fluorescence at the minimum [$Ca^{2+}$].
16. Change the solution by perfusing fresh IC solution containing saturating [$Ca^{2+}$] (200 μM) to record the fluorescence at maximum [$Ca^{2+}$] (*see* **Note 54**).

17. Stop the recording.
18. If possible, export the mean fluorescence intensity (FI) measured for each ROI and each time point at the two excitation wavelengths (Fig. 3b), otherwise export the images sequence acquired as .tif files (if possible, export separate files for each wavelength).
19. Refer to Subheading 3.6.5 for postmeasurement analysis.

### 3.6.5 Post Measurement Analysis

1. If your acquisition software of choice allows to export FI data collected from each ROI, start the analysis from **step 13**.
2. Otherwise, open a .tif image sequence for one excitation wavelength (e.g., $\lambda_{ex} = 400$ nm) with an analysis software of your choice. Here we refer on analysis performed with Fiji, however similar plugins/commands can be found in other analysis software.
3. With one of the selection tools (e.g., rectangle) draw a ROI where the fluorescence of the probe is absent (i.e., no cells are present); this ROI is referred as background (BG) ROI and represents the autofluorescence level at the coverslip.
4. Follow the menu Analyze > Tools > ROI Manager (keyboard shortcut [Ctrl + t]), to open the ROI Manager window and add the drawn BG ROI (keyboard shortcut [t]).
5. Draw one ROI for each cell where to measure the fluorescence (*see* **Note 55**) and add each of them to the ROI Manager.
6. Select all the ROIs in the ROI Manager window and select "Measure" from the list on the right of the ROI Manager window.
7. On the Results window, select Set Measurement from the Results menu and check only Mean Grey Value; the output data in the Results window is the mean of the FI in each ROI over time, obtained upon illumination at 400 nm.
8. Copy and paste the FI values ($\lambda_{ex} = 400$ nm) for each ROI into an analysis software, for example Microsoft Excel.
9. Without closing the ROI Manager window, open the .tiff image sequence corresponding to the second excitation wavelength (e.g., $\lambda_{ex} = 350$ nm).
10. Repeat **steps 6–9** to obtain the mean of the FI over time obtained upon illumination at 350 nm in the same ROIs.
11. Copy and paste the FI values ($\lambda_{ex} = 350$ nm) for each ROI into an analysis software, for example, Microsoft Excel.
12. For each wavelength, subtract from the FI value recorded for each ROI at a certain time point, the FI value of the background ROI corresponding to the same time point.

13. Plot time-course $F/F_0$ (Fig. 3b) for each wavelength. $F_0$ value is calculated as the mean of 10 points recorded at the beginning of the experiment, after baseline is stable, or when minimal $[Ca^{2+}]$ is obtained (i.e., upon cell permeabilization and EGTA perfusion).
14. Calculate for each time point the $R$ between the FI recorded upon excitation at the two $\lambda_{ex}$ as $R = FI_{350}/FI_{400}$.
15. Plot time-course $R$ values of the selected ROIs (Fig. 3b, c).
16. Calculate the mean $R$ value in the presence of minimum $[Ca^{2+}]$ ($R_{min}$) and maximum $[Ca^{2+}]$ ($R_{max}$): the DR for mt-fura-2 in situ can be calculated as $DR = R_{max}/R_{min}$.
17. $R_{min}$ and $R_{max}$ values obtained in each experiment can be used to convert the $R$ data into $R$% values (*see* **Note 56**) (Fig. 3d), as follows:

$$R\% = \left(\frac{R - R_{min}}{R_{max} - R_{min}}\right) \times 100$$

18. Calculate parameters of interest using an analysis software such as Origin or Prism GraphPad. Examples of useful parameters related to the kinetics of $Ca^{2+}$ uptake by mitochondria that can be extrapolated from the experiment described in Subheading 3.6.4 are as follows:
    (a) *Peak Height*: gives an estimation of the maximal $[Ca^{2+}]$ reached within mitochondria upon stimulation;
    (b) *Peak Area*: AUC (calculated using plugins for integral measurement) gives an estimation of the $Ca^{2+}$ entering mitochondria during the stimulus;
    (c) *Uptake Rate*: (calculated using plugins of Origin software for derivative calculus on the first points during influx) indicates the speed of $Ca^{2+}$ increase within mitochondrial matrix.

## 4 Notes

1. Mt-fura-2/COOH and mt-fura-2/AM are not commercially available yet. They have been prepared in the laboratories of the authors through a 20 steps synthesis [8]. The authors would be willing to provide them based on a MTA.
2. NaOH is used to alkalinize solutions containing higher $Na^+$ (compared to $K^+$) ions concentration (i.e., EC solution), KOH instead is used to alkalinize solutions containing higher $K^+$ (compared to $Na^+$) concentration (i.e., IC solution).

3. It is preferable, if possible, to use well-separated excitation wavelengths, to avoid interference between the fluorophores. For colocalization studies, we transfected cells with mt-RFP.
4. Or another IP3-generating stimulus, depending on the cell type used.
5. Solution changes or drug additions are generally obtained through a perfusion system to ensure fast exchanging of solutions. Set the perfusion pump flow rate at 2–3 mL/min; the solution in the perfusion chamber should be completely exchanged in less than 1 min. Please note that some hydrophobic drugs, such as the ionophore ionomycin, stick to plastic tubes. In these cases, abundant washing of the perfusion system with 2% BSA is mandatory to wash away the drug from the tubes. As a recommended alternative, hydrophobic drugs can be added manually with a pipette after stopping the perfusion (*see* **Note 6**).
6. Manual addition can be used as an alternative to perfusion. It is advisable to practice with manual additions before starting an experiment, since they should be performed quickly but carefully, to avoid changing in the focus. Furthermore, the solution has to be mixed within a few seconds from the addition, to ensure a homogeneous bathing of cells. If manual addition of stimuli is performed, it is advisable that the volume of the addition is about the 10% of the solution present in the imaging chamber.
7. Imaging chambers can be found as "open" or "closed." In case you decide to use a perfusion system for solution exchange, ensure that it fits with the imaging chamber.
8. The temperature of each device should be set in order to guarantee that the solution in the chamber remains at 37 °C during the experiment. When setting up the system, the actual temperature of the solution bathing cells should be verified using a thermocouple probe.
9. The wavelengths of maximum absorption determine the optimal excitation wavelengths for the probe. Moreover, recording absorption spectra allows to determine the maximum concentration of the dye that guarantees the linear proportionality of fluorescence with probe concentration (i.e., $A < 0.1$).
10. The concentration of the probe may need optimization. The maximum value of absorbance recorded along the spectrum should be about 0.2–0.3. In case you record too high or too low absorbance values, repeat the experiment decreasing or increasing the concentration of the dye, respectively.
11. Generally, for high-affinity probes the concentration of EGTA that allows chelation of virtually all $Ca^{2+}$ present in solution is

at least 2–3× the [$Ca^{2+}$]. Considering that the contaminant [$Ca^{2+}$] present in standard solutions does not exceed 3 μM, a concentration of EGTA higher than 10 μM is adequate to record spectra at minimal [$Ca^{2+}$].

12. Conventionally, spectra are represented in terms of molar extinction coefficient at each wavelength ($\varepsilon_\lambda$).
13. It is suggested to increase [$Ca^{2+}$] until no variations in the absorbance spectra are observed; final [$Ca^{2+}$] will be about 50–100× the expected $K_d$ value.
14. Between sequential experiments, the cuvettes are washed with milliQ water, then with EGTA (100–200 μM), then absolute EtOH and finally flushed out with the solvent of the upcoming experiment (generally solution S).
15. Absorbance spectra of the -AM form are necessary to calculate the quantum yield of the probe in its protected form (*see* Subheading 3.3.3).
16. In order to obtain a precise fluorometric characterization, it is crucial to determine the optimal slit width and the amplification power of the PMT. These parameters are necessary to achieve the higher signal intensity without reaching the saturation of the detector for each of the three forms of the probe analyzed (-AM, –COOH-$Ca^{2+}$-bound and –COOH-$Ca^{2+}$-free). Narrow slits allow to record a high-resolution spectrum, but high PMT power, required if the probe brightness is low, could amplify also the background noise; on the contrary, it is possible to increase the slit width while reducing the PMT, in order to record a higher signal–noise ratio spectrum at the expense of a loss of resolution. Excitation and emission slits can be set with different widths: in general, when recording an excitation spectrum, keep the excitation slit narrower than the emission slit. Vice versa, when recording an emission spectrum, emission slit should be narrower than the excitation slit.
17. A trial-and-error approach must be used to achieve the best combination of the parameters, taking into account the experimental set up and spectra obtained with other compounds. As an example, with our experimental set up we record excitation fluorescence spectra of commercial fura-2/COOH (0.5 μM at 37 °C) as follows: slit width = 2.5/5 nm or 5/10 nm (excitation/emission) and PMT = 800 or 600; for mt-fura-2 (2 μM at 37 °C) the optimized setup is slit width = 5/10 nm and PMT = 800 V.
18. Affinity of a probe for $Ca^{2+}$ is defined by the dissociation constant of the following equilibrium:

$$P - Ca^{2+} \rightleftharpoons P + Ca^{2+} \qquad K_d = \frac{[P][Ca^{2+}]}{[P - Ca^{2+}]}$$

$pK_d$ value for a ratiometric probe is represented by the intercept of the linear fitting of $p[Ca^{2+}]$ versus $p\left[\beta \times \left(\frac{R-R_{min}}{R_{max}-R}\right)\right]$, obtained by plotting the experimental data at two different wavelengths, according to Grynkiewicz equation:

$$p[Ca^{2+}] = pK_d + p\left[\beta \times \left(\frac{R - R_{min}}{R_{max} - R}\right)\right]$$

where $K_d$ is the dissociation constant of the equilibrium between the probe and $Ca^{2+}$ at 37 °C, $R = \frac{F_{\lambda_1}}{F_{\lambda_2}}$, $\beta = \frac{F_{\lambda_2,Ca^{2+}_{min}}}{F_{\lambda_2,Ca^{2+}_{max}}}$, $F_{\lambda_1}$is $F$value measured at $\lambda_1$ before the isosbestic point, and $F_{\lambda_2}$ is the $F$value measured at $\lambda_2$ after isosbestic point.

19. DR is a dimensionless measure that represent the ratio between the largest and smallest value that the ratio $R$ can assume.

$$DR = \frac{R_{max}}{R_{min}}$$

DR varies when changing the couple of excitation wavelengths used, thus a crucial step in the characterization of a probe is the evaluation of the wavelengths that optimize this parameter.

20. Excitation interval should cover the wavelength range where absorption is detected for either (or both) mt-fura-2/COOH-$Ca^{2+}$-bound or -unbound (*see* Subheading 3.1, **step 1**).

21. We set $\lambda_{em} = 530$ nm as an intermediate wavelength between the maximum emission of mt-fura-2/COOH $Ca^{2+}$-bound (maximum $\lambda_{em} = 520$ nm) and $Ca^{2+}$-free form (maximum $\lambda_{em} = 540$ nm), as determined in Subheading 3.3.1.

22. Volume additions of at least 6 μL is recommended, in order to reduce the error in pipetting. Total volume of additions at the end of the titration must be less than 5% of the initial volume, in order to reduce the dilution of the probe and the $Ca^{2+}$ ion.

23. It is suggested to record several spectra in the range of concentrations closed to the expected value of $K_d$. When two subsequent spectra show minimal variations, rise the volume or the $[Ca^{2+}]$ added (i.e., using for the addition solutions at increasing $[Ca^{2+}]$: 0.1–1–10–100–1000 mM). For mt-fura-2 ($K_d$ ~ 1.5 μM) an example of subsequent additions is the following: 0.1, 0.2, 0.8, 1.2, 1.6, 2.0, 2.5, 5.0, 10, 20, 60, and 500 μM (each value represents the final $[Ca^{2+}]$).

24. Generally, residual [$Ca^{2+}$] ranges between 500 nM and 3 μM. A $Ca^{2+}$-buffered solution can be prepared by adding to the medium H-EDTA (1 mM), EGTA (2 mM), and an amount of $CaCl_2$ suitable to obtain a free [$Ca^{2+}$] below residual [$Ca^{2+}$]. The free [$Ca^{2+}$] has to be estimated using Maxchelator or analogous software and then checked by fluorometric measurements with fura-2 as described in Subheading 3.1.
25. A quick method to determine the wavelengths in which Dynamic Range achieve maximum value provides for the evaluation of the wavelengths where the cumulative plot of $\beta(\lambda)$ (for $\lambda > \lambda_{isosbestic}$) and $\beta^{-1}(\lambda)$ for ($\lambda < \lambda_{isosbestic}$) reach the two maximum values. $DR_{max}$ can be determined by the ratio between $R_{max}$ and $R_{min}$ at the wavelengths of the two maxima of the plot. The choice of two wavelengths close to maxima of the plot ($\lambda_1$ and $\lambda_2$) allow to work with a DR value close to $DR_{max}$.
26. Residual [$Ca^{2+}$] in the solutions is not negligible for high and medium affinity probes. Measure it as reported in Subheading 3.1 and be sure to consider it when calculating [$Ca^{2+}$] in each solution used.
27. Fluorescence QY is a property of a specific compound in a solvent at a given temperature that represents the probability of a radiative decay compared with other possible nonradiative decay and defined by the ratio:

$$\Phi_{fl} = \frac{\#_{\text{photons emitted}}}{\#_{\text{photons absorbed}}}$$

    Experimentally, fluorescence QY can be determined using a comparative method, that is, by measuring the fluorescence emitted by a fluorophore of known QY compared with the compound of interest at the same experimental conditions (excitation wavelength, slit width, PMT voltage, scan speed, etc.).
28. Standard reference must have absorbance and emission wavelengths similar to the sample compound. For mt-fura-2, Quinine Sulfate in $H_2SO_4$ 0.1 M has been used as standard reference ($\Phi$ = 0.54 at 25 °C, $\lambda_{abs}$: 274–400 nm, $\lambda_{em}$: 400–600 nm, $A_{max}$ = 0.025 (2.5 μM) at 350 nm [12])
29. The temperature can be different for the probes and the standard reference but must be kept constant during the measure for each compound. Quinine sulfate standard QY is calculated at 25 °C, while mt-fura-2 QY has been evaluated at 37 °C.
30. Temperature controllers are usually slower in cooling down than warming up the system, thus it is recommended to start the recordings at the lowest temperature (e.g., 25 °C used for the standard reference quinine sulfate) and then heat to higher temperature (e.g., 37 °C used for mt-fura-2).

31. All the emission fluorescence spectra must be corrected with standard methods (e.g., using the instrument specific correction curve) in order to normalize the data to the sensitivity of the detector at the different wavelengths.
32. The QY of the different forms of the probe has been determined by plotting for the probe and the standard reference the area under the curve (AUC) of emission spectra versus the absorbance value at the wavelength of excitation. The slope of the plots allows to calculate QY according to the following equation:

$$\Phi_x = \Phi_{ST} \times \frac{Grad_x}{Grad_{ST}} \times \frac{\eta_x^2}{\eta_{ST}^2}$$

where $\Phi$ indicates the QY, *Grad* the slope of the plot and $\eta$ the refractive index of the solvents. Subscribe "$x$" is referred to the compound under examination and "*ST*" is referred to the standard reference. Both must be excited at the same wavelength (e.g., slopes calculated for mt-fura-2/AM has been compared with those of Quinine Sulfate obtained upon excitation at 361 nm).

33. Between subsequent experiments, the imaging chambers must be properly cleaned. The chamber is completely disassembled and immersed in 2% BSA solution for at least 15 min while stirring and then rinsed with deionized water. For a deeper cleanse it is possible to scrub all the pieces of the imaging chamber with a toothbrush with liquid soap and then rinse with deionized water.
34. Low signals are usually recorded below the excitation wavelength of 350 nm due to lower permeability of objectives to UV light.
35. Mitochondria are subcellular organelles where a consistent production of reactive oxygen species (ROS) has been observed. These species could in principle interfere with the fluorescence of the probe. For this reason, the exclusion of any effect due to ROS (in the typical timescale of a biological experiment) is important in the frame of the optical characterization of a mitochondriotropic probe.
36. Fura-based probes show affinity for alkaline earth metals and transition double charged metals [11]. Compared to $Ca^{2+}$ ion, a negligible affinity has been observed for $Mg^{2+}$, a very low affinity for $Ba^{2+}$ and $Sr^{2+}$, and a high affinity for $Zn^{2+}$ (with substantial increase of brightness). These cations can be calibrated as described for $Ca^{2+}$, determining $K_d$, DR, $\varepsilon$, and $\Phi$ values. Transition double charged metals with *d* orbitals partially filled, for example $Mn^{2+}$, $Fe^{2+}$, or $Cu^{2+}$, usually act as quenchers of fluorescence.

37. pH-dependent equilibria of the BAPTA-carboxylic moieties could affect either $Ca^{2+}$ binding or fluorescence properties of the dye. There are two main possibilities: (1) mt-fura-2/COOH-$Ca^{2+}$-bound form: protons could act as competitive ions with $Ca^{2+}$ altering the affinity for the cation (2) mt-fura-2/COOH-$Ca^{2+}$-free form: variations of pH could change the protonation state of the carboxylic moieties leading to a variation of fluorescence independent from [$Ca^{2+}$].
38. For HeLa cells, glass coverslips are untreated. Some cell types require specific treatments (e.g., poly-L-lysine) in order to stick to glass.
39. The standard loading protocol we propose presents only slight modifications compared to the classical fura-2 loading protocol (see, e.g., [13]). The major change we made is the omission of the organic-anion transport inhibitor sulfinpyrazone in the loading mix. Sulfinpyrazone is used to favor the trapping of the fura-2 probe into the cytosol. We reasoned that leaving the physiological plasma membrane extrusion mechanisms unaffected would result in the extrusion of the mt-fura-2 probe that has not been efficiently internalized in mitochondria.
40. Pluronic F-127 is a nonionic surfactant used to avoid the precipitation of the -AM form of the probe when diluted in aqueous media.
41. **Important**! Follow carefully the indicated order when adding the components of the loading mix. In particular, it is crucial to add mt-fura-2 directly on the Pluronic F-127 and mix well before the addition of EC solution, in order to avoid agglomeration and precipitation of the probe.
42. The optimal incubation time could vary among cell lines, due for example to the different amount of esterases present within the cells or polarization of mitochondria.
43. In HeLa cells we obtained a satisfactory loading at 37 °C. However, the optimal incubation temperature during the loading have to be determined for each cell type. It has been shown using fura-2/AM that compartmentalization is favored by higher temperatures [14].
44. The washing step is necessary for the proper hydrolysis of the AM groups of the internalized probe. Longer washing time may be necessary for different cell lines, however note that the probe could be extruded from the organelles/cells. In mitochondria, we believe that this is caused by the flickering of PTP.
45. In the case of cells or tissues where transfection is not an option, mitochondria can be stained by loading the cells with TMRM, MitoTracker or other fluorescent, mitochondria-targeted probes. Attention must be paid that excitation spectra do not overlap with that of mt-fura-2.

46. The probe is excited by UV-light illumination. The confocal microscope used have to be equipped for UV imaging. Particularly, a UV laser line and a UV-permeant objective are mandatory.
47. To allow the equilibration of the cells on the coverslip with the extracellular-like medium and avoid pH and temperature oscillations, perfuse with warmed EC saline for 1–5 min before starting the recording.
48. Set the exposure time based on the characteristics of your instrument and the loading efficiency of the probe. The interval between subsequent exposures varies in function of the experimental protocol and the cellular process analyzed; for example, faster acquisition is required when evaluating kinetics, such as $Ca^{2+}$ uptake rate. Most commonly, we use 50–200 ms exposure for each wavelength and 1–5 s interval between subsequent acquisitions. Whenever the sample is not illuminated by excitation light, the illumination source output is blocked by a shutter or the monochromator is moved to a not-toxic wavelength which does not excite the fluorescent probe (810 nm).
49. If the microscope allows live monitoring of fluorescence intensity and R, draw ROIs around the cells present in the field of view. Draw also one ROI where the signal in absent (i.e., cells are not present) to monitor the background fluorescence during the experiment (Fig. 3a).
50. Record for 2 min in order to check whether cells are equilibrated with the perfusing solution. When the R value is stable over time, the experiment can start.
51. To trigger ER $Ca^{2+}$ release, cells are perfused with EC medium containing histamine or another IP3-generating stimulus, adequate for the cell type of choice. In order to increase ER $Ca^{2+}$ release, IP3-generating stimulus can be applied together with SERCA pump inhibitor cyclopiazonic acid (CPA, 20 μM). In case you wish to exclude any possible contribution due to entrance of $Ca^{2+}$ from extracellular environment, histamine application has to be performed in $Ca^{2+}$-free, EGTA (500 μM)-containing EC solution.
52. The concentration of digitonin and the duration of the permeabilization have to be optimized for each experiment, since they can be highly variable, due for example to the concentration of cells on the coverslip.
53. Mitochondrial depolarization induced by CCCP application is necessary to allow the passive equilibration of $[Ca^{2+}]$ between the solution applied and the mitochondrial matrix. Cyclosporin A is applied to prevent PTP opening probability.

54. High [$Ca^{2+}$] may result in precipitation of $Ca_3(PO_4)_2$ salt, avoid the presence of phosphates in the solutions. The application of [$Ca^{2+}$] higher than 200 μM can result in the exit of mt-fura-2 from mitochondria. This is probably due to PTP opening.
55. The ROIs outlined in one series of files (e.g., upon $\lambda_{ex} = 400$ nm) will be applied later to the other series of files (e.g., upon $\lambda_{ex} = 350$ nm). The FI will be measured in the same regions for the two excitation wavelengths.
56. Calculating *R*% values allow to normalize *R* values to minimum and maximum *R* values obtained in each coverslip. This represents an easy but quite accurate way to compare different conditions, even though without calculating real [$Ca^{2+}$].

## Acknowledgments

The original work by the authors has been supported by grants from the University of Padua (STARS Grants programme "CHEM PROCALIM" to A.M.) and Fondazione Cassa di Risparmio di Padova e Rovigo (CARIPARO) Foundation (Starting Grant 2015 to D.P.).

### References

1. Rizzuto R, De Stefani D, Raffaello A, Mammucari C (2012) Mitochondria as sensors and regulators of calcium signalling. Nat Rev Mol Cell Biol 13:566–578. https://doi.org/10.1038/nrm3412
2. De Stefani D, Rizzuto R, Pozzan T (2016) Enjoy the trip: calcium in mitochondria back and forth. Annu Rev Biochem 85:161–192. https://doi.org/10.1146/annurev-biochem-060614-034216
3. Pendin D, Greotti E, Filadi R, Pozzan T (2015) Spying on organelle $Ca^{2+}$ in living cells: the mitochondrial point of view. J Endocrinol Investig 38:39–45. https://doi.org/10.1007/s40618-014-0178-2
4. Pendin D, Greotti E, Lefkimmiatis K, Pozzan T (2017) Exploring cells with targeted biosensors. J Gen Physiol 149(1):1–36. https://doi.org/10.1085/jgp.201611654
5. Suzuki J, Kanemaru K, Iino M (2016) Genetically encoded fluorescent indicators for Organellar calcium imaging. Biophys J 111:1119–1131. https://doi.org/10.1016/j.bpj.2016.04.054
6. Tsien RY (1980) New calcium indicators and buffers with high selectivity against magnesium and protons: design, synthesis, and properties of prototype structures. Biochemistry 19:2396–2404. https://doi.org/10.1021/bi00552a018
7. Tsien RY (1981) A non-disruptive technique for loading calcium buffers and indicators into cells. Nature 290:527–528. https://doi.org/10.1038/290527a0
8. Pendin D, Norante R, De Nadai A et al (2019) A synthetic fluorescent mitochondria-targeted sensor for ratiometric imaging of calcium in live cells. Angew Chem Int Ed Engl 58:9917–9922. https://doi.org/10.1002/anie.201902272
9. Rizzuto R, Brini M, Pizzo P et al (1995) Chimeric green fluorescent protein as a tool for visualizing subcellular organelles in living cells. Curr Biol 5:635–642. https://doi.org/10.1016/S0960-9822(95)00128-X
10. Filippin L, Magalhães PJ, Di Benedetto G et al (2003) Stable interactions between mitochondria and endoplasmic reticulum allow rapid accumulation of calcium in a subpopulation of mitochondria. J Biol Chem 278:39224–39234. https://doi.org/10.1074/jbc.M302301200

11. Grynkiewicz G, Poenie M, Tsien RY (1985) A new generation of $Ca^{2+}$ indicators with greatly improved fluorescence properties. J Biol Chem 260:3440–3450. https://doi.org/10.1016/S0021-9258(19)83641-4
12. Melhuish WH (1961) Quantum efficiencies of fluorescence of organic substances: effect of solvent and concentration of the fluorescent solute. J Phys Chem 65:229–235. https://doi.org/10.1021/j100820a009
13. Kipanyula MJ, Contreras L, Zampese E et al (2012) $Ca^{2+}$ dysregulation in neurons from transgenic mice expressing mutant presenilin 2. Aging Cell 11:885–893. https://doi.org/10.1111/j.1474-9726.2012.00858.x
14. Malgaroli A, Milani D, Meldolesi J, Pozzan T (1987) Fura-2 measurements of cytosolic free $Ca^{2+}$ in monolayers and suspensions of various types of animal cells. J Cell Biol 105:2145–2155. https://doi.org/10.1083/jcb.105.5.2145

# Chapter 13

# Sequence-Specific Control of Mitochondrial Gene Transcription Using Programmable Synthetic Gene Switches Called MITO-PIPs

**Takuya Hidaka, Hiroshi Sugiyama, and Ganesh N. Pandian**

## Abstract

Mitochondria possess multiple copies of mitochondrial DNA (mtDNA) that encode 37 genes and their transcription and replication get controlled by unique molecular codes different from that in the nuclear DNA. The mtDNA has been gaining increased attention as one of the critical therapeutic targets as mutations in them impair the function of mitochondria and cause mitochondrial diseases like MELAS. In this chapter, we describe artificial control of mitochondrial transcription based on mtDNA sequence information with a new type of compounds termed MITO-PIPs, which encompasses two domains: pyrrole–imidazole polyamide as DNA recognition domain and mitochondrial penetrating peptide as the mitochondria-targeting domain. Because MITO-PIPs are amenable to tunability, they can be expanded as a synthetic strategy to modulate mitochondrial gene(s) on demand.

**Key words** MITO-PIP, Mitochondrial DNA, Pyrrole–imidazole polyamide, DNA binding ligand, Transcription, Fmoc solid-phase synthesis

## 1 Introduction

Mitochondria have essential roles in cellular functions like energy production, programmed cell death, and calcium homeostasis. Mitochondria possess ~16.6 kbp circular DNA encoding 37 genes, including 13 critical subunits of the oxidative phosphorylation system. Because a high level of reactive oxygen species is generated during energy production by the oxidative phosphorylation system, mtDNA shows a higher mutation rate than nuclear DNA. While most of these mutations have no significant effect, some mutations impair mitochondrial functions and cause mitochondrial diseases like MELAS, Leigh syndrome and MERRF [1]. It is also reported that mtDNA mutations are related to other diseases like cancer and diabetes [2, 3], so mtDNA has been

Volkmar Weissig and Marvin Edeas (eds.), *Mitochondrial Medicine: Volume 1: Targeting Mitochondria*, Methods in Molecular Biology, vol. 2275, https://doi.org/10.1007/978-1-0716-1262-0_13,

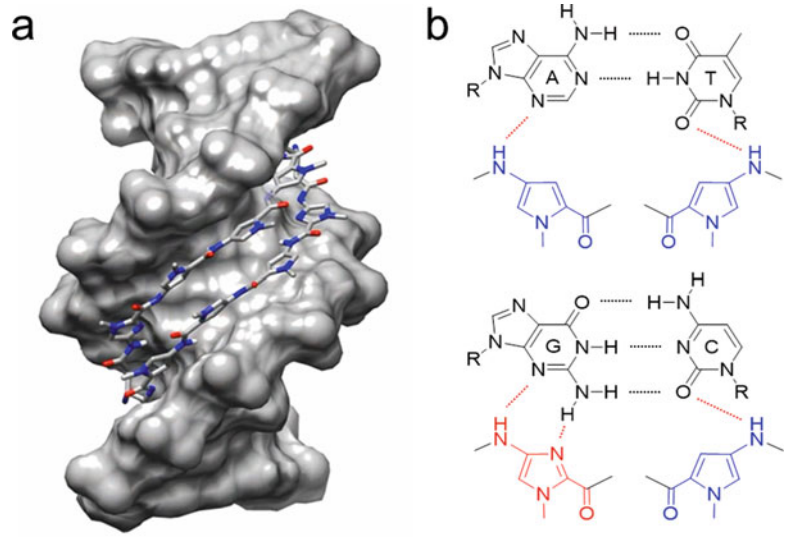


**Fig. 1** (**a**) Crystal structure of DNA-PIP complex (PDB accession number: 3OMJ) [5]. (**b**) Rule of DNA recognition by PIPs. Py–Py pairs recognize A–T or T–A base pairs and Im–Py pairs recognize G–C base pairs [6, 7]

gaining increasing attention as one of the important therapeutic targets.

Pyrrole–imidazole polyamides (PIPs) are compounds mainly composed of *N*-methyl-pyrrole (Py) and *N*-methyl-imidazole (Im), which bind to the minor groove of double-stranded DNA in a sequence-specific manner (Fig. 1a) [4, 5]. Antiparallel Py–Py pairs recognize A–T or T–A base pairs while Im/Py pairs recognize G–C base pairs (Fig. 1b) [6, 7]. Based on this binding rule, the target sequence of PIP can be programed by rearranging Py and Im rings. This programmable property has been applied to gene switches which can control transcription based on DNA sequence information and fluorescence probe to visualize the specific region of DNA [8, 9]. PIPs usually localize into nuclei due to their affinity to DNA, but the introduction of the mitochondria-penetrating peptide can reroute the ligands to mitochondria [10, 11]. We named the ligands "MITO-PIPs" and reported that a MITO-PIP targeting light-strand promoter (LSP) region (MITO-PIP-LSP, Fig. 2a) can repress the expression of *ND6*, a downstream gene of LSP, by inhibiting mitochondrial transcription factor A (TFAM) binding to LSP region (Fig. 2b) [12].

In this chapter, we describe Fmoc solid-phase synthesis and cellular evaluation of MITO-PIP-LSP. Although this chapter mainly explains about MITO-PIP-LSP, other MITO-PIPs targeting different sequences can be prepared by following a similar protocol.

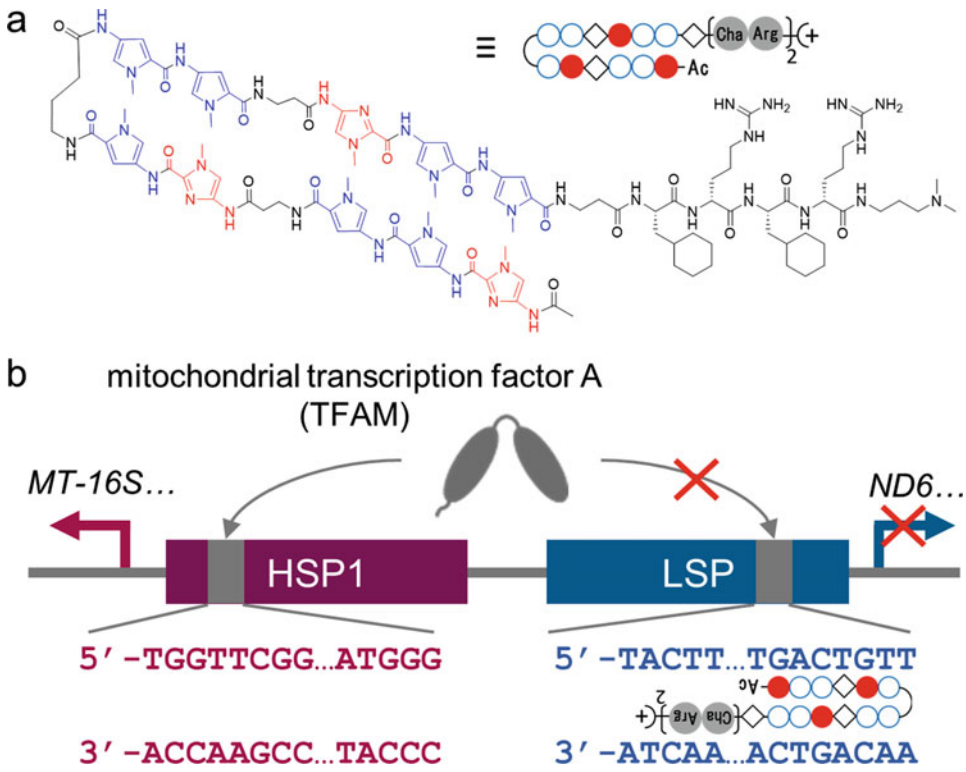


**Fig. 2** (**a**) Chemical structure of MITO-PIP-LSP and its schematic illustration. (*Cha* cyclohexylalanine, *Arg* d-arginine). (**b**) Mechanism of LSP-specific transcription repression by MITO-PIP-LSP. Binding of mitochondrial transcription factor A (TFAM) to LSP site is inhibited by MITO-PIP-LSP and expression of LSP downstream genes are repressed

## 2 Materials

MITO-PIPs can be synthesized by Fmoc solid-phase synthesis. Coupling reactions are moisture sensitive, so use super dehydrated solvent or peptide synthesis grade reagents in the synthesis (*see* **Note 1**). Solutions required for synthesis should be freshly prepared just before the synthesis.

### *2.1 MITO-PIP-LSP Synthesis*

1. Fmoc-Arg(Pbf)-Alko resin.
2. Fmoc deblocking solution: 20% piperidine in dimethylformamide (DMF).
3. Coupling solution: *N*-Methyl-2-pyrrolidone (NMP) solution containing 0.2 M of HCTU and 0.2 M of each Fmoc-unit (Fmoc-Py-COOH, Fmoc-Im-COOH, Fmoc-β-Ala-OH, Fmoc-GABA-OH, Fmoc-D-Arg(Pbf)-OH, and Fmoc-Cha-OH) (*see* **Note 2**).

4. Activation solution: 0.6 M of *N*,*N*-diisopropylethylamine (DIEA) in DMF.
5. Washing solution: DMF (peptide synthesis grade).
6. Capping solution: 20% acetic anhydride in DMF.
7. Methanol.
8. *N*,*N*-Dimethylaminopropylamine.
9. Diethyl ether.
10. Pbf deblocking solution: trifluoroacetic acid–triisopropylsilane–$H_2O$ (95:2.5:2.5%, v/v).
11. 2.5 mL plastic reaction vessel with filter.
12. Desiccator connected to a vacuum pump.
13. Reversed-phase chromatography system.
14. Vacuum freeze dryer.
15. High-performance liquid chromatography (HPLC) system equipped with a C18 column.
16. Solvent for HPLC: acetonitrile and $H_2O$–0.1% TFA.
17. Instrument for mass spectrometry like ESI-MS or MALDI-TOFMS.

### 2.2 Cellular Evaluation of MITO-PIP-LSP

1. HeLa cells.
2. Growth medium: Dulbecco's Modified Eagle Medium supplemented with 10% fetal bovine serum and 1% MEM nonessential amino acids solution.
3. DMSO (cell-culture grade).
4. Reagents required for reverse-transcription quantitative PCR (RT-qPCR): RNA extraction kit, reverse transcription kit, qPCR master mix, and PCR primers (Table 1).
5. Nano spectrophotometer (e.g., NanoDrop).

**Table 1**
**Sequence of each primers for RT-qPCR**

| Primer name | Sequence |
|---|---|
| *MT-16S* forward | 5′-ACTTTGCAAGGAGAGCCAAA |
| *MT-16S* reverse | 5′-GCTATCACCAGGCTCGGTAG |
| *ND6* forward | 5′-GGGTTAGCGATGGAGGTAGG |
| *ND6* reverse | 5′-GATCCTCCCGAATCAACCCT |

## 3 Methods

We use an automated peptide synthesizer for Fmoc solid-phase synthesis of MITO-PIPs, but the whole procedure can be also performed manually. Carry out all procedures at room temperature, unless otherwise specified (*see* **Note 3**).

### 3.1 Solid-Phase Synthesis of MITO-PIP-LSP

1. Add 1 mL of NMP to Fmoc-Arg(Pbf)-Alko resin (~50 μmol of monomer on resin) in a 2.5 mL plastic reaction vessel and shake at room temperature for 30 min (*see* **Note 4**).
2. Remove NMP and wash the resin with 0.6 mL of Washing solution once.
3. Add 0.5 mL of deblocking solution to the resin and mix at room temperature for 4 min to remove Fmoc protecting group. Repeat this step twice.
4. Wash the resin with 0.6 mL of Washing solution five times.
5. Add 0.33 mL of Activation solution to 1 mL of Coupling solution containing Fmoc-unit which should be introduced in the cycle and shake at room temperature for 3 min. HCTU activates the carboxy group of Fmoc-unit in the presence of a nonnucleophilic base like DIEA.
6. Transfer whole solution prepared in **step 5** to washed resin and perform coupling reaction for 1 h at room temperature (*see* **Note 5**).
7. After the coupling reaction, wash the resin with 0.6 mL of Washing solution five times.
8. Repeat **steps 3**–**7** to sequentially introduce each unit to make the desired structure. In the case of MITO-PIP-LSP, the following sequential structure should be synthesized: (Resin)-Arg(Pbf)–Cha–Arg(Pbf)–Cha–β-Ala–Py–Py–Im–β-Ala–Py–Py–GABA–Py–Im–β-Ala–Py–Py–Im (*see* **Note 6**).
9. After the final washing, repeat **steps 3** and **4** to remove the final Fmoc group.
10. Add 0.5 mL of Capping solution and shake for 5 min to acetylate the amine group of the last unit.
11. Wash the resin with methanol (2 mL) and dry in a desiccator in vacuo. The dried resin can be stored at 4 °C.

### 3.2 Cleavage and Purification of MITO-PIP

1. Add *N*,*N*-dimethylaminopropylamine (1 mL) to the dried resin and shake at 55 °C for 3 h. Synthesized MITO-PIP-LSP is cleaved from the resin at this step and the solution turns into yellowish color (*see* **Note 7**).
2. Transfer solution (without the resin) to diethyl ether (40 mL) in a 50 mL centrifuge tube. Because MITO-PIPs cannot be

dissolved into diethyl ether, cleaved MITO-PIP-LSP forms white–yellow precipitate. Centrifuge at 9900 × *g* for 10 min to make a pellet and remove supernatant. Dry the pellet in a desiccator in vacuo.

3. Purify the crude MITO-PIP-LSP by reversed-phase chromatography. We purify MITO-PIPs using the CombiFlash Rf with 4.3 g C18 RediSep Rf reversed-phase flash column (Teledyne Isco, Inc) or by reversed-phase HPLC using a Jasco Engineering UV2075 HPLC UV/vis detector and a PU-2080 plus series system with a preparative C18 column. Acetonitrile and $H_2O$–0.1% TFA are used as mobile phases.
4. Lyophilize the sample to remove the solvent. The purified sample is subjected to reversed-phase HPLC using acetonitrile and $H_2O$–0.1% TFA as a solvent for purity quantification and mass spectrometry like ESI-MS or MALDI-TOFMS for compound characterization.

### 3.3 Cellular Evaluation of MITO-PIP

1. Seed HeLa cells on a 12-well plate at the concentration of $5 \times 10^4$ cells/well 1 day prior to the treatment.
2. Prepare 10 mM DMSO solution of MITO-PIP-LSP. Because the amount of MITO-PIP-LSP used in cellular experiments can be very small (less than 0.5 mg), it is recommended to determine the concentration by using an extinction coefficient of 9900 $M^{-1}$ $cm^{-1}$ per one pyrrole or imidazole moiety at $\lambda_{max}$ near 310 nm. Measure absorption spectra using a nano spectrophotometer (e.g., NanoDrop) and use maximum absorbance value in 300–310 nm for calculation (*see* **Note 8**).
3. After cell attachment, replace medium with fresh medium supplemented with MITO-PIP-LSP (1–10 μM) and incubate at 37 °C in 5% $CO_2$. Samples containing the same amount of DMSO without MITO-PIP-LSP are used as a negative control.
4. After the compound treatment, extract total RNA and perform reverse transcription to synthesize cDNA using reagent kits which are commercially available. Check expression level of each mitochondrial gene (*ND6* as LSP and *MT-16S* as HSP1 downstream gene) by quantitative PCR using the primers listed in Table 1. Calculate the relative expression ratio ([*ND6*]/[*MT-16S*]) normalized to the negative control from determined Cp value (*see* **Note 9**).

## 4 Notes

1. All reagents for synthesis should be warmed to room temperature before opening caps and drying solid reagents in a desiccator in vacuo will help to improve coupling efficiency.

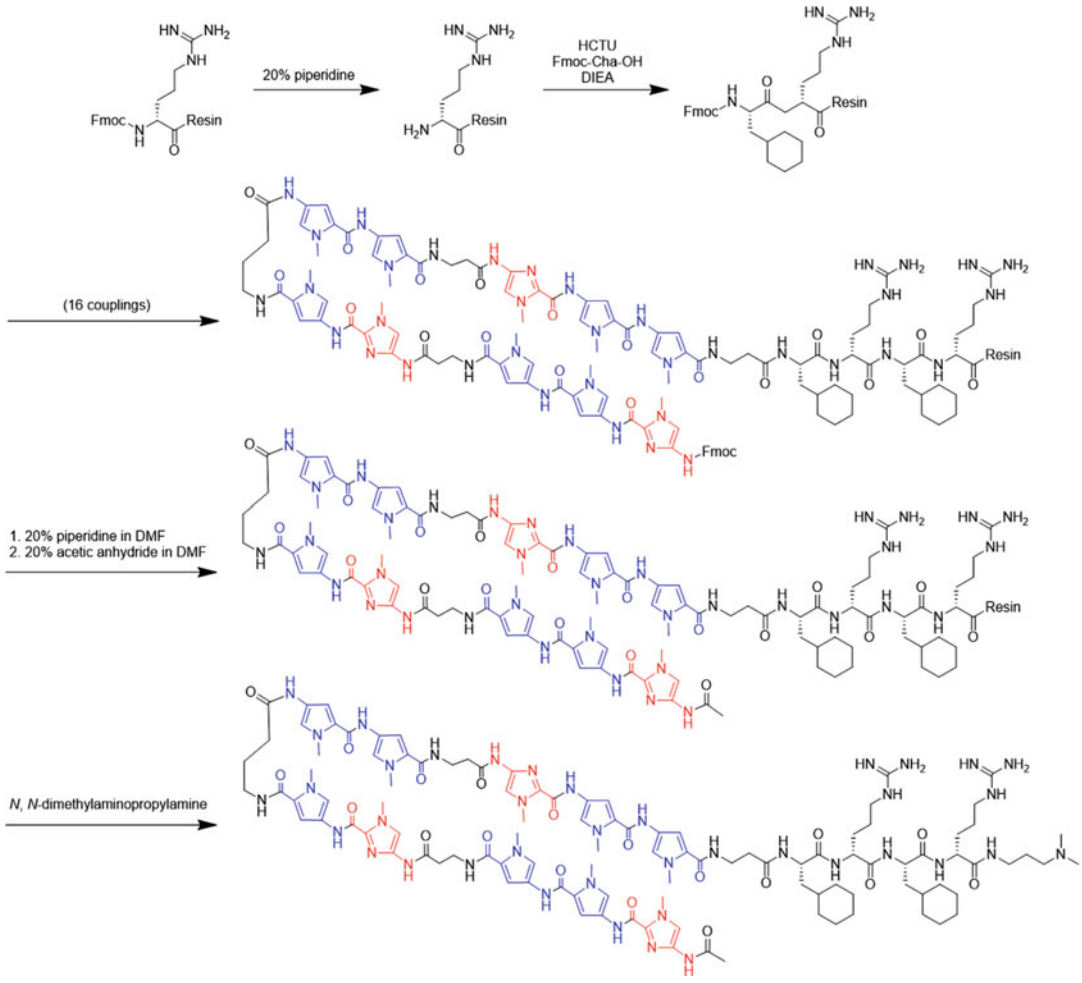


**Fig. 3** Synthetic scheme of MITO-PIP-LSP

2. Prepare required Fmoc-units depending on the structure of MITO-PIP you want to synthesize. Although DMF can be used as a solvent of Coupling solution, Fmoc-Im-OH has better solubility to NMP.
3. The synthetic scheme of MITO-PIP-LSP is shown in Fig. 3.
4. You can change the first resin depending on the structure of MITO-PIP you want to synthesize.
5. If the coupling efficiency is low, the coupling reaction time can be extended. We usually use four equivalents of HCTU, each Fmoc-unit and DIEA to the monomer on resin, but the amount of reagent can be modified based on coupling efficiency and reagent cost.
6. The order of Fmoc-units can be modified depending on the structure of MITO-PIP you want to synthesize.

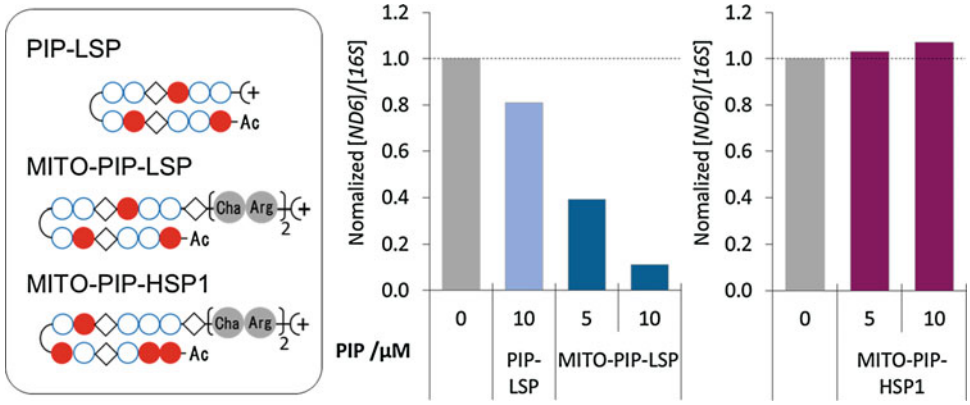


**Fig. 4** Example of RT-qPCR result. HeLa cells were treated with each compound for 24 h and the relative expression level of downstream genes ([*ND6*]/[*MT-16S*]) was quantified by RT-qPCR [12]

7. If you use 3,3′-diamine-*N*-methyldipropylamine instead of *N*, *N*-dimethylaminopropylamine, synthesized MITO-PIPs have amine group at C-terminus which can be used for coupling reaction to introduce other functional compounds (e.g. fluorescence dye) with a carboxy group.
8. For example, if maximum absorbance value in 300–310 nm of 100-fold diluted MITO-PIP-LSP solution is determined to be 0.99 using NanoDrop (optical path length = 0.1 cm), the concentration of the original solution is calculated from the following formula:

$$C = \frac{\text{Abs}}{9900 \times n \times c} \times \text{DF} = \frac{0.99}{9900 \times 10 \times 0.1} \times 100 = 1 \times 10^{-2}(\text{M})$$

where $n$ is total number of Py and Im rings, $c$ is optical path length (cm), and DF is dilution factor.

9. We reported that [*ND6*]/[*MT-16S*] ratio is downregulated to ~40% at 5 μM and ~10% at 10 μM of MITO-PIP-LSP in HeLa cells after 24 h treatment. Other compounds like PIP-LSP (no peptide) and MITO-PIP targeting HSP1 site (MITO-PIP-HSP1) do not show a significant difference in expression ratio (Fig. 4) [12].

## References


1. Gorman GS et al (2016) Mitochondrial diseases. Nat Rev Dis Primers 2:16080
2. Chatterjee A, Mambo E, Sidransky D (2006) Mitochondrial DNA mutations in human cancer. Oncogene 25:
3. Maassen JA, Lemkes HHPJ et al (2004) Mitochondrial diabetes: molecular mechanisms and clinical presentation. Diabetes 53:S103–S109
4. Chenoweth DM, Dervan PB (2010) Structural basis for cyclic Py-Im polyamide allosteric inhibition of nuclear receptor binding. J Am Chem Soc 132:
5. Kielkopf CL, Rees DC et al (1998) A structural basis for recognition of a·T and T·a base pairs in the minor groove of B-DNA. Science 282:111–115
6. Kielkopf CL, Baird EE, Dervan PB, Rees DC (1998) Structural basis for G·C recognition in the DNA minor groove. Nat Struct Biol 5:104–109
7. Trauger JW, Baird EE, Dervan PB (1996) Recognition of DNA by designed ligands at subnanomolar concentrations. Nature 382:559–561
8. Namasivayam GP, Sugiyama H et al (2014) Distinct DNA-based epigenetic switches trigger transcriptional activation of silent genes in human dermal fibroblasts. Sci Rep 4:3843
9. Kawamoto Y, Sugiyama H et al (2016) Targeting 24bp within telomere repeat sequences with tandem tetramer pyrrole–imidazole polyamide probes. J Am Chem Soc 138:
10. Horton KL, Kelley SO et al (2008) Mitochondria-penetrating peptides. Chem Biol 15:375–382
11. Yousif LF, Stewart KM, Horton KL, Kelley SO (2009) Mitochondria-penetrating peptides: sequence effects and model cargo transport. Chembiochem 10:2081–2088
12. Hidaka T, Namasivayam GP, Sugiyama H et al (2017) Creation of a synthetic ligand for mitochondrial DNA sequence recognition and promoter-specific transcription suppression. J Am Chem Soc 139:

# Chapter 14

# Targeting the Mitochondrial Genome Via a MITO-Porter: Evaluation of mtDNA and mtRNA Levels and Mitochondrial Function

**Yuma Yamada and Hideyoshi Harashima**

## Abstract

Genetic mutations and defects in mitochondrial DNA (mtDNA) are associated with certain types of mitochondrial dysfunctions, ultimately resulting in the emergence of a variety of human diseases. To achieve an effective mitochondrial gene therapy, it will be necessary to deliver therapeutic agents to the innermost mitochondrial space (the mitochondrial matrix), which contains the mtDNA pool. We recently developed a MITO-Porter, a liposome-based nanocarrier that delivers cargo to mitochondria via a membrane-fusion mechanism. In this chapter, we discuss the methodology used to deliver bioactive molecules to the mitochondrial matrix using a Dual Function (DF)-MITO-Porter, a liposome-based nanocarrier that delivers it cargo by means of a stepwise process, and an evaluation of mtDNA levels and mitochondrial activities in living cells. We also discuss mitochondrial gene silencing by the mitochondrial delivery of antisense RNA oligonucleotide (ASO) targeting mtDNA-encoded mRNA using the MITO-Porter system.

**Key words** Mitochondria, Mitochondrial drug delivery, Nucleic acid delivery, MITO-Porter, Mitochondrial RNA knockdown, Mitochondrial matrix, Mitochondrial DNA, Mitochondrial gene therapy

## 1 Introduction

Mitochondrial dysfunction has recently been implicated in a variety of human diseases [1–3]. It is now generally accepted that genetic mutations and defects in mitochondrial DNA (mtDNA) are associated with certain types of mitochondrial dysfunction, which are the ultimate cause these disorders. Therefore, an effective mitochondrial gene therapy and diagnosis would be expected to have great medical benefits. To achieve such an innovative strategy in which the mitochondrial genome is the target, it will be necessary to deliver therapeutic agents to the innermost mitochondrial space (the mitochondrial matrix), which contains the mtDNA pool, in diseased cells.

Volkmar Weissig and Marvin Edeas (eds.), *Mitochondrial Medicine: Volume 1: Targeting Mitochondria*, Methods in Molecular Biology, vol. 2275, https://doi.org/10.1007/978-1-0716-1262-0_14,

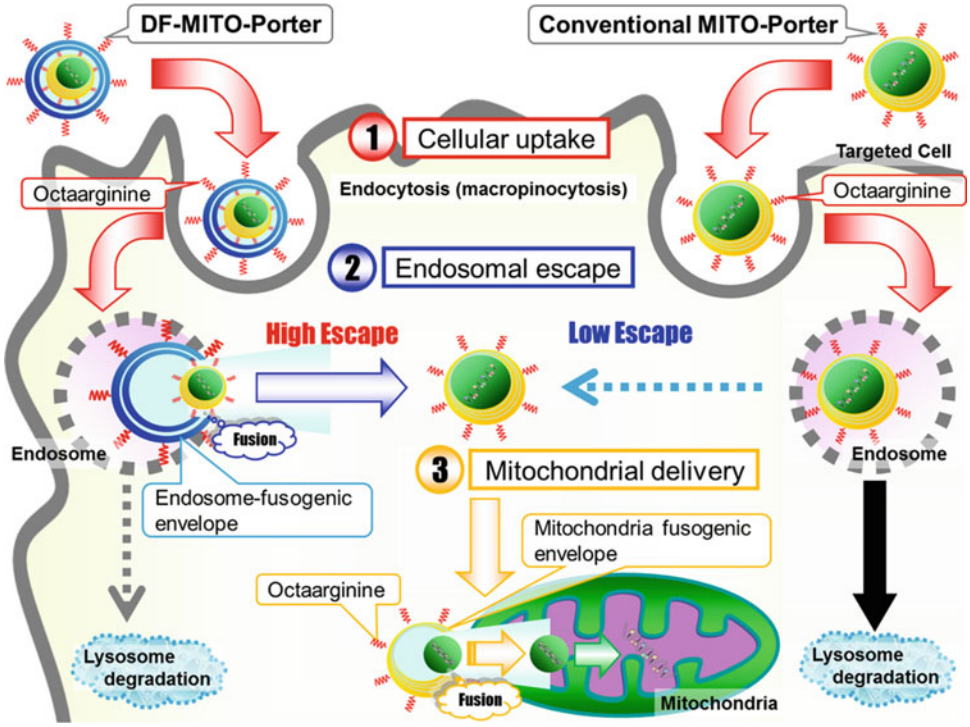


**Fig. 1** Schematic diagram illustrating the intracellular trafficking events associated with the Dual Function (DF)-MITO-Porter and the conventional MITO-Porter. Modification of the outer envelope-surface with a high density of octaarginine greatly assists the efficient uptake of both the DF-MITO-Porter and the conventional MITO-Porter by cells (first step). The DF-MITO-Porter efficiently escapes from endosomes via membrane fusion, a process that is mediated by the outer endosome-fusogenic lipid membranes (second step), whereas the efficiency of escape for the conventional MITO-Porter is low. A greater fraction of the conventional MITO-Porter undergoes endosomal degradation compared with the DF-MITO-Porter. Finally, the carrier fuses with the mitochondrial membrane to deliver its cargo to mitochondria (third step). Thus, the DF-MITO-Porter would be more efficient than the conventional MITO-Porter in the process of endosomal escape [20]

In previous studies, we proposed an original and innovative strategy for penetrating the mitochondrial membrane via membrane fusion, that is, the development of a MITO-Porter system (Fig. 1) [4–6]. To determine the optimal composition of mitochondrial fusogenic lipid, we screened for fusogenic activities directed at mitochondria by monitoring the cancellation of fluorescence resonance energy transfer (FRET) using various octaarginine (R8)-modified liposomes (R8-LPs). R8 was selected as a cytosol delivery device for the MITO-Porter, because it has been reported that R8-LPs are efficiently taken up by cells mainly through macropinocytosis [7]. We also expected that R8, which mimics TAT, might have mitochondrial targeting activity [5, 8]. We succeeded in identifying lipid compositions that promote both the fusion of the MITO-Porter with the mitochondrial membrane and the release of its cargo to the intra-mitochondrial compartment in living cells [4, 9]. We also verified that the MITO-Porter delivered cargoes to the mitochondrial matrix, using propidium iodide, as a

probe to detect mtDNA, and the results showed that this system can be used to efficiently visualize mtDNA within living cells [10]. Based on our previous report, we concluded that the MITO-Porter has the ability to deliver chemicals to the mitochondrial matrix. Current studies regarding MITO-Porter include the fields of autophagy [11], cancer therapy [12], antioxidant therapy [13, 14], and mitochondrial gene therapy [15–17].

In first topic of this chapter, our strategies for delivering bioactive molecules to the mitochondrial matrix are described. The approach involves the use of a Dual Function (DF)-MITO-Porter, which possesses mitochondria-fusogenic inner and endosome-fusogenic outer envelopes with cargos encapsulated within it (Fig. 1) [18, 19]. Intracellular observations showed that mitochondrial delivery by the DF-MITO-Porter was significantly higher than that for a conventional MITO-Porter [18, 20]. To validate mitochondrial genome targeting using a DF-MITO-Porter, the DNase I protein was packaged in the carrier as a cargo. It would be expected that the mtDNA would be digested, as the mitochondrial delivery of the DNase I proteins progressed. In addition, the levels of mtDNA and the mitochondrial activity were evaluated after the mitochondrial delivery of DNase I was complete.

As a second topic, we discuss the mitochondrial delivery of an antisense RNA oligonucleotide (ASO) which performs mitochondrial RNA knockdown to regulate mitochondrial function [21–23]. Mitochondrial delivery of the ASO induces the knockdown of the targeted mitochondria-encoded mRNA and protein, namely, the cytochrome c oxidase subunit II (COX2), a component of the mitochondrial respiratory chain (*see* **Note 1**). Furthermore, the mitochondrial membrane potential was depolarized by the down regulation of the respiratory chain as the result of the mitochondrial delivery of ASO (Fig. 2).

## 2 Materials

Prepare all solutions using ultrapure water (prepared by purifying deionized water to a sensitivity of 18 MΩ-cm at 25 °C) and commercially available reagent-grade reagents. Prepare and store all reagents at room temperature (unless otherwise indicated).

### 2.1 Lipids

1. 1,2-Dioleoyl-*sn*-glycero-3-phosphatidyl ethanolamine (DOPE).
2. Egg yolk phosphatidyl choline (EPC).
3. 5-Cholesten-3-ol 3-hemisuccinate (CHEMS).
4. Phosphatidic acid (PA).
5. Sphingomyelin (SM).

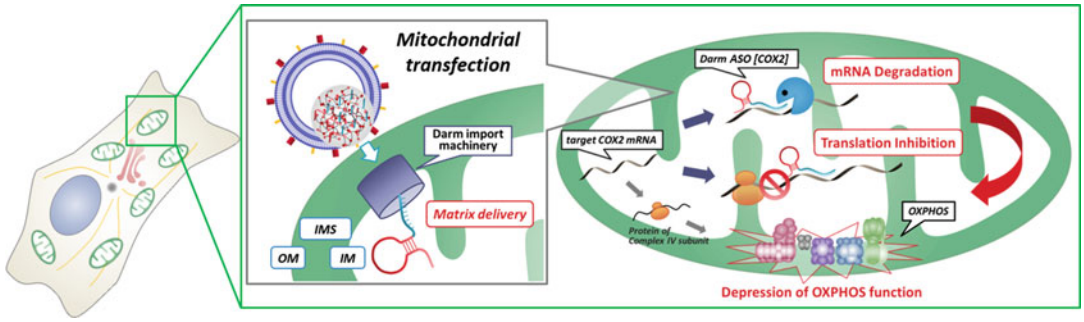


**Fig. 2** Conceptual image of mitochondrial delivery and gene silencing. After reaching to the mitochondria, a nanoparticle of Darm (a mitochondrial tRNA import signal) modified ASO is delivered to the IMS by the MITO-Porter carrier via membrane fusion with the OM of a mitochondrion, and is then imported into the mitochondrial matrix via the Darm import machinery. In this experiment, the mRNA that codes for COX2 was chosen as the target. COX2 is one of mitochondrial proteins to regulate mitochondrial OXPHOS function as a subunit of Complex IV. If the binding of Darm ASO [COX2] to the target mRNA is successful, the target mRNA would be degradation or translation from the target mRNA inhibited. Finally, the expression levels of target mitochondrial protein would be decreased, followed by a reduction in mitochondrial OXPHOS function. Darm ASO [COX2], Darm modified antisense 2′-OMe RNA which targeted cytochrome c oxidase subunit II (COX2); IM, inner membrane; IMS, intermembrane space; OM, outer membrane; OXPHOS, oxidative phosphorylation [22]

6. Stearyl octaarginine (STR-R8) (Kurabo Industries Ltd., Osaka, Japan) [24].
7. Cholesteryl (Chol)-GALA (cholesteryl- WEAALAEALAEA LAEHLAEALAEALEALAA -$NH_2$) (KURABO Industries Ltd) [25, 26].

### 2.2 Liposome Preparation

1. Lipid stock solutions: Dissolve 1 mM Lipid in 100% ethanol (*see* **Notes 2–4**). Store at −20 °C.
2. HEPES buffer: 10 mM 2-[4-(2-Hydroxyethyl)-1-piperazinyl] ethanesulfonic acid, pH 7.4. Store at 4 °C.
3. DNase I protein (from bovine pancreas, Grade II) (Roche Diagnostics GmbH, Mannheim Germany).
4. DNase I protein sol.: 1 mg/mL DNase I protein in HEPES buffer. Store at −80 °C (*see* **Note 5**).
5. Darm modified antisense 2′-*O*-Methyl (2′-OMe) RNA targeting COX II (Darm ASO [COX2]) (5′-GGGACUGUAGCU CAAUUGGUAGAGCAUCUUGCGCUGCAUGUGCCAU-3′) and Darm-modified 2′-OMe RNA nontargeting COX2 (Darm Mock) (5′-GGGACUGUAGCUCAAUUGGUAGAG CAUCGACAAGCGCACCGAU-3′) (Hokkaido System Science Co., Ltd., Sapporo, Japan) [21].
6. Polyethyleneimine (PEI) (a linear, 10 kDa molecule).
7. Bath-type sonicator (85 W) (Aiwa Co., Tokyo, Japan).

8. Probe-type sonicator ((Digital Sonifier 250) (Branson Ultrasonics Co., Danbury, CT, USA).
9. Zetasizer Nano ZS (Malvern, Worcestershire, UK).

### 2.3 Cell Cultures

1. HeLa cells: HeLa human cervix carcinoma cells (RIKEN Cell Bank, Tsukuba, Japan).
2. DMEM: Dulbecco's modified Eagle medium.
3. FBS: Inactivate fetal bovine serum (Life Technologies Corporation).
4. Penicillin G Potassium.
5. Streptomycin sulfate.
6. DMEM [+]: DMEM supplemented with 10% FBS, penicillin (100 U/mL), and streptomycin (100 μg/mL).
7. 6-well plate.
8. 24-well plate.
9. PBS (−): Dissolve the powdered Dulbecco's Phosphate buffered saline (−) in Water. Autoclave.

### 2.4 Evaluation of the Levels of mtDNA

1. GenElute Mammalian Genome DNA Miniprep kit (Sigma-Aldrich).
2. NanoDrop: NanoDropLITE (Thermo Fisher Scientific, Waltham, MA, USA).
3. Finnzyme Taq DNA Polymerase with dNTP Mix (Thermo Fisher Scientific) includes Taq DNA polymerase, 10× Taq buffer, and 10 mM deoxynucleoside triphosphates (dNTPs).
4. Oligodeoxynucleotides in purified form for primer (Sigma Genosys Japan, Ishikari, Japan).
5. Sequence of forward primer ND 6: 5′-ATAGGATCCTCCC GAATCAA-3′ (*see* **Note 6**).
6. Sequence of reverse primer ND 6: 5′-GTTTTAGTGGGGT TAGCGAT-3′ (*see* **Note 6**).
7. Thermal Cycler: S1000 Thermal Cycler (Bio-Rad Laboratories, Hercules, CA, USA).
8. 6× Loading dye (Toyobo Co. Ltd., Osaka, Japan).
9. Agarose gel.
10. TAE: 40 mM Tris–HCl, 40 mM acetic acid, 1 mM EDTA, pH 8.0 in Water.
11. Mupid-2plus (Advance Co. Ltd., Tokyo, Japan).
12. Image Quant LAS 4000 (GE Healthcare UK Ltd., England).

### 2.5 Evaluation of Mitochondrial Activity

1. Tetra Color ONE reagent (Seikagaku Biobusiness Corporation, Tokyo, Japan).
2. Plate reader: Benchmark plus micro plate reader (Bio-Rad Laboratories).

### 2.6 Quantification of Target Mitochondrial mRNA Levels

1. RNeasy Mini Kit (Qiagen, Hilden, Germany).
2. TURBO DNA-free Kit (Thermo Fisher Scientific [Ambion]).
3. High Capacity RNtA-to-cDNA kit (Thermo Fisher Scientific [Applied Biosystems]).
4. THUNDERBIRD SYBR qPCR Mix (TOYOBO CO., LTD.).
5. Sequence of the forward primer for mitochondrial mRNA coding COX2 (target mRNA): 5′- ATCATCCTAGTCCT CATCG-3′.
6. Sequence of the reverse primer for mitochondrial mRNA coding COX2 (target mRNA): 5′-GATTTGATGGTAAGGGAGG -3′.
7. Sequence of the forward primer for β-actin mRNA encoded in nuclear DNA (internal control RNA): 5′- GGGACGACATG GAGAAAATC-3′.
8. Sequence of the reverse primer for β-actin mRNA encoded in nuclear DNA (internal control RNA): 5′-GAAGGTCTCAAA CATGATCTGG-3′.
9. LightCycler 480 (Sigma-Aldrich Co. LLC. [Roche]).

### 2.7 Evaluation of Mitochondrial Membrane Potential

1. JC-1 (Thermo Fisher Scientific [Invitrogen]).
2. Hoechst 33342 (DOJINDO LABORATORIES, Kumamoto, Japan).
3. Carbonyl cyanide 4-(trifluoromethoxy) phenylhydrazone (FCCP) (Thermo Fisher Scientific [Invitrogen]).
4. Confocal laser scanning microscopy CLSM (FV10i-LIV; Olympus Corporation, Tokyo, Japan).

## 3 Methods

Carry out all procedures at room temperature, unless otherwise specified.

### 3.1 Construction of DF-MITO-Porter Encapsulating DNase I

The construction of the DF-MITO-Porter encapsulating DNase I involves the following three steps: the construction of nanoparticles containing DNase I; coating the nanoparticles with a mitochondria-fusogenic envelope; further coating the endosome-fusogenic envelope [18], based on our previous report regarding gene packaging with two-different types of lipid layers [27].

**Table 1**
**Lipid composition of the properties of SUV**

| | Lipid composition | Component before evaporation to form lipid film | | Total lipid concentration of SUV[a] | Note |
|---|---|---|---|---|---|
| SUV(D/S/C) | DOPE/SM/CHEMS (9/2/1, molar ratio) | 1 mM DOPE | 675 μL | 0.6 mM | Mitochondrial fusogenic SUV for inner |
| | | 1 mM SM | 150 μL | | |
| | | 1 mM CHEMS | 75 μL | | |
| | | $CHCl_3$ | 750 μL | | |
| SUV(E/C) | EPC/CHEMS (9/2, molar ratio) | 1 mM EPC | 675 μL | 0.55 mM | Non fusogenic SUV for inner envelopes |
| | | 1 mM CHEMS | 150 μL | | |
| | | $CHCl_3$ | 750 μL | | |
| SUV(D/P) | DOPE/PA (7/2, molar ratio) | 1 mM DOPE | 642 μL | 0.55 mM | Endosome-fusogenic SUV for outer envelopes |
| | | 1 mM PA | 183 μL | | |
| | | $CHCl_3$ | 750 μL | | |

[a]Total lipid concentration of SUV in 1.5 mL HEPES buffer after sonication

1. Mix the DNase I protein solution (1 mg/mL) and STR-R8 in 100 μL of HEPES buffer at a ratio of 1:1 (v/v) (STR-R8/DNase I protein molar ratio of 10) (*see* **Note 7**), and incubate the resulting mixture at 25 °C to form positively charged nanoparticles.
2. Form lipid films on the bottom of a glass tube following the lipid composition list shown in Table 1 (*see* **Note 8**). Add 1.5 mL of HEPES buffer to the dried lipid film on the bottom of a glass tube, and then incubate the mixture for 10–15 min at room temperature to allow hydration to occur (*see* **Note 9**). Sonicate the suspensions using a bath-type sonicator for 30–60 s to generate empty vesicles, then sonicate the resulting vesicles using a probe-type sonicator for 10 min on ice to generate small unilamellar vesicles (SUVs).
3. Mix the suspension of complexed DNase I nanoparticles (0.5 mg/mL) and suspended mitochondrial fusogenic SUV (D/S) or a nonfusogenic SUV (E/C) at a ratio of 1:3 (v/v) to coat the complexed DNase I nanoparticles with a double-lipid envelope, as described in a previous study [27, 28]. Add the STR-R8 solution (10 mol% of lipids) to the resulting suspension, and then incubate the solution for 30 min at room temperature after gentle mixing, to modify the R8 on the surface of the envelopes (*see* **Note 10**).

4. Mix the resulting suspension of lipid envelopes and an endosome-fusogenic SUV (D/P) (total lipid concentration: 0.6 mM) at a ratio of 1:2 (v/v) to generate particles with a double endosome-fusogenic envelope. Modify the surface of the envelopes with R8 (10 mol% R8 of lipids) as described above (*see* **Note 11**), to produce the DF-MITO-Porter and a control carrier with nonmitochondrial fusogenic inner envelope.
5. Measure the particle diameters of the liposomes using a quasi-elastic light scattering method, and determine the $\zeta$-potentials by electrophoretically using laser doppler velocimetry (Zetasizer Nano ZS) (*see* **Notes 12** and **13**).

### 3.2 Cell Cultures and the Mitochondrial Delivery of DNase I Using DF-MITO-Porter

1. Seed HeLa cells ($2 \times 10^5$ cells/well) on a 6-well plate with 2 mL DMEM [+] for mtDNA detection assay, or HeLa cells ($1 \times 10^4$ cells/well) on a 24 well plate with 500 μL DMEM [+] for mitochondrial activity assay (*see* **Note 14**).
2. Incubate the cells for 24 h at 37 °C under an atmosphere of 5% $CO_2$–air.
3. Wash the cells with ice-cold PBS (−), and incubate them with the DNase I protein encapsulated carriers in serum-free DMEM (applied dose of DNase I: 6 μg) (*see* **Notes 15** and **16**).
4. Wash the cells with ice-cold PBS (−) after a 3 h incubation under an atmosphere of 5% $CO_2$–air at 37 °C, and further incubate the cells in DMEM [+] for 21 h in the absence of the carriers.

### 3.3 Evaluation of the Levels of mtDNA After Mitochondrial Delivery of DNase I Using DF-MITO-Porter System

To verify that mtDNA levels were decreased after the mitochondrial delivery of DNase I using the DF-MITO-Porter, the mtDNA levels within the cells are evaluated by means of a PCR assay to detect the ND6 genes coded in the mtDNA.

1. After the mitochondrial delivery of DNase I using the DF-MITO-Porter, wash the cells with ice-cold PBS (−), trypsinize them, suspend the cells in DMEM [+] and isolate the cells in the form of a precipitate by centrifugation (1800 × *g*, 4 °C, 3 min). Wash the pellets with PBS (−) and precipitate again by centrifugation (1800 × *g*, 4 °C, 3 min).
2. To evaluate the levels of mtDNA using PCR, isolate cellular DNA from cell lysates and purify by means of a GenElute Mammalian Genome DNA Miniprep kit. Determine the concentrations and purity of the DNA by NanoDrop and dilute to 10 ng/μL with water (*see* **Note 17**).
3. Place PCR tubes on ice, place aliquots of the PCR master mix into individual PCR tubes and add template DNA for each

**Table 2**
**Reaction components for the PCR assay**

| Component[a] | 25 μL of reaction | Final concentration |
|---|---|---|
| 10× *Taq* buffer | 2.5 μL | 1× |
| 10 mM dNTPs | 0.5 μL | 200 μM |
| 100 μM forward primer | 0.125 μL | 0.5 μM |
| 100 μM reverse primer | 0.125 μL | 0.5 μM |
| Template DNA (10 ng/μL) | 1 μL | 10 ng |
| *Taq* DNA polymerase (5 U/μL) | 0.125 μL | 0.625 U/25 μL PCR |
| Wafer | to 25 μL | |

[a]Component includes PCR master mix (10× Taq Buffer buffer, 10 mM dNTPs, primers, and Taq DNA polymerase) and Template DNA

**Table 3**
**Thermocycling conditions for routine PCR**

| Step | Temp | Time |
|---|---|---|
| Initial denaturation | 94 °C | 2 min |
| 30 cycles | 94 °C<br>55 °C<br>72 °C | 30 s<br>30 s<br>45 s |
| Final extension | 72 °C | 10 min |
| Hold | 4 °C | |

25 μL of reaction volume, as shown in Table 2. Gently mix the samples and spin down to collect the droplets (*see* **Notes 18**).

4. Quickly transfer the samples to a thermocycler that had been preheated to the denaturation temperature (94 °C) and start the PCR in thermocycling conditions, as shown in Table 3.
5. Mix 5 μL of PCR products and 1 μL of 6× Loading dye, apply the mixture to each well with 2% agarose gel in TAE and then run electrophoresis using Mupid-2plus at 100 V for 30 min.
6. To detect DNA, incubate the agarose gel after electrophoresis in an ethidium bromide solution for 30 min at room temperature. After incubation, wash the agarose gel with water three times.
7. Visualize the DNA bands by UV after ethidium bromide staining using Image Quant LAS 4000 (*see* **Notes 19** and **20**).

### 3.4 Evaluation of Mitochondrial Activity After the Mitochondrial Delivery of DNase I

In this experiment, mitochondrial activity would be predicted to be inversely proportional to the efficiency of the mitochondrial delivery of DNase I. Mitochondrial activity was evaluated by measuring the activity of mitochondrial dehydrogenase after the delivery of DNase I by the DF-MITO-Porter.

1. After the mitochondrial delivery of DNase I using the DF-MITO-Porter, wash the cells with ice-cold PBS (−) and add 250 μL of DMEM [+] to the cell suspension.
2. Add 25 μL of Tetra Color ONE reagent DMEM [+] to the cells of each well and incubate the cells at 37 °C for 1 h under an atmosphere of 5% $CO_2$–air.
3. After incubation, measure the absorbance (wave length at 450 nm for sample and 630 nm for reference) at 37 °C after shaking for 5 s, use a plate reader to determine mitochondrial dehydrogenase activity (*see* **Notes 21** and **22**).
4. Estimate the mitochondrial activity (%), which is calculated as follows:

$$\text{Mitochondrial activity } (\%) = (AS_{450} - AS_{630})/(AU_{450} - AU_{630}) \times 100$$

where AS, AU represent the absorbance at 450 nm or 630 nm, for cells that were treated and untreated with samples, respectively (*see* **Note 23**).

### 3.5 Construction of a MITO-Porter Encapsulating Nanoparticles of ASO

The MITO-Porter encapsulating ASO–PEI nanoparticles was constructed by the hydration method [29, 30]. The construction of the MITO-Porter that contains encapsulated ASO requires the following steps: (1) the formation of a nanoparticle of ASO with a PEI via electrostatic interactions, (2) packaging the ASO nanoparticle in a mitochondrial fusogenic lipid envelope modified with GALA (an endosomal escape device), followed by modifying the carrier with the R8 peptide (a cellular uptake and mitochondrial targeting device) [22] (Fig. 5).

1. Mix a solution of ASO [Darm ASO [COX2] or Darm Mock] and a linear PEI (10 kDa) solution in 10 mM HEPES buffer (pH 7.4) at a nitrogen–phosphate (N/P) ratio of 5 to form a positively charged ASO–PEI nanoparticle.
2. Form lipid films (175 nmol lipid) on the bottom of a glass tube following the lipid composition [DOPE–SM–CHEMS–Chol-GALA (lipid ratio of 9:2:3:0.2)] (*see* **Note 24**).
3. Add 250 μL of HEPES buffer containing the ASO–PEI complex (1094 pmol ASO) to the dried lipid film on the bottom of a glass tube, and then incubate for 10–15 min at room temperature to allow hydration to occur (*see* **Note 9**). Sonicate the suspensions using a bath-type sonicator for 30–60 s to generate vesicles.

4. Add the STR-R8 solution (10 mol% of lipids) to the resulting suspension, and then incubate for 30 min at room temperature after gentle mixing, to modify the R8 on the surface of the envelopes, to produce the MITO-Porter (ASO [COX2]/PEI) and a control carrier [MITO-Porter (Mock/PEI)] encapsulating Darm Mock.
5. Measure the particle diameters of the liposomes using a quasi-elastic light scattering method, and determine the $\zeta$-potentials by electrophoretically using laser doppler velocimetry (Zetasizer Nano ZS) (*see* **Notes 13**, **25**, and **26**).

### 3.6 Cell Culture and the Mitochondrial Transfection of ASO Using MITO-Porter

1. Seed HeLa cells ($2 \times 10^5$ cells/well) on a 6-well plate with 2 mL of DMEM [+] for quantification of the target mitochondrial mRNA levels, or HeLa cells ($1 \times 10^5$ cells/dish) on a 35 mm dish with 2 mL DMEM [+] for the evaluation of the mitochondrial membrane (*see* **Note 14**).
2. Incubate the cells at 37 °C for 24 h under an atmosphere of 5% $CO_2$–air.
3. Wash the cells with ice-cold PBS (−), and incubate them with the ASO encapsulated MITO-Porters in serum-free DMEM (*see* **Notes 27** and **28**).
4. Wash the cells with ice-cold PBS (−) after a 3 h incubation at 37 °C under an atmosphere of 5% $CO_2$–air, and further incubate the cells in DMEM [+] for 21 h for the quantification of target mitochondrial mRNA levels, or 45 h for the evaluation of the mitochondrial membrane in the absence of the carriers.

### 3.7 Quantification of Target Mitochondrial mRNA Levels After Mitochondrial Transfection of ASO Using MITO-Porter System

To evaluate the antisense effect by the delivered Darm ASO [COX2] in the mitochondrial genomic system, the level of expression of target COX2 mRNA was evaluated by quantitative RT-PCR.

1. After the mitochondrial transfection of ASO using the MITO-Porter, purify the total RNA with an RNeasy Mini Kit, followed by DNase I digestion to degrade the DNA in total RNA samples using a TURBO DNA-free Kit (*see* **Note 29**). Then, reverse transcribe the resulting RNA suspension using a High Capacity RNA-to-cDNA kit (*see* **Note 29**). Determine the concentrations and purity of the DNA by NanoDrop and dilute to 10 ng/μL with water (*see* **Note 17**).
2. Perform a quantitative PCR analysis on the cDNA using the THUNDERBIRD SYBR qPCR Mix and LightCycler 480. Use the primers for mitochondrial mRNA coding COX2 (the target mRNA) and β-actin mRNA encoded in nuclear DNA (internal control RNA). Perform all reactions using a volume of 5 μL.

3. Calculated relative COX2–β-actin mRNA expression levels as the amount of DNA derived from COX2 mRNA divided by the amount of DNA derived from β-actin mRNA (*see* **Notes 30** and **31**).

### 3.8 Evaluation of Mitochondrial Membrane Potential After Mitochondrial Transfection of ASO

The ASO [COX2] used in this study targets mRNA that codes for the COX2 subunit, a component of the mitochondrial electron transport chain, complex IV. When a defect in the mitochondrial oxidative phosphorylation (OXPHOS) system is created by an antisense effect, a decrease in mitochondrial membrane potential is induced. The mitochondrial membrane potential was evaluated after the transfection of the MITO-Porter by means of a JC-1 assay (*see* **Note 32**).

1. After the mitochondrial transfection of ASO using the MITO-Porter, at 30 min and 10 min before acquiring the fluorescence images, the cells were stained with JC-1 (final concentration, 10 μM) to observe the mitochondrial membrane potential and Hoechst 33342 (final concentration, 5 μg/mL) to stain the nuclei, respectively.
2. After the incubation, the cells were washed with phenol red free serum containing DMEM, and then observed by CLSM (FV10i-LIV).
3. The cells were excited with a 405 nm light, a 473 nm light and a 559 nm light from an LD laser. Images were obtained using an FV10i-LIV equipped with a water-immersion objective lens (UPlanSApo 60×/NA. 1.2) and a dichroic mirror (DM405/473/559/635).
4. The following filters were set for the observation: Ch1: 455/50 (blue) for Hoechst 33342, Ch2: 490/50 (green) for monomeric form of JC-1, Ch3: 570/50 (red) for aggregated form of JC-1 (*see* **Note 33**) (Fig. 6).

## 4 Notes

1. COX2 is one of the mitochondrial proteins that make up complex IV of the electron transport system that functions in the inner membrane of mitochondria. When the ASO was delivered to mitochondria, it became bound to the target COX2 mRNA in mitochondria, followed by the degradation of the target mRNA or the inhibition of translation. In addition, the expression level of the target COX2 protein of the mitochondrial respiratory chain complex subunit would be expected to decrease the mitochondrial membrane potential and decrease overall ATP production, eventually resulting in cell death (Fig. 2).

2. Dissolve the lipid by sonication using a bath type sonicator, when the lipid does not readily dissolve in the solvent.
3. Dissolve the lipid in 100% ethanol–chloroform (1:1, v/v) when PA is used, and store the solution in a glass tube not a plastic tube.
4. Incubate the lipid stocks at room temperature before use.
5. Thaw the DNase I protein solution on ice before use. Do not repeat thawing and freezing.
6. Polymerase chain reaction (PCR) assays to detect the mitochondrial NADH dehydrogenase 6 (ND6) gene are performed in order to detect the mtDNA from HeLa cell lysates. These primers anneal the 106–251 sequence in the ND6 region of the mitochondrial genome (146 bp length).
7. Gentle mixing during this procedure is recommended.
8. Check that a thin lipid film is formed. If optimization of the lipid film is needed, dry the solvent again after the addition of 1.5 mL of a 100% ethanol–chloroform (1:1, v/v) solution to the glass tubes.
9. Mix the lipid suspension using a vortex mixer before sonication.
10. For the DF-MITO-Porter, the inner envelope has a mitochondria-fusogenic composition [DOPE–SM–CHEMS–STR-R8 (9:2:1:1, molar ratio)]. As a negative control, a non-fusogenic inner envelope was prepared using the lipid composition (EPC–CHEMS–STR-R8 [9:2:1, molar ratio]) [4, 18].
11. The outer envelope had an endosome-fusogenic composition (DOPE–PA–STR-R8 [7:2:1, molar ratio]) [18, 27, 31].
12. The particle diameters of the DF-MITO-Porter should be around 150 nm and the $\zeta$-potentials should be around +30 mV [18].
13. We find that it is best to prepare the carriers fresh each time.
14. Culture the HeLa cells at 37 °C in DMEM [+] under an atmosphere of 5% $CO_2$–air.
15. HeLa cells should be incubated in 1 mL of serum-free DMEM on a 6-well plate for the mtDNA detection assay. HeLa cells should be incubated in 250 μL of serum-free DMEM on a 24-well plate for the mitochondrial activity assay.
16. The outer envelopes of the carriers used in this experiment are composed of DOPE–PA–STR-R8 (7:2:1, molar ratios). It has been reported that high-density R8-modified liposomes are taken up mainly through macropinocytosis and then delivered to the cytosol [7].
17. Store at −20 °C. Thaw the DNA on ice before use.

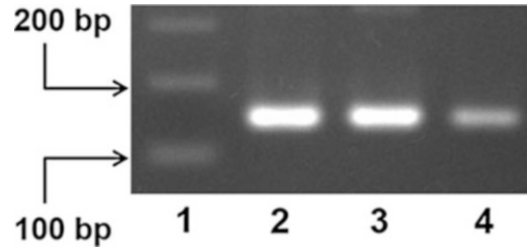


**Fig. 3** Evaluation for the levels of mtDNA after the mitochondrial delivery of DNase I. DNase I proteins encapsulated in the DF-MITO-Porter or the control carrier with low mitochondrial fusion activity were incubated with HeLa cells. Cellular DNA samples were collected and then subjected to PCR. The PCR products were detected by ethidium bromide staining after separation by electrophoresis. PCR assays for the ND6 gene (146 bp) detection were performed in order to detect mtDNA. Lane 1, 100 bp DNA Ladder; lane 2, Nontreatment; lane 3, control carrier with low mitochondrial fusion activity [EPC–CHEMS–STR-R8]; lane 4, DF-MITO-Porter [DOPE–SM–CHEMS–STR-R8]. ND6, mitochondrial NADH dehydrogenase 6 [19].

18. To minimize the possibility of pipetting errors and to save time by reducing the number of reagent transfers, prepare a PCR master mix by adding water, 10× Taq Buffer nonautogenic, 10 mM dNTPs, primers and Taq DNA polymerase, then add the template DNA from HeLa cell lysate solutions to each tube.
19. Figure 3 shows agarose gel electrophoresis data for the PCR products derived from mtDNA. In the case of the DF-MITO-Porter with inner envelopes composed of DOPE–SM–CHEMS–STR-R8 (9:2:1:1), the mtDNA levels were decreased (Lane 4), whereas the effect of carriers with a low mitochondrial fusion activity with inner envelopes composed of EPC–CHEMS–STR-R8 (9:2:1) on mtDNA levels was negligible (Lane 2) [19].
20. It was confirmed that, a decrease in nuclear DNA levels was not detected in the case of the DF-MITO-Porter with inner envelopes composed of DOPE–SM–CHEMS–STR-R8 (9:2:1:1) [19].
21. The assay is based on the cleavage of the tetrazolium salt 2-(2-Methoxy-4-nitrophenyl)-3-(4-nitrophenyl)-5-(2,4-disulfophenyl)-2*H*-tetrazolium, monosodiumsalt (WST)-8 by mitochondrial dehydrogenase in viable cells, leading to the generation of a formazan dye.
22. The inner envelope of the DF-MITO-Porter and control carrier used in this experiment is composed of DOPE–SM–CHEMS–STR-R8DOPE–SM–CHEMS–STR-R8 (9:2:1:1, molar ratios) and EPC–CHEMS–STR-R8 (9:2:1, molar ratios), respectively [19].

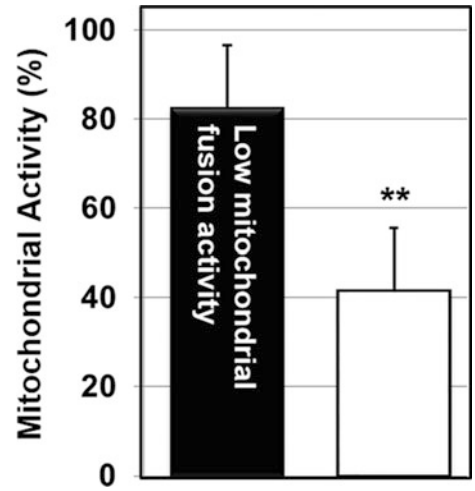


**Fig. 4** Mitochondrial delivery of DNase I using the DF-MITO-Porter. DNase I (0.5 μg) encapsulated in the DF-MITO-Porter or the control carrier with a low mitochondrial fusion activity were incubated with HeLa cells. Mitochondrial activity was then evaluated by measuring mitochondrial dehydrogenase activity. Data are represented as the mean ± S.D. ($n = 3$–4). **Significant differences between control carrier with low mitochondrial fusion activity [EPC–CHEMS–STR-R8] and DF-MITO-Porter [DOPE–SM–CHEMS–STR-R8] ($p < 0.01$ by a two-tailed unpaired Student's *t*-test) [19]

23. As shown in Fig. 4, the use of the DF-MITO-Porter with inner envelopes composed of DOPE–SM–CHEMS–STR-R8 (9:2:1:1) resulted in a significant decrease in mitochondrial activity, whereas the effect of carriers with a low mitochondrial fusion activity with inner envelopes composed of EPC/CHEMS/STR-R8 (9:2:1) on mitochondrial activity was negligible.
24. Confirm that a thin lipid film is formed. If optimization of the lipid film is needed, dry the solvent again after adding 250 μL of 100% ethanol–chloroform (1:1, v/v) to the glass tubes.
25. The particle diameters of the MITO-Porter should be less than 200 nm and the ζ-potentials should be around +30 mV [18].
26. The packaging of ASO in the MITO-Porter [160 mol lipid–RNA ratio] via a nanoparticle packaging method showed a tenfold higher packaging efficiency than when the conventional method was used [1680 mol lipid–RNA ratio] [18].
27. The carriers used in this experiment contain STR-R8. It has been reported that high-density R8-modified liposomes are taken up mainly through macropinocytosis and then delivered to the cytosol [7].

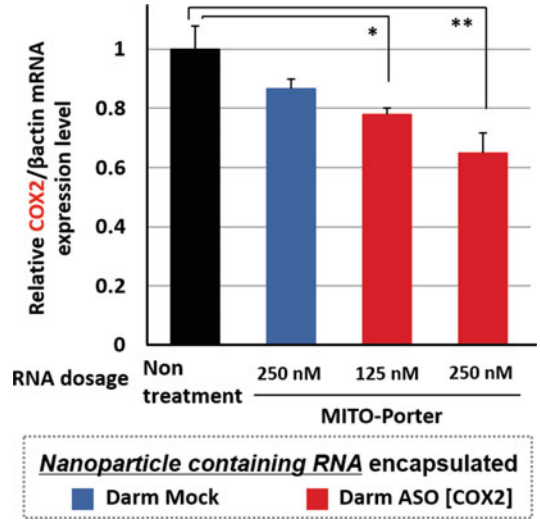


**Fig. 5** Evaluation of mitochondrial mRNA expression levels after transfection by the MITO-Porter system. After 24 h transfection of nanoparticles containing RNA (Darm Mock or Darm ASO [COX2]) by MITO-Porter (ASO–PEI), the knockdown effect of mitochondrial mRNA (COX2 encoded in mtDNA) was evaluated by quantitative RT-PCR. Relative mRNA expression levels were normalized with the value of nontreated cells as 1. In this experiment, β-actin mRNA encoded in nuclear DNA was used as an internal control. Bars indicate the mean with SEM ($n = 3$–7). Significant differences between nontreatment and others were detected (**$p < 0.01$, *$p < 0.05$ by one-way ANOVA analysis, followed by Bonferroni's correction). N.S., no significant difference [22]

28. HeLa cells were incubated in 1 mL of serum-free DMEM on a 6-well plate for the mtDNA detection assay. HeLa cells were incubated in 250 μL of serum-free DMEM on a 24 well plate for the mitochondrial activity assay.
29. These experiments should be performed according to the manufacturer's suggested protocol.
30. Figure 5 provides information on the quantification of the target mitochondrial mRNA expression levels by a quantitative PCR analysis. In the case of the MITO-Porter (ASO [COX2]/PEI), the COX2 mRNA levels were significantly decreased, whereas the effect of the MITO-Porter (Mock/PEI) on target mitochondrial mRNA expression levels was negligible [22].
31. It was confirmed that, no change in the expression level of COX2 mRNA was observed when Darm ASO [COX2] was transfected using a commercially available gene transfer reagent, LFN RNAi MAX [22].
32. JC-1 is a mitochondrial membrane potential-dependent staining reagent that shows a green fluorescence in the monomer state, but red when the monomer has undergone aggregation.

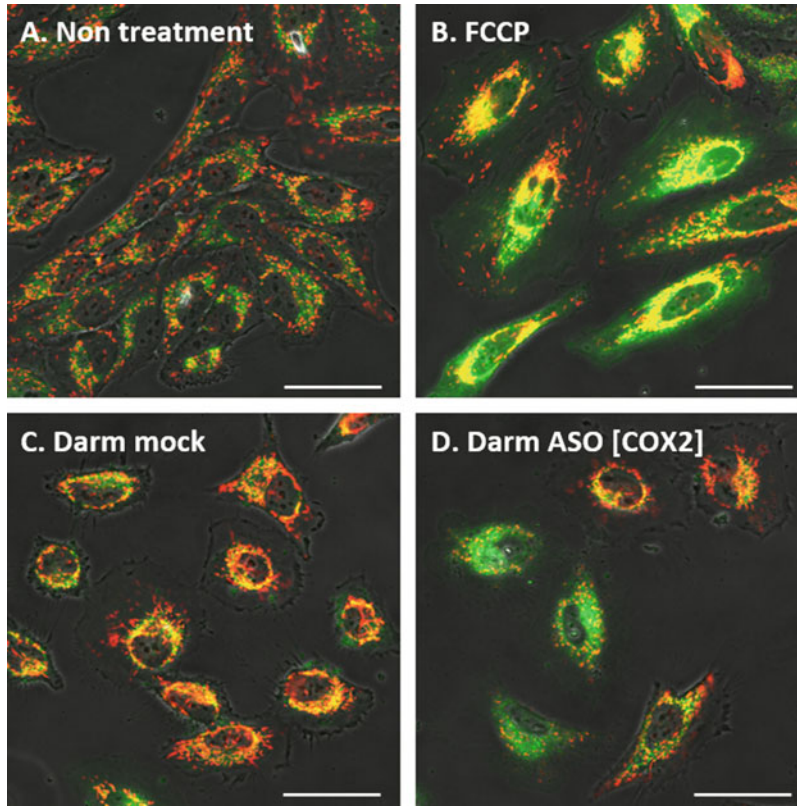


**Fig. 6** CLSM image of mitochondrial membrane potential using JC-1 at 48 h after the transfection of nanoparticles containing RNA by MITO-Porter (**a**, Nontreatment; **b**, FCCP; **c**, Darm Mock; **d**, Darm ASO [COX2]). The accumulation of JC-1 in normal mitochondria with a high membrane potential results in the production of a fluorescent red signal (**a**), while a fluorescent green signal is produced in the case of mitochondria that have lost their membrane potential (**b**). Scale bars, 50 mm

In normal cells, JC-1 accumulates in mitochondria, depending on the mitochondrial membrane potential, and shows a strong red fluorescence (Fig. 6a). On the other hand, when an uncoupling agent (FCCP), which lowers the mitochondrial membrane potential is added to the cells, JC-1 diffuses into the cytoplasm from mitochondria, resulting in the generation of a strong green fluorescence caused by the monomeric form of JC-1 (Fig. 6b).

33. As shown in Fig. 6, a strong green fluorescence appeared in the case of MITO-Porter (ASO [COX2]/PEI) (Fig. 6d), whereas, red-colored mitochondria were observed in the case of the MITO-Porter (Mock/PEI) (Fig. 6c).

## Acknowledgements

This work was supported, in part by, the Grant-in-Aid for Young Scientists (A) and Grant-in-Aid for Challenging Exploratory Research from the Ministry of Education, Culture, Sports, Science and Technology of Japanese Government (MEXT), and the A-STEP feasibility study program in Japan Science and Technology Agency (JST). We also wish to thank Dr. Milton Feather for his helpful advice in writing the manuscript.

### References

1. Chen H, Chan DC (2009) Mitochondrial dynamics--fusion, fission, movement, and mitophagy--in neurodegenerative diseases. Hum Mol Genet 18(R2):R169–R176
2. Kyriakouli DS, Boesch P, Taylor RW, Lightowlers RN (2008) Progress and prospects: gene therapy for mitochondrial DNA disease. Gene Ther 15(14):1017–1023
3. Schapira AH (2006) Mitochondrial disease. Lancet 368(9529):70–82
4. Yamada Y, Akita H, Kamiya H, Kogure K, Yamamoto T, Shinohara Y, Yamashita K, Kobayashi H, Kikuchi H, Harashima H (2008) MITO-porter: a liposome-based carrier system for delivery of macromolecules into mitochondria via membrane fusion. Biochim Biophys Acta 1778(2):423–432
5. Yamada Y, Harashima H (2008) Mitochondrial drug delivery systems for macromolecule and their therapeutic application to mitochondrial diseases. Adv Drug Deliv Rev 60 (13-14):1439–1462
6. Kogure K, Akita H, Yamada Y, Harashima H (2008) Multifunctional envelope-type nano device (MEND) as a non-viral gene delivery system. Adv Drug Deliv Rev 60(4-5):559–571
7. Khalil IA, Kogure K, Futaki S, Harashima H (2006) High density of octaarginine stimulates macropinocytosis leading to efficient intracellular trafficking for gene expression. J Biol Chem 281(6):3544–3551
8. Del Gaizo V, Payne RM (2003) A novel TAT-mitochondrial signal sequence fusion protein is processed, stays in mitochondria, and crosses the placenta. Mol Ther 7 (6):720–730
9. Yamada Y, Akita H, Harashima H (2012) Multifunctional envelope-type nano device (MEND) for organelle targeting via a stepwise membrane fusion process. Methods Enzymol 509:301–326
10. Yasuzaki Y, Yamada Y, Harashima H (2010) Mitochondrial matrix delivery using MITO-porter, a liposome-based carrier that specifies fusion with mitochondrial membranes. Biochem Biophys Res Commun 397(2):181–186
11. Yamada Y, Daikuhara S, Tamura A, Nishida K, Yui N, Harashima H (2019) Enhanced autophagy induction via the mitochondrial delivery of methylated beta-cyclodextrin-threaded polyrotaxanes using a MITO-porter. Chem Commun (Camb) 55(50):7203–7206
12. Satrialdi, Munechika R, Biju V, Takano Y, Harashima H, Yamada Y (2020) The optimization of cancer photodynamic therapy by utilization of a pi-extended porphyrin-type photosensitizer in combination with MITO-porter. Chem Commun (Camb) 56 (7):1145–1148
13. Hibino M, Yamada Y, Fujishita N, Sato Y, Maeki M, Tokeshi M, Harashima H (2019) The use of a microfluidic device to encapsulate a poorly water-soluble drug CoQ10 in lipid nanoparticles and an attempt to regulate intracellular trafficking to reach mitochondria. J Pharm Sci 108(8):2668–2676
14. Yamada Y, Takano Y, Satrialdi, Abe J, Hibino M, Harashima H (2020) Therapeutic strategies for regulating mitochondrial oxidative stress. Biomol Ther 10(1):83
15. Yamada Y, Fujishita N, Harashima H (2020) A nanocarrier for the mitochondrial delivery of nucleic acids to cardiomyocytes. Nucleosides Nucleotides Nucleic Acids 39:141–155
16. Ishikawa T, Somiya K, Munechika R, Harashima H, Yamada Y (2018) Mitochondrial transgene expression via an artificial mitochondrial DNA vector in cells from a patient with a mitochondrial disease. J Control Release 274:109–117
17. Kawamura E, Maruyama M, Abe J, Sudo A, Takeda A, Takada S, Yokota T, Kinugawa S, Harashima H, Yamada Y (2020) Validation of gene therapy for mutant mitochondria by delivering mitochondrial RNA using a MITO-porter, a liposome-based nano device. Mol Ther Nucl Acids 20:687–698

18. Yamada Y, Furukawa R, Yasuzaki Y, Harashima H (2011) Dual function MITO-porter, a Nano carrier integrating both efficient cytoplasmic delivery and mitochondrial macromolecule delivery. Mol Ther 19(8):1449–1456
19. Yamada Y, Harashima H (2012) Delivery of bioactive molecules to the mitochondrial genome using a membrane-fusing, liposome-based carrier, DF-MITO-porter. Biomaterials 33(5):1589–1595
20. Yamada Y, Kawamura E, Harashima H (2012) Mitochondrial-targeted DNA delivery using a DF-MITO-porter, an innovative nano carrier with cytoplasmic and mitochondrial fusogenic envelopes. J Nanopart Res 14(8):1013–1027
21. Furukawa R, Yamada Y, Kawamura E, Harashima H (2015) Mitochondrial delivery of antisense RNA by MITO-porter results in mitochondrial RNA knockdown, and has a functional impact on mitochondria. Biomaterials 57:107–115
22. Kawamura E, Hibino M, Harashima H, Yamada Y (2019) Targeted mitochondrial delivery of antisense RNA-containing nanoparticles by a MITO-porter for safe and efficient mitochondrial gene silencing. Mitochondrion 49:178–188
23. Yamada Y, Fukuda Y, Sasaki D, Maruyama M, Harashima H (2020) Development of a nanoparticle that releases nucleic acids in response to a mitochondrial environment. Mitochondrion 52:67–74
24. Futaki S, Ohashi W, Suzuki T, Niwa M, Tanaka S, Ueda K, Harashima H, Sugiura Y (2001) Stearylated arginine-rich peptides: a new class of transfection systems. Bioconjug Chem 12(6):1005–1011
25. Kakudo T, Chaki S, Futaki S, Nakase I, Akaji K, Kawakami T, Maruyama K, Kamiya H, Harashima H (2004) Transferrin-modified liposomes equipped with a pH-sensitive fusogenic peptide: an artificial viral-like delivery system. Biochemistry 43(19):5618–5628
26. Kusumoto K, Akita H, Ishitsuka T, Matsumoto Y, Nomoto T, Furukawa R, El-Sayed A, Hatakeyama H, Kajimoto K, Yamada Y, Kataoka K, Harashima H (2013) Lipid envelope-type nanoparticle incorporating a multifunctional peptide for systemic siRNA delivery to the pulmonary endothelium. ACS Nano 7(9):7534–7541
27. Akita H, Kudo A, Minoura A, Yamaguti M, Khalil IA, Moriguchi R, Masuda T, Danev R, Nagayama K, Kogure K, Harashima H (2009) Multi-layered nanoparticles for penetrating the endosome and nuclear membrane via a stepwise membrane fusion process. Biomaterials 30(15):2940–2949
28. Lee RJ, Huang L (1996) Folate-targeted, anionic liposome-entrapped polylysine-condensed DNA for tumor cell-specific gene transfer. J Biol Chem 271(14):8481–8487
29. Yamada Y, Tabata M, Yasuzaki Y, Nomura M, Shibata A, Ibayashi Y, Taniguchi Y, Sasaki S, Harashima H (2014) A nanocarrier system for the delivery of nucleic acids targeted to a pancreatic beta cell line. Biomaterials 35 (24):6430–6438
30. Kogure K, Moriguchi R, Sasaki K, Ueno M, Futaki S, Harashima H (2004) Development of a non-viral multifunctional envelope-type nano device by a novel lipid film hydration method. J Control Release 98(2):317–323
31. El-Sayed A, Khalil IA, Kogure K, Futaki S, Harashima H (2008) Octaarginine- and octalysine-modified nanoparticles have different modes of endosomal escape. J Biol Chem 283(34):23450–23461

# Chapter 15

# mTRIP, an Imaging Tool to Investigate Mitochondrial DNA Dynamics in Physiology and Disease at the Single-Cell Resolution

**Laurent Chatre and Miria Ricchetti**

## Abstract

Mitochondrial physiology and metabolism are closely linked to replication and transcription of mitochondrial DNA (mtDNA). However, the characterization of mtDNA processing is poorly defined at the single-cell level. We developed mTRIP (*m*itochondrial *T*ranscription and *R*eplication *I*maging *P*rotocol), an imaging approach based on modified fluorescence in situ hybridization (FISH), which simultaneously reveals mitochondrial structures committed to mtDNA initiation of replication as well as the mitochondrial RNA (mtRNA) content at the single-cell level in human cells. Also specific RNA regions, rather than global RNA, can be tracked with mTRIP. In addition, mTRIP can be coupled to immunofluorescence for in situ protein tracking, or to MitoTracker, thereby allowing for simultaneous labeling of mtDNA, mtRNA, and proteins or mitochondria, respectively. Altogether, qualitative and quantitative alterations of the dynamics of mtDNA processing are detected by mTRIP in human cells undergoing physiological changes, as well as stress and dysfunction. mTRIP helped elucidating mtDNA processing alterations in cancer cells, and has a potential for diagnostic of mitochondrial diseases.

**Key words** Mitochondrial DNA, FISH , Imaging, mTRIP, Mitochondrial disease, Transcription, DNA replication, Single-cell

## 1 Introduction

Mitochondria are highly dynamic organelles that can fuse and divide to produce a variety of morphologies ranging from individual entities to interconnected tubular networks, which are functional to cell growth, cell physiology, and disease [1, 2]. In eukaryotes, mitochondria play a central role in the energy metabolism that is regulated by the nuclear genome as well as the organelle genome. In mammals, individual mitochondria carry multiple copies of double-stranded circular mtDNA, packed into nucleoids structures and autonomously replicated and transcribed [3, 4]. The human mtDNA is a 16.5 kbp molecule coding for

Volkmar Weissig and Marvin Edeas (eds.), *Mitochondrial Medicine: Volume 1: Targeting Mitochondria*, Methods in Molecular Biology, vol. 2275, https://doi.org/10.1007/978-1-0716-1262-0_15,

two ribosomal RNAs, 22 transfer RNAs, and 13 protein-coding genes that are transcribed into polycistronic precursor RNAs and then processed to mature mRNAs, rRNAs, and tRNAs ([5]) (Fig. 1). The dynamics of mtDNA replication are still debated, and distinct models are proposed ([6–8], for reviews *see* [9–11]). Nevertheless, in these models initiation of replication takes place at the $O_H$ origin, and the nascent heavy (H) strand may subsequently pause about 700 nucleotides downstream generating the 7S DNA, which produces a characteristic triple displacement loop or D-loop [12]. mtDNA replication and transcription have been extensively characterized by biochemical approaches, which assess values within large cell populations. In addition, superresolution imaging revealed, at the single cell level, that mtDNA replication occurs only in a subset of nucleoids [13, 14]. These findings underscore the urgency of combined protein and DNA analysis of mitochondrial substructures. However, classic FISH procedures may damage protein epitopes and are therefore not suitable also for immunofluorescence analysis, thereby limiting the simultaneous track of mitochondrial nucleic acids and proteins.

mTRIP, a novel imaging protocol based on modified FISH, identifies mitochondrial entities engaged in the mtDNA initiation of replication, and can simultaneously reveal the mitochondrial RNA (mtRNA) content in single human cells. Moreover mTRIP can be coupled to immunofluorescence, making possible the combined detection of mtDNA initiation of replication, mtRNA content, and proteins of choice in single human cells [15] (Fig. 2). MtDNA initiation of replication is identified by the mREP probe, which targets a specific DNA region located upstream of the replication origin $O_H$ and within in the regulatory D-loop. Probe mREP recognizes only DNA in an open structure; therefore, the double-stranded mitochondrial genome that is not engaged in replication initiation is not detected by mREP. mTRANS, a mix of three DNA probes located on different regions of the mitochondrial genome, detects specific mtRNAs which are considered representative of global mtRNA levels (Fig. 1).

We generally associate mTRIP analysis of mitochondrial nucleic acids with immunofluorescence of a mitochondrial outer membrane protein (TOM22 or TOMM22) to identify the mitochondrial network. These labeling allow for the detection and quantification of at least three classes of mitochondrial subpopulations: (1) replication initiation active and transcript-positive (Ia-Tp); (2) replication initiation silent and transcript-positive (Is-Tp); and (3) replication initiation silent and transcript-negative (Is-Tn) [15], revealing that individual mitochondria are strongly heterogeneous within human cells (Fig. 3a–d). This heterogeneity is functional to physiological changes, as during the cell cycle [16], and can be also affected during stress and disease [15]. mTRIP can be also associated with MitoTracker analysis, which detects mitochondria in living cells, based on its binding to thiol groups present

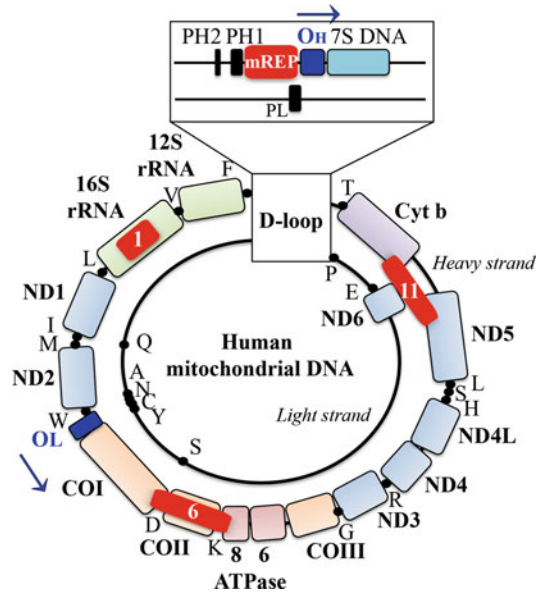


**Fig. 1** Schematic representation of the human mitochondrial DNA and probes used in mTRIP. The H (heavy) and light (L) strands of the mitochondrial genome are indicated in the external and inner circle, respectively, with the position and name of single genes within. tRNA genes are indicated with a black dot and the corresponding letter. All genes are located on the H-strand, with the exception of *ND6* and several tRNAs, located on the L-strand. Magnification of the D-loop region (which contains H-strand origin of replication ($O_H$) and promoters of both H (PH1 and PH2) and L (PL) strands) is shown on top. Blue arrows indicate the direction of DNA replication from $O_H$ and $O_L$. The position of probe mREP and probes 1, 6, and 11 is indicated with a red box. mTRANS is a mix of probes 1, 6, and 11, which targets rRNA as well as several coding genes and tRNA on both strands

in the organelle (Fig. 3e–h). Other probes than mREP and mTRANS can be produced to target specific regions of interest in the mitochondrial genome (*see* Ref. 15). For instance, mTRIP labeling with either a LSP (Light Strand Promoter)-specific probe or an ND6 (NADH-ubiquinone oxidoreductase chain 6)-specific probe was combined with immunostaining of the mitochondrial transcription factor and DNA binding protein TFAM for colocalization experiments. *ND6* is the only gene located in the L-strand of the mitochondrial genome (*see* Fig. 1), and is a component of the respiratory complex I. mTRIP contributed to show that the mitochondrial fraction of the protooncogene MDM2 directly impacts on TFAM binding to the LSP, thereby affecting *ND6* transcription and thereby the respiratory complex I function in cancer cells [17]. Described and novel mTRIP probes, combined with a variety of immunofluorescence and mitochondrial markers (Fig. 4) should help decipher mtDNA dynamics and their impact under physiological changes, including stress, and in disease.

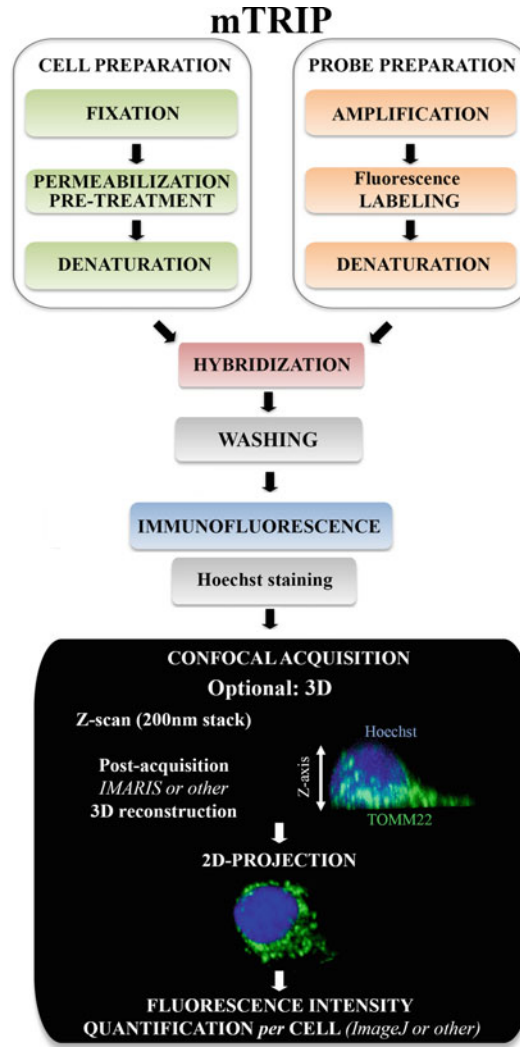


**Fig. 2** Scheme of mTRIP labeling. Summary and chronology of steps of mTRIP labeling described in detail in this document. After labeling, 3D confocal acquisition and the subsequent treatment of acquisitions are shown. 3D acquisition is necessary for fluorescence quantification of the entire cell volume, but also 2D acquisition of a single plan (and thereby fluorescence quantification of this single plan) can be performed (not shown here)

Notably, the mREP and mTRANS probes alone can act as markers of functional mtDNA processing. The investigation of functional mtDNA processing in single cells has relevance beyond classical mitochondrial activity (oxidative phosphorylation). For instance, mTRIP labeling with these two probes contributed to demonstrate that mtDNA acquired from the host mouse by mtDNA-depleted grafted cancer cells was not only present but also fully functional in individual cells a few days after grafting

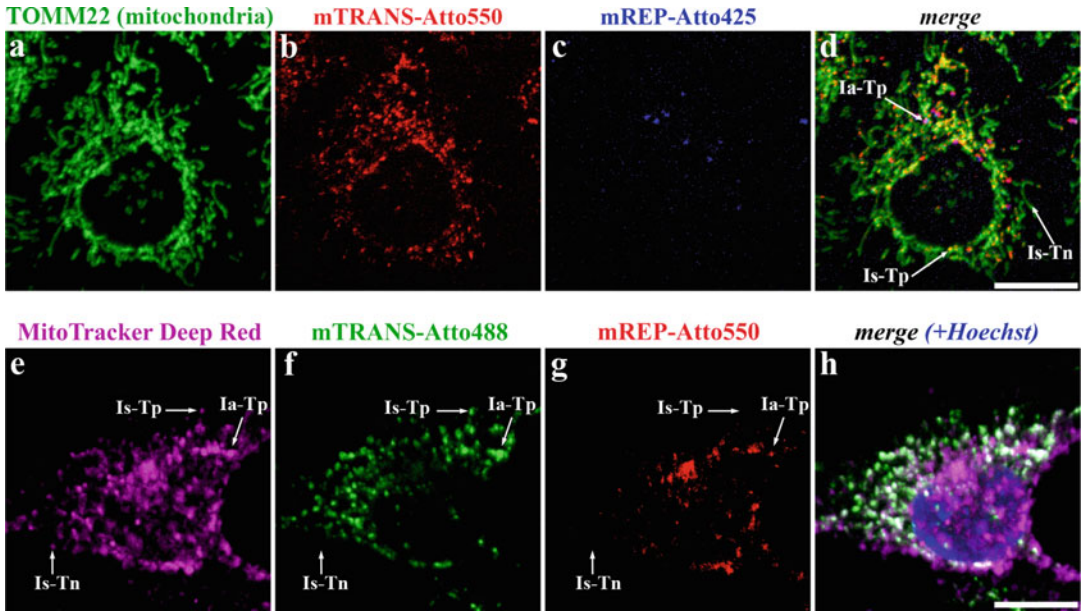


**Fig. 3** mTRIP colabeling with either immunofluorescence mitochondrial proteins or Mitotracker. Panels a-d: Colabeling of TOMM22 immunofluorescence (green, panel **a**), mTRANS (red, panel **b**), and mREP (blue, panel **c**) probes, shows mitochondrial initiation of replication, transcription, and mitochondrial network, respectively. In merge, mREP essentially colocalizes with mTRANS (purple; arrow; Ia-Tp, replication Initiation active and Transcript positive), and independent mTRANS labeling (orange; arrow; Is-Tp, replication Initiation silent and Transcript active), as well as replication Initiation silent and Transcript negative mitochondrial structures (green; arrow, Is-Tn) are also observed. Panels (**e**–**h**) Colabeling of MitoTracker Deep Red (purple; panel **e**), mTRANS (green; panel **f**), mREP (red, panel **g**), and merge (panel **h**, which was also counterstained with Hoechst, blue, for nucleus detection). MitoTracker labeling results in a more diffused signal than immunofluorescence and mTRIP, therefore colocalization with other markers appears less defined in panel **h** than in panel **d**. Ia-Tp, Is-Tp, and Is-Tn mitochondrial structures are detected also with this colabeling (presence or absence of labeling in panels **e**–**g** is shown rather than in merge, because of the limited resolution of the combined fluorescence signal by visual detection). Scale bars = 10 μm

[18]. This work demonstrated that acquisition and processing of host mtDNA, and thereby restoration of mitochondrial respiration, are essential for tumorigenesis, although not for ATP production but rather pyrimidine biosynthesis through dihydroorotate dehydrogenase (DHODH) reactivation [18]. In another study, mTRIP detection of mtDNA initiation of replication using the mREP probe helped understanding the dynamics of mtDNA synthesis/depletion. Indeed, a novel function of the endonuclease G (EndoG) both as a stimulator of mtDNA replication initiation and mtDNA depletion was identified [19, 20]. In this study, experiments that included the mTRANS probe contributed to demonstrate that removal of damaged mtDNA by EndoG is compensated by mtDNA replication to maintain mtDNA transcription and mitochondria homeostasis.

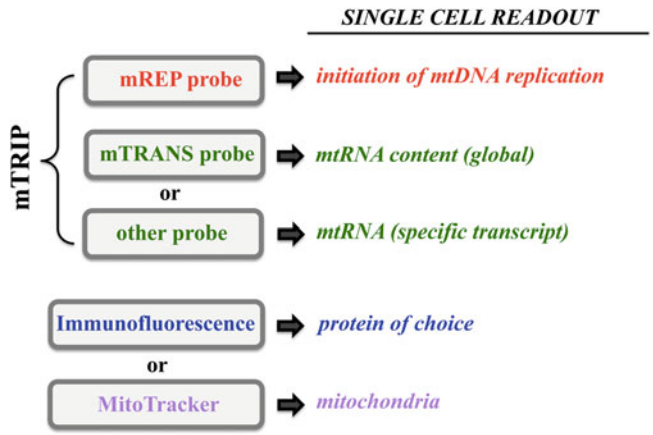


**Fig. 4** Single-cell analysis with mTRIP alone and in combination with other approaches. The readouts of distinct mTRIP probes alone and in combination with immunofluorescence or MitoTracker labeling are indicated

mTRIP is therefore a versatile and powerful tool to investigate single cell dynamics of mitochondrial DNA processing in physiology and disease.

## 2 Materials

Prepare all solutions using ultrapure water when needed. Follow all waste disposal regulations when disposing of waste materials.

### 2.1 Probe Preparation and Labeling

1. Lysis buffer to extract total genomic DNA: 0.2% SDS, 5 mM EDTA, 0.2 mg/ml Proteinase K in 1× phosphate buffered saline (PBS) buffer.
2. Sodium acetate 3 M, pH 5.2, cold ultrapure isopropanol and ultrapure water.
3. Taq DNA polymerase (we recommend LA Taq DNA polymerase TaKaRa).
4. Primers for PCR amplification of the mREP probe from total genomic DNA:

   Coordinates of all primers are according to NC_012920 GenBank.

   mREP (98 nucleotides, nt): coordinates 446-544.

   Forward 5′-ACATTATTTTCCCCTCCC-3′.

   Reverse 5′-GGGGTATGGGGTTAGCAG-3′.
5. Primers for PCR amplification of the mTRANS probe from total genomic DNA:

   mTRANS is an equimolar mix of three DNA probes: probe 1, probe 6, and probe 11.

Primers for PCR amplification of DNA probe 1 (961 nt):

Forward 5′-ACCAGACGAGCTACCTAAGAACAG-3′.

Reverse 5′-CTGGTGAAGTCTTAGCATGT-3′.

Primers for PCR amplification of DNA probe 6 (1118 nt):

Forward 5′-CTACCACACATTCGAAGAACC-3′.

Reverse 5′-CGTTCATTTTGGTTCTCAGGG-3′.

Primers for PCR amplification of DNA probe 11 (1420 nt):

Forward 5′-CATACCTCTCACTTCAACCTC-3′.

Reverse 5′-TGAGCCGAAGTTTCATCATGC-3′.

6. PCR products cleanup system kit (*see* **Note 1**).
7. Labeling of purified mREP and mTRANS PCR products. It is strongly recommended to label the DNA probes by Nick-translation using Atto425 or Atto488 or Atto550 or Atto647 NT Labeling Kit (JenaBioscience) (*see* **Note 2**).

   Labeled and purified mREP and mTRANS probes must be aliquoted and stored at −20 °C in the dark.

### 2.2 Cell Treatment

1. Tissue culture plates 6-well (12-well or 24-well plates are reasonable alternatives for culture of rare primary cells or slow growing cells).
2. Microscope glass coverslips 18 mm diameter.
3. 2% Paraformaldehyde (PFA) in 1× PBS (mix 5 ml of 16% PFA with 35 ml of 1× PBS).
4. 2% PFA can be stored at 4 °C for a couple of weeks.
5. Permeabilization buffer: 0.5% Triton X-100 in 1× PBS (mix 50 μl of 100% Triton X-100 with 9550 μl 1× PBS).
6. 20× saline sodium-citrate (SSC) buffer: 150 mM NaCl, 15 mM $Na_3Citrate \times 2H_2O$, pH 7.0). For SSC preparation, dissolve 175.3 g of NaCl and 88.2 g of sodium citrate in 800 ml of ultrapure water. Adjust the pH to 7.0 with 14 N solution of HCl. Adjust the volume to 1 l with additional ultrapure water. Sterilize by autoclaving. Store at room temperature up to 6 months.
7. Pretreatment buffer for permeabilized cells: 50% formamide–2× SSC in 1× PBS. Store the solution at room temperature up to 6 months in the dark.
8. Denaturation buffer for permeabilized cells: 70% formamide–2× SSC in 1× PBS.

   Store the solution at room temperature up to 6 months in the dark.

### 2.3 mTRIP Hybridization

1. Parafilm.
2. Hybridization buffer: 10% dextran sulfate–50% formamide–2× SSC in 1× PBS).
   Store the solution at room temperature up to 6 months in the dark (*see* **Note 3**).
3. 100 ng/μl salmon sperm DNA: dilute stock salmon sperm DNA with 1× PBS.
   Store the solution at −20 °C.
4. Washing buffer A: 2× SSC in 1× PBS.
5. Washing buffer B: 1× SSC in 1× PBS.
6. Washing buffer C: 0.1× SSC in 1× PBS.

### 2.4 mTRIP Coupled to Immuno-fluorescence

1. Parafilm.
2. Blocking buffer: 5% bovine serum albumin (BSA) in 1× PBS. The solution can be stored at 4 °C several weeks (*see* **Note 4**).
3. Primary antibody (*see* **Note 5**): we recommend the use of unconjugated rabbit polyclonal anti-TOMM22 to label mitochondria.
4. Fluorescence-conjugated secondary antibody (*see* **Note 6**): we recommend the use of Cy5 (or similar) conjugated goat secondary anti-rabbit antibody.
5. Hoechst 33342.

### 2.5 mTRIP Coupled to MitoTracker®

MitoTracker® Probes, Invitrogen. Select a MitoTracker probe with appropriate spectral characteristics for successive labeling with mTRIP. Here we used MitoTracker® Deep Red (655 nm).

### 2.6 Imaging Equipment

1. Confocal microscope.
2. Optional for 3D imaging: 3D-reconstruction imaging software.
3. Quantification—imaging software such as Image J.

## 3 Methods

mTRIP principles are summarized in Fig. 2.

### 3.1 Extraction of Total Genomic DNA

It is strongly recommended to use primary cells such as IMR90 at early passages (and not cancer-derived or immortalized cell lines) (*see* **Note 7**).

1. Add 200 μl of fresh lysis buffer to the cell pellet at 50 °C for 3 hours (h).
2. Incubate at 50 °C for 3 h.
3. Add 20 μl of sodium acetate 3 M, pH 5.2.

4. Add 200 µl of cold ultrapure isopropanol.
5. Incubate at −20 °C for 15 min.
6. Centrifuge at 16,100 × *g* at 4 °C for 30 min.
7. Carefully discard the supernatant.
8. Add 500 µl of 70% ethanol.
9. Centrifuge at 16,100 × *g* at 4 °C for 5 min.
10. Carefully discard the supernatant.
11. Dry the DNA pellet for 5 min at room temperature. The pellet should be transparent after drying.
12. Resuspend the DNA pellet in 100 µl of ultrapure water.
13. Incubate at 4 °C overnight.
14. Quantify the total genomic DNA. Dilute in ultrapure water, if needed.
15. Storage: −20 °C.

### 3.2 Preparation and Labeling of the DNA Probe

1. Amplify the mREP probe by PCR using at least 100 ng/µl of total genomic DNA and LA Taq DNA polymerase (Recommendation: annealing temperature: 56 °C; extension: 68 °C).
2. Amplify the mTRANS component probe 1 by PCR using at least 100 ng/µl of total genomic DNA and LA Taq DNA polymerase (recommendation: annealing temperature: 56 °C; extension: 68 °C).
3. Amplify the mTRANS component probe 6 by PCR using at least 100 ng/µl of total genomic DNA and LA Taq DNA polymerase (recommendation: annealing temperature: 56 °C; extension: 68 °C).
4. Amplify the mTRANS component probe 11 by PCR using at least 100 ng/µl of total genomic DNA and LA Taq DNA polymerase (recommendation: annealing temperature: 56 °C; extension: 68 °C).
5. Purify the PCR products using 2% agarose electrophoresis gel and conventional PCR products cleanup kit.
6. Estimate the amount of the purified PCR product. **It is essential to get 1 µg of PCR product at a concentration of 75 ng/µl or higher.** If this amount of DNA product is not reached, one can concentrate the DNA by sodium acetate and isopropanol precipitation, then resuspend in the appropriate volume of ultrapure water to reach the required concentration. Note that precipitation of highly diluted DNA is not recommended at it may result in salt concentration higher than necessary, in spite of intense washing.

***Be careful as the following steps are dedicated to DNA probes fluorescent labeling by nick translation and are crucial***

***for mTRIP. Consider that no other technique of DNA labeling than nick translation has been tested in this context.***

7. Choose the fluorescence label for mREP and mTRANS DNA probes (*see* **Note 8**). If mTRIP is coupled to immunofluorescence and Hoechst 33342, resulting in four-color channels, the recommended choice is mREP labeled with Atto550 NT kit, mTRANS labeled with Atto488 NT kit, immunofluorescence with a Cy5-conjugated secondary antibody, and Hoechst.
8. Preparation of the mREP DNA probe:
   (a) Resuspend 1 μg of pure PCR product in a maximum volume of 14 μl in a 0.2 ml thin-wall 8-tube strip with caps for regular thermal cycler (PCR machine).
   If the volume is smaller, adjust to 14 μl with PCR-grade water from the kit.
9. Preparation of the mTRANS DNA mix probes.
   (a) Mix 333 ng of mTRANS probe 1, 333 ng of mTRANS probe 6, and 333 ng of mTRANS probe 11 (equimolar amounts of the three probes) for a final amount of 1 μg of DNA mix, in maximum volume of 14 μl in a 0.2 ml thin-wall 8-tube strip with caps for regular thermal cycler (PCR machine).
   If the volume is smaller adjust to 14 μl with PCR-grade water from the kit.
   **The following steps are identical for mREP and mTRANS fluorescence labeling.**
10. Gently mix 14 μl of template DNA with 2 μl of 10× NT labeling buffer on ice.
11. Add 2 μl of Atto488 or Atto550 NT labeling mix.
12. Add 2 μl of 10× Enzyme mix.
13. Ensure sample homogeneity by gently mixing.
14. Incubate the mix at 15 °C for 90 min, for example in a regular thermal cycler, in the dark.
15. Add 5 μl of NT Kit Stop buffer to stop the reaction.
16. Transfer the reaction mixture in 1.5 ml Eppendorf tube.
17. Add 2 μl of 3 M pH 5.2 sodium acetate.
18. Add 14 μl of ultrapure cold isopropanol.
19. Gently mix the sample.
20. Incubate at −20 °C for 15 min in the dark.
21. Centrifuge at 16,100 × *g* at 4 °C for 30 min.
22. Discard the supernatant.
23. Add 500 μl of 70% ethanol.
24. Centrifuge at 16,100 × *g* at 4 °C for 5 min.

25. Discard the supernatant.
26. Add 500 µl of 70% Ethanol.
27. Centrifuge at 16,100 × *g* at 4 °C for 5 min.
28. Discard the supernatant.
29. Resuspend the fluorescence-labeled DNA probe in 50 µl of ultrapure water to get a final concentration of 20 ng/µl.
30. Store the labeled DNA probe at −20 °C in the dark.

### 3.3 Prehybridization of the DNA Probe

To reduce bench timing, the steps in this section can be done in parallel with the steps of Subheading 3.4.

1. Choice 1: **ONE probe**, preparation of the reaction mixture (in a 1.5 ml tube):

   If only one probe (e.g., mREP or mTRANS) is used, the reaction mix is done in a final volume of 25 µl per coverslip. Gently mix 2 µl of 20 ng/µl of fluorescent DNA probe (40 ng DNA probe are used per coverslip at a final concentration of 1.6 ng/µl) with 4 µl of 100 ng/µl salmon sperm DNA (400 ng of salmon sperm DNA are used for 40 ng of DNA probe, and *per* coverslip) and 19 µl of hybridization buffer.
2. Choice 2: **TWO probes**, preparation of the reaction mixture (in a 1.5 ml tube):

   If two probes (mREP *and* mTRANS) are used, the reaction mix is done in a final volume 25 µl per coverslip. Gently mix 2 µl of 20 ng/µl fluorescent mREP probe (40 ng of DNA probe are used per coverslip; final concentration 1.6 ng/µl) and 2 µl of 20 ng/µl fluorescent mTRANS probe (40 ng DNA probe are used per coverslip; final concentration 1.6 ng/µl) with 8 µl of 100 ng/µl of salmon sperm DNA (800 ng of salmon sperm DNA are used for 2× 40 ng of DNA probes and per cove slip) and 13 µl of hybridization buffer.
3. Denaturation: incubate the reaction mixture at 80 °C for 10 min in the dark.
4. Precooling step: transfer the denatured reaction mixture containing tube at 37 °C for at least 30 min in the dark. This time can be extended to a maximum of 1 h at 37 °C in the dark. This step helps lowering unspecific binding of salmon sperm DNA versus specific binding of DNA probes. Keep denatured reaction mixture under these conditions until the end of Subheading 3.4.

### 3.4 Preparation of Cells on Coverslip

1. Culture cells under appropriate culture conditions in (6-wells or 12-wells) culture plates containing a clean coverslip at the bottom of each well. Ideally cells should be grown at about 50–60% confluence to avoid plans with packed cell during microscope analysis.

If mTRIP is coupled to MitoTracker labeling, incubate live cells with MitoTracker® (e.g., MitoTracker® Deep Red) for 1 h in appropriate culture conditions (*see* **Note 9**).

2. Discard the culture medium.
3. Wash cells once with 1× PBS.
4. Add 2% PFA at room temperature.
5. Incubate for 20 min at room temperature.
6. Discard PFA.
7. Wash 2× with 1× PBS. At this step, PFA-fixed cells can be stored in 1× PBS for several weeks at 4 °C.
8. Discard PBS from the coverslip.
9. Permeabilize cells with 0.5% Triton X-100 in 1× PBS for 5 min at 4 °C.
10. Discard the Triton X-100.
11. Wash 4× with 1× PBS.

    **OPTIONAL: if required, at this step permeabilized cells can be incubated with specific nucleases for the time recommended by the manufacturer (generally 1 h at 37 °C). After incubation, wash 4× with 1× PBS (*see* Note 10).**
12. Discard PBS.
13. Pretreat the permeabilized cells by adding pretreatment buffer (50% formamide–2× SSC in 1× PBS).
14. Incubate at room temperature for 30 min.
15. Discard the pretreatment buffer.
16. Add 70% formamide–2× SSC in 1× PBS.
17. Put the 6-well culture plate (with, at the bottom of each well, a coverslip with pretreated permeabilized cells) on the top of a metal block heater at 75 °C for 5 min to denature the sample.
18. Immediately transfer the 6-well culture plate on ice (4 °C) and keep on ice at least 1 min and not longer than 10 min (*see* **Note 11**).

### 3.5 mTRIP Hybridization

1. Put a 25 µl drop of denatured and precooled reaction mixture which contains DNA probe(s) on an appropriate surface of Parafilm (at least 3.6 × 3.6 cm for 18 mm diameter coverslip). For multiple labeling, use a single surface of Parafilm with enough room for multiple and well separated drops.
2. Put the coverslip upside down, with the face containing cells (samples previously undergone denaturation) directly on the drop.

3. Incubate at 37 °C for 15 h either at the top of a heating metal block in the dark (cover with plastic top to set dark) or on a humid chamber at 37 °C in the dark.

### 3.6 mTRIP Washing

1. After 15 h incubation, remove the coverslip from Parafilm and put it back into a clean cell culture plate (6-well plate).

   ***The following steps must be performed in the dark:***

2. Wash 2× with 2× SSC in 1× PBS for 2 min at room temperature (RT) with gentle shaking.
3. Wash 2× with 1× SSC in 1× PBS for 2 min at RT with gentle shaking.
4. Wash 2× with 0.1× SSC in 1× PBS for 2 min at RT with gentle shaking.
5. Wash 2× with 1× PBS for 2 min at RT with gentle shaking.

   ***At this point, either label the sample by immunofluorescence, and in this case go to Subheading 3.7 (mTRIP coupled to immunofluorescence) or do not label the sample by immunofluorescence (this is also the case for MitoTracker labeling), and in this case:***

6. Incubate the coverslip for 1 h in the dark with 10 μg/ml Hoechst 33342 in 1× PBS.
7. Wash 5× with 1× PBS.
8. Mount the coverslip on a clean and dry glass slide using the favorite mounting buffer or a drop of 50% glycerol in 1× PBS.
9. Seal the slide with varnish and keep the mounted slide in a dark and clean box either at room temperature if confocal analysis is done the done the same day, or at 4 °C until confocal analysis is done (it is recommended to analyze the slide not later than 2 weeks from labeling).

### 3.7 mTRIP Coupled to Immunofluorescence

Follow the immunofluorescence (IF) protocol suggested below, (*see* **Note 12**).

1. Incubate the coverslip with 5% BSA in 1× PBS at RT for 1 h in the dark.
2. Wash 2× in 1× PBS for 2 min at RT with gentle shaking.
3. Dilute the primary antibody (anti-TOMM22 (1:200), recommended for assessing the mitochondrial network) in 1% BSA and 1× PBS.
4. Put a 50 μl drop of diluted primary antibody mix on an appropriate surface of Parafilm.
5. Put the coverslip upside down, with the face containing cells directly on the drop.

6. Incubate at RT for 1 h in the dark. The incubation time depends on the primary antibody.
7. Wash 3× in 1× PBS for 2 min at RT with gentle shaking.
8. Dilute secondary antibody (1:1000) in 1% BSA and 1× PBS, and add 10 μg/ml of Hoechst 33342.
9. Put a 50 μl drop of diluted secondary antibody mix on an appropriate surface of Parafilm.
10. Put the coverslip upside down, with the face containing cells directly on the drop.
11. Incubate at RT for 1 h in the dark.
12. Wash 5× in 1× PBS for 2 min at RT with gentle shaking.
13. Mount the coverslip on a clean and dry slide using the favorite mounting buffer or a drop of 50% glycerol in 1× PBS.
14. Seal the slide with varnish and keep the mounted slide in a dark and clean box either at room temperature if confocal analysis is done the same day, or at 4 °C until confocal analysis is done (it is recommended to analyze the slide not later than 2 weeks from labeling).

### 3.8 Imaging Acquisition and Fluorescence Intensity Quantification

1. Acquisition for subsequent quantification is done with confocal microscope (*see* **Note 13**).
2. One can do either two-dimensional (2D) or three-dimensional (3D) acquisition. In the last case 3D reconstruction of the image should follow 3D acquisition.
3. With image format (.tiff) of the acquired image, one can quantify the fluorescence intensity *per* cell using the Image J software.

   A 3D-reconstructed human cell stained by mTRIP is shown in Fig. 3 (panels b, c, f, g). The mTRIP procedure is covered by a patent application for commercial use (*see* **Note 14**), which also includes tissues sections (*see* **Note 15**).

## 4 Notes

1. Wizard® SV Gel, PCR clean-Up system (Promega), and NucleoSpin® Extract II (Macherey-Nagel) worked well in our hands.
2. Labeling of DNA probes with other techniques than Nick Translation has not been tested. We do not exclude that other DNA probes labeling techniques are compatible with mTRIP.
3. It is strongly recommended to prepare the hybridization buffer several days (at least 2 days) before the experiment as dextran sulfate takes a long time to dissolve.

4. Alternative blocking buffers can also be used.
5. Unconjugated rabbit polyclonal anti-TOMM22 is used to illuminate the mitochondrial network. However, you can use other primary antibodies for detecting the mitochondrial network, or other cellular structures or proteins of interest.
6. The choice of the secondary antibody-conjugated fluorescence depends on the available spectra after exclusion of the fluorophore(s) used for DNA probes (mTRIP). All combinations compatible with available fluorophores and the equipment (fluorescence filters) of your microscope can be used.
7. Cancer and immortalized cell lines may have mutated and highly heteroplasmic mitochondrial genomes.
8. The fluorescence color of the DNA probes can be different from the ones used here, and for this, appropriate fluorophores must be selected.
9. In this case, use mREP-Atto550 and mTRANS-Atto-488 for mTRIP labeling, and Hoechst.
10. Treatment with DNaseI (recommended 100 U/ml) or RNaseA (recommended 100 μg/ml) allows identification of the DNA and RNA components of the mTRIP signal. Treatment with RNaseH (recommended 100 U/ml) allows identification of RNA/DNA structures, usually at replication origins and in transcription bubbles. For combined use of nucleases and the respective readouts on mitochondrial nucleic acids by mTRIP, *see* Ref. 15.
11. Do not keep denatured samples at room temperature, as this condition will interfere with the hybridization step. Keep the samples always on ice until hybridization.
12. The favorite IF procedure, if different form the one described here, can alternatively be performed.
13. Reliable quantification requires fluorescence measurement of the cell volume. Cell surface (2D-acquisition) can also be acquired instead of cell volume, but the corresponding quantification will not measure the total cell fluorescence.
14. mTRIP tool is covered by patent applications: EP2500436 and WO2012123588 "Method, probe and kit for DNA in situ hybridization and use thereof."
15. mTRIP can be used with paraformaldehyde-fixed human cells and paraffin-embedded human tissue sections (method not described here).

## Acknowledgments

This work was supported by Association Nationale contre le Cancer (ARC 4022 and SFI20111204038), PTR-Institut Pasteur (PTR217), DARRI-Institut Pasteur (projects P790319 and PasteurInnov 14/152), and Agence Nationale pour la Recherche (ANR 11BSV202502).

### References

1. Chan DC (2020) Mitochondrial dynamics and its involvement in disease. Annu Rev Pathol 15:235–259
2. Tilokani L, Nagashima S, Paupe V, Prudent J (2018) Mitochondrial dynamics: overview of molecular mechanisms. Essays Biochem 62:341–360
3. Barshad G, Marom S, Cohen T, Mishmar D (2018) Mitochondrial DNA transcription and its regulation: An evolutionary perspective. Trends Genet 34:682–692
4. Farge G, Falkenberg M (2019) Organization of DNA in mammalian mitochondria. Int J Mol Sci 20:2770
5. Ojala D, Montoya J, Attardi G (1981) tRNA punctuation model of RNA processing in human mitochondria. Nature 290:470–474
6. Chang DD, Clayton DA (1985) Priming of human mitochondrial DNA replication occurs at the light-strand promoter. Proc Natl Acad Sci U S A 82:351–355
7. Clayton DA (1991) Replication and transcription of vertebrate mitochondrial DNA. Annu Rev Cell Biol 7:453–478
8. Holt IJ, Lorimer HE, Jacobs HT (2000) Coupled leading- and lagging-strand synthesis of mammalian mitochondrial DNA. Cell 100:515–524
9. Gustafsson CM, Falkenberg M, Larsson NG (2016) Maintenance and expression of mammalian mitochondrial DNA. Annu Rev Biochem 85:133–160
10. Ricchetti M (2018) Replication stress in mitochondria. Mutat Res 808:93–102
11. Yasukawa T, Kang D (2018) An overview of mammalian mitochondrial DNA replication mechanisms. J Biochem 164:183–193
12. Nicholls TJ, Minczuk M (2014) In D-loop: 40 years of mitochondrial 7S DNA. Exp Gerontol 56:175–181
13. Kukat C, Wurm CA, Spahr H, Falkenberg M, Larsson NG, Jakobs S (2011) Super-resolution microscopy reveals that mammalian mitochondrial nucleoids have a uniform size and frequently contain a single copy of mtDNA. Proc Natl Acad Sci U S A 108:13534–13539
14. Brown TA, Tkachuk AN, Shtengel G, Kopek BG, Bogenhagen DF, Hess HF, Clayton DA (2011) Superresolution fluorescence imaging of mitochondrial nucleoids reveals their spatial range, limits, and membrane interaction. Mol Cell Biol 31:4994–5010
15. Chatre L, Ricchetti M (2013) Large heterogeneity of mitochondrial DNA transcription and initiation of replication exposed by single-cell imaging. J Cell Sci 126:914–926
16. Chatre L, Ricchetti M (2013) Prevalent coordination of mitochondrial DNA transcription and initiation of replication with the cell cycle. Nucleic Acids Res 41:3068–3078
17. Arena G, Cisse MY, Pyrdziak S, Chatre L, Riscal R, Fuentes M, Arnold JJ, Kastner M, Gayte L, Bertrand-Gaday C, Nay K, Angebault-Prouteau C, Murray K, Chabi B, Koechlin-Ramonatxo C, Orsetti B, Vincent C, Casas F, Marine JC, Etienne-Manneville S, Bernex F, Lombes A, Cameron CE, Dubouchaud H, Ricchetti M, Linares LK, Le Cam L (2018) Mitochondrial MDM2 regulates respiratory complex I activity independently of p53. Mol Cell 69:594–609. e8
18. Bajzikova M, Kovarova J, Coelho AR, Boukalova S, Oh S, Rohlenova K, Svec D, Hubackova S, Endaya B, Judasova K, Bezawork-Geleta A, Kluckova K, Chatre L, Zobalova R, Novakova A, Vanova K, Ezrova Z, Maghzal GJ, Magalhaes Novais S, Olsinova M, Krobova L, An YJ, Davidova E, Nahacka Z, Sobol M, Cunha-Oliveira T, Sandoval-Acuna C, Strnad H, Zhang T, Huynh T, Serafim TL, Hozak P, Sardao VA, Koopman WJH, Ricchetti M, Oliveira PJ, Kolar F, Kubista M, Truksa J, Dvorakova-Hortova K, Pacak K, Gurlich R, Stocker R, Zhou Y, Berridge MV, Park S, Dong L, Rohlena J, Neuzil J (2019) Reactivation of dihydroorotate dehydrogenase-driven pyrimidine biosynthesis restores tumor growth of respiration-deficient cancer cells. Cell Metab 29:399–416. e10

19. Wiehe RS, Gole B, Chatre L, Walther P, Calzia E, Palmer A, Gebhardt JCM, Ricchetti M, Wiesmuller L (2018) Correction: endonuclease G promotes mitochondrial genome cleavage and replication. Oncotarget 9:27908

20. Wiehe RS, Gole B, Chatre L, Walther P, Calzia E, Ricchetti M, Wiesmuller L (2018) Endonuclease G promotes mitochondrial genome cleavage and replication. Oncotarget 9:18309–18326

# Chapter 16

# Development of Mitochondria-Targeted Imaging Nanoplatforms by Incorporation of Fluorescent Carbon Quantum Dots

**Ye Zhang and Hong Bi**

## Abstract

Multifunctional nanoplatforms are promising scaffolds for biomedical applications such as bioimaging, chemical/biological sensors, drug delivery, and cancer diagnosis and/or treatments. Mitochondria play crucial roles in metabolism of eukaryotic cells; therefore, mitochondria-targeting molecule such as triphenylphosphonium (TPP) is attached onto the magnetic mesoporous silica nanoparticle ($Fe_3O_4$@m$SiO_2$). In order to track the nanoparticles, fluorescent carbon quantum dots (CDs) were conjugated to the $Fe_3O_4$@m$SiO_2$. The as-constructed $Fe_3O_4$@m$SiO_2$–TPP/CQD nanoplatform showed minimal cytotoxicity in various cell lines such as A549, CHO, HeLa, SH-SY5Y, HFF, and HMEC-1. External magnetic field-assisted uptake of the nanoplatform by tumor cell has been achieved promptly. More importantly, conjugation with CQDs endows the nanoplatform multicolored fluorescence that can remain bright and stable inside cells for a long time. This nanoplatform provides a multifunctional platform in targeting, imaging, and agent delivery for mitochondria-related disease diagnosis and treatment.

**Key words** Mitochondria targeting, Carbon quantum dots, Bioimaging, Nanoplatform, Magnetic targeting

## 1 Introduction

The development of inorganic multifunctional nanoplatforms integrating magnetic, fluorescent, and porous properties all in one system has excellent potential biomedical applications. These nanoplatforms are not only used as efficient contrast agents for localized imaging of the disease but also could deliver the therapeutic drugs to the targeted sites as well as monitor the real-time therapeutic effects. As one of the commonly used components in the constructed nanoplatform, superparamagnetic iron oxide ($Fe_3O_4$) nanoparticles are considered to be ideal $T_2$ contrast agents in magnetic resonance imaging (MRI), magnetic-targeted carriers in drug delivery system, and magnetohyperthermia (MHT) agents in

Volkmar Weissig and Marvin Edeas (eds.), *Mitochondrial Medicine: Volume 1: Targeting Mitochondria*, Methods in Molecular Biology, vol. 2275, https://doi.org/10.1007/978-1-0716-1262-0_16,

tumor therapy [1, 2]. Combination of magnetic $Fe_3O_4$ with fluorescent molecule/quantum dots could yield dual-modality imaging probe for noninvasive and high spatial resolution MRI, as well as high sensitivity and resolution fluorescence imaging for real-time image-guided therapy and monitoring [3, 4]. It is well known that mesoporous silica ($mSiO_2$) nanomaterials have been widely applied in biomedical field due to their high surface areas, large pore volume, uniform and ordered mesopores, as well as facile surface functionalization. As a result of these properties, $mSiO_2$ could serve as an ideal vehicle for loading drugs, genes, and proteins, and further delivering them to the targeted sites. To construct mesoporous silica nanoparticles with specificity in targeting and imaging ability, one strategy is to prepare magnetic mesoporous silica ($Fe_3O_4$@$mSiO_2$) nanoparticles with core–shell structure. In the presence of an external magnetic field, $Fe_3O_4$@$mSiO_2$ nanoparticles have been used in direct tumor-targeting therapeutic agent delivery, T cell-activated antitumor therapy, cell sorting, and cellular uptake modulation [5–8].

Subcellular-targeting imaging and therapy have emerged as an important technique in cancer diagnosis and therapy. The efficacy of treatment would be enhanced and the side effects be decreased when the concentration of drugs or photosensitizers in their site of action is increased. Mitochondria are not only vital cellular organelles to supply energy for cells, but also critical regulators of cell apoptosis. Delivering therapeutic agents specific to mitochondria and regulate mitochondrion function has become an effective method for cancer treatment [9]. Because of the negative membrane potential of the mitochondrial inner membrane, various lipophilic cationic species, such as triphenylphosphonium (TPP), could be attached to small molecules, liposomes, and nanoparticles to deliver cargo to mitochondria [10]. The biosafety of TPP group has been validated in a phase II clinical trial of MitoQ (a TPP-modified mitochondria targeted antioxidant mitoquinone) through oral administration for 12 months [11]. Moreover, TPP is easily introduced to small molecules or nanocarriers by chemical synthesis. And the conjugation of TPP does not affect the physicochemical properties of these molecules and carriers because TPP group is small.

Since they were first synthesized in 2004, carbon quantum dots (CQDs) have aroused significant interest in biomedical field due to their outstanding photoluminescence properties and excellent biocompatibility. CQDs is new kind of carbon materials, which shows quasi-spherical structure with the size less than 10 nm. Different from the well-studied II/VI semiconductor quantum dots, good water solubility, and low cytotoxicity enable CQDs predominant applications in long time bioimaging and cargo delivery [12]. The quantum yield of CQDs can be enhanced not only by doping heteroatoms such as nitrogen, phosphorus, sulfur, and fluorine but also by surface functionalization, which introduce new surface

state of CQDs to exhibit excellent optical or photocatalytic properties [13, 14]. We have prepared one kind of nitrogen-doped CQDs in the size of 2–3 nm with a high quantum yield (22% in ethanol) and low cytotoxicity through pyrolysis of konjac flour (KF) [15]. Experiment data proved that CQDs have remarkable cell imaging ability and easy surface modification aptness. In the last decade, more and more nanoplatforms were presented by integrating the targeting and therapeutic moieties (drug/gene/photosensitizer/photothermal agent) with the fluorescent CQDs to generate "all in one" theranostic reagent [16]. Based on this concept, we constructed a mitochondria-targeting multifunctional nanoplatform through conjugating as-synthesized CQDs with a TPP-modified $Fe_3O_4$@m$SiO_2$ nanoparticles ($Fe_3O_4$@m$SiO_2$–TPP/CQDs) for magnetic field targeting and enhancing cellular uptake, long time mitochondria imaging, as well as potential drug delivery [17]. In this report, we describe a robust protocol for formulating $Fe_3O_4$@m$SiO_2$–TPP/CQDs nanoplatforms for mitochondria-targeting imaging of A549, CHO, HeLa, SH-SY5Y, HFF, and HMEC-1 cell lines.

## 2 Materials

### 2.1 Equipment for Synthesis

1. Stirring/heating plate with magnetic stirrer bar.
2. Electromechanical stirring with Teflon stirring rod.
3. Oven (>200 °C capable).
4. Oil bath with temperature probe.
5. Vacuum pump (weak vacuum, 100 mbar sufficient).
6. Vacuum line (<20 mbar).
7. Rotary evaporator attached to vacuum line.
8. Muffle (>800 °C capable).
9. Centrifuge.
10. Balance.
11. 11 Dynamic Light Scattering (DLS) instrument.
12. NMR spectrometer.
13. Lyophilizer.
14. Plate reader.
15. Transmission electron microscope (TEM) instrument.
16. Confocal laser scanning microscope (CLSM).
17. Thermometer.
18. Clamp stand and appropriate clamps.
19. 100 mL three-necked round bottomed flask.

20. 250 mL three-necked round bottomed flask.
21. 100 mL round bottomed flask.
22. Condenser (appropriate to fit flask) and connections to attach water.
23. Buchner flask and Buchner funnel with filter paper.
24. Beaker.
25. Sample vials.
26. 1 mL syringes and appropriate needles.
27. 5 mL syringes and appropriate needles.

### 2.2 Synthesis of $Fe_3O_4$@$mSiO_2$

1. Ferrous ammonium sulfate ($FeSO_4{\cdot}(NH_4)_2SO_4{\cdot}6H_2O$) ($\geq$99.5%).
2. Sodium hydroxide (NaOH) ($\geq$96.0%).
3. Oleic acid (OA).
4. Ethanol.
5. Ultra-pure water,
6. *n*-Hexane.
7. Cetyltrimethylammonium bromide (CTAB) ($\geq$99.0%).
8. Chloroform.
9. Tetraethyl orthosilicate (TEOS).
10. Ethyl acetate (EtOAc).
11. Ammonium nitrate ($NH_4NO_3$) ($\geq$98.0%).

### 2.3 Synthesis of $Fe_3O_4$@$mSiO_2$–TPP

1. Triphenylphosphonium (TPP).
2. α-Bromobutyric acid (98.0%).
3. Toluene.
4. Diethyl ether.
5. 3-Aminopropyltriethoxysilane (APTES) ($\geq$98.0%).
6. Dimethylformamide (DMF).
7. Thionyl chloride ($\geq$99.0%).

### 2.4 Synthesis of $Fe_3O_4$@$mSiO_2$–TPP/CQD Nanoplatform

1. Konjac flour (KF) (food-grade, 50 wt%).
2. Ethanol.
3. Ultrapure water.

### 2.5 Cytotoxicity Assay

1. Human pulmonary adenocarcinoma cells (A549).
2. Chinese hamster ovary cell line (CHO).
3. Human cervical cancer cells (HeLa).
4. Human neuroblastoma (SH-SY5Y).
5. Human foreskin fibroblast cells (HFF).

6. Human microvascular endothelial cells (HMEC-1).
7. Dulbecco's modified Eagle's medium (DMEM).
8. MCDB131 medium.
9. Fetal bovine serum (FBS, added to growth media as 10% vol/vol).
10. Sterile Penicillin–Streptomycin Solution stabilized, with 10,000 units penicillin and 10 mg streptomycin/mL (Pen./Strep.).
11. Trypsin.
12. Centrifuge at 100–2000 × *g*.
13. Cell culture plastic dishes, 96-well plates.
14. Phosphate buffered saline (PBS): 8 g NaCl, 0.2 g KCl, 3.63 g $Na_2HPO_4 \cdot 12H_2O$ and 0.24 g $KH_2PO_4$ in 1 L of $H_2O$, autoclaved sterilization.
15. Multichannel pipettor.
16. Pipette(s) capable of dispensing at 10 μL, 200 μL, and 1 mL.
17. 3-(4,5-Dimethylthiazol-2-yl)-2,5-diphenyltetrazolium bromide (MTT).
18. Microplate reader with excitation 570 nm and 630 nm.

### 2.6 Cell Imaging

1. Φ35 mm confocal laser dish.
2. 4% paraformaldehyde
3. PBS.

### 2.7 Mitochondria Colocalization

1. Φ35 mm confocal laser dish.
2. PBS.
3. 4% paraformaldehyde.
4. MitoTracker® Red CMXRos (Thermo Fisher Scientific).
5. MitoTracker™ Green FM (Thermo Fisher Scientific).

## 3 Methods

### 3.1 Synthesis of $Fe_3O_4$@$mSiO_2$

First, uniform magnetite $Fe_3O_4$ nanoparticles are prepared according to a typical liquid-solid-solid method.

1. In a 100 mL three-necked round bottomed flask, add 2.0 g of NaOH, then rest the flask in an electromechanical stirring with Teflon stirring rod.
2. Add 20 mL of OA and 20 mL of ethanol into the flask simultaneously, stir the mixture for 20 min at 600 rpm to form a creamy yellow solution (*see* **Note 1**).

3. In a 50 mL beaker, 2.35 g of $FeSO_4 \cdot (NH_4)_2SO_4 \cdot 6H_2O$ dissolve in 40 mL ultrapure water to obtain the $Fe^{2+}$-rich precursor.
4. Add the $Fe^{2+}$-rich precursor into the flask rapidly, stir the brown solution for 15 min at room temperature.
5. Transfer the prepared suspension to a 100 mL Teflon-lined autoclave, place in the oven and heat up to 180 °C, continue to keep for 10 h.
6. Pure the products into a 200 mL beaker, add 20 mL of *n*-hexane in the beaker to extract the products. After standing for 30 min, mixture in the beaker is layered. Suck the black *n*-hexane solution out by a pipette to separate the $Fe_3O_4$ nanoparticles.
7. The $Fe_3O_4$ nanoparticles in *n*-hexane are stored in a glass sample vial and put in a 4 °C refrigerator (*see* **Note 2**).

   Next, OA-capped $Fe_3O_4$ are transferred to water-soluble $Fe_3O_4$ by a phase-transfer method.
8. Determine the concentration of $Fe_3O_4$ in *n*-hexane by weighting dried 1 mL of $Fe_3O_4$/*n*-hexane. Weight an empty 5 mL sample tube and record the value. Pipet 1 mL of $Fe_3O_4$/*n*-hexane into the 5 mL sample tube, add 2 mL ethanol into the tube and ultrasound for a few seconds. Separate the $Fe_3O_4$ by a magnet and discard the mixed solution of *n*-hexane and ethanol. Add 2 mL ethanol into the tube and ultrasound for a few seconds to disperse $Fe_3O_4$ in ethanol, separate the $Fe_3O_4$ by the magnet again, repeat twice. Use $N_2$ gas flow or oven to remove residual organic solvents, and weight the sample tube containing nanoparticles again, record the value. Calculate the concentration of $Fe_3O_4$ in *n*-hexane with the unit of mg per mL.
9. Pipet approximately 15 mg of $Fe_3O_4$ nanoparticles in a sample tube and wash excess OA away as abovementioned. Redisperse these 15 mg of $Fe_3O_4$ nanoparticles in 1 mL of chloroform.
10. Add 0.2 g of CTAB and 10 mL ultrapure water in a 50 mL beaker and stir for 20 min until CTAB totally dissolved.
11. Place the beaker in a 60 °C ultrasound machine, and add 1 mL $Fe_3O_4$/chloroform solution into the CTAB–$H_2O$ solution drop by drop. When all $Fe_3O_4$ nanoparticles being added, the beaker mouse is sealed with plastic wrap and continually ultrasound for 20 min. And then, take the plastic wrap away and continually ultrasound for another 20 min to allow the chloroform totally to volatilize (*see* **Note 3**).

    Subsequently, $Fe_3O_4$@m$SiO_2$ nanoparticles are synthesized via sol-gel method.

12. Transfer the $Fe_3O_4$-CTAB-$H_2O$ into a 250 mL three-necked round bottomed flask, add the ultrapure water until the total volume of solution is 160 mL. Place the flask in the electromechanical stirring at the speed of 400 rpm. Turn on the oil-bath and adjust to 60 °C. Warm the solution and add NaOH (2.0 M) to adjust the pH of solution around 12.
13. Use 1 mL syringe to add 0.8 mL of TEOS into the flask drop by drop under stirring.
14. Add 8 mL of EtOAc into the flask slowly by 5 mL syringe under stirring.
15. Increase the speed to 1000 rpm and stir for 30 s. Age the suspensions for 3 h.
16. Centrifuge the suspensions at 13,523 × *g* for 20 min to collect the products ($Fe_3O_4$@m$SiO_2$). Wash the products with ethanol three times.
17. Redisperse the collected $Fe_3O_4$@m$SiO_2$ in 10 mg/mL of $NH_4NO_3$-ethanol solution by ultrasound. Place the round-bottom flask and condenser in an oil bath. Warm and keep the temperature at 80 °C. Reflux the mixture at 80 °C for 3 h to remove residual CTAB.
18. Centrifuge the mixture at 13,523 × *g* for 20 min to collect the products, discard the supernatant and wash the products with ethanol three times.
19. Resuspend $Fe_3O_4$@m$SiO_2$ nanoparticles in ethanol and store at room temperature.

### 3.2 Synthesis of $Fe_3O_4$@m$SiO_2$–TPP

First, synthesize (carboxyethyl)triphenylphosphonium bromide (CTPB).

1. Weight out 2.63 g TPP in the 100 mL round-bottom flask containing the magnetic bar. Add 30 mL toluene into the flask. Place the flask fitted with condenser in an oil-bath and adjust the temperature to 40 °C.
2. After TPP powder is dissolved completely, add 0.20 g α-bromobutyric acid into the flask rapidly with continuous stirring and then reflux the mixture. The boiling point of toluene is about 110 °C.
3. When the boiling temperature is reached, continue to heat the reaction under reflux for 4 h for complete conversion into the product.
4. Remove the reaction from oil by moving clamp arm bearing the flask upward. Cool the products to room temperature.
5. Filter under vacuum to collect the white solid CTPB. Wash the filter cake by 30 mL diethyl ether three times. Dry the materials in vacuum oven at 40 °C for 2 h.

Next, modify amine to the surface of $Fe_3O_4$@m$SiO_2$.

6. Dry a sufficient amount of $Fe_3O_4$@m$SiO_2$ in vacuum oven at 60 °C overnight. Weight 0.10 g of $Fe_3O_4$@m$SiO_2$ and suspend in 50 mL of toluene in a round-bottom flask by ultrasound.
7. Place the flask and condenser in an oil-bath. Keep stirring and then turn on heat to reflux.
8. When the boiling temperature is reached, add 1 mL APTES into the flask by 1 mL syringe under stirring. Keep refluxing overnight (*see* **Note 4**).
9. Turn off heat and cool to room temperature. Centrifuge the mixture at 13,523 × *g* for 20 min to collect the $Fe_3O_4$@m-$SiO_2$–$NH_2$, discard the supernatant and wash the products with ethanol three times.

   Subsequently, modify TPP to the surface of $Fe_3O_4$@m$SiO_2$ nanoparticles.
10. Dry a certain amount of $Fe_3O_4$@m$SiO_2$–$NH_2$ in vacuum oven at 60 °C overnight. Weight 0.20 g of $Fe_3O_4$@m$SiO_2$–$NH_2$ and suspend in 20 mL of DMF in a three-necked round bottomed flask by ultrasound.
11. Place the flask in oil-bath and warm the oil to 60 °C.
12. Add 0.1 g of CTPB and 0.5 mL of thionyl chloride into the flask under stirring *see* **Note 5**).
13. Keep the temperature at 60 °C and stir overnight.
14. Turn off heat and cool to room temperature. Centrifuge the mixture at 13,523 × *g* for 20 min to collect the $Fe_3O_4$@m-$SiO_2$–TPP. Discard the supernatant and wash the products with ethanol several times until the pH of supernatant reach around 7.
15. Dry the products in vacuum oven at 60 °C overnight to obtain $Fe_3O_4$@m$SiO_2$–TPP nanoparticles.

### 3.3 Synthesis of Carbon Quantum Dots

1. Add 1 g of KF powder into a 25 mL porcelain crucible and pure the powder on the bottom of the crucible uniformly.
2. Put the crucible in the middle of the muffle furnace.
3. Increase the temperature from room temperature to 470 °C at a speed of 5 °C/min. Keep the temperature at 470 °C for 1.5 h.
4. Turn off heat and cool to room temperature.
5. Ground the carbonized solid into fine powder by a mortar. Put the fine powder into a 100 mL beaker and add 25 mL of ethanol into the beaker. Ultrasound the mixture for 30 min and further stir overnight to extract the CQDs.

6. Filtrate the mixture with a 0.22 μm Nylon filter membrane and dry the filtrate in an oven at 60 °C to obtain brown-yellow powder.
7. Redisperse the powder in 15 mL ultrapure water by ultrasound for 30 min.
8. Filtrate the mixture with a 0.22 μm MCE filter membrane to remove the residual inorganic salts and hydrophilic organic components. Dry the filtrate in an oven at 60 °C to obtain the brown-yellow powder.
9. Redisperse the powder in 20 mL ethanol by ultrasound. Repeat the abovementioned (**steps 6–8**) extracting procedure with ethanol and ultrapure water three times.
10. Freeze dry the last extracting aqueous filtrate to obtain the purified CQDs.

### 3.4 Construction of the $Fe_3O_4$@$mSiO_2$–TPP/CQD Nanoplatform

1. Add 2 mg of $Fe_3O_4$@$mSiO_2$–TPP and 1 mL of ethanol in a 2 mL centrifuge tube. Disperse the nanoparticles in ethanol by ultrasound.
2. Disperse 0.5 mg of as-prepared CQD powder in 0.5 mL ethanol by ultrasound.
3. Add the CQD ethanol solution into the tube containing $Fe_3O_4$@$mSiO_2$–TPP, ultrasound for 30 min, and then transfer the tube to a shaker and shake overnight.
4. Collect $Fe_3O_4$@$mSiO_2$–TPP/CQD nanoparticles by centrifugation at 13,523 × *g* for 20 min. Discard the supernatant and wash the products with ethanol three times to remove the excess CQDs.

### 3.5 Physical Characterization the $Fe_3O_4$@$mSiO_2$–TPP/CQD Nanoplatform

1. CTPB will be characterized by using a 400 MHz Bruker NMR spectrometer to confirm the structure. The characteristic features of the CTPB peak at different chemical shifts in $^1$H NMR spectrum are as follows (triplet, broad singlet, and multiplet are abbreviated as t, bs, and m, respectively): $^1$H-NMR in d-$D_2O$: ppm $\delta$ 1.78–1.87 (m), 2.43–2.47 (t), 3.17–3.24 (m), 7.54–7.74 (m, from phenyl groups in TPP).
2. TPP modification on the surface of $Fe_3O_4$@$mSiO_2$ will be characterized by $^1$H NMR spectrum. Employ mesoporous silica nanoparticles instead of the $Fe_3O_4$@$mSiO_2$ to rule out the possible disturbance caused by the magnetic $Fe_3O_4$ cores. The peak at 7.66 ppm originating from aromatic protons of the TPP group indicates a successful conjugation of TPP onto the surface of nanoparticles.
3. Particle size and surface zeta potential, morphology, and fluorescent property of nanoparticles ($Fe_3O_4$@$mSiO_2$, $Fe_3O_4$@$mSiO_2$–TPP, CQDs, and $Fe_3O_4$@$mSiO_2$–TPP/CQDs) will be

characterized by Nano Zeta Potential Analyzer (Delsa 440SX Beckman Coulter Limited, USA), transmission electron microscope (200 kV JEM-2100 TEM, JEOL Ltd. Japan), and fluorescence spectrophotometer (Hitachi F-4500, Japan).

### 3.6 Cytotoxicity Assay

Evaluate the cytotoxicity of $Fe_3O_4$@m$SiO_2$, $Fe_3O_4$@m$SiO_2$–TPP, CQDs, and $Fe_3O_4$@m$SiO_2$–TPP/CQDs in A549, CHO, HeLa, SH-SY5Y, HFF, and HMEC-1 cells using a standard MTT assay.

1. Seed each kind of cells in transparent 96-well cell culture plates at a density of $1 \times 10^4$ cells per well. Use complete DMEM medium (containing 10% FBS and 100 U/mL penicillin/streptomycin) for A549, CHO, HeLa, SH-SY5Y, and HFF cells. Use complete MCDB131 (containing 10% FBS, 10 ng/mL MVGS, and 100 U/mL penicillin/streptomycin) for HMEC-1 cells, *see* **Note 5**).
2. Allow cells to attach to the bottom of the plates overnight.
3. When the cells in each well are about 60–70% confluent, discard the medium and add the fresh complete medium containing different concentrations of nanoparticles-based samples (such as 50, 100, 200, 300, and 400 μg/mL) in each well. Make sure the final volume is 100 μL in each well.
4. Culture cells for another 24 h.
5. Add 10 μL of MTT solution (5 mg/mL in PBS, 0.22 μm sterile filtration) in each well, including controls, and then incubate the assay plates at 37 °C for 4 h (*see* **Note 6**).
6. Remove assay plates from 37 °C incubator, and remove all MTT-containing medium carefully and slowly (*see* **Note 7**).
7. Add 150 μL of DMSO in each well.
8. Shake the assay plates on an orbital shaker for 15 min, making sure all purple precipitate has dissolved.
9. Insert the assay plate in the plate reader and measure the absorbance in each well at 570 nm. The reference wavelength set as 630 nm (*see* **Note 8**).
10. Calculate results of absorbance data, and plot percent cell viability as following equation:

$$\text{Cell viability } (\%) = \frac{\text{OD}_{\text{sample}}}{\text{OD}_{\text{control}}} \times 100\%$$

### 3.7 Cell Imaging

1. Seed $5 \times 10^4$ cells of A549, CHO, HeLa, SH-SY5Y, HFF, and HMEC-1 on the Φ35 mm confocal laser dishes, respectively.
2. Culture cells for 24 h, discard the medium and add 1 mL of fresh medium containing 100 μg/mL of $Fe_3O_4$@m$SiO_2$–TPP/CQDs in each dish.

3. Culture cells for another 24 h.
4. Discard the medium, and wash cells with PBS for three times.
5. Add 500 μL of 4% paraformaldehyde in each dish for 15 min at room temperature.
6. Discard the paraformaldehyde solution, and wash cells with PBS for twice, finally add 1 mL of PBS in each dish.
7. Place the dishes in the confocal laser scanning microscope, observe and take photos under the excitation of 405, 488, and 559 nm laser, respectively.

### 3.8 Mitochondria Colocalization

1. Seed cells on the Φ35 mm confocal laser dishes at a density of $5 \times 10^4$ per dish.
2. Allow cells to attach to the bottom of the dish for 24 h.
3. Remove the medium and add the fresh medium containing 100 μg/mL of $Fe_3O_4$@m$SiO_2$–TPP/CQDs in each dish.
4. Culture cells for another 12 or 24 h.
5. Discard the nanoparticles medium and wash the cells with PBS for three times.
6. Apply 0.5 mL of organelle fluorescent dye solution per dish, and coincubate for 30 min at 37 °C. Use MitoTracker® Red CMXRos to colocalization with mitochondria when nanoplatforms in cells excited by 405 nm laser to show blue fluorescence. Use MitoTracker™ Green FM to colocalization with mitochondria when nanoplatforms in cells excited by 559 nm laser to show red fluorescence. The working concentration of these dyes is 20 nM diluted in PBS.
7. Discard the dye solution, and carefully wash cells three times using PBS.
8. Add 1 mL PBS in each dish, and view the dishes using the CLSM with the appropriate Ex/Em fluorescent filters (375 nm/445 nm filter for nanoplatforms showing blue fluorescence, 470 nm/515 nm filter for MitoTracker™ Green FM, and 525 nm/580 nm filter for MitoTracker® Red CMXRos or nanoplatforms showing red fluorescence.).
9. Use Image J software to merge the acquired colored image stacks and determine the resulting Pearson's coefficient of colocalization.

## 4 Notes

1. Make sure all NaOH granules or flakes dissolve when stirring the mixture solution. If the room temperature is below 20 °C, turn on a water-bath and keep at 25–30 °C. This will result in small, monodispersed $Fe_3O_4$ crystals.

2. The bottle cap of the glass vial should be entangled with a sealing film. Make sure the concentration of $Fe_3O_4$ in *n*-hexane does not change due to the high volatility of *n*-hexane.
3. Keep the temperature of whole ultrasound process not lower than 60 °C. The obtained $Fe_3O_4$ solution is clear and bright, if precipitation appears, it means the phase transfer is failed.
4. Use 1 mL syringe with needle to take APTES out in a glovebox or under $N_2$ atmosphere.
5. Store thionyl chloride in tightly closed containers in a dry, cool, well-ventilated area away from heat and light. It fumes when add to the flask. Ensure the circulating water in condensate turn on and leave the mouse of condenser open to allow the gas overflow.
6. The MTT addition procedure should be performed in the dark, and the assay plates should be coated with silver paper to shield from light.
7. When remove the MTT medium, aspirate the medium using the pipette carefully, do not take the generated purple precipitate away.
8. The absorbance value of each well between 0.75 and 1.25 is credible.

## Acknowledgments

This work was supported by the National Natural Science Foundations of China (Grant No. 51272002) and the Technology Foundation for Selected Overseas Chinese Scholar, Ministry of Personnel of China (No. [2013]-385).

### References

1. Xu CJ, Sun SH (2013) New forms of superparamagnetic nanoparticles for biomedical applications. Adv Drug Deliv Rev 65:732–743
2. Kievit FM, Zhang MQ (2011) Surface engineering of iron oxide nanoparticles for targeted cancer therapy. Acc Chem Res 44:853–862
3. Hong X, Li J, Wang M, Xu J et al (2004) Fabrication of magnetic luminescent nanocomposites by a layer-by-layer self-assembly approach. Chem Mater 16(21):4022–4027
4. Jing LM, Ding K, Kershaw SV et al (2014) Magnetically engineered semiconductor quantum dots as multimodal imaging probes. Adv Mater 26:6367–6386
5. Bakandritsos A, Papagiannopoulos A, Anagnostou EN et al (2012) Merging high doxorubicin loading with pronounced magnetic response and bio-repellent properties in hybrid drug nanocarriers. Small 8:2381–2393
6. Perica K, Tu A, Richter A et al (2014) Magnetic field-induced T cell receptor clustering by nanoparticles enhances T cell activation and stimulates antitumor activity. ACS Nano 2014:2252–2260
7. Amendola V, Meneghetti M, Granozzi G et al (2011) Top-down synthesis of multifunctional iron oxide nanoparticles for macrophage labelling and manipulation. J Mater Chem 21:3803–3813
8. Liu Q, Zhang JX, Xia WL et al (2012) Magnetic field enhanced cell uptake efficiency of magnetic silica mesoporous nanoparticles. Nanoscale 4:3415–3421

9. Weinberg SE, Chandel NS (2015) Targeting mitochondria metabolism for cancer therapy. Nat Chem Biol 11(1):9
10. Zielonka J, Joseph J, Sikora A et al (2017) Mitochondria-targeted triphenylphosphonium-based compounds: syntheses, mechanisms of action, and therapeutic and diagnostic applications. Chem Rev 117 (15):10043–10120
11. Snow BJ, Rolfe FL, Lockhart MM et al (2010) A double-blind placebo-controlled study to assess the mitochondria-targeted antioxidant MitoQ as a disease-modifying therapy in Parkinson's disease. Mov Disord 25:1670–1674
12. Arcudi F, Đorević L, Prato M (2019) Design, synthesis, and functionalization strategies of tailored carbon nanodots. Acc Chem Res 52 (8):2070–2079
13. Zhou J, Zhou H, Tang J et al (2017) Carbon dots doped with heteroatoms for fluorescent bioimaging: a review. Microchim Acta 184 (2):343–368
14. Ding C, Zhu A, Tian Y (2013) Functional surface engineering of C-dots for fluorescent biosensing and in vivo bioimaging. Acc Chem Res 47(1):20–30
15. Teng X, Ma C, Ge C et al (2014) Green synthesis of nitrogen-doped carbon dots from konjac flour with "off-on" fluorescence by $Fe^{3+}$ and L-lysine for bioimaging. J Mater Chem B 2(29):4631–4639
16. Du J, Xu N, Fan J et al (2019) Carbon dots for in vivo bioimaging and theranostics. Small 15: e1805087
17. Zhang Y, Shen Y, Teng X, Yan M, Bi H, Morais PC (2015) Mitochondria-targeting nanoplatform with fluorescent carbon dots for long time imaging and magnetic field-enhanced cellular uptake. ACS Appl Mater Interfaces 7:10201–10212

# Chapter 17

# Norbormide-Based Probes and Their Application for Mitochondrial Imaging in *Drosophila Melanogaster*

**Alessia Forgiarini, Zifei Wang, Sergio Bova, Margaret Anne Brimble, Brian Hopkins, David Rennison, and Genny Orso**

## Abstract

Fluorescent live imaging on *Drosophila melanogaster* is a microscopy technique in rapid expansion. The growing number of probes available to detect cellular components and the relatively easy genetic manipulation of fruit fly make this model one of the most used for in vivo analysis of several physiological and/or pathological processes. Here we describe the chemical synthesis of two norbormide-derived BODIPY-conjugated fluorescent probes ($NRB^{MC009}$ and $NRB^{ZLW0047}$). Moreover, we describe the larval dissection method, and subsequent live imaging acquisition. Both probes are able to label mitochondria in different *Drosophila* larval tissues, which allows for the characterization of mitochondrial morphological alterations by using a simple and quick method that avoids the fixation artefacts that often occur in immunofluorescence studies.

**Key words** Norbormide, Fluorescent probes, Live imaging, Confocal microscopy, *Drosophila melanogaster*

## 1 Introduction

*Drosophila melanogaster* is a highly versatile model widely used to investigate biochemical pathways and disease-related morphological alterations in vivo. It is particularly insightful when used in combination with fluorescent tools and live imaging microscopy, that allow the real time visualization of tissue and cellular structures during the development of biological processes [1–6]. The GAL4/UAS system is a powerful binary tool for cell- or tissue-specific expression of wild type/mutated genes and RNA interference, useful for genetic screens and for fluorescence-tagged protein expression and imaging [7, 8].

We recently used the rat-specific toxicant norbormide (NRB) as a scaffold for the development of new fluorescent probes by conjugating it to either nitrobenzoxadiazole (NBD) or boron-

Volkmar Weissig and Marvin Edeas (eds.), *Mitochondrial Medicine: Volume 1: Targeting Mitochondria*, Methods in Molecular Biology, vol. 2275, https://doi.org/10.1007/978-1-0716-1262-0_17,

dipyrromethene (BODIPY) fluorophores. We found that both were able to clearly label intracellular structures such as mitochondria, endoplasmic reticulum (ER), Golgi apparatus, and lipid droplets (LDs) in various cell lines, in the absence of cytotoxic effects [9, 10]. Subsequently, we investigated the live cell imaging applications of the green BODIPY FL derivative $NRB^{MC009}$ and a newly developed red BODIPY TMR derivative $NRB^{ZLW0047}$, on dissected *Drosophila* third instar larvae [11]. Both compounds were rapidly internalized by most tissues (except the central nervous system), and showed a preferential localization to the mitochondria and endoplasmic reticulum of wild-type *Drosophila* larvae, as well as in tissues of mutant lines exhibiting morphological alterations to the mitochondria [11].

Rapid internalization, a bright signal, compatibility with other available fluorescent probes and GFP-tagged proteins, and a lack of toxicity make $NRB^{MC009}$ and $NRB^{ZLW0047}$ useful screening tools for characterizing mitochondrial morphology and disease-related alterations by live cell microscopy studies in *Drosophila melanogaster*.

## 2 Materials

### 2.1 Norbormide-Based Probes Synthesis

1. BODIPY FL (3-[4,4-difluoro-5,7-dimethyl-4-bora-3a,4a-diaza-s-indacene-3-yl]propionic acid) [12] and BODIPY TMR (3-[4,4-difluoro-1,3-dimethyl-5-(4′-methoxyphenyl)-4-bora-3a,4a-diaza-*s*-indacene-2-yl]propionic acid) [13], along with their corresponding *N*-hydroxysuccinimide esters, BODIPY FL NHS ester [10, 11, 14] and BODIPY TMR NHS ester [13], respectively, are prepared using partially modified literature methods.
2. *N*-2′-Aminoethyl-endo-5-(α-hydroxy-α-2-pyridylbenzyl)-7-(α-2-pyridylbenzylidene)-5-norbornene-2,3-dicarboximide [9] is also prepared using literature methods.
3. Flash chromatography is performed using silica gel (Riedel-de Haën, particle size 0.032–0.063 mm).
4. Nuclear Magnetic Resonance (NMR) spectra are recorded on a Bruker AVANCE 400 ($^1$H, 400 MHz) spectrometer at 298 K. For $^1$H NMR data, chemical shifts are described in parts per million (ppm) relative to tetramethylsilane ($\delta$ 0.00) and are reported consecutively as position ($\delta_H$), relative integral, multiplicity (s = singlet, br s = broad singlet, m = multiplet), coupling constant ($J$/Hz) and assignment.
5. Mass spectra are recorded on a VG-70SE mass spectrometer (EI, CI, and FAB). High-resolution mass spectra are recorded at a nominal resolution of 5000.

### 2.2 Drosophila *Larva Dissection*

1. *Drosophila* standard food: dissolve 10 g of agar in 1 l of hot water (approximately at 80 °C), and add 27 g of yeast, 66 ml of unsulfured molasses, and 22 g of precooked cornmeal. Cook at 85 °C for 20 min and then add 2.6 g of methylparaben dissolved in 15 ml of ethanol 96%. Cool the food to 50–60 °C and pour it in the desired *Drosophila* tubes. Let it solidify at room temperature, plug the tubes with raw cotton balls, and store them at 18 °C.
2. *Drosophila melanogaster* strains used: $w^{[1118]}$ (BL-5905), Tubulin-Gal4 (BL-5138), and UAS-Mito-GFP (BL-8443, Bloomington Drosophila Stock Center) and UAS-$Marf^{RNAi}$ (ID 40478, Vienna Drosophila Resource Center).
3. Dissecting instruments: entomological stainless-steel pins (Ø 0.10 mm), microdissection steel forceps (Dumont #2, #5, and #55), and scissors (2.5 mm cutting edge).
4. Pin preparation: collect one steel pin at a time and clamp it with the #2 forceps approximately 2 mm from the tip, bend it at 90° and cut the excess with small pliers.
5. Depression glass spot plate.
6. SYLGARD dissection dish: mix SYLGARD 184 base silicone elastomer and SYLGARD 184 curing agent (10:1 ratio by weight) and gently pipette for a few minutes. Set the tube down until almost all the bubbles have been cleared. Apply the viscous solution into a culture dish of the desired diameter and cure it for 10 min at 150 °C, 20 min at 125 °C, 45 min at 100 °C, 10 h at 65 °C, or 48 h at room temperature (*see* **Note 1**).
7. Hemolymph-like saline (HL3): 70 mM NaCl, 5 mM KCl, 1.5 mM $CaCl_2$, 20 mM $MgCl_2$, 10 mM $NaHCO_3$, 5 mM trehalose, 115 mM sucrose, 5 mM sodium HEPES, pH 7.2. Weigh 0.409 g of NaCl, 0.037 g of KCl, 0.017 g of $CaCl_2$, 0.190 g of $MgCl_2$, 0.084 g of $NaHCO_3$, 0.189 g of trehalose, 3.937 g of sucrose, and 0.119 g of HEPES in about 90 ml of milliQ water. Adjust pH to 7.2 using $NaHCO_3$, transfer to a measuring cylinder, and add milliQ water to a volume of 100 ml (*see* **Note 2**).
8. HL3-glutamate saline: before use, dilute glutamate stock solution 1:10 in HL3 saline to reach the final concentration of 10 mM (*see* **Note 3**).
9. $NRB^{MC009}$ and $NRB^{ZLW0047}$ stock solutions: weigh the desired amount of $NRB^{MC009}$ or $NRB^{ZLW0047}$ powders and dissolve them in dimethylsulfoxide (DMSO) to obtain 20 mM solutions. Store them at −20 °C (*see* **Note 4**).

10. Staining solutions: dilute stock solutions in HL3-glutamate saline in order to obtain 500 nM $NRB^{MC009}$ solution or 1 μM $NRB^{ZLW0047}$ solution and use them immediately.

### 2.3 Image Acquisition

1. Square borosilicate glass coverslips 22 × 22 mm (thickness 0.13 mm) and black enameled entomological pins (Ø 0.15 mm).
2. Microscopes:
   (a) Stereo microscope equipped with dual arm fiber optic light source for *Drosophila* larva dissection.
   (b) Confocal microscope, equipped with oil/water immersion or dry objectives of desired magnification (e.g., 5×, 20×, 40×, or 60×), and the respective acquisition software (*see* **Note 5**).
3. Immersion oil for microscopy (if needed).

## 3 Methods

### 3.1 Norbormide Probe Synthesis

1. Preparation of $NRB^{MC009}$ (Fig. 1a). A solution of *N*-2-′-aminoethyl-endo-5-(α-hydroxy-α-2-pyridylbenzyl)-7-(α-2-pyridylbenzylidene)-5-norbornene-2,3-dicarboximide (90 mg, 0.16 mmol), BODIPY FL NHS ester (69 mg, 0.18 mmol) and diisopropylethylamine (31 μl, 0.18 mmol) in dichloromethane (5 ml) is stirred at room temperature for 16 h. The mixture is washed with water, the separated aqueous phase further extracted with dichloromethane (2 × 10 ml), the combined organic layers dried over anhydrous magnesium sulfate, filtered, and the solvent removed in vacuo. Purification by preparative thin-layer chromatography (petroleum ether–ethyl acetate, 1:2) afforded $NRB^{MC009}$ as a mixture of endo stereoisomers (red solid; 100 mg, 0.12 mmol, 71%). $^1$H NMR (400 MHz, $CDCl_3$) $\delta$ 2.22 (3H, s, $CH_3$), 2.50 (3H, s, $CH_3$), 2.51–2.58 (2H, m, $NHCOCH_2CH_2$ or $NHCOCH_2CH_2$), 3.20–3.72 (8.2H, m, $NHCOCH_2CH_2$ or $NHCOCH_2CH_2$, $NCH_2CH_2NHCO$, H-2, H-3, W/H-4), 3.83–3.90 (0.8H, m, U/H-1, V/H-1, Y/H-4), 4.08 (0.1H, m, U/H-4), 4.29 (0.3H, m, V/H-4), 4.42–4.49 (0.6H, m, W/H-1, Y/H-1), 5.40 (br s, OH), 5.61–5.64 (0.7H, m, V/H-6, Y/H-6), 6.04–6.07 (1H, m, Ar), 6.19 (0.1H, m, U/H-6), 6.23 (0.2H, m, W/H-6), 6.26 (br s, OH), 6.27 (br s, OH), 6.29–6.31 (1H, m, Ar), 6.36 (m, NH), 6.47 (m, NH), 6.61 (m, NH), 6.75–7.60 (18H, m, CH, Ar), 8.36–8.63 (2H, m, αPyr). *m/z* (ESI+, 70 eV) calcd for $C_{49}H_{43}BF_2N_6NaO_4$ $[M + Na]^+$: 851.3307; found: 851.3335.

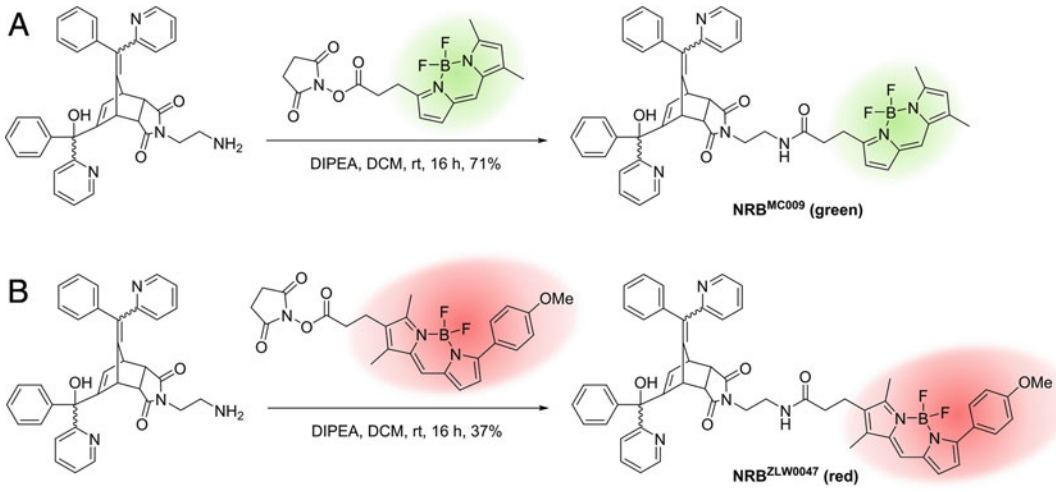


**Fig. 1** Synthesis of norbormide probes $NRB^{MC009}$ (**a**) and $NRB^{ZLW0047}$ (**b**)

2. Preparation of $NRB^{ZLW0047}$ (Fig. 1b). A solution of *N*-2-′-aminoethyl-endo-5-(α-hydroxy-α-2-pyridylbenzyl)-7-(α-2-pyridylbenzylidene)-5-norbornene-2,3-dicarboximide (111 mg, 0.20 mmol), BODIPY TMR NHS ester (110 mg, 0.22 mmol), and diisopropylethylamine (35 μl, 0.20 mmol) in dichloromethane (7 ml) is stirred at room temperature for 16 h. The mixture is washed with water, the separated aqueous phase further extracted with dichloromethane (20 ml), the combined organic layers washed with brine (3 × 20 ml), dried over anhydrous magnesium sulfate, filtered, and the solvent removed in vacuo. Purification by preparative thin-layer chromatography (petroleum ether–ethyl acetate, 1:3) afforded $NRB^{ZLW0047}$ as a mixture of endo stereoisomers (purple solid; 70 mg, 0.074 mmol, 37%). $^1$H NMR (400 MHz, $CDCl_3$) $\delta$ 2.18–2.20 (3H, m, $CH_3$), 2.22–2.26 (2H, m, $NHCOC\mathit{H}_2CH_2$ or $NHCOCH_2C\mathit{H}_2$), 2.47–2.48 (3H, m, $CH_3$), 2.72–2.75 (2H, m, $NHCOC\mathit{H}_2CH_2$ or $NHCOCH_2C\mathit{H}_2$), 3.24–3.84 (7H, m, $NC\mathit{H}_2C\mathit{H}_2NHCO$, H-2, H-3, U/H-1, V/H-1, W/H-4, Y/H-4), 3.84–3.85 (3H, m, $OCH_3$), 4.02 (0.1H, m, U/H-4), 4.30 (0.3H, m, V/H-4), 4.44 (0.4H, m, Y/H-1), 4.47 (0.2H, m, W/H-1), 5.15 (br s, OH), 5.22 (br s, OH), 5.51 (0.3H, m, V/H-6), 5.53 (0.4H, m, Y/H-6), 6.14 (0.1H, m, U/H-6), 6.20 (0.2H, m, W/H-6), 6.28 (br s, OH), 6.29 (br s, OH), 6.47–6.53 (1H, m, Ar), 6.77–7.59 (20H, m, CH, Ar), 7.82–7.88 (2H, m, Ar), 8.38–8.64 (2H, m, αPyr). *m/z* (ESI+, 70 eV) calcd for $C_{56}H_{49}BF_2N_6NaO_5$ $[M + Na]^+$: 957.3727; found: 957.3745.

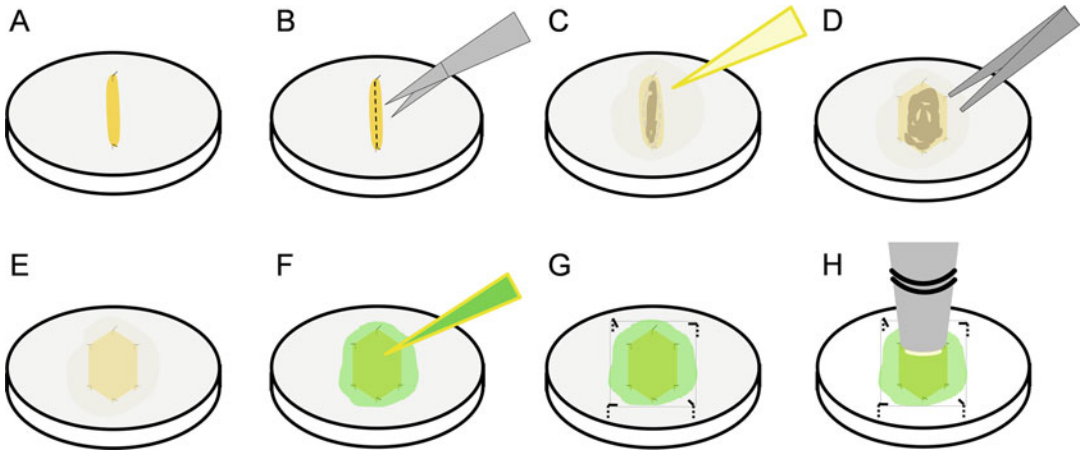


**Fig. 2** Schematic *Drosophila* larval dissection method. Fasten the larva with two pins, one in the lower and one in the upper body (**a**). Make an incision along the dorsal midline (**b**) and cover the larva with HL3-glutamate saline (**c**). Pin the lateral flaps to stretch the fillet (**d**) and remove the unnecessary organs (**e**). Replace the saline with the desired staining solution (**f**), lay over a glass coverslip fastened with four pins (**g**) and proceed to image acquisition (**h**)

### *3.2* Drosophila *Larva Dissection*

All dissection procedures are performed using a stereomicroscope equipped with dual arm fiber optic light source to allow a clear visualization of the dissected larva.

1. Choose and collect carefully third instar *Drosophila* larvae from the tube using the microdissection forceps (*see* **Note 6**).
2. Quickly wash them by immersing in a concave well of a spot glass plate containing phosphate buffered saline (PBS) without calcium or magnesium. Dry by putting them on a paper towel and lay them down on the SYLGARD dissection dish (*see* **Note 7**).
3. Using the forceps to hold the larva, pin it between the posterior spiracles and above the mouth hooks, straighten the larval body out (Fig. 2a), and cut along the dorsal midline (Fig. 2b, *see* **Note 8**).
4. Add 100 μl of HL3-glutamate saline and fasten the lateral flaps with four pins to stretch the body wall (Fig. 2c, d, *see* **Note 9**).
5. As needed, leave all larval organs on the muscle fillet, or remove the unnecessary organs for single tissue acquisition (Fig. 2e, *see* **Note 10**).
6. Remove HL3 saline, and add 50 μl of the staining solution (Fig. 2f).
7. Cover the dissected fillet with a glass coverslip, fasten it with four 0.15 mm pins (Fig. 2g, *see* **Note 11**), and leave at room temperature for 15 min.

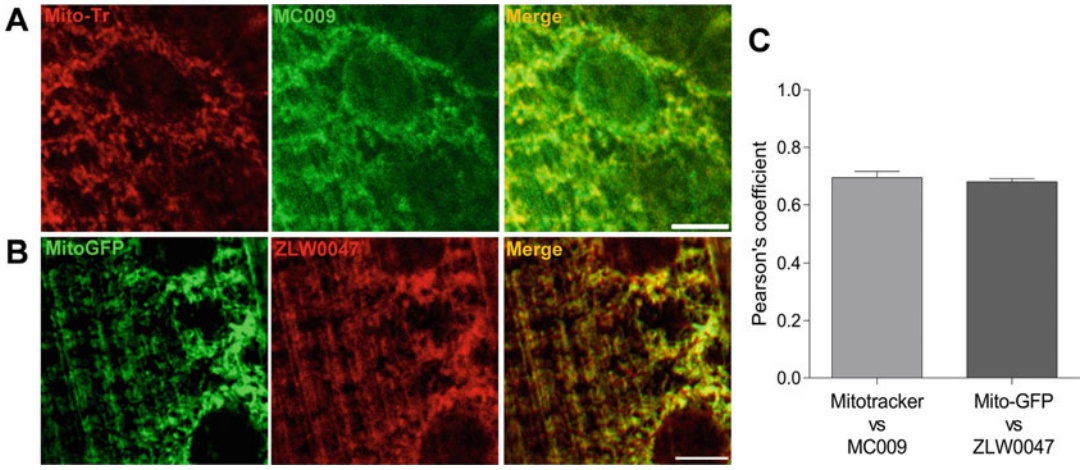


**Fig. 3** $NRB^{MC009}$ and $NRB^{ZLW0047}$ mitochondrial distribution in larval muscles. Confocal live imaging of third instar larval muscles 6–7 from segment A3 of (**a**) $w^{[1118]}$ labeled with MitoTracker™ 1 μM (mitochondria marker, red) together with $NRB^{MC009}$ 500 nM (green) and of (**b**) *UAS-Mito-GFP/Tubulin-Gal4* (mitochondrial marker, green) labeled with $NRB^{ZLW0047}$ 1 μM (red). Magnification 60×; scale bars 10 μm. (**c**) Graph of Pearson's correlation coefficients between the probes and the mitochondrial markers in *Drosophila* larval muscles. Data are expressed as mean ± SEM, $n \geq 10$

### 3.3 Image Acquisition

Confocal microscope settings could vary depending on microscope type and brand. Use the lower laser intensity and pinhole aperture to obtain a bright and well-defined signal (*see* **Note 12**).

1. Prepare microscope for acquisition, add the immersion oil over the cover glass, and proceed to imaging (Fig. 2h).
2. The probes could be used alone, or together with other fluorescent dyes (Fig. 3a) or fluorescent-tagged proteins (Fig. 3b, *see* **Note 13**), and could be used on both wild type larvae, to label physiologic mitochondria morphology, as well as in *Drosophila* pathologic models, to highlight mitochondrial disease-related phenotypes (Fig. 4). They also could be effective at screening for any effects on mitochondrial morphology due to pharmacological treatments or stressors applied on *Drosophila* larvae.

## 4 Notes

1. SYLGARD is difficult to wash out: handle the compounds wearing gloves and clean up any spills with paper towels. Dish could be totally or partially filled with SYLGARD solution, depending on the use and personal preferences. Be careful to put the dishes on a flat surface during the curing process, to ensure a horizontal levelling.

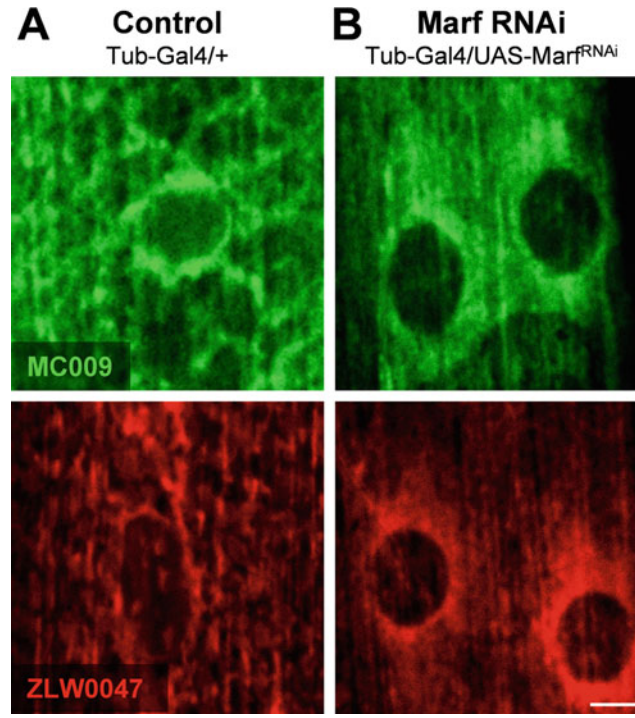


**Fig. 4** NRB$^{MC009}$ and NRB$^{ZLW0047}$ highlight pathologic mutation-related mitochondrial phenotypes. Confocal live imaging of *Drosophila* muscles 6–7 from segment A3 of (**a**) control (*Tubulin-Gal4/+*), and (**b**) Marf downregulation (*UAS-Marf$^{RNAi}$/Tubulin-Gal4*), labeled with NRB$^{MC009}$ 500 nM (green) or NRB$^{ZLW0047}$ 1 μM (red). Magnification 60×; scale bar 10 μm

2. HL3 saline should be stored at 4 °C for short term use or at −20 °C for longer periods.
3. Prepare a stock solution 100 mM of L-glutamate in water: weigh 169 mg of L-glutamic acid monosodium salt hydrate and dissolve it in 10 ml of milliQ water. Store at −20 °C. Glutamate addition is important to arrest muscle contraction and desensitize postsynaptic glutamate receptors, necessary to acquire focused images [15].
4. It is advantageous to make small aliquots of the probe stock solutions to prevent their possible degradation due to repeated freezing/thawing cycles.
5. Images are processed and analyzed using Fiji, a flexible and widely used open source software, that bundles together many popular and useful ImageJ plugins [16].
6. Third instar larvae can be recognized on tube walls because they stop feeding and climb away from the food. Be careful and gentle not to damage the larval bodies when clamping them with the forceps.

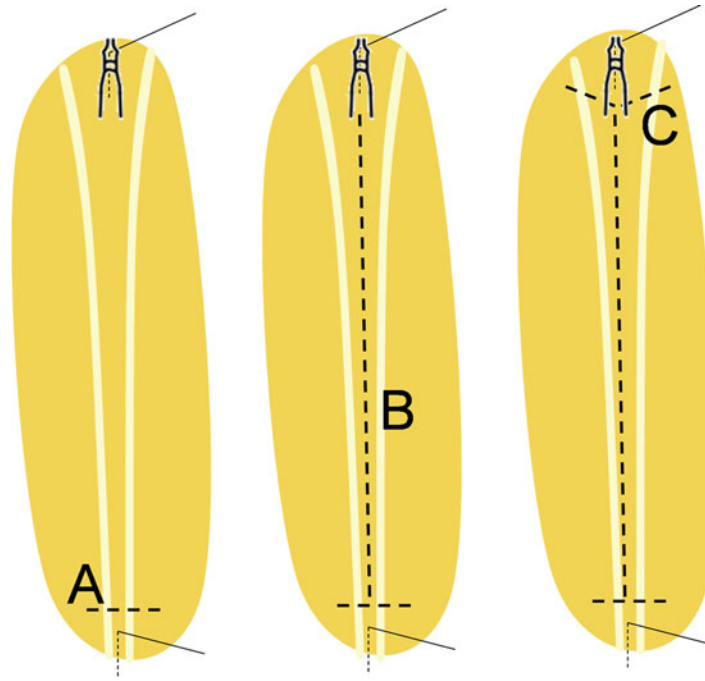


**Fig. 5** Larval incision procedure. Make a small horizontal cut with the microdissection scissors in the lower body (**a**), then cut between the main dorsal tracheae (white vertical lines) until the mouth hook (**b**), without damaging the interior organs, and then make two small lateral incisions (**c**)

7. Be sure that the SYLGARD dish is clean before putting the larvae over it. Before starting to dissect, it is recommended to clean the dish with ethanol 70% to avoid sample contamination. It may be convenient to keep a reserved SYLGARD dish for each probe used because fluorescent molecules may be absorbed by the silicone polymer, eliciting false staining results.
8. Pins must be well pointed, to avoid lacerations of the larval body. While cutting with the micro scissors be careful not to damage the larval muscle fillet and the organs. Make an initial horizontal small incision of the cuticle at the bottom of the larval body (Fig. 5a), then cut along the dorsal midline (between the two main tracheae) to the mouth hook (Fig. 5b), and lastly make two little cuts laterally (Fig. 5c).
9. Dissection process must be rapid (within 5 min) and the larvae have to be always covered by HL3-glutamate saline, to avoid drying. The larval fillet must be well stretched and flat, but it is necessary to be careful not to tear the muscles.
10. For whole larva imaging keep the inner organs as intact as possible while dissecting, and use a low magnification objective to acquire the entire body fillet (e.g., 5× objective). To access

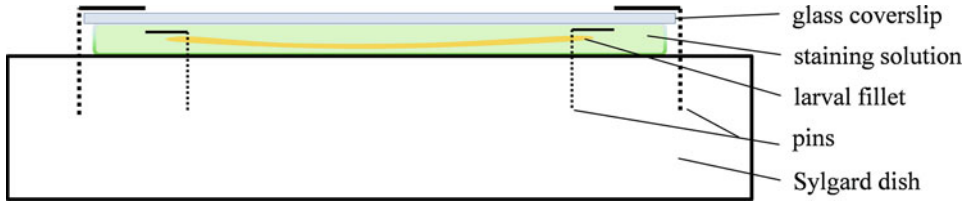


**Fig. 6** Acquisition chamber scheme. The larval fillet (in orange) is fastened on the SYLGARD dish (in white) with entomological pins, immersed in the staining solution (in green), and covered with a glass coverslip (in light blue) secured with pins

deep inside a single tissue, for example muscle, it is recommended to take off the other organs without damaging the fillet and acquire the images with a higher magnification objective (e.g., 40× or 60×).

11. The "acquisition chamber" consists of a cover glass lying above the SYLGARD dish (Fig. 6), which allows the dissected larva to be submerged by the staining solution for the entire acquisition time. The glass coverslip also allows the use of upright confocal microscopes without damaging dry objectives and allows the use of oil objectives if it is necessary to obtain more defined images. It is also possible to perform the acquisition from water objectives, if available on the microscope, through direct immersion into the staining solution (without using the cover glass). If this method is preferred, be careful to clean thoroughly the objective after use: fluorescent probe residues could contaminate subsequent experiments.
12. It is important to verify that the fluorescent signal is either due to the probe labeling or to larval tissues autofluorescence. In order to determine the fluorescent source, dissected larvae are imaged in HL3-glutamate saline without fluorescent probes using identical microscope settings as that used for labeled tissue acquisitions. To avoid false positives, the autofluorescence signal must be almost null.
13. $NRB^{MC009}$ and $NRB^{ZLW0047}$ signals are not specific and exclusive to mitochondria, but the high Pearson's colocalization coefficients between the probes and data generated using available mitochondrial markers (Fig. 2c) suggest that most of the signal represents mitochondrial labeling.

## Acknowledgments

This work was supported by the New Zealand Ministry of Business, Innovation and Employment's Endeavour Fund C09X1710 and by the University of Padova, project n. 148125/14.

## References


1. Aldaz S, Escudero LM, Freeman M (2010) Live imaging of *Drosophila* imaginal disc development. Proc Natl Acad Sci U S A 107:14217–14222. https://doi.org/10.1073/pnas.1008623107
2. Tan FHP, Azzam G (2017) *Drosophila melanogaster*: deciphering Alzheimer's disease. Malays J Med Sci 24:6–20. https://doi.org/10.21315/mjms2017.24.2.2
3. Musselman LP, Kühnlein RP (2018) Drosophila as a model to study obesity and metabolic disease. J Exp Biol 221:jeb163881. https://doi.org/10.1242/jeb.163881
4. Chatterjee S (2014) Artefacts in histopathology. J Oral Maxillofac Pathol 18:S111–S116. https://doi.org/10.4103/0973-029X.141346
5. Mushtaq Z, Choudhury SD, Gangwar SK et al (2016) Human Senataxin modulates structural plasticity of the neuromuscular junction in drosophila through a Neuronally conserved TGFβ signalling pathway. Neurodegener Dis 16:324–336. https://doi.org/10.1159/000445435
6. Orso G, Martinuzzi A, Rossetto MG et al (2005) Disease-related phenotypes in a drosophila model of hereditary spastic paraplegia are ameliorated by treatment with vinblastine. J Clin Invest 115:3026–3034. https://doi.org/10.1172/JCI24694
7. Duffy JB (2002) GAL4 system in drosophila: A fly geneticist's swiss army knife. Genesis 34:1–15. https://doi.org/10.1002/gene.10150
8. Rodríguez A del V, Didiano D, Desplan C (2011) Power tools for gene expression and clonal analysis in drosophila. Nat Methods 9:47–55. https://doi.org/10.1038/nmeth.1800
9. D'Amore C, Orso G, Fusi F et al (2016) An NBD derivative of the selective rat toxicant Norbormide as a new probe for living cell imaging. Front Pharmacol 7:315. https://doi.org/10.3389/fphar.2016.00315
10. D'Amore C, Orso G, Forgiarini A et al (2018) Synthesis and biological characterization of a new Norbormide derived Bodipy FL-conjugated fluorescent probe for cell imaging. Front Pharmacol 9:1055. https://doi.org/10.3389/fphar.2018.01055
11. Forgiarini A, Wang Z, D'Amore C et al (2019) Live applications of norbormide-based fluorescent probes in *Drosophila melanogaster*. PLoS One 14:e0211169. https://doi.org/10.1371/journal.pone.0211169
12. Gießler K, Griesser H, Göhringer D et al (2010) Synthesis of 3′-BODIPY-labeled active esters of nucleotides and a chemical primer extension assay on beads. Eur J Org Chem 2010:3611–3620. https://doi.org/10.1002/ejoc.201000210
13. Meltola NJ, Wahlroos R, Soini AE (2004) Hydrophilic labeling reagents of Dipyrrylmethene-BF2 dyes for two-photon excited Fluorometry: syntheses and Photophysical characterization. J Fluoresc 14:635–647. https://doi.org/10.1023/B:JOFL.0000039350.94256.53
14. Sorkin MR, Walker JA, Brown JS, Alabi CA (2017) Versatile platform for the synthesis of orthogonally cleavable Heteromultifunctional cross-linkers. Bioconjug Chem 28:907–912. https://doi.org/10.1021/acs.bioconjchem.7b00033
15. Chen K, Augustin H, Featherstone DE (2008) Effect of ambient extracellular glutamate on drosophila glutamate receptor trafficking and function. J Comp Physiol A 195:21. https://doi.org/10.1007/s00359-008-0378-3
16. Schindelin J, Arganda-Carreras I, Frise E et al (2012) Fiji: an open-source platform for biological-image analysis. Nat Methods 9:676–682. https://doi.org/10.1038/nmeth.2019

# Chapter 18

# Live-Cell Assessment of Reactive Oxygen Species Levels Using Dihydroethidine

**Sander Grefte and Werner J. H. Koopman**

## Abstract

Reactive oxygen species (ROS) play an important role in cellular (patho)physiology. Empirical evidence suggests that mitochondria are an important source of ROS, especially under pathological conditions. Here, we describe a method for ROS measurement using dihydroethidium (HEt) and live-cell microscopy.

**Key words** MitoSOX Red®, Mitochondrial membrane potential, Fluorescence imaging

## Abbreviations

| | |
|---|---|
| FCCP | carbonyl cyanide-p-trifluoromethoxyphenylhydrazone |
| HEt | dihydroethidium |
| HT | HEPES-Tris |
| mito-HEt | mito-dihydroethidium |
| ROS | reactive oxygen species |
| TPP | triphenylphosphonium |
| $\Delta\psi$ | mitochondrial membrane potential |

## 1 Introduction

Reactive oxygen species (ROS) can damage cellular biomolecules, but are also increasingly recognized as signaling molecules [1–4]. Among other sources, mitochondria are considered to be important contributors to ROS generation during healthy and pathological conditions [5]. The primary ROS superoxide ($O_2^{\cdot-}$) is produced by membrane-bound parts of the respiratory chain and a number of soluble mitochondrial proteins. Although $O_2^{\cdot-}$ cannot traverse membranes and has only limited reactivity with biological targets, it might function as a redox signal in mitochondria

Volkmar Weissig and Marvin Edeas (eds.), *Mitochondrial Medicine: Volume 1: Targeting Mitochondria*, Methods in Molecular Biology, vol. 2275, https://doi.org/10.1007/978-1-0716-1262-0_18,

[6–8]. Since mitochondrial signaling and cellular function are intricately linked, it is important to measure mitochondrial $O_2^{\cdot-}$ in the proper context—that is, the living cell. However, it has proven difficult to develop fluorescent probes or sensors that are specific for $O_2^{\cdot-}$ and sensitive enough to compete with superoxide dismutase (SOD), which converts $O_2^{\cdot-}$ to hydrogen peroxide at an extremely high rate [9]. Quantifying the oxidation of dihydroethidium (HEt) is a widely applied strategy to detect $O_2^{\cdot-}$ in living cells. HEt is membrane-permeable and reacts with $O_2^{\cdot-}$ to form the specific fluorescent product 2-hydroxyethidium (2-OH-$Et^+$) (Fig. 1a). In addition, HEt can act as a hydride acceptor, leading to oxidative formation of the nonspecific fluorescent product ethidium ($Et^+$) [10–12]. Whereas the fluorescence excitation peaks of 2-OH-$Et^+$ (Fig. 1b; upper blue curve) and $Et^+$ (lower blue curve) overlap at around 500 nm, 2-OH-$Et^+$ has one additional peak at 396 nm which has been used for more specific detection of 2-OH-$Et^+$ [9]. Still, the latter approach should be considered semiquantitative and not fully $O_2^{\cdot-}$-specific given the unknown reactivity of $O_2^{\cdot-}$ with SOD, the possible oxidation of HEt by cytochrome *c* and because HEt can catalyze $O_2^{\cdot-}$ dismutation [9, 13]. Given its lipophilic nature, HEt oxidation can in principle occur everywhere in the cell. Both 2-OH-$Et^+$ and $Et^+$ are positively charged and therefore accumulate: (1) in the nucleus where they intercalate with nucleic acids, and (2) in the mitochondrial matrix due to the inside-negative membrane potential ($\Delta\psi$) of this organelle. In an attempt to utilize $\Delta\psi$, a mitochondria-targeted variant of HEt was developed (MitoSOX Red®, aka Mito-HEt). The latter consists of HEt extended with a cationic triphenylphosphonium (TPP) side group [9]. Below we describe the critical loading procedure for different intact cells and methods to measure HEt-oxidizing ROS using live cell microscopy.

## 2 Materials

### 2.1 General

1. Cells cultured on a glass coverslip (ø24 mm, Thermo Scientific, Etten-Leur, The Netherlands) placed in a 35-mm CellStar tissue culture dish (Sigma-Aldrich) or disposable incubation chamber (Willco Wells BV) (*see* **Note 1**).
2. A microscope system with the following setup or similar; a monochromator (Polychrome IV, TILL Photonics) allowing for excitation with 405 and/or 490 nm light, a 525DRLP dichroic mirror (Omega Optical Inc.) and 565ALP emission filter (Omega Optical Inc) and an image capturing device (e.g., a CoolSNAP HQ monochrome CCD-camera (Roper Scientific)). The microscope should be equipped with an environmental control system to sustain cell viability.

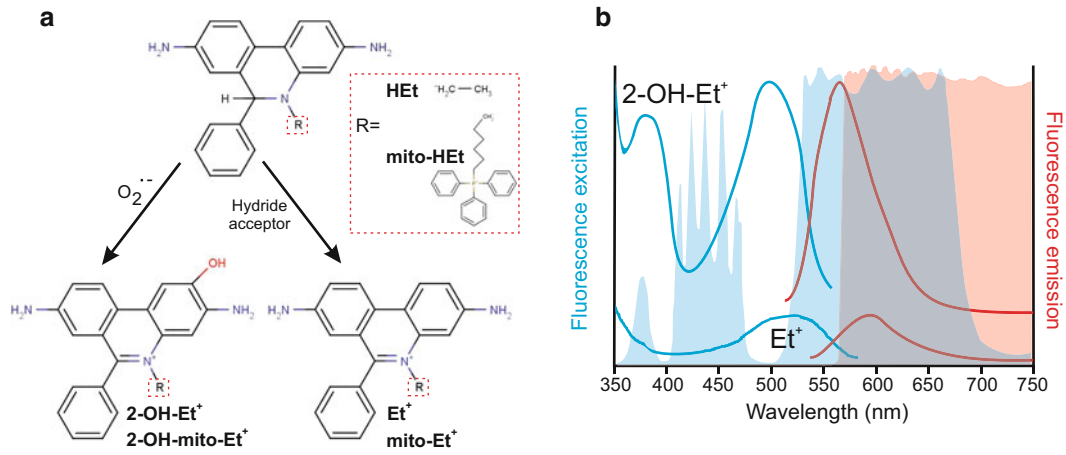


**Fig. 1** Chemical structures and excitation spectra of HEt and mito-Het. (**a**) HEt and mito-HEt specifically react with $O_2^{\cdot -}$ to form the reaction product 2-OH-(mito-)$Et^+$ and (mito-)$Et^+$ as a nonspecific by-product. The inset shows the HEt- and mito-HEt-specific groups. (Figure was adapted from [17]). (**b**) Fluorescence excitation (blue) and emission (red) spectra of 2-OH-$Et^+$ (top traces) and $Et^+$ (lower traces) superimposed with the excitation and emission filters used in our microscope setup. (Figure was adapted from [18]. This figure was reproduced (with permission) from Ref. 19)

3. 5× HEPES buffer: 662.2 mM NaCl, 50 mM HEPES, 21.06 mM KCl, 6.1 mM $MgCl_2$ (*see* **Note 2**).
4. 1× HEPES-Tris buffer: 10 mM HEPES, 132 mM NaCl, 4.2 mM KCl, 1.2 mM $MgCl_2$, 1.0 mM $CaCl_2$, 5.5 mM D-glucose. Adjust the pH to 7.4 using Tris-base (*see* **Note 3**).

### *2.2 Dihydroethidium (HEt)*

1. HEt stock solution (31.7 mM in DMSO): Dissolve 1 mg of HEt powder (Invitrogen) in 100 µl DMSO. Prepare 10 µl aliquots in brown Eppendorf tubes, overlay with $N_2$ gas and store at −20 °C (*see* **Note 4**).
2. HEt working solution (5 mM in DMSO): Thaw an aliquot of HEt stock solution and add 53.4 µl of DMSO to yield the 5 mM HEt working solution.

### *2.3 Mito-Dihydroethidium (Mito-HEt)*

Mito-HEt working solution (500 µM in DMSO): Dissolve 50 µg of MitoSOX Red® powder (Invitrogen) in 132 µl DMSO. Prepare 4 µl aliquots in brown Eppendorf tubes, overlay with $N_2$ gas and store at −20 °C.

## 3 Methods

### *3.1 Microscopy Imaging of Dihydroethidium (HEt) Oxidation*

1. Seed the cells at such densities that the cells are 70–80% confluent at the time of imaging. This allows for subtraction of the background signal (*see* **Note 5**).

2. Transfer the cells to an incubator close to the microscope system at least 1 h prior to imaging (*see* **Note 1**).
3. Aliquot 2 μl of HEt working solution in Eppendorf tubes.
4. Take 1 ml of medium from the culture dish, add it to the aliquoted HEt and vortex for 5–10 s to prepare a final concentration of 10 μM (*see* **Note 6**).
5. Replace the rest of the medium from the dish by the medium–HEt solution.
6. Incubate the cells in a 37 °C, 5% $CO_2$ incubator for exactly 10 min (*see* **Note 7**).
7. Wash the coverslip three times with 1 ml PBS.
8. Replace the PBS by prewarmed HT buffer and mount the coverslip in a Leiden chamber on the microscope [14]. When using oil-based objectives be careful to remove all excess buffer from the bottom of the coverslip with a tissue to avoid optical artifacts.
9. Start loading of a next coverslip as soon as loading of the current one is complete.
10. Preferably, take images at both 405 and 490 nm excitation. Set the exposure time to 100 ms.
11. Record at least 10 different images, each containing ~15 cells (*see* **Notes 8** and **9**).

### *3.2 Microscopy Imaging of Mito-Dihydroethidium (Mito-HEt) Oxidation*

1. Seed the cells at such densities that the cells are 70–80% confluent at the time of imaging. This allows for subtraction of the background signal.
2. Transfer the cells to an incubator close to the microscope system at least 1 h prior to imaging.
3. Thaw the 4 μl mito-HEt contents of a brown Eppendorf tube.
4. Take 1 ml of medium from the culture dish, add it to mito-HEt and vortex for 5–10 s to prepare a final concentration of 2 μM (*see* **Note 10**).
5. Replace the rest of the medium from the dish by the medium–mito-HEt solution.
6. Incubate the cells in a 37 °C, 5% $CO_2$ incubator for exactly 10 min (*see* **Note 7**).
7. Wash the coverslip three times with 1 ml phosphate buffered saline (PBS).
8. Replace the PBS by prewarmed HT buffer and mount the coverslip in a Leiden chamber on the microscope [14]. When using oil-based objectives be careful to remove all excess buffer from the bottom of the coverslip with a tissue to avoid focusing problems.

9. Start loading of a next coverslip as soon as loading of the current one is complete.
10. Preferably, take images at both 405 and 490 nm excitation. Set the exposure time to 500 ms.
11. Record an image sequence of one field of view, acquiring one image every 5 or 10 s for a total of at least 2 min (*see* **Note 11**).

### 3.3 Image Analysis

1. Open the raw images in an image analysis program such as Metamorph® (Molecular Devices Corporation, Palo Alto, CA, USA), Image Pro Plus (Media Cybernetics) or the open-source software FIJI (http://fiji.cs/).
2. Draw circular regions of interest (ROIs) in: (1) a mitochondria-dense area, (2) surrounding the nucleus, and (3) just outside each individual cell to correct for background intensity (*see* **Note 9**).
3. Export the average ROI gray value to a spreadsheet program such as Excel (Microsoft) and calculate the background-subtracted values of the mitochondria and the nucleus of each cell.

## 4 Notes

1. Due to the positive charge of mito-HEt and the reaction products of HEt oxidation, the fluorescence intensity measured in the mitochondria is $\Delta\psi$-dependent (Fig. 2). Since the mitochondrial membrane potential is very sensitive to environmental changes (e.g., temperature, pH), we advise to culture the cells in separate dishes and to allow for cells to recover in an incubator close to the microscope system at least 1 h prior to imaging. In addition, we have noticed that HEt can react with residues on a number of glass-bottom culture dishes, leading to fluorescent "spots" in the background. Therefore, always check background levels for disturbances.
2. We store a large volume of 5× HEPES buffer at 4 °C, which is stable for at least 6 months.
3. We advise to make the 1×HT buffer supplemented with the required substrates at the day of imaging. We routinely use 5.5 mM D-glucose for human skin fibroblasts and myoblasts/fibers, whereas HEK293 cells are imaged in HT buffer containing 25 mM D-glucose. In addition, one can consider supplementing pyruvate and/or glutamine. If necessary, the HT buffer can be stored for ~1 week at 4 °C.
4. Always keep HEt solutions protected from light and air.

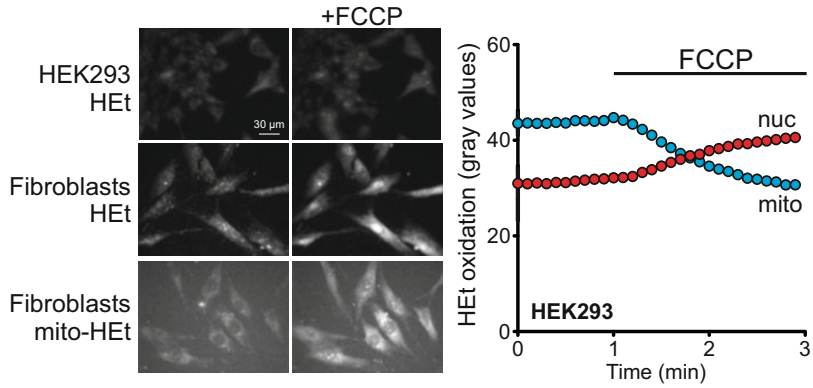


**Fig. 2** Localization of HEt oxidation products is dependent on the membrane potential. Addition of the mitochondrial protonophore carbonyl cyanide-p-trifluoromethoxyphenylhydrazone (FCCP; 0.5 µM) acutely induces translocation of fluorescent HEt and mito-HEt oxidation products from the mitochondria to the nucleus in HEK293 cells and human skin fibroblasts. (This figure was reproduced (with permission) from Ref. 19)

5. Proper background correction close to the cells is of particular importance when the fluorescent signal is close to the background intensity. Such a background correction is challenging when confluency exceeds 80%. Therefore, adjust the seeding condition according to the number of days the cells are cultured.
6. We prefer to load the cells with HEt in the collected cell culture medium to detect ROS levels in the exact cell culture conditions. However, we have noticed lower fluorescence intensities in medium-loaded cells as compared to cells loaded with HEt in the HT buffer. This is possibly caused by binding of the HEt to proteins present in the medium (i.e., serum), but might also be due to increased fluorescence levels in HT medium (Fig. 3a).
7. The HEt incubation time should be determined experimentally for each cell line separately. To be able to semiquantitively measure HEt oxidation, the increase in fluorescence intensity from oxidation products should be linear. To that end, we mount unloaded cells onto the microscope system in HT buffer, start imaging every 10 s and add the required HEt in HT buffer in 1:1 ratio. We then calculate the maximum time of incubation in which the increase is still linear. An incubation time of 10 min is most often used for HEK293 and human skin fibroblasts (Fig. 3b). However, in some cell types such as primary mouse myotubes it appears to be safer to use shorter incubation times because the signal increase deviates from linearity within 10 min (Fig. 3c).
8. When attempting to image HEt oxidation using 405 nm excitation, we advise to use the 490 nm light to locate cells and find

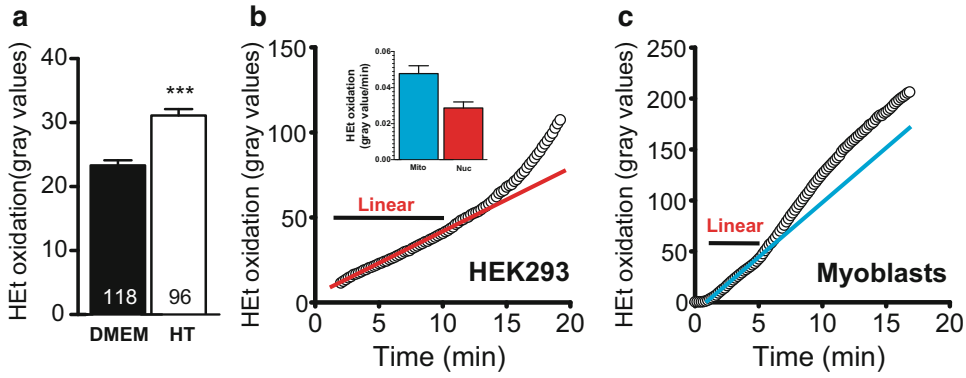


**Fig. 3** HEt loading procedure in intact cells. (**a**) HEK293 cells were incubated with HEt for exactly 10 min in the collected cell culture medium (DMEM) or washed and incubated for exactly 10 min in HT buffer. HEt oxidation was measured at 490 nm. The data presented represent the mean ± SE of two different experiments. Statistical significance was assessed using a Mann–Whitney test. Numerals within bars indicate the number of analyzed cells. (**b**) Representative trace of nuclear HEt oxidation fluorescence intensity at 490 nm excitation light in HEK293 cells. Up to approximately 10 min the increase remains linear. Note that the mitochondrial increase occurs faster in these cells than in the nucleus. (**c**) Representative trace of mitochondrial HEt oxidation fluorescence intensity at 490 nm in myoblasts. The increase is linear during 4.5 min. (This figure was reproduced (with permission) from Ref. 19)

a good focus, because in our experimental setup fluorescence intensity is higher at 490 nm than at 405 nm excitation (Fig. 4a). Moreover, we routinely only measure fluorescence from 490 nm excitation since, in some cell types, the 405 nm signal is too low for reliable quantification. However, relative changes in emission fluorescence observed at 405 and 490 nm excitation are similar, justifying the use of 490 nm as a measure of HEt oxidation [15].

9. It is sufficient to have only a portion of the cells in the field of view, since only part of the cell is analyzed.
10. We advise to use a mito-HEt concentration that is as low as possible, but still revealing detectable levels of fluorescence. In theory, the positive charge accumulating in the mitochondrial matrix might interfere with mitochondrial bioenergetics and therefore report incorrect HEt oxidation values. In addition, it was reported that nuclear fluorescence occurred at concentrations as low as 2 μM and therefore to use a concentration of mito-HEt between 0.1 and 2.5 μM [9].
11. Removing excess HEt after incubation effectively removes all nonoxidized HEt and therefore the signal remains stable for at least 10 min of continuous imaging [16]. The TPP moiety of Mito-HEt induces accumulation of nonoxidized Mito-HEt in the mitochondrial matrix that is insensitive to washing. Consequently, the fluorescence signal continues to increase after washing and therefore we advise to measure the slope of the increase after loading and washing (Fig. 4b).

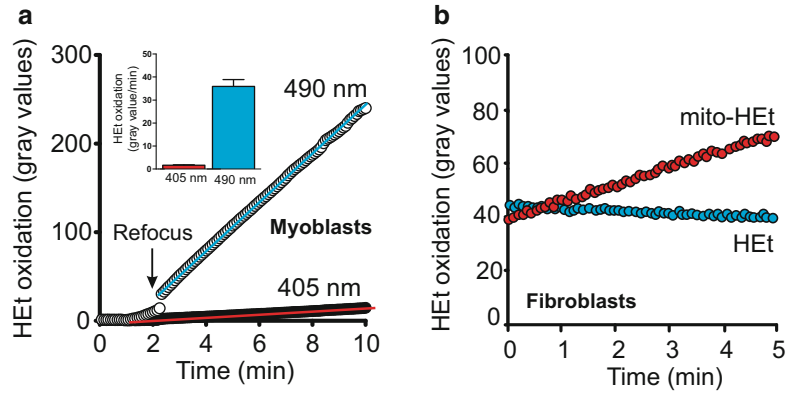


**Fig. 4** Fluorescence intensity from 405 and 490 nm excitation and measurement of HEt versus mito-HE oxidation. (**a**) Simultaneous measurement of HEt oxidation using 405 and 490 nm excitation light in myoblasts. (**b**) Human skin fibroblasts were incubated with 10 μM HEt or 1 μM mito-HEt, washed, and imaged every 5 s using 490 nm excitation light. Staining with HEt yields end-point signals, whereas mito-HEt signals continue to increase in time. (This figure was reproduced (with permission) from Ref. 19)

## Acknowledgments

We are grateful to Dr. A.S. De Jong and Dr. Marleen Forkink (Dept. of Biochemistry, Radboudumc) for performing the HEt and Mito-HEt experiments.

*Potential competing interests*: Werner J.H. Koopman is a scientific advisor of Khondrion. This SME had no involvement in the data collection, analysis, and interpretation; writing of the manuscript; and the decision to submit the manuscript for publication.

### References

1. Distelmaier F, Valsecchi F, Forkink M et al (2012) Trolox-sensitive reactive oxygen species regulate mitochondrial morphology, oxidative phosphorylation and cytosolic calcium handling in healthy cells. Antioxid Redox Signal 17:1657–1669
2. Finkel T (2012) Signal transduction by mitochondrial oxidants. J Biol Chem 287:4434–4440
3. Willems PHGM, Rossignol R, Dieteren CEJ, Murphy MP, Koopman WJH (2015) Redox homeostasis and mitochondrial dynamics. Cell Metab 22:207–218
4. Murphy MP, Holmgren A, Larsson NG et al (2011) Unraveling the biological roles of reactive oxygen species. Cell Metab 13:361–366
5. Brown GC, Borutaite V (2012) There is no evidence that mitochondria are the main source of reactive oxygen species in mammalian cells. Mitochondrion 12:1–4
6. Tormos KV, Anso E, Hamanaka RB et al (2011) Mitochondrial complex III ROS regulate adipocyte differentiation. Cell Metab 14:537–544
7. Zhou L, a Aon M, Almas T et al (2010) A reaction-diffusion model of ROS-induced ROS release in a mitochondrial network. PLoS Comput Biol e1000657:6
8. Murphy M (2009) How mitochondria produce reactive oxygen species. Biochem J 417:1–13
9. Robinson KM, Janes MS, Pehar M et al (2006) Selective fluorescent imaging of superoxide in vivo using ethidium-based probes. Proc Natl Acad Sci U S A 103:15038–15043

10. Zhao H, Kalivendi S, Zhang H et al (2003) Superoxide reacts with hydroethidine but forms a fluorescent product that is distinctly different from ethidium: potential implications in intracellular fluorescence detection of superoxide. Free Radic Biol Med 34:1359–1368
11. Zhao H, Joseph J, Fales HM et al (2005) Detection and characterization of the product of hydroethidine and intracellular superoxide by HPLC and limitations of fluorescence. Proc Natl Acad Sci U S A 102:5727–5732
12. Xiao Y, Meierhofer D (2019) Are hydroethine-based probes reliable for reactive oxygen species detection? Antioxid Redox Signal 31:359–367
13. Benov L, Sztejnberg L, Fridovich I (1998) Critical evaluation of the use of hydroethidine as a measure of superoxide anion radical. Free Radic Biol Med 25:826–831
14. Ince C, Beekman RE, Verschragen G (1990) A micro-perfusion chamber for single-cell fluorescence measurements. J Immunol Methods 128:227–234
15. Forkink M, Smeitink JAM, Brock R et al (2010) Detection and manipulation of mitochondrial reactive oxygen species in mammalian cells. Biochim Biophys Acta 1797:1034–1044
16. Koopman W, Verkaart S, Visch H et al (2005) Inhibition of complex I of the electron transport chain causes $O_2^{\cdot -}$-mediated mitochondrial outgrowth. Am J Physiol Cell Physiol 288:C1440–C1450
17. Zielonka J, Vasquez-Vivar J, Kalyanaraman B (2008) Detection of 2-hydroxyethidium in cellular systems: a unique marker product of superoxide and hydroethidine. Nat Protoc 3:8–21
18. Zielonka J, Kalyanaraman B (2010) Hydroethidine- and fluorescence is not a reliable indicator of intracellular superoxide formation: another inconvenient truth. Free Radic Biol Med 48:983–1001
19. Forkink M, Willems PHGM, Koopman WJH, Grefte S (2015) Chapter 15: reactive oxygen species quantification using hydroethidium. Meth Mol Biol 1264:161–169

# Chapter 19

# Protein Supercomplex Recording in Living Cells Via Position-Specific Fluorescence Lifetime Sensors

**Bettina Rieger and Karin B. Busch**

## Abstract

Our group has previously established a strategy utilizing fluorescence lifetime probes to image membrane protein supercomplex (SC) formation in situ. We showed that a probe at the interface between individual mitochondrial respiratory complexes exhibits a decreased fluorescence lifetime when a supercomplex is formed. This is caused by electrostatic interactions with the adjacent proteins. Fluorescence lifetime imaging microscopy (FLIM) records the resulting decrease of the lifetime of the SC-probe. Here we present the details of our method for performing SC-FLIM, including the evaluation of fluorescence lifetimes from the FLIM images. To validate the feasibility of the technique for monitoring adaptive SC formation, we compare data obtained under different metabolic conditions. The results confirm that SC formation is dynamic.

**Key words** Respiratory supercomplexes, Mitochondria, FLIM, Fluorescence sensor, Live cell imaging

## 1 Introduction

The formation of supercomplexes of proteins that catalyze successive reactions is not uncommon in biology. The respiratory supercomplex from the OXPHOS system is a prominent example from the field of bioenergetics. Three out of five membrane complexes in the inner mitochondrial membrane, the proton pumps NADH: ubiquinone oxidoreductase (CI), cytochrome c reductase (CIII), and complex IV cytochrome c oxidase (CIV) constitute the respiratory chain (RC) also named electron transport chain (ETC). Those three complexes are found to form supercomplexes [1, 2]. As an alternative to CI, succinate dehydrogenase (CII) is able to deliver electrons (from $FADH_2$) to CIII and then to CIV. Electrons from $NADH/H^+$ (or $FADH_2$) finally reduce oxygen to water. This reaction is exergonic and the energy is used to pump electrons from the matrix site (*n*-site) into the intermembrane (intra-cristae) space (*p*-site), which is thereby acidified. The generated proton

Volkmar Weissig and Marvin Edeas (eds.), *Mitochondrial Medicine: Volume 1: Targeting Mitochondria*, Methods in Molecular Biology, vol. 2275, https://doi.org/10.1007/978-1-0716-1262-0_19,

electrochemical gradient, referred to as proton motive force (PMF), drives ATP synthesis by complex V ($F_OF_1$ ATP synthase) [3]. The high abundance of integral OXPHOS complexes in the inner mitochondrial membrane suggests a densely packed system with a calculated average distance between (homogeneously) distributed complexes of a few nanometers [4]. The so-called plasticity model assumes a dynamic situation of adaptive assembly and disassembly of complexes I, III, and IV into supercomplexes [5]. Major assemblies of the composition $CI/CIII_2$ and $CI/CIII_2/CIV$ were found (Schägger and Pfeiffer, 2000; Dudkina et al., 2005; Wittig et al., 2006). Recently, Cryo EM-single particle analysis finally yielded putative structures for isolated $CI/CIII_2/CIV$, where CIV is facing CIII with the site that is opposite from the site that is mediating CIV dimerization [6–9]. Despite the bundle of evidence for supercomplex formation, it has been criticized that the previous stoichiometric and structural data is based on the solubilization of supercomplexes with mild detergents [10] from tissue and could be artifacts at worst. Thus, a proof of supercomplex assembly in situ was due.

Here, we present fluorescence lifetime imaging microscopy (FLIM) as a technique for monitoring (dynamic) supercomplex formation in living cells. It is based on recording the fluorescence lifetime of a constructed SC sensor, CoxVIIIa-sEcGFP [11]. The method exploits the fact that the fluorescence lifetime of a fluorochrome is dependent on its nanoenvironment. An excited fluorochrome in a neighborhood with high macromolecular crowding has the possibility of multiple electrodynamic interactions, resulting in decreased fluorescence lifetime $\tau$. This is also true for a sensor positioned in a protein complex/supercomplex [12]. In order to find a suitable position of a fluorescent SC sensor, it is recommendable to first perform computational modelling using existent structures. In our case, several models were constructed with Green Fluorescent Protein (GFP) at different positions of in the respiratory supercomplex $CI/CIII_2/CIV$ [6–8] (Fig. 1a). Therefore, GFP was fused to the subunits CoxVIIIa and CoxVIIc in CIV. The Fusion of GFP to these subunits appeared to be suitable to sense SC assembly due to the specific localization of the subunits at the interface between CI, CIII, and CIV in a supercomplex. After generation of the genetically encoded fluorescent protein fusion constructs CoxVIIIa-sEcGFP and CoxVIIc-sEcGFP, respectively, HeLa cells were transfected, correct expression was verified (*see* **Note 1**) and stable cell lines were generated. The pH-sensitive GFP derivative chosen was sEcGFP, which would allow parallel recording of pH values [13] (*see* **Note 2**). However, other GFP derivatives can be used as well (*see* **Note 3**). As the FLIM data clearly show, the positioning of the fluorescent protein at the interface between CIII and CIV at CoxVIIIa-sEcGFP resulted in a significant decrease in fluorescence lifetime, indicating a supercomplex environment. In contrast, the lifetime probes positioned

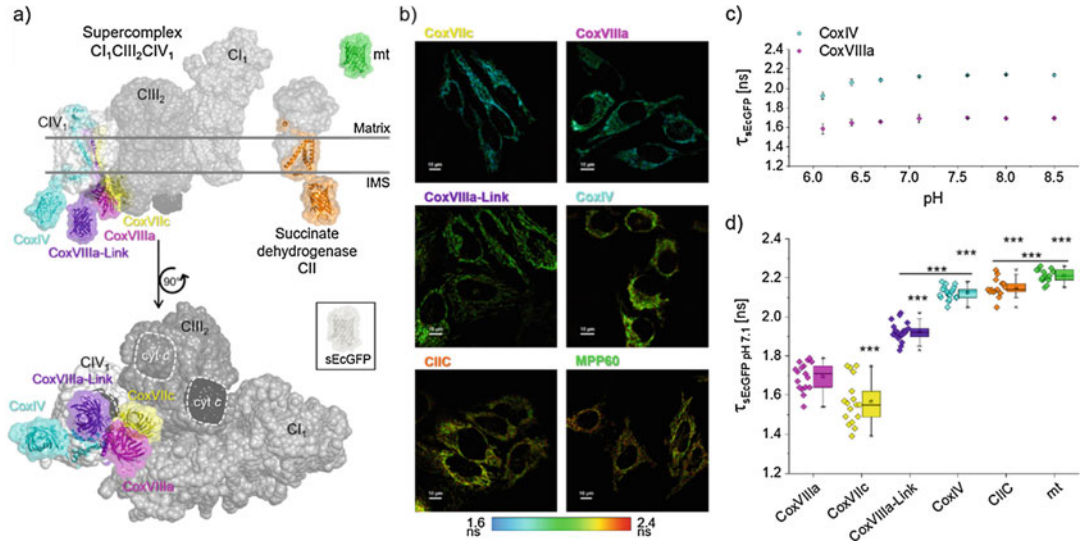


**Fig. 1** Fluorescent proteins attached to OXPHOS subunits CoxVIIIa and CoxVIIc report specific molecular crowding at the contact site of supercomplexes such as $CI_1CIII_2CIV_1$. (**a**) 3D maps of CII and the $CI_1CIII_2CIV_1$ supercomplex model (Dudkina et al., 2011) showing the side view (top) and the view of the supercomplex from the *p*-side (complex I in gray, complex III in darker gray, and complex IV in light gray, cytochrome *c* in black). The fluorescent protein sEcGFP was fused to different subunits of respiratory complexes: CoxVIIc (yellow), CoxVIIIa (pink), CoxVIIIa-Link (violet), CoxIV (cyan), and CIIC/SDHC (orange), and to a short matrix targeting sequence mt (green). Selected fitting models are shown. (**b**) Intensity – lifetime images of HeLa cells expressing the different fusion constructs reveal clear differences in fluorescence lifetimes. FLIM was conducted with a TCS SP8 SMD confocal laser scanning microscope from Leica equipped with a 63x water objective (37 °C and 5% $CO_2$). Scale bars: 10 μm or 20 μm, as indicated. (**c**) pH dependene of the fluorescence lifetime of sEcGFP-constructs. (**d**) Lifetime constants $\tau_{amp}$ of six different sEcGFP-constructs (CoxVIIIa—pink, CoxVIIc—yellow, CoxVIIIa-Linker—violet, CoxIV—cyan, subunit C of SDH—orange, and of matrix-targeted soluble sEcGFP—green) determined in cells clamped at pH 7.1 with 20 mM BES and ionophores. Measurements were performed at 37 °C without $CO_2$. Generally, cells were incubated in different buffers (20 mM MES, 20 mM BES or 20 mM HEPPSO), whose pH was adjusted differently. To exclude any interference with mitochondrial activity, oxidative phosphorylation was inhibited by treatment with 5 μg/mL oligomycin, 10 μM Carbonylcyanid-m-chlorphenylhydrazon (CCCP) and 1 μM Nigericin. Data points represent means (one data point per cell), error bars represent s.d. (d) or s.e.m. (c). $N = 2–3$ biological replicates. (Adapted from [11])

at the surface of the supercomplex (e.g., CoxIV-sEcGFP) (Fig. 1b), displayed no decrease in lifetime. Subunits positioned comparably close to the *p*-side membrane surface but at complexes that are not involved in supercomplex formation (CII subunit C-sEcGFP) showed no decrease in lifetime. Also, a lifetime probe in the matrix volume did not show the specific shortening of fluorescence lifetimes as found for CoxVIIIa-sEcGFP [11]. To verify, if indeed the embedding of a sensor in the SC was the cause for the lifetime shortening, a construct with an inserted linker between the fluorescent sensor and CoxVIIIa was also tested. The

insertion of the linker, composed of the C-terminal sequence of CoxVIIb, was designed to enhance the distance of the sensor protein to the subunit CoxVIIIa at the SC interface. The insertion of the linker resulted in a significant prolongation of the lifetime of the fusion protein CoxVIIIa-link-sEcGFP, indicating a partial escape from the molecular crowd (Fig. 1b). Before using the sensor-fusion proteins for further studies, a functional assay (*see* **Note 4**) was performed to test whether labeling would impact on function (data not shown). We measured oxygen consumption rates. While the cell line stably expressing CoxVIIc-sEcGFP had lower oxygen consumption rates (OCR), CoxVIIIa-sEcGFP expression had no effect on respiration. Thus, the sensor-tagged subunit CoxVIIIa (*see* **Note 5**) does not interfere with mitochondrial function. Therefore, CoxVIIIa-sEcGFP was chosen as the putative SC-sensor.

Since it is known that the fluorescence lifetime of a fluorescent protein is pH sensitive to some extent, we also performed fluorescence lifetime imaging at different pH values within cells [13]. We found that the pH sensitivity of the fluorescence lifetime was negligible at physiological pH values above pH 6.7 in the microcompartments analyzed (Fig. 1c). Furthermore, comparison of fluorescence lifetimes in cells with pH adjusted to pH 7.1 showed that the significant lifetime differences between the different sensor constructs (Fig. 1d) also existed under equalized pH conditions and thus are not the result of pH differences.

In order to demonstrate the feasibility of SC-sensing, we conducted FLIM of cells supplied with different sugar supply. As cancer cells, HeLa usually mainly use glycolysis to generate ATP. However, they can increase respiration and oxidative phoshorylation when glucose is restricted and glutamine is supplied instead (reverse Warburg effect) [14]. The supply of galactose also has this effect [15]. Galactose moreover enhances supercomplex formation of respiratory chain complexes [16], which we were able to confirm via our noninvasive live cell imaging technique [17] using stable HeLa cell lines expressing the supercomplex sensor CoxVIIIa-sEcGFP. CoxIV-sEcGFP was used as negative control (Fig. 2a–d). In galactose, the fluorescence lifetime of CoxVIIIa-sEcGFP decreased significantly, while no effect on the lifetime of the control sensor was observed. Taken together, this data clearly demonstrates that FLIM with a SC-sensor at the interface/contact site within a supercomplex (here CoxVIIIa-sEcGFP in CI/$CIII_2$/CIV) is a suitable tool to record dynamic supercomplex formation by determining changes in the fluorescence lifetime of the sensor.

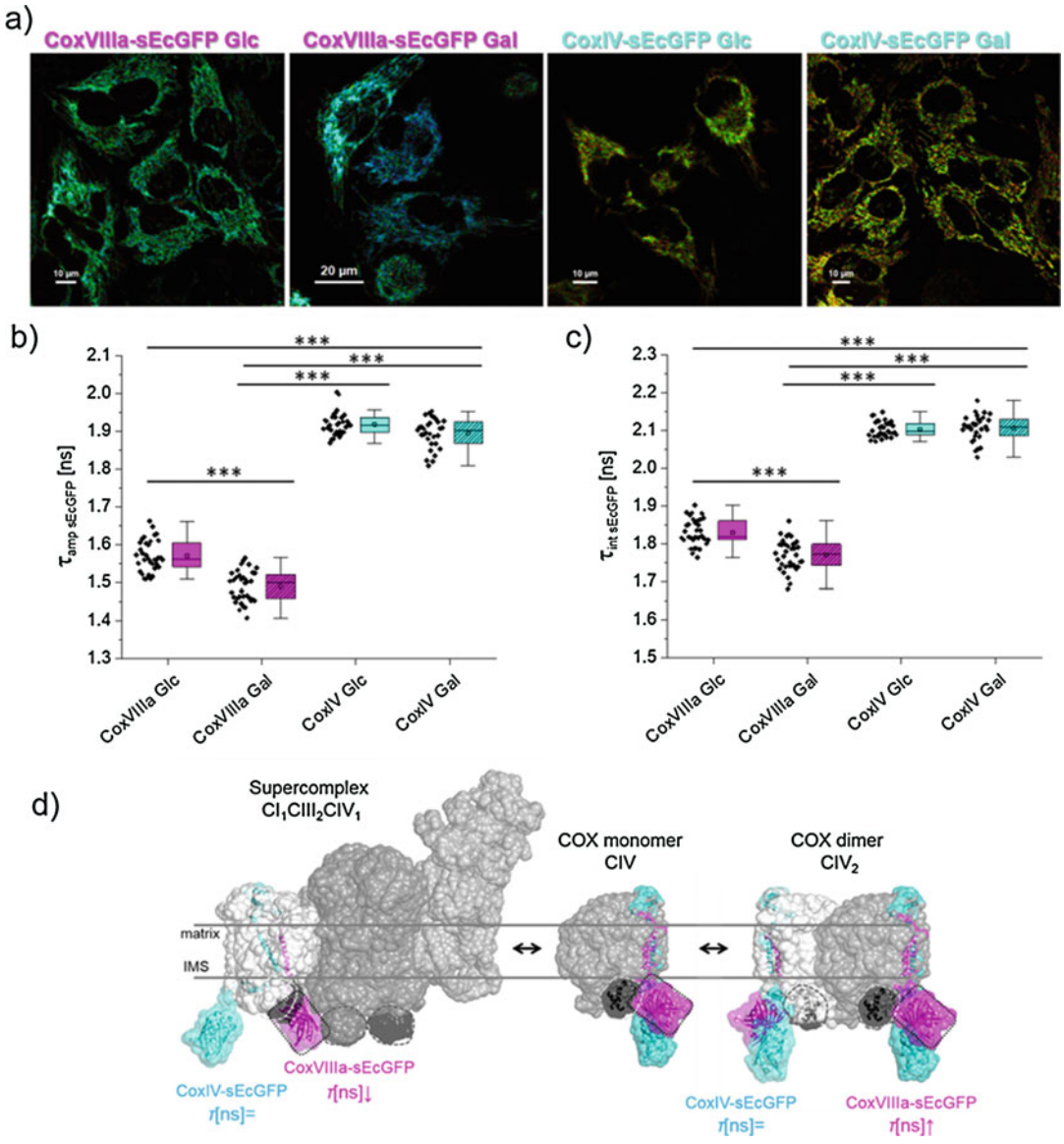


**Fig. 2** Decreased fluorescence lifetime of sEcGFP fused to CoxVIIIa in OXPHOS dependent cells. (**a**) Fluorescence lifetime images of CoxVIIIa-sEcGFP or CoxIV-sEcGFP, in cells supplied with 10 mM glucose or 10 mM galactose (stable CoxVIIIa-sEcGFP expressing HeLa cell lines). (**b**) Corresponding average fluorescence lifetimes $\tau_{amp}$. determined from time-correlated single photon counting (TCSPC) histograms. For the analysis, fluorescence lifetimes were calculated by fitting the fluorescence decay with a biexponential model. (**c**) Corresponding average fluorescence lifetimes $\tau_{int}$. (**d**) Positions of CoxVIIIa-sEcGFP and CoxIV-sEcGFP in the supercomplex (Dudkina et al., 2011) and in monomeric and dimeric CIV, respectively. CoxVIIIa-sEcGFP is exposed to a dense molecular environment in a supercomplex, especially under galactose conditions, and an aqueous environment in single CIV(2). In contrast, CoxIV-sEcGFP is always exposed to an aqueous environment. Data (mean values $\pm$ s.d.) in (**b**) and (**c**) was analyzed by One-Way ANOVA with post hoc Scheffe test ($***p < 0{:}001$; $**p < 0{:}01$; and $*p < 0{:}05$). $N = 2$–3 biological replicates. Scale bars: 10 µm or 20 µm, as indicated (**a**). FLIM is carried out with a TCS SP8 SMD confocal laser scanning microscope from Leica equipped with a 63x water objective (37 °C and 5% $CO_2$). (Adapted from [18] and [11])

## 2 Materials

### 2.1 Confocal Laser Scanning Microscopes

For microscopy, the cells are seeded on coverslips in 3 cm dishes (70% confluency) and maintained in medium containing glucose or galactose for 48 h. For imaging, the coverslips are mounted in a homemade cell chamber (alternatively, commercially available glas-bottom dishes with 8 chambers were used) and supplied with 1 mL of medium. Cells are imaged using an inverted confocal fluorescence microscope (TCS SP8 SMD, Leica) equipped with a 63× water Objective (N.A. 1.2) and a tunable white light laser (WLL). Live cells are microscoped at 37 °C supplied with 5% $CO_2$. The fluorescence lifetime of excited CoxVIIIa-sEcGFP or CoxIV-sEcGFP is recorded by Time-Correlated Single Photon Counting (TCSPC). HyD's with GaASP photocathodes are used as detectors for two-color imaging and FLIM (fluorescence lifetime imaging microscopy). sEcGFP is excited with a 488 nm pulsed (20 MHz) laser line from the tunable white light laser. For FLIM, emitted photons with a wavelength between 500 and 550 nm are recorded. The acquisition is performed until at least 1000 photons are reached in the brightest pixel. Data analysis is performed with SymphoTime™ software (64 bit, Picoquant). The instrumental response function (IRF) is calculated and the fluorescence lifetime histogram is fitted with a biexponential fit after subtracting the IRF. Only the fluorescence of the mitochondrial network of a cell is analyzed. Usually, from biexponential fits, the average lifetime $\tau_{amp}$ is calculated [18].

### 2.2 Chemicals

1. 0.1 M and 1 M HCl (Roth)
2. 0.1 M and 1 M NaOH (AppliChem)
3. 1 μM nigericin (Enzo Life, BML-CA421-0005)
4. 10 μM Carbonylcyanid-m-chlorphenylhydrazon (CCCP, Sigma, C-2759)
5. 10 μM Oligomycin (Millipore, 495455)

### 2.3 Plasmids

For eukaryotic expression of sEcGFP, the full-length protein-coding region of superecliptic pHluorin (F64L/S65T/S147D/N149Q/V163A/S175G/S202F/Q204T/A206T; a gift from Jürgen Klingauf, Münster) was inserted by PCR amplification into a modified pSEMS-26 m vector from NEB Biosciences (formerly Covalys Biosciences), substituting the original snap-ORF. The following fusion constructs, in which the respective subunits of the OXPHOS complexes are joined to the N terminus of sEcGFP, have been generated:

1. mt-sEcGFP. As targeting sequence, the mitochondrial targeting sequence of the mitochondrial processing peptidase

(MPP), was added to the 5′ end of the sEcGFP-encoding segment in the sEcGFP-vector [11].

2. For measurements in the intermembrane space, CoxVIIc-, CoxVIIIa-, CoxIV-, and CIIC-sEcGFP were assembled behind the CMV promoter and at the 5′ end of sEcGFP in the sEcGFP-vector [11].
3. To increase sensor distance to the membrane by C-terminal extension of CoxVIIIa, we used part of the C-terminal sequence of CoxVIIb (TCCCCTGTTG GCAGAGTTAC CC CAAAGGAA TGGAGGAATC AG) to insert a linker between CoxVIIIa and sEcGFP (resulting in CoxVIIIa-Link-sEcGFP) [11].

### 2.4 Cells

HeLa cells, a cervix cancer cell line, were purchased from the Leibniz Institute (DSMZ-German, Collection of Microorganisms and Cell Cultures).

### 2.5 Media and Buffers

1. Glucose growth medium: Minimal Essential Medium Eagle with Earle's salts and phenol red (Sigma, M2279), 10% fetal bovine serum (FBS) Supreme (PAN-Biotech, P30-3031), 1% (v/v) HEPES (4-(2-hydroxyethyl)piperazine-1-1ethanesulfonic acid (Sigma, H0887), 1% (v/v) nonessential amino acids NEA (Sigma, M7145).
2. Galactose growth medium: XF Base Medium Minimal DMEM (Agilent Seahorse XF, 102353–100), 10 mM D-galactose (Roth, 4985.1), 10% fetal bovine serum (FBS) Superior, 1% (v/v) HEPES (4-(2-hydroxyethyl)piperazine-1-1ethanesulfonic acid, 1% (v/v) nonessential amino acids NEA, 4% (v/v) alanyl-glutamine (Sigma, G8541), 2.2 g/L $NaHCO_3$ (Sigma, S8761).
3. Selective growth medium: Growth medium, 0.8 mg/mL G418 disulfate salt (Sigma, A1720-5G).
4. Calcium chloride for transfection: 2.5 M $CaCl_2$ (AppliChem, A3587.0500) solution.
5. HBS buffer (pH 7 ± 0.05) for transfection: 50 mM HEPES (Roth, HN77.4) , 280 mM NaCl (Roth, 3957.1), 1.5 mM $Na_2HPO_4$ (AppliChem, A3567.0500)
6. Washing buffer: PBS buffer (Sigma, D8537), pH 7.4 without $Ca^{2+}$ and $Mg^{2+}$.
7. Detaching buffer: 10% Trypsin–EDTA (PAN-Biotech, P10–024100), 1% HEPES, 1% $NaHCO_3$, 1% penicillin–streptomycin (Sigma, P0781).
8. Calibration buffers: 125 mM KCl (Serva, 26868), 20 mM NaCl (Roth, 3957.1), 0.5 mM $CaCl_2$ (AppliChem,

A3587.0500), 0.5 mM $MgSO_4$ (AppliChem, A1037.0500) in milliQ $H_2O$ with either 20 mM MES hydrate (Sigma, M2933-25G), 20 mM BES (Sigma, B4554-25G) or 20 mM HEPPSO (Sigma Aldrich, R426725-1G).

### 2.6 Software

1. SymphoTime® software (64 bit, PicoQuant).
2. ImageJ (MacBiophotonics).
3. OriginPro (OriginLab).

### 2.7 Specific Equipment

TC dishes 35, standard (Sarstedt, 83.3900) plus Precision cover slips, 24 mm (Roth, PK26.1) or rather µ-Slide 8 Well with ibiTreat (ibidi, 80826) for microscopy.

## 3 Methods

### 3.1 Cell Culture

#### 3.1.1 Cultivation

1. Cultivate HeLa cells in T25 cell culture flasks, with 5 mL growth medium at 37 °C and 5% $CO_2$.
2. Passage cells when they reach confluency.

#### 3.1.2 Passaging

1. Aspirate the old medium from confluent cells grown in T25 flasks.
2. Wash the cells with 4 mL washing buffer.
3. Aspirate the washing buffer.
4. Add 1 mL detaching medium to detach cells from the flask surface.
5. Incubate the flask at 37 °C and 5% $CO_2$ until the cells are removed from the bottom (2–5 min).
6. Stop the reaction when all cells are detached by adding 4 mL fresh growth medium.
7. Pipet several times up and down to homogenize the cell solution.
8. Transfer 1 mL to a new T 25 flask and fill up to 5 mL with fresh growth medium.

#### 3.1.3 Cell Transfection

For transfection with the fusion constructs, the calcium phosphate method is used [19].

1. Seed $5 \times 10^3$ to $1 \times 10^4$ cells into a 60 mm Cellstar® tissue culture dish and 4 mL growth medium. Transfect when the cells reach 60–80% confluency (approx. after 8–24 h).
2. Pipet 10 µL plasmid solution, containing 10 µg pure DNA in an Eppendorf tube.
3. Add 50 µL $CaCl_2$ solution (2.5 M).
4. Mix by carefully pipetting up and down once.

5. Wait for 30 s.
6. Add 440 µL milliQ $H_2O$.
7. Pipet 500 µL HBS buffer (pH 7 ± 0.05) in another Eppendorf tube.
8. Vortex the HBS Buffer in the Eppendorf tube.
9. Add the 500 µL buffered DNA–$CaCl_2$ solution by dropping it into the HBS Buffer during vortexing.
10. Replace the growth medium of the HeLa cells in the 60 mm Cellstar® tissue culture dishes with 4 mL fresh growth medium.
11. Pipet the DNA solution in single drops into the 60 mm Cellstar® tissue culture dishes filled with the fresh medium. Increase the height of pipetting to avoid "dancing" of drops onto the medium surface, which can lead to inhomogeneous DNA concentration in the sample.
12. Incubate the transfected HeLa cells at 37 °C and 5% $CO_2$ overnight.
13. After 8–18 h, wash twice with 4 mL washing buffer and add 4 mL fresh growth medium.
14. Let the cells grow for several hours after replacing the growth medium.
15. Passage the cells into several µ-Slide 8 Well with ibiTreat. Therefore, wash the cells with 4 mL washing buffer (PBS), aspirate the PBS and add 1 mL detaching medium. Incubate the flask at 37 °C and 5% $CO_2$ until the cells are removed from the bottom. Stop the reaction when all cells are detached by adding 3 mL fresh growth medium. Pipet several times up and down to homogenize the cell solution. Transfer 15,000–30,000 cells per well into the µ-Slide 8 Well. Total well volume with fresh medium should be 200 µL.
16. In order to have good expression levels of your protein of interest, image the transfected cells 36–72 h after transfection.
17. At day of imaging:
    (a) Wash each well with 200 µL washing buffer.
    (b) Add 200 µL fresh growth medium per well.
    (c) Keep the cells at 37 °C and 5% $CO_2$ until imaging.

### *3.1.4 Generation of Stable Transfected Cell Lines*

For generation of a stable cell line, the transfected plasmid has to be integrated into the cell genome of the target cell. The advantage is a stable, long-term expression of the protein of interest with mostly homogeneous (*see* **Note 6**) and moderate expression levels.

1. Seed, transfect, wash, and detach cells as described under Subheading 3.1.3.

2. Split cells into 3 60 mm Cellstar® tissue culture dishes, fill up to 4 mL with fresh growth medium.
3. After 24 h, replace growth medium in each dish with 4 mL selective growth medium.
4. During a period of 10–14 days, change selective growth medium every 2–3 days.
5. Colonies (visible by eye) which grow in the selective medium are from stable transfected cells and can be isolated as follows.
6. Incubate cells with detaching buffer until cells round and start to detach.
7. Pick colonies with 200 µL pipette (absorbing 50 µL should be enough) and transfer into a 96-well cell culture plate, where 150 µL selective growth medium has been added before (one colony per well). Incubate at 37 °C and 5% $CO_2$ and change selective growth medium every 2–3 days.
8. When cells are confluent, passage them into a 24-well cell culture plate. Change selective growth medium every 2–3 days.
9. When cells are confluent, passage them into a T25 flask. Change selective growth medium every 2–3 days.
10. Continue proliferation in selective growth medium in the T25 flask until confluency is reached, then passage and freeze leftovers.

### 3.2 Preparation of Stable Transfected Cells for Imaging

1. Passage the cells in T25 flasks as described in Subheading 3.1.2. and seed into µ-Slide 8 Well with ibiTreat. Transfer 30,000 cells per well for imaging the next day or 15,000 cells per well for imaging after two days into the µ-Slide 8 Well. Total well volume with fresh medium should be 200 µL.
2. At day of imaging:
   (a) Wash each well with 200 µL washing buffer.
   (b) Add 200 µL fresh growth medium per well.
   (c) Keep the cells at 37 °C and 5% $CO_2$ until imaging.

### 3.3 Fluorescence Lifetime Imaging

1. Start temperature control (37 °C).
2. Switch on the microscope, the computer(s)/monitor(s), the scanner, the laser(s), and the Time Tagger and Time-Correlated Single Photon Counting (TCSPC) system including for example the HydraHarp 400.
3. Start the microscope software.
4. Start the SymphoTime® 64 software (*see* **Note 7**) and generate a new workspace. Make sure that the correct data channel and an appropriate TCSPC resolution is selected.

5. An internal GaASP photocathode is used as detector for FLIM => Start its cooling system to decrease background.
6. Clean the objective with a KIMTECH Science Precision Wipe.
7. Place a small droplet of water (or immersion oil if an oil objective is used) on the pupil of the water-objective.
8. Mount the μ-Slide 8 Well. Be sure that two clips are positioned at the edges of the slide.
9. Start the $CO_2$ supply (set to 5%).
10. Preadjust the objective position/the focal plane.
11. Start the fluorescence mercury lamp (select a very low intensity, if possible) and select the GFP filter cube. Open the shutter and search for cells with fluorescent signals (*see* **Note 8**). After focusing, close the shutter again.
12. Turn the safety interlock key to On-1. Switch from TCS SP8 to FLIM=> Setup Imaging. Start imaging the cells with GFP settings (WLL ex. 488 nm, em. 500–550 nm). Use sufficient laser intensity, an appropriate zoom and adjust the z position to get the mitochondria focused.
13. Switch from Setup *Imaging* to Setup *FLIM*. Choose a format of 256 × 256 pixel and a scan speed of 100 Hz (scan direction X: Unidirectional). Operate the white light laser (Output power = 70%) at 20 MHz and restrict emission of the internal GAsP detector to 525/50 nm. Default pinhole setting (1 Airy disk) and default acquisition mode xyz is used.
14. Setup FLIM: Run FLIM Test and adjust the laser power to avoid oversaturation.
15. Measurements: Start recording by clicking on Run FLIM.
16. Perform the acquisition until at least 1000 photons in the brightest pixel is reached (can be selected in Measurements/Acquisition).
17. Give a name to the generated FLIM image. This can be done after slowly clicking twice on the file.

### 3.4 FLIM Evaluation

1. Double click on the File ending with _OFLIM.pqres in the SymphoTime software. The software opens the FLIM/intensity image, the Lifetime histogram and the time correlated single photon counting (TCSPC) histogram (Fig. 3).
2. Adjust the lifetime pseudo color scale if you like.
3. Choose free ROI or paint ROI to select one cell in the image by holding down the left mouse button while defining the ROI.
4. Select N-Exponential Reconvolution as fitting model and choose ROI as decay option to fit the complete fluorescence lifetime decay of the ROI (*see* **Note 9**). This will subtract the

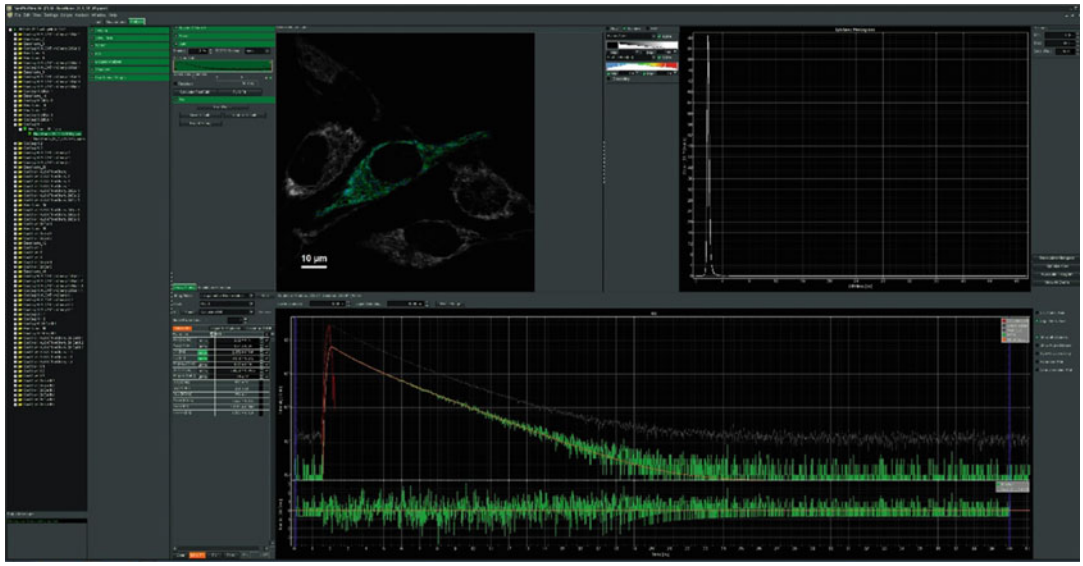


**Fig. 3** FLIM evaluation with biexponential fit of the fluorescence decay curve

IRF = instrument response function (*see* **Note 10**). Perform a biexponential fit of the fluorescence decay curve (Model Parameters: $n = 2$). The fitted curve should overlay well with the decay curve, resulting in a chi-squared test value approaching 1 and residuals that are randomly spread around 0 (*see* **Note 11**).

5. Click on initial fit. Besides the lifetimes of the two lifetime components and their amplitudes, the software also calculates the average lifetimes $\tau_{int}$ (equals the average time that the fluorophore remains in the excited state) and $\tau_{amp}$ (proportional to the steady state intensity), which you can export (*see* **Note 12**).

## 4 Notes

1. Correct localization of mitochondria-targeted fusion constructs can be checked by costaining mitochondria with MitoTracker™ Red FM.
2. In addition to SC-FLIM, you can determine the local pH when you use sEcGFP as a sensor by performing ratio imaging [13].
3. You can perform SC-FLIM also with other fluorescent proteins. We have tried and would like to recommend Clover and mCitrine [11]. If possible, use sensors with a monoexponential decay.
4. Check possible negative side effects on bioenergetic performance by performing for example a mitochondrial stress test in an Extracellular flux analyzer (Agilent/Seahorse).

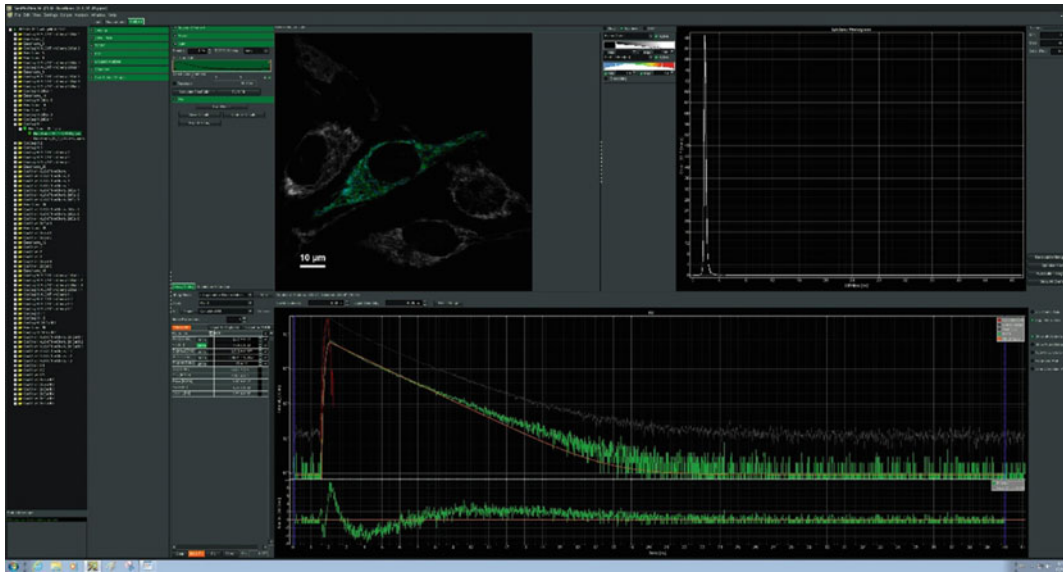


**Fig. 4** FLIM evaluation with monoexponential fit of the fluorescence decay curve

Alternatively, you could check the mitochondrial membrane potential via specific fluorescent dyes or perform clear native electrophoresis for in-gel catalytic activity assays of mitochondrial complexes I–V.

5. Perform a Western Blot following blue or clear native electrophoresis as additional experiment to show that your sensor-tagged subunit is still used as building block for the respiratory complex.
6. Stable transfected cells show more homogeneous protein expression levels and are easier to handle than transiently transfected cells. Check if the fluorescence lifetimes of transient transfected cells differ from that of stable cell lines.
7. When starting the SymphoTime® software, you might also have to adjust the offset of the synchronization signal and GAsP detector channel manually, so that the entire TCSPC histogram is displayed properly (as shown).
8. For imaging, better select ROIs with equally bright cells to get a similar number of the photon counts in all of them.
9. Using a pulsed white light laser (WLL) for FLIM can result in a small extra peak at the end of your histogram. Make sure that you exclude this peak from your fit by setting the boundary for the longe time before this peak.
10. You can use the calculated IRF or import an IRF measured by yourself, for example by using Erythrosin B as a fluorescent dye. This might be necessary when your fluorescence contains components with extremely fast decay (short lifetimes).

11. You can try to perform a monoexponential fit of the fluorescence decay curve (Model Parameters: $n = 1$). When the chi-squared test and the residuals look like in Fig. 4, then it is not an appropriate fitting model. For an appropriate fit, the residuals trace should not show any trends.
12. Principally, $\tau_{amp}$ is rather used for FLIM-FRET.

## References


1. Wittig I, Carrozzo R, Santorelli FM, Schagger H (2006) Supercomplexes and subcomplexes of mitochondrial oxidative phosphorylation. Biochim Biophys Acta 1757:1066–1072
2. Dudkina NV, Heinemeyer J, Sunderhaus S, Boekema EJ, Braun HP (2006) Respiratory chain supercomplexes in the plant mitochondrial membrane. Trends Plant Sci 11:232–240
3. Mitchell P (2011) Chemiosmotic coupling in oxidative and photosynthetic phosphorylation. 1966. Biochim Biophys Acta 1807:1507–1538
4. Lenaz G (1988) Role of mobility of redox components in the inner mitochondrial membrane. J Membr Biol 104:193–209
5. Acin-Perez R, Fernandez-Silva P, Peleato ML, Perez-Martos A, Enriquez JA (2008) Respiratory active mitochondrial supercomplexes. Mol Cell 32:529–539
6. Guo R, Zong S, Wu M, Gu J, Yang M (2017) Architecture of human mitochondrial respiratory Megacomplex I2III2IV2. Cell 170 (1247–1257):e1212
7. Letts JA, Fiedorczuk K, Sazanov LA (2016) The architecture of respiratory supercomplexes. Nature 537:644–648
8. Althoff T, Mills DJ, Popot JL, Kuhlbrandt W (2011) Arrangement of electron transport chain components in bovine mitochondrial supercomplex I1III2IV1. EMBO J 30:4652–4664
9. Dudkina NV, Kudryashev M, Stahlberg H, Boekema EJ (2011) Interaction of complexes I, III, and IV within the bovine respirasome by single particle cryoelectron tomography. Proc Natl Acad Sci U S A 108:15196–15200
10. Shinzawa-Itoh K, Shimomura H, Yanagisawa S, Shimada S, Takahashi R, Oosaki M, Ogura T, Tsukihara T (2016) Purification of active respiratory Supercomplex from bovine heart mitochondria enables functional studies. J Biol Chem 291:4178–4184
11. Rieger B, Shalaeva DN, Sohnel AC, Kohl W, Duwe P, Mulkidjanian AY, Busch KB (2017) Lifetime imaging of GFP at CoxVIIIa reports respiratory supercomplex assembly in live cells. Sci Rep 7:46055
12. Sohnel AC, Kohl W, Gregor I, Enderlein J, Rieger B, Busch KB (2016) Probing of protein localization and shuttling in mitochondrial microcompartments by FLIM with sub-diffraction resolution. Biochim Biophys Acta 1857:1290–1299
13. Rieger B, Junge W, Busch KB (2014) Lateral pH gradient between OXPHOS complex IV and F(0)F(1) ATP-synthase in folded mitochondrial membranes. Nat Commun 5:3103
14. Warburg O (1956) On respiratory impairment in cancer cells. Science 124:269–270
15. Rossignol R, Gilkerson R, Aggeler R, Yamagata K, Remington SJ, Capaldi RA (2004) Energy substrate modulates mitochondrial structure and oxidative capacity in cancer cells. Cancer Res 64:985–993
16. Balsa E, Soustek MS, Thomas A, Cogliati S, Garcia-Poyatos C, Martin-Garcia E, Jedrychowski M, Gygi SP, Enriquez JA, Puigserver P (2019) ER and nutrient stress promote assembly of respiratory chain supercomplexes through the PERK-eIF2alpha axis. Mol Cell 74:877–890.e876
17. Lyamzaev KG, Panteleeva AA, Karpukhina AA, Galkin II, Popova EN, Pletjushkina OY, Rieger B, Busch KB, Mulkidjanian AY, Chernyak BV (2019) Novel fluorescent mitochondria-targeted probe MitoCLox reports lipid peroxidation in response to oxidative stress in vivo. Oxidative Med Cellular Longevity 2020:3631272
18. Rieger B, Krajčová A, Duwe P, Busch KB (2019) ALCAT1 overexpression affects supercomplex formation and increases ROS in respiring mitochondria. Oxidative Med Cellular Longevity 2019:9186469
19. Graham FL, van der Eb AJ (1973) A new technique for the assay of infectivity of human adenovirus 5 DNA. Virology 52:456–467

# Chapter 20

# Identification of Peroxynitrite by Profiling Oxidation and Nitration Products from Mitochondria-Targeted Arylboronic Acid

**Jacek Zielonka, Adam Sikora, Radoslaw Podsiadly, Micael Hardy, and B. Kalyanaraman**

## Abstract

The development of boronic probes enabled reliable detection and quantitative analysis of hydrogen peroxide, other nucleophilic hydroperoxides, hypochlorite, and peroxynitrite. The major product, in which boronate moiety of the probe is replaced by the hydroxyl group, is, however, common for all those oxidants. Here, we describe how *ortho*-isomer of mitochondria-targeted phenylboronic acid can be used to detect and differentiate peroxynitrite-dependent and independent probe oxidation. This method highlights detection and quantification of both the major, phenolic product and the minor, peroxynitrite-specific cyclic and nitrated products of probe oxidation.

**Key words** Hydrogen peroxide, Peroxynitrite, Mitochondria-targeted probes, Boronic probes, *o*-MitoPhB$(OH)_2$, HPLC-MS

## 1 Introduction

Boronate-based probes were developed over the last decade for detection of hydrogen peroxide ($H_2O_2$) and peroxynitrite ($ONOO^-$) in biological systems [1–3]. Mitochondria-targeted boronate probes were developed to monitor hydrogen peroxide in mitochondria [4–8]. Boronates react directly and stoichiometrically with both $H_2O_2$ and $ONOO^-$ [9, 10]. This is in contrast to more classical fluorogenic probes (e.g., dichlorodihydrofluorescein, DCFH and dihydrorhodamine, DHR), which need the catalyst (e.g., iron, heme proteins) or react with the products of $ONOO^-$ decomposition [11–13]. Additionally, in contrast to boronates, both DCFH and DHR form intermediate radical species that reduce oxygen to superoxide radical anion [11, 14]. However, most boronates lack specificity needed to distinguish between

Volkmar Weissig and Marvin Edeas (eds.), *Mitochondrial Medicine: Volume 1: Targeting Mitochondria*, Methods in Molecular Biology, vol. 2275, https://doi.org/10.1007/978-1-0716-1262-0_20,

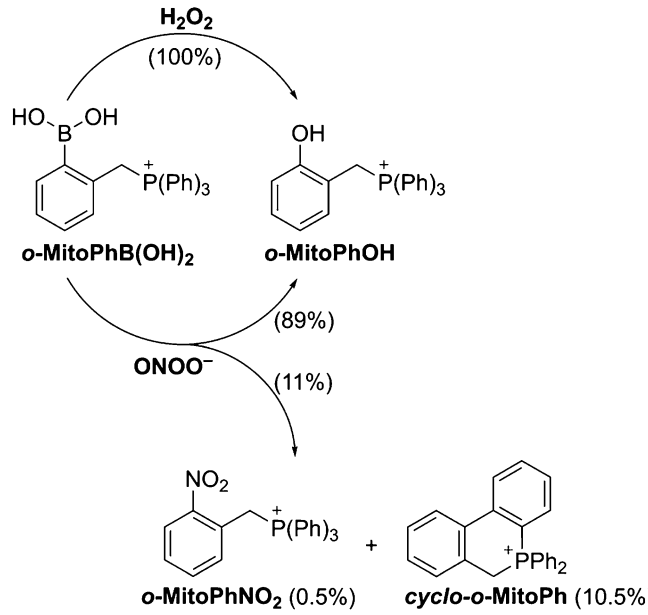


**Fig. 1** Scheme of oxidation of *o*-MitoPhB(OH)$_2$. *o*-MitoPhB(OH)$_2$ is oxidized to *o*-MitoPhOH by both $ONOO^-$ and $H_2O_2$. However, *cyclo*-*o*-MitoPh and *o*-MitoPhNO$_2$ are formed only in reaction between *o*-MitoPhB(OH)$_2$ and $ONOO^-$ as the minor products, with the yields of 10.5% and 0.5%, respectively [21]

hydrogen peroxide, other nucleophilic hydroperoxides and peroxynitrite in a complex biological system, as discussed below [2, 9, 15–17]. In a simple system when bolus amounts of the reactants are quickly mixed this limitation can be overcome due to significant differences of the reaction rate constants. The rate constant of the reaction of boronates with peroxynitrite is six orders of magnitude higher than of the analogous reaction with hydrogen peroxide [2, 9]. For example, under the conditions when the reaction with $ONOO^-$ is completed within 100 ms, the reaction with $H_2O_2$ was not completed even after 12 h [9]. The situation is, however, different when the oxidants react with the probe in biological systems, with the oxidants continuously produced during the incubation with the probe. Therefore, we proposed the use of specific inhibitors of oxidants formation and/or specific scavengers of the oxidants to differentiate between different species responsible for oxidation of boronate probes in cells [2, 18]. We have previously reported a formation of both major, phenolic product (*o*-MitoPhOH) and minor, nitrated product (*o*-MitoPhNO$_2$) during the reaction of peroxynitrite with *ortho*-isomer of mitochondria-targeted phenylboronic acid (*o*-MitoPhB(OH)$_2$, Fig. 1) [19, 20]. More recently, we have identified an additional, more abundant minor product, *cyclo*-*o*-MitoPh (Fig. 1) [21, 22]. These minor products are specific for $ONOO^-$ reaction and are not produced by any other oxidant. Therefore the proposed method provides also an opportunity to distinguish between two

biological nitrating pathways: peroxynitrite-dependent and myeloperoxidase/hydrogen peroxide/nitrite-dependent [21]. Here, we show how this unique chemistry can be utilized to selectively detect peroxynitrite in cellular systems [23, 24]. The method is based on probing the oxidants ($ONOO^-$ and $H_2O_2$) in cells by incubation of cells with *o*-MitoPhB$(OH)_2$ followed by extraction and HPLC-MS/MS analysis of the products formed [21, 25]. We describe the protocol for probe preparation, processing of biological samples, and HPLC-MS-based analysis of the products formed.

## 2 Materials

### 2.1 Components for the Synthesis of o-MitoPhB$(OH)_2$

1. 2 g of triphenylphosphine.
2. 200 ml of anhydrous diethyl ether.
3. 1 g of 2-(bromomethyl)phenylboronic acid.
4. 100 ml of dichloromethane
5. Argon gas.

### 2.2 Cell Incubation Components

1. Cell growth medium (for RAW 264.7 cells): DMEM containing 10% FBS, 100 U/ml penicillin, and 0.1 mg/ml streptomycin).
2. Assay medium: DPBS supplemented with 5.5 mM glucose and 0.33 mM pyruvate (*see* **Note 1**).
3. Solution of 50 mM *o*-MitoPhB$(OH)_2$ (for description of synthesis *see* Subheading 3.1) in DMSO.

### 2.3 Cell Extraction Components

1. Cell lysis buffer: 10 ml DPBS containing 0.1% Triton X-100 spiked with 1 μM mixture of internal standards, place on ice (can be stored at 4 °C) (*see* **Note 2**).
2. 100 ml of ice-cold acetonitrile containing 0.1% (v/v) formic acid.
3. 10 ml of ice-cold acetonitrile containing 0.1% (v/v) formic acid and 1 μM mixture of internal standards, place on ice (can be stored for a short term at 4 °C).
4. Protein assay reagent (Bradford reagent).
5. BSA in lysis buffer: 20 mg/ml BSA. Prepare a series of BSA solutions by serial dilutions with the final concentrations of 0.5, 1.0, 1.5, 2, 3, 4, 5, 7, and 10 mg/ml. Keep the solutions on ice.

### 2.4 HPLC Analysis Components

1. HPLC mobile phase: 0.1% formic acid in water (mobile phase A) and 0.1% formic acid in acetonitrile (mobile phase B) (*see* **Note 3**).
2. Solution of *o*-MitoPh$NO_2$ (50 mM) in DMSO (*see* **Note 4**).

3. Solution of *o*-MitoPhB$(OH)_2$ (50 mM) in DMSO.
4. Solution of *o*-MitoPhOH (50 mM) in DMSO (*see* **Note 4**).
5. Solution of *cyclo-o*-MitoPh (50 mM) in DMSO (*see* **Note 5**).
6. Water–acetonitrile (3:1) mixture containing 0.1% (v/v) formic acid, spiked with 1 μM mixture of the internal standards. This will be a solvent for preparation of standards for HPLC calibration.
7. Mixture of the standards of *o*-MitoPhB$(OH)_2$, *o*-MitoPhOH, and *o*-MitoPh$NO_2$ and *cyclo-o*-MitoPh (0.1 mM each) in water–acetonitrile (3:1) solvent containing 0.1% formic acid spiked with 1 μM mixture of the internal standards. Prepare serial dilutions down to 1 nM concentration. Use the solvent for standards prepared in the previous step.

## 3 Methods

### 3.1 Preparation of o-MitoPhB$(OH)_2$

1. The preparation of the o-MitoPhB$(OH)_2$ probe should be carried out inside a hood with well-working ventilation!
2. Prepare a solution of triphenylphosphine (1.048 g, 4.0 mmol) in anhydrous diethyl ether (30 ml).
3. Add 2-(bromomethyl)phenylboronic acid (0.856 g, 4.0 mmol) with constant stirring under argon atmosphere.
4. Stir the reaction mixture for 46 h (using magnetic stirrer) at room temperature under argon atmosphere.
5. A crystalline precipitate of bromide salt of o-MitoPhB$(OH)_2$ should be obtained.
6. Filter the suspension. Keep the solid and discard the filtrate.
7. Wash the solid with anhydrous diethyl ether (30 ml). Filter the suspension again and keep the solid.
8. Dissolve the solid in dichloromethane (in a minimum volume, <5 ml) and precipitate the compound back by addition of diethyl ether (1:10). Filter the powder and keep the solid. Repeat this step once more.
9. Leave the solid to dry. A white powder should be obtained with the melting point of 225–226 °C. Test the identity and purity of the synthesized probe (*see* **Note 6**).

### 3.2 Cell Incubation with the Probe

1. Prepare the cells according to the experimental conditions to be tested for peroxynitrite formation (*see* **Note 1**).
2. Add *o*-MitoPhB$(OH)_2$ to obtain the final concentration of 50 μM (*see* **Notes 7** and **8**).
3. Incubate the cells for 1 h.

4. Collect an aliquot of the medium (0.1 ml) in 1.5 ml microcentrifuge tube and freeze in liquid nitrogen.
5. Remove the rest of medium and wash the cells twice with ice-cold DPBS.
6. Add 1 ml of ice-cold DPBS and harvest the cells, place the cell suspension in 1.5 ml microcentrifuge tube and spin down the cells by quick centrifugation. Remove the supernatant and freeze the cell pellet in liquid nitrogen.
7. Frozen cell pellets and media can be stored at −80 °C for at least 1 week before analysis.

### 3.3 Extraction of the Products

#### 3.3.1 Cell Pellets

1. Preload one set of 1.5 ml microcentrifuge tubes with 0.1 ml of 0.1% formic acid in acetonitrile and place on ice.
2. Preload a second set of 1.5 ml microcentrifuge tubes with 0.1 ml of 0.1% formic acid in water and place on ice.
3. Prepare a clear-bottom 96-well plate for protein assay and place on ice.
4. Place the tubes with frozen cell pellets on ice.
5. Add 0.2 ml of the lysis buffer spiked with a mix of internal standards (1 μM each) and lyse the cells by 10 syringe strokes using a 0.5 ml insulin syringe with the needle 28 Gauge × 0.5 in. (0.36 mm × 13 mm).
6. Transfer 0.1 ml of the cell lysates into the tubes containing ice-cold 0.1% formic acid in acetonitrile, vortex for 10 s, and place on ice. Transfer 3 × 2 μl of the cell lysate aliquots into 3 wells on 96-well plate for the protein assay.
7. Incubate the mixtures of cell lysates with acetonitrile for 30 min on ice.
8. During incubation measure the protein concentration in the cell lysates using Bradford assay and plate reader with absorption detection (*see* **Note 9**).
9. Vortex the tubes again for 5 s and centrifuge for 30 min at 20,000 × *g* at 4 °C.
10. Place the tubes back on ice and transfer 0.1 ml aliquots of the supernatants into the second set of tubes, containing 0.1% formic acid in water.
11. Vortex the tubes for 5 s and centrifuge for 15 min at 20,000 × *g* at 4 °C.
12. Transfer 0.15 ml of the supernatants into HPLC vials preloaded with conical inserts, seal the vials and place on ice. Once all solutions have been transferred, place the vials in HPLC autosampler precooled to 4 °C.

#### 3.3.2 Media

1. Preload one set of 1.5 ml microcentrifuge tubes with 0.1 ml of 0.1% formic acid in water and place on ice.
2. Place the tubes with frozen media on ice.
3. Add 0.1 ml of the ice-cold 0.1% formic acid in acetonitrile spiked with internal standards (1 μM each) to each tube, vortex for 10 s, and place on ice.
4. Incubate the mixtures of media with acetonitrile for 30 min on ice.
5. Vortex the tubes again for 5 s and centrifuge for 30 min at 20,000 × *g* at 4 °C.
6. Place the tubes back on ice and transfer 0.1 ml aliquots of the supernatants into the tubes containing 0.1% formic acid in water.
7. Vortex the tubes for 5 s and centrifuge for 15 min at 20,000 × *g* at 4 °C.
8. Transfer 0.15 ml of the supernatants into HPLC vials preloaded with conical inserts, seal the vials and place on ice. Once all solutions have been transferred, place the vials in HPLC autosampler precooled to 4 °C.

### 3.4 HPLC-MS/MS Analysis of the Extracts

1. Install the column Kinetex Phenyl-Hexyl 50 mm × 2.1 mm, 1.7 μm (Phenomenex) in the HPLC-MS/MS system. The column should be equipped with a UHPLC column filter or guard column to extend the column lifetime.
2. Equilibrate the column with the mobile phase (75% of mobile phase A and 25% mobile phase B).
3. Setup the HPLC-MS/MS method and detection parameters according to Tables 1 and 2, respectively (*see* **Note 10**).
4. Test the system by three injections of standards (10 μM) for the reproducibility of retention times and peak intensities for all analytes and internal standards, as shown in Fig. 2.
5. Run the analysis of the batch of samples.
6. Include the system and column wash with water–methanol (1:1) mixture at the end of batch.
7. Quantify each analyte based on the specific MRM transitions and calibration curves constructed in the concentration range relevant to the samples analyzed (*see* **Note 11**).
8. When appropriate, normalize the concentrations of analytes to the protein levels in cell lysates, as determined by Bradford method.
9. Increase in peak intensities of both *o*-MitoPhOH, *cyclo*-*o*-MitoPh, and *o*-MitoPh$NO_2$ (Fig. 3) indicates formation of $ONOO^-$, while formation of *o*-MitoPhOH, but not *o*-MitoPh$NO_2$ (Fig. 4) indicates the presence of other oxidants, most commonly $H_2O_2$ (*see* **Note 12**).

**Table 1**
**HPLC method parameters**

| | | | |
|---|---|---|---|
| Flow rate | 0.5 ml/min | | |
| Gradient | 0 min | 75% A | 25% B |
| | 2 min | 68.3% A | 31.7% B |
| | 4 min | 0% A | 100% B |
| | 4.5 min | 0% A | 100% B |
| | 5 min | 75% A | 25% B |
| Diverter valve | 0 min | Waste | |
| | 1.0 min | Detector | |
| | 4.0 min | Waste | |

**Table 2**
**MS/MS detection parameters**

| Analyte | Dominant MRM transition | Reference MRM transition | Reference MRM to dominant MRM intensities ratio | Retention time (min) |
|---|---|---|---|---|
| *o*-MitoPhB $(OH)_2$ | 397.00 > 135.00 | 397.00 > 379.05 | 0.8 | 1.61 |
| *o*-MitoPhB $(OH)_2$-$d_{15}$ | 412.20 > 117.10 | 412.20 > 135.10 | 0.55 | 1.57 |
| *o*-MitoPhOH | 369.00 > 107.10 | 369.00 > 183.05 | 0.4 | 1.95 |
| *o*-MitoPhOH-$d_{15}$ | 384.10 > 278.10 | 384.10 > 107.10 | 1.0 | 1.90 |
| *o*-MitoPhNO$_2$ | 397.90 > 262.05 | 397.90 > 351.10 | 0.25 | 2.13 |
| *o*-MitoPhNO$_2$-$d_{15}$ | 413.10 > 277.15 | 413.10 > 113.00 | 0.85 | 2.08 |
| *Cyclo-o*-MitoPh | 351.10 > 183.05 | 351.10 > 165.05 | 0.7 | 2.15 |
| *o*-MitoPhCH$_3$ | 367.00 > 105.05 | 367.00 > 79.05 | 0.1 | 2.78 |

## 4 Notes

1. The medium used may be selected according to experimental design, and cell culture needs. However, it is preferred that when monitoring extracellular $ONOO^-$ and/or $H_2O_2$, the components of the medium capable of scavenging those oxidants should be avoided, if possible. For example, pyruvate in the medium may efficiently compete with boronate probes for $H_2O_2$.

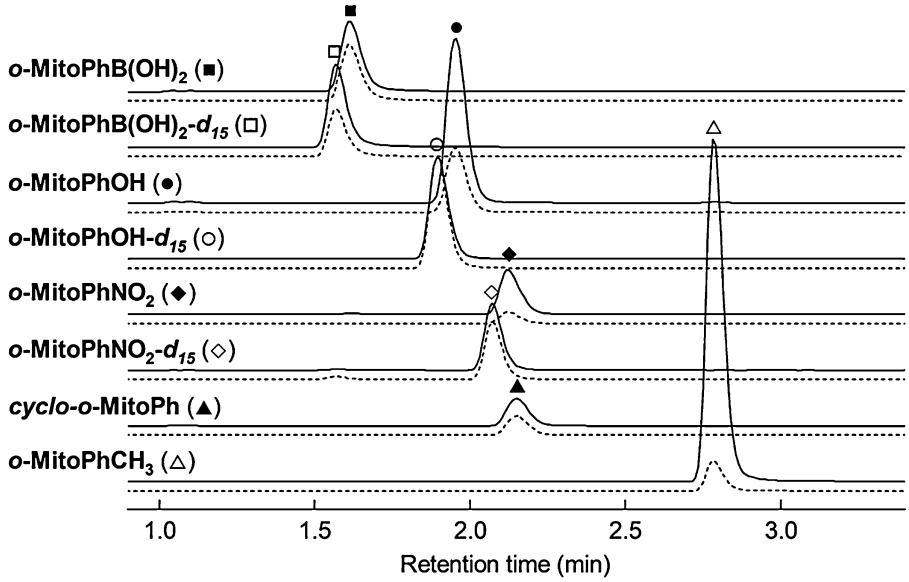


**Fig. 2** HPLC-MS/MS detection of *o*-MitoPhB(OH)$_2$, *o*-MitoPhOH, *cyclo*-*o*-MitoPh, and *o*-MitoPhNO$_2$. The chromatograms have been obtained with the described method by injection of 20 μl of the mixture of *o*-MitoPhB(OH)$_2$, *o*-MitoPhOH, *cyclo*-*o*-MitoPh, and *o*-MitoPhNO$_2$ (solid symbols) and corresponding internal standards (open symbols) (1 μM each). For each compound two MRM transitions are shown: dominant (solid lines) and reference (dashed lines). HPLC-MS/MS traces were recorded using the parameters shown in Table 2. The traces have not been scaled and thus represent the actual intensities of each MRM transition in the equimolar mixture

2. Internal standards for *o*-MitoPhB(OH)$_2$, *o*-MitoPhOH, and *o*-MitoPhNO$_2$ are their isotopologs containing deuterated triphenylphosphonium moiety (Fig. 2). These are not commercially available but can be synthesized in analogous ways as *o*-MitoPhB(OH)$_2$, *o*-MitoPhOH, and *o*-MitoPhNO$_2$, (*see* **Note 4**, for description of synthesis of *o*-MitoPhB(OH)$_2$ *see* Subheading 3.1), but starting with commercially available triphenylphosphine-$d_{15}$. As *cyclo*-*o*-MitoPh is not synthesized from triphenylphosphine, we do not have deuterated isotopolog for use as an internal standard. Instead, we use (2-methylbenzyl) triphenylphosphonium (*o*-MitoPhCH$_3$) as an internal standard for *cyclo*-*o*-MitoPh (Fig. 2).
3. LC-MS (preferably UHPLC-MS) grade solvents and formic acid should be used. After preparation, mobile phase should be passed through a 0.2 μm filter. Prepare only the amount of mobile phase, which is necessary for the experiment. Do not store the mobile phase for longer than 2–3 days to avoid any growth of the biological matter.
4. The standards of the products *o*-MitoPhOH and *o*-MitoPhNO$_2$ are commercially available, but can be also synthesized. The phenolic product can be prepared by allowing

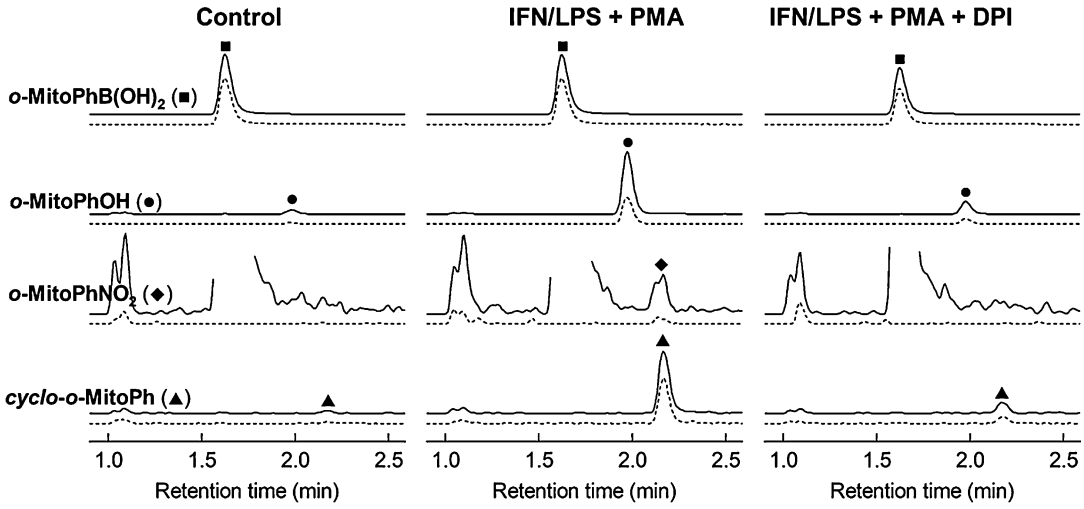


**Fig. 3** HPLC-MS/MS analysis of the extracts of RAW 264.7 macrophages activated to produce peroxynitrite. To produce peroxynitrite RAW 264.7 cells were pretreated overnight with interferon γ (IFN, 50 U/ml) and lipopolysaccharide (LPS, 1 μg/ml) followed by addition of PMA (1 μM) in the presence or absence of diphenyleneiodonium (DPI, 1 μM). During stimulation with PMA, *o*-MitoPhB(OH)$_2$ (50 μM) was present and incubated for 1 h. Cell pellets were collected and processed as described in the protocol. The intensities of *o*-MitoPhOH were multiplied by a factor of 10 and intensities of *cyclo-o*-MitoPh and *o*-MitoPhNO$_2$ were multiplied by 200 and 2000, respectively, to fit the same scale as of *o*-MitoPhB(OH)$_2$. Solid lines represent the dominant transitions used for quantification and the dashed lines represent the reference transitions used for confirmation of peak identity

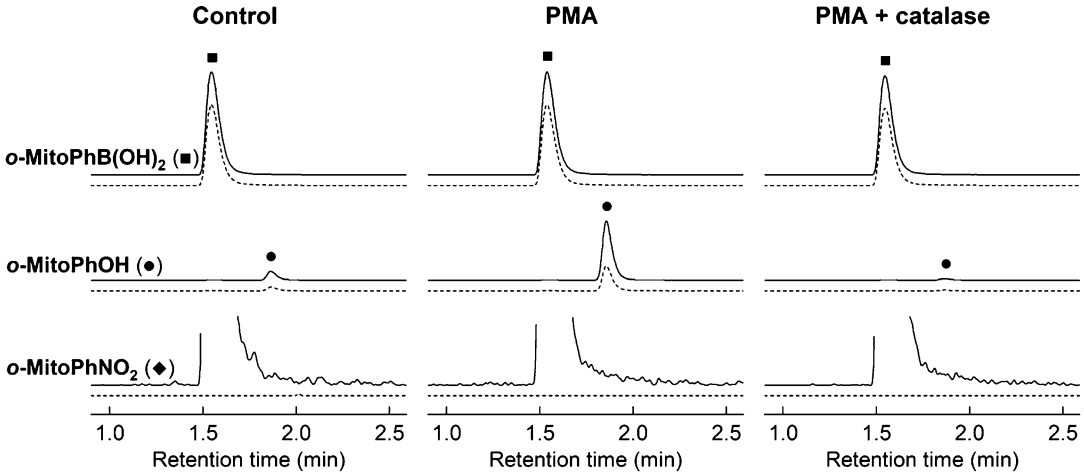


**Fig. 4** HPLC-MS/MS analysis of the media of neutrophil-like cells activated to produce hydrogen peroxide. To produce hydrogen peroxide, HL60 cells differentiated for 4 days with *all-trans* retinoic acid were stimulated with PMA (1 μM) in the presence and absence of catalase (1 kU/ml) and cotreated with *o*-MitoPhB(OH)$_2$. Aliquots of media were collected after 30 min and processed and analyzed as described in the protocol. The intensities of *o*-MitoPhOH were multiplied by a factor of 5 and intensities of *o*-MitoPhNO$_2$ were multiplied by 1000, to fit the same scale as of *o*-MitoPhB(OH)$_2$

*o*-MitoPhB(OH)$_2$ to react with hydrogen peroxide, followed by addition of catalase to remove excess $H_2O_2$. The nitrated product can be synthesized in an analogous protocol as described for *o*-MitoPhB(OH)$_2$, but starting with 2-nitrobenzyl bromide instead of 2-(bromomethyl)phenylboronic acid.

5. *Cyclo*-*o*-MitoPh is not commercially available should be synthesized according to the published method [21]. If only small amounts of *cyclo*-*o*-MitoPh are needed, it may be also produced by reacting *o*-MitoPhB(OH)$_2$ with $ONOO^-$, followed by HPLC-based purification. The identity of the isolated fraction and the extent of contamination by *o*-MitoPh$NO_2$ need to be determined. In our experience, sufficient chromatographic resolution between the peaks of *cyclo*-*o*-MitoPh and *o*-MitoPh$NO_2$ can be obtained using Raptor Biphenyl column (Restek, Bellefonte, PA, USA; 100 mm × 2.1 mm, 2.7 μm).
6. Purity of synthesized *o*-MitoPhB(OH)$_2$ should be tested by HPLC and the compound repurified, if needed. The identity should be confirmed by NMR [20, 26] and HRMS ($C_{25}H_{23}BO_2P^+$, $m/z = 397.1535$) [19, 20] analyses.
7. The concentration of *o*-MitoPhB(OH)$_2$ used for probing of $ONOO^-$ should be chosen so as it does not interfere with mitochondrial function. We did not observe significant effects of 50 μM *o*-MitoPhB(OH)$_2$ on the rate of oxygen consumption by RAW 264.7 cells or MiaPaCa-2 pancreatic cancer cells [25].
8. When exposing cells to *o*-MitoPhB(OH)$_2$ it is preferred to add the medium containing the probe, rather than directly adding a solution of concentrated *o*-MitoPhB(OH)$_2$ in DMSO, to avoid local exposure of cells to high concentrations of DMSO.
9. If plate reader with absorption detection is not available, protein measurements can be carried out using regular spectrophotometer. The volume of cell lysate needed for the assay may be higher, depending on the volume of the spectrophotometer cell.
10. To protect the detector, only portion of eluate is flowed into mass detector. This is achieved by using a diverter valve, which directs the flow into waste before 1 min and after 4 min after injection. Between 1 min and 4 min the flow is directed into the detector and the signals recorded.
11. For each compound two MRM transitions (pairs of parent ion/daughter ion) are recorded. The primary (dominant) transition is used for quantification, while the secondary (reference) transition is used for confirmation of the identity of the analyte. If the ratio of reference to dominant MRM transitions

(Table 2) is outside the range allowed (typically ±30%), the peak is rejected and not used for quantification. Due to similar *m/z* values of *o*-MitoPhB$(OH)_2$ and *o*-MitoPh$NO_2$, there is a small peak of the boronate appearing in the channel of the nitro derivative (Fig. 2, a peak at 1.55 min), which may show up as the dominant peak, when *o*-MitoPhB$(OH)_2$ is in high excess comparing to *o*-MitoPh$NO_2$ (Fig. 3). This peak is not, however, observed in the reference channel, exemplifying the usefulness of the reference transitions for peak identification.

12. The identity of the oxidizing species can be tested by application of specific inhibitors and/or scavengers and/or identification of ONOO-specific products (13;15). Confirmation of peroxynitrite involvement may be obtained by testing the inhibitory effects of inhibitors of nitric oxide synthase, for example L-NAME [18, 20]. Detection of $ONOO^-$ marker products, *cyclo-o*-MitoPh and *o*-Mito$PhNO_2$, is sufficient to confirm the involvement of $ONOO^-$ in probe oxidation [21], as shown in Fig. 3. The inhibitory activity of catalase on the yield of *o*-MitoPhOH and the lack of formation of *o*-Mito$PhNO_2$ (Fig. 4) indicates the involvement of $H_2O_2$ and not $ONOO^-$ in probe oxidation.

## Acknowledgments

This work was supported by NIH grant R01CA208648 (B.K.). JZ was supported in part by Institutional Research Grant IRG #16-183-31 from the American Cancer Society and the MCW Cancer Center. MH was supported, in part, by the French National Research Agency ANR-16-CE07-0023-01. AS was supported by Polish National Science Center within the SONATA BIS program (Grant Number 2015/18/E/ST4/00235). RP was supported by a grant from Polish National Science Centre (NCN) within the SONATA BIS 6 program (Grant no. 2016/22/E/ST4/00549).

### References

1. Lippert AR, Van de Bittner GC, Chang CJ (2011) Boronate oxidation as a bioorthogonal reaction approach for studying the chemistry of hydrogen peroxide in living systems. Acc Chem Res 44:793–804
2. Zielonka J, Sikora A, Hardy M, Joseph J, Dranka BP, Kalyanaraman B (2012) Boronate probes as diagnostic tools for real time monitoring of peroxynitrite and hydroperoxides. Chem Res Toxicol 25:1793–1799
3. Sikora A, Zielonka J, Debowska K, Michalski R, Smulik-Izydorczyk R, Pieta J, Podsiadly R, Artelska A, Pierzchala K, Kalyanaraman B (2020) Boronate-based probes for biological oxidants: A novel class of molecular tools for redox biology. Front Chem 8:580899
4. Dickinson BC, Chang CJ (2008) A targetable fluorescent probe for imaging hydrogen peroxide in the mitochondria of living cells. J Am Chem Soc 130:9638–9639
5. Cocheme HM, Quin C, McQuaker SJ, Cabreiro F, Logan A, Prime TA, Abakumova I, Patel JV, Fearnley IM, James AM, Porteous CM, Smith RA, Saeed S, Carre

JE, Singer M, Gems D, Hartley RC, Partridge L, Murphy MP (2011) Measurement of $H_2O_2$ within living Drosophila during aging using a ratiometric mass spectrometry probe targeted to the mitochondrial matrix. Cell Metab 13:340–350

6. Cocheme HM, Logan A, Prime TA, Abakumova I, Quin C, McQuaker SJ, Patel JV, Fearnley IM, James AM, Porteous CM, Smith RA, Hartley RC, Partridge L, Murphy MP (2012) Using the mitochondria-targeted ratiometric mass spectrometry probe MitoB to measure $H_2O_2$ in living Drosophila. Nat Protoc 7:946–958
7. Dickinson BC, Lin VS, Chang CJ (2013) Preparation and use of MitoPY1 for imaging hydrogen peroxide in mitochondria of live cells. Nat Protoc 8:1249–1259
8. Zielonka J, Joseph J, Sikora A, Hardy M, Ouari O, Vasquez-Vivar J, Cheng G, Lopez M, Kalyanaraman B (2017) Mitochondria-targeted triphenylphosphonium-based compounds: syntheses, mechanisms of action, and therapeutic and diagnostic applications. Chem Rev 117:10043–10120
9. Sikora A, Zielonka J, Lopez M, Joseph J, Kalyanaraman B (2009) Direct oxidation of boronates by peroxynitrite: mechanism and implications in fluorescence imaging of peroxynitrite. Free Radic Biol Med 47:1401–1407
10. Sikora A, Zielonka J, Lopez M, Dybala-Defratyka A, Joseph J, Marcinek A, Kalyanaraman B (2011) Reaction between peroxynitrite and boronates: EPR spin-trapping, HPLC analyses, and quantum mechanical study of the free radical pathway. Chem Res Toxicol 24:687–697
11. Wardman P (2007) Fluorescent and luminescent probes for measurement of oxidative and nitrosative species in cells and tissues: progress, pitfalls, and prospects. Free Radic Biol Med 43:995–1022
12. Kalyanaraman B (2011) Oxidative chemistry of fluorescent dyes: implications in the detection of reactive oxygen and nitrogen species. Biochem Soc Trans 39:1221–1225
13. Zielonka J, Kalyanaraman B (2018) Small-molecule luminescent probes for the detection of cellular oxidizing and nitrating species. Free Radic Biol Med 128:3–22
14. Zielonka J, Kalyanaraman B (2012) Methods of investigation of selected radical oxygen/nitrogen species in cell-free and cellular systems. In: Pantopoulos K, Schipper HM (eds) Principles of free radical biomedicine, vol I. Nova Science Publishers, New York, pp 201–264
15. Zielonka J, Sikora A, Joseph J, Kalyanaraman B (2010) Peroxynitrite is the major species formed from different flux ratios of co-generated nitric oxide and superoxide: direct reaction with boronate-based fluorescent probe. J Biol Chem 285:14210–14216
16. Michalski R, Zielonka J, Gapys E, Marcinek A, Joseph J, Kalyanaraman B (2014) Real-time measurements of amino acid and protein hydroperoxides using coumarin boronic acid. J Biol Chem 289:22536–22553
17. Truzzi DR, Augusto O (2017) Influence of $CO_2$ on hydroperoxide metabolism. In: Vissers MC, Hampton M, Kettle AJ (eds) Hydrogen peroxide metabolism in health and disease. CRC Press, Boca Raton, FL, pp 81–99
18. Zielonka J, Zielonka M, Sikora A, Adamus J, Joseph J, Hardy M, Ouari O, Dranka BP, Kalyanaraman B (2012) Global profiling of reactive oxygen and nitrogen species in biological systems: high-throughput real-time analyses. J Biol Chem 287:2984–2995
19. Sikora A, Zielonka J, Adamus J, Debski D, Dybala-Defratyka A, Michalowski B, Joseph J, Hartley RC, Murphy MP, Kalyanaraman B (2013) Reaction between peroxynitrite and triphenylphosphonium-substituted arylboronic acid isomers: identification of diagnostic marker products and biological implications. Chem Res Toxicol 26:856–867
20. Zielonka J, Sikora A, Adamus J, Kalyanaraman B (2015) Detection and differentiation between peroxynitrite and hydroperoxides using mitochondria-targeted arylboronic acid. Methods Mol Biol 1264:171–181
21. Zielonka J, Zielonka M, VerPlank L, Cheng G, Hardy M, Ouari O, Ayhan MM, Podsiadły R, Sikora A, Lambeth JD, Kalyanaraman B (2016) Mitigation of NADPH oxidase 2 activity as a strategy to inhibit peroxynitrite formation. J Biol Chem 291:7029–7044
22. Rios N, Radi R, Kalyanaraman B, Zielonka J (2020) Tracking isotopically labeled oxidants using boronate-based redox probes. J Biol Chem 295:6665-6676
23. Zielonka J, Joseph J, Sikora A, Kalyanaraman B (2013) Real-time monitoring of reactive oxygen and nitrogen species in a multiwell plate using the diagnostic marker products of specific probes. Methods Enzymol 526:145–157
24. Hardy M, Zielonka J, Karoui H, Sikora A, Michalski R, Podsiadly R, Lopez M, Vasquez-Vivar J, Kalyanaraman B, Ouari O (2018) Detection and characterization of reactive oxygen and nitrogen species in biological systems by monitoring species-specific products. Antioxid Redox Signal 28:1416–1432

25. Cheng G, Zielonka M, Dranka B, Kumar SN, Myers CR, Bennett B, Garces AM, Dias Duarte Machado LG, Thiebaut D, Ouari O, Hardy M, Zielonka J, Kalyanaraman B (2018) Detection of mitochondria-generated reactive oxygen species in cells using multiple probes and methods: potentials, pitfalls, and the future. J Biol Chem 293:10363–10380

26. Morrison DE, Issa F, Bhadbhade M, Groebler L, Witting PK, Kassiou M, Rutledge PJ, Rendina LM (2010) Boronated phosphonium salts containing arylboronic acid, closo-carborane, or nido-carborane: synthesis, X-ray diffraction, in vitro cytotoxicity, and cellular uptake. J Biol Inorg Chem 15:1305–1318

# Chapter 21

# Mitochondrial Coenzyme Q10 Determination Via Isotope Dilution Liquid Chromatography–Tandem Mass Spectrometry

**Erik Hedman and Outi Itkonen**

## Abstract

Coenzyme Q10 ($CoQ_{10}$) is an essential part of the mitochondrial respiratory chain. Here, we describe an accurate and sensitive liquid chromatography tandem mass spectrometry (LC-MS/MS) method for determination of mitochondrial $CoQ_{10}$ in isolated mitochondria. In the assay, mitochondrial suspensions are spiked with $CoQ_{10}$-[$^2H_9$] internal standard (IS), extracted with organic solvents and $CoQ_{10}$ quantified by LC-MS/MS using multiple reaction monitoring (MRM).

**Key words** Ubiquinone, Coenzyme Q10, Isotope dilution, LC-MS/MS, Mitochondrial disease

## 1 Introduction

Coenzyme Q10 ($CoQ_{10}$), also called ubiquinone, is an essential part of the mitochondrial respiratory chain. The high transfer energy containing electrons of NADH and $FADH_2$ formed in the glycolysis, fatty acid oxidation, and the citric acid cycle are transferred to $O_2$ by the respiratory chain in a process called oxidative phosphorylation (OXPHOS). In this way, the energy in the diet is transformed to adenosine triphosphate (ATP) for cellular functions [1]. In the respiratory chain, $CoQ_{10}$ transfers reducing equivalents from respiratory complexes I and II to complex III [2]. Apart from its role in the respiratory chain, $CoQ_{10}$ also allows protons to be extruded from the mitochondrial matrix to the intermembrane space [3], acts as pro- or antioxidant [4], has a role in pyrimidine biosynthesis [5] and modulates apoptosis [6].

Disorders in OXPHOS chain cause lack of energy in cells and tissues resulting in heterogeneous symptoms in the patient. Patients with primary and secondary $CoQ_{10}$ deficiency have been reported [7–11]. There are no curative treatments for OXPHOS

Volkmar Weissig and Marvin Edeas (eds.), *Mitochondrial Medicine: Volume 1: Targeting Mitochondria*, Methods in Molecular Biology, vol. 2275, https://doi.org/10.1007/978-1-0716-1262-0_21,

disorders. However, some patients with $CoQ_{10}$ deficiency benefit from substitution of $CoQ_{10}$ [12, 13], the treatment with $CoQ_{10}$ is also relatively cheap and lacks severe side effects. $CoQ_{10}$ quantification may be used to aid in diagnosis of mitochondrial $CoQ_{10}$ deficiency and to identify patients for potentially effective substitution therapy [14].

The reported assays for $CoQ_{10}$ in biological samples are based on liquid chromatography (LC) with ultraviolet (UV) [15–18], electrochemical (EC) [19–23], mass spectrometric (MS) [24], tandem mass spectrometric (MS/MS) [25–30], and high resolution mass spectrometric (HRMS) detection [31]. Most techniques have also been used to simultaneously determine the reduced and the oxidized form of $CoQ_{10}$ [19, 23, 28, 31]. The highest sensitivity and specificity are reached by LC-MS/MS technology employing an isotopically labeled internal standard [27, 31, 32].

## 2 Materials

Always use reagents of the highest analytical quality and deionized water with a resistance of 18 MΩ at +25 °C. The performance of the analytical balance, spectrophotometer, and the LC-MS/MS instrument should be assured either by an external quality assurance scheme or by the procedures of the respective instrument manufacturer.

### 2.1 Mitochondrial Isolation

1. Homogenizing buffer: 100 mM KCl, 50 mM $KH_2PO_4$, 50 mM Tris(hydroxymethyl)amino methane, 5 mM $MgCl_2$, 1.8 mM ATP, 1 mM (EDTA), pH 7.2. Weigh 1.86 g KCl (p.a.), 1.70 g potassium dihydrogen phosphate, 1.51 g Tris (hydroxymethyl)-amino methane, 0.254 g magnesium chloride hexahydrate, 0.101 g ethylenediaminetetraacetic acid ($EDTAx2H_2O$), dipotassium salt, and 0.248 g adenosine-5-′-triphosphate, disodium salt. Add 200 mL of water into a 250 mL beaker. Under mixing with a magnetic stirrer, add the weighed reagents. Adjust the pH to 7.2 with 1 M HCl. Transfer the solution into a volumetric flask and make up to 250 mL with water. Mix well. Store in 3 mL aliquots at −20 °C in plastic vials. Use within a year.
2. Resuspension solution: 250 mM sucrose, 15 mM $KH_2PO_4$, 2 mM $MgAc_2$, 0.5 mM EDTA, 0.5 g/L albumin, pH 7.2. Weigh 0.25 g human albumin (essentially fatty acid free) and put aside (*see* **Note 1**). Weigh 42.8 g sucrose, 1.02 g $KH_2PO_4$, 0.215 g magnesium acetate tetrahydrate, and 0.101 g $EDTAx2H_2O$, dipotassium salt. Add 400 mL of water into a 500 mL beaker. Under stirring with a magnetic stirrer, add the weighed reagents except albumin (*see* **Note 1**). Adjust the pH to 7.2 with 5 M KOH. Add albumin to the solution and stir

until dissolved. Transfer the solution into a volumetric flask and make up to 500 mL with water. Mix well. Store in 4 mL aliquots at −20 °C in plastic vials. Use within a year.

3. Cooled (+4 °C) centrifuge for Eppendorf tubes with a speed up to 15,000 × *g*.
4. Homogenizer (60 rpm), Potter-Elvehjem homogenizer tube (inner diameter 8.0 mm, frosted walls) with a Teflon pestle (diameter 7.8 mm).

### 2.2 Assay of $CoQ_{10}$

1. Spectrophotometer and quartz cuvettes.
2. $CoQ_{10}$ calibrator stock solution: 400–700 μmol/L (μM). Prepare a stock solution by weighing 20–30 mg of $CoQ_{10}$. Make up to 50 mL in a volumetric flask with chloroform (p.a.) and mix thoroughly (*see* **Note 2**). The actual $CoQ_{10}$ concentration of the stock solution is calculated based on the molar absorptivity of $CoQ_{10}$. Set the spectrophotometer at 275 nm. Blank with chloroform. Read the absorbance of the $CoQ_{10}$ solution and calculate the concentration (*see* **Note 3**). Divide into 1.5 mL aliquots into glass (borosilicate) vials and store at −80 °C.
3. Working calibrators: Prepare a 1000 nM working calibrator by diluting the stock solution with mobile phase A (*see* **item 13** below) in a 50 mL volumetric flask (*see* **Note 4**). Mix well. Divide into 1.5 mL aliquots into glass (borosilicate) vials and store at −80 °C. Other working calibrators are prepared freshly into Eppendorf tubes as follows:

   500 nM, mix 250 μL of 1000 nM solution and 250 μL of mobile phase A,

   250 nM, mix 250 μL of 1000 nM solution and 750 μL of mobile phase A,

   100 nM, mix 100 μL of 1000 nM solution and 900 μL of mobile phase A,

   10 nM, mix 100 μL of 100 nM solution and 900 μL of mobile phase A,

   1 nM, mix 100 μL of 10 nM solution and 900 μL of mobile phase A.
4. Stable isotope-labeled internal standard (IS): Prepare a 1.2 mM (1 g/L) stock solution of IS ($CoQ_{10}$-[$^2H_9$] in chloroform). Mix well (*see* **Note 2**). Store as 1.5 mL aliquots in glass vials at −80 °C. Prepare a 0.5 μM IS working solution in mobile phase A by diluting 10.4 μL of IS stock solution to 25 mL in a volumetric flask. Store as 1.0 mL aliquots in Eppendorf tubes at −80 °C.
5. Ethanol–hexane (2 + 5): Mix 80 mL of ethanol and 200 mL of hexane.

6. Multitube vortexer.
7. Sample concentrator SBH CONC/1.
8. Block heater SBH 130D/3.
9. Freeze bath, Lauda ECO Silver RE1050.
10. Ultrahigh-performance liquid chromatograph with a binary pump, degasser, column oven (+60 °C) and autosampler.
11. Triple quadrupole mass spectrometer with an electrospray ion source (we use an Xevo TQ-S with electrospray ionization ion source from Waters).
12. Acquity UPLC™ BEH C18 analytical column (we use a 2.1 × 100 mm, 1.7 μM particle size from Waters).
13. Mobile phase A, 82% (v/v) methanol, 18% 1-propanol containing 500 μM ammonium acetate. Mix 205 mL of methanol (MS grade), 45 mL of 1-propanol and 125 μL of 1 M ammonium acetate (*see* **Note 5**).
14. Mobile phase B, 50% methanol, 50% 1-propanol containing 500 μM ammonium acetate. Mix 125 mL of methanol (MS grade), 125 mL of 1-propanol, and 125 μL of 1 M ammonium acetate.

### 2.3 Assay of Citrate Synthase Activity

1. Triton X-100 solution: 2% Triton X-100 (v/v). Let Triton X-100 reach room temperature. Add approx. 20 mL water to a 25 mL volumetric flask. Transfer 500 μL Triton X-100 to the flask (*see* **Note 6**). Add water up to 25 mL and mix on magnetic stirrer for 10 min. Transfer the solution to a tinted glass bottle. May be stored refrigerated up to 1 month.
2. Homogenization buffer: 53 mM $KH_2PO_4$, 1.05 mM EDTA. Dissolve 1.79 g $KH_2PO_4$ and 0.105 g EDTA-$K_2$ in 200 ml of water. Adjust pH to 7.5 with 5 M KOH and add up water to 250 mL. Store 2.85 mL aliquots of the solution at −20 °C for up to 1 year.
3. Homogenization buffer with Triton X-100: 50 mM $KH_2PO_4$, 1 mM EDTA, 0.1% Triton X-100 (v/v). Add 150 μL 2% Triton X-100 to one tube of Homogenization buffer. Prepare on the day for use.
4. Pre CS-A: Tris 120 mM; 5,5′-dithiobis(2-nitrobenzoic acid) (DTNB) 0.48 mM. Dissolve 2.9 g Tris(hydroxymethyl)-aminomethane in approx. 180 mL of water. Adjust pH to 8.1 with 5 M HCl. Add 38 mg DTNB and adjust to a final volume of 200 mL with water (*see* **Note 7**). Mix and store in 2.5 mL aliquots at −20 °C for up to 1 year.
5. Acetyl-CoA 1.2 mM: Work in ice bath. Dissolve 25 mg of Acetyl-CoA in 21.7 mL of water. Mix the solution with magnetic stirrer. Store in 500 μL aliquots at −20 °C for up to 1 year.

6. *CS-A:* Tris 100 mM; DTNB 0.40 mM; acetyl-CoA 0.2 mM. Mix one tube of Pre CS-A and one tube of acetyl-CoA 1.2 mM. Prepare on the day for use. Must be used within 2 h.
7. CS-B: Oxaloacetate 12.5 mM. Weigh 2–3 mg oxaloacetate in a tube. Add water to a concentration of 1.65 mg oxaloacetate/mL. Mix. Prepare on the day for use.
8. Automated filter photometer. In our laboratory we use the Indiko™ clinical chemistry system from ThermoFisher Scientific.

## 3 Methods

### 3.1 Isolation of Mitochondria

For isolation of mitochondria, use published standard procedures like that described for muscle samples in [33] (*see* **Note 8**).

1. Homogenize the muscle sample (roughly 100 mg of *tibialis anterior*) for 4 min in a homogenizer fitted with a Teflon pestle. Use a volume (μL) of homogenizing buffer that corresponds to muscle weight (mg) × 20 (minimum 700 μL) (*see* **Note 9**).
2. Centrifuge first the homogenate for 3 min at 650 × *g* and then the supernatant for 3 min at 15,000 × *g*.
3. Wash the pelleted mitochondria with 300 μL of homogenizing buffer, centrifuge for 3 min at 15,000 × *g* and resuspend the pellet in *resuspension solution* in a volume (μL) corresponding to muscle weight (mg) × 4 (minimum 200 μL) (*see* **Notes 10** and **11**). The mitochondrial suspension is stored in 10 μL aliquots at −80 °C until assay (*see* **Note 12**).

### 3.2 Sample and Calibrator Preparation

1. Dilute 10 μL of the mitochondrial suspension with 240 μL of water (*see* **Note 13**).
2. Transfer 100 μL of calibrators and diluted mitochondrial solution into 10 mL glass tubes (*see* **Note 14**).
3. Add 20 μL of IS working solution and vortex-mix. Calibrators are now ready for analysis.
4. To QA and patient samples, add 300 μL of 1-propanol and mix.
5. Centrifuge at 10,000 × *g* for 2 min at room temperature.
6. Transfer 350 μL of the upper phase into 10 mL glass tubes.
7. Add 3 mL of ethanol–hexane (2 + 5) and vortex-mix for 3 min in a multitube vortexer.
8. Add 4 mL of water and turn the glass tubes upside down 5 times.
9. Let the tubes stand for 15 min at room temperature.
10. Let the tubes stand in the freeze bath for 10 min at −35 °C.

11. Transfer the upper phase into clean glass tubes. Evaporate to dryness under a flow of nitrogen at +37 °C (*see* **Note 15**).
12. Dissolve the residue in 100 μL of mobile phase A and transfer into autosampler vials.

### 3.3 LC-MS/MS Analysis

1. Set up a chromatographic method with a flow rate of 600 μL/min and the following gradient.
   (a) $t = 0$ min, $B = 1\%$
   (b) $t = 0.40$ min, $B = 1\%$
   (c) $t = 2.00$ min, $B = 40\%$
   (d) $t = 2.50$ min, $B = 99\%$
   (e) $t = 2.85$ min, $B = 99\%$
   (f) $t = 2.86$ min, $B = 1\%$
   (g) $t = 3.50$ min, $B = 1\%$
2. Set the column oven at +60 °C and adjust the injection volume to 10 μL (*see* **Note 16**). The MS is operated in positive ion mode with the ion source spray voltage at +3000 V, desolvation gas temperature at +350 °C. The desolvation gas setting is 1200 L/h, cone gas 150 L/h, and collision gas (Ar) setting 0.15 mL/min. For MRM transitions, collision energy, capillary voltage, and dwell times, *see* Table 1.
3. Equilibrate the LC system with mobile phase A and keep the column at +60 °C for 20 min (*see* **Note 17**). It is good practice to do multiple injections of a system suitability test (SST) before calibrators and patients' samples are analyzed (*see* **Note 18**).
4. Inject the calibrators and extracted samples to the LC-MS/MS. $CoQ_{10}$ and the IS elute at a retention time of about 1.5 min.

### 3.4 Determination of Citrate Synthase Activity

The activity of citrate synthase (CS) is generally accepted as a matrix enzyme and a marker for mitochondrial abundance in a sample. Clinically, the most important application of $CoQ_{10}$ assay is detection of $CoQ_{10}$ deficiency of the respiratory chain. For this purpose, normalization of the $CoQ_{10}$ concentration in relation to CS activity, that is, mitochondrial abundance, is likely to reflect the available $CoQ_{10}$ content more accurately [27]; however, normalization with protein as well as CS has also been proposed [7]. CS activity in the sample is determined by following the reduction of 5,5′-dithiobis (2-nitrobenzoic acid) (DTNB) at 405 nm coupled to the reduction of Coenzyme A in the presence of oxaloacetate [33]. Prior to the CS assay the mitochondrial membranes are permeabilized by diluting the mitochondrial suspension in a hypotonic solution containing the detergent Triton X-100.

**Table 1**
**MRM transitions used for quantification of $CoQ_{10}$ and internal standard**

| Analytes | MRM transition (m/z) | Dwell time (s) | CV (V) | CE (V) |
|---|---|---|---|---|
| $CoQ_{10}$ (target) | 863.8 → 197.0 | 0.1 | 12 | 30 |
| $CoQ_{10}$ (qualifier) | 863.8 → 109.0 | 0.1 | 12 | 38 |
| $CoQ_{10}$-[$^2H_9$] (IS) | 872.9 → 206.1 | 0.1 | 44 | 34 |

*CV* capillary voltage, *CE* collision energy

#### 3.4.1 Procedure

1. Load the reagents CS-A and CS-B in the instrument.
2. Prepare each sample by thawing a 10 μL aliquot of mitochondrial suspension and dilute it in 240 μL Homogenization buffer with Triton X-100 solution.
3. Load the diluted samples in the instrument and start the assay.
   (a) 20 μL of diluted sample is mixed with 125 μL CS-A and 95 μL water in a cuvette.
   (b) The reaction mixture is incubated for 300 s in +37 °C.
   (c) 10 μL of CS-B is added.
   (d) After a lag phase of 60 s the reaction rate is registered under 72 s at the wavelength 405 nm.
4. All samples are analysed in duplicate. The analysis time is approx. 15 min for 10 samples.
5. The reaction rate before the addition of CS-B is basically negligible, and no blank correction is made.

### 3.5 Calculation of the Results

Review peak integration and construct a calibration curve based on the ratio of the peak areas of $CoQ_{10}$ and IS using $1/x^2$ weighted linear least-squares regression by the instrument software (*see* **Notes 19** and **20**).

#### 3.5.1 $CoQ_{10}$

#### 3.5.2 Citrate Synthase

The reaction rate is registered as Δ absorbance/min (typically 0.05 abs/min). The citrate synthase activity is calculated by multiplying the reaction rate with a factor 22,978 to achieve the final result with the unit μM/min/L (U/L) (*see* **Note 21**).

## 4 Notes

1. The pH of the solution is low before adjustment. To prevent albumin denaturation, first adjust the pH to 7.2 and then add albumin.
2. We found it important to dissolve the stock calibrator into chloroform because $CoQ_{10}$ showed poor solubility in 1-propanol. Especially at −20 °C $CoQ_{10}$ tends to precipitate in 1-propanol but not in chloroform.

3. Calculate the concentration of $CoQ_{10}$ according to the equation $c\,(M) = A_{275\ nm}/(\varepsilon \times l)$, where $A_{275\ nm}$ is the absorbance, $\varepsilon$ is 14.3 $mM^{-1}$ $cm^{-1}$ (the molar absorptivity of $CoQ_{10}$), and $l$ is the sample path length (cm).
4. The volume of the stock solution to be diluted is calculated according to the equation: Stock solution volume (mL) = 1 μM × working calibrator volume (mL)/stock solution concentration (μM).
5. To ensure efficient mixing of the mobile phases it is important that also mobile phase A contains 1-propanol.
6. If possible, use a positive displacement pipette. Wipe the outside of the pipette tip clean before final transfer! Push out Triton X-100 under the water surface in the flask. Aspire and dispense below the water surface a few times to rinse pipette inside.
7. Make sure that pH has been adjusted before DTNB is added to the Tris-solution!
8. Enriched mitochondria from any tissue or cell line can be used for the $CoQ_{10}$ assay. The present procedure has been optimized for isolation of muscle mitochondria.
9. Avoid foaming and high pressure during homogenization.
10. All reagents and materials are cooled and kept ice-cold during the entire isolation procedure.
11. Practically all mitochondrial $CoQ_{10}$ is oxidized during sample pretreatment and no ubiquinol oxidation is needed for quantification of total $CoQ_{10}$ in isolated mitochondria [27].
12. Mitochondrial $CoQ_{10}$ is stable for several years at −80 °C and at least 4 weeks at −20 °C when stored in concentrated (0.25 mg/μL) rather than in dilute suspensions [27].
13. A mitochondrial suspension corresponding to 0.01 mg wet weight/μL is optimal for analysis of $CoQ_{10}$ in human muscle mitochondria. Different cells and tissues contain varying amounts of mitochondria and therefore, optimal dilution depends on the samples used and needs to be tested.
14. It is highly recommended to prepare your own quality assurance (QA) samples to ascertain assay quality. Treat QA samples identically to unknown samples.
15. For rapid evaporation of the solvents we recommend the TurboVap® evaporator (Caliper Life Sciences) with the temperature set at +37 °C.
16. The MS settings are instrument dependent and must be optimized.

17. Proper equilibration of the LC column prior to analysis and a thorough clean-up procedure after analysis is essential for repeated high-quality analysis.
18. For accurate and repeatable analysis, always inspect the ion source spray prior to analysis, run a blank sample and SST, for example a calibrator or specifically prepared solution of the analyte, and record the signal-to-noise ratio, response area and retention time for each assay series.
19. The method linearity depends on the instrumentation and should be validated in each laboratory. In our laboratory, the linear range is 1–1000 nM (0.864–863 ng/mL) with an LOQ of 0.8 nM (691 pg/mL) only slightly higher than the original publication [27]. The mean mitochondrial $CoQ_{10}$ concentration in *quadriceps (vastus lateralis)* muscle has been previously reported to $CoQ_{10}$/CS 1.7 nmol/U (95% CI 1.6–1.7 nmol/U) [27]. However, we emphasize the importance of establishing a laboratory specific reference range. In our laboratory, the mean mitochondrial $CoQ_{10}$/CS in *tibialis anterior* was 1.7 nmol/U (95% CI 1.2–2.4 nmol/U), $n = 51$.
20. The automatically calculated results are expressed as nmol/L. To express the result as nmol/Unit CS, the obtained result (nM) must be multiplied by 25 (since the suspension was diluted 25 times, **step 1** in Subheading 3.2).
21. The factor 22,978 is calculated as $25 \times 250 \times 1000/13.6/20$ where:
    25 = dilution factor of pretreated sample
    250 = final volume of assay mixture (μL)
    1000 = conversion between mmol and μmol
    13.6 = molar extinction coefficient for DTNB ($mM^{-1}$ $cm^{-1}$)
    20 = sample volume in the assay (μL).

## References


1. Kroger A, Klingenberg M (1973) The kinetics of the redox reactions of ubiquinone related to the electron-transport activity in the respiratory chain. Eur J Biochem 34(2):358–368. https://doi.org/10.1111/j.1432-1033.1973.tb02767.x
2. Sun IL, Sun EE, Crane FL, Morre DJ, Lindgren A, Low H (1992) Requirement for coenzyme Q in plasma membrane electron transport. Proc Natl Acad Sci U S A 89 (23):11126–11130. https://doi.org/10.1073/pnas.89.23.11126
3. Trumpower BL (1990) The protonmotive Q cycle. Energy transduction by coupling of proton translocation to electron transfer by the cytochrome bc1 complex. J Biol Chem 265 (20):11409–11412
4. Ernster L, Forsmark-Andree P (1993) Ubiquinol: an endogenous antioxidant in aerobic organisms. Clin Investig 71(8 Suppl): S60–S65. https://doi.org/10.1007/bf00226842
5. Lopez-Martin JM, Salviati L, Trevisson E, Montini G, DiMauro S, Quinzii C, Hirano M, Rodriguez-Hernandez A, Cordero MD, Sanchez-Alcazar JA, Santos-Ocana C, Navas P (2007) Missense mutation of the COQ2 gene causes defects of bioenergetics and de novo pyrimidine synthesis. Hum Mol

Genet 16(9):1091–1097. https://doi.org/10.1093/hmg/ddm058

6. Papucci L, Schiavone N, Witort E, Donnini M, Lapucci A, Tempestini A, Formigli L, Zecchi-Orlandini S, Orlandini G, Carella G, Brancato R, Capaccioli S (2003) Coenzyme q10 prevents apoptosis by inhibiting mitochondrial depolarization independently of its free radical scavenging property. J Biol Chem 278(30):28220–28228. https://doi.org/10.1074/jbc.M302297200
7. Emmanuele V, Lopez LC, Berardo A, Naini A, Tadesse S, Wen B, D'Agostino E, Solomon M, DiMauro S, Quinzii C, Hirano M (2012) Heterogeneity of coenzyme Q10 deficiency: patient study and literature review. Arch Neurol 69(8):978–983. https://doi.org/10.1001/archneurol.2012.206
8. Freyer C, Stranneheim H, Naess K, Mourier A, Felser A, Maffezzini C, Lesko N, Bruhn H, Engvall M, Wibom R, Barbaro M, Hinze Y, Magnusson M, Andeer R, Zetterstrom RH, von Dobeln U, Wredenberg A, Wedell A (2015) Rescue of primary ubiquinone deficiency due to a novel COQ7 defect using 2,4-dihydroxybensoic acid. J Med Genet 52 (11):779–783. https://doi.org/10.1136/jmedgenet-2015-102986
9. Kishita Y, Pajak A, Bolar NA, Marobbio CM, Maffezzini C, Miniero DV, Monne M, Kohda M, Stranneheim H, Murayama K, Naess K, Lesko N, Bruhn H, Mourier A, Wibom R, Nennesmo I, Jespers A, Govaert P, Ohtake A, Van Laer L, Loeys BL, Freyer C, Palmieri F, Wredenberg A, Okazaki Y, Wedell A (2015) Intra-mitochondrial methylation deficiency due to mutations in SLC25A26. Am J Hum Genet 97(5):761–768. https://doi.org/10.1016/j.ajhg.2015.09.013
10. Salviati L, Trevisson E, Doimo M, Navas P (2017) Primary coenzyme Q10 deficiency. In: Adam MP, Ardinger HH, Pagon RA et al (eds) GeneReviews((R)). University of Washington, Seattle, WA
11. Kwong AK, Chiu AT, Tsang MH, Lun KS, Rodenburg RJT, Smeitink J, Chung BH, Fung CW (2019) A fatal case of COQ7-associated primary coenzyme Q10 deficiency. JIMD Rep 47(1):23–29. https://doi.org/10.1002/jmd2.12032
12. Caglayan AO, Gumus H, Sandford E, Kubisiak TL, Ma Q, Ozel AB, Per H, Li JZ, Shakkottai VG, Burmeister M (2019) COQ4 mutation leads to childhood-onset ataxia improved by CoQ10 administration. Cerebellum 18 (3):665–669. https://doi.org/10.1007/s12311-019-01011-x
13. Rotig A, Appelkvist EL, Geromel V, Chretien D, Kadhom N, Edery P, Lebideau M, Dallner G, Munnich A, Ernster L, Rustin P (2000) Quinone-responsive multiple respiratory-chain dysfunction due to widespread coenzyme Q10 deficiency. Lancet 356(9227):391–395. https://doi.org/10.1016/S0140-6736(00)02531-9
14. Yubero D, Allen G, Artuch R, Montero R (2017) The value of coenzyme Q10 determination in mitochondrial patients. J Clin Med 6 (4):37. https://doi.org/10.3390/jcm6040037
15. Benoist JF, Rigal O, Nivoche Y, Martin C, Biou D, Lombes A (2003) Differences in coenzyme Q10 content in deltoid and quadriceps muscles. Clin Chim Acta 329(1–2):147–148. https://doi.org/10.1016/s0009-8981(02)00423-0
16. Hirano M, Garone C, Quinzii CM (2012) CoQ(10) deficiencies and MNGIE: two treatable mitochondrial disorders. Biochim Biophys Acta 1820(5):625–631. https://doi.org/10.1016/j.bbagen.2012.01.006
17. Ogasahara S, Engel AG, Frens D, Mack D (1989) Muscle coenzyme Q deficiency in familial mitochondrial encephalomyopathy. Proc Natl Acad Sci U S A 86(7):2379–2382. https://doi.org/10.1073/pnas.86.7.2379
18. Laaksonen R, Riihimaki A, Laitila J, Martensson K, Tikkanen MJ, Himberg JJ (1995) Serum and muscle tissue ubiquinone levels in healthy subjects. J Lab Clin Med 125 (4):517–521
19. Menke T, Niklowitz P, Adam S, Weber M, Schluter B, Andler W (2000) Simultaneous detection of ubiquinol-10, ubiquinone-10, and tocopherols in human plasma microsamples and macrosamples as a marker of oxidative damage in neonates and infants. Anal Biochem 282(2):209–217. https://doi.org/10.1006/abio.2000.4579
20. Miles MV, Tang PH, Miles L, Steele PE, Moye MJ, Horn PS (2008) Validation and application of an HPLC-EC method for analysis of coenzyme Q10 in blood platelets. Biomed Chromatogr 22(12):1403–1408. https://doi.org/10.1002/bmc.1072
21. Pastore A, Giovamberardino GD, Bertini E, Tozzi G, Gaeta LM, Federici G, Piemonte F (2005) Simultaneous determination of ubiquinol and ubiquinone in skeletal muscle of pediatric patients. Anal Biochem 342(2):352–355. https://doi.org/10.1016/j.ab.2005.02.018
22. Tang PH, Miles MV, DeGrauw A, Hershey A, Pesce A (2001) HPLC analysis of reduced and oxidized coenzyme Q(10) in human plasma. Clin Chem 47(2):256–265

23. Schou-Pedersen AMV, Schemeth D, Lykkesfeldt J (2019) Determination of reduced and oxidized coenzyme Q10 in canine plasma and heart tissue by HPLC-ECD: comparison with LC-MS/MS quantification. Antioxidants (Basel) 8(8):253. https://doi.org/10.3390/antiox8080253
24. Li L, Pabbisetty D, Carvalho P, Avery MA, Avery BA (2008) Analysis of CoQ10 in rat serum by ultra-performance liquid chromatography mass spectrometry after oral administration. J Pharm Biomed Anal 46(1):137–142. https://doi.org/10.1016/j.jpba.2007.10.019
25. Arias A, Garcia-Villoria J, Rojo A, Bujan N, Briones P, Ribes A (2012) Analysis of coenzyme Q(10) in lymphocytes by HPLC-MS/MS. J Chromatogr B Analyt Technol Biomed Life Sci 908:23–26. https://doi.org/10.1016/j.jchromb.2012.09.027
26. Duberley KE, Hargreaves IP, Chaiwatanasirikul KA, Heales SJ, Land JM, Rahman S, Mills K, Eaton S (2013) Coenzyme Q10 quantification in muscle, fibroblasts and cerebrospinal fluid by liquid chromatography/tandem mass spectrometry using a novel deuterated internal standard. Rapid Commun Mass Spectrom 27(9):924–930. https://doi.org/10.1002/rcm.6529
27. Itkonen O, Suomalainen A, Turpeinen U (2013) Mitochondrial coenzyme Q10 determination by isotope-dilution liquid chromatography-tandem mass spectrometry. Clin Chem 59(8):1260–1267. https://doi.org/10.1373/clinchem.2012.200196
28. Ruiz-Jimenez J, Priego-Capote F, Mata-Granados JM, Quesada JM, Luque de Castro MD (2007) Determination of the ubiquinol-10 and ubiquinone-10 (coenzyme Q10) in human serum by liquid chromatography tandem mass spectrometry to evaluate the oxidative stress. J Chromatogr A 1175 (2):242–248. https://doi.org/10.1016/j.chroma.2007.10.055
29. Schaefer WH, Lawrence JW, Loughlin AF, Stoffregen DA, Mixson LA, Dean DC, Raab CE, Yu NX, Lankas GR, Frederick CB (2004) Evaluation of ubiquinone concentration and mitochondrial function relative to cerivastatin-induced skeletal myopathy in rats. Toxicol Appl Pharmacol 194(1):10–23. https://doi.org/10.1016/j.taap.2003.08.013
30. Teshima K, Kondo T (2005) Analytical method for ubiquinone-9 and ubiquinone-10 in rat tissues by liquid chromatography/turbo ion spray tandem mass spectrometry with 1-alkylamine as an additive to the mobile phase. Anal Biochem 338(1):12–19. https://doi.org/10.1016/j.ab.2004.12.007
31. Pandey R, Riley CL, Mills EM, Tiziani S (2018) Highly sensitive and selective determination of redox states of coenzymes Q9 and Q10 in mice tissues: application of orbitrap mass spectrometry. Anal Chim Acta 1011:68–76. https://doi.org/10.1016/j.aca.2018.01.066
32. Louw R, Smuts I, Wilsenach KL, Jonck LM, Schoonen M, van der Westhuizen FH (2018) The dilemma of diagnosing coenzyme Q10 deficiency in muscle. Mol Genet Metab 125 (1–2):38–43. https://doi.org/10.1016/j.ymgme.2018.02.015
33. Wibom R, Hagenfeldt L, von Dobeln U (2002) Measurement of ATP production and respiratory chain enzyme activities in mitochondria isolated from small muscle biopsy samples. Anal Biochem 311(2):139–151. https://doi.org/10.1016/s0003-2697(02)00424-4

# Chapter 22

# Janus-Type Mesoporous Silica Nanoparticles for Sequential Tumoral Cell and Mitochondria Targeting

**Maria Rocio Villegas, Victoria Lopez, Verónica Rodríguez-García, Alejandro Baeza, and María Vallet-Regí**

## Abstract

The development of nanoparticles has provided a powerful weapon in the fight against cancer due to the discovery of their selective accumulation in tumoral tissues, known as *enhanced permeation and retention* (EPR) effect (Peer et al, Nat Nanotechnol 2:751–760, 2007). Tumoral tissues require afastformation of blood vessels to sustain this rapid growth.

**Key words** Nanomedicine, Janus nanoparticles, Sequential targeting, Mitochondria targeting, Antitumoral therapy

## 1 Introduction

The development of nanoparticles has provided a powerful weapon in the fight against cancer due to the discovery of their selective accumulation in tumoral tissues, known as *enhanced permeation and retention* (EPR) effect [1]. Tumoral tissues require a fast formation of blood vessels to sustain this rapid growth. The accelerated angiogenesis is chaotically carried out yielding tumoral blood vessels which present high porosity and tortuosity [2]. Thus, when the nanoparticles reach the tumoral tissue, they pass through these pores accumulating there, whereas they cannot escape from healthy blood vessels. Additionally, tumoral tissues usually present an inefficient drainage as a consequence of the collapse of lymphatic vessels [3]. Therefore, the extravasated nanoparticles are not cleared from the tissue remain there during long periods of time. This paramount discovery opened a new way to deliver chemotherapeutic agents to malignant neoplastic tissues by

Maria Rocio Villegas, Victoria Lopez, and Verónica Rodríguez-García contributed equally to this work.

Volkmar Weissig and Marvin Edeas (eds.), *Mitochondrial Medicine: Volume 1: Targeting Mitochondria*, Methods in Molecular Biology, vol. 2275, https://doi.org/10.1007/978-1-0716-1262-0_22,

loading them within nanometric carriers. Nanocarrier selectivity against tumoral cells has been enhanced by the attachment of targeting groups on their surface. These targeting agents are molecules such as antibodies [4], aptamers [5], vitamins [6], peptides [7], or synthetic small molecules [8], which bind specifically to certain cell membrane receptors overexpressed by cancerous cells. Interestingly, nanoparticles have also been functionalized with targeting agents able to recognize cellular organelles which enhance the efficacy of many chemotherapeutic drugs designed to act on then [9]. Thus, nanoparticles decorated with cellular and organelle targeting moieties have demonstrated improved capacity to destroy tumoral cells [10]. Many of these designs involves the random attachment of targeting agents on the particle surface, which implies a lack of control in the amount and space location of each targeting moiety. Recently, Ma and coworkers have studied in silico what is the most efficient configuration of targeting agents in dual-targeted nanocarriers concluding that Janus-type nanoparticles yield the higher engulfment by cell membrane [11]. Here, we have developed a robust methodology to asymmetrically decorate the surface of mesoporous silica nanoparticles (MSN) with a cellular targeting agent (folic acid) in one hemisphere and a mitochondria targeting group (triphenylphosphine) on the other side. The presence of triphenylphosphine, which is a cationic group, leads to an accumulation of nanoparticles on the highly negative mitochondria membrane [12] These Janus nanoparticles (J-MSN) were loaded with a potent cytotoxic drug, topotecan, and their therapeutic efficacy was evaluated using human prostate cancer cells (LNCaP) because these cells overexpress folate-binding proteins on their membrane [13]. Healthy preosteoblastic cells (MC3T3-E1) were used as control due to their lower expression of folate receptors. The results showed an enhanced selectivity and cytotoxic capacity of the dual-targeted J-MSN in comparison with nanoparticles functionalized with only one targeting moiety or none [14].

## 2 Materials

### 2.1 Solutions and Buffers

1. EtOH (95%): 57 mL of EtOH (99%) in 3 mL distilled water.
2. PBS 1×: Add 8 g of NaCl, 0.2 g of KCl, 1.44 g of $Na_2HPO_4$, and 0.24 g of $KH_2PO_4$ to 800 mL of distilled water. Then, adjust pH to 7.4 through the addition of HCl. Finally, fill up to 1 L with distilled water.

### 2.2 Cell Lines and Cell Culture Reagents

1. Mouse osteoblastic cell line MC3TE-E1 (subclone 4, CRL-2593; American Type Culture Collection, Manassas, VA).

2. Androgen-sensitive human prostate cancer cell line (CRL-1740; American Type Culture Collection, Manassas, VA).
3. α-Minimum essential medium (for MC3T3-E1 cell line),
4. Dulbecco's modified Eagle's medium (DMEM, for LNCaP cell line).
5. Fetal bovine serum (FBS).
6. L-glutamine, 200 Mm, 100SX.
7. Antibiotic Antimycotic 100X.
8. 0.05% Trypsin–ethylenediaminetetraacetic acid 1× (0.05% trypsin–EDTA 1×).
9. Trypan blue.
10. Solution of 4′,6-diamidine-2′-phenylindole dihydrochloride (DAPI) is prepared at a concentration of 1–5 $mg{\cdot}mL^{-1}$ in water. This solution is stored at 4 °C and protected from light.
11. Solution of MitoTracker Red FM is prepared at 1 mM in anhydrous dimethylsulfoxide (DMSO). This solution is stored at 4 °C, protected from light.

### 2.3 Cell Culture Equipment

1. Evos FL cell imaging system equipped with three light-emitting diode (LED) light cubes ($\lambda_{ex}$ [nm], $\lambda_{em}$ [nm]): 4′,6-diamidine-2′-phenylindole (DAPI; [257/44],[447/60], green fluorescent protein (GFP; [470/22],[525/50]), and red fluorescent protein (RFP; [531/40],[593/40]), from AMG (Advance Microscopy Group).
2. Synergy 4 S4MFTA Multi-Detection Microplate Reader with power supply for Biotek Laboratory Instruments 100-240VAC, 50/60 Hz,250 W.
3. Thermo Spectronic Unicam UV-510 UV–visible spectrophotometer (UV500Series, wavelength range 190–900 nm, 120–240 V, 50/60 Hz, 350vA).
4. Flow cytometer FACSCan (Becton Dickinson).

## 3 Methods

Carry out all procedures at room temperature, unless otherwise specified.

### 3.1 MSN Synthesis

#### 3.1.1 Synthesis of APTES-FITC

To carry out cell internalization studies, MSN must be covalently labeled with a fluorophore. So that, the first step of the synthesis is the chemical link of the silica precursor (APTES, aminopropyltriethoxy silane) with FITC fluorophore (Fluorescein isocyanate) (*see* **Note 1**).

1. Dissolve a mass of 4 mg of FITC in 0.5 mL of EtOH and 10 μL of APTES.
2. Stir the mixture with a magnetic stirrer for 2 h at 200 rpm.

### 3.1.2 Synthesis of MSN Labeled with FITC

Once the fluorescein is covalently linked to APTES, the synthesis of the mesoporous silica nanoparticles (MSN) is carried out. To create the structure of ordered pores into the silica particles surfactant CTAB (cetyltrimethylammonium bromide) is used (*see* **Note 2**).

1. Prepare 1.75 mL of alkaline aqueous solution of NaOH 2 M.
2. Pour 240 mL of deionized water and 1.75 mL of the previous NaOH solution in a flask to create a reaction medium.
3. Dissolve 500 mg of CTAB in the alkaline aqueous medium stirring for 15 min at 350 rpm and 80 °C in a magnetic stirrer.
4. Cover the flask opening with a septum.
5. In parallel, add the APTES-FITC agent previously synthesized to 2.5 mL of tetraethylorthosilicate (TEOS) (*see* **Note 3**).
6. With the help of a syringe and a needle, add dropwise the mixture obtained in **step 5** in the flask of **step 3** during 20 min without removing the septum cover. Prick the septum with a needle in case of overpressure.
7. Once added this solution, continue stirring the mixture 2 h at 350 rpm and 80 °C (*see* **Note 4**).
8. Remove the septum and pour the content of the flask into centrifuge tubes.
9. Centrifuge the centrifuge tubes for 10 min at 800 rpm and 25 °C.
10. Discard the liquid phase, add water and stir manually until dispersion of particles.
11. Repeat **step 9** and discard the liquid phase.

### 3.1.3 Removal of Surfactant in MSN

The ordered pores will be used to load antitumor drugs. Therefore, it is necessary to remove the surfactant which remains inside the silica network.

1. Add 200 mg of $NH_4NO_3$ to 60 mL of EtOH (95%) solution and stir until complete dissolution.
2. Add 200 mg of $NH_4NO_3$ to this solution and stir until complete dissolution.
3. Add the nanoparticles prepared in Subheading 3.1.2 to this solution and stir for 2 h at 300 rpm and 60 °C employing a reflux condenser to avoid EtOH evaporation.
4. Pour the product in centrifuge tubes and centrifuge for 5 min at 14,600 × *g*.

5. Discard the liquid phase.
6. Repeat **steps 1–6** twice more.
7. Add de-ionized water in the centrifuge tubes, stir manually until dispersion of the particles and centrifuge again.
8. Discard the liquid phase.
9. Add pure EtOH in the Eppendorf tubes, stir manually until redispersion of the particles and centrifuge again.
10. Repeat **step 10**.
11. Discard the liquid phase.
12. Dry the washed solid in a vacuum oven at room temperature for 24 h.

The surface charge of nanoparticles is characterized by Zeta potential, their size is measured by dynamic light scattering (DLS) and scanning electron microscopy (SEM). The presence of residual surfactant inside pores is determined by Fourier-Transform Infrared spectroscopy (FTIR), thermogravimetric analysis (TGA) and $N_2$ adsorption. (See Characterization Techniques).

### *3.2 Asymmetric Functionalization of MSN (Fig. 1)*

#### *3.2.1 Step 1: Attachment of Amino Groups Employing a Pickering Emulsion Method (Fig. 2)*

1. Add 4.4 mL of pure EtOH, 11.6 mL of milliQ water, 200 mg of MSN synthesized in the previous step, and 2 mg of CTAB to a Schlenk Tube with two nozzles.
2. Sonicate the Schlenk Tube 5 min.
3. Add 0.5 g of paraffin to the Schlenk Tube.
4. Heat the mixture at 70 °C in a water bath (point at which the paraffin melts).
5. Once the paraffin is melted, heat the upper part of the tube with a heater to ensure a uniform temperature.
6. When the tube is completely heated at 70 °C, place it quickly on a Vortex stirrer for 80 s (*see* **Note 5**).
7. Then, place the Schlenk Tube under cold water so that the paraffin droplets solidify embedding partially the nanoparticles.
8. Filter the mixture with a 0.45 μm nylon pore filter paper in a Kitasato flask employing a vacuum pump.
9. Now, the exposed surface of MSN will be functionalized (**steps 10–12**).
10. Place the filtered paraffin mass in an Erlenmeyer flask together with 14 mL of EtOH, 1.5 mL of $NH_3$, and 0.5 mL of APTES (*see* **Note 6**).
11. Put the flask in a in a Ecotron for 12 h at 150 rpm and 30 °C.
12. Repeat **step 8**.

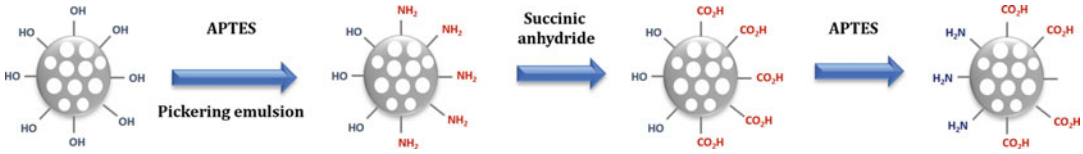


**Fig. 1** Asymmetrization process of MSN

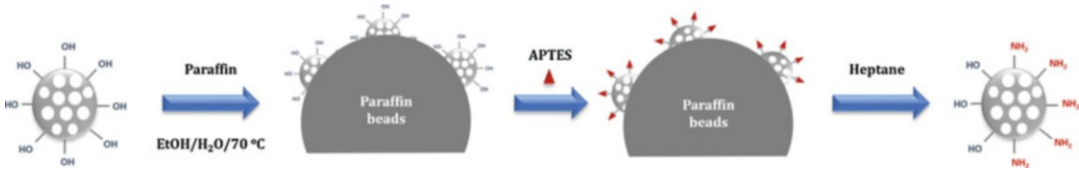


**Fig. 2** Attachment of amino groups on one hemisphere of MSN

*3.2.2 Paraffin Removal*

1. Add paraffin/nanoparticles harvested in Subheading 3.2.1 to 100 mL of Heptane (a non-polar solvent) in a flask.
2. Sonicate the mixture 30 min.
3. Filter the mixture with a 0.45 μm nylon pore filter paper in a Kitasato flask employing a vacuum pump.
4. Repeat **steps 1–3** two more times.
5. Dry in a vacuum oven harvesting MSN-$NH_2$.

*3.2.3 Step 2: Attachment of Carboxylic Acid Groups*

1. Place 200 mg of dried MSN-$NH_2$ and 40 mg of succinic anhydride on a 25 mL two-neck flask with a magnet inside and deoxygenate the flask (*see* **Note 7**).
2. Inject 10 mL of dry THF in the flask and stir the suspension during 12 h under $N_2$ atmosphere.
3. Filter the obtained nanoparticles with a 0.45 μm nylon pore filter paper in a Kitasato flask employing a vacuum pump and wash them with THF and water yielding MSN-$CO_2H$.

*3.2.4 Step 3: Attachment of Amino Groups*

1. Introduce 130 mg of MSN-$CO_2H$ in two-neck flask and deoxygenate the flask (*see* **Note 7**).
2. Inject 10 mL of dry toluene onto the flask and stir at 80 °C.
3. Once the temperature is reached, add 0.15 mL of APTES.
4. Set the temperature at 110 °C and stir the suspension overnight.
5. Filter the obtained nanoparticles with a 0.45 μm nylon pore filter paper in a Kitasato flask employing a vacuum pump and wash them with toluene and ethanol yielding $NH_2$-MSN-$CO_2H$.

### 3.3 Attachment of Targeting moieties on $NH_2$-MSN-$CO_2H$

#### 3.3.1 Attachment of Folic Acid to Prepare Folic-MSN-$CO_2H$

1. Introduce 22 mg (50 mmol) of folic acid in a two-neck flask with a magnet inside and remove the air (*see* **Note 7**).
2. Inject 2 mL of DMF–DMSO (4:1) solution in the two-neck flask and stir until complete dissolution of folic acid.
3. Add to this flask 36 mg of DCC and 38 mg of NHS previously dissolved in 0.5 mL of deoxygenated DMF–DMSO (4:1) mixture and stir during 30 min at room temperature under $N_2$ atmosphere.
4. Add the solution obtained in the previous step in a two-neck flask which contains 50 mg of $NH_2$-MSN-$CO_2H$ suspended in 3 mL of deoxygenated DMF–DMSO (4:1).
5. Stir the resulting suspension under $N_2$ atmosphere overnight.
6. Filter the obtained nanoparticles with a 0.45 μm nylon pore filter paper in a Kitasato flask employing a vacuum pump and wash them with DMF–DMSO (4:1), water and acetone yielding Folic-MSN-$CO_2H$.

#### 3.3.2 Attachment of Triphenylphosphine to Prepare $H_2N$-MSN-TPP

1. Mix 12 mg of DCC, 13 mg of NHS, and 100 mg of $H_2N$-MSN-$CO_2H$ in a two-neck flask with a magnet and deoxygenate the flask (*see* **Note 7**).
2. Add 2 mL of dry DMF and stir the suspension during 15 min under $N_2$ atmosphere at room temperature.
3. Add 5 μL of DIPEA to this suspension and after that, inject 41 mg of TPP derivative (synthesized according with the protocol described elsewhere[12]) previously dissolved in 0.5 mL of deoxygenated DMF.
4. Stir the mixture overnight under $N_2$ atmosphere.
5. Filter the obtained nanoparticles with a 0.45 μm nylon pore filter paper in a Kitasato flask employing a vacuum pump and wash them with DMF, water and acetone yielding $H_2N$-MSN-TPP.

#### 3.3.3 Synthesis of Dual-Targeted Nanoparticles Folic-MSN-TPP

1. Introduce 22 mg (50 mmol) of folic acid in a two-neck flask with a magnet inside and remove the air (*see* **Note 7**).
2. Inject 2 mL of DMF–DMSO (4:1) solution in the two-neck flask and stir until complete dissolution of folic acid.
3. Add to this flask 36 mg of DCC and 38 mg of NHS previously dissolved in 0.5 mL of deoxygenated DMF–DMSO (4:1) mixture and stir during 30 min at room temperature under $N_2$ atmosphere.
4. Add the solution obtained in the previous step in a two-neck flask which contains 50 mg of $H_2N$-MSN-TPP in 3 mL of DMF–DMSO (4:1).
5. Stir the resulting suspension under $N_2$ atmosphere overnight.

6. Filter the obtained nanoparticles with a 0.45 μm nylon pore filter paper in a Kitasato flask employing a vacuum pump and wash them with DMF–DMSO (4:1), water and acetone yielding Folic-MSN-TPP.

The surface charge of nanoparticles is characterized by Zeta potential. Their size is measured by dynamic light scattering (DLS). Asymmetrization process is evaluated following the change in surface charge after each step. The presence of each functional group is confirmed by FTIR after each synthetic step. Additionally, the introduction of amino groups only on one side of MSN is confirmed by transmission electron microscopy employing gold nanoparticles as contrast agents (see Characterization Techniques).

### 3.4 Loading Nanoparticles with Topotecan

1. Place 50 mg of each of the four sets of MSNs, namely, $NH_2$-MSN-$CO_2H$, MSN-Fol, MSN-TPP, and Fol-MSN-TPP, in different two-neck flasks with a magnet inside and dry the nanoparticles at 80 °C under vacuum during 4 h. Protect the flasks with aluminum foil to maintain in darkness the nanoparticles and topotecan. in a dark glass vial to avoid light interactions, as the Topotecan is light sensitive.
2. Add 5 mL of an aqueous solution of TOP (3 mg·$mL^{-1}$) and stir the suspension at room temperature during 48 h.
3. Filter the nanoparticles to remove the excess TOP and wash three times with water.
4. The amount of drug loaded in each system is determined from the difference between fluorescence measurements of the initial and recovered solutions ($\lambda_{exc} = 400$, $\lambda_{em} = 540$ nm). In all cases, the amount of TOP loaded is around 5% in weight.

### 3.5 In Vitro Nanoparticle Uptake and cytotoxicity Evaluation

#### 3.5.1 Laminar Flow Cabinets Use

The laminar flow hood, which presents vertical flow, is designed to avoid samples from contamination and protect laboratory workers from the biological samples. All the cell protocols described are carried out within a laminar flow hood whenever possible. As safe considerations, the worker should be wearing laboratory coat, eye protection, gloves, and closed shoes. The main rules to work in a laminar flow cabin are: [15].

1. Turn on the UV light and laminar flow for approximately 30 min before using the laminar flow hood.
2. Turn off the UV light (*see* **Note 8**).
3. Turn on the light.
4. Put on your gloves and sterilized them before approaching the hood by spraying them with ethanol and rubbing your hands together (*see* **Note 9**).

5. Thoroughly wash laminar flow hood by spraying with 70% ethanol, diluted bleach or other disinfectant and dry with paper.
6. After proper sterilization spraying with 70% ethanol, place all the reactants, solutions and materials required for the experiment inside the cabinet. Any object that is introduced in the hood must be previously disinfected,
7. Always work away from the grille toward the inside of the cab (work area).
8. While working inside the hood, always keep flasks, bottles, conical tubes, and other containers closed excepting the moment of their use in order to avoid contamination. In addition, avoid the contact of pipettes with containers as it can transfer traces of contamination between sterile materials.
9. Once the work has been completed inside the booth, secure all reagents, dissolutions, and materials before extraction to maintain their sterility. Clean all material in contact with cells using bleach and ethanol after use.
10. Once the hood is empty, clean all surfaces with ethanol. If there is a liquid spill containing cells, perform a prior disinfecting with bleach.
11. Turn off the laminar flow and turn on the UV light for 30 minutes.
12. After 30 min, turn off the UV light.

### 3.5.2 Cell Line Culture

Biological experiments will be carried out inside the laminar flow cabin, whenever possible. All media and solutions used during the following protocols, such as PBS 1X, cell culture medium, and fluorescent dye, are brought to room temperature prior to their use.

1. Incubate culture cell line of interest (mouse osteoblastic cell line MC3T3-E1 and androgen-sensitive LNCaP cells) using a suitable culture medium (*see* **Note 10**) in a hatcher (*see* **Note 11**) to 80% confluency.
2. When the cell cultures are at 80% confluence or above, trypsinize the cells and placed them into 24-well plates to carry out uptake and cell viability experiments.

   To trypsinize the cells proceed as follows (*see* **Note 12**):

   (a) Remove cell culture flask from the incubator and introduce it into the laminar flow cabinet.

   (b) Remove cell culture medium and dispose it in bleach.

   (c) Wash twice the cell culture with sterile PBS 1×, pH 7.4 (*see* **Note 13**).

(d) Dispense enough trypsin–EDTA (*see* **Note 14**) solution into cell culture flask to completely cover the monolayer of cells (approximately 3–5 mL to cell culture flask with a surface of 175cm$^2$) and place into an incubator for 2–5 min until all cells detach (*see* **Note 15**). After this time the cells should be in suspension (*see* **Note 16**).

(e) Take the cell culture bottle out of the incubator and put it back into the laminar flow cabinet.

(f) It is advisable to add medium (approximately 10 mL) (*see* **Note 10**) to the cell suspension in trypsin–EDTA as soon as possible in order to inhibit further proteolytic activity of trypsin, which could damage the cells.

(g) Transfer the cell suspension by serological pipette to a 50 mL conical tube.

(h) Centrifuge at room temperature at 1500 rpm for 5 min.

(i) Take the conical tube out of the centrifuge and put it back into the laminar flow cabinet.

(j) Remove the supernatant and suspend cells in 4 mL of cell medium by gently pipetting the cell suspension to break up the clumps.

3. Then, count the cells using any commercial automated cell counter or any other protocol. In order differentiate the living cells from the dead; add 100 μL of trypan blue to a small amount of the medium with cells, approximately 100 μL. The trypan blue enters the cells and while the living cells can expel it, in the dead cells it is retained and is therefore marked with a blue color. The automatic cell counter can differentiate them and provide the real number of living cells per mL.

4. Finally, plate cells at a density of 20,000 cells·cm$^{-2}$ in 1 mL of α-minimum essential medium (for MC3T3-E1 cell line) or Dulbecco's modified Eagle's medium (DMEM, for LNCaP cell line) in 24-well plate and incubate them at 37 °C in a humidified atmosphere of 5% $CO_2$ for different times (*see* **Note 17**). All cell studies described below will be performed on both types of cultures.

### *3.5.3 Nanoparticle Uptake Studies by Flow Cytometry*

1. After 24 h of incubation, remove the cell culture from the incubator and place it in the laminar flow cabinet.

2. Carefully remove cell culture medium by aspiration and delete in bleach.

3. Add 1 mL of fresh medium with and without MSNs sample (6 μg·mL$^{-1}$) (*see* **Note 18**) using P1000 micropipette to each well of both cell culture. In this step the types of samples used are $NH_2$-MSN-$CO_2H$, MSN-Fol, MSN-TPP, and Fol-MSN-TPP, also medium without nanoparticles is used as control culture.

4. Introduce 24-well plate with cells into incubator (*see* **Note 11**).
5. Incubate cells in absence or presence of MSNs sample during 2 h.
6. Remove cell culture from incubator and put it into laminar flow cabinet.
7. Remove cell culture medium with or without MSNs.
8. Wash the cell culture with PBS 1× twice (*see* **Note 13**).
9. Add 500 μL of trypsin–EDTA solution per well for cell detachment (*see* **Note 14**).
10. Remove the 24-well plate from the laminar flow cabinet and introduce it into the incubator for 2–5 min (*see* **Note 15**). After this time the cells should be in suspension (*see* **Note 16**).
11. Take the cell culture bottle out of the incubator and put it back into the laminar flow cabinet.
12. It is advisable to add medium (approximately 1 mL) to cell suspension in trypsin–EDTA as soon as possible in order to inhibit further proteolytic activity of trypsin, which could damage cells.
13. Transfer the cell suspension of each well by micropipette to a 2 mL Eppendorf tube.
14. Centrifuge the Eppendorf tubes at room temperature and 1500 rpm for 5 min.
15. Take the Eppendorf tubes out of the centrifuge and put them back into the laminar flow cabinet.
16. Remove the supernatant and resuspend the cells in 300 μL of fresh cell culture medium by gently pipetting the cell suspension to scatter clumps.
17. Quench the fluorescence outside cells by adding trypan blue in each well (reaching a final concentration of 0.4%). The surface fluorescence is quenched to eliminate the fluorescence of the nanoparticles that are on the membrane of the cell and ensure that the fluorescence signal measured in the cytometer is due to the fluorescent nanoparticles which are located inside the cells, that is to say, which have been engulfed by cells.
18. If the cytometry analysis is not performed immediately, storage cells in presence of ice and never for more than 1 h.
19. Perform flow cytometric measures using an excitation wavelength of 488 nm and measure green fluorescence signal at 530 nm in a FACScan machine. Analyze at least 10,000 cells in each sample for statistical significance.
20. Analyze the results using the appropriate software (Fig. 3).

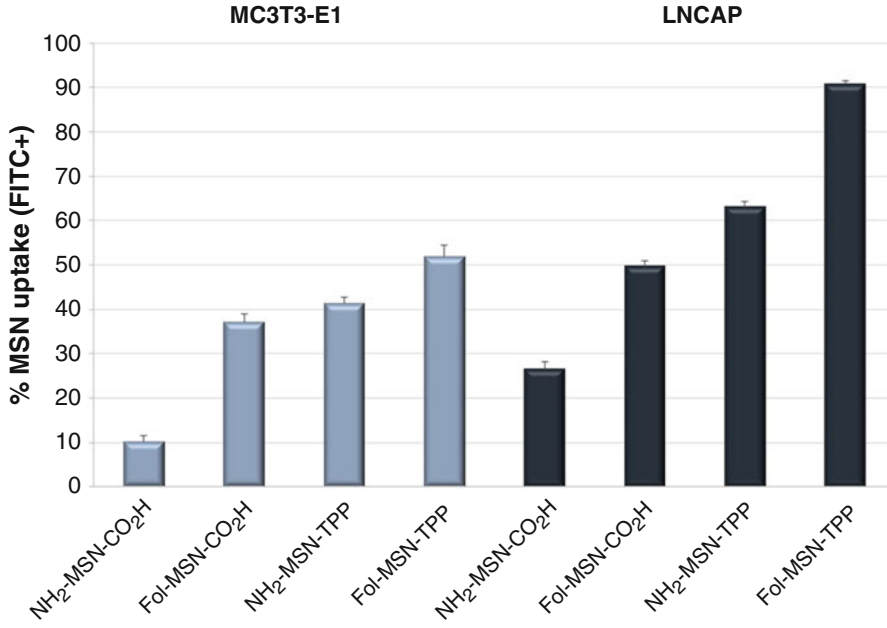


**Fig. 3** MSN-derivatives uptake evaluation by flow cytometry. (Reprinted (Adapted) with permission from López, Victoria, et al. "Janus mesoporous silica nanoparticles for dual targeting of tumor cells and mitochondria." . ACS applied materials & interfaces 2017, 9, 26697-26706. Copyright (2017) American Chemical Society)

*3.5.4 Nanoparticle Uptake Studies by Fluorescent Microscopy*

1. Incubate cells placed in a 24-well plate in an incubator until cultures reach 50–70% confluences.
2. Remove the cell culture from the incubator and place it in the laminar flow cabinet.
3. Remove cell culture medium by aspiration and delete in bleach.
4. Add 1 mL of fresh medium with or without MSNs sample (6 $\mu g \cdot mL^{-1}$) (*see* **Note 18**) to each well of both cell culture. In this step the types of samples used are $NH_2$-MSN-$CO_2H$, MSN-Fol, MSN-TPP, and Fol-MSN-TPP, also medium without nanoparticles is used as control culture.
5. Introduce 24-well plate with cells into incubator.
6. Incubate cells in absence or presence of MSNs sample during 2 h.
7. Remove cell culture from incubator and put it into laminar flow cabinet.
8. Remove cell culture medium with or without MSNs.
9. Wash the cell culture with PBS 1× twice (*see* **Note 13**) to remove all nanoparticles that have not been internalized by the cells.

10. Dilute 1 mM MitoTracker® stock solution to the final working concentration in the appropriate cell culture medium (*see* **Notes 19–21**).
11. To stain mitochondria of adherent cells, incubate cells for 15–45 min (*see* **Note 20**) with MitoTracker Red FM working solution under growth conditions (*see* **Note 11**). Staining is produced by passive diffusion of the MitoTracker, which contains a mildly thiol-reactive chloromethyl moiety, across the plasma membrane and by subsequent accumulation in the active mitochondria.
12. Once staining is complete replace the staining solution with fresh prewarmed cell culture medium and wash the cell culture with cell culture medium twice (*see* **Note 13**).
13. To fix the cells, carefully remove the medium covering the cells and replace it with freshly prepared and prewarmed at 37 °C cell culture medium containing 2–4% formaldehyde for 5–15 min.
14. Then, prepare a solution 1 $\mu g \cdot mL^{-1}$of DAPI in methanol for nucleic acid staining (*see* **Note 22**). DAPI is a blue fluorescent dye, cell permeable, which binds to double stranded complex.
15. Add 500 μL of DAPI solution per well and put the plate into the incubator for 15 min.
16. After incubation wash the wells with methanol (using a similar protocol to that detailed to PBS 1× in **Note 13**).
17. Add 500 μL of sterile PBS 1× and take pictures by fluorescent microscopy (Evos FL cell imaging system equipped with three light-emitting diode (LED) light cubes ($\lambda_{ex}$ [nm], $\lambda_{em}$ [nm]): 4′,6-diamidine-2′-phenylindole (DAPI; [257/44],[447/60], green fluorescent protein (GFP; [470/22],[525/50]), and red fluorescent protein (RFP; [531/40],[593/40]), from AMG (Advance Microscopy Group)) (Fig. 4).

*3.5.5 Cell Viability Evaluation After Incubation with Topotecan-Loaded Mesoporous Silica Nanoparticles*

1. Cells are cultured in 24-well plate following the procedure described in Subheading 3.5.2.
2. After 24 h of incubation, remove the cell culture from the incubator and place it in the laminar flow cabinet.
3. Remove cell culture medium by aspiration and delete in bleach.
4. Add 1 mL of fresh medium with MSNs ($NH_2$-MSN-$CO_2H$, MSN-Fol, MSN-TPP, and Fol-MSN-TPP) loaded or not with TOP (see **Note 18**). In this step use two concentrations of nanoparticles different (6 $\mu g \cdot mL^{-1}$ or 100 $\mu g \cdot mL^{-1}$) for each type of sample. Also, medium without any type of nanoparticles is used as control culture.
5. Introduce the 24-well plate with the cells into incubator.

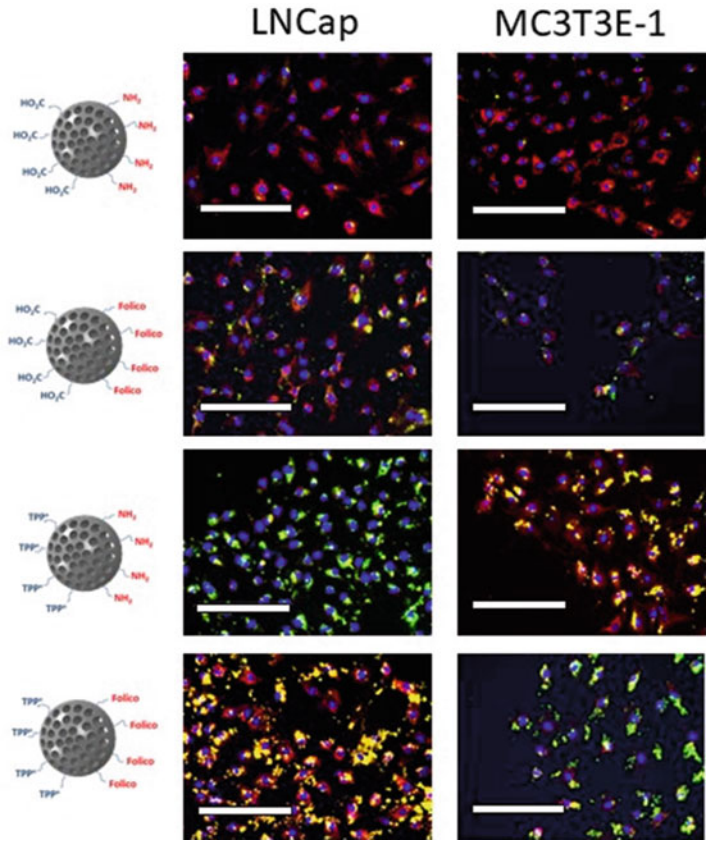


**Fig. 4** MSN derivative uptake evaluation by fluorescence microscopy. White bars correspond to 200 μm. (Reprinted (Adapted) with permission from López, Victoria, et al. "Janus mesoporous silica nanoparticles for dual targeting of tumor cells and mitochondria." ACS applied materials & interfaces 2017, 9, 26697-26706. Copyright (2017) American Chemical Society)

6. Incubate Cells in absence or presence of sample at different concentration (6 $\mu g \cdot mL^{-1}$ or 100 $\mu g \cdot mL^{-1}$) during 6 h.
7. Remove cell culture from incubator and put it into laminar flow cabinet.
8. Remove cell culture medium with or without nanoparticles.
9. Wash with sterile PBS 1× to eliminate nanoparticles that have not been engulfed by cells (*see* **Note 13**).
10. Add 1 mL of fresh medium and kept the 24-well plate into the incubator for 48 h more.
11. Remove cell culture from the incubator and put it into laminar flow cabinet.
12. Remove cell culture medium with or without nanoparticles.
13. Wash with sterile PBS 1× (*see* **Note 13**).

14. Prepare a solution of MTS according with the protocol described elsewhere [15] (previously brought to 37 °C and protected from light) in growth medium (1 mL of MTS per 6 mL of medium).
15. 500 μL of MTS solution is added per each well and placed into the incubator protected from light for 1–4 h.
16. Record the absorbance at 490 nm using a well plate reader.

## 3.6 Characterization Techniques

These measurements are carried out employing Malvern Zetasizer equipment and their respective protocols. The samples are prepared as follows:

### 3.6.1 Zeta Potential and DLS Measurements

1. Suspend the silica nanoparticles in HPLC water (1 mg/mL).
2. Sonicate 3 min sto avoid aggregates before introducing the solution into the cell.
3. When adding the suspension to the cell avoid the formation of bubbles.
4. The measurements, both size and Z potential, are carried out at room temperature.

### 3.6.2 Thermogravimetric Analysis (TGA)

Thermogravimetry (TG) is defined as the technique that measures the weight change of a sample respect to temperature by subjecting the sample to a temperature-controlled program in a controlled atmosphere. In this case, this technique is used to measure the organic matter of the nanoparticles in the different steps of the synthesis.

1. Heat 19 mg of sample in air atmosphere from 30 °C to 600 °C at a rate of 5 °C/minute.
2. A mass versus temperature curve is obtained from which we obtain the percentage of mass lost in said temperature range.

### 3.6.3 Fourier Transform Infrared Spectroscopy

Fourier Transform Infrared spectroscopy (FTIR) is used in the characterization of different compounds to identify the functional groups present in the samples. This technique is based on the infrared light energy being absorbed by the sample, causing molecular vibrations. This excitation causes the change in amplitude in the chemical bonds that will be measured.

1. Mix a small amount of sample with a highly purified salt that does not present absorption peaks in the IR spectrum (as potassium bromide).
2. Crush and press the mixture in order to form a pill through which the light can pass.

### 3.6.4 Analysis of Textural Properties of MSN by $N_2$ Adsorption

Gas adsorption technique is used to characterize the pores and surface of the nanoparticles. The amount of gas adsorbed at a given temperature for different relative pressures of gas is known as an adsorption isotherm. The *Type IV* is characteristic of mesoporous materials; it presents an increase in the significant amount absorbed at intermediate relative pressures and occurs through a multilayer filling mechanism. (The IUPAC recognizes three types of pore according to its size: macropore (>50 nm), mesopore (2–50 nm) and micropores (<2 nm)).

The measurement of the specific surface is carried out using the Brunauer–Emmett–Teller (BET) method, which estimates the area of the solid from the amount of gas needed to form a monolayer and the area occupied by one of the adsorbed molecules.

### 3.6.5 Scanning Electron Microscopy (SEM)

Scanning electron microscope is based on inducing a thin beam of accelerated electrons, with energies from a few hundred eV to a few tens of keV, on a thick, opaque to the electrons sample. The beam focuses on the surface of the sample and scans it. The samples destined to the SEM must meet two conditions: they must be dry and conductive.

1. Dry the samples in a vacuum oven the night before their observation.
2. Support geometry will depend on the SEM used. The sample should be conveniently adhered to said support, usually by using a carbon tape (to make it conductive) with double adhesive face.
3. Use a Metallizer to provide a gold coat to the samples by sputtering.

### 3.6.6 Asymmetrization Characterization by Transmission Electronic Microscopy (TEM)

In order to verify the correct Asymmetrization, a characterization by TEM is carried out. This test consists of mixing aminated nanoparticles (MSNs-$NH_2$) with gold nanoparticles. Gold nanoparticles present high affinity by amino groups, so these are strongly attracted by them. Thus, it is possible to check whether gold nanoparticles appear only in one nanoparticle hemisphere by transmission electron microscopy and, therefore, whether the asymmetrization process has been carried out correctly. The steps to perform this assay consists in:

1. Weight 0.5 mg of mesoporous silica nanoparticles (MSNs) and amino functionalized mesoporous silica nanoparticles (MSNs-$NH_2$) on a high-precision balance.
2. Introduce each sample in a 15 mL falcon tube.
3. Add 0.5 mL of miliQ water in each falcon and use ultrasound bath in order to obtain a correct dispersion, that nanoparticles are in a stable suspension.

4. Introduce 10 mL of 5 nm spherical gold nanoparticles (AuNP) using a 10 mL-micropipette in each tube. In this case gold nanoparticle concentration is $5.5 \cdot 10^{13}$particles/ml (commercial information).
5. Keep the mixture (0.5 mg of nanoparticles (MSNs) and amino functionalized nanoparticles (MSNs-$NH_2$) during 12 h at room temperature under stirring.
6. After 12 h, isolate mesoporous silica nanoparticles by centrifugation during 10 min at 5000 rpm. This centrifugation allows separate gold nanoparticles that have not reacted and remain in the supernatant due to their small size and high colloidal stability from the silica nanoparticles with or without gold nanoparticles on their surface, which precipitate due to their larger size.
7. Suspend the precipitate in 10 mL of water using ultrasound bath during 2–3 min in order to ensure that all gold nanoparticles in the precipitate are MSNs joined.
8. Centrifugate samples during 10 min at 5000 rpm.
9. Resuspend samples in 10 mL of water.
10. Place one drop of each sample, in stable suspension, on a copper strip for transmission electron microscopy.
11. Analyze the micrographs by statistical analysis. Then, at least 50 nanoparticles are counted and grouped into three groups, naked nanoparticles (MSNs that not present AuNP), uniform nanoparticles (MSNs that present AuNP in both hemispheres) and Janus nanoparticles (MSNs that only present AuNP in one of their hemispheres) (Fig. 5).

## 4 Notes

1. In this phase, a covalent bonding occurs between the isocyanate group of the dye and the amine group of APTES.
2. It is required the use of surfactant molecules in solution at a certain value of concentration (critical micellar concentration) for the synthesis of ordered porous materials, so that the molecules form micellar aggregates. These micelles, in turn, are grouped together forming supramicellar structures. In general, as the concentration of surfactants increases under moderate temperatures, the cylindrical micelles are grouped first, forming a hexagonal phase.
3. A fundamental condition for obtaining mesoporous nanoparticles is that there is an attractive interaction between the surfactant and the silica precursor (TEOS (tetraethylorthosilicate) and APTES-FITC) to ensure the inclusion of the steering

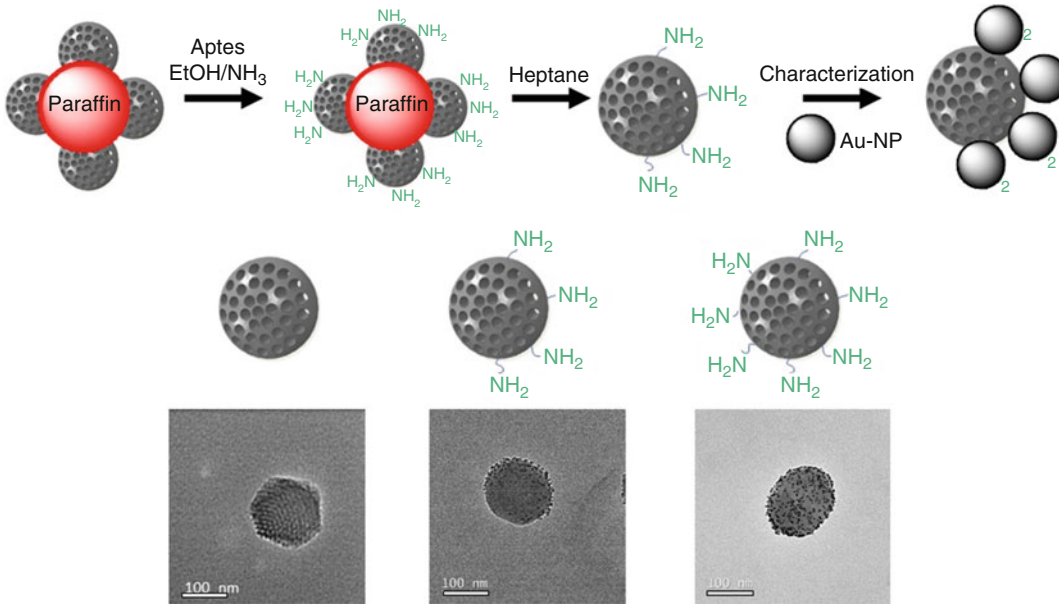


**Fig. 5** Gold nanoparticles in contact with MSN and MSN-$NH_2$. (Reprinted (Adapted) with permission from López, Victoria, et al. "Janus mesoporous silica nanoparticles for dual targeting of tumor cells and mitochondria." ACS applied materials & interfaces 2017, 9, 26697-26706. Copyright (2017) American Chemical Society)

structure (cylindrical micelles) and without phase separation. APTES-FITC and TEOS experience a polycondensation reaction in the alkaline medium in presence of CTAB micelles, being finally covalently integrated into the final inorganic network.

4. An important factor to consider is the temperature of the polycondensation reaction, since at temperatures higher than 60 °C the diameter of the particles drops to the range of 100 nm, critical to exploit the EPR effect.
5. At this point, the paraffin will take the form of micrometric droplets since it is not soluble in water. At the same time, with the help of CTAB, the nanoparticles will be partially embedded in the surface of the droplet, in such a way that half of the nanoparticle will remain inside the droplet and the other half facing the outside.
6. The ammonia provides a basic means that causes the silanol groups of the APTES (Si-OH) to become silanates (Si-O-) causing another polycondensation reaction and getting the particles embedded in the paraffin with its outer part functionalized with amino groups.
7. How reactives are deoxygenated/dried?

The flask used is a two-neck flask. One neck is connected by PTFE key to the $N_2$/vacuum line and the other one is sealed with a septum. Once MSN and succinic anhydride are added, the air is removed applying vacuum during 3 h and then $N_2$ is introduced in the flask. After this, solvent can be added with a syringe through the septum without introducing air in the flask.

8. The most of laminar flow hoods are equipped with ultraviolet (UV) lights, which reduce contamination by causing DNA damage to potential contaminants. It is important to know that such light is also harmful to laboratory worker who should not look directly at a UV light, as it can produce eye damage. UV light can also cause skin burns, then it should always be tuned off during working time in the hood.
9. Users hands should remain in the hood whenever possible during the experiment. The hand cleanliness is decreased each time nonsterile items are touched; therefore the disinfecting procedure should be repeat periodically. Face, hair or clothing must not be touch under any circumstances while working on the hood.
10. α-minimum essential medium is used for MC3T3-E1 cell line, whereas Dulbecco's modified Eagle's medium (DMEM) is used for LNCaP cell line. Both media contain 10% heat-inactivated fetal bovine serum (FBS) and 1% of antibiotic antimycotic. FBS is previously inactivated by incubation in a water bath at 50 °C for 1 h.
11. Each cell type must be incubated under growth conditions. In this case incubator conditions are 37 °C and a humidified atmosphere of 5% $CO_2$.
12. Cell culture medium, PBS 1×, and trypsin should be brought to 37 °C prior to their use with cell cultures.
13. The procedure for washing a cell monolayer with PBS 1x involves the following steps.
    (a) Add 10 mL of sterile PBS 1× in the cell culture flasks or 1 mL in each well in 24-well plate and wash the cell monolayer by gentle movements to remove remaining cellular medium.
    (b) Remove PBS 1× by aspiration.
    (c) Repeat the procedure twice in order to delete all traces of cell culture medium.
    (d) The procedure is the same when the cell culture is washed with culture medium so, in this case, the PBS is replaced by culture medium.

14. It is advisable to distribute the commercial bottle of trypsin in small quantity containers (depending on the periodicity of use) in order to reduce the freeze-thaw cycles.
15. The time required to detach cells from the cell culture flask depend on cell type, population density, potency of trypsin, serum concentration in the growth medium, and time since last subculture. Considering that trypsin causes cellular damage, the process of trypsinization should be minimized as much as possible.
16. When the cells are adhered to the surface of the culture bottle the medium has a transparent appearance whereas when trypsin detaches them, these remain in suspension and the medium presents a cloudy appearance.
17. In order to continue with cell culture a part of the cells must be subculture in a cell culture bottle with 15–20 mL of the corresponding growth medium.
18. Nanoparticle suspensions in sterile PBS 1× should be obtained by means of smooth and periodic pipette movements. Occasionally, and only if necessary, the solution can be introduced into an ultrasonic bath in order to obtain a stable suspension although the submersion period should not be long. This is especially critical when the nanoparticles are loaded with a cytotoxin, as the ultrasonic bath could produce a premature release of the toxic agent. In order to obtain statistically significant data, each type of sample is added to three wells to have three replicates.
19. When using the MitoTracker reagent or the DAPI, the cabin light must be turned off so that these reagents are not exposed to light.
20. Before opening a MitoTracker vial it is necessary to bring it to room temperature. Then, in order to prepare a stock solution, the lyophilized MitoTracker ® should be dissolved in anhydrous dimethylsulfoxide (DMSO) to a final concentration of 1 mM. Store of the MitoTracker® dyes solutions must be frozen at $\leq -20$ °C and protected from light.
21. In order to avoid mitochondrial toxicity from overloading and reduce potential artifacts, the concentration of the MitoTracker working solution must be kept as low as possible.
22. DAPI storage conditions (protect from light).
    (a) Stock solution: 1–5 mg·mL $^{-1}$ in water is stable at −15 to −25 °C for about 12 months.
    (b) Working solution: working solution is obtained by diluting the stock solution with methanol to a final concentration of 1 μg·mL $^{-1}$ which is stable at 2–8 °C for 6 months.

## Acknowledgments

Author contributions: All authors contributed to manuscript preparation. The final version of the manuscript was approved by all authors. The authors declare no competing financial interest. This work was supported by European Research Council, ERC-2015-AdG (VERDI), Proposal No. 694160. The authors wish to thank the ICTS Centro Nacional de Microscopia Electrónica (Spain) and CAI Cytometer and Fluorescence Microscopy of the Universidad Complutense de Madrid (Spain) for assistance with microscopy.

### References

1. Peer D, Karp JM, Hong S, Farokhzad OC, Margalit R, Langer R (2007) Nanocarriers as an emerging platform for cancer therapy. Nat Nanotechnol 2:751–760
2. Jain RK, Stylianopoulos T (2010) Delivering nanomedicine to solid tumors. Nat Rev Clin Oncol 7:653–664
3. Fang J, Nakamura H, Maeda H (2011) The EPR effect: unique features of tumor blood vessels for drug delivery, factors involved, and limitations and augmentation of the effect. Adv Drug Deliv Rev 63:136–151
4. Vivek R, Thangam R, NipunBabu V, Rejeeth C, Sivasubramanian S, Gunasekaran P, Muthuchelian K, Kannan S (2014) Multifunctional HER2-antibody conjugated polymeric nanocarrier-based drug delivery system for multi-drug-resistant breast cancer therapy. ACS Appl Mater Interfaces 6:6469–6480
5. Lao Y, Phua KKL, Leong KW (2015) Aptamer nanomedicine for cancer therapeutics : barriers and potential for translation. ACS Nano 9:2235–2254
6. Vlashi E, Kelderhouse LE, Sturgis JE, Low PS (2013) Effect of folate-targeted nanoparticle size on their rates of penetration into solid tumors. ACS Nano 7:8573–8582
7. Field LD, Delehanty JB, Chen Y, Medintz IL (2015) Peptides for specifically targeting nanoparticles to cellular organelles: quo Vadis ? Acc Chem Res 48:1380–1390
8. Villaverde G, Alfranca A, Gonzalez-Murillo A, Melen GJ, Castillo RR, Ramírez M, Baeza A, Vallet-Regí M (2019) Molecular scaffolds as double-targeting agents for the diagnosis and treatment of neuroblastoma. Angew Chemie Int Ed 58:3067–3072
9. Ma X, Gong N, Zhong L, Sun J, Liang XJ (2016) Future of nanotherapeutics: targeting the cellular sub-organelles. Biomaterials 97:10–21
10. Pan L, Liu J, He Q, Shi J (2014) MSN-mediated sequential vascular-to-cell nuclear-targeted drug delivery for efficient tumor regression. Adv Mater 26:6742–6748
11. Xia Q, Ding H, Ma Y (2017) Can dual-ligand targeting enhance cellular uptake of nanoparticles? Nanoscale 9:8982–8989
12. Smith R, Porteous CM, Gane AM, Murphy MP (2003) Delivery of bioactive molecules to mitochondria in vivo. Proc Natl Acad Sci 100:5407–5412
13. Hattori Y, Maitani Y (2005) Folate-linked nanoparticle-mediated suicide gene therapy in human prostate cancer and nasopharyngeal cancer with herpes simplex virus thymidine kinase. Cancer Gene Ther 12:796–809
14. López V, Villegas MR, Rodríguez V, Villaverde G, Lozano D, Baeza A, Vallet-Regí M (2017) Janus mesoporous silica nanoparticles for dual targeting of tumor cells and mitochondria. ACS Appl Mater Interfaces 9:26697–26706
15. Bykowski T, Holt JF, Stevenson B (2019) Aseptic technique. Curr Protoc Essent Lab Tech 18:1–13

# Chapter 23

# Split Green Fluorescent Protein–Based Contact Site Sensor (SPLICS) for Heterotypic Organelle Juxtaposition as Applied to ER–Mitochondria Proximities

**Tito Calì and Marisa Brini**

## Abstract

In the last decades, membrane contact sites (MCSs) have been the object of intense investigation in different fields of cell physiology and pathology and their importance for the correct functioning of the cell is now widely recognized. MCS between any known intercellular organelles, including endoplasmic reticulum (ER), mitochondria, Golgi, endosomes, peroxisomes, lysosomes, lipid droplets, and the plasma membrane (PM), have been largely documented and in some cases the molecules responsible for the tethering also identified. They represent specific membrane hubs where a tightly coordinated exchange of ions, lipids, nutrients, and factors required to maintain proper cellular homeostasis takes place. Their delicate, dynamic, and sometimes elusive nature prevented and/or delayed the development of tools to easily image interorganelle proximity under physiological conditions and in living organisms. Nowadays, this aspect received great momentum due to the finding that MCSs' dysregulation is involved in several pathological conditions. We have recently developed modular, split-GFP-based contact site sensors (SPLICS) engineered to fluoresce when homo- and heterotypic juxtapositions between ER and mitochondria occur over a range of specific distances. Here we describe in detail, by highlighting strengths and weaknesses, the use and the application of these novel genetically encoded SPLICS sensors and how to properly quantify short- and long-range ER–mitochondria interactions.

**Key words** Endoplasmic reticulum, Mitochondria, Organelle contact sites, SPLICS, ER–Mitochondria tethering, Split GFP

## 1 Introduction

### *1.1 Old and New Approaches to Detect Organelle Contact Sites*

Physical and functional connections between two opposing organelle membranes, known as membrane contact sites (MCSs), occur in distinct domains and are essential for the regulation of a multitude of cellular processes [1]. In the past few years it has convincingly been shown that dysregulation in this communication is

Tito Calì and Marisa Brini contributed equally to this work.

Volkmar Weissig and Marvin Edeas (eds.), *Mitochondrial Medicine: Volume 1: Targeting Mitochondria*, Methods in Molecular Biology, vol. 2275, https://doi.org/10.1007/978-1-0716-1262-0_23,

associated with a number of pathological conditions. For these reasons, the study and the characterization of the contact sites as well as the search for their possible modulators are now very challenging.

Contact sites between selected organelles are considered as intracellular hubs where the general function of each organelle can be specifically tuned to perfectly cope with the cellular and/or environmental needs. A mutual cooperation ensures the coordination of essential physiological processes such as the binding and the transport of molecules/ions between the two compartments, as well as the engaging of the organelle during the process of biogenesis, the positioning and the dynamics of various protein complexes that required the concerted action of two different organelles. In all eukaryotes one of the largest organelles, the endoplasmic reticulum (ER), forms MCSs with mitochondria, Golgi, endosomes, peroxisomes, lysosomes, lipid droplets, and the plasma membrane (PM), but we also know that mitochondria can form selective contacts with the same partners of the ER. The interaction between ER and mitochondria is the best characterized so far, however the tools we have in our hands to explore it can be tricky. The oldest and more consolidate approach to elucidate the structure of ER–mitochondria contacts and to calculate their distance is the electron microscopy (EM) [2–6]. Starting from 1958 EM studies produced a complete and detailed view of the ER–mitochondria contacts: different 3D reconstructions of these structures were generated by serial, tilt-angle tomography in yeast cells [5] as well as by focused ion beam scanning EM at 4-nm resolution in neurons from mice brain slices [7], and by soft X-ray tomography with 50-nm resolution in mammalian lymphoblastoid cells [8]. However, the acquisition and reconstruction processes for these 3D approaches remain laborious and not easily accessible to all the laboratories. Therefore, despite very informative, this methodology is not yet widely applicable. Pioneeringly, the existence of the mitochondria associated membranes fraction (MAM) has been proven during cell-fractionation experiments in which subcompartmentalized ER membranes cosedimented with mitochondria [9]. To date, this approach, eventually validated by EM, is still considered the standard method when the presence/abundance of specific players at the ER–mitochondria interface has to be investigated [10]. However, the EM analysis is not able to generate sufficient data for statistical comparisons of organelle geometry. Other methods, mainly based on the colocalization of ER and mitochondrial markers and/or organelle targeted fluorescent proteins, are described in the literature and substantially contributed to analyze ER–mitochondria contacts architecture [11–14], but none of them has yet been applied to quantify the overall extent or the geometry of the interface, being their major limitation linked to insufficient confocal microscope resolution to detect the physiologically relevant interfaces, which are believed to be in a range below the 100–200 nm.

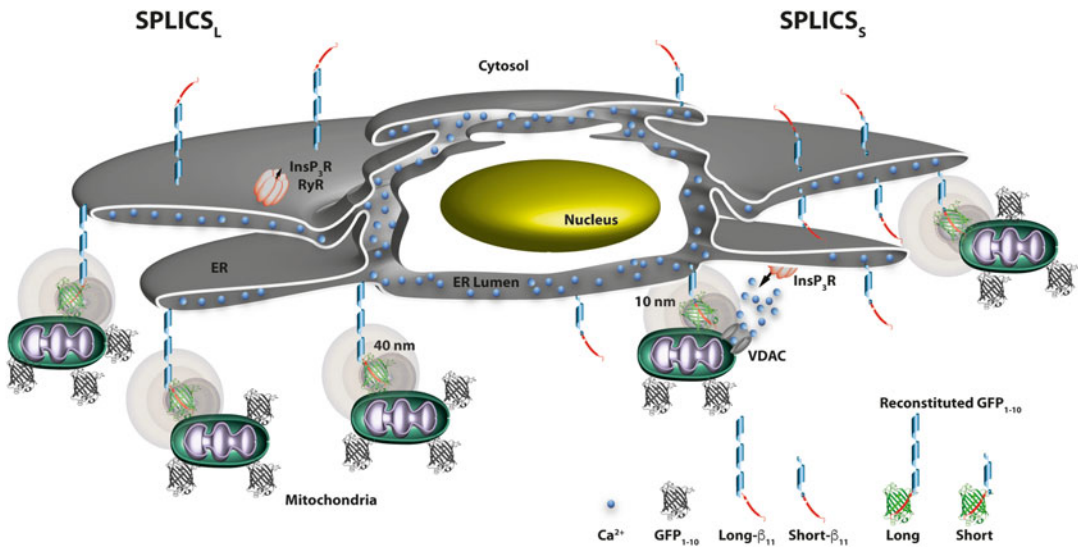


**Fig. 1** The cartoon summarizes the concept that ER–mitochondria tethering occurs at different distance in the cells. The two SPLICS probes, SPLICS$_L$ and SPLICS$_S$, were designed to monitor contact sites in the long (40 nm) and in the short (10 nm) range. The short-range contact sites are those involved in $Ca^{2+}$ transfer from ER to mitochondria. *InsP3* inositol 1,4,5 trisphosphate receptor, *RyR* ryanodine receptor, *VDAC* voltage-gated anion channel

The in situ proximity ligation assay (PLA) is another approach that has successfully been employed to visualize and quantify endogenous ER–mitochondria interactions in fixed cells by using pairs of primary antibodies against proteins on opposing membranes [15]. However, despite of this technique is widely used [16–18] it can only be applied upon cells fixation and is limited by the availability as well as by the specificity of the antibodies. More recently, a tool based on the system of rapamycin-inducible linkers tagged with a pair of fluorophores able to generate Förster resonance energy transfer (FRET) [19] has been developed for the specific detection and quantification of ER–mitochondria contact points. Major limitations in the use of this FRET-based probe are due to the need of equimolar expression of the two moieties [20] and, even more critical, to the need of rapamycin application, a potent inducer of autophagy [21], to reach maximal FRET signal, thus limiting its applications in in vivo settings. Novel tools based on a bifluorescence complementation system have been recently developed to measure interorganelle proximity [22–27], however, one missing aspect was the possibility to easily image them over a range of distances in living cells. On this respect, we have designed modular, split-GFP based contact site sensors (SPLICS) engineered to fluoresce when organelles are in close proximity (Fig. 1). The power of our probe is that it has been generated in two different variants suited to efficiently measure narrow (8–10 nm) and wide (40–50 nm) juxtapositions between ER and mitochondria

(SPLICS$_{S/L}$). Thanks to these characteristics it has permitted to document not only the existence of at least two types of contact sites in human cells and in vivo in *D. rerio* Rohon Beard (RB) sensory neurons, but also to unravel that they are differently modulated by genetic or pharmacological treatments [23]. Short- and long-range organelle contact sites between the ER and mitochondria can now be easily imaged and quantified under physiological conditions in vitro and in vivo with a high signal-to-noise ratio and over a dark background. Here we describe SPLICS sensors application and a semiautomated quantification protocol that we have set up to make the quantification of contact sites fast and accurate. The reliability of our genetically encoded SPLICS sensors is increasingly acknowledged by their successful employment in many laboratories to quantify the extent of ER–mitochondria interactions under physiological and pathological conditions [28–37].

### 1.2 The Split GFP Approach: Fiat Lux

Since its cloning in 1992 [38] the *Aequorea Victoria* green fluorescent protein (avGFP), an 11-stranded barrel structure of 238 amino acids [39], underwent several cycles of "evolution" that have improved its properties making it an extraordinary tool for the study of cells and organisms biology [40, 41]. In 1995, avGFP was evolved by site-directed mutagenesis to optimize its brightness and excitation efficiency at 488 nm excitation wavelength. The introduction of a S65T substitution accelerates the chromophore maturation and promotes the formation of hydrogen bonds that stabilize the anionic state, resulting in a fluorescent protein characterized by a brightness fivefold higher than that of avGFP and by a unique excitation peak at 489 nm [42]. One year later, the F64L mutation was introduced, leading to improved chromophore maturation at 37 °C which represents a great advancement for all the GFP application in mammals [43]. Sequence "humanization" of the S65T/F64L double mutant avGFP gave rise to the "enhanced-GFP" (eGFP), which combines a high expression efficiency in mammalian cells with a 30-fold increase in brightness in respect with the avGFP [44, 45]. Additional variants, such as the folding reporter GFP (frGFP) which includes folding mutations F99S, M153T and V163A, have been created in order to increase the folding efficiency in *E. Coli* and to reduce possible defect due to the fusion of the GFP moiety with other proteins [46, 47]. A big improvement that has certainly paved the road to the development of novel biosensors for a number of cellular processes has been the generation of the stable superfolder GFP variant (sfGFP) [48]. Six novel mutations in respect to the frGFP substantially increase sfGFP folding kinetics and render it completely unaffected by the fusion to poorly folded proteins and resistant to chemical/thermal denaturation. Starting from this variant, in 2015 Waldo's laboratory developed a splitGFP, in which the sfGFP moiety was truncated between β-strand 10 and 11 and

whose N- and C-terminal fragments were both mutated to optimize their suitability for fluorescence complementation and solubility. By cutting one by one the loops that connect each β-strand of sfGFP, the ability of each isolated β-strand to bind and restore fluorescence of the GFP moiety was tested and a proper cutoff site at position 214/215 was identified. After one random screen and three additional rounds of directed evolution on both the $GFP_{1–10}$ and the strand $\beta_{11}$ fragment, a stable, soluble bipartite splitGFP system with favorable association kinetics was born. The resulting splitGFP is optimized for self-association of its fragments and for minimal disturbance by fusion partners [49]. Compared to sfGFP the $GFP_{1–10}/\beta_{11}$ system, whose complementary fragments are nonfluorescent per se, incorporated 10 additional mutations. Nowadays the sfGFP-based self-associating bipartite split-GFP systems have been widely exploited to monitor cellular parameters as different as expression, localization, association, and trafficking of proteins within the cell [31, 50–55].

Our lab, for the first time, employed this system to monitor contact sites between intracellular organelles. Considering the high interest in the characterization of the ER–mitochondria communication, we have focused our attention on developing specific sensors to monitor contact sites between these two organelles [28]. To this aim the nonfluorescent $GFP_{1–10}$ moiety was targeted to the cytosolic face of the outer mitochondrial membrane (OMM-$GFP_{1–10}$), while the $\beta_{11}$ fragment was targeted to the ER membrane by creating two versions of fusion proteins containing aminoacidic linkers of different lengths in order to follow short- (≈8–10 nm) and long- range (≈40–50 nm) ER–mitochondria interactions [3]. In particular we generated an ER-Short $\beta_{11}$ version where the $\beta_{11}$ sequence was fused to a 29 aa spacer and an ER-Long $\beta_{11}$ version containing a 146 aa spacer. The resulting split GFP-based contact site sensors ($SPLICS_{S/L}$) were remarkably able to identify narrow and wide ER–mitochondria apposition lying in a range of around 10 and 50 nm and to promptly monitor how they responded to pharmacological and genetic manipulations known to affect ER–mitochondria tethering. We have shown that they work efficiently not only in different stable cells lines but also in primary cultures of different origins and in vivo in zebrafish sensory neurons. To date, they are the only genetically encoded sensors proven to efficiently detect ER–mitochondria contact sites in vivo [28].

## 2 Materials

All the materials and the methods described in the following sections are adapted to Hela cells, a model cell line we have chosen to set up this methodological approach. We and others have further validated it in other cell types different for embryological origin and

cell culture conditions. None of the specific conditions required for cell cultures or transfection according the cell specificity should in principle impact on the use of $SPLIC_{S/L}$ probes. Therefore, the protocol described below can be adapted. We only recommend to follow a standard method in the quantification procedure based on fixed criteria to be applied to the different samples that have to be compared. The protocol can be optimized starting from the plugins we describe below.

Prepare all solutions using ultrapure water, unless otherwise specified.

### 2.1 Cell Culture and Transfection

1. Cell type: HeLa cells.
2. Culture plate: 24- or 6-well cell culture plate.
3. 13 or 24 mm diameter round glass coverslips.
4. Culture medium: Dulbecco's modified Eagle's medium (DMEM) High glucose supplemented with 10% foetal bovine serum (FBS), 100 U/ml penicillin, and 100 μg/ml streptomycin.
5. Phosphate buffer saline solution (PBS): 140 mM NaCl, 2 mM KCl, 1.5 mM $KH_2PO_4$, 8 mM $Na_2HPO_4$ pH 7.4.
6. Trypsin solution.
7. Krebs Ringer Buffer (KRB): 125 mM NaCl, 5 mM KCl, 1 mM $Na_3PO_4$, 1 mM $MgSO_4$, 20 mM HEPES, pH 7.4, 37 °C containing 1 mM $CaCl_2$, 5.5 mM glucose.
8. Transfection reagents for calcium phosphate procedure: 2.5 M $CaCl_2$, HEPES buffered saline (HBS; 2× stock): 280 mM NaCl, 50 mM HEPES, 1.5 mM $Na_2HPO_4$, pH 7.12.
9. Transfection reagents for other transfection protocols are available from common suppliers of laboratory reagents.
10. DNA constructs: vectors encoding $SPLICS_S$ and $SPLICS_L$ ([28]), that is, OMM-$GFP_{1–10}$ and either the ER-Short $\beta_{11}$ or the ER-Long $\beta_{11}$ probes.
11. Antibodies: primary antibodies against GFP, secondary fluorophore conjugated antibodies.

### 2.2 DNA Purification

Plasmid DNA for cell transfection can be extracted using commercially available kits for DNA purification on large scale and following the manufactures instructions.

DNA working aliquots can be stored at −20 °C.

## 3 Methods

### 3.1 Protocol for Monitoring Basal ER–Mitochondria Contact Sites with $SPLICS_S$ and $SPLICS_L$

1. Maintain cells in their growth medium at 37 °C and 5% $CO_2$ until the day before the transfection.
2. The day before the transfection, seed HeLa cells (or other cell types) on 13 mm coverslips in a 24-well plate at low confluence ($3–4 \times 10^4$ cells/well) or 24 mm coverslips in a 6-well plate at low confluence ($2 \times 10^5$ cells/well).
3. Change the culture media with fresh DMEM 30 min before the transfection.
4. Cotransfect cells with the OMM-$GFP_{1–10}$ and either the ER-Short $\beta_{11}$ or the ER-Long $\beta_{11}$ probe (to detect short- and long-range ER–mitochondria contact sites, respectively) using calcium phosphate transfection protocol. For cotransfections, use a 1:1 ratio of OMM-$GFP_{1–10}$ and either the ER-Short $\beta_{11}$ or the ER-Long $\beta_{11}$ DNA, that is, a total of 4 μg for 13 mm coverslips and a total of 12 μg for 24 mm coverslips (*see* **Notes 1–6**). Cotransfection with a mitochondrial marker (mtRFP) or staining mitochondria with a specific dye (TMRM or Mito-Tracker) is strongly suggested (*see* **Note 7**). You can adjust transfection protocol according to the cell line. No limitations or side effect for the use of cationic lipids or PEI or electroporation or viral infection (*see* **Note 8**). Stable clones can also be generated (*see* **Note 9**).
5. Calcium phosphate precipitates can be toxic to HeLa cells; therefore, carefully remove them after 8–12 h of transfection by washing 3× with PBS. For other transfection procedures please refer to the manufactures protocol.
6. After waiting 24/36 h to achieve a good probe expression, the coverslips can either be fixed (with 3.7% (vol/vol) formaldehyde in PBS for 20 min and washed three times with PBS) and mounted on microscope glass or placed in the imaging chamber containing 1 ml of KRB/$Ca^{2+}$ buffer for live imaging.
7. Put the coverslip/chamber on the confocal microscope stage and bring the cells into focus using visible light. Possibly select a field with sparse cells. In our laboratory Leica SP5-TCS-II-RS inverted confocal microscope with excitation laser's wavelength of 488 nm is routinely employed to image ER–mitochondria contacts. HCX Plan APO 63×/numerical aperture 1.40 oil-immersion objective or other objectives with high numerical aperture and resolving power should be used.
8. Check the fluorescence emission at 488 nm excitation wavelength. Select cells that have a good signal-to-noise ratio with nonaltered mitochondria morphology, and images of good quality (*see* **Notes 10** and **11**).

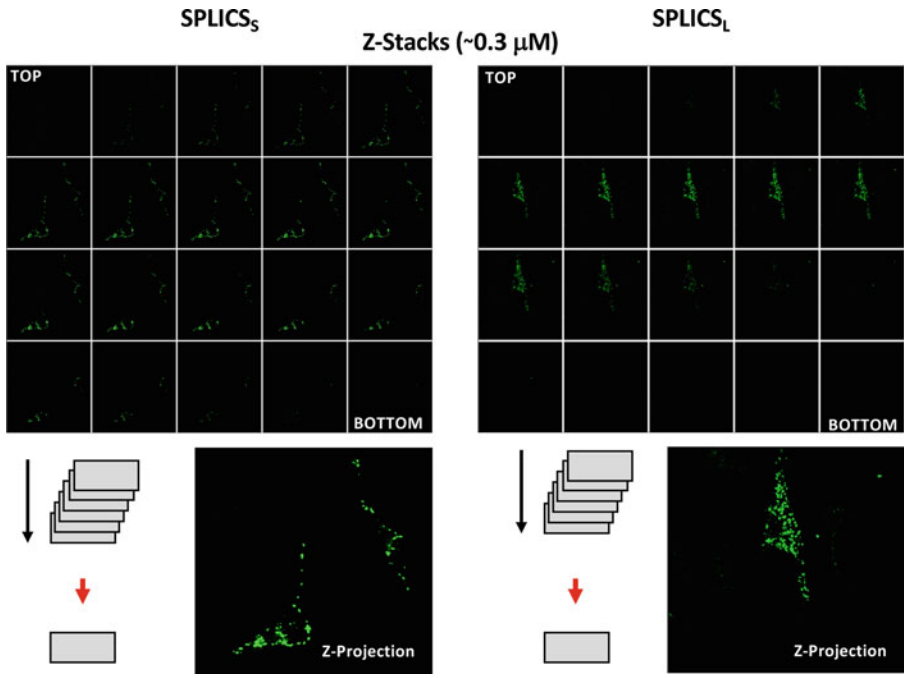


**Fig. 2** An example of Z-stack acquisition showing the ER–mitochondria contacts in all the planes and the Z-projection reconstitution

9. For all the acquired images set the following parameters: scanning mode as *xyz*, pinhole at 1 airy unit, format at 1024 × 1024, speed at 200 Hz, and pixel size around 100 nm.
10. To properly image ER–mitochondria contacts, it is recommended to acquire a Z-stack for the whole depth of the cell by sampling at 300 nm in the Z plane (*see* **Note 12**). *See* Fig. 2 as an example.
11. Process the complete z-stack using ImageJ (National Institutes of Health (NIH)). First convolve the images and then select the cells using the freehand selection of ImageJ in the drawing/selection polygon tool. Then proceed with the ER–mitochondria contacts quantification using the "Quantification 1" plugin.

    You can download "Quantification 1" plugin from https://drive.google.com/file/d/18KG4SwUIUBhegxfH_WZR44pLigtK_mm/view?usp=sharing.
12. Obtain a 3D reconstruction of the image resulting from the "Quantification 1" plugin using the Volume J plugin (http://bij.isi.uu.nl/vr.htm).
13. Threshold a selected face of the 3D rendering and use it to count short or long contact sites through the "Quantification 2" plugin (*see* **Note 13**).

You can download "Quantification 2" plugin from https://drive.google.com/file/d/1qqrHH5yMwC0JmyMxUigzkZjB-e4ppW5E/view?usp=sharing.

### 3.2 Protocol for Quantifying Basal ER–Mitochondria Contact Sites with $SPLICS_S$ and $SPLICS_L$

The protocol is illustrated in Fig. 3.

1. A Z-Stack covering the whole volume of the cell is acquired every 0.3 μM in order to acquire the number of the contact sites occurring over different Z-planes of the cell.
2. Open the Z-stacks with the FIJI software (from Image J) and apply the convolve filter. A matrix will appear with a number in the center. This number is usually correct, but sometimes it should be increased by one unit to improve the image. We discourage to decrease this value since it will lead to loss of signal. The changes must be applied to all the stacks.
3. A Gaussian Blur filter must then be applied to the convolved stacks. Even in this case a window will appear with a sigma (radius) value. We usually increase this value up to 1.5 or 2 to blur the image in order to reduce noise. Apply to all the stacks. The "Quantification 1" Plugin will provide with the blurred image that must be contrasted. The contrast of the blurred image should be slightly adjusted (Image, Adjust, Brightness/contrast) in order to reduce the blurring. Changes should be applied to all the stacks.
4. The processed image stacks are now ready to be 3D rendered. This process can be performed through the VolumeJ plugin, but cannot be automated since some settings must be adjusted.
5. Make sure that the correct stack is selected for rendering from the volume stack window.
6. Select the Isosurface rendering algorithm.
7. Set the Z-stack depth (0.3 μM) in the third panel of the aspect ratios.
8. Set the trilinear Interpolation mode.
9. Set the cine-total rotation to 180°.
10. Set the cine-frame increment at 20°.
11. Render the 3D stack with the render cine mode.
12. The VolumeJ plugin will give a series of 3D rendered images representing each plane of the total volume tilted by 20° for a total of a 180° rotation (a total of 9 images to be saved as image sequence).
13. The first and the last 3D rendered image will thus represent the top and the bottom of the cell and can be opened with the "Quantification 2" plugin to quantify the number of contact sites. Alternatively, the image must be thresholded (*see* **Note**

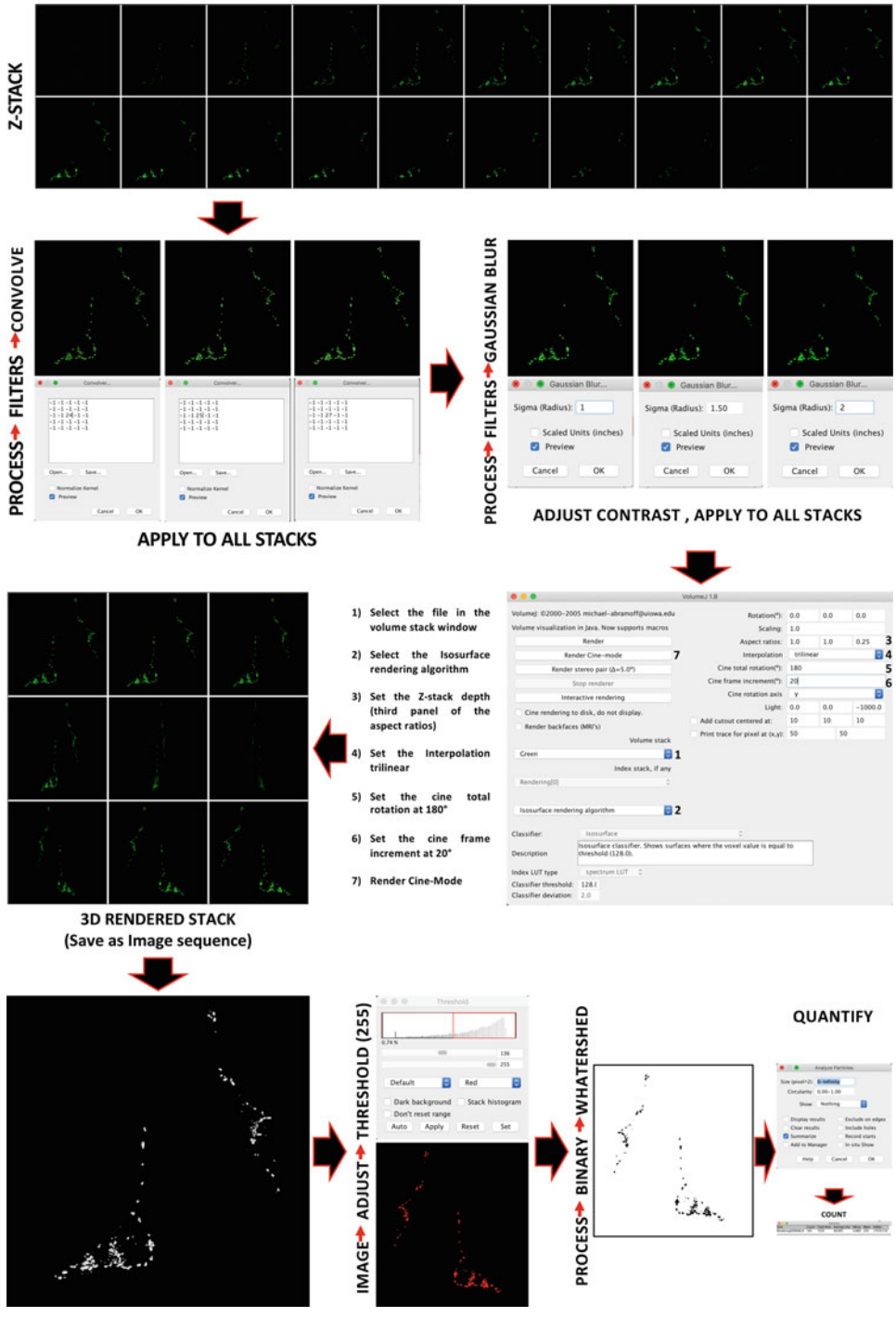


**Fig. 3** A flowchart illustrating the procedure for setting up the standard protocol for fluorescent dots quantification. For details see the Methods section

**13**) and the watershed binary process must be applied before the final quantification with the Analyze particle tool of FIJI software is performed. In general, we do prefer to count the number of objects per cell, though the Analyze particle tool will give additional parameters such as the volume or the intensity.

## 4 Notes

1. A good attachment and a homogenously distribution of the cells on the well/coverslip greatly enhances the efficiency of transfection. Try to avoid the accumulation of cells at the center of the well/coverslip.
2. Use the appropriate plastic tubes to prepare the transfection solution: polypropylene tubes are recommended when transfecting with the calcium phosphate procedure; avoid polystyrene tubes when transfecting with cationic lipids because of their propensity to bind them.
3. When SPILCS probes are cotransfected with other protein/s whose action on ER–mitochondria contact sites will be investigated, use a larger amount of cDNA expressing the probe (2:1 or 3:1 protein/SPLICS ratio) in order to avoid the possibility that the signals measured comes from cells transfected only with the SPLICS probe, thus underestimating the effect of the protein of interest. In any case, if the analysis of contact sites is performed in fixed cells, it is convenient to perform an immunocytochemistry analysis against the protein of interest.
4. Changing the culture medium of HeLa cells before the addiction of the transfection solution greatly enhances the efficiency of transfection.
5. Calcium phosphate precipitates are toxic for the cells. Carefully remove them after 12 h by washing the cells with PBS. Wash cells gently in order to avoid cells detachment.
6. Performing the experiment at least 24 h after transfection ensures both an ideal expression of the SPLICS probe (and, possibly, of the coexpressed protein of interest) and a full recovery of the transfected cells.
7. Targeting at the OMM is usually critical since can be accompanied by changes in the mitochondria morphology when expression levels are high. Thus, when working in transient transfection we strongly encourage to check the mitochondrial architecture in order to avoid misinterpretation of the results. The mitochondria architecture must be as in control/untransfected cells, for example, in HeLa cells under basal conditions mitochondria appears as a filamentous network. Therefore, the

contact sites number should be assessed in those cells whose mitochondria morphology is preserved.

8. The cDNAs for SPLICS expression could be easily cloned in viral expression system (adenoviral, adeno-associated viral, or lentiviral) and used to transduce cells resistant to transfection or primary cultures. We obtained preliminary evidence that the SPLICS probes, upon viral infection, work even in mouse primary neuronal cultures (not published).
9. The protocol described above refers to transient transfection, which is generally preferred in order to avoid the selection stable clones with peculiar characteristics. However, stable clones expressing $SPLICS_S$ or $SPLICS_L$ can be generated either upon selection with geneticin (whose resistance is conferred by pCDNA3) or upon cotransfection with additional plasmids conferring resistance to other antibiotics. In this case it is opportune to follow some tips, which are as follows.

   All the plasmids must be linearized at a single site. Choose a site of restriction that does not interfere with their expression. The reporter–selection ratio should be at least 5:1. Cotransfection works best using calcium phosphate coprecipitation, but also electroporation and cationic lipids methods can be used. The antibiotic concentration used to select clones should be first titrated on untransfected cells setting it at 2–3× the amount that kills 100% of the cells. Using less will give you false positives; using more will kill even transfected cells. Serum source and concentration should not be varied until stable clones are generated. Once clones are selected, they should be screened for expression and reconstitution of the GFP fluorescent signal. Discard negative clones as well as clones with mistargeted mitochondrial OMM $GFP_{1\text{-}10}$ or ER β S11 signal. Mitochondrial OMM $GFP_{1\text{-}10}$ distribution can be verified either by immunocytochemistry analysis using commercial anti-GFP antibodies or by complementation with a cytosolic untargeted reporter protein tagged with β S11 fragment, which can reconstitute GFP signal on the cytosolic surface of the outer mitochondrial membrane. β S11 localization on the ER surface can be verified by complementation with untargeted $GFP_{1\text{-}10}$ and the appearance of a green fluorescent signal with a reticular distribution. Transfectants should be cultured for a few passages and then reanalyzed. Some of the highest expressors could become negative because they took up too much DNA and were unstable. For long term culture, use media containing the selectable drug at 1× the amount used above. It is not necessary to use more, be conscious that these drugs are quite expensive.

10. Set up the best conditions for your expression system avoiding very strong overexpression and always check the correct targeting of the GFP 1-10 moiety by immunocytochemistry using primary antibodies against GFP. Be aware that in the case of high level of expression some mistargeting may occur or mitochondrial morphology could be affected. If this is the case reduce the amounts of transfected plasmids or the time of expression.
11. Verify that the ER and mitochondria morphologies were not affected by the transfection procedure. This could compromise the real evaluation of the number of ER–mitochondria contact sites.
12. It is strongly required to perform a Z-Stack analysis of the whole cell volume in order to be sure to quantify properly all the ER–mitochondria interactions. Indeed, as also shown in Fig. 2, organelle contact sites are not formed only on a single confocal plane rather they are distributed throughout the whole volume and area of the cell. Acquiring only single planes will inevitably lead to misinterpretations of the results. The Z-stack should be just above the resolution limit of the confocal microscope, that is, at around 0.3 μM. Acquisition of bigger stacks, for example, at 0.4 or 0.5 μM, although it is not forbidden, might cause the loss of some contacts thus leading to an underestimation of the results. To improve the image quality, we suggest acquiring them at a resolution of 1024 × 1024 and a speed of 200 Hz.
13. The 3D rendered image must be thresholded in order to quantify the number of contact sites. This procedure is not easy to standardize due to the heterogeneous nature in terms of size of the contact sites monitored, for this reason we encourage to count the number of objects monitored per cell. In this case the threshold must be set in order to consider all the 3D rendered dots in the cell. Increasing or decreasing the threshold level above or below the 3D rendered signal will inevitably lead to underestimation or overestimation of the contacts number, respectively. The "Quantification 2" plugin will then apply the watershed binary filter.

## References

1. Phillips MJ, Voeltz GK (2016) Structure and function of ER membrane contact sites with other organelles. Nat Rev Mol Cell Biol 17 (2):69–82. https://doi.org/10.1038/nrm.2015.8
2. Mannella CA, Buttle K, Rath BK, Marko M (1998) Electron microscopic tomography of rat-liver mitochondria and their interaction with the endoplasmic reticulum. Biofactors 8 (3-4):225–228
3. Csordas G, Renken C, Varnai P, Walter L, Weaver D, Buttle KF, Balla T, Mannella CA, Hajnoczky G (2006) Structural and functional features and significance of the physical linkage between ER and mitochondria. J Cell Biol 174

(7):915–921. https://doi.org/10.1083/jcb.200604016
4. de Brito OM, Scorrano L (2008) Mitofusin 2 tethers endoplasmic reticulum to mitochondria. Nature 456(7222):605–610. https://doi.org/10.1038/nature07534
5. Murley A, Lackner LL, Osman C, West M, Voeltz GK, Walter P, Nunnari J (2013) ER-associated mitochondrial division links the distribution of mitochondria and mitochondrial DNA in yeast. elife 2:e00422. https://doi.org/10.7554/eLife.00422
6. Friedman JR, Lackner LL, West M, DiBenedetto JR, Nunnari J, Voeltz GK (2011) ER tubules mark sites of mitochondrial division. Science 334(6054):358–362. https://doi.org/10.1126/science.1207385
7. Wu Y, Whiteus C, Xu CS, Hayworth KJ, Weinberg RJ, Hess HF, De Camilli P (2017) Contacts between the endoplasmic reticulum and other membranes in neurons. Proc Natl Acad Sci U S A 114(24):E4859–E4867. https://doi.org/10.1073/pnas.1701078114
8. Elgass KD, Smith EA, LeGros MA, Larabell CA, Ryan MT (2015) Analysis of ER-mitochondria contacts using correlative fluorescence microscopy and soft X-ray tomography of mammalian cells. J Cell Sci 128 (15):2795–2804. https://doi.org/10.1242/jcs.169136
9. Rusinol AE, Cui Z, Chen MH, Vance JE (1994) A unique mitochondria-associated membrane fraction from rat liver has a high capacity for lipid synthesis and contains pre-Golgi secretory proteins including nascent lipoproteins. J Biol Chem 269 (44):27494–27502
10. Wieckowski MR, Giorgi C, Lebiedzinska M, Duszynski J, Pinton P (2009) Isolation of mitochondria-associated membranes and mitochondria from animal tissues and cells. Nat Protoc 4(11):1582–1590. https://doi.org/10.1038/nprot.2009.151
11. Filadi R, Greotti E, Turacchio G, Luini A, Pozzan T, Pizzo P (2015) Mitofusin 2 ablation increases endoplasmic reticulum-mitochondria coupling. Proc Natl Acad Sci U S A 112(17): E2174–E2181. https://doi.org/10.1073/pnas.1504880112
12. Rizzuto R, Brini M, Murgia M, Pozzan T (1993) Microdomains with high Ca2+ close to IP3-sensitive channels that are sensed by neighboring mitochondria. Science 262 (5134):744–747
13. Brunstein M, Wicker K, Herault K, Heintzmann R, Oheim M (2013) Full-field dual-color 100-nm super-resolution imaging reveals organization and dynamics of mitochondrial and ER networks. Opt Express 21 (22):26162–26173. https://doi.org/10.1364/OE.21.026162
14. Bottanelli F, Kromann EB, Allgeyer ES, Erdmann RS, Wood Baguley S, Sirinakis G, Schepartz A, Baddeley D, Toomre DK, Rothman JE, Bewersdorf J (2016) Two-colour live-cell nanoscale imaging of intracellular targets. Nat Commun 7:10778. https://doi.org/10.1038/ncomms10778
15. Tubbs E, Rieusset J (2016) Study of endoplasmic reticulum and mitochondria interactions by in situ proximity ligation assay in fixed cells. J Vis Exp (118):54899. https://doi.org/10.3791/54899
16. Gomez-Suaga P, Paillusson S, Stoica R, Noble W, Hanger DP, Miller CC (2017) The ER-mitochondria tethering complex VAPB-PTPIP51 regulates autophagy. Curr Biol 27 (3):371–385. https://doi.org/10.1016/j.cub.2016.12.038
17. Stoica R, Paillusson S, Gomez-Suaga P, Mitchell JC, Lau DH, Gray EH, Sancho RM, Vizcay-Barrena G, De Vos KJ, Shaw CE, Hanger DP, Noble W, Miller CC (2016) ALS/FTD-associated FUS activates GSK-3beta to disrupt the VAPB-PTPIP51 interaction and ER-mitochondria associations. EMBO Rep 17 (9):1326–1342. https://doi.org/10.15252/embr.201541726
18. Paillusson S, Gomez-Suaga P, Stoica R, Little D, Gissen P, Devine MJ, Noble W, Hanger DP, Miller CCJ (2017) Alpha-Synuclein binds to the ER-mitochondria tethering protein VAPB to disrupt Ca2+ homeostasis and mitochondrial ATP production. Acta Neuropathol 134(1):129–149. https://doi.org/10.1007/s00401-017-1704-z
19. Csordas G, Varnai P, Golenar T, Roy S, Purkins G, Schneider TG, Balla T, Hajnoczky G (2010) Imaging interorganelle contacts and local calcium dynamics at the ER-mitochondrial interface. Mol Cell 39 (1):121–132. https://doi.org/10.1016/j.molcel.2010.06.029
20. Naon D, Zaninello M, Giacomello M, Varanita T, Grespi F, Lakshminaranayan S, Serafini A, Semenzato M, Herkenne S, Hernandez-Alvarez MI, Zorzano A, De Stefani D, Dorn GW 2nd, Scorrano L (2016) Critical reappraisal confirms that Mitofusin 2 is an endoplasmic reticulum-mitochondria tether. Proc Natl Acad Sci U S A 113 (40):11249–11254. https://doi.org/10.1073/pnas.1606786113
21. Ravikumar B, Duden R, Rubinsztein DC (2002) Aggregate-prone proteins with

polyglutamine and polyalanine expansions are degraded by autophagy. Hum Mol Genet 11 (9):1107–1117

22. Shi F, Kawano F, Park SE, Komazaki S, Hirabayashi Y, Polleux F, Yazawa M (2018) Optogenetic control of endoplasmic reticulum-mitochondria tethering. ACS Synth Biol 7(1):2–9. https://doi.org/10.1021/acssynbio.7b00248
23. Cieri D, Vicario M, Giacomello M, Vallese F, Filadi R, Wagner T, Pozzan T, Pizzo P, Scorrano L, Brini M, Calì T (2017) SPLICS: a split green fluorescent protein-based contact site sensor for narrow and wide heterotypic organelle juxtaposition. Cell Death Differ 25 (6):1131–1145. https://doi.org/10.1038/s41418-017-0033-z
24. Yang Z, Zhao X, Xu J, Shang W, Tong C (2018) A novel fluorescent reporter detects plastic remodeling of mitochondria-ER contact sites. J Cell Sci 131(1):jcs208686. https://doi.org/10.1242/jcs.208686
25. Harmon M, Larkman P, Hardingham G, Jackson M, Skehel P (2017) A bi-fluorescence complementation system to detect associations between the endoplasmic reticulum and mitochondria. Sci Rep 7(1):17467. https://doi.org/10.1038/s41598-017-17278-1
26. Kakimoto Y, Tashiro S, Kojima R, Morozumi Y, Endo T, Tamura Y (2018) Visualizing multiple inter-organelle contact sites using the organelle-targeted split-GFP system. Sci Rep 8(1):6175. https://doi.org/10.1038/s41598-018-24466-0
27. Shai N, Yifrach E, van Roermund CWT, Cohen N, Bibi C, IJ L, Cavellini L, Meurisse J, Schuster R, Zada L, Mari MC, Reggiori FM, Hughes AL, Escobar-Henriques M, Cohen MM, Waterham HR, Wanders RJA, Schuldiner M, Zalckvar E (2018) Systematic mapping of contact sites reveals tethers and a function for the peroxisome-mitochondria contact. Nat Commun 9(1):1761. https://doi.org/10.1038/s41467-018-03957-8
28. Cieri D, Vicario M, Giacomello M, Vallese F, Filadi R, Wagner T, Pozzan T, Pizzo P, Scorrano L, Brini M, Cali T (2018) SPLICS: a split green fluorescent protein-based contact site sensor for narrow and wide heterotypic organelle juxtaposition. Cell Death Differ 25 (6):1131–1145. https://doi.org/10.1038/s41418-017-0033-z
29. Gómez-Suaga P, Pérez-Nievas BG, Glennon EB, Lau DHW, Paillusson S, Mórotz GM, Calì T, Pizzo P, Noble W, Miller CCJ (2019) The VAPB-PTPIP51 endoplasmic reticulum-mitochondria tethering proteins are present in neuronal synapses and regulate synaptic activity. Acta Neuropathol Commun 7(1):35. https://doi.org/10.1186/s40478-019-0688-4
30. Yeshaw WM, van der Zwaag M, Pinto F, Lahaye LL, Faber AI, Gomez-Sanchez R, Dolga AM, Poland C, Monaco AP, van ISC, Grzeschik NA, Velayos-Baeza A, Sibon OC (2019) Human VPS13A is associated with multiple organelles and influences mitochondrial morphology and lipid droplet motility. elife 8:e43561. https://doi.org/10.7554/eLife.43561
31. Cieri D, Vicario M, Vallese F, D'Orsi B, Berto P, Grinzato A, Catoni C, De Stefani D, Rizzuto R, Brini M, Cali T (2018) Tau localises within mitochondrial sub-compartments and its caspase cleavage affects ER-mitochondria interactions and cellular Ca(2+) handling. Biochim Biophys Acta Mol basis Dis 1864 (10):3247–3256. https://doi.org/10.1016/j.bbadis.2018.07.011
32. Filadi R, Leal NS, Schreiner B, Rossi A, Dentoni G, Pinho CM, Wiehager B, Cieri D, Calì T, Pizzo P, Ankarcrona M (2018) TOM70 sustains cell bioenergetics by promoting IP3R3-mediated ER to mitochondria Ca 2+ transfer. Curr Biol 28(3):369–382.e6. https://doi.org/10.1016/j.cub.2017.12.047
33. Granatiero V, Giorgio V, Cali T, Patron M, Brini M, Bernardi P, Tiranti V, Zeviani M, Pallafacchina G, De Stefani D, Rizzuto R (2016) Reduced mitochondrial Ca transients stimulate autophagy in human fibroblasts carrying the 13514A>G mutation of the ND5 subunit of NADH dehydrogenase. Cell Death Differ 23(2):231–241. https://doi.org/10.1038/cdd.2015.84
34. Doghman-Bouguerra M, Granatiero V, Sbiera S, Sbiera I, Lacas-Gervais S, Brau F, Fassnacht M, Rizzuto R, Lalli E (2016) FATE1 antagonizes calcium- and drug-induced apoptosis by uncoupling ER and mitochondria. EMBO Rep 17(9):1264–1280. https://doi.org/10.15252/embr.201541504
35. Cali T, Ottolini D, Vicario M, Catoni C, Vallese F, Cieri D, Barazzuol L, Brini M (2019) splitGFP technology reveals dose-dependent ER-mitochondria Interface modulation by alpha-Synuclein A53T and A30P mutants. Cell 8(9):1072. https://doi.org/10.3390/cells8091072
36. Berenguer-Escuder C, Grossmann D, Massart F, Antony P, Burbulla LF, Glaab E, Imhoff S, Trinh J, Seibler P, Grunewald A, Kruger R (2019) Variants in Miro1 cause alterations of ER-mitochondria contact sites in fibroblasts from Parkinson's disease patients.

J Clin Med 8(12):2226. https://doi.org/10.3390/jcm8122226

37. Carreras-Sureda A, Jana F, Urra H, Durand S, Mortenson DE, Sagredo A, Bustos G, Hazari Y, Ramos-Fernandez E, Sassano ML, Pihan P, van Vliet AR, Gonzalez-Quiroz M, Torres AK, Tapia-Rojas C, Kerkhofs M, Vicente R, Kaufman RJ, Inestrosa NC, Gonzalez-Billault C, Wiseman RL, Agostinis P, Bultynck G, Court FA, Kroemer G, Cardenas JC, Hetz C (2019) Non-canonical function of IRE1alpha determines mitochondria-associated endoplasmic reticulum composition to control calcium transfer and bioenergetics. Nat Cell Biol 21(6):755–767. https://doi.org/10.1038/s41556-019-0329-y
38. Prasher DC, Eckenrode VK, Ward WW, Prendergast FG, Cormier MJ (1992) Primary structure of the Aequorea victoria green-fluorescent protein. Gene 111(2):229–233. https://doi.org/10.1016/0378-1119(92)90691-h
39. Tsien RY (1998) The green fluorescent protein. Annu Rev Biochem 67:509–544. https://doi.org/10.1146/annurev.biochem.67.1.509
40. Cubitt AB, Heim R, Adams SR, Boyd AE, Gross LA, Tsien RY (1995) Understanding, improving and using green fluorescent proteins. Trends Biochem Sci 20(11):448–455. https://doi.org/10.1016/s0968-0004(00)89099-4
41. Heim R, Prasher DC, Tsien RY (1994) Wavelength mutations and posttranslational autoxidation of green fluorescent protein. Proc Natl Acad Sci U S A 91(26):12501–12504. https://doi.org/10.1073/pnas.91.26.12501
42. Heim R, Cubitt AB, Tsien RY (1995) Improved green fluorescence. Nature 373(6516):663–664. https://doi.org/10.1038/373663b0
43. Cormack BP, Valdivia RH, Falkow S (1996) FACS-optimized mutants of the green fluorescent protein (GFP). Gene 173(1 Spec No):33–38. https://doi.org/10.1016/0378-1119(95)00685-0
44. Zhang G, Gurtu V, Kain SR (1996) An enhanced green fluorescent protein allows sensitive detection of gene transfer in mammalian cells. Biochem Biophys Res Commun 227(3):707–711. https://doi.org/10.1006/bbrc.1996.1573
45. Yang TT, Cheng L, Kain SR (1996) Optimized codon usage and chromophore mutations provide enhanced sensitivity with the green fluorescent protein. Nucleic Acids Res 24(22):4592–4593. https://doi.org/10.1093/nar/24.22.4592
46. Waldo GS, Standish BM, Berendzen J, Terwilliger TC (1999) Rapid protein-folding assay using green fluorescent protein. Nat Biotechnol 17(7):691–695. https://doi.org/10.1038/10904
47. Crameri A, Whitehorn EA, Tate E, Stemmer WP (1996) Improved green fluorescent protein by molecular evolution using DNA shuffling. Nat Biotechnol 14(3):315–319. https://doi.org/10.1038/nbt0396-315
48. Pedelacq JD, Cabantous S, Tran T, Terwilliger TC, Waldo GS (2006) Engineering and characterization of a superfolder green fluorescent protein. Nat Biotechnol 24(1):79–88. https://doi.org/10.1038/nbt1172
49. Cabantous S, Terwilliger TC, Waldo GS (2005) Protein tagging and detection with engineered self-assembling fragments of green fluorescent protein. Nat Biotechnol 23(1):102–107. https://doi.org/10.1038/nbt1044
50. Calì T, Ottolini D, Soriano ME, Brini M (2015) A new split-GFP-based probe reveals DJ-1 translocation into the mitochondrial matrix to sustain ATP synthesis upon nutrient deprivation. Hum Mol Genet 24(4):1045–1060. https://doi.org/10.1093/hmg/ddu519
51. Vicario M, Cieri D, Vallese F, Catoni C, Barazzuol L, Berto P, Grinzato A, Barbieri L, Brini M, Calì T (2019) A split-GFP tool reveals differences in the sub-mitochondrial distribution of wt and mutant alpha-synuclein. Cell Death Dis 10(11):857. https://doi.org/10.1038/s41419-019-2092-1
52. Cabantous S, Waldo GS (2006) In vivo and in vitro protein solubility assays using split GFP. Nat Methods 3(10):845–854. https://doi.org/10.1038/nmeth932
53. Chun W, Waldo GS, Johnson GV (2007) Split GFP complementation assay: a novel approach to quantitatively measure aggregation of tau in situ: effects of GSK3beta activation and caspase 3 cleavage. J Neurochem 103(6):2529–2539. https://doi.org/10.1111/j.1471-4159.2007.04941.x
54. Kaddoum L, Magdeleine E, Waldo GS, Joly E, Cabantous S (2010) One-step split GFP staining for sensitive protein detection and localization in mammalian cells. BioTechniques 49(4):727–728, 730, 732 passim. https://doi.org/10.2144/000113512
55. Pinaud F, Dahan M (2011) Targeting and imaging single biomolecules in living cells by complementation-activated light microscopy with split-fluorescent proteins. Proc Natl Acad Sci U S A 108(24):E201–E210. https://doi.org/10.1073/Pnas.1101929108

# Chapter 24

# Qualitative Characterization of the Rat Liver Mitochondrial Lipidome Using All Ion Fragmentation on an Exactive Benchtop Orbitrap MS

**Irina G. Stavrovskaya, Rose M. Gathungu, Susan S. Bird, and Bruce S. Kristal**

## Abstract

Untargeted lipidomics profiling by liquid chromatography–mass spectrometry (LC-MS) allows researchers to observe the occurrences of lipids in a biological sample without showing intentional bias to any specific class of lipids and allows retrospective reanalysis of data collected. Typically, and in the specific method described, a general extraction method followed by LC separation is used to achieve nonspecific class coverage of the lipidome prior to high resolution accurate mass (HRAM) MS detection. Here we describe a workflow including the isolation of mitochondria from liver tissue, followed by mitochondrial lipid extraction and the LC-MS conditions used for data acquisition. We also highlight how, in this method, all ion fragmentation can be used to identify species of lower abundances, often missed by data dependent fragmentation techniques. Here we describe the isolation of mitochondria from liver tissue, followed by mitochondrial lipid extraction and the LC-MS conditions used for data acquisition.

**Key words** Mitochondria, Lipidomics, LC-MS, Cardiolipins, Lysophospholipids, HCD

## 1 Introduction

Mitochondria are intracellular membrane-enclosed organelles that play crucial role in bioenergetics, biosynthesis of critical cellular constituents, the regulation of cell survival, and the execution of cell death pathways [1, 2]. Lipids are essential to mitochondrial viability, and they are involved in the regulation of the wide range of mitochondrial functions, such as maintenance of membrane structural composition and fluidity, membrane fusion and fission, electron transport and oxidative phosphorylation, signal transduction, interaction with other cellular constituencies such as proteins and glycoproteins, and energy storage [3–5]. The role of lipids in mitochondrial function is, for example, exemplified by mitochondrial phospholipid cardiolipin (CL). CL, which is almost exclusively

Volkmar Weissig and Marvin Edeas (eds.), *Mitochondrial Medicine: Volume 1: Targeting Mitochondria*, Methods in Molecular Biology, vol. 2275, https://doi.org/10.1007/978-1-0716-1262-0_24,

found in the inner mitochondrial membrane, plays multiple key roles in the regulation of mitochondrial metabolism, including regulation of essential enzymatic activities involved in electron transport and oxidative phosphorylation, and assembly of respiratory supercomplexes [5–7]. Recent studies suggest a critical role of mitochondrial lipid cardiolipin in apoptotic cell death pathway [8] and regulation of mitochondrial dynamics [9].

Mitochondrial lipids are also both a major target for oxidative damage by reactive oxygen species produced during respiration and a major source of lipid peroxides and peroxidation by-product (e.g., hydroxyalkenals, γ-isoketoaldehydes) production that serve to amplify oxidative damage under pathophysiological conditions [10–14]. Development of analytical methods for accurate quantitative and qualitative analysis of all lipid classes and species that contribute to and reflect mitochondrial function is therefore highly important.

Liquid chromatography with high resolution accurate mass (HRAM)-MS is widely used to study the biochemical species (proteins, metabolites, lipids, etc) that comprise a biological sample [15–17]. These techniques offer the speed, sensitivity and specificity necessary to determine the biochemical composition of a system by providing both qualitative and relative quantitative results. This is imperative for a successful nontargeted lipidomics analysis, where all lipid species are considered of potential biological importance and therefore there can be no deliberate analytical bias is given toward any of the eight lipid categories established and defined by LIPID MAPS [18].

By using HRAM instrumentation, such as the Exactive benchtop Orbitrap MS, for both full scan and all ion fragmentation (AIF), a broad picture of the lipidome is captured and the electronic data record obtained can easily be used for both primary and retrospective analysis. LC separation followed by HRAM detection in combination with MS/MS fragmentation allows both known and unknown species to be structurally elucidated and monitored. Using the method described herein, containing both LC and MS with AIF MS/MS, the identification of more than 350 unique lipids in serum, mitochondria and premature infant fecal samples have been found and reported [19–22].

Specifically, using the approach described, we have identified 26 structurally unique CL species and two monolysocardiolipins (MLCL)—$(18:2)_3$ and $(18:2)_2(18:1)$ in liver mitochondria isolated from healthy male Fisher 344 × Brown Norway F1 rats, and revealed the patterns of dietary-mediated regulation of these species [22]. All CL species were characterized by four fatty acid chains. Furthermore, this method enabled us to detect 36 CL species in a pooled sample drawn from the livers of selectively bred polygenetic obesity prone (OP) and resistant (OR) Sprague-Dawley rats, 22 of them were characterized by four fatty acid

chains, and 14 species as carbon to double bond ratio (unpublished data, IS NORC study). Twenty-eight structurally unique CLs and two MLCLs were identified in mitochondria isolated from skeletal (gastrocnemius) muscles of OP and OR rats. Forty-six CL species, with the most dominant (18:1/22:6/20:4/20:4) specie, were detected in nonsynaptosomal mitochondria isolated from brains of C57BL/6 J alpha-synuclein knockout mice (unpublished data). We were able to detect an elevation of the range of proinflammatory lysophospholipids such as lysophosphatidylcholines (LPCs)—(16:1), (18:1) and (18:2) in mitochondria isolated from the livers of OP and OR rats.

## 2 Materials

### 2.1 Liver Mitochondria Isolation [23]

1. Isolation buffer IB1: 240 mM D-sucrose, 10 mM HEPES, pH 7.4, 1 mM ethylene glycol-bis(2-aminoethylether)-*N,N,N′,N′*-tetraacetic acid (EGTA) stock with pH 7.2 adjusted by KOH, 5 g/1 L bovine serum albumin (BSA, Sigma-Aldrich, fatty acid free). Dissolve 82.152 g of D-sucrose in 900 mL of distilled water. Add 10 mL of 1 M HEPES-KOH and 20 mL of 0.5 M EGTA-KOH. Adjust pH to 7.4 with KOH. Bring the solution to 1 L with water. Add 5 g of fatty acid free bovine serum albumin (BSA, Sigma-Aldrich), do not shake it, leave it overnight at 4 °C to dissolve completely (*see* **Notes 1–5**).
2. Petri dish.
3. 50 mL plastic disposable beaker.
4. Potter-Elvehjem glass–Teflon homogenizers 40 mL and 15 mL volume.
5. 50 mL round-bottom centrifuge tubes.
6. Fixed angle JA-20 centrifuge rotor and appropriate centrifuge, (both, Beckman, USA), both prechilled to 4 °C.
7. Secure the pestle in the chuck of the electrical motor.
8. Isolation buffer IB2: 240 mM D-sucrose, 10 mM HEPES, pH 7.4. Dissolve 82.152 g/1 L D-sucrose, 2.38 g/1 L HEPES, pH 7.4, adjusted by KOH. Bring the solution to 1 L with water. Sterilize the solution using sterile vacuum filter units (*see* **Notes 1–5**).
9. Bicinchoninic acid kit (Sigma-Aldrich, USA) to determine mitochondrial protein concentration and 1.0 mg/mL BSA as a standard solution (*see* **Note 6**).
10. Spectrophotometer, Uvikon 943, or equivalent.
11. Washing buffer: 125 mM KCl, 10 mM HEPES, pH 7.4. Dissolve 9.32 g/1 L KCL, 2.38 g/1 L HEPES, pH 7.4 adjusted by KOH. Bring the solution to 1 L with water. Sterilize the solution using sterile vacuum filter units (*see* **Notes** 1–5).

### 2.2 Mitochondrial Lipid Extraction

1. 1.5 mL Fisher brand siliconized low-retention microcentrifuge tubes (Fisher Scientific, Pittsburgh PA)
2. Microcentrifuge floating rack.
3. Mechanical ultrasonic cleaner.
4. 10 mL Falcon tubes
5. Thermo Scientific Savant SPD111V P1.
6. ACS grade dimethyl sulfoxide (DMSO).
7. ACS grade dichloromethane (DCM).
8. LC-MS grade methanol (MeOH).
9. LC-MS grade isopropanol (IPA).
10. LC-MS grade acetonitrile (ACN).
11. All water ($H_2O$) is deionized to attain a sensitivity of 18 M Ω cm at 25 °C.
12. Lipid internal standard solution: 1.5 mL, enough for 50 samples; Combine 37.50 μL of a 2 mg/mL solution of 1,1′,2,2-′-tertraoleoyl cardiolipin ($CL(18:1)_4$) (Avanti Polar Lipids), 30 μL each of a 2.5 mg/mL solution of 1,2-diheptadecanoyl-*sn*-glycero-3-phosphocholine (PC(17:0/17:0) and 1,2-dimyristoyl-*sn*-glycero-3-[phospho-rac-(1-glycerol)] (PG(14:0/14:0) (Avanti Polar Lipids), 15 μL of a 5 mg/mL solution of 11-O-hexadecyl-*sn*-glycero-3-phosphocholine (lysoPC(16:0)) (Enzo Chemicals) and 75 μL of a 1 mg/mL solution of 1,2-dipalmitoyl-*sn*-glycero-3-phospho-L-serine (PS(16:0/16:0) (Avanti Lipids) followed by 1297.5 μL of 2:1 DCM–MeOH. All standards are dissolved in 2:1 mixture of DCM–MeOH prior to mixing and stored a −20 °C.
13. LC-MS internal standard: Create 100 mL of a 5 μg/mL working concentration solution of LC-MS internal standard 1,2-diheptadecanoyl*sn*-glycero-3-[phospho-rac-(1-glycerol)] (PG 17:0/17:0) by adding 200 μL of a 2.5 mg/mL stock solution to 100 mL of a 63:30:5 ACN–IPA–$H_2O$ mixture.

### 2.3 LC-MS Analysis

1. LC-MS grade acetonitrile with 0.1% formic acid.
2. Ascentis Express $C_{18}$ 2.1 × 150 mm 2.7 μm column (Sigma-Aldrich, St. Louis, MO).
3. Column hot pocket thermostated column heater (Thermo Fisher Scientific, San Jose, CA).
4. Thermo Fisher Scientific PAL autosampler, (Thermo Fisher Scientific, San Jose, CA).
5. Accela quaternary HPLC pump (Thermo Fisher Scientific, San Jose, CA).

6. Exactive benchtop Orbitrap mass spectrometer with HCD (Thermo Fisher Scientific, San Jose, CA) and heated electrospray ionization (HESI) probe.
7. Mobile phase A is prepared by dissolving 630 mg of ammonium formate into a mixture of 600 mL water and 400 mL ACN with 0.1% formic acid. This bottle is then sonicated for several minutes to remove any gases from mixing solvents.
8. Mobile phase B is prepared by dissolving 630 mg of ammonium formate into 1 mL of water before adding to 900 mL of IPA and 100 mL of ACN with 0.1% formic acid. This bottle is then sonicated for several minutes to facilitate dissolution and remove any gases from mixing solvents.
9. SIEVE v 2.1 Differential Analysis Software (Thermo Fisher Scientific, San Jose CA).

## 3 Methods

### 3.1 Liver Mitochondria Isolation

1. All isolation steps have to be done on ice, and all operations have to be carried out at 0-4 °C as described previously [22, 24] (*see* **Note 7**). Alternative mitochondrial isolation approaches from liver and/or other tissue are also expected to provide suitable starting material, although the user should be aware of the characteristics of any given preparation with regards, for example, to purity. The use of other preparations would replace **steps 1–12** of this protocol.
2. Take liver tissue (8–10 g) from the animal (*see* **Note 8**) and place it immediately in Petri dish containing ice-cold 20–30 mL of the isolation buffer #1 (IB1). Wash out blood.
3. Transfer liver tissue in a 50 mL plastic disposable beaker containing 20–30 mL of IB1, and mince the tissue with scissors, or use a press.
4. Pour the suspension in Potter-Elvehjem glass–Teflon homogenizer and add IB1 to a total volume of 40 mL.
5. Homogenize the suspension using 7-8 up-and-down strokes with the pestle rotating at 500–600 rpm (*see* **Notes 9** and **10**). The suspension should look homogeneous.
6. Transfer the obtained homogenate into 50 mL round-bottom centrifuge tubes. Centrifuge the tubes at 1000 × *g* for 10 min (*see* **Note 11**).
7. Collect the supernatant and centrifuge it at 11,000 × *g* for 10 min. (*see* **Note 12**).
8. Collect the pellet and resuspend it in 15 mL of IB1 in the Potter-Elvehjem glass–Teflon homogenizer using 4-5 up-and-down strokes by hand. Suspension should look

homogeneous. Adjust volume to 40 mL, mix, and centrifuge the suspension at 11,000 × *g* for 10 min.

9. Resuspend the pellet in 15 mL of isolation buffer #2 (IB2) in the Potter-Elvehjem glass–Teflon homogenizer with 4-5 up-and-down strokes by hand. The suspension should look homogeneous. Adjust volume to 40 mL, mix, and centrifuge the suspension at 11,000 × *g* for 10 min.
10. Resuspend final pellet in 0.5 mL of IB2 and store on ice (*see* **Note 13**).
11. Add 10 μL of mitochondrial suspension into 990 μL of IB2 to measure protein concentration by bicinchoninic acid -based method using BSA as a standard (see sigmaaldrich.com for details).
12. Aliquot mitochondrial sample by 1 mg of protein, resuspend it in 125 mM KCl, 10 mM HEPES, pH 7.4 buffer, centrifuge at 11,000 × *g* for 10 min, remove supernatant and freeze as dry pellets at −80 °C for further analysis.

### 3.2 Mitochondrial Lipid Extraction

1. Add 40 μL DMSO to each aliquot of mitochondria (containing 1 mg of protein) (*see* **Notes 14**).
2. Place each mitochondria–DMSO sample into the floating microcentrifuge rack and sonicate for 1 h to disrupt the membranes.
3. Pipet 10 μL from each sample into a 10 mL Falcon tube to create a mitochondrial pool sample. The pool samples will be processed for quality control (QC) and lipid identification studies.
4. Add 5 μL of lipid internal standard to each 30 μL mitochondria sample, this includes samples from the study and pool samples created in **step 3**.
5. Add 190 μL of MeOH to each sample and vortex for 10 s.
6. Next add 380 μL of DCM and vortex for 20 s (*see* **Notes 15** and **16**).
7. Finally, add 120 μL of water to induce phase separation.
8. Vortex samples for 10 s and allow to equilibrate at room temperature for 10 min.
9. Centrifuge each sample at 8000 × *g* for 10 min at 10 °C (*see* **Note 17**).
10. Using a 500 μL pipette, transfer 320 μL of the lower lipid-rich DCM layer to a clean microcentrifuge tube. Be careful to push the pipette tip along the side of the container when piercing the protein disk as not to disrupt the phase separation or transfer any protein with the lipid-rich DCM layer.

11. Evaporate the samples to dryness under vacuum using a speed-vac (*see* **Note 18**).
12. Reconstitute samples in 300 μL of LC-MS internal standard (PG (17:0/17:0)) before LC-MS analysis (*see* **Note 19**).

### 3.3 LC-MS Conditions

1. Separate 10 μL lipid extracts on an Ascentis Express $C_{18}$ 2.1 × 150 mm 2.7 μm column connected to a Thermo Fisher Scientific PAL autosampler, Accela quaternary HPLC pump and an Exactive benchtop Orbitrap mass spectrometer equipped with a heated electrospray ionization (HESI) probe (*see* **Notes 20** and **21**).
2. Run separations for 30 min with mobile phase A and B consisting of 60:40 water–ACN in 10 mM ammonium formate and 0.1% formic acid and 90:10 IPA–ACN also with 10 mM ammonium formate and 0.1% formic acid, respectively.
3. The gradient starts at 32% B for 1.5 min; from 1.5 to 4 min increases to 45% B, from 4 to 5 min increases to 52% B, from 5 to 8 min to 58% B, from 8 to 11 min to 66% B, from 11 to 14 min to 70% B, from 14 to 18 min to 75% B, from 18 to 21 min to 97% B, during 21–25 min 97% B is maintained; from 25 to 30 min solvent B is decreased to 32% and then maintained. The flow rate is 260 μL/min.
4. Maintain the column oven temperature at 45 °C and set the temperature of the autosampler to 4 °C. The same LC conditions and buffers are used for all MS experiments.
5. Set the spray voltage to 3.5 kV, whereas the heated capillary and the HESI probe are held at 250 °C and 350 °C, respectively.
6. Set the sheath gas flow to 25 units and the auxiliary gas to 15 units.
7. Hold these conditions constant for both positive and negative ionization mode acquisitions.
8. The instrument is tuned by direct infusion of PG (17:0/17:0) in positive mode and PC (19:0) in the negative mode (*see* **Notes 20** and **22**) and external mass calibration is performed using the standard calibration mixture and protocol from ThermoFisher approximately every 5 days.

### 3.4 Full Scan Profiling Experiments

1. Operate the MS in high resolution mode, corresponding to a resolution of 60 k and a 2 Hz scan speed and hold the scan range between *m/z* 120–2000.
2. Mitochondrial lipid extracts are profiled by injecting each sample once, in randomized order, with pool samples, blanks and IS mixture injections spread throughout the analysis.

### 3.5 Lipid Identification Studies

1. Run HCD experiments on the pool, lipid IS mixture and blank samples only.
2. Perform these experiments by alternating between full scan acquisitions and HCD scans, both run at 2 Hz. Three different HCD energies, 30, 60, and 100 eV, are used in separate experiments in both positive and negative mode.

### 3.6 Data Analysis

All LC-MS profiling samples are analyzed using the MS label free differential analysis software package SIEVE v 1.3 or higher (Thermo Fisher Scientific and Vast Scientific, Cambridge, MA). (*see* **Notes 23** and **24**).

The frame *m/z* values are used to do batch searches on the Metlin database [23], the human metabolome database (HMDB) [25] and the LIPID MAPS database [26] and those matches are confirmed using the intact molecule's exact mass observed during the analysis, RT regions based on the lipid IS mixture elution times run throughout the sequence and HCD fragmentation patterns that chromatographically align with the intact exact mass extracted ion chromatograms for the parent compound (*see* **Note 25**).

## 4 Notes

1. Use deionized water (Milli-Q, "Millipore") for mitochondrial buffer preparation.
2. Airtight glass containers or Thermo Scientific Nalgene disposable bottles are strongly recommended for storage of mitochondrial buffers.
3. Sterilize all buffers by filtering through 0.22 μm membrane (we recommend to use Thermo Scientific Nalgene disposable filter units that come with bottles). The buffers are stable for at least 3 months if kept sterile.
4. Do not freeze isolation and incubation buffers.
5. The buffer composition for mitochondria isolation and incubation may vary. For example, examination of the literature will show changes in relative concentrations of sucrose and/or mannitol, in the choice of buffering agent and counter ion, the inclusion/exclusion of divalent cation chelators, osmolarity, and ionic strength. The buffers described have been used by our lab for upstream respiration and/or calcium overload experiments and subsequent downstream lipidomics studies.
6. Alternative protein concentration approaches can be used, but linear range and potential interference must be examined.
7. Quality and purity of isolated mitochondria is very important, because contamination of mitochondrial preparation with cytosolic structures can interfere/mask lipid profiling results.

8. Animals have to be sacrificed, and liver tissue has to be removed and placed in ice-cold buffer as quickly as possible.
9. During tissue homogenization steps, do not draw a vacuum and avoid bubble creation.
10. Avoid very fast pestle rotation during homogenization.
11. Do not use detergents to clean centrifuge tubes.
12. Carefully remove fat from centrifuge tube walls with a delicate wiper after second centrifugation.
13. Make final mitochondria suspension rather concentrated than diluted (we recommend a concentration of 60–80 mg/mL of mitochondria).
14. Minimize contamination in mass spectrometry:

    Do not store organic solvents used for the sample preparation in plastic tubes. PEG contaminants and plasticizers such phthalates can leach out of plastic into the sample and make their way to the LC-MS system. Always use glass bottles.

    If you have to use detergent to wash the glassware, be sure to rinse them with large volume of deionized water before use. Detergents contain PEG materials which can contaminate reversed phase columns and cause ion suppression in mass spectrometry.
15. Dichloromethane is a harmful organic solvent with some evidence of carcinogenic effects. It must be handled wearing safety gloves and in a fume hood at all times. Be sure to read dichloromethane MSDS before use.
16. Dichloromethane has a high vapor pressure at room temperature that makes it difficult to be accurately measured and transferred using pipettes. To minimize loss of DCM through evaporation during pipetting, pipet up and down several times in DCM to ensure the inside of pipette tip is saturated with CDM vapors.
17. Centrifugation of the sample at 4 °C helps keep the DCM layer cool. Transfer the DCM layer while it is still cool. Cold DCM is easier to transfer using pipette tips and less prone to loss via evaporation.
18. Before drying the lipid extracts in a vacuum centrifuge, cool the extracts down in a −20 °C freezer. This will help minimize exposure to DCM vapors when opening and placing sample tubes in the vacuum centrifuge, in case the instrument is not placed in a fume hood.
19. Reconstitute the samples with the appropriate solvent right before LC-MS analysis. Avoid keeping the reconstituted samples for prolonged time before LC-MS analysis to minimize potential lipid degradation. Store the extra samples in a −80 °C freezer.

20. MS Preparation for Lipidomics Profiling: Mass calibration: Mass calibration should be done to the instrument vendor's specifications. On the Exactive in our laboratory, mass calibrations are done weekly. Calibrations are done separately in positive and negative ion modes.

    MS Tuning: Tuning of the MS is done to optimize ion transmission through the ion optics to the analyzer. Tuning is therefore performed at the operating LC FLOW rate and the compound chosen as the tuning compound should have similar ESI characteristics as your molecules of interest and should be at the same concentration as a majority of molecules being analyzed. As an example, for our LC-MS analysis, we tee-in (using a splitter) 2.5 μg/mL of PG 17:0/17:0 flowing at 10 μL/min and 50:50 of mobile phase A and Mobile Phase B at a flow of 250 μL/min (total flow into MS is 260 μL/mL). The final concentration of PG 17:0/17:0 into the MS is ~100 ng/mL.

    LC Solvents: Always use LC-MS grade solvents to avoid contamination of mass spectrometer with impurities. To assist with solubilization of ammonium formate in mobile phase B, first dissolve it in ~1 mL of deionized water.

21. Analysis of lipid samples by reversed-phase LC-MS: Lipids, (especially triglycerides) are very hydrophobic and thus they tend to stick to the injector port which leads to carryover from sample-to-sample. To avoid carryover, it is important to flush the injector port thoroughly. We usually flush the injector port with 50:50 acetonitrile: isopropanol and 50:50 isopropanol–dichloromethane (10× with each). The isopropanol in dichloromethane wets the needle and prevents drying (which can ruin the needle plunger). It is also is important to ensure that the solvent used for flushing area is miscible.

22. Tuning the ESI source parameters (e.g., temperature, source voltages and gas flow rates) is important to ensure that lipids are transmitted optimally to the analyzer. Additionally, if the source parameters are not optimized; for example, if the source voltages are set too high, lipids can fragment in the ionization source. This In-source fragmentation (ISF) of lipids can be problematic if the resulting ion masses correspond to the masses of another lipid thus leading to misannotation of fragment ions as true lipids [27, 28].

    In the negative ionization mode, lipids that are prone to ISF to produce lower mass fragment ions that look like other lipids include: (a) Phosphocholine which lose a methyl group to produce fragment ions with the same mass as PEs, (b) glycosyl-ceramides and ceramide phosphates, which lose their glycosyl and phosphate group, respectively, to form a fragment with the same mass as their respective ceramide

(c) the fragmentation of all PLs (i.e., PG, PI, PS, PC) which after the loss of their head groups, form in-source fragments with the same exact mass as phosphatidic acid, and iv) PLs also fragment in-source to produce ions that correspond to masses of free fatty acids and their respective lysoforms [27]. In the positive ionization mode, lipids that fragment in-source include cholesteryl esters which lose their fatty acyl chain to form ions that correspond to free cholesterol, and, TGs which lose one or two of their three fatty acyl chains to produce ions that correspond to DGs and MGs respectively [29].

23. The framing parameters in these experiments are set at 0.01 Daltons for the *m/z* window and 1.00 min for the RT window; 1000 is used at the intensity threshold. Peaks under this intensity will normally be background or too low to quantify robustly. These parameters can be adjusted based on your own data. A pool from the middle of the sample sequence should be used as a qualitative reference and for relative quantitation, and frames built off the reference are then applied to all samples in the experiment. If a different reference is used, the intensity values may change slightly, however, the overall lipid ratios should be the same.

24. Chromatographic alignment and framing using Sieve: For Sieve analysis on the LC-MS lipidomics data, the small molecule, chromatographic alignment and framing and the nondifferential single class analysis options are used. Positive and negative ion data are analyzed separately and only the full scan raw data is used for alignment and framing. The framing parameters used are determined by the user. The *m/z* window chosen depends on the mass accuracy of the instrument used. The retention time window chosen should be large enough to enable correct chromatographic alignment to account for retention time drifts over time, but not too large so as to minimize false positives. We therefore, typically use 1 min for the retention time window and an intensity threshold of 1000 (to ensure that as many features as possible are identified but without picking out the noise).

25. Lipid Identification: To assist with lipid identification of the lipids obtained from the framing data, HCD analysis (done separately in the positive and negative modes) is performed on a pooled sample. HCD fragmentation is done at three energies 30 eV (low energy), 60 eV (medium energy), and 100 eV (high energy).

    Lipid identification is done by matching the retention time of extracted ion chromatogram of a particular exact mass and its fragments obtained using the all ion fragmentation data. This alignment helps in distinguishing lipids with the same exact mass but different fatty acyl chains. *See also* **Note 22**.

## Acknowledgments

These studies were funded by U01-ES16048 (BSK, PI) and P30-DK040561 (W. Allan Walker, PI). The authors thank ThermoFisher for the loan of an Exactive Benchtop orbitrap for demonstration testing (later purchased) and financial support for scientific meeting attendance.

*Financial Disclosures*

IGS and RMG have no financial disclosures.

SSB currently works for ThermoFisher.

BSK is the inventor of general metabolomics-related IP that has been licensed to Metabolon via Weill Medical College of Cornell University, for which he receives royalty payments via Weill Medical College of Cornell University. He also has a small equity interest in the company. Metabolon offers biochemical profiling services and is developing molecular diagnostic assays detecting and monitoring disease. Metabolon has no rights or proprietary access to the research results presented and/or new IP generated under these grants/studies. BSK's interests were reviewed by the Brigham and Women's Hospital and Partners Healthcare in accordance with their institutional policy. Accordingly, upon review, the institution determined that BSK's financial interest in Metabolon does not create a significant financial conflict of interest (FCOI) with this research. The addition of this statement where appropriate was explicitly requested and approved by BWH.

## References

1. Kroemer G, Galluzzi L, Brenner C (2007) Mitochondrial membrane permeabilization in cell death. Physiol Rev 87:99–163
2. Rasola A, Bernardi P (2007) The mitochondrial permeability transition pore and its involvement in cell death and in disease pathogenesis. Apoptosis 12:815–833
3. Osman C, Voelker D, Langer T (2011) Making heads or tails of phospholipids in mitochondria. J Cell Biol 192:7–16
4. Horvath SE, Daum G (2013) Lipids of mitochondria. Prog Lipid Res 52:590–614
5. Claypool SM, Koehler CM (2012) The complexity of cardiolipin in health and disease. Trends Biochem Sci 37:32–41
6. Pfeiffer K, Gohil V, Stuart RA, Hunte C, Brandt U, Greenberg ML, Schagger H (2003) Cardiolipin stabilizes respiratory chain supracomplexes. J Biol Chem 278:52873–52880
7. Klingenberg M (2009) Cardiolipin and mitochondrial carriers. Biochim Biophys Acta 1788:2048–2058
8. Kagan VE, Tyurin VA, Jiang J, Tyurina YY, Ritov VB, Amoscato AA, Osipov AN, Belikova NA, Kapralov AA, Kini V, Vlasova II, Zhao Q, Zou M, Di P, Svistunenko DA, Kurnikov IV, Borisenko GG (2005) Cytochrome c acts as a cardiolipin oxygenase required for release of proapoptotic factors. Nat Chem Biol 1:223–232
9. Kameoka S, Adachi Y, Okamoto K, Iijima M, Sesaki H (2018) Phosphatidic acid and cardiolipin coordinate mitochondrial dynamics. Trends Cell Biol 28:67–76
10. Lesnefsky EJ, Hoppel CH (2008) Cardiolipin as an oxidative target in cardiac mitochondria in the aged rat. Biochim Biophys Acta 1777:1020–1027
11. Esterbauer H, Schaur RJ, Zollner H (1991) Chemistry and biochemistry of 4-hydroxynonenal, malonaldehyde and related aldehydes. Free Radic Biol Med 11:81–128
12. Stavrovskaya IG, Baranov SV, Guo X, Davies SS, Roberts LJ 2nd, Kristal BS (2010) Reactive gamma-ketoaldehydes formed via the

isoprostane pathway disrupt mitochondrial respiration and calcium homeostasis. Free Radic Biol Med 49:567–579

13. Keller JN, Mattson MP (1998) Roles of lipid peroxidation in modulation of cellular signalling pathways, cell dysfunction, and death in the nervous system. Rev Neurosci 9:105–116
14. Kristal BS, Park BK, Yu BP (1996) 4-Hydroxynonenal is a potent inducer of the mitochondrial permeability transition. J Biol Chem 271:6033–6038
15. Ejsing CS, Moehring T, Bahr U, Duchoslav E, Karas M, Simons K, Shevchenko A (2006) Collision-induced dissociation pathways of yeast sphingolipids and their molecular profiling in total lipid extracts: a study by quadrupole TOF and linear ion trap-orbitrap mass spectrometry. J Mass Spectrom 41:372–389
16. Wikoff WR, Anfora AT, Liu J, Schultz PG, Lesley SA, Peters EC, Siuzdak G (2009) Metabolomics analysis reveals large effects of gut microflora on mammalian blood metabolites. Proc Natl Acad Sci U S A 106:3698–3703
17. Picotti P, Clément-Ziza M, Lam H, Campbell DS, Schmidt A, Deutsch EW, Röst H, Sun Z, Rinner O, Reiter L, Shen Q, Michaelson JJ, Frei A, Alberti S, Kusebauch U, Wollscheid B, Moritz RL, Beyer A, Aebersold RA (2013) Complete mass-spectrometric map of the yeast proteome applied to quantitative trait analysis. Nature 494:266–270
18. Fahy E, Subramaniam S, Brown HA, Glass CK, Merrill AH Jr, Murphy RC, Raetz CR, Russell DW, Seyama Y, Shaw W, Shimizu T, Spener F, van Meer G, VanNieuwenhze MS, White SH, Witztum JL, Dennis EA (2005) A comprehensive classification system for lipids. J Lipid Res 46:839–861
19. Bird SS, Marur VR, Sniatynski MJ, Greenberg HK, Kristal BS (2011) Lipidomics profiling by high-resolution LC-MS and high-energy collisional dissociation fragmentation: focus on characterization of mitochondrial cardiolipins and monolysocardiolipins. Anal Chem 83:940–949
20. Bird SS, Marur VR, Sniatynski MJ, Greenberg HK, Kristal BS (2011) Serum lipidomics profiling using LC-MS and high-energy collisional dissociation fragmentation: focus on triglyceride detection and characterization. Anal Chem 83:6648–6657
21. Gregory KE, Bird SS, Gross VS, Marur VR, Lazarev AV, Walker WA, Kristal BS (2013) Method development for fecal lipidomics profiling. Anal Chem 85:1114–1123
22. Stavrovskaya IG, Bird SS, Marur VR, Sniatynski MJ, Baranov SV, Greenberg HK, Porter CL, Kristal BS (2013) Dietary macronutrients modulate the fatty acyl composition of rat liver mitochondrial cardiolipins. J Lipid Res 54:2623–2635
23. Smith CA, O'Maille G, Want EJ, Qin C, Trauger SA, Brandon TR, Custodio DE, Abagyan R, Siuzdak G (2005) METLIN: a metabolite mass spectral database. Ther Drug Monit 27:747–751
24. Stavrovskaya IG, Narayanan MV, Zhang W, Krasnikov BF, Heemskerk J, Young SS, Blass JP, Brown AM, Beal MF, Friedlander RM, Kristal BS (2004) Clinically approved heterocyclics act on a mitochondrial target and reduce stroke-induced pathology. J Exp Med 200:211–222
25. Wishart DS, Knox C, Guo AC, Eisner R, Young N, Gautam B, Hau DD, Psychogios N, Dong E, Bouatra S, Mandal R, Sinelnikov I, Xia J, Jia L, Cruz JA, Lim E, Sobsey CA, Shrivastava S, Huang P, Liu P, Fang L, Peng J, Fradette R, Cheng D, Tzur D, Clements M, Lewis A, De Souza A, Zuniga A, Dawe M, Xiong Y, Clive D, Greiner R, Nazyrova A, Shaykhutdinov R, Li L, Vogel HJ, Forsythe I (2009) HMDB: a knowledgebase for the human metabolome. Nucleic Acids Res 37:D603–D610
26. Fahy E, Sud M, Cotter D, Subramaniam S (2007) LIPID MAPS online tools for lipid research. Nucleic Acids Res 35:W606–W612
27. Gathungu RM, Larrea P, Sniatynski MJ, Marur VR, Bowden JA, Koelmel JP, Starke-Reed P, Hubbard VS, Kristal BS (2018) Optimization of electrospray ionization source parameters for lipidomics to reduce misannotation of in-source fragments as precursor ions. Anal Chem 90:13523–13532
28. Criscuolo A, Zeller M, Fedorova M (2020) Evaluation of lipid in-source fragmentation on different orbitrap-based mass spectrometers. J Am Soc Mass Spectrom 31:463–466
29. Höring M, Ejsing CS, Hermansson M, Liebisch G (2019) Quantification of cholesterol and cholesteryl ester by direct flow injection high-resolution Fourier transform mass spectrometry utilizing species-specific response factors. Anal Chem 91:3459–3466

# Chapter 25

# Live Imaging of Mitochondria in Kidney Tissue

**Milica Bugarski, Susan Ghazi, and Andrew M. Hall**

## Abstract

Kidneys are highly aerobic organs and their function is tightly coupled to mitochondrial energy production. Renal tubular cells, particularly the proximal tubule (PT), require an abundance of mitochondria to provide sufficient energy for regulating fluid and electrolyte balance. Meanwhile, mitochondrial defects are implicated in a range of different kidney diseases. Multiphoton microscopy (MP) is a powerful tool that allows detailed study of mitochondrial morphology, dynamics, and function in kidney tissue. Here, we describe how MP can be used to image mitochondria in kidney tubular cells, either ex vivo in tissue slices or in vivo in living rodents, using both endogenous and exogenous fluorescent molecules. Moreover, changes in mitochondrial signals can be followed in real time in response to different insults or stimuli, in parallel with other important readouts of kidney tubular function, such as solute uptake and trafficking.

**Key words** Mitochondria, Kidney, Fluorescence imaging, Multiphoton microscopy

## 1 Introduction

The kidney is a highly metabolic organ and plays an important role in maintaining water, electrolyte, and acid–base homeostasis in the body. Specifically, metabolically intense reabsorption and excretion processes occur in the kidney, which place high energy demands on the renal tubule, and in particular the proximal tubule (PT). Accordingly, PTs possess a high density of mitochondria and are almost entirely dependent on aerobic respiration to generate ATP [1]. This renders them vulnerable to mitochondrial insults, such as ischemia and toxins, which are frequent causes of kidney disease in humans. While there are various nonimaging techniques available to investigate mitochondrial function, fluorescence microscopy has the distinct advantage of allowing for simultaneous assessment of mitochondrial structure, function, and dynamics in situ. Multiphoton (MP) microscopy is a type of fluorescence imaging ideally suited to working with intact tissues, due to a greater laser penetrance and less phototoxicity in comparison to standard confocal imaging [2].

Volkmar Weissig and Marvin Edeas (eds.), *Mitochondrial Medicine: Volume 1: Targeting Mitochondria*, Methods in Molecular Biology, vol. 2275, https://doi.org/10.1007/978-1-0716-1262-0_25,

We have demonstrated previously that mitochondrial structure and function can be imaged in rodent kidneys ex vivo and in vivo, using multiphoton excitation of endogenous and exogenous fluorophores. The ex vivo kidney slice preparation model has the advantage that structural integrity is relatively well preserved, but experimental conditions can be more tightly controlled than in living animals. For example, dyes, drugs, and metabolites can be directly applied to the tissue and changes in fluorescence signal recorded in real time [3]. However, there are some limitations of the slice model, including the possibility to introduce damage or artifacts via the slicing process itself. Furthermore, the nervous innervation of the kidney is lost and tissue slices have no exposure to circulating hormones and cytokines that are important in regulating kidney function. Intravital MP microscopy allows the exciting possibility to study cell and organelle function within intact, working organs [4]. A major advantage of this approach is that mitochondrial signals can be coimaged with other important readouts of kidney function, such as blood flow, glomerular filtration, tubular flow, and solute uptake and transport [5–7]. However, these advantages have to be weighed against the practical challenges of in vivo imaging, such as maintaining the health of the animal and achieving sufficient loading of dyes into cells. Moreover, only tubules in the outer cortex can be visualized.

A range of different aspects of mitochondrial function can be assessed in kidney tissue using fluorescence imaging. For example, endogenous autofluorescence signals, such as NADH and flavoproteins (FP), can provide label free readouts concerning redox state and substrate metabolism [8]. Meanwhile, uptake of voltage or pH sensitive probes can be used to assess mitochondrial membrane potential ($\Delta\Psi_m$) and pH gradients ($\Delta pH_m$) across the inner mitochondrial membrane, respectively. Examples of such dyes include tetramethylrhodamine, methyl ester (TMRM) and Rhodamine 123, which are both voltage sensitive [9], and 5-(and-6)-carboxy SNARF-1, acetoxymethyl ester, acetate (C-SNARF-1), which is pH sensitive [10].

## 2 Materials

### 2.1 Kidney Slices

Prepare all solutions using ultrapure deionized water and analytical grade reagents.

#### 2.1.1 Kidney Slice Buffer

1. 1 L 10× slice buffer stock solution: 118 mM NaCl, 4.7 mM KCl, 1.2 mM $KH_2PO_4$, 10 mM $NaHCO_3$, 10 mM HEPES. Weigh 68.96 g NaCl, 3.5 g KCl, 1.63 g $KH_2PO_4$, 8.4 g $NaHCO_3$, and 28.83 g HEPES. Add 800 mL of water and mix. Make up to a total volume of 1 L. Store at room temperature (RT).

2. 1 L of 1× slice buffer (make one day prior to experiment): 100 mL 10× slice buffer; 1.8 mM $CaCl_2$, 1.44 mM $MgSO_4$, 5 mM glucose, 5 mM sodium pyruvate, 2.5 mM sodium butyrate, and 2.5 mM sodium lactate. Weigh 0.2 g $CaCl_2$, 0.17 g $MgSO_4$, 0.9 g glucose, 0.55 g sodium pyruvate, 0.28 g sodium butyrate, and 0.28 g sodium lactate. Add 100 mL of 10× slice buffer and make up to 1 L with water. Split the 1× buffer solution into two parts, put one on ice and the other heating on 37 °C. Mix and adjust the pH of both buffers to 7.4 on appropriate temperature (4 °C or 37 °C) (*see* **Note 1**) while gassing with continuous supply of 95% $O_2$ and 5% $CO_2$ (Oxycarbon medicinal). Once pH is set, store both buffer solutions at 4 °C.

*2.1.2 Anesthesia*

1. Prepare anesthetic prior to experiment: mix ketamine (170 mg/kg) and xylazine (10 mg/kg) in 1× PBS.

*2.1.3 Setup for Slicing and Imaging*

1. Temperature controller, inline heater, heated chamber, grids, and harps (Warner Instruments, Hamden, CT, USA).
2. Perfusion pump (Watson-Marlow Pumps, Cornwall, UK).
3. Polyethylene tubing, ID: 0.58 mm, 1.14 mm, or 2.05 mm (Warner Instruments, Hamden, CT, USA and Watson-Marlow Pumps, Cornwall, United Kingdom).
4. Oxycarbon gas bottle (Oxycarbon medizinal, Pangas AG, Hauptsitz, Switzerland).
5. Liquid glue (Loctite—Henkel Adhesives, Düsseldorf, Germany).

*2.1.4 Mitochondrial Toxins*

1. 100 mM stock solution of respiratory chain uncoupler FCCP, dissolved in ethanol. Keep aliquots at −20 °C. Working solution of FCCP: 5 μM dissolved in 1× slice buffer.
2. 500 mM stock solution of respiratory chain inhibitor sodium cyanide, dissolved in water. Keep aliquots at −20 °C. Working solution of sodium cyanide: 5 mM dissolved in 1× slice buffer (*see* **Note 2**).

*2.1.5 Mitochondrial Dyes*

1. Voltage dependent dye Rhodamine 123 (Molecular Probes, Eugene, OR, USA): 50 mM stock solution dissolved in DMSO. Keep aliquots at −20 °C. Working solution of Rhodamine 123: 50 nM dissolved in 1× slice buffer (*see* **Note 3**).
2. pH dependent dye C-SNARF-1 (Molecular Probes, Eugene, OR, USA): 1 mM of stock solution dissolved in DMSO (*see* **Note 4**). Working solution of C-SNARF-1: 10 μM in 1× slice buffer (*see* **Note 5**).

### 2.2 Intravital Imaging of the Kidney

#### 2.2.1 Agarose

1. 4.5% agarose in 0.9% NaCl solution: weigh 0.9 g of NaCl and dissolve in 100 mL of water. Once NaCl is dissolved, add 4.5 g of agarose. Heat up and stir thoroughly until agarose is boiled and dissolved. Store in aliquots at −20 °C (*see* **Note 6**).

#### 2.2.2 Surgery

1. Surgical tools (forceps, clamps, fine scissors, spring scissors), needle and thread (FST, Heidelberg Germany).
2. Tissue glue—Histoacryl Flexible (Braun, Hessen, Germany).
3. Polyethylene tubing (ID 0.28 mm) for cannulating the jugular vein (Fisher Scientific, Loughborough, UK).
4. Feedback loop warming system—Complete Homeothermic Blanket System with Flexible Probe (Harvard apparatus, Holliston, MA, USA).
5. Pump 11 Elite—Standard Infuse/Withdraw Programmable Syringe Pumps (Harvard apparatus, Holliston, MA, USA).

#### 2.2.3 Anesthesia

1. Isoflurane connected to oxygen bottle source—VetFlo (Kent Scientific Corporation, Torrington, CT, USA).

#### 2.2.4 Dyes

1. Voltage-dependent dye TMRM (Molecular Probes, Eugene, OR, USA): 50 mM stock solution dissolved in DMSO. Keep aliquots at −20 °C. Final concentration, prepared prior to experiment: 0.4 mg/kg dissolved in 0.9% NaCl.
2. Dextran Alexa 647 (Molecular Probes, Eugene, OR, USA): 2 mg/ml stock solution dissolved in 1× PBS. Store in aliquots at −80 °C. Final concentration, prepared prior to experiment: 2 mg/kg dissolved in 0.9% NaCl.

## 3 Methods

### 3.1 Kidney Slices

#### 3.1.1 Slicing

1. Inject ketamine–xylazine mix intraperitoneally and wait until the animal is deeply anaesthetized. Quickly remove the kidneys by pulling them out from the renal artery using tweezers (*see* **Note 7**). After the removal of capsule, one pole of the kidney is mounted and cut with a vibratome (Microm HM 650 V, Thermo Scientific, Waltham, MA, USA) into thin sections (*see* **Note 8**). Tissue is kept oxygenated at 4 °C in 1× slice buffer until used at the microscope.

#### 3.1.2 Setup at the Microscope

1. Make the perfusion system by connecting the 1× slice buffer supply to the slices chamber, using polyethylene tubing (*see* Fig. 1a). Use an inline heater to keep the temperature at 37 °C.
2. Mount the slices into an open-bath heated chamber platform using anchor harps to keep the kidney slices stable and ensure no movement occurs during the imaging (*see* Fig. 1b, c). Set the heated platform on a microscopic stage underneath an objective and perfuse with oxygenated 1× slice buffer at 37 °C.

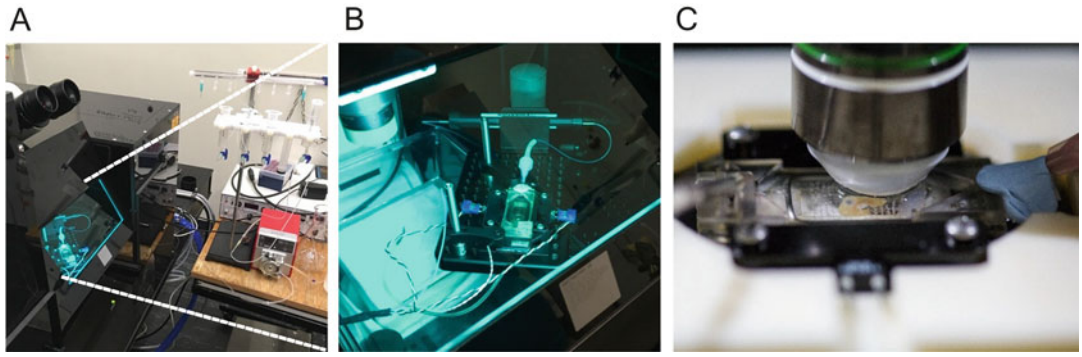


**Fig. 1** Setup for imaging of kidney slices (**a**) Perfusion system, temperature controller and perfusion pump supplying the slice buffer to the chamber. (**b**) Open-bath slice chamber mounted on a microscope platform. Inline and chamber heaters keep the temperature of the buffer at 37 °C. (**c**) The kidney slice is stabilized within the chamber using anchor harps

#### *3.1.3 Imaging*

1. Autofluorescence signals: Mitochondria are known to emit autofluorescence signals originating from NAD and FPs [11]. NADH emits fluorescence in the blue range (420–480 nm) when in reduced state [12], with a maximum two photon excitation at 700–750 nm (*see* **Note 9**). FPs emit in the green range when in oxidized state, but their fluorescence properties depend on the type of protein within which they are contained [11]. We found that maximum excitation for FPs in mitochondria was at 850–900 nm, while the maximum emission occurred at 560–590 nm [8] (*see* Fig. 2a). To test the redox sensitivity of the NADH signal, apply the respiratory chain uncoupler FCCP (5 μM) and inhibitor cyanide (5 mM). Mitochondrial NADH signal should decrease in response to FCCP, and increase in response to cyanide (*see* Fig. 2b).
2. To assess the mitochondrial signal with Rhodamine 123, slices should be incubated for 30 minutes at RT with 50 nm Rhodamine 123 in gassed 1× slice buffer. This dye is excited at 850 nm and the fluorescence signal emitted at 500–550 nm (*see* Fig. 2c).
3. For mitochondrial pH signals, incubate slices for 15 min with 10 μM C-SNARF-1 in gassed 1× slice buffer at RT (*see* **Note 5**). This dye is excited at 800 nm and fluorescence emission is recorded at 565–605 nm and 625–675 nm wavelengths simultaneously. pH values can be derived by ratiometric measurements of the emission recordings at both wavelengths [10] (*see* **Note 10**).

### *3.2 Intravital Imaging of the Kidney*

Maintenance of the health of the animal while under anesthesia is vital to maintain normal kidney function and obtain reliable and reproducible results. The check the depth of anesthesia it is sufficient to monitor respiration rate and the lack of withdrawal reflexes

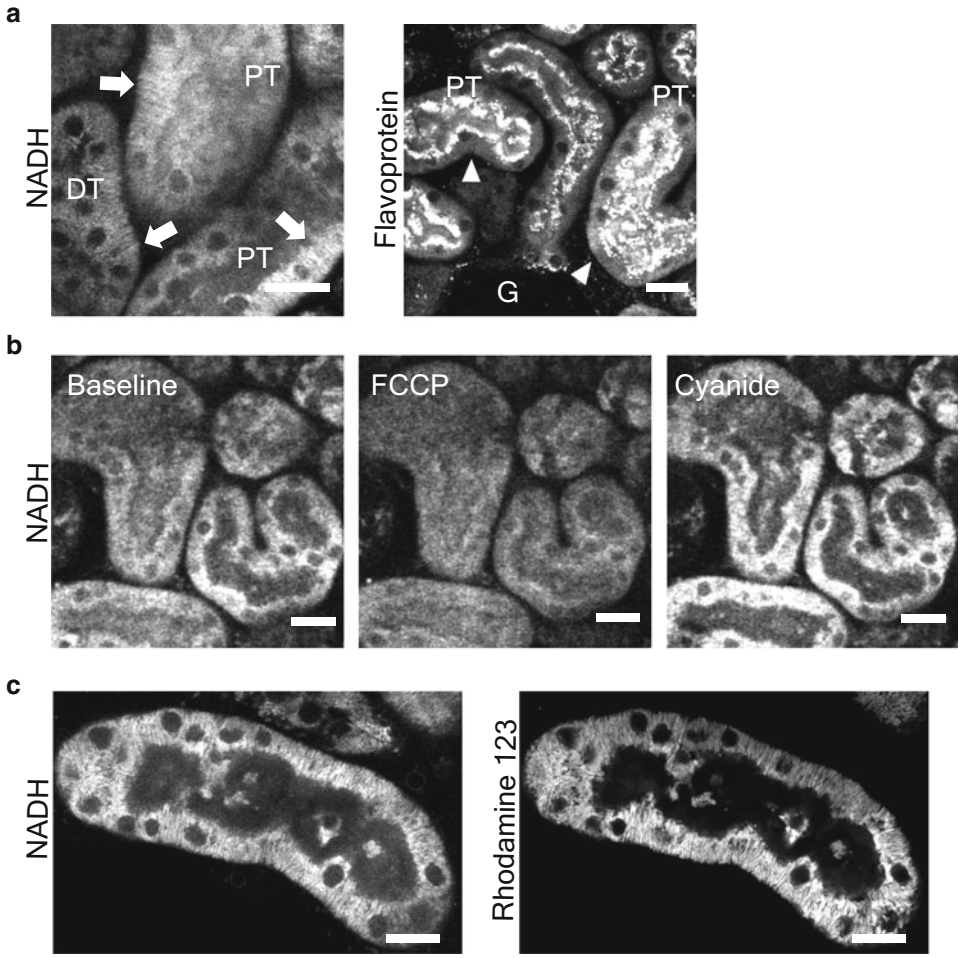


**Fig. 2** Imaging of mitochondria in kidney slices. (**a**) Example images of metabolic autofluorescence signals in the mouse kidney cortex. Mitochondrial NADH signal (arrows) was excited at 700–750 nm and visualized at 420–500 nm. Flavoprotein signal in mitochondria (arrowheads) was excited at 900 nm and collected at 515–560 nm. (**b**) NADH redox state can be manipulated with respiratory chain (RC) uncouplers and inhibitors. For example, the uncoupler FCCP (5 μm) decreases NADH fluorescence, while the inhibitor cyanide (5 mM) increases it. (**c**) Coimaging of NADH signal and the mitochondrial membrane potential-dependent dye Rhodamine 123. Scale bars = 20 μm. *PT* proximal tubule, *DT* distal tubule, *G* glomerulus. (All images were taken from Bugarski M et al., (2018) Am J Physiol Renal Physiol. 315(6):F1613-F1625)

following tail or leg pinch. Animals need to be on a temperature-controlled stage and body temperature should be closely monitored and regulated at all times. A rectal temperature probe coupled to a thermometer is an established method to follow the animal's core temperature in real time. Because prolonged periods of anesthesia could lead to decrease in blood pressure, it is important to control this parameter during image acquisition. Blood pressure can be recorded with a transducer/amplifier system connected to the arterial catheter or by commercially available noninvasive blood-pressure monitoring devices [13].

#### 3.2.1 Surgery

1. Animals need to be deeply anesthetized with isoflurane before starting the surgery. The right jugular vein needs to be cleaned, cut, and cannulated with polyethylene tubing in order to access the vascular system, in which dyes will be injected. Once cannulated, ensure the vein is tightly sutured with thread and apply Histoacryl flexible glue on top.

#### 3.2.2 Externalization of the Kidney

1. Exposure of the organ is accomplished via a small flank incision in the abdomen. The left kidney is externalized and rested on the cover slide of the microscopic stage and agarose is poured to ensure support to the kidney and stable conditions for acquiring images (*see* **Note 11**).

#### 3.2.3 Imaging

1. Finding the region of interest: visualize the capsule by exciting at 850 nm and collecting emission light in the blue and green channels (330–550 nm). Zoom in to visualize the kidney cortex and kidney tubules. S1 and S2 segments of proximal tubules can be distinguished by characteristic autofluorescence signals [8] (*see* **Notes 9** and **12**).
2. Application of dyes: these are prepared in 0.9% NaCl and applied with the pump 11 elite system, in 100 μL volume, with 300 μL/min infusion rate.
3. Coimaging of TMRM and Dextran: The tubular and vascular compartments can be visualized by using fluorescent molecules of different sizes that are either freely filtered or retained in the circulation, respectively. To visualize filtration and endocytosis of dextran Alexa 647, excite at 1120 nm and acquire images in the far-red channel (660–740 nm). After 30 min, TMRM can be injected at the same volume and rate. Optimal settings for this dye are 850 nm excitation and 580–630 nm emission wavelengths (*see* Fig. 3). The rate of GFR can be calculated by drawing regions of interest (ROIs) in the vasculature and measuring the decay of fluorescence signal [15]. Tubular flow can be assessed by the decay of fluorescence signal emitted by the freely filtered molecules inside the tubular lumen.

## 4 Notes

1. pH of the buffer is temperature dependent. Make sure you set the pH on the adequate temperature (4 °C or 37 °C), while gassing. Important: it takes a couple of hours until the pH is stable; therefore, we suggest to prepare the buffers 1 day before your experiment.
2. Sodium cyanide is alkaline. Measure the pH of your working solution and correct it to pH of 7.4 before applying it to the kidney slice.

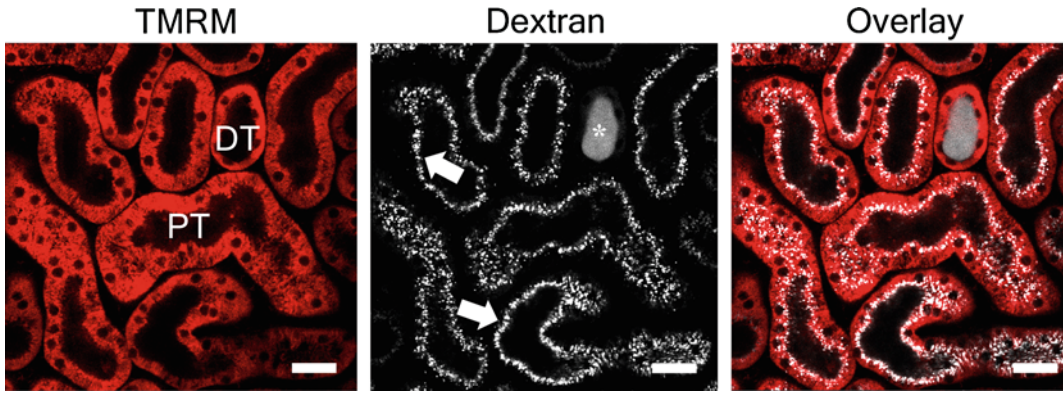


**Fig. 3** Intravital multiphoton imaging of the kidney. The mitochondrial membrane potential ($\Delta\psi_m$)–dependent dye tetramethyl rhodamine methyl ester (TMRM) is taken up by tubules in vivo and localizes to mitochondria. Dextran Alexa 647 (10 kD), a marker for fluid-phase endocytosis [14], is rapidly filtered from the blood and taken up apically into proximal tubules (arrows). Luminal wasting of concentrated dextran (*) can be observed in the distal tubule. Scale bars = 30 μm. *PT* proximal tubule, *DT* distal tubule

3. Rhodamine 123 is a cationic fluorescent dye that accumulates in the negatively charged interior of mitochondria. It is important to use low concentrations (10–50 nM range) of Rhodamine 123 in order to avoid autoquenching of this dye in the mitochondria [16].
4. It is important to freshly prepare the stock solution of C-SNARF-1 on the day of the experiment and keep it at RT.
5. C-SNARF-1 can be toxic to tissue slices, especially at 37 °C, as the dye accumulates more potently into the cells. As an alternative, you can perform the experiment at RT to preserve the health of the slice for a longer period of time.
6. Wait approx. 1 h for agarose to dissolve. Important: place agarose powder in 0.9% NaCl on RT. If the solution is preheated the agarose will not melt.
7. To maintain the health of the tissues slices, it is crucial to supply them continuously with nutrients and oxygen. Therefore, kidneys have to be externalized fast and immediately placed on ice in oxygenated 1× slice buffer. Under these conditions, the slices remain usable up to about 6–8 h.
8. Slices of kidney tissue can be cut from either cortex or the medulla. If you are interested in imaging the cortical region of the kidney, we suggest to cut 250 μm thick cross-sections. For imaging the medulla, make sagittal 280 μm thick sections.
9. When imaging autofluorescence signals be careful with repetitive and high-laser power imaging, due to phototoxicity. Make sure you optimize the zoom, format and speed of image acquisition, along with the laser power you will use.

10. C-SNARF-1 has a dual emission peak (at 580 and 640 nm) and mitochondrial pH values from tissue slices can be derived by ratiometric measurements at wavelengths corresponding to the maxima emission. First, the dye has to be calibrated in vitro, as in situ calibration is not feasible in tissue slices. For the calibration, you use Tris buffered solution (1 M) with a range of different pH values (pH 5.0—9.0) and add C-SNARF-1 in a final concentration of 2 μM. The intensity ratios derived at the two wavelengths have then to be plotted in a linear calibration plot as in eq. 1 [17], where R is the ratio of the fluorescence intensities (F) $F\lambda_1/F\lambda_2$ measured at two wavelengths $\lambda_1$ (580 nm) and $\lambda_2$ (640 nm). The subscripts $A$ and $B$ indicate the values of the most acidic and most basic pH respectively. The $p\mathrm{K_A}$ is equal to the intercept of this linear plot.

$$p\mathrm{H} = pK_A - \log\left[\frac{R - R_B}{R_A - R} \times \frac{F_{B(\lambda 2)}}{F_{A(\lambda 2)}}\right]$$

This calibration curve can subsequently be used to deduct pH values from raw images of tissue slices derived at the two different emission wavelengths. To measure the pH signal specifically inside the mitochondria, you can draw small ROIs in your image around the mitochondrial region of the cell.

11. A small suture should be made around the abdominal incision. After externalization of the kidney close the suture to ensure that the kidney does not return to the abdominal cavity. However, do not tight it too strong in order to avoid ischemia.
12. Check if the tubular lumen is open. If the lumens are collapsed, due to low blood pressure, there will be no delivery of the fluorescent probes to the kidney tubules. Reducing isoflurane anesthesia or injecting small volume of 0.9% NaCl to the jugular vein could help with increasing the blood pressure, which is usually accompanied by opening of collapsed lumens.

## Acknowledgments

This work was supported by The Swiss National Centre for Competence in Research (NCCR) Kidney Control of Homeostasis and by a project grant from the Swiss National Science Foundation. The authors also acknowledge support from The Zurich Centre for Microscopy and Image Analysis and The Zurich Centre for Integrative Human Physiology.

## References


1. Bagnasco S, Good D, Balaban R, Burg M (1985) Lactate production in isolated segments of the rat nephron. Am J Physiol 248: F522–F526
2. Fujita K (2007) Two-photon laser scanning fluorescence microscopy. Tanpakushitsu Kakusan Koso 52:1778–1779
3. Hall AM, Unwin RJ, Parker N, Duchen MR (2009) Multiphoton imaging reveals differences in mitochondrial function between nephron segments. J Am Soc Nephrol 20:1293–1302
4. Weigert R, Sramkova M, Parente L et al (2010) Intravital microscopy: a novel tool to study cell biology in living animals. Histochem Cell Biol 133:481–491
5. Molitoris BA, Sandoval RM (2005) Intravital multiphoton microscopy of dynamic renal processes. Am J Physiol 288:1084–1089
6. Peti-Peterdi J, Toma I, Sipos A, Vargas SL (2009) Multiphoton imaging of renal regulatory mechanisms. Physiology 24:88–96
7. Hall AM, Crawford C, Unwin RJ et al (2011) Multiphoton imaging of the functioning kidney. J Am Soc Nephrol 22:1297–1304
8. Bugarski M, Martins JR, Haenni D, Hall AM (2018) Multiphoton imaging reveals axial differences in metabolic autofluorescence signals along the kidney proximal tubule. Am J Physiol Renal Physiol 315:F1613–F1625
9. Scaduto RC, Grotyohann LW (1999) Measurement of mitochondrial membrane potential using fluorescent rhodamine derivatives. Biophys J 76:469–477
10. Bassnett S, Reinisch L, Beebe DC (1990) Intracellular pH measurement using single excitation-dual emission fluorescence ratios. Am J Physiol 258:C171–C178
11. Chance B, Schoener B, Oshino R et al (1979) Oxidation-reduction ratio studies of mitochondria in freeze-trapped samples. NADH and flavoprotein fluorescence signals. J Biol Chem 254:4764–4771
12. Mayevsky A, Chance B (2007) Oxidation-reduction states of NADH in vivo: from animals to clinical use. Mitochondrion 7:330–339
13. Dunn KW, Sutton TA, Sandoval RM (2007) Live-animal imaging of renal function by multiphoton microscopy. Curr Protoc Cytom 41:12.9.1–12.9.18
14. Gekle M, Mildenberger S, Freudinger R, Silbernagl S (1995) Endosomal alkalinization reduces J(max) and K(m) of albumin receptor-mediated endocytosis in OK cells. Am J Physiol 268:F899–F906
15. Wang E, Sandoval RM, Campos SB, Molitoris BA (2010) Rapid diagnosis and quantification of acute kidney injury using fluorescent ratiometric determination of glomerular filtration rate in the rat. Am J Physiol Renal Physiol 299:1048–1055
16. Perry SW, Norman JP, Barbieri J et al (2011) Mitochondrial membrane potential probes and the proton gradient: a practical usage guide. BioTechniques 50:98–115
17. Owen S (1992) Comparison of Spectrum-shifting intracellular pH. Anal Biochem 204:65–71

# Chapter 26

# Time-Resolved Imaging of Mitochondrial Flavin Fluorescence and Its Applications for Evaluating the Oxidative State in Living Cardiac Cells

**A. Marcek Chorvatova, M. Cagalinec, and D. Chorvat Jr**

## Abstract

Time-resolved fluorescence spectrometry is a highly valuable technological tool to detect and characterize mitochondrial metabolic oxidative changes by means of endogenous fluorescence. Here, we describe detection and measurement of endogenous mitochondrial flavin fluorescence directly in living cardiac cells using fluorescence lifetime imaging microscopy (FLIM) after excitation with 473 nm picoseconds (ps) laser. Time-correlated single photon counting (TCSPC) method is employed.

**Key words** Mitochondrial oxidative state, Endogenous flavin fluorescence, FLIM, TCSPC, Energy metabolism

## 1 Introduction

Fluorescence lifetime imaging and spectroscopy has made an important impact in the field of monitoring of the mitochondrial metabolic processes implicated in energy production in living cells and tissues [1–4]. Naturally occurring endogenous fluorophores and their fluorescence (also called autofluorescence) offer the possibility to study noninvasively mitochondrial metabolic processes. Despite their lower fluorescence yield when compared to fluorescence probes or dyes, endogenous fluorophores are highly advantageous for noninvasive tracking of changes in mitochondrial metabolic state by natural means. To evaluate mitochondrial metabolism, NAD(P)H and flavoproteins were proposed to be the marker of the metabolic oxidative state thanks to their principal role in energy production [5–7]. Addition of the time resolution, fluorescence spectroscopy enabled a deeper insight into metabolic processes thanks to the ability to distinguish individual fluorophores involved in energy production [8, 9]. Fluorescence lifetime is an internal property of the fluorophore. In general, it depends on

Volkmar Weissig and Marvin Edeas (eds.), *Mitochondrial Medicine: Volume 1: Targeting Mitochondria*, Methods in Molecular Biology, vol. 2275, https://doi.org/10.1007/978-1-0716-1262-0_26,

the ability of a fluorophore to transfer energy to its environment—and thus on the physicochemical characteristics of such environment, while being independent on the fluorophore concentration.

Endogenous fluorescence is an intrinsic property of living cells and while NAD(P)H is stimulated after excitation of the sample by ultraviolet (UV) light, flavins and flavoproteins are excited by visible light [4, 6, 8, 9]. This is particularly true in energetically highly active cells, such as cardiac myocytes [10–12]. Endogenous fluorescence results predominantly from mitochondria [13, 14] and it is therefore a good practice to verify the mitochondrial localisation of the recorded images of cellular autofluorescence and/or to compare them with AF distribution. Flavins are best excited in the range from 400 to 500 nm [13, 15] and their fluorescence occurs with maximum at 490–560 nm. After binding, flavins are reduced into FADH, a nonfluorescing molecule [8, 9, 12, 15]. Time-resolved approach identified two fluorescence decay components: 1.8–2.0 ns for the "free" form of flavins and 0.4–0.6 ns for, most likely, flavins "bound" to enzymes of the mitochondrial ETC (electron transport chain), in other words, "in use flavins" [3, 8, 9]. At lower wavelengths, fluorescence of NAD(P)H (emitting up to 500 nm) can affect the recording of the flavin fluorescence [16–18]. For the best results it is crucial to darken the experimental setup as much as possible: enclose it into a light-impermeable box/cover, or prevent the outside light to enter the laboratory.

Different types of flavins can be distinguished by different metabolic modulation [4–6, 9]. Modulation of the processes of energy production enables to study their roles in the cell metabolic state and can also provide a "calibration" of the metabolic oxidative state. OXPHOS (oxidative phosphorylation) can be either inhibited to reduce the oxidation, leaving the cells in a fully reduced state; or uncoupled from energy production, thus inducing a fully oxidized state [4–6, 19].

Both flavins and NAD(P)H can serve as metabolic oxidative state modulators. Although for spectral region where the NAD(P)H emits there is also a marginal collagen fluorescence, in the spectral regions where the flavins emits there are not only several types and forms of flavins emitting in a wide spectral band from 480 to approximately 560 nm, but also several other absorbing and emitting fluorophores (lipofuscins, melanin, riboflavin, porphyrins, etc.) [8–10]. Ability to detect and to distinguish between different forms of flavins by spectrally and time-resolved fluorescence is therefore highly useful to gather closer insight into the mitochondrial metabolism of various tissues [3, 12, 19] and, consequently, to understand changes that occur during either physiological (aging, differentiation) or pathophysiological conditions linked with modifications in mitochondrial metabolic oxidative state such as inflammations, transplanted tissue rejections, hypoxia, and/or cancer [4, 15, 16, 20]. Here, we describe flavin fluorescence lifetime imaging microscopy in cardiac cells isolated from rat hearts.

## 2 Materials

### 2.1 Solutions

Prepare all solutions using ultrapure water (produced by purifying the deionized water to attain the resistivity of 18 MΩ.cm at 25 °C). Adjust pH in all solutions to 7.35 with 1 mol/l NaOH, osmolarity 330 mosm/l.

1. **Solution 1Ca**: 135 mM NaCl, 5.4 mM KCl, 1.2 mM $MgSO_4$, 1 mM $CaCl_2$, 1.2 mM $NaH_2PO_4$, 10 mM HEPES; 10 mM glucose, 10 mM creatine, 10 mM taurine.
2. **Solution 0Ca-EGTA**: 135 mM NaCl, 5.4 mM KCl, 1.2 mM $MgSO_4$, 1.2 mM $NaH_2PO_4$, 0.1 mM EGTA, 10 mM HEPES; 10 mM glucose, 10 mM creatine, 10 mM taurine.
3. **Solution 50μM Ca**: 135 mM NaCl, 5.4 mM KCl, 1.2 mM $MgSO_4$, 0.05 mM $CaCl_2$, 1.2 mM $NaH_2PO_4$, 10 mM HEPES; 10 mM glucose, 10 mM creatine, 10 mM taurine.
4. **Enzymatic solution**: 135 mM NaCl, 5.4 mM KCl, 1.2 mM $MgSO_4$, 0.02 mM $CaCl_2$, 1.2 mM $NaH_2PO_4$, 10 mM HEPES; 10 mM glucose, 10 mM creatine, 10 mM taurine and 0.05–0.2 mg/ml Liberase TM (Roche, Cat. No. 5 40 127,001).
5. **BSA-enzymatic solution** equals to the Enzymatic solution with addition of 1% (w./v.) of BSA.

### 2.2 Drug Preparation

1. Prepare rotenone at 1 mM stock solution in water and store at −20 °C. Use at final concentration of 1μM.
2. Prepare 2, 4-dinitrophenol (DNP) at 1 mM stock solution in DMSO and store at −20 °C. Use at final concentration of 50μM.

## 3 Methods

### 3.1 Microscopy

1. All procedures were carried out at room temperature (*see* **Notes 1** and **2**).
2. Prepare cardiac cells (see Cell preparation for microscopy).
3. For image acquisition, keep myocytes in the solution 2.1.1 (*see* **Note 3**).
4. Based on the employed objective, choose the right thickness of the microscope cover slip. For example, for C-Apochromat 40×, we used the No.#1 (0.13–0.16 mm) glass cover slip bottoms to seed the cells onto.
5. FLIM images were recorded using time-correlated single photon counting (TCSPC) technique [2] (*see* **Note 4**), following excitation with a 473 nm picosecond laser diode (BDL-473,

Becker & Hickl, Germany, *see* **Note 5**) Axiovert 200 LSM 510 Meta (Carl Zeiss, Germany) equipped with C-Apochromat 40×, 1.2 W corr NA. The laser beam was reflected to the sample through an epifluorescence path of the laser scanning confocal microscope. The emitted fluorescence was separated from laser excitation using LP500 nm and detected by HPM 100–40 photomultiplier array employing SPC-830 TCSPC board (both Becker & Hickl, Germany). The setup was kept in the darkness.

### 3.2 Cell Preparation for Microscopy

1. Isolate left ventricular myocytes based on retrograde Langendorff perfusion with the solution 2.1.4. See [7, 22] for details. The protocol is optimized for a rat weighting 200–400 g.
2. After removing the heart with sufficiently long ascending aorta, mount the aorta immediately to the cannula of the Langendorff system. Secure the aorta with a thread.
3. First perfuse the heart with the solution 2.1.1. to clean the heart from the blood (usually up to 5 min). At the end the dripping solution should be completely transparent.
4. Then perfuse with the solution 2.1.2 for 5 min to stop the contractions of the heart.
5. Consequently, perfuse the heart with solution 2.1.4 driven by a peristaltic pump at a rate of 3 ml/min until the tissue become soft (usually ~9 min).
6. Remove the right ventricle and cut the left ventricle gently into small pieces.
7. Filter the suspension through 100μm nylon mesh.
8. Centrifuge at 50 × *g* for 1 min and replace the supernatant with the Solution 2.1.3.
9. Digest the remaining tissue with the Solution 2.1.5. for 5 min.
10. Repeat the **steps 10–12** until the tissue is dissolved completely (usually 4–5 batches of myocytes).
11. Use the batch with highest yield of rod-shaped cardiac cells for further experiments. Centrifuge the batch at 50 × *g* for 1 min and replace the supernatant with the fresh solution 2.1.3. to completely remove the enzyme.
12. Increase gradually the concentration of $Ca^{2+}$ in this batch to 100, 250, 500, and 1000μM in 5 min intervals to keep the myocytes calcium tolerant (*see also* **Note 3** for other cell solutions). Use the myocytes up to 8 h after isolation, or until degradation of the cells quality (observed, namely, by the presence of hypercontracted cell edges).

### 3.3 Fluorescence Lifetime Imaging of Flavin Fluorescence in Living Cells

1. Put cover slips with cells onto a microscopy stage.
2. Prepare recording setup: for flavin measurements, based on its excitation/emission characteristics (as detailed in the Introduction), use excitation at 473 nm (or below, *see* **Note 5**) with an appropriate emission filter. To collect maximum fluorescence, use LP 500 nm of below. *See* **Note 6** on how to gather spectrally resolved data.
3. Create recording protocol: collect high resolution time-resolved images of cells for 120 s with ADC (analog-to-digital converter) resolution 256 to record image size of 256 × 256 pixels (*see* Fig. 1 for illustration). To improve data resolution, *see* **Note 7**. For recording of fast processes, *see* **Note 8**.
4. When the recording is finished, save data in a corresponding file.
5. Verify the mitochondrial localisation of the endogenous fluorescence and absence of the nuclear one from the recorded images.

### 3.4 Testing Mitochondrial Presence

1. Fluorescence probe Rhodamine 123 can be employed to evaluate the presence of mitochondria in living cells (*see* **Note 9**). Apply Rhodamine 123 in external medium at final concentration of 1μM to the cells. Leave for 10 min and then replace with clean external medium.
2. Put cover slips with cells onto a microscopy stage.
3. Prepare recording setup: based on excitation/emission properties of the probes (500/530 nm for Rhodamine 123 [23]), we have used excitation with 473 nm picoseconds laser and LP 500 nm.
4. Create recording protocol: collect high resolution time-resolved images of cells for 120 s with ADC resolution 256 (*see* Fig. 2 for illustration; same recording setup and protocol can be employed for the measurement of flavin endogenous fluorescence). Verify the mitochondrial localisation of the Rhodamine 123 fluorescence from the recorded confocal images.

### 3.5 Reducing Mitochondrial Oxidation by OXPHOS Inhibition

1. Prepare rotenone at 1–5μM in water.
2. Apply rotenone to unstained cells by gently replacing external medium with external medium + rotenone, or by adding higher concentration of rotenone to the solution with cells and shaking gently.
3. Leave rotenone to act for 10 min at room temperature (*see* **Note 1**): cells are now in a fully reduced state.
4. Verify that the fluorescence intensity has decreased and fluorescence lifetime shifted toward shorter lifetimes (shifting toward

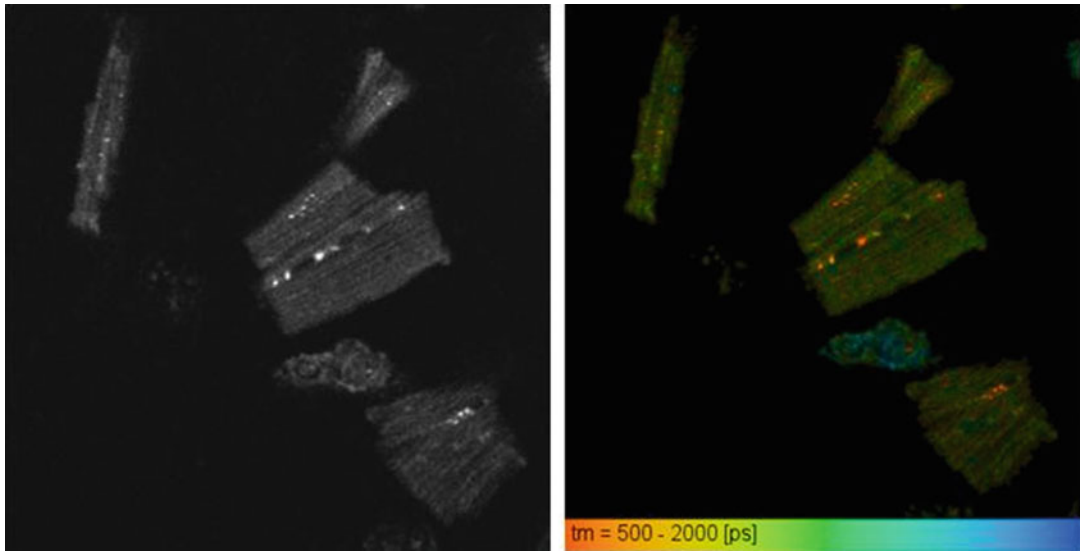


**Fig. 1** Intensity (left) and FLIM (right) image of flavin fluorescence recorded in cardiomyocytes in control conditions after excitation with 473 nm picosecond laser diode and emission with LP 500 nm. Fluorescence decay image scale is between 0.5 and 2.0 ns

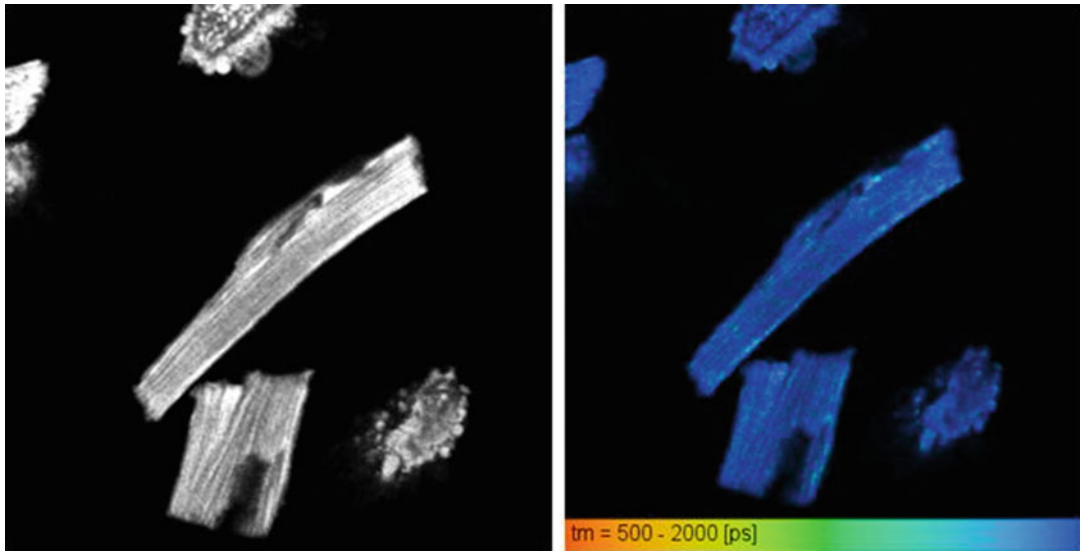


**Fig. 2** Intensity (left) and FLIM (right) image of Rhodamine 123-stained cardiomyocytes after excitation with 473 nm picosecond laser diode and emission with LP 500 nm. Fluorescence decay image scale is between 0.5 and 2.0 ns

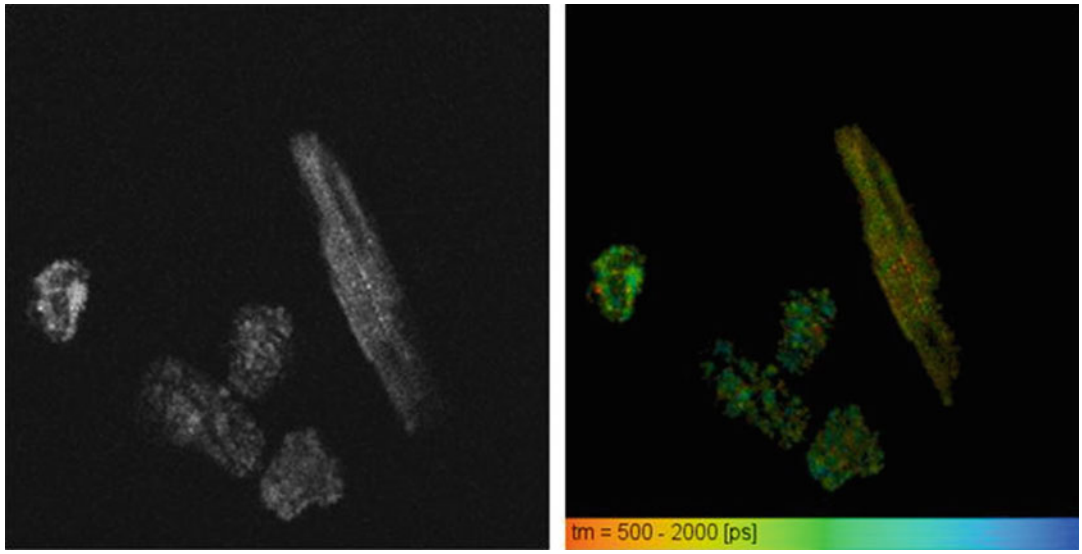


**Fig. 3** Intensity (left) and FLIM (right) image of flavin fluorescence recorded in cardiomyocytes in a reduced state, in the presence of rotenone (1μM) after excitation with 473 nm picosecond laser diode and emission with LP 500 nm. Fluorescence decay image scale between is 0.5 and 2.0 ns. Note low intensity in the presence of the rotenone

yellow colors, see example at Fig. 3, however, with significantly decreased fluorescence, verify the precision of the lifetime estimation, namely, by checking the goodness of the fit with $\chi^2$ value). *See* **Notes 10–12** for testing of other metabolic modulators.

5. Record corresponding images using exactly the same protocol that was employed in control conditions to insure comparability.
6. Use cells for up to 20–25 min, or until the deterioration of their viability (*see* **Note 7**).

### *3.6 Increasing Mitochondrial Oxidation by Uncoupling of Respiratory Chain*

1. Prepare DNP at 50μM in the external medium.
2. Apply DNP to cells by gently replacing external medium with external medium + DNP.
3. Leave DNP to act for 10–15 min at room temperature (*see* **Note 2**): cells are now in a fully oxidized state following uncoupling of ATP synthesis.
4. Verify that fluorescence intensity has increased and fluorescence lifetime shifted toward longer lifetimes (shifting toward blue colors, see example at Fig. 4). *See* **Note 10** for use of other metabolic uncouplers.

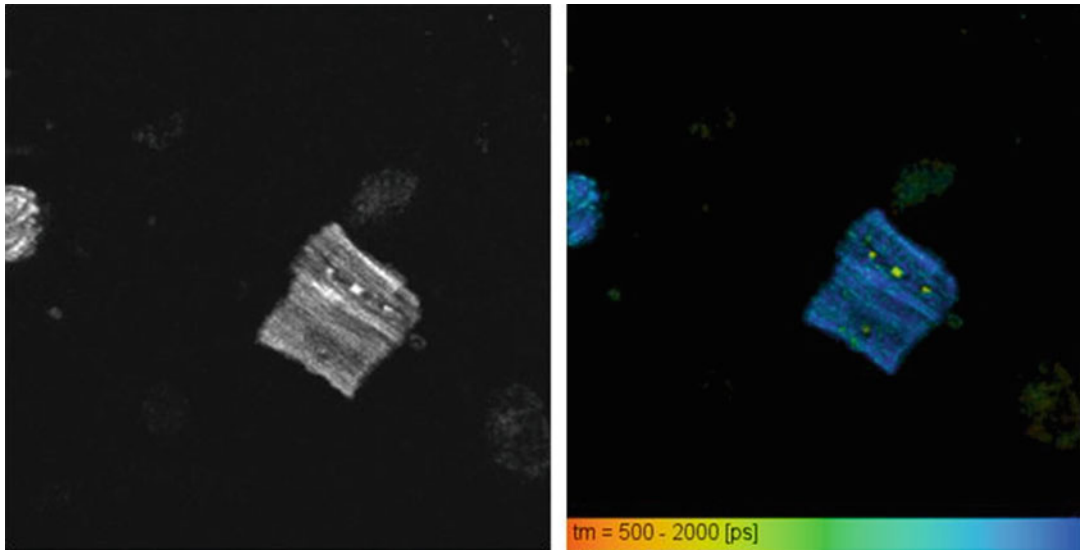


**Fig. 4** Intensity (left) and FLIM (right) image of flavin fluorescence recorded in cardiomyocytes in an oxidized state in the presence of DNP (50μM) after excitation with 473 nm picosecond laser diode and emission with LP 500 nm. Fluorescence decay image scale between is 0.5 and 2.0 ns

5. Record corresponding images using exactly the same protocol that was employed in control conditions to insure comparability.
6. Use cells for up to 20–25 min, or until the deterioration of their viability (*see* **Note 7**).

### 3.7 Analysis

Use SPCImage software to perform first estimation of intensity and fluorescence decays in the recorded images.

1. Send data to SPCImage, or import the recorded image.
2. Calculate decay matrix (for a selected channel or the whole image).
3. Use the predefined instrument response function (IRF) (or *see* **Note 13** to use the recorded IRF).
4. To improve image, use export color-coded images.
5. If the result is not good (e.g., bright specks are present in the image), go to "Options/Intensity" tab and turn the "Autoscale" off.
6. Keep an eye on the goodness of the fit represented by chi squared value ($\chi^2$): usually, it should not be higher than 1.2 (*see* **Note 14** on how to improve $\chi^2$).
7. For advanced analysis, refer to linear unmixing of individual components [11], or phasor approach [24].

## 4 Notes

1. Procedures can be carried out at 35–36 °C using an on-stage incubator for tracking temperature-dependent changes. In such case, do not forget to use preheated solutions for cell preparation and verify that the level of photobleaching [25] did not increase.
2. Oxygenation of the solution by different $O_2/N_2$ mixture can be insured by an on-stage incubator/controller.
3. Self-designed external solution can be replaced by PBS, depending on the type of the isolated and/or cultured cells used. Remember to check that the applied solution does not contain molecules fluorescing in the detected spectral range, most commonly the Phenol red, and that the medium is able to maintain the cells alive for the necessary measurement time, without affecting their metabolism and/or viability. For example, D-MEM without phenol red, FluoroBrite™ D-MEM medium, can be successfully used for cultured cells.
4. Alternative to TCSPC, frequency-modulated (amplitude domain) approach can be employed to evaluate fluorescence lifetimes [1].
5. Excitation by 473 nm ps laser can be replaced by shorter wavelength, namely 445 nm ps laser. Use an appropriate LP (long pass) or BP (band pass) filter.
6. To gather spectrally resolved data, specific narrow BP filters can be employed accordingly. For the most effective detection of the flavin fluorescence, we recommend to use either BP filter to record wavelengths in the range 490–590 nm, or LP filter to detect wavelengths longer than 500 nm to cut off the excitation pulse and its reflections. For example, to record spectrally resolved flavin fluorescence, BP 490 ± 10 nm and BP 540 ± 10 nm can be used to evaluate "bound" and "free" flavins respectively. Another possibility is to use a monochromator in front of the detector with the advantage of choosing the exact wavelength detected.
7. Always verify the state of the recorded cells before and after recording. Discard all recordings during which the cells presented change in their shape and/or state. In case of cardiac cells, do not use cells presenting hypercontractions. Consequently, although shorter recordings are more suitable, the length of the recording has to be appropriate to reach a sufficient number of photons for multiexponential decay data analysis (for more details, refer to [2] or the Becker & Hickl TCSPC handbook https://www.becker-hickl.com/literature/handbooks/).

8. The recording time can be adjusted depending on the rapidity of the studied processes. For fast processes, synchronized recording can be considered, as described in [26].
9. Other fluorescence probes for viability testing can also be used, depending on the cell type and/or setup characteristics.
10. Effect of metabolic modulators can vary depending on the cell type and/or pathway that it employs. To test the oxidative phosphorylation, we have employed rotenone (the inhibitor of the Complex I) and DNP to inhibit and/or uncouple the ATP production by the respiratory chain, respectively. At the same time, rotenone can be replaced by CCCP and/or cyanides (NaCN or KCN, the inhibitors of the Complex IV), while 9,10-Dinitrophenol can be replaced by FCCP [4].
11. In cells preferentially using glycolysis instead of oxidative phosphorylation [4, 27, 28], modulators mentioned in the **Note 10** would induce only limited effect and other pathways, such as modulation of glucose production etc. need to be tested.
12. Comparably, sensitivity of cells to oxidative stress can be tested by applying compounds such as hydrogen peroxide [4, 7, 24].
13. For precise evaluation of the fluorescence lifetimes, measure the IRF [20] and apply it for the fluorescence lifetime data analysis. The Becker & Hickl SPCImage analysis software does not require the measured IRF, fast lifetime verification can be done with the predefined IRF. However, IRF measurement should always be performed on the new sample and verified regularly to achieve a precise lifetime evaluation, especially in case of very short lifetimes. IRF measurement could also be needed when custom analysis software is employed.
14. Goodness of the fit can be enhanced (the $\chi^2$ lowered) by optimizing the offset and scatter parameters in the analysis, but also by improving the recorded image, for example, by insuring that less background light is entering the setup—darkening of the setup can significantly improve the goodness of the fit (for more details, refer to [2] or the Becker & Hickl TCSPC handbook https://www.becker-hickl.com/literature/handbooks/).

## Acknowledgments

This project has received funding from the European Union's Horizon 2020 Research and Innovation Programme under grant agreement no 871124 Laserlab-Europe (the Integrated Initiative of European Laser Infrastructures LASERLAB-EUROPE V), from the Slovak Research and Development Agency under the grant

agreement APVV-15-0302 (CAMYS) as well as the VEGA Grant Agency under contracts no. 2/0070/21 and 2/0121/19.
All experiments conformed to the European directive 2010/63/EU and to Act No. 377/2012 of the Government of the Slovak Republic and were carried out in compliance with the guidelines for the care and use of laboratory animals, approved by the Ethical committee of the Centre of Biosciences, Slovak Academy of Sciences and by the State Veterinary and Food Administration of the Slovak Republic (approval No. Ro-4433/16-221/3 and Ro-2498/18-221).

## References


1. Lakowicz JR (2006) Principles of fluorescence spectroscopy. Springer, New York
2. Becker W (2005) Advanced time-correlated single photon counting techniques. Springer, New York
3. Chorvat D Jr, Chorvatova A (2009) Multi-wavelength fluorescence lifetime spectroscopy: a new approach to the study of endogenous fluorescence in living cells and tissues. Laser Phys Lett 6:175–193
4. Horilova J, Mateasik A, Revilla R, Raible F, Chorvat D Jr, Marcek Chorvatova A (2015) Fingerprinting of metabolic states by NAD(P)H fluorescence lifetime spectroscopy in living cells: a review. Med Photonics 27:16–23; review
5. Chance B, Cohen P, Jobsis F, Schoener B (1962) Intracellular oxidation-reduction states in vivo. Science 137:499–508
6. Chance B, Ernster L, Garland PB, Lee CP, Light PA, Ohnishi T, Ragan CI, Wong D (1967) Flavoproteins of the mitochondrial respiratory chain. Proc Natl Acad Sci U S A 57:1498–1505
7. Chorvatova A, Aneba S, Mateasik A, Chorvat D Jr, Comte B (2013) Time-resolved fluorescence spectroscopy investigation of the effect of 4-hydroxynonenal on endogenous NAD(P)H in living cardiac myocytes. J Biomed Opt 18:67009
8. Chorvatova A, Chorvat D Jr (2014) Review of tissue fluorophores and their spectroscopic characteristics. In: Marcu L, French P, Elson D (eds) Fluorescence lifetime spectroscopy and imaging for tissue biomedical diagnostics. CRC Press Publ, Boca Raton, pp 47–84
9. Berezin MY, Achilefu S (2010) Fluorescence lifetime measurements and biological imaging. Chem Rev 110:2641–2684
10. Marcek Chorvatova A (2014) Chapter 12: Autofluorescence-assisted examination of cardiovascular system physiology and pathology. In: Heikal A, Ghukasyan V (eds) Natural biomarkers for cellular metabolism: biology, techniques, and applications, Cellular and clinical imaging, Periasamy A (series ed). Taylor and Francis, pp 245–271
11. Chorvatova A, Mateasik A, Chorvat D Jr (2013) Spectral decomposition of NAD(P)H fluorescence components recorded by multi-wavelength fluorescence lifetime spectroscopy in living cardiac cells. Laser Phys Lett 10:125703
12. Chorvat D Jr, Chorvatova A (2006) Spectrally resolved time-correlated single photon counting: a novel approach for characterization of endogenous fluorescence in isolated cardiac myocytes. Eur Biophys J Biophys Lett 36:73–83
13. Blinova K, Carroll S, Bose S, Smirnov AV, Harvey JJ, Knutson JR, Balaban RS (2005) Distribution of mitochondrial NADH fluorescence lifetimes: steady-state kinetics of matrix NADH interactions. Biochemistry 44:2585–2594
14. Mayevsky A, Rogatsky GG (2007) Mitochondrial function in vivo evaluated by NADH fluorescence: from animal models to human studies. Am J Physiol Cell Physiol 292: C615–C640
15. Konig K, Riemann I (2003) High-resolution multiphoton tomography of human skin with subcellular spatial resolution and picosecond time resolution. J Biomed Opt 8:432–439
16. Jamme F, Kascakova S, Villette S, Allouche F, Pallu S, Rouam V, Refregiers M (2013) Deep UV autofluorescence microscopy for cell biology and tissue histology. Biol Cell 105:277–288
17. Vishwasrao HD, Heikal AA, Kasischke KA, Webb WW (2005) Conformational dependence of intracellular NADH on metabolic state revealed by associated fluorescence anisotropy. J Biol Chem 280:25119–25126

18. Lakowicz JR, Szmacinski H, Nowaczyk K, Johnson ML (1992) Fluorescence lifetime imaging of free and protein-bound NADH. Proc Natl Acad Sci U S A 89:1271–1275
19. Romashko DN, Marban E, O'Rourke B (1998) Subcellular metabolic transients and mitochondrial redox waves in heart cells. Proc Natl Acad Sci U S A 95:1618–1623
20. Chorvat D Jr, Chorvatova A (2006) Spectrally resolved time-correlated single photon counting: a novel approach for characterization of endogenous fluorescence in isolated cardiac myocytes. Eur Biophys J Biophys Lett 36:73–83
21. Feenstra KA (2002) Long term dynamics of proteins and peptides. Ponsen & Looijen, Wageningen, pp 119–143
22. Cagalinec M et al (2019) Calcium signaling and contractility in cardiac myocyte of wolframin deficient rats. Front Physiol 10:172
23. Schneckenburger H, Stock K, Lyttek M, Strauss WS, Sailer R (2004) Fluorescence lifetime imaging (FLIM) of rhodamine 123 in living cells. Photochem Photobiol Sci 3:127–131
24. Stringari C, Nourse JL, Flanagan LA, Gratton E (2012) Phasor fluorescence lifetime microscopy of free and protein-bound NADH reveals neural stem cell differentiation potential. PLoS One 7:e48014
25. Chorvatova A, Mateasik A, Chorvat D Jr (2011) Laser-induced photobleaching of NAD(P)H fluorescence components in cardiac cells resolved by linear unmixing of TCSPC signals. Proc SPIE 7903:790326-1–790326-9
26. Chorvat D Jr, Abdulla S, Elzwiei F, Mateasik A, Chorvatova A (2008) Screening of cardiomyocyte fluorescence during cell contraction by multi-dimensional TCSPC. Proc SPIE 6860:686029-1–686029-12
27. Warburg O (1956) On the origin of cancer cells. Science 123:309–314
28. Gatenby RA, Gillies RJ (2004) Why do cancers have high aerobic glycolysis? Nat Rev Cancer 4:891–899

# Chapter 27

# Mito-SinCe$^2$ Approach to Analyze Mitochondrial Structure–Function Relationship in Single Cells

**B. Spurlock and K. Mitra**

## Abstract

The cross talk between mitochondrial dynamic structure, determined primarily by mitochondrial fission and fusion events, and mitochondrial function of energetics, primarily ATP and ROS production, is widely appreciated. Understanding the mechanistic details of such cross talk between mitochondrial structure and function needs integrated quantitative analyses between mitochondrial dynamics and energetics. Here we describe our recently designed approach of mito-SinCe$^2$ that involves high resolution confocal microscopy of genetically expressed ratiometric fluorescent probes targeted to mitochondria, and its quantitative analyses. Mito-SinCe$^2$ analyses allows for quantitative analyses of mitochondrial structure–function relationship in single cells toward understanding the role of mitochondria and their heterogeneity in various physiological and pathological conditions.

**Key words** Mitochondrial Dynamics, Fission, Fusion, Mitochondrial Energetics, ATP, Redox State, Confocal Microscopy, Single Cell, Structure–Function Relationships, Ratiometric Probes, Quantitative analyses

## 1 Introduction

Mitochondria change shape through the processes of fission and fusion, the dynamic balance of which dictates the structure of mitochondria in a cell at a given time. Understanding the mechanisms by which mitochondrial dynamics (primarily fission and fusion) and energetics impact each other requires integrated quantitative analyses of these mitochondrial properties within the same cells. Tools to measure mitochondrial energetics are fairly well developed, and quantification of mitochondrial dynamics and its impact on mitochondrial structure has been attempted with varying degrees of utility [1–6]. To address the critical need for integrated analyses, we developed a high resolution confocal microscopy based approach to analyze mitochondrial structure–function relationship in single cells. We call this approach mito-SinCe$^2$ (mito-SinCe-

Volkmar Weissig and Marvin Edeas (eds.), *Mitochondrial Medicine: Volume 1: Targeting Mitochondria*, Methods in Molecular Biology, vol. 2275, https://doi.org/10.1007/978-1-0716-1262-0_27,

SQuARED: *Sin*gle *Ce*ll *S*imultaneous *Qu*antification of *A*TP or *Re*dox with *D*ynamics of *Mito*chondria) [7].

Mito-SinCe$^2$ analyzes live cells expressing genetically encoded ratiometric fluorescent probes to obtain steady-state metrics for mitochondrial fission, fusion, matrix continuity and diameter (mitochondrial dynamics) and ATP or redox state (mitochondrial energetics). Applying these metrics, we developed a robust multivariate approach to measure relationships between mitochondrial dynamics and energetics across a broad range of cell types and conditions [7].

Mito-SinCe$^2$ analyses can be conducted on any cells that can express the fluorescent probes, including primary cells isolated from animal models or patients. Additionally, experiments can be designed to study the impact of any stimuli (that do not impact fluorescence microscopy) on the mitochondrial dynamics and energetics of single cells over time. The probes used in this protocol are targeted to the mitochondrial matrix, but mito-SinCe$^2$ can also be applied to probes targeted to other mitochondrial compartments. The advent of high throughput, high resolution confocal microscopes will allow improvement of the current low throughput mito-SinCe$^2$ approach. Thus, mito-SinCe$^2$ is a valuable technique in exploring robust quantitative relationships between mitochondrial dynamics and energetics as well as any heterogeneity in such relationships in any given populations of cells.

The mito-SinCe$^2$ approach has two distinct arms (Fig. 1a): Dynamics-ATP and Dynamics-Redox. The Dynamics-ATP arm uses the matrix-targeted ratiometric mito-GO-ATeam2 FRET probe [8, 9]. The normalized FRET signal ($FL_{FRET/488}$) measures relative matrix ATP levels while the direct excitation of the FRET acceptor (Ex-555) is used to obtain information about steady-state mitochondrial dynamics (Fig. 1a, b). The Dynamics-Redox arm uses the redox-sensitive mito-roGFP [9, 10] and the mito-PhotoSwitchable-mOrange (mito-PSmO) [11–13]. The ratio of mito-roGFP signal ($FL_{405/488}$) measures the relative matrix oxidation state. Steady-state fission, fusion, and diameter metrics are obtained from the basal mito-PSmO fluorescence (Ex-555), and the decrease over time of the normalized photoswitched pool ($FL_{639/555}$) measures the relative matrix continuity of a cell (Fig. 1a, b). Neither mito-PsmO2 nor mito-roGFP can be used with mito-GO-ATeam2 due to overlapping fluorescence spectra (Fig. 1b). Therefore, the matrix continuity assay is only compatible with the Dynamics-Redox arm of mito-SinCe$^2$. Note that although mito-SinCe$^2$ involves bivariate and multivariate analyses of steady state energetics and dynamics metrics, each of the metrics can be also used separately depending on the experimental objective.

**a**

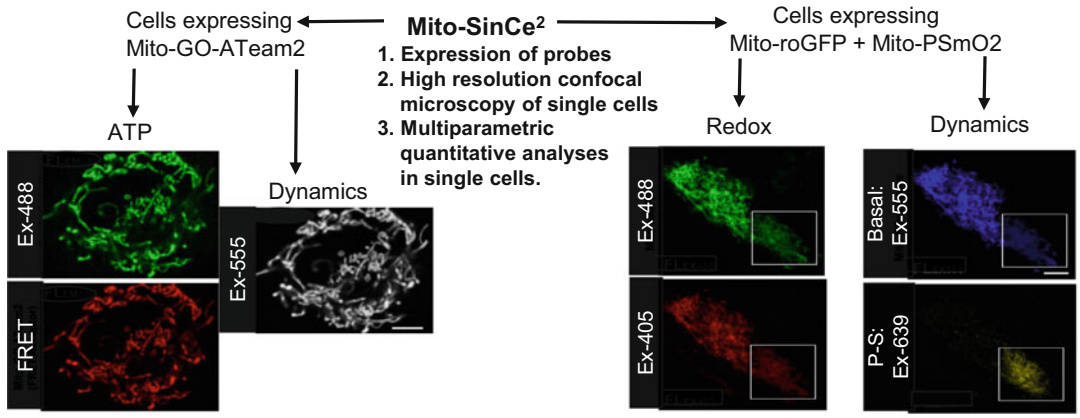


**b**

| Probe | Excitation Laser (nm) | Description | Detector Filters | Arm | Ratio | Output |
|---|---|---|---|---|---|---|
| Mito-GO-ATeam 2 | 488 | **1.** No FRET | SP 555 | ATP | $FL_{FRET/488}$ (**2 / 1**) | [ATP] |
| | | **2.** FRET | LP 560 | | | |
| | 555 | **3.** Direct Ex. of FRET Probe | LP 560 | | N.A. | [Fission], [Fusion(1-10)], [Diameter] |
| Mito-ro-GFP | 405 | **1.** Oxidized | 420-475 + BP 500-610 | Redox | $FL_{405/488}$ (**1 / 2**) | [Oxidation] |
| | 488 | **2.** Reduced | | | | |
| Mito-PSmO | 555 | **3.** Basal Signal | 420-475 + BP 500-610 | | N.A. | [Fission], [Fusion(1-10)], [Diameter] |
| | 639 | **4.** Photo-Switched | LP 640 | | $FL_{639/555}$ (**4 / 3**) | [Matrix Continuity] |

**Fig. 1** Overview of the mito-SinCe$^2$ approach. (**a**) Flow chart showing two arms of mito-SinCe$^2$ with representative micrographs of each fluorescence channel of each probe used for mito-SinCe$^2$ analyses. (**b**) Table summarizing the microscopy-based use of the probes for mito-SinCe$^2$ analyses to obtain energetics and dynamics metrics

## 2 Materials

### *2.1 Cell Culture*

1. Materials used for standard cell culture, as optimized by the user.
2. Glass bottom Lab-Tek or MatTek chambers.

### 2.2 Confocal Microscope (Parameters Described Herein Were Optimized on a Zeiss LSM700) Equipped with

1. 40× Plan-apochromat 1.4NA/Oil objective or better
2. 405 nm, 488 nm, 555 nm, and 639 nm lasers
3. Multiple channel detector system (Fig. 1b).
4. Temperature and $CO_2$ controlled chamber.
5. Definite Focus (as in Zeiss LSM700) or similar.

### 2.3 Software

1. Image analysis software (e.g., proprietary ZEN Black, Blue (from Zeiss), open source ImageJ) capable of (1) exporting subsets of channels or optical slices, (2) drawing and cutting out Regions of Interest (ROIs) within images, (3) creating maximum intensity projections, (4) measuring fluorescence intensities, and (5) exporting 3D images as TIFFs.
2. Mac running OSX 10.10 or later with (1) iGraph R-package installed, (2) MitoGraph v2.1 (https://github.com/vianamp/MitoGraph) [14] (*see* **Note 1**) and (3) accompanying analysis R script saved in a Desktop folder named "MitoGraph".
3. Appropriate statistics software (Excel, SPSS, R, etc.).

### 2.4 Plasmids

1. Mito-GO-ATeam2.
2. Mito-roGFP.
3. Mito-PSmO.
4. Any other desired probes with compatible Excitation/Emission spectra.

### 2.5 Plasmid Expression System

Plasmid expression system for transfection (we recommend Fugene, *see* **Note 2**), lentiviral transduction (packaging cell line, e.g., HEK293T and packaging vectors like psPax2, pCMV-VSV-G).

### 2.6 Drugs or Metabolites for Validation

Drugs or metabolites for validation including but not limited to Oligomycin (mitochondrial ATP synthase inhibitor, CCCP (uncoupler), Antimycin (mitochondrial Complex III inhibitor), t-BH (oxidizing agent), DTT (reducing agent) and Galactose (to replace glucose as carbon source).

## 3 Methods

### 3.1 Expressing Mito-SinCe$^2$ Probes

1. Seed cells in glass bottom live cell chambers using standard techniques. Allow cells to settle/attach overnight or as optimized for transfection or transduction.
2. Express probes using preferred transfection/transduction technique, making sure to minimize cell death and stress (*see* **Note 3**). For the Dynamics-ATP arm, express mito-GO-ATeam2

FRET probe. For the Dynamics-Redox arm, co-express mito-PSmO and mito-roGFP probes.

3. Allow transfection/transduction to proceed for at least 24 h or as optimized. Lines stably expressing the probes (optional, *see* **Note 3**) can be generated by selecting cells with particular drug resistance as follows: (1) for the Dynamics-ATP arm select cells expressing mito-GO-ATeam2 with neomycin (1 mg/mL) for 48 h. Thereafter, maintain in selection media as needed to maintain expression, and (2) for the Dynamics-Redox arm express probes sequentially beginning with mito-roGFP, selecting expressing cells with hygromycin (0.2 mg/mL) for 48 h, followed by mito-PSmO, selecting cells with puromycin (2 μg/mL) for 48 h. Repeat selection protocol as needed to maintain expression.
4. To limit the impact of depletion of metabolites or changes in pH on mitochondria, replace media in live cell chamber with 200 μL media (equilibrated to 37 °C, 5% $CO_2$) and incubate for at least 1 h before microscopy.

### 3.2 Confocal Microscopy

#### 3.2.1 Turn on Microscope

Turn on microscope and set incubator temperature to 37 °C and $CO_2$ to 5%. When temperature and $CO_2$ stabilize, mount the live cell chamber with cells expressing probes on the microscope.

#### 3.2.2 Perform 3D Confocal Microscopy to Obtain and Validate Mito-SinCe$^2$ Energetics and Dynamics Metrics

1. Adjust parameters to acquire 512 × 512 pixel images of transfected cells at optical zoom 3 with 1 Airy unit pinhole and 0.5 μm *Z* interval. Use a scan speed of 8 (pixel dwell time of 2.55 μs) and a bit-depth of 12. Take the sum of the signal of two scans. Adjust image offset appropriately to obtain distinct dark pixels (*see* **Note 4**). Be sure to capture at least one optical slice with all dark pixels above and below the required *Z* range to cover the cells (*see* **Note 5**).
2. Design multichannel image acquisition to rule out cross talk and cross excitations, with automated switching lasers between channels after each scanned line (*see* **Note 6**). *See* Fig. 1b for excitation laser and detector filters for each probe used on an LSM 700. This can be modified based on the microscope being used. After optimizing laser power and gain for each channel, do not adjust these parameters for any image where the data are compared.
3. Once all parameters are optimized, acquire 3D images (*Z*-stacks) of transfected cells. Set a target cell number for each experiment and scan control and experimental groups on the same day. Change oil on the objective as needed.

*3.2.3 Validate Probes for New Cell Lines*

1. Use appropriate drugs that modify mitochondrial energetics and/or dynamics. (1) Validate ATP metric from mito-GO-ATeam2 by treating cells with the mitochondrial ATP-synthase inhibitor Oligomycin (10 μg/mL). (2) Validate redox state metric from mito-roGFP by treating cells with *tert*-butyl hydroperoxide (*t*-BH, 0.5 mM) and subsequently with 1,4-dithiothreitol (DTT, 1 mM). (3) Validate steady-state dynamics metrics from mito-GO-ATeam2 and mito-PSmO by treating cells with carbonyl cyanide m-chlorophenyl hydrazone (CCCP, 5 μM) to inhibit fusion allowing unopposed fission. Before beginning microscopy, make and equilibrate a 2× stock of treatment media.
2. While treatment media is equilibrating, use the lowest possible zoom to preselect all fields that will be imaged in one well/dish. Take preliminary 2D images of zoomed out areas to facilitate recognizing and finding selected fields quickly between scans. Next, acquire the pretreatment 3D images (as described in Subheading 3.2.2) of each of the preselected fields. Quickly remove half of the culture media (100 μL) from the well/dish while the chamber is still mounted. Replace with the same volume of the 2× treatment media (100 μL) and incubate cells at 37 °C and 5% $CO_2$ for optimized duration (*see* **Note 7**). Acquire posttreatment 3D images (as described in Subheading 3.2.2) of the same fields without changing the culture media. Stop imaging at the time limit and analyze only fields with both pre- and posttreatment images. Repeat this process for 2 wells/dishes (target 30 cells or as many as possible) per treatment. This validation protocol can also be used to study the impact of exogenous agents like inhibitors, metabolites, and growth factors on mitochondrial dynamics and energetics.

*3.2.4 Perform Pulse–Chase Microscopy Experiment to Measure Mitochondrial Matrix Continuity (Fig. 2) in Conjunction with Redox State (Dynamics-Redox Arm;* see ***Note 8****)*

1. First, design the "pulse" protocol for 488 nm laser induced photoswitching. *See* Fig. 1b for excitation lasers and detection filters of the basal and photo-switched fluorescence of mito-PSmO. Adjust scanning parameters as in Subheading 3.2.2 with the following modifications: (1) Take 2D time-lapse images instead of 3D images, and (2) open the pinhole to 2 Airy Units. Then, optimize photoswitching parameters (i.e., laser power and iterations) for maximal photoswitching within a 50 × 50 pixel rectangular ROI drawn inside the mitochondrial population of a transfected cell, as follows: (1) Select a putative field of cells expressing mito-PSmO. (2) Perform time-lapse imaging (with no designated time interval) to obtain a pre photoswitching image, followed by photoswitching, and two post photoswitching images. First, keep the iterations fixed and vary the power of the 488 nm photoswitching laser from

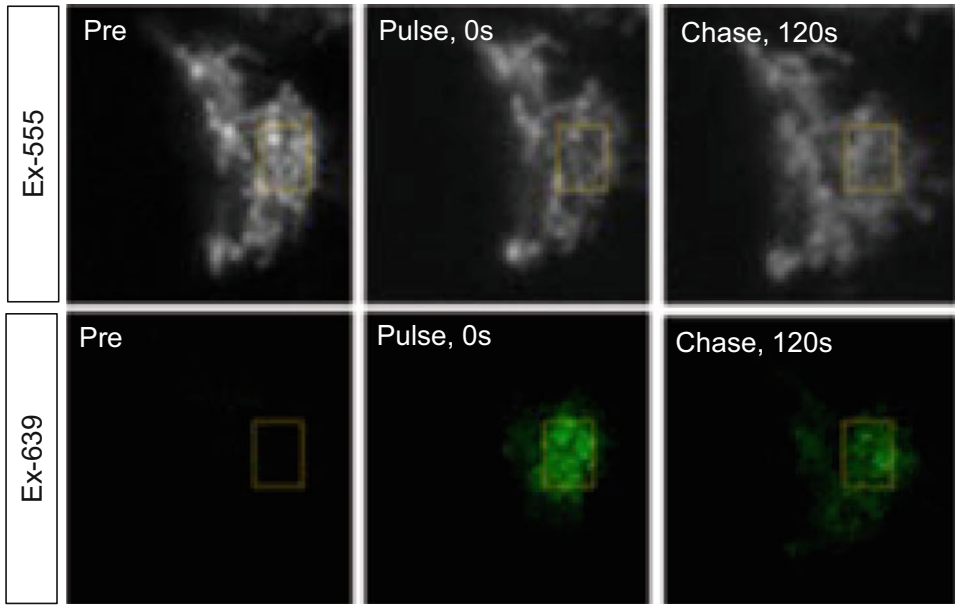


**Fig. 2** The pulse–chase protocol used to determine matrix continuity. A representative cell expressing mito-PSmO is shown with its basal (white) and photo-switched (green) fluorescence. With the photoswitching pulse in the ROI (yellow box), the basal fluorescence decreases and photoswitched fluorescence increases. Within the chase time period of 120 s the photoswitched fluorescence decreases due to diffusion of the probe through the continuous matrix in fused mitochondrial elements

10% to 100% in steps of 10. Thereafter, vary the iterations from 1 through 20 in the steps of 2 at the optimal laser power. (3) For each ROI, determine the increase in the photoswitched pool and decrease in the basal pool after the pulse (see image processing and analysis for pulse–chase experiment below at Subheading 3.3.3, **step 1**). Choose the settings with the maximum photoswitching efficiency, or increase in fluorescence intensity of the photoswitched pool. We achieved maximal photoswitching with two iterations of our 488 nm laser at 90% power (*see* **Note 9**). Only cells with 3× increase in photoswitched pool are considered for further analyses.

2. Next, design the time-lapse "chase" protocol. Set the experiment to run for 2 min post-photoswitching with scans every 15 s. To maintain the desired focus, turn on Definite Focus and set it to trigger with every third scan of the pulse–chase time-lapse series.
3. To ensure selection of cells with optimal mito-PSmO expression, set a threshold signal of the prephotoswitching mito-PSmO basal fluorescence. First, draw 50 × 50 pixel ROIs within the mitochondrial populations of 20 cells. Next, run the optimized photoswitching protocol. For each ROI determine the photoswitching efficiency. Select all ROIs that show at

least a 3× increase in the intensity of the photo-switched pool. Choose 3–5 ROIs with the lowest prephotoswitching basal fluorescence. Set the mean of the prephotoswitching basal fluorescence of these ROIs as a minimum threshold. For all future pulse–chase experiments, only proceed with cells that meet this threshold (*see* **Note 10**).

4. Once the protocol is optimized, begin experiment to determine matrix continuity, metrics for steady-state fission, fusion, and diameter, and redox state. Select a putative field of cells expressing both mito-PSmO and mito-roGFP using the pulse–chase scanning parameters. Before initiating pulse–chase experiment, obtain a separate image for determining redox state and steady-state dynamics metrics as described in Subheading 3.2.2. Redox state determination must be done before photoswitching because the photoswitching is expected to bleach mito-roGFP signal. Finally, begin the pulse–chase experiment. Turn off mito-roGFP channels and revert to acquisition parameters optimized for photoswitching and time-lapse imaging (*see* Subheading 3.2.4, **steps 1** and **2**). Adjust focus to maximize visible mitochondrial area and/or fluorescence intensity. Draw a 50 × 50 pixel photoswitching ROI within each cell in the field. Cells and mitochondria may shift between selection and scanning. If needed, readjust ROIs and focus. Execute the pulse–chase protocol.
5. It will be necessary to obtain a bleaching rate for each experiment. To that end, execute the pulse–chase protocol on ROIs drawn around the entire perimeter of at least five cells (*see* **Note 11**).

#### *3.2.5 Validate Matrix-Continuity Metric for New Cell Lines*

First, incubate one well with DMSO (vehicle) for 2 h at 37 °C and 5% $CO_2$. Incubate a second well with CCCP (5 μM) for 2 h at 37 °C and 5% $CO_2$. Conduct pulse–chase experiment as in Subheading 3.2.4.

### *3.3 Image Processing and Analysis*

#### *3.3.1 Obtain Energetics Metrics, [ATP] and [Oxidation], from 3D Images of Ratiometric Probes as Follows*

1. Obtain Mean Fluorescence Intensities (MFI) for each fluorescence channel as follows: First, obtain maximum intensity projections of all optical slices of each of the acquired 3D confocal images, including the "pre" images from the pulse–chase experiment. Thereafter, use a free hand tool to draw ROIs around the mitochondrial population of each transfected cell in the maximum intensity projections. Obtain the background fluorescence by drawing ROIs (any shape, but ~10% of the area of the measurement ROIs) in the nucleus or cytosol of each transfected cell. Do not include any mitochondrial elements in the background ROI. For each cell, export the MFI values for all channels from both mitochondrial and background ROIs into a spreadsheet.

2. Use the MFIs to calculate and validate energetics metrics. For each cell, subtract the background MFI from the mitochondrial MFI of all channels. Calculate [ATP] for each cell using the following formula: *[ATP] = [FRET MFI/Ex-488 MFI]* (Fig. 1b). Validate [ATP] by calculating [Oligomycin-sensitive ATP] as $[ATP]_{pre\text{-}Oligo}/[ATP]_{post\text{-}Oligo}$. The mean of [Oligomycin-sensitive ATP] for the scanned cells should be >1 for successful validation (*see* **Note 12**). Calculate [Oxidation] for each cell using the following formula: *[Oxidation] = Ex-405 MFI/Ex-488 MFI* (Fig. 1b). Validate [Oxidation] by calculating [*t*-BH-induced Oxidation] as $[Oxidation]_{pre\text{-}tBH}/[Oxidation]_{post\text{-}tBH}$. The mean of this value for the scanned cells should be <1 for successful validation. Next, calculate [DTT-induced Reduction] as $[Oxidation]_{pre\text{-}DTT}/[Oxidation]_{post\text{-}DTT}$. This value should be >1 for successful validation. Finally, Compare [ATP] and [Oxidation] of control to experimental groups as appropriate.

### 3.3.2 Obtain Value of Dynamics Metrics of Steady-State [Fission], [Fusion(1-10)], and [Diameter] (Fig. 1b) from 3D Images Using MitoGraph v2.1 Analysis Software [7, 14] as Follows

1. Prepare files for MitoGraph analyses. For both Dynamics-ATP and Dynamics-Redox arms, subset Ex-555 channel (Fig. 1b) for each 3D image stack. Then, draw ROIs around the mitochondrial populations of each transfected cell to cut each into a separate 3D image stack. Save each cut image stack in TIFF format (still as 3D stacks). Image file names should have no spaces or hyphens and contain fewer than 9 characters. Move the TIFF images to a separate, descriptively named folder on the Desktop of the MitoGraph computer. Folder name should have no spaces or hyphens (e.g., FolderName).
2. Perform MitoGraph analyses. To run MitoGraph, first open Terminal. For images acquired with the parameters recommended herein, enter the following command string to run the MitoGraph software:

```
cd ~/Desktop/MitoGraph
```

```
./MitoGraph -path ~/Desktop/FolderName -xy 0.104 -z 0.5 -analyze
```

```
(-xy designates the pixel size in µm, and -z designates the optical slice height in µm.)
```

MitoGraph execution will generate various files in "FolderName." The relevant files for this protocol are the binary images (*.png) and the list of mitochondrial measurements (*.mitograph). As a quality control step, ensure adequate thresholding of mitochondrial signal by selecting 3–5 cells at random and comparing their z-projected binary images created by the MitoGraph software to maximum intensity projections of the raw images created in the

image processing software (e.g., Zen Black, ImageJ). If there are cells where these images do not largely match discard these cells and check all binary images against the maximum intensity projections of the raw files. Now select the *.mitograph files and import them (*see* **Note 13**) into a spreadsheet (Fig. 3, blue outline). Each file describes the mitochondrial network of a single cell. For MitoGraph utility beyond the scope of this protocol, see the original paper [14]. As a quality control step for each cell, discard components with reported lengths or volumes that are physical impossibilities (e.g., V = 0, Thickness > 2 that cannot be verified by manually measuring in image analysis software; Fig. 3, red outline; see limitation 6).

3. Calculate the various Dynamics metrics using the following formulae: $[Fission] = N/\Sigma L$ where $N$ is the number of components and $\Sigma L$ is the total length of all mitochondria in the cell (Fig. 3, gold outline); $[\text{Fusion}(1, 3, 5, 10)] = (\Sigma(L_{1,3,5,10})/\Sigma L) \times 100$, where $L_n$ is the summed length of one ($L_1$), three ($L_3$), five ($L_5$) or ten ($L_5$) longest components (*see* **Note 14**; Fig. 3, gold outline); $[Diameter] = \sum_{n=1}^{N} \frac{V_n}{V_T} d_n$, where $V_n$ is the volume of individual components, $V_T$ is the total mitochondrial volume, and $d_n$ is the thickness of individual components derived from component length and volume assuming cylindrical mitochondria (Fig. 3, gold outline). As a quality control step, compare binary images of outlier cells to the maximum intensity projections of the raw images for those cells. If they do not largely match, these cells can be discarded. As another quality control step, ensure [Fission] and [Fusion(1-10)] are significantly inversely correlated (as in Fig. 4a, where cells were treated with CCCP or galactose (replacing glucose) for 2 h to cover the extremes of fission or fusion, respectively).
4. Validate [Fission], [Fusion(1-10)], and [Diameter] by calculating [CCCP-induced Fission] as $[\text{Fission}]_{\text{pre-CCCP}}/[\text{Fission}]_{\text{post-CCCP}}$. The mean of this value for the scanned cells should be <1 for successful validation. Next, calculate [CCCP-reduced Fusion(1-10)] as $[\text{Fusion(1-10)}]_{\text{pre-CCCP}}/[\text{Fusion (1-10)}]_{\text{post-CCCP}}$. This value should be >1 for successful validation. [Diameter] Finally, calculate [Inhibitor-sensitive Diameter] as $[\text{Diameter}]_{\text{pre-Inhibitor}}/[\text{Diameter}]_{\text{post-inhibitor;}}$ Here, inhibitor can be any drug(s) that leads to swelling of mitochondria in the cells of choice, while we found when cells treated with Oligomycin, followed by CCCP, followed by Antimycin leads to appreciable increase in diameter. The mean of this value for the scanned cells should be <1 for successful validation. Compare [Fission], [Fusion(1-10)], and [Diameter] metrics of control and experimental groups as appropriate.

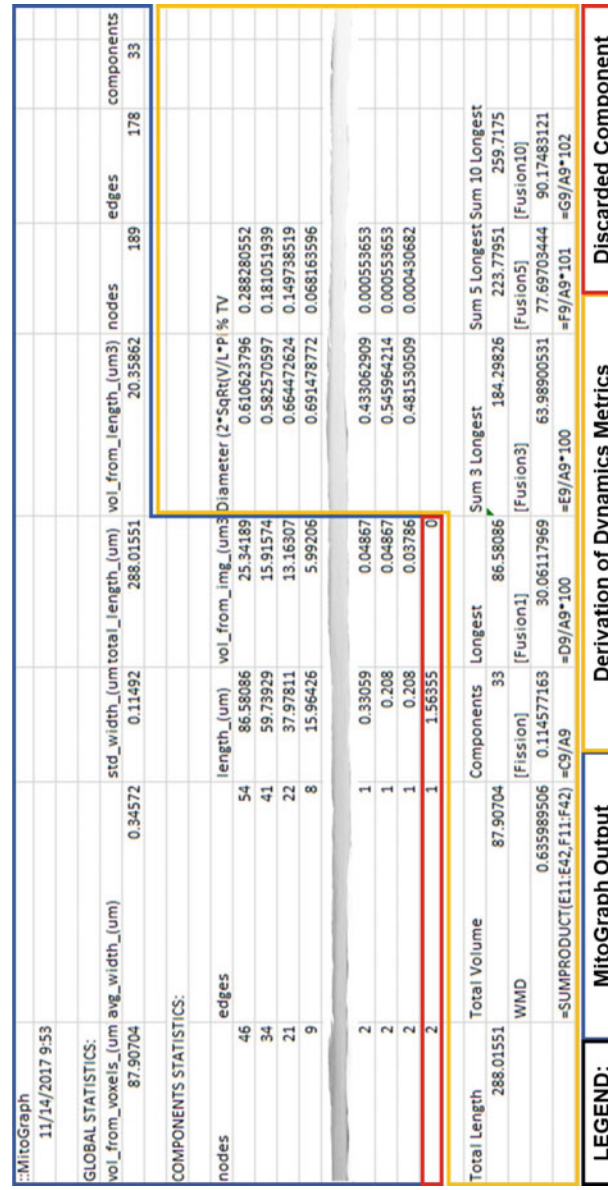


**Fig. 3** Representative results from MitoGraph v2.1 analyses for a single cell to obtain [Fission], [Fusion] and [Diameter] metrics. The blue outline encompasses the raw output from the *.mitograph file, the gold outline encompasses the derivation of the dynamics metrics using Excel, and the red outline highlights an example of a component that must be discarded

*3.3.3 Obtain [Matrix-Continuity] from Pulse–Chase Time-Lapse Images as Follows*

1. Obtain MFIs of the time-lapse sequence: Use a freehand tool to draw ROIs around each photo-converted pool at time point 2 (immediately after photoswitching). Then, determine background fluorescence by drawing ROIs (any shape, ~10% of the area of the measurement ROIs) in the nucleus or cytosol of

each transfected cell, being careful not to include any mitochondrial elements at any time point. As a quality control step, use background corrected Ex-639 MFIs to determine photoswitching efficiency as *Ex-639 MFI*$_{post\text{-}pulse}$/*Ex-639 MFI*$_{pre\text{-}pulse}$. Discard any cells where photoswitching efficiency is $<3$. For cells with photoswitching efficiency of $\geq 3$, ideally use the same photoswitching efficiency ROIs to measure MFI for all time points. However, carefully examine the cell at each time point and if necessary, draw new ROIs to account for movement of the photoswitched pool. Use as few ROIs as possible per cell. Name the ROIs for the cell and the time points they cover. Then, export the background and experimental MFIs of Ex-555 and Ex-639 channels for each cell at all time points ($t = 0$ s to $t = 120$ s, Fig. 2) to a spreadsheet. Compile the values from the appropriate ROIs to get the real time lapse of the MFIs of the photo-converted pool of each cell. Correct each by subtracting the background MFI for each time point.

2. Calculate the [Matrix-continuity] metric. Calculate $FL_{639/555}$ ratio as *Ex-639 MFI/Ex-555 MFI* for each time point. For all time points calculate Normalized $FL_{639/555}$ as $FL_{639/555}$ *at* $t_n$/$FL_{639/555}$ at $t_1$ and plot the MFIs for each cell against the time in seconds. Determine the equation for the parabolic fit to the above plot. Take the linear coefficients (as in Fig. 4b, where the linear coefficient is $-0.0025$ for the CCCP treated cell and $-0.0118$ for the CNT cell) and multiply them by $-1$. Report this value as the [Matrix-continuity]. Obtain a control bleaching rate by performing the [Matrix-continuity] calculations using the whole cell bleaching ROIs. Report values lower than bleaching (including negative values) as 0.
3. Validate [Matrix-Continuity] by making boxplots of [Matrix-continuity] for DMSO and CCCP treated cells. Successful validation requires CCCP treated cells to have reduce [Matrix-continuity] compared to DMSO treated cells (as in Fig. 4c).

*3.3.4 To Measure the Impact of Exogenous Agents (EA) on Mitochondrial Energetics and Dynamics Use Similar Steps to Validation of [ATP], [Oxidation], [Fission], [Fusion(1-10)], and [Diameter] (as Described in Subheading 3.3.1,* ***step 2****)*

For Energetics metrics, determine $[ATP]_{pre}/[ATP]_{post}$ or $[Oxidation]_{pre}/[Oxidation]_{post}$ to obtain [EA sensitive Energetics] metrics. For Dynamics metrics, determine $[Fission]_{pre}/[Fission]_{post}$, $[Fusion5]_{pre}/[Fusion5]_{post}$ and $[Diameter]_{pre}/[Diameter]_{post}$ to obtain [EA sensitive Dynamics] metrics.

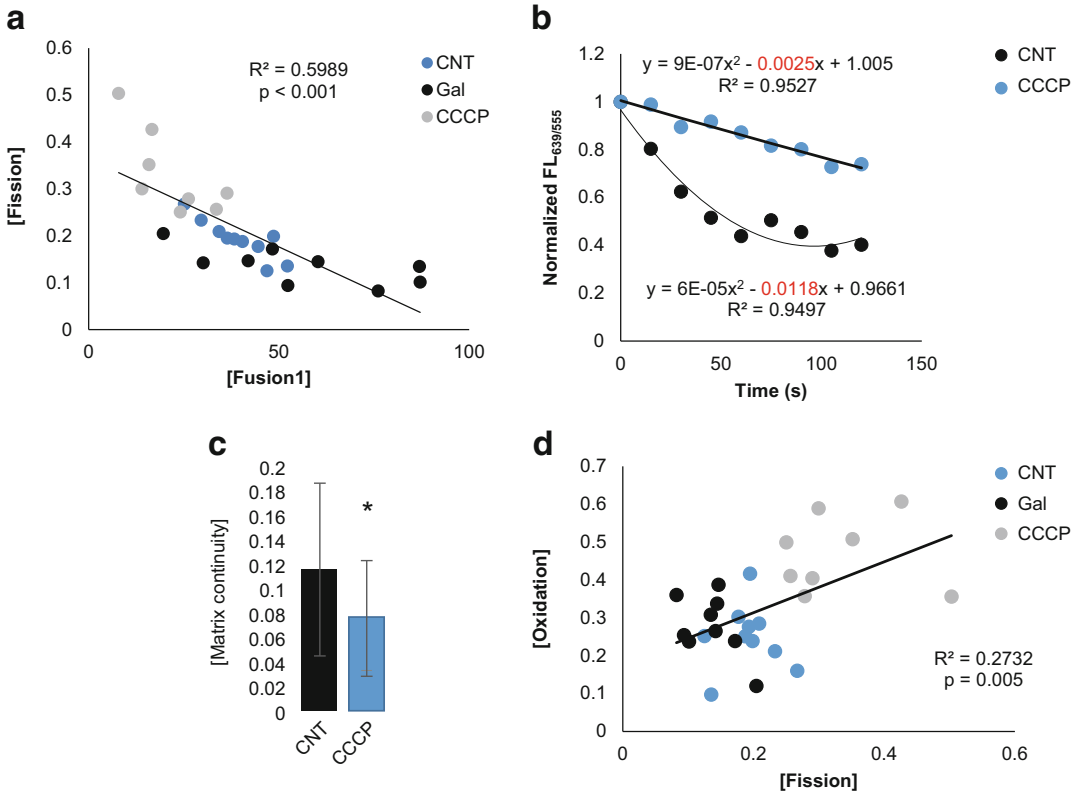


**Fig. 4** Representative regression analyses of mito-SinCe$^2$ metrics. (**a**) Linear regression, with $R^2$ and $p$ values, showing inverse relationship between [Fission] and [Fusion1] metrics where CCCP treated cells occupy extreme [Fission] and galactose treated cells occupy extreme [Fusion]. (**b**) Parabolic fit of pulse–chase time-lapses of two cells, a control and a cell treated with CCCP, and the derivation of [Matrix-continuity] for both cells using the negative linear coefficient, highlighted in red in the equations for the fit. (**c**) Bar graph showing the mean for all cells in each group in experiment depicted in **b**. (**d**) Linear regression analysis, with $R^2$ and $p$ values, showing the significant relationship between [Fission] and [Oxidation] as an example of a bivariate mito-SinCe$^2$ analysis

#### *3.3.5 For Mito-SinCe$^2$ Analyses, Plot [Dynamics] Against [Energetics] Metrics for Single Cells in Control and Experimental Groups*

Use statistical software of choice to compare distributions with appropriate hypothesis testing and determine relationships. The simplest mito-SinCe$^2$ bivariate relationship can be studied using standard regression analyses. For example, linear regression analysis of the data points obtained in the experiment described in Subheading 3.3.2, **step 3** revealed a significant relationship between [Fission] and [Oxidation] (Fig. 4d). Other examples of potential bivariate and multivariate statistical analyses include K-means clustering, partial least square discriminant analysis (PLS-DA), and nonlinear regression analyses [7].

### *3.4 Limitations of Mito-Since$^2$*

1. Nonuniformity of mitochondrial signal: Mitochondrial structures with nonuniform fluorescence intensities can cause artifactual output from the MitoGraph v2.1 software. Therefore, fluorescence intensity of dynamics probes must be similar

across mitochondria within a cell to avoid artifacts in the calculation of steady-state dynamics metrics. For example, cells exhibiting nonuniformity of mito-GO-ATeam2 of signal have to be excluded from the analyses [7]. Additionally, when swollen mitochondrial regions within the mitochondrial network have high MFI, the thin linking mitochondrial regions are thresholded out by MitoGraph v2.1, causing underestimated [Fusion(1-10)] values in these cells [7].

2. Impact of image resolution: MitoGraph v2.1, as with all image analysis software, is limited by the resolution of the image. The resolution recommended here may lead to metrics with underreport fission (and over-report fusion) in cells with compactly clustered mitochondrial components which are nonetheless highly fragmented. Additionally, the recommended *Z* interval causes universal overestimation of average diameter. For this reason, restrict conclusions to relative differences between cells and treatments and refrain from reporting [Diameter] in μm.
3. Impact of intracellular mitochondrial heterogeneity: Mito-SinCe$^2$ was designed to compare average mitochondrial parameters in individual cells. [Dynamics] metrics do not reflect intracellular heterogeneity of shape or number of mitochondrial components.
4. Impact of mitochondrial turnover: In some conditions, [Dynamics] metrics may be nonnegligibly influenced by the balance of mitophagy and mitochondrial biogenesis.
5. Impact of particular probes: The possible impact of a particular probe on mitochondrial shape and energetics must be considered when drawing conclusions from MitoSinCe$^2$. In particular, mitochondrial dyes (e.g., MitoTracker dyes) can impact mitochondrial energetics. We recommend restricting analyses to genetically encoded fluorophores where possible.
6. Impact of skeletonization on [Diameter]: In MitoGraph v2.1, each recognized element has at least two nodes and one edge. To ensure this, small mitochondrial components that are reduced to a single pixel by skeletonizing are arbitrarily given a second pixel on the *xy* plane. When these components are elongated along the *xz* plane, the edge that was imposed on *xy* may not represent the major axis of the small mitochondrial component. This can lead to physically impossible values for Length or Volume of certain elements. Our protocol includes quality control steps of filtering these cases.
7. Mito-SinCe$^2$ does not address the kinetics of fission and fusion: The mito-SinCe$^2$ method and [Dynamics] metrics quantify only the fission or fusion state at given time points and not the rates of fission or fusion. Additionally, transient fusion events that do not result in change in mitochondrial shape impact [Matrix-Continuity] but not [Fusion(1-10)].

## 4 Notes

1. MitoGraph v3.0 is now available. The primary differences between these versions of the software relate to ex post facto utility.
2. We primarily expressed probes using the Fugene reagent after optimizing manufacturer's protocol.
3. Although transfection stress can be avoided by generating cell lines stably expressing the probes for mito-SinCe$^2$ analyses, the sensitivity of the mito-roGFP to report steady-state [Oxidation] may be reduced in the stable cells. This is because the ro-GFP participate in the cellular redox homeostasis system thus changing it.
4. The parameters recommended here are minimum requirements. Higher resolution is possible with proper precautions to limit and control for bleaching.
5. A dark optical slice from a separate scan can be appended to the stack during image processing if necessary. In the Zen software this is accomplished by subsetting the single slice and stitching it together with the desired 3D image.
6. Set up channels with the excitation parameters of one fluorophore and the detector of another. Adjust parameters to limit cross-talk and cross-excitation.
7. To avoid introduction of the undue effects of prolonged drug incubation take the following precautions: (1) Using either the literature or extended time-lapse imaging of transfected cells after treatment, set a strict scanning time window for each round of imaging to ensure optimal effect of treatment while minimizing the changes due to long term exposure to the treatment. (2) Determine how many images can be taken with perfect technique within that time window and select that many fields for future experiments.
8. The pulse–chase assay described here for determining matrix continuity is distinct from published assays for quantifying fission/fusion dynamics over time, typically a period of 30 m or more [3].
9. Photoswitching efficiency will change over the lifetime of the laser so periodic reoptimization is required.
10. Eventually, users will develop a visual appreciation for which cells will and will not work for the pulse–chase experiment, and the initial check of these cells can be skipped to save time.
11. Loss of fluorescence through bleaching impacts the photoswitched mito-PSmO signal more quickly than the basal signal. This bleaching disparity causes relative loss of Ex-639 even

where there is little or no actual matrix continuity. These bleaching controls, therefore, set the [Matrix-continuity] floor.

12. If desired, the validation treatments can be used to establish a ceiling or a floor for [ATP] or [Oxidation] and experimental values reported as % $ATP_{max}$ or % oxidized.
13. The following macro can be used to import multiple files at once into a single Excel file:

```
Sub CombineTextFiles()'updateby Extendoffice 20151015
Dim xFilesToOpen As Variant
Dim I As Integer
Dim xWb As WorkbookDim xTempWb As Workbook
Dim xDelimiter As StringDim xScreen As BooleanOn Error GoTo
ErrHandlerxScreen = Application.ScreenUpdatingApplication.
ScreenUpdating = False
xDelimiter = "|"xFilesToOpen = Application.GetOpenFilename
("Text Files (*.txt;*.mitograph), *.txt", , "Kutools for
Excel", , True)
If TypeName(xFilesToOpen) = "Boolean" Then
MsgBox "No files were selected", , "Kutools for Excel"
GoTo ExitHandler
End If
I = 1
Set xTempWb = Workbooks.Open(xFilesToOpen(I))
xTempWb.Sheets(1).Copy
Set xWb = Application.ActiveWorkbook
xTempWb.Close False
xWb.Worksheets(I).Columns("A:A").TextToColumns _
Destination:=Range("A1"), DataType:=xlDelimited, _
TextQualifier:=xlDoubleQuote, _
ConsecutiveDelimiter:=False, _
Tab:=True, Semicolon:=False, _
Comma:=False, Space:=False, _
Other:=False, OtherChar:="|"
Do While I < UBound(xFilesToOpen)
I = I + 1
Set xTempWb = Workbooks.Open(xFilesToOpen(I))
With xWb
xTempWb.Sheets(1).Move after:=.Sheets(.Sheets.Count)
.Worksheets(I).Columns("A:A").TextToColumns _
Destination:=Range("A1"), DataType:=xlDelimited, _
TextQualifier:=xlDoubleQuote, _
ConsecutiveDelimiter:=False, _
Tab:=True, Semicolon:=False, _
Comma:=False, Space:=False, _
Other:=False, OtherChar:=xDelimiter
End With
```

```
Loop
ExitHandler:
Application.ScreenUpdating = xScreen
Set xWb = Nothing
Set xTempWb = Nothing
Exit Sub
ErrHandler:
MsgBox Err.Description, , "Kutools for Excel"
Resume ExitHandler
End Sub
```

14. [Fusion1] is the most sensitive of the [Fusion] metrics while [Fusion10] is the most reflective of the whole cell fusion state at the expense of sensitivity. We found that [Fusion5] was the most appropriate fusion metric for our purposes, but the appropriate metric for new systems must be optimized.

## Acknowledgments

We acknowledge Drs. S. Rafelski and M. Vienna for developing the MitoGraph v2.1 software and for help with accessing and understanding its capabilities; Dr. P. Gupta for helping to develop the MitoSinCe2 approach in its earliest stages; D. Parker for performing some of the experiments from which we took example data; and J. Wirth for the custom-built Excel macro. This work was supported by the National Institutes of Health (NIH) [R33ES025662] grant to B.S. and K.M.

### References

1. Harwig MC, Viana MP, Egner JM, Harwig JJ, Widlansky ME, Rafelski SM, Hill RB (2018) Methods for imaging mammalian mitochondrial morphology: A prospective on MitoGraph. Anal Biochem 552:81–99. https://doi.org/10.1016/j.ab.2018.02.022
2. Iannetti EF, Smeitink JA, Beyrath J, Willems PH, Koopman WJ (2016) Multiplexed high-content analysis of mitochondrial morphofunction using live-cell microscopy. Nat Protoc 11 (9):1693–1710. https://doi.org/10.1038/nprot.2016.094
3. Karbowski M, Cleland MM, Roelofs BA (2014) Photoactivatable green fluorescent protein-based visualization and quantification of mitochondrial fusion and mitochondrial network complexity in living cells. Methods Enzymol 547:57–73. https://doi.org/10.1016/B978-0-12-801415-8.00004-7
4. Mitra K, Wunder C, Roysam B, Lin G, Lippincott-Schwartz J (2009) A hyperfused mitochondrial state achieved at G1-S regulates cyclin E buildup and entry into S phase. Proc Natl Acad Sci U S A 106(29):11960–11965. https://doi.org/10.1073/pnas.0904875106
5. Ouellet M, Guillebaud G, Gervais V, Lupien St-Pierre D, Germain M (2017) A novel algorithm identifies stress-induced alterations in mitochondrial connectivity and inner membrane structure from confocal images. PLoS Comput Biol 13(6):e1005612. https://doi.org/10.1371/journal.pcbi.1005612
6. Parker DJ, Moran A, Mitra K (2017) Studying mitochondrial structure and function in drosophila ovaries. J Vis Exp (119):e54989. https://doi.org/10.3791/54989
7. Spurlock B, Gupta P, Basu MK, Mukherjee A, Hjelmeland AB, Darley-Usmar V, Parker D,

Foxall ME, Mitra K (2019) New quantitative approach reveals heterogeneity in mitochondrial structure-function relations in tumor-initiating cells. J Cell Sci 132(9):jcs230755. https://doi.org/10.1242/jcs.230755

8. Nakano M, Imamura H, Nagai T, Noji H (2011) Ca(2)(+) regulation of mitochondrial ATP synthesis visualized at the single cell level. ACS Chem Biol 6(7):709–715. https://doi.org/10.1021/cb100313n
9. Vevea JD, Alessi Wolken DM, Swayne TC, White AB, Pon LA. (2013) Ratiometric biosensors that measure mitochondrial redox state and ATP in living yeast cells. J Vis Exp (77):50633. https://doi.org/10.3791/50633
10. Waypa GB, Marks JD, Guzy R, Mungai PT, Schriewer J, Dokic D, Schumacker PT (2010) Hypoxia triggers subcellular compartmental redox signaling in vascular smooth muscle cells. Circ Res 106(3):526–535. https://doi.org/10.1161/CIRCRESAHA.109.206334
11. Beretta CA, Dross N, Engel U, Carl M (2016) Tracking cells in GFP-transgenic zebrafish using the photoconvertible PSmOrange system. J Vis Exp (108):e53604. https://doi.org/10.3791/53604
12. Pletnev S, Shcherbakova DM, Subach OM, Pletneva NV, Malashkevich VN, Almo SC, Dauter Z, Verkhusha VV (2014) Orange fluorescent proteins: structural studies of LSSmOrange, PSmOrange and PSmOrange2. PLoS One 9(6):e99136. https://doi.org/10.1371/journal.pone.0099136
13. Subach OM, Patterson GH, Ting LM, Wang Y, Condeelis JS, Verkhusha VV (2011) A photoswitchable orange-to-far-red fluorescent protein, PSmOrange. Nat Methods 8 (9):771–777. https://doi.org/10.1038/nmeth.1664
14. Viana MP, Lim S, Rafelski SM (2015) Quantifying mitochondrial content in living cells. Methods Cell Biol 125:77–93. https://doi.org/10.1016/bs.mcb.2014.10.003

# Chapter 28

# Computer-Aided Prediction of Protein Mitochondrial Localization

**Pier Luigi Martelli, Castrense Savojardo, Piero Fariselli, Giacomo Tartari, and Rita Casadio**

## Abstract

Protein sequences, directly translated from genomic data, need functional and structural annotation. Together with molecular function and biological process, subcellular localization is an important feature necessary for understanding the protein role and the compartment where the mature protein is active. In the case of mitochondrial proteins, their precursor sequences translated by the ribosome machinery include specific patterns from which it is possible not only to recognize their final destination within the organelle but also which of the mitochondrial subcompartments the protein is intended for. Four compartments are routinely discriminated, including the inner and the outer membranes, the intermembrane space, and the matrix. Here we discuss to which extent it is feasible to develop computational methods for detecting mitochondrial targeting peptides in the precursor sequence and to discriminate their final destination in the organelle. We benchmark two of our methods on the general task of recognizing human mitochondrial proteins endowed with an experimentally characterized targeting peptide (TPpred3) and predicting which submitochondrial compartment is the final destination (DeepMito). We describe how to adopt our web servers in order to discriminate which human proteins are endowed with mitochondrial targeting peptides, the position of cleavage sites, and which submitochondrial compartment are intended for. By this, we add some other 1788 human proteins to the 450 ones already manually annotated in UniProt with a mitochondrial targeting peptide, providing for each of them also the characterization of the suborganellar localization.

**Key words** Targeting peptide, Prediction of subcellular localization, Arginine motifs, Cleavage site, Machine and deep learning

## 1 Introduction

### *1.1 Targeting Peptides and Mitochondrial Localization*

Recent estimates in mammals indicate that mitochondrial proteomes comprise from about 1500 to 2500 protein types, all participating into biological processes involving to different extent the mitochondrion [1, 2]. Large-scale proteomics experiments, based mainly on mass spectrometry and green fluorescent protein (GFP) tagging, allow characterizing proteins localized in the

Volkmar Weissig and Marvin Edeas (eds.), *Mitochondrial Medicine: Volume 1: Targeting Mitochondria*, Methods in Molecular Biology, vol. 2275, https://doi.org/10.1007/978-1-0716-1262-0_28,

mitochondrial space [3]. Consequently, different databases gather the currently available data and therefrom annotate mammalian proteins based on direct assays or upon sequence similarity detection. Among them, MitoMiner (http://mitominer.mrc-mbu.cam.ac.uk) [4] and MitoCarta (http://www.broadinstitute.org/pubs/MitoCarta/) [5] currently list 2231 and 1158 human mitochondrial proteins, respectively. Targeting peptides have different compositional and structural features, which may unravel the different types of translocating protein machineries in different eukaryotic species. Apparently, the mitochondrial sequence precursors may carry also characteristic arginine-rich motifs at the N-terminal position [6].

In humans, the mitochondrial genome encodes only for 13 protein chains that are part of the respiratory complexes, labeled as I, III, IV, and V. The nuclear genome encodes for the large majority of the remaining mitochondrial proteins, synthesized at cytosolic ribosomes, and therefrom translocated to the different submitochondrial localizations (outer and inner mitochondrial membranes, intermembrane space, and matrix). Different protein machineries, which recognize protein precursors harboring either N-terminal cleavable signals or internal non-cleavable signals, control the import into the mitochondrion and the sorting towards submitochondrial compartments [6–8]. The most characterized and widespread mechanism involves the detection of a N-terminal presequence, called targeting peptide, which directs the protein across the translocase complexes located at the outer and inner mitochondrial membranes and which is then proteolytically cleaved, when the protein reaches the final destination. In the genomic era, the detection of targeting peptides starting from the protein sequence is an important step in order to characterize the function, the localization and the sequence of the mature protein and to discriminate mitochondrial from nonmitochondrial proteins in the genome. After detection of targeting peptides, a further step towards the full functional characterization of any mitochondrial protein is the discrimination of a specific localization within the organelle.

### 1.2 Available Computational Methods for Targeting peptide Detection

The dataset of experimentally characterized targeting peptides is still very small, and its analysis reveals that they are very variable in length and in covalent structure composition. This hampers the adoption of simple alignment methods for the detection of targeting peptides in uncharacterized proteins. Furthermore, the cleavage site is quite heterogeneous, and although common motifs have been recognized [6], they are not sufficient to perform prediction based on pattern matching.

Different computational methods can help the annotation of targeting peptides in proteins when experimental data are not available. Most of the available methods implement statistical or machine-learning approaches, such as neural networks (NNs),

support vector machines (SVMs), hidden Markov models (HMMs), grammatical-restrained hidden conditional random fields (GRHCRFs), extreme learning machines (ELMs), and deep learning [9–16]. Machine learning methods can extract rules of association between input features derived from the protein residue sequence and output features to be predicted. After training on the few available proteins with experimentally characterized targeting peptides and cleavage sites, a machine learning based method can infer the presence or not (with an associated likelihood) of targeting peptides and cleavage sites, taking as input the protein sequence. The generalization capability of the different methods routinely depends on the different implementations, training procedures, training datasets, and input encodings. In order to evaluate the generalization power, the predictive performance of a method is statistically validated on the same training dataset with a leave-one-out procedure and, in addition, on a blind data set of data experimentally validated. Based on the number of correct and incorrect evaluations, different scoring indexes can be computed in order to measure and compare the reliability of the different tools.

Table 1 lists the most recent available tools for the prediction of targeting peptides (all of them are publicly available as web servers). They differ in many implementation aspects, such as the method, the adopted training set and the input encoding. In particular, all but MitoProt [17] and iPSORT [18] are based on machine learning approaches, and all but MitoProt and MitoFates [16] have been trained on datasets containing both mitochondrial and plastidic targeting peptides. All methods take as input the protein residue sequence, translated from its coding sequence and different physical and chemical features that are again derived directly from the sequence, without the necessity of any functional or structural information. All the predictors compute a probability for the presence of a targeting peptide by analyzing an N-terminal portion of the precursor protein, ranging from 40 to 160 residues and depending on the method. MitoProt, PredSL [10], MitoFates, TargetP [11, 13], and TPpred [12, 14, 15] are also able to predict the position of the cleavage site along the protein sequence. During the years, some of the methods such as TargetP and TPpred have been updated and improved. For instance, TPpred v2 [14] is dedicated only to mitochondrial transit peptides and, over the first version, it improves the detection of cleavage sites adopting the occurrence of known sequence motifs [6]. TPpred v3 [15] adopts different machine learning approaches (GRHCRFs, ELMs, and SVMs) and it is able to predict also plastidic peptides in plants, discriminating plastidic from mitochondrial peptides and improving cleavage-site prediction by exploiting the occurrence patterns of newly discovered, organelle-specific sequence motifs around peptide cleavage sites.

**Table 1**
**Computational methods available for the prediction of mitochondrial targeting peptides**

| Tool name (references) | Type[a] | Site | Method | Input encoding[b] | Web server |
|---|---|---|---|---|---|
| MitoProt [17] | Mito | Yes | Discriminant function | 47 physicochemical properties | http://ihg.gsf.de/ihg/mitoprot.html |
| iPSORT [18] | Mito Plast | No | Rule-based algorithm | 434 propensity scales | http://ipsort.hgc.jp/ |
| Predotar [9] | Mito Plast | No | NN | Residue sequence Hydrophobicity Charged residues | https://urgi.versailles.inra.fr/predotar/predotar.html |
| PredSL [10] | Mito Plast | Yes | NN, HMM, scoring matrices | Residue sequence | http://hannibal.biol.uoa.gr/PredSL |
| TPpred, TPpred2, TPpred3 [12, 14, 15] | Mito Plast | Yes | GRHCRF Nto1-ELM SVM | Residue sequence Hydrophobicity Charged residues Hydrophobic moment Cleavage-site motifs | https://tppred3.biocomp.unibo.it |
| MitoFates [16] | Mito | Yes | SVM | Residue sequence Residue physicochemical properties | http://mitf.cbrc.jp/MitoFates/cgi-bin/top.cgi |
| TargetP1.1, TargetP2 [11, 13] | Mito Plast | Yes | NN DeepLearning | Residue sequence Hydrophobicity Charged residues | http://www.cbs.dtu.dk/services/TargetP/ |

*Mito* mitochondrial, *Plast* plastidic
[a]The targeting peptide type predicted
[b]Features considered by the method

An important issue to be considered in developing and adopting a predictor is that the proportion of proteins endowed with a targeting peptide with respect to the whole proteome is expected to be quite small (≈2–4%). In this situation, even a small rate of incorrect predictions in the negative set would lead to a large amount of proteins misclassified as "carrying a targeting peptide."

### *1.3 Available Computational Methods for Discrimination of Submitochondrial Localization*

In the past years, the definition of reliable computational methods for discriminating protein localization at submitochondrial level has been significantly hampered by a substantial lack of curated information available on public databases, such as UniProtKB. Recently, thanks to the improvement of experimental techniques allowing fine-grain assessment of protein localization [19], a few methods capable of predicting protein submitochondrial localization have appeared in literature [20–23]. In Table 2, we list the main

**Table 2**
**Computational methods available for the prediction of submitochondrial localization**

| Tool name (references) | Compartments[a] | Method | Input encoding[b] | Web server |
|---|---|---|---|---|
| SubMito-PSPCP [20] | 3 | SVM | Pseudo AA composition | https://www.pufengdu.org/bioinfo/submito-pspcp/ |
| TetraMito [21] | 3 | SVM | Tetrapeptide words | http://lin.uestc.edu.cn/server/TetraMito |
| SubMitoPred [22] | 4 | SVM | Composition PFam domains | http://proteininformatics.org/mkumar/submitopred/ |
| DeepMito [23] | 4 | CNN | Residue properties Evolutionary information | http://busca.biocomp.unibo.it/deepmito/ |

[a]The number of distinct compartments predicted
[b]Features considered by the method

approaches available to date. Only the two most recent methods, namely SubMitoPred [22] and our DeepMito [23], are able to predict the four main mitochondrial compartments: outer and inner membranes, intermembrane space, and matrix. All methods but DeepMito are based on SVMs leveraging protein features such as canonical and pseudo amino acid composition or tetrapeptide compositions. DeepMito is the first method adopting deep learning, specifically convolutional neural networks (CNNs), to the task at hand. In several benchmarks, DeepMito has been proven to be the top-scoring and most balanced method for predicting submitochondrial localization [23].

## 2 Materials

### 2.1 Benchmark Dataset

UniProtKB (release Nov 2019) [24] contains 90,489 complete human sequences (not considering fragments). In this set, we identified proteins having manually curated evidence for the presence of the N-terminal mitochondrial targeting peptide (see https://www.uniprot.org/help/evidences for evidence codes used in the UniProtKb database). We retained only mitochondrial targeting peptides with known and unambiguous assignment of the cleavage site and excluded annotations labeled as "by similarity", "potential", "probable", or "not cleaved". With this procedure, the positive dataset (DB+) consists of 450 protein sequences (Table 3). The negative dataset (DB-) comprises 19,800 proteins with manually curated non-mitochondrial localization, as derived from the subcellular localization feature of UniProtKB and/or from the gene ontology (GO) annotations in the cellular component aspect.

**Table 3**
**The human protein dataset**

| Total | DB+[a] | DB-[a] | DB*[a] |
|---|---|---|---|
| 90,489 | 450 | 19,800 | 70,497 |

The human protein dataset was downloaded from UniProtKB (release Nov 2019) as described in Subheading 2.1
[a]DB+: mitochondrial proteins with a manually curated annotation of the mitochondrial targeting peptide, DB-: proteins with a manually curated annotation of nonmitochondrial localization; DB*: the remaining human protein set

**Table 4**
**Submitochondrial localizations of the human protein dataset**

| Localization | DB+# | DB*# | Total# |
|---|---|---|---|
| Outer membrane | 9 | 135 | 144 |
| Inner membrane | 86 | 192 | 278 |
| Intermembrane space | 5 | 20 | 25 |
| Matrix | 187 | 126 | 313 |
| *Single localization* | *287* | *473* | *760* |
| *Multiple localization* | *94* | *89* | *183* |
| Total | 381 | 562 | 943 |

# Number of proteins

GO annotations were obtained from the UniProtKB GO Annotation (GOA) database (release 12/11/2019, https://www.ebi.ac.uk/GOA/). The remaining 70,497 proteins form the DB* dataset, contain: (a) mitochondrial proteins (annotated either in GO or UniProtKB) without curated annotation of the targeting peptide, (b) proteins manually annotated with a subcellular localization that is compatible with the mitochondria (e.g., "cytoplasm", "membrane", "ribosome"), (c) proteins annotated with a localization (either mitochondrial or not) without manually curated evidence, and (d) proteins lacking any annotation for subcellular localization. DB* is also used to predict new potential targeting peptides with TPpred3.

In Table 4, we show statistics of available manually curated annotations for submitochondrial localization of proteins in the human protein set. In particular we considered (1) proteins endowed with the mitochondrial targeting peptide (i.e., the DB+ dataset) and (2) proteins contained in DB*, annotated with mitochondrial localization but lacking targeting peptide. Four mitochondrial compartments are considered: inner and outer membranes, intermembrane space, and matrix. Out of 450 proteins, 85% (381) of proteins contained in DB+ set (i.e., endowed with a mitochondrial targeting peptide) are also annotated at the

submitochondrial level. In DB*, 1396 proteins are annotated as mitochondrial (with manually curated assertions). Of these, 562 (40%) have also annotations at the submitochondrial level.

Some 183 proteins out of 943 have multiple submitochondrial localizations: the vast majority of multi-localized proteins reside in the inner membrane and/or in the matrix (128 proteins).

We used the remaining large fraction of 760 proteins with single localization to score DeepMito in discriminating submitochondrial compartments.

The datasets are available at our http://biocomp.unibo.it/savojard/hs.dec2019.benchmark.tar.gz.

### 2.2 Length and Residue Composition of Targeting Peptides

The length of experimentally annotated targeting peptides in human proteins (DB+) ranges from 7 to 117 residues, with an average length of 38 residues and a standard deviation of 19 residues (Fig. 1).

The overall residue composition of proteins included in DB+ and DB- datasets shows only minor differences, lower than 2%, proving that the whole composition is not sufficient to perform a prediction (Fig. 2). On the contrary, the composition of human targeting peptides is quite peculiar, since they are strongly enriched in alanine, leucine, and arginine and are depleted in isoleucine, asparagine, aspartic acid, glutamic acid, and lysine. These data are in agreement with previous observations carried out on larger, non–organism-specific datasets [12].

### 2.3 Features of the Cleavage Site

Compositional features of the region surrounding the cleavage site are important for the interaction between the protein precursor and their peptidase complexes, and they can be visualised with a sequence logo obtained by piling up the 20-residue-long segments centred on each one of the cleavage sites of the DB+ dataset (Fig. 3). The logo represents the positional composition of the segments, with letters whose heights are proportional to the information content of each residue [25]. Values range from 0 (low information equivalent to uniform composition) to $\log_2(20) = 4.3$ (high information, corresponding to highly conserved residues). It is evident that the information in the surrounding regions of the cleavage site is moderate, although positions -2 and -3 appears significantly richer in arginine (R), positions 0 and 1 are richer in serine (S) and alanine (A), and position 1 is also moderately richer in histidine (H).

These features reflect also the presence of previously recognized motifs around the cleavage site [6]: (a) R2 = RX|X, (b) R3 = RXX|[SAX], (c) R10 = RX[FLI]XX[TSG]XXXX|X, and (d) Rnone = X|X[SX]. In this representation, the character "|" indicates the cleavage position, the wildcard character X represents any residue, and the residues enclosed in square brackets indicate alternative choices. Table 5 shows the number of cleavage sites in

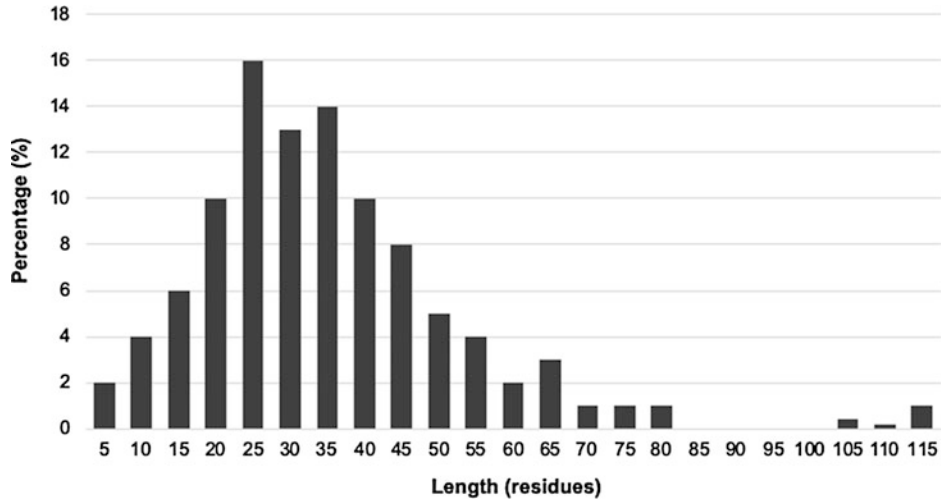


**Fig. 1** Length distribution of targeting peptides in DB+ dataset

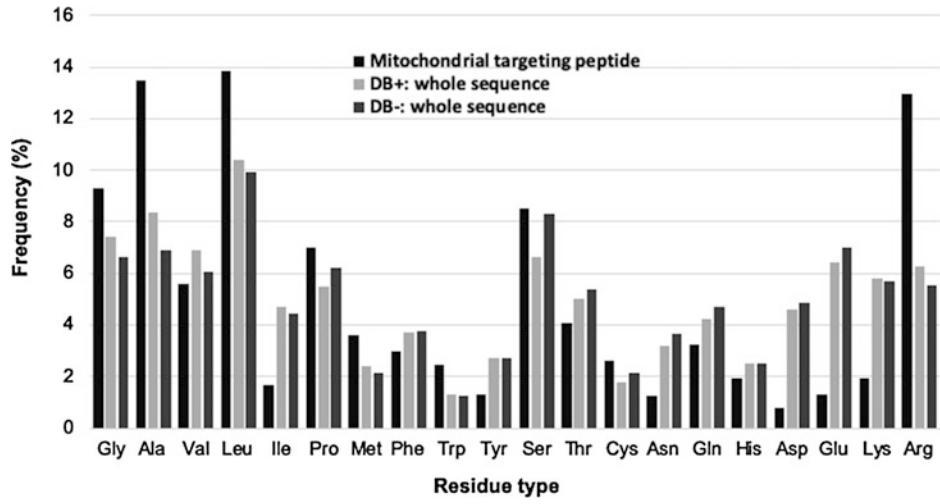


**Fig. 2** Residue composition of our benchmark datasets. Composition of targeting peptides is reported with *black bars*. *Light and dark grey bars* represent the composition of the whole sequences included in DB+ and DB- datasets, respectively

DB+, matching with each one of the motifs. When the multiple choice contains a wildcard character, the patterns have been split, as in the case of R3a (RXX|[SA]) and R3b (RXX|X). The pattern X|XX was not considered. Since the patterns are not mutually exclusive, a single cleavage site can match with more than one of them (Table 6). On the overall, 321 out of 450 (71%) sites match with at least one pattern, and the most represented are, as expected, the shortest ones: R2 and Rnone.

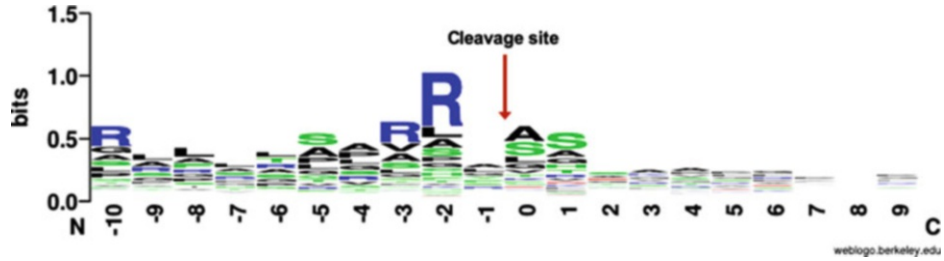


**Fig. 3** Sequence logo of the sequence segments surrounding the cleavage site. Sequence logo is computed by the WebLogo server (http:/weblogo.berkeley.edu) [25]. Position "1" is the first residue of the mature protein. Color codes cluster residues in apolar (*black*), polar (*green*), positively charged (*blue*), and negatively charged (*red*). *Height of each letter* indicates the information content of the corresponding residue in the input profile. Information is measured in bits and ranges between 0 and $\log_2(20) \approx 4.3$

**Table 5**
**Regular expression in cleavage sites of the positive data set (DB+)**

| Motif Name | Motif expression | Mapped cleavage sites in DB+ |
|---|---|---|
| R2 | RX\|X | 188 |
| R3a | RX[YFL]\|[SA] | 50 |
| R3b | RX[YFL]\|X | 63 |
| R10 | RX[FLI]XX[TSG]XXXX\|X | 55 |
| Rnone | X\|XS | 110 |

*R* arginine, *S* serine, *Y* tyrosine, *F* phenylalanine, *L* leucine, *I* isoleucine, *T* threonine, *G* glycine, *X* wildcard (any of 20 residues), | cleavage site

**Table 6**
**Regular expression in cleavage sites of the positive data set (DB+)**

| Number of motifs mapping the cleavage sites | Number of proteins |
|---|---|
| 0 | 129 |
| 1 | 198 |
| 2 | 103 |
| 3 | 18 |
| 4 or more | 2 |

DB+ contains the human proteins with an experimentally detected targeting peptide

### *2.4 Compositions of Proteins Residing in Different Mitochondrial Compartments*

Figure 4 shows residue compositions of proteins belonging to the four mitochondrial compartments. These distributions were computed on the complete set of 943 proteins with manually curated evidence for mitochondrial sublocalization (*see* Table 4). From Fig. 4, it is clear that, overall, no remarkable differences are observed in the composition of proteins in the four compartments

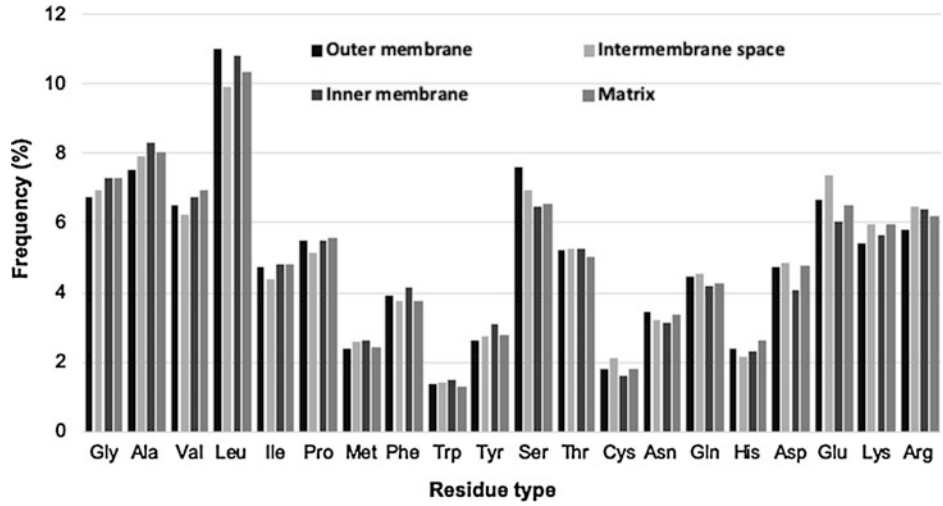


**Fig. 4** Composition of proteins localized in different mitochondrial subcompartments

(average difference is less than 1%). This suggests that discriminative features are not related to global protein characteristics but instead need to be identified at a local level such as the presence of specific sequence motifs. Appropriate machine-learning approaches, such as convolutional neural networks, can be very effective in this task.

## 3 Methods

### 3.1 TPpred3

Our TPpred predictor [15] is organized as a pipeline consisting of three cascading prediction steps: (1) the preliminary detection of the targeting peptide and the corresponding cleavage-site at the N-terminus of the query sequence; (2) the classification of the detected targeting sequence into mitochondrial or chloroplastic (only executed if plant proteins are provided in input); and (3) the refinement of the cleavage-site prediction exploiting the occurrence pattern of newly discovered, organelle-specific cleavage-site sequence motifs.

Preliminary TP detection and site prediction is performed using the same method adopted in TPpred3 [15], including a probabilistic graphical model based on Grammatical Restrained Hidden Conditional Random Fields (GRHCRFs), and a machine-learning framework that has been proven effective in addressing sequence labelling tasks [26]. Indeed, similarly to hidden Markov models (HMMs), GRHCRFs allow to cast into a model the grammatical restraints of the problem at hand, and at the same time, they share with neural networks (NNs) and support vector machines (SVMs) the ability to deal with complex input encodings, consisting of several features besides the residue

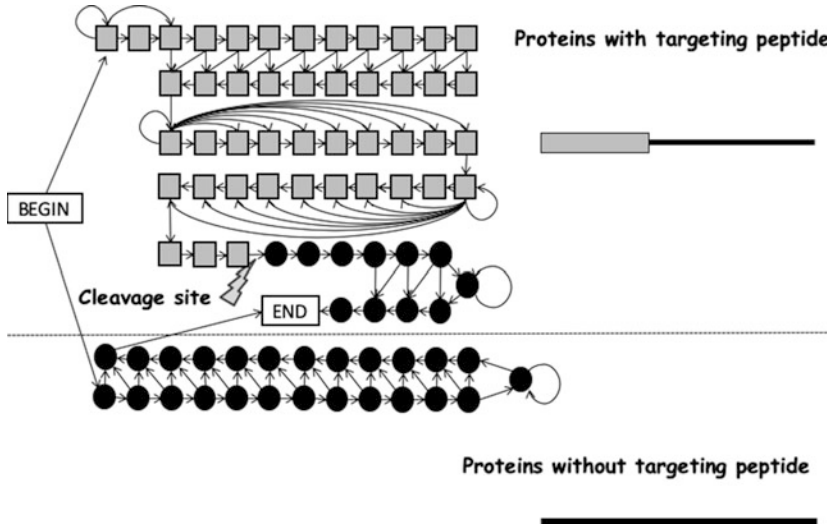


**Fig. 5** Graphical model of TPpred3. TPpred3 is based on grammatical-restrained conditional random fields (GRHCRFs) [26]. *Gray squares* represent states describing targeting peptides, while *black circles* represent nontargeting peptide states. *The upper submodel* represents proteins endowed with targeting peptide and the *lower submodel* represents proteins devoid of targeting peptide

sequence [26]. The GRHCRF model implemented in TPpred3 is depicted in Fig. 5, where grey boxes represent targeting peptide positions and black circles represent other positions. The model consists of two major submodels describing proteins endowed or not with a targeting peptide (the upper and the lower submodels in Fig. 5, respectively). All states and transitions are associated with potential functions, related to the probability for each residue in the sequence to be generated by a particular state. Each potential function mixes the different components of the input encoding, namely, the residue sequence, the local average hydrophobicity (computed on a 7-residue window centred around each residue), the local average positive and negative charge, and the local hydrophobic moments (computed considering the ideal alpha-helical and beta-strand conformations).

In the second step, if the query protein is from a plant organism, the preliminary identified targeting peptide is classified into mitochondrial or chloroplastic using a special architecture of neural network known as N-to-1 Extreme Learning Machine [15, 27]. The network takes as input the protein N-terminal sequence up to the cleavage-site predicted at the previous step and provides in output a binary classification (mitochondrial or chloroplastic). This prediction step is performed only when the input protein is from a plant organism. In the case of nonplant proteins, the detected targeting peptide is directly classified as mitochondrial and passed to the next step.

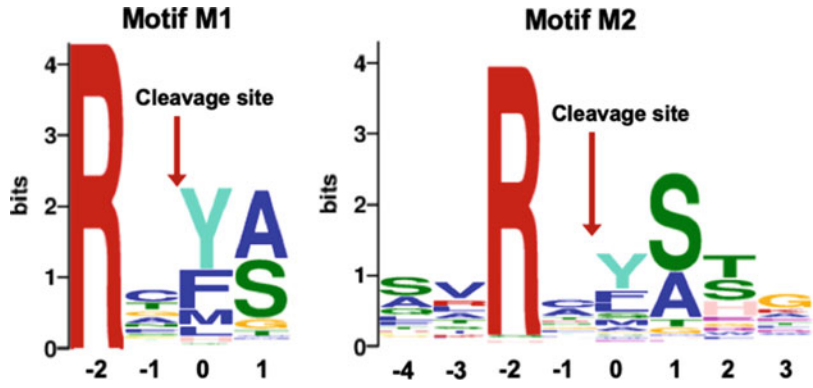


**Fig. 6** The two mitochondrial-specific motifs found around targeting peptide cleavage sites by extensive motif discovery [15]

In the final third step, using the outcome of the classification performed at step two, the preliminary cleavage site identified at the first step is refined exploiting information derived from organelle-specific sequence motifs surrounding the site of cleavage. These motifs were discovered and extracted by means of an extensive motif discovery procedure on two datasets of experimentally verified targeting peptides [15]. Specifically, for cleavage sites of mitochondrial targeting peptides we identified the two motifs M1 and M2 depicted in Fig. 6 as sequence logos. Previously discovered short motifs [6] listed in Table 5 are included into the longer, more general motifs M1 and M2 found and adopted in TPpred3 to refine cleavage site position.

The overall pipeline has been trained using the same dataset adopted for the previous versions of TPpred [12, 14], including a positive dataset of 297 nonredundant proteins endowed with a mitochondrial (202) or plastidic (95) targeting peptide and a negative dataset of 8010 nonredundant proteins from animal, plants, and fungi [12].

In summary, for a given query sequence, TPpred3 provides the probability of having a targeting peptide at the N-terminus, the predicted type of targeting sequence (mitochondrial or chloroplastic) and the position of the cleavage site.

### *3.2 Benchmarking TPpred3 on the Human Protein Datasets*

We evaluate the performance of TPpred3 on the DB+ and DB- datasets. The method computes the probability of carrying a targeting peptide and the position of the cleavage site.

For an overall evaluation of the targeting peptide discriminative power, the receiver operating characteristic (ROC) curve of the method is computed by plotting the true-positive rate (TPR or recall) versus the false-positive rate (FPR), defined as

$$\mathrm{TPR} = \frac{\mathrm{TP}}{\mathrm{TP} + \mathrm{FN}} \tag{1}$$

$$\mathrm{FPR} = \frac{\mathrm{FP}}{\mathrm{TN} + \mathrm{FP}} \tag{2}$$

where TP and TN are the numbers of correct (true) predictions in the positive and negative classes, respectively, while FP and FN count the incorrect (false) predictions in the same classes.

The area under the ROC curve (AUC) ranges between 0 and 1, and it measures how far the predictors are from a random predictor that would score with AUC equal to 0.5. Our method performs very well, scoring with AUC values higher than 0.98.

When the cleavage site position along the sequence is predicted, considering a seventeen residue-long window centered at the cleavage site, the rate of correct prediction is 40% with perfect matching and 69% for an error lower or equal to 10 residues. TPpred3 is available as a web server (https://tppred3.biocomp.unibo.it).

### 3.3 DeepMito

DeepMito [23] has been recently implemented for protein submitochondrial localization prediction. DeepMito is able to discriminate the four different mitochondrial compartments (the two membranes (inner and outer), the intermembrane space, and the matrix). The method is based on a deep learning approach, and in particular a convolutional neural network, specifically designed to extract relevant patterns from protein sequences and to map them with respect to the four mitochondrial compartments.

Each sequence is encoded using evolutionary information, in the form of Position Specific Scoring Matrices (PSSMs) as obtained running PSI-BLAST against the UniRef90 reference cluster database and residue physical–chemical attributes. DeepMito was trained and tested in cross-validation on a dataset comprising 424 high-quality, non-redundant proteins extracted from UniProtKB/SwissProt (release February 2018) and experimentally annotated as being localized into one of the four mitochondrial compartments. In all comparative experiments, DeepMito outperformed other approaches, showing, in particular, a very high robustness with respect to class imbalance. Details can be found in the reference paper [23]. DeepMito is available as web server (http://busca.biocomp.unibo.it/deepmito) and as command-line tool executable as a Docker container (https://hub.docker.com/r/bolognabiocomp/deepmito).

### 3.4 Benchmarking DeepMito on the Human Protein Datasets

Performance of DeepMito was assessed on the set comprising 760 mitochondrial proteins endowed with manually curated localization into a single submitochondrial compartment (multilocalized proteins were excluded from the benchmark, *see* Table 4, Subheading 2.1). Each protein is classified by DeepMito into one of four compartments, including the outer and the inner membranes, the intermembrane space, and the matrix. The classification was scored

**Table 7**
**Prediction of human protein submitochondrial localization with DeepMito**

| Compartment | $MCC_c$ |
|---|---|
| Outer membrane (144) | 0.61 |
| Intermembrane space (25) | 0.44 |
| Inner membrane (278) | 0.50 |
| Matrix (313) | 0.55 |

*$MCC_c$* Matthews correlation coefficient for compartment *c*

by computing the Matthews Correlation Coefficient (MCC) for each compartment, defined as

$$\mathrm{MCC_c} = \frac{(\mathrm{TP_c} \times \mathrm{TN_c} - \mathrm{FP_c} \times \mathrm{FN_c})}{\sqrt{(\mathrm{TP_c} + \mathrm{FP_c}) \times (\mathrm{TP_c} + \mathrm{FN_c}) \times (\mathrm{TN_c} + \mathrm{FP_c}) \times (\mathrm{TN_c} + \mathrm{FN_c})}} \quad (3)$$

where $TP_c$, $TN_c$, $FP_c$, and $FN_c$ are true positive, true negative, false positive, and false negative predictions, respectively, with respect to compartment $c \in \{\text{outer}, \text{inner}, \text{intermembrane}, \text{matrix}\}$. Results are listed in Table 7. MCC scores range from 0.44 for intermembrane space (the most difficult class to predict, given the small number of proteins) to 0.61 for the outer membrane compartment. These results are in line with what obtained in different benchmarks previously performed [23] and highlight the ability of DeepMito to provide balanced performances across the different compartments.

### 3.5 TPpred3 and DeepMito at Work on the Human Genome

In this section we show how to adopt both TPpred3 and DeepMito to discover and annotate new mitochondrial proteins. Both predictors are now part of the BUSCA pipeline available in our lab (http://busca.biocomp.unibo.it) [28].

TPpred3 is adopted to annotate new potential targeting peptides in the human proteome, predicting the DB* dataset. Out of 70,497 sequences, 1788 are predicted to carry a targeting peptide (Table 8). The large majority of the new predictions (1134 out of 1788) involve proteins that are lacking any annotation for the subcellular localization in UniProt fields (including the Gene Ontology annotation). Other 414 proteins are annotated to be located either in mitochondria or in compatible localizations. Finally, 240 proteins are localized in other compartments, although with non-experimental annotations.

The set of new potential mitochondrial proteins were then analyzed using DeepMito to assess their submitochondrial localization. Some 92 out of 1788 proteins were already endowed with manually curated submitochondrial localization. We ran DeepMito on the remaining 1696 proteins lacking annotations at

**Table 8**
**TPpred3 at work: the newly annotated precursor proteins in the human proteome**

| | | Protein evidence level | | | | |
|---|---|---|---|---|---|---|
| **Annotation** | **Total** | **Protein** | **Transcript** | **Homology** | **Predicted** | **Uncertain** |
| Mitochondrial | 395 | 215 | 99 | 50 | 30 | 1 |
| Compatible subcellular localization | 19 | 6 | 9 | 2 | 0 | 2 |
| Non experimental nonmitochondrial localization | 240 | 94 | 106 | 10 | 30 | 0 |
| Non annotated for subcellular localization | 1134 | 376 | 445 | 17 | 284 | 12 |
| Total | 1788 | 691 | 659 | 79 | 344 | 15 |

**Table 9**
**DeepMito at work: subcompartments for newly annotated mitochondrial proteins**

| | | Compartment | | | |
|---|---|---|---|---|---|
| **Annotation** | **Total** | **Outer membrane** | **Inner membrane** | **Intermembrane space** | **Matrix** |
| Mitochondrial | 303 | 11 | 161 | 8 | 123 |
| Compatible subcellular localization | 19 | 2 | 12 | 2 | 3 |
| Non experimental nonmitochondrial localization | 240 | 50 | 89 | 23 | 78 |
| Non annotated for subcellular localization | 1134 | 83 | 384 | 91 | 576 |
| Total | 1696 | 146 | 646 | 124 | 780 |

suborganelle level. The result of the complete analysis is shown in Table 9, in which DeepMito predictions are joined to available annotations for subcellular localization.

The vast majority of proteins are predicted as localized in the matrix or in the inner membrane. Indeed, these are the compartments expected to include the largest fraction of proteins [23].

The list of the proteins predicted by TPpred3 with a targeting peptide and the predicted cleavage sites as well as localizations annotated by DeepMito are available at http://biocomp.unibo.it/savojard/hs.dec2019.mitoset.tsv.gz.

### *3.6 How to Predict Mitochondrial Localization with TPpred3*

TPpred3 is available as a web server and it requires as input only the residue sequence of the proteins:

1. Write or download the sequence to be predicted in FASTA format.

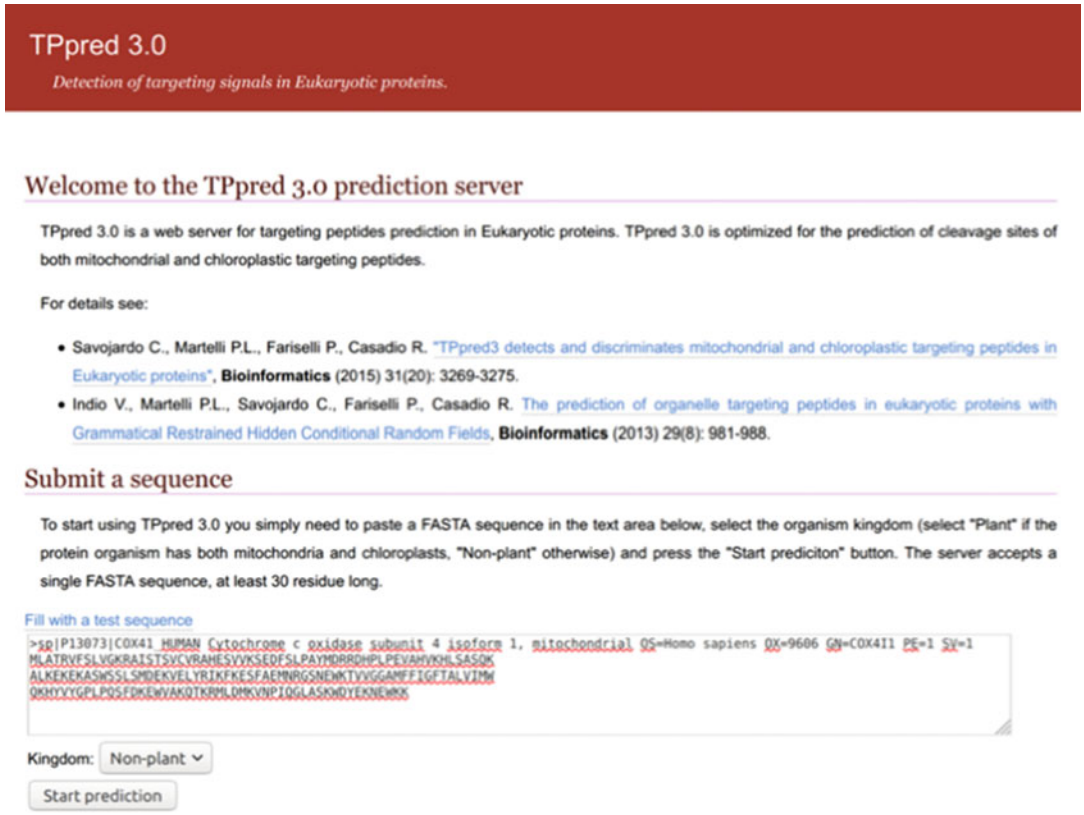


**Fig. 7** Input page of TPpred3, http:/tppred3.biocomp.unibo.it/

2. Go to the website http://tppred3.biocomp.unibo.it/ (Internet Explorer 6 and upper, Firefox, and Google Chrome were tested and support the prediction server). *See* Fig. 7.
3. Copy and paste the sequence in the corresponding field (only one sequence at the time) (Fig. 7).
4. Choose the kingdom the protein belongs to among Plant or Non-plant (Fig. 7).
5. Submit the request and wait for results (approximately 10 s per protein sequence).

### *3.7 How to Read the Results of TPpred3*

1. The first section of the result page reports: (a) the name of the input sequence, (b) the length of the input sequence, and (c) the probability that the input sequence contains a N-terminal mitochondrial targeting peptide, as computed by TPpred3, and the position of the cleavage site.
2. The second section reports the annotation of the targeting peptide along the sequence (Fig. 8).

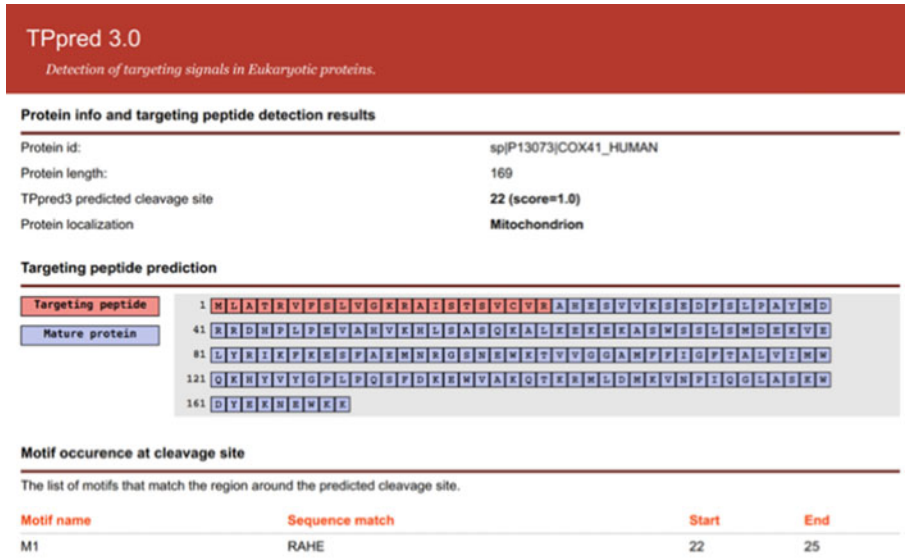


**Fig. 8** Typical TPpred3 output. The output page reports the name of the input sequence, its length, and the probability that it contains a mitochondrial targeting peptide and cleavage site, as computed by TPpred3. The second section reports the annotation of the targeting peptide along the sequence, and the third section lists mitochondrial-specific sequence motifs (M1 or M2) matching the region around the predicted cleavage site

3. The third section lists mitochondrial-specific sequence motifs (M1 or M2) motifs matching the region around the predicted cleavage site, reporting the exact start and end positions of the match.

### 3.8 How to Predict Submitochondrial Localization with DeepMito

DeepMito is available as a web server and can analyze up to 200 sequences in a single job:

1. Write or download the sequence(s) to be predicted in FASTA format.
2. Go to the website http://busca.biocomp.unibo.it/deepmito/ (Internet Explorer 6 and upper, Firefox, and Google Chrome were tested and support the prediction server). *See* Fig. 9.
3. Copy and paste the sequence in the corresponding field (up to 200 sequences) (Fig. 9).
4. Submit the request and wait for results (approximately 1 or 2 m per protein sequence).

### 3.9 How to Read DeepMito Results

1. The first section of the results page reports (a) the job identifier, (b) the job submission time, and (c) the number of sequences submitted (*see* Fig. 10).

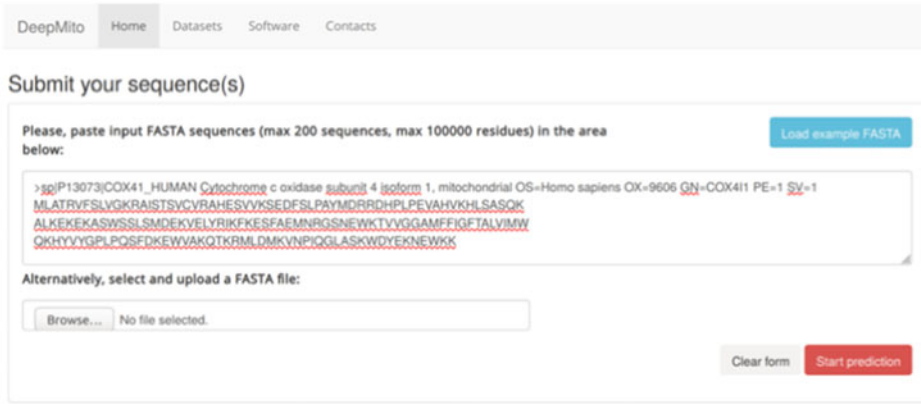


**Fig. 9** Input page of DeepMito, http:/busca.biocomp.unibo.it/deepmito

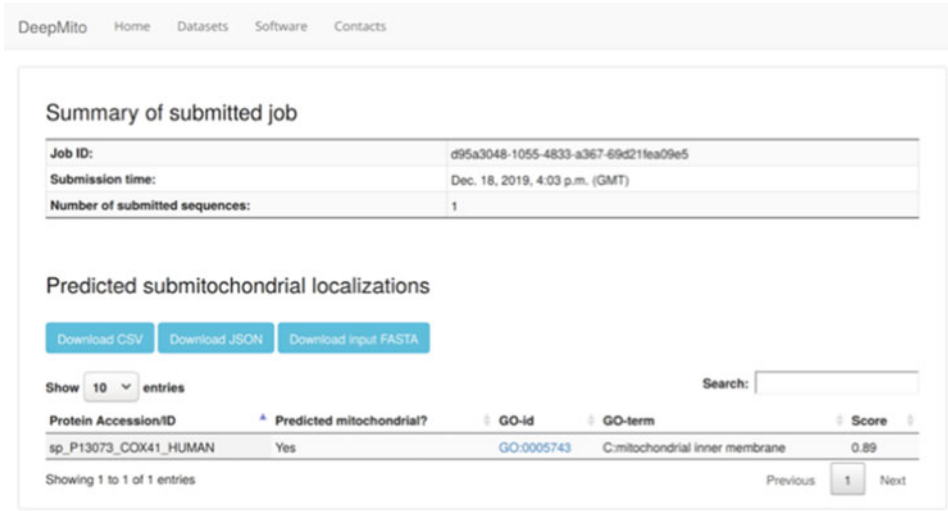


**Fig. 10** Typical DeepMito output. The output page reports the job identifier, date of submission, number of sequences, and the name of the input sequences. The second section reports, for each submitted sequence, the protein identifier, whether the protein is predicted as mitochondrial or not, the predicted compartments as GO term in the cellular component and the prediction score

2. The second section reports, for each submitted sequence, (a) the sequence identified, as extracted from the user-provided FASTA, (b) whether the protein is mitochondrial or not (as predicted by TPpred3 and BaCelLo [29]), (c) the predicted mitochondrial subcompartment as a GO cellular component term, and (d) a numerical value in the range [0,1] representing the prediction score.

## Acknowledgments

This work was supported by the following projects: PRIN 2017 project 2017483NH8 (to C.S.) (Italian Ministry for University and Research: MIUR).

### References

1. Goffart S, Martinsson P, Malka F, Rojo M, Spelbrink JN (2007) The mitochondria of cultured mammalian cells: II. Expression and visualization of exogenous proteins in fixed and live cells. Methods Mol Biol 372:17–32
2. Meisinger C, Sickmann A, Pfanner N (2008) The mitochondrial proteome: from inventory to function. Cell 134:22–24
3. Pagliarini DJ, Calvo SE, Chang B, Sheth SA, Vafai SB, Ong S-E et al (2008) A mitochondrial protein compendium elucidates complex I disease biology. Cell 134:112–123
4. Smith AC, Blackshaw JA, Robinson AJ (2012) MitoMiner: a data warehouse for mitochondrial proteomics data. Nucleic Acids Res 40: D1160–D1167
5. Calvo SE, Clauser KR, Mootha VK (2016) MitoCarta2.0: an updated inventory of mammalian mitochondrial proteins. Nucleic Acids Res 44:D1251–D1257
6. Mossmann D, Meisinger C, Vögtle F-N (2012) Processing of mitochondrial presequences. Biochim Biophys Acta 1819:1098–1106
7. Schmidt O, Pfanner N, Meisinger C (2010) Mitochondrial protein import: from proteomics to functional mechanisms. Nat Rev Mol Cell Biol 11:655–667
8. Wiedemann N, Pfanner N (2017) Mitochondrial machineries for protein import and assembly. Annu Rev Biochem 86:685–714
9. Small I, Peeters N, Legeai F, Lurin C (2004) Predotar: a tool for rapidly screening proteomes for N-terminal targeting sequences. Proteomics 4:1581–1590
10. Petsalaki EI, Bagos PG, Litou ZI, Hamodrakas SJ (2006) PredSL: a tool for the N-terminal sequence-based prediction of protein subcellular localization. Genomics Proteomics Bioinformatics 4:48–55
11. Emanuelsson O, Brunak S, von Heijne G, Nielsen H (2007) Locating proteins in the cell using TargetP, SignalP and related tools. Nat Protoc 2:953–971
12. Indio V, Martelli PL, Savojardo C, Fariselli P, Casadio R (2013) The prediction of organelle-targeting peptides in eukaryotic proteins with grammatical-restrained hidden conditional random fields. Bioinformatics 29:981–988
13. Almagro Armenteros JJ, Salvatore M, Emanuelsson O, Winther O, von Heijne G, Elofsson A et al (2019) Detecting sequence signals in targeting peptides using deep learning. Life Sci Alliance 2:e201900429
14. Savojardo C, Martelli PL, Fariselli P, Casadio R (2014) TPpred2: improving the prediction of mitochondrial targeting peptide cleavage sites by exploiting sequence motifs. Bioinformatics 30:2973–2974
15. Savojardo C, Martelli PL, Fariselli P, Casadio R (2015) TPpred3 detects and discriminates mitochondrial and chloroplastic targeting peptides in eukaryotic proteins. Bioinformatics 31:3269–3275
16. Fukasawa Y, Tsuji J, Fu S-C, Tomii K, Horton P, Imai K (2015) MitoFates: improved prediction of mitochondrial targeting sequences and their cleavage sites. Mol Cell Proteomics 14:1113–1126
17. Claros MG, Vincens P (1996) Computational method to predict mitochondrially imported proteins and their targeting sequences. Eur J Biochem 241:779–786
18. Bannai H, Tamada Y, Maruyama O, Nakai K, Miyano S (2002) Extensive feature detection of N-terminal protein sorting signals. Bioinformatics 18:298–305
19. Thul PJ, Åkesson L, Wiking M, Mahdessian D, Geladaki A, Ait Blal H et al (2017) A subcellular map of the human proteome. Science 356: eaal3321
20. Du P, Yu Y (2013) SubMito-PSPCP: predicting protein submitochondrial locations by hybridizing positional specific physicochemical properties with pseudoamino acid compositions. Biomed Res Int 2013:263829
21. Lin H, Chen W, Yuan L-F, Li Z-Q, Ding H (2013) Using over-represented tetrapeptides to predict protein submitochondria locations. Acta Biotheor 61:259–268
22. Kumar R, Kumari B, Kumar M (2018) Proteome-wide prediction and annotation of mitochondrial and sub-mitochondrial proteins

by incorporating domain information. Mitochondrion 42:11–22

23. Savojardo C, Bruciaferri N, Tartari G, Martelli PL, Casadio R (2020) DeepMito: accurate prediction of protein sub-mitochondrial localization using convolutional neural networks. Bioinformatics 36(1):56–64
24. UniProt Consortium (2019) UniProt: a worldwide hub of protein knowledge. Nucleic Acids Res 47:D506–D515
25. Crooks GE, Hon G, Chandonia J-M, Brenner SE (2004) WebLogo: a sequence logo generator. Genome Res 14:1188–1190
26. Fariselli P, Savojardo C, Martelli PL, Casadio R (2009) Grammatical-restrained hidden conditional random fields for bioinformatics applications. Algorithms Mol Biol 4:13
27. Savojardo C, Fariselli P, Casadio R (2011) Improving the detection of transmembrane -barrel chains with N-to-1 extreme learning machines. Bioinformatics 27:3123–3128
28. Savojardo C, Martelli PL, Fariselli P, Profiti G, Casadio R (2018) BUSCA: an integrative web server to predict subcellular localization of proteins. Nucleic Acids Res 46:W459–W466
29. Pierleoni A, Martelli PL, Fariselli P, Casadio R (2006) BaCelLo: a balanced subcellular localization predictor. Bioinformatics 22:e408–e416

# INDEX



Volkmar Weissig and Marvin Edeas (eds.), *Mitochondrial Medicine: Volume 1: Targeting Mitochondria*, Methods in Molecular Biology, vol. 2275, https://doi.org/10.1007/978-1-0716-1262-0,

## D



## E



## F

## G



## H



## I



## J



## K



## L



## M

## N



## O



## P



## Q

## R



## S



## T

## U



## V



## W



## X



## Z